Dissertation zur Erlangung des Doktorgrades
der Fakultät für Chemie und Pharmazie
der Ludwig-Maximilians-Universität München

Experimental and Theoretical Characterization of Multinary Nitrides

Robin Alexander Niklaus

aus

München, Deutschland

2019

Erklärung

Diese Dissertation wurde im Sinne von §7 der Promotionsordnung vom 28. November 2011 von Herrn Prof. Dr. Wolfgang Schnick betreut.

Eidesstattliche Versicherung

Diese Dissertation wurde eigenständig und ohne unerlaubte Hilfe erarbeitet.

München, den 07.11.2019

.....

(Robin Alexander Niklaus)

Dissertation eingereicht am	05.08.2019
1. Gutachter:	Prof. Dr. Wolfgang Schnick
2. Gutachter:	Prof. Dr. Ján Minár
Mündliche Prüfung am	21.10.2019

FÜR MEINE ELTERN

„Ihr Weise, mit der Wissenschaft,

Die Welten zu bewegen,

Gebt einem matten Herzen Kraft,

Ein Fünkchen neu Vermögen,

Ach einen Tropfen Lebenssaft,

sich jugendlich zu regen —

Ich laß′ euch eure Wissenschaft

Die Welten zu bewegen.“

(Johann Gottfried von Herder, Die Mechanik des Herzens *Zerstreute Blätter*, **1787**)

“I was taught that the way of progress was neither swift nor easy”

(Marie Curie, *Pierre Curie*, Macmillan, **1923**)

Acknowledgments

Mein besonderer Dank gebührt Prof. Dr. Wolfgang Schnick, dafür, dass er mir die Möglichkeit gegeben hat meine Dissertation in seinem Arbeitskreis anfertigen zu dürfen. Ich bedanke mich des Weiteren für die nahezu unbegrenzten Entfaltungsfreiheiten sowohl die bereitgestellten Mittel und Geräte betreffend, als auch hinsichtlich der Ausarbeitung meiner wissenschaftlichen Untersuchungen und Kooperationen. Ich bin außerdem dankbar für die stete Unterstützung beim Besuch nationaler und internationaler Tagungen die mir zusätzlich wichtige Erfahrungen eingebracht haben.

Ebenfalls gebührt mein besonderer Dank Prof. Dr. Ján Minár für die Übernahme des Koreferats meiner Dissertation und dafür, dass er mir über den Verlauf meiner ganzen Promotion hinweg stets beratend zur Seite gestanden hat. Ich bin darüber hinaus dankbar für die vielfältigen und fruchtbaren Kooperation die im Rahmen meiner Dissertation entstandenen sind, sowie für die Bereitstellung rechentechnischer Ressourcen welche entscheidend zu den vielen Ergebnissen dieser Arbeit beigetragen haben.

Ich danke Prof. Dr. Hubert Huppertz, Prof. Dr. Hans-Christian Böttcher sowie Prof. Dr. Lena Daumann und Prof. Dr. Konstantin Karaghiosoff für das Begutachten meiner Dissertation und ihre Beteiligung im Prüfungskomitee während der mündlichen Verteidigung.

Ich danke insbesondere allen aktuellen und ehemaligen Arbeitskreismitgliedern des Lumileds Teams, Dr. Philipp Pust, Dr. Sebastian Schmiechen, Dr. Dajana Durach, Dr. Christine Pösl, Dr. Philipp Strobel, Dr. Christian Maak, Dr. Philipp Bielec, Peter Wagatha, Eugenia Elzer, Lisa Gamperl, und Tobias Giftthaler für die vielen konstruktiven Diskussionen und die gute Stimmung im Team. Besonders Philipp Strobel und Christian Maak möchte ich für ihre stete Hilfsbereitschaft und die gemeinsamen entstandenen Kooperationen danken.

Den Mitarbeitern des Lumileds Phosphor Center Aachen möchte ich meinen ganz besonderen Dank aussprechen. Dr. Peter J. Schmidt als ständigen Ansprechpartner und für seine Hilfsbereitschaft bei diversen Fragestellungen, sowie Volker Weiler, Cora Hecht, Petra Huppertz und Detlef Wiechert für zahlreiche Lumineszenzmessungen von Pulverproben und Einkristallen.

Dr. Dominik Baumann, Sebastian Vogel und Dr. Eva-Maria Bertschler danke ich für die diversen Kooperationen zu Hochdruckumwandlungen der Phosphoroxidnitride und Lithium Nitridophosphate.

Christian Minke und Dr. Christian Maak danke ich außerdem für das Messen unzähliger EDX Spektren.

Außerdem danke ich Thomas Miller und Wolfgang Wünschheim für das technische Instandhalten des Arbeitskreises, sowie ihre Hilfe bei diversen damit verbundenen Fragestellungen. Olga Lorenz danke ich außerdem für ihre Kompetenz als Ansprechpartnerin allen weiteren organisatorischen Fragen

Besonders möchte ich meinen ehemaligen und aktuellen Laborkollegen Dr. Lukas Neudert, Dr. Christine Pösl, Dr. Philipp Strobel, Lucien Eisenburger, Eugenia Elzer und Dr. Christian Maak für die schöne Zeit und die zahlreichen Laborabende, sowie die daraus entstandenen Freundschaften danken.

Weiterer Dank gebührt selbstverständlich auch meinen Kollegen, Dr. Jonas Häusler, Otto Zeeman und Peter Wagatha für die gute Atmosphäre in der Schreibstube.

Außerdem möchte ich allen bisher unerwähnten Mitgliedern des AK Schnick, des AK Lotsch und des AK Johrendt für die schönen und lustigen Kaffeeküchengespräche, und die stets tolle arbeitskreisübergreifende Atmosphäre danken.

Ich danke außerdem besonders meiner Freundin Julia sowie allen meinen guten Freunden aus München dafür, dass sie Teil meines Lebens und über die Jahre hinweg auch wie eine Familie für mich geworden sind.

Mein größter Dank gebührt meinen beiden Eltern Eva und Mathias die mich immer bestmöglich in meinem Leben und meinen Entscheidungen unterstützt und bekräftigt haben.

Table of Contents

1 Introduction

1.1 Applications and Developments of Solid-State Materials in Modern Technology

Solid-state materials take on vital roles in various technical applications starting from electrolytes for (lithium) batteries[1] to the vast majority being used in (opto)electronic devices such as photoreceivers, -multipliers, -voltaics for power generation, or light emitting diodes (LEDs) for illumination and backlighting purposes in displays.[2–7] Over the last decades the importance and growth of these application fields has not only increased due to technical advancements but also due to changes in political climate. Since around the 1990s the energy revolution was increasingly expedited by substantiations of the impending climate change. Subsequent developments of different climate scenarios and climate targets such as efficient reduction of CO_2-emissions aimed at amending or obverting current climate trends.[8–15] With the concomitant increase in public and political awareness towards healthier lifestyles and less polluting technologies in general, the focus has shifted towards cleaner power generation and renewable energy sources. The latter is, for instance, reflected by U.S. department of energy forecasts, postulating an increase of 139% in renewable energy until 2050 with a main increase of 94% from wind power and photovoltaics.[16] In turn, research on the development of both efficient and environmentally friendly materials for photocatalysis, electromobility, and semiconductor applications has probably never been more in the spotlight than it is today.[17–19] One of the most noticeable developments within recent years was the gradual increase in substitution of incandescent lamps by compact fluorescent lamps (CFLs) and LEDs. However, with regard to modern illuminants LEDs have the edge over CFLs and conventional light sources, both in terms of energy efficiency and environmental friendliness.[20] According to data ascertainments and forecasts from the U.S. department of energy (DOE) LEDs will thus, become the dominant light source as soon as 2030 with a U. S. market sales penetration of 86% for residential housing and 65–86% for commercial lighting by 2035. For the lighting sector this will result in energy savings of 55–75%, depending on the assumption of either past development trends or the realization of a more aggressive DOE plan towards LED adoption.[21,22] Similar positive trends are also reported for Europe, where LED lamp and luminaire installments of 8 and 9% were reported for 2016 with a projected increase to 53 and 58% in 2024.[23,24]

Amongst the myriad of investigated material classes eligible for the design of semiconducting materials with potential optoelectronic applications nitride materials comprise but a fraction. Some are, however, prominent and well established materials, such as (Al,Ga)N and (In,Ga)N solid solutions commonly used for band gap engineering and application in semiconductor devices.[25] However, throughout the search for complementary or replacement materials to (In,Ga)N, especially such containing more earth abundant materials,[25] nitrides have become increasingly prominent within the last two decades. Since then the fundamental research on nitrides has given birth to a vast variety of nitride material classes with great diversity regarding their individual structures and properties. Some prominent classes include II-IV-N_2 type nitrides

as potential alternatives to (In,Ga)N, structurally diverse (oxo)nitridosilicates as high-temperature ceramics and efficient luminescence materials (phosphors) for LEDs. Equally diverse (oxo)nitridophosphates may also exhibit luminescence but are of further interest as lithium conductor materials. In addition phosphorus (oxo)nitride materials are of interest for fundamental science with regard to high-pressure synthesis and phase transitions in analogy to isoelectronic silica phases within the earth's interior.
Beyond the plurality of experimental investigations, the immense contemporaneous progress of first principles calculations throughout the last decades must not to be disregarded, as it has led to a vast playground for theoreticians to tackle electronic properties that are difficult to explore experimentally. *Ab initio* structure predictions may even offer the possibility to give impulses independent from experiment and contribute to materials search efforts of experimentalists.

1.2 Benefits of Computational Methods in Solid-State Chemistry

Quantum mechanics dates back to the derivation of Planck's constant in 1900 and the quantization of light by Einstein in 1905. Following the de Broglie relation about the wave-particle duality, the establishment of Schrödinger's equation in 1926 laid the foundation for the ensuing (quantum) wave mechanics.[26] Thereupon followed the development of quantum chemistry, up to its extensive significance that it bears today. In addition the perpetual progress in computational power largely facilitated the evolution of quantum mechanics, resulting in a plurality of modern implementations such as quantum chemical programs.[27]
Owing to this digital revolution, the principal possibilities in addressing all fundamental materials properties of interest on a computational basis nowadays appear hardly limited. Accordingly, in recent years the use and development of high throughput computational screening methods has gained a lot of popularity.[28,29] Approaches therein may vary from evolutionary algorithms aiming at the *ab initio* structure prediction of novel compounds, to dedicated screening procedures, machine learning or even a combination of the latter.[30-33] Thus, interesting compounds with desired material properties may be identified and predicted. Some examples in the field of nitride chemistry comprise the prediction of novel perovskites, mapping the stability of known and predicted ternary (nitride) compounds, specifically screening for (earth abundant) nitride semiconductors or screening for oxonitrides with regard to photocatalytic water splitting.[25,34–37] As such, high throughput screening methodologies can be quite powerful and a profit for the scientific community as a whole. With consideration to the vast number of investigated compounds, high throughput methods, however, also require efficient processing of large amounts of data, unrestricted access to (super)computer centers, and usually balance between computation speed and accuracy.[29]

Yet, even for the individual researcher modern quantum chemical programs offer a tremendous choice of assets with respect to the calculation of specific properties for materials of interest. For solid-state chemistry, which usually involves calculating compounds with a large number of atoms, density functional theory (DFT) based programs are usually the most efficient choice in

order to treat electronic and further derived material properties. Such properties may involve, but are not limited to, electronic structure optimization, the determination of the electronic band gap, optical absorption, phase transitions, thermodynamics or predicting the relative structural stability. The determination of these properties can be beneficial to individually characterize a novel or existing material, contribute to experimental findings or corroborate the latter.

1.3 Impact of Nitrides on the Research of (Opto)Electronic Materials

1.3.1 Solid State Lighting: Historical Development of LED and Nitride-based Phosphor Research

The first commercial red LED was constructed as early as 1962 with n-type doped $GaAs_{1-x}P_x$ whereas construction plans for blue (respectively UV) emitting LEDs were reported for p-doped GaN by 1971–1972.[38–43] Yet due to low efficiencies it took until the early 1990s when advancements made in metal-organic vapor epitaxial growth of GaN, GaAs and novel materials such as AlInGaP enabled higher internal quantum efficiencies for LEDs.[39,44,45] One of the most important developments therein was the fabrication of an efficient blue LED, which was enabled in 1991 through enhancements by Nakamura who used metal-organic chemical vapor deposition and thermal annealing of Mg doped GaN layers.[43,46,47] Throughout the 1990s, subsequent fabrication processes of (In,Ga)N and (Al,In,Ga)N further pushed the band gap engineering of nitride materials in order to access an increased range of spectral emissions.[39,48–50] The advancements towards efficient blue LEDs were considered so essential for the development of white light LEDs, that in 2014 Nakamura, Akasaki and Amano were awarded the Nobel Prize in Physics for their contributions.[39,43,51]

A white light emitting LED can principally be devised from three primary red, green and blue LEDs where the white light results from color mixing. There are, however, no efficient primary LEDs available to uniformly cover the entirety of the visible spectral region, especially in the so called yellow gap.[52] In addition balancing of different primary LED sources to achieve white light with a stable and constant color temperature requires complex setups.[53] An alternative approach for white light generation are phosphor-converted LEDs (pc-LEDs), in which a blue- or UV-LED is combined with green to red emitting phosphor materials. Therein, the phosphor materials are effectively excited by partial amounts of the respective blue (UV) LED light, so that white light results from the color combination of the excited phosphor materials with the remainder of the non-converted light from the primary LED source. In contrast to the sole combination of primary LEDs, pc-LEDs are simpler to construct and in principal only limited by the quantum efficiency and emission profile of the phosphor materials, which makes them more cost-efficient.[52,53] The accessible color gamut for pc-LED setups results from the combination of a blue LED with phosphor materials in the red, yellow and green spectral region, and can be exemplified within the *Commission Internationale de l'Eclairage* (CIE) 1931 color space diagram as seen in Figure 1.1 using a number of commercially applied efficient phosphor materials.

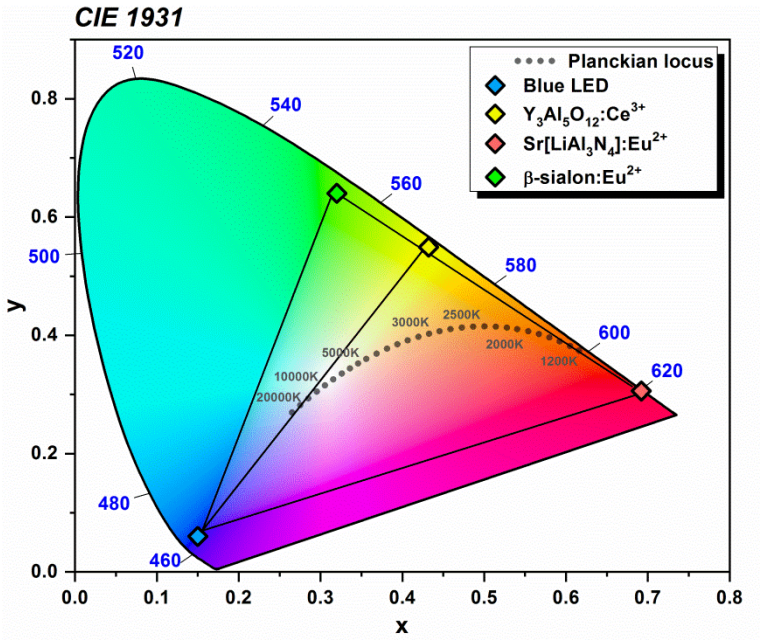

Figure 1.1 CIE 1931 color space within the visible spectrum (nm-scale, blue values) with CIE coordinates of a commercial blue LED, alongside phosphors emitting in the yellow (YAG:Ce^{3+}), red ($Sr[LiAl_3N_4]:Eu^{2+}$) and green (β-sialon:Eu^{2+}) spectral region, which can be used to produce any color within the spanned color gamut by color mixing. CIE coordinates for different correlated color temperatures (CCT) in K for an ideal blackbody radiator indicate the planckian locus used to determine the CCT of a LED.

Using a setup of a blue LED along with the prominent broadband green-yellow emitting phosphor $Y_3Al_5O_{12}:Ce^{3+}$ (YAG:Ce), for which systematic studies on its luminescence and elemental substitutions had been carried out since the 1960s,[54–57] the first efficient white pc-LED was patented by Shimizu and the Nichia Company in 1996.[58,59] With increasing LED performance, the design of warm-white LEDs gained in importance for residential housing illumination around the early 2000s.[39] Lumileds, for example, utilized additional red emitters such as $CaS:Eu^{2+}$ to balance the cold-white emission of YAG:Ce within their first warm-white pc-LEDs.[60] Following the early 2000s there was a subsequent demand for suitable solid-state phosphor materials inducing a steep increase in research, synthesis and characterization of prospect material classes. A key feature for the sought after phosphor materials are sufficiently large band gaps, typically beyond 3 eV. This allows a localization of electronic states of activator ions in-between the valence and conduction band of the host material.

The most prominent activator ions for this purpose constitute lanthanide metals with partially occupied 4*f* and unoccupied 5*d* orbitals. While 4*f* orbitals are highly contracted, the 5*d* orbitals protrude further from the atomic core. Compared to the narrow line emissions of parity forbidden $4f^n \rightarrow 4f^{n-1}$ transitions that are observed for a multitude of lanthanide activated compounds, spin- and parity-allowed $4f^x5d^0 \rightarrow 4f^{x-1}5d^1$ transitions are typically observed for Ce^{3+} and Eu^{2+} activated compounds.[61] The latter typically exhibit broadband emission, due to line-broadening from *d*-orbital interactions with the surrounding ligand field.

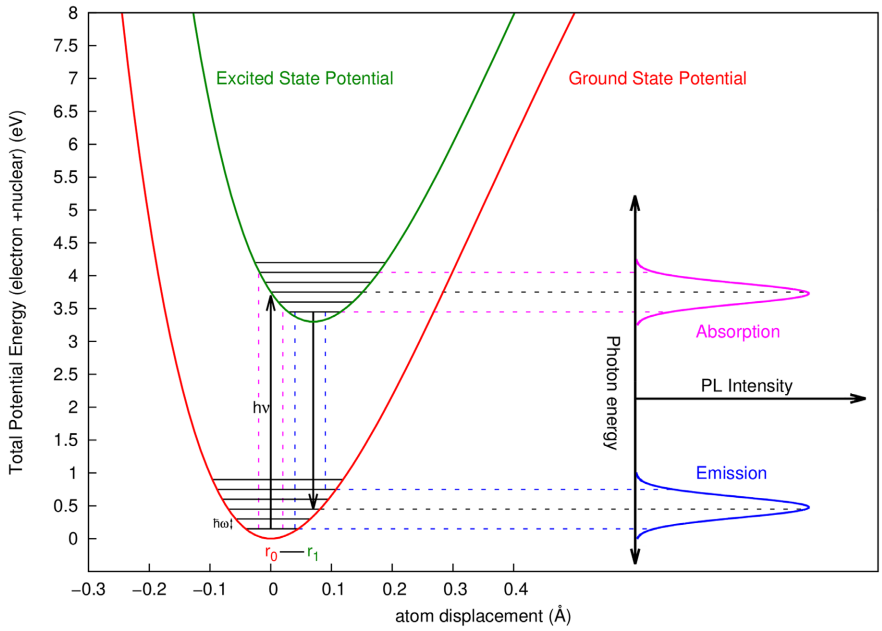

Figure 1.2 Schematic illustration of the energetic (*hν*) excitation and emission process of an electron between ground and excited state potentials according to the configurational coordinate model. The Stokes shift corresponds to the energy difference between absorption and emission resulting from the displacement of the two potentials. Black arrows indicate the highest transition probabilities resulting in the photo-absorption and -emission maxima.

Upon illuminating Ce^{3+} and Eu^{2+} doped phosphors with light of suitable energy to overcome the energy difference between the 4*f* and 5*d* states, electrons are excited from the electronic $4f^x5d^0$ ground state to an electronically and vibrationally excited $4f^{x-1}5d^1$ configuration. Depending on the strength of electron-phonon coupling this process causes the locally surrounding atoms to deviate from their equilibrium position in response to the creation of a charge-density hole, in turn also inducing slight changes in the activator-ligand distances. Within the simplified configurational coordinate diagram illustrated in Figure 1.2, the electron then quickly relaxes to the lowest vibronic excited state, before falling back to the ground state potential. Upon recombination of the electron with its created charge-density hole, the local atoms relax back to equilibrium. However, the electron-phonon interaction (i.e. scattering on lattice vibrations) reduces the energy of the emitted photon, causing a redshift to the overall emission spectra.[62] The difference between absorption and emission maxima is further termed the Stokes shift.

Nitrides exhibit great potential as suitable phosphor materials, when doped with Eu^{2+} because their spectral emissions are typically redshifted when compared to oxides. This redshift is due to the increased covalency in nitrides leading to a higher nephelauxetic effect.[61,63,64] Especially nitridosilicates and nitridophosphates are auspicious to explore as they often exhibit highly covalent networks with sufficiently large band gaps. As such in 1997 red luminescence was discovered for $Eu_2Si_5N_8$, and shortly after $Sr_2Si_5N_8$:Eu^{2+} was found in 2000, becoming one of the earlier prominent orange-emitting phosphor materials.[65–67] With its high quantum efficiency and low thermal emission quenching up to typical LED operating temperatures of 400 K, $Sr_2Si_5N_8$:Eu^{2+} still finds application in automotive turning lights as well as retrofit LEDs.[68]

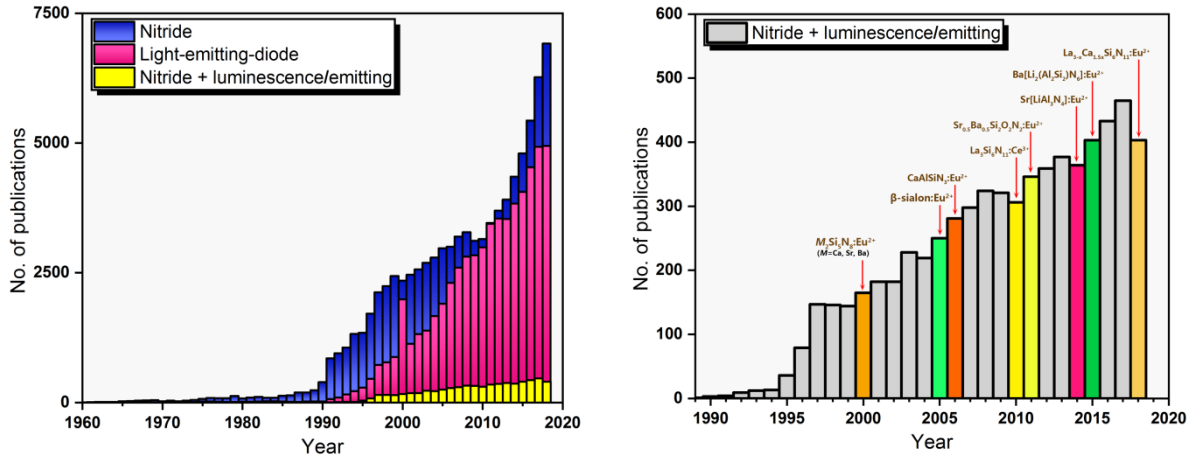

Figure 1.3 Left: Number of publications within chemistry, physics and materials science tagged under *nitride*, *light*+*emitting*+*diodes* and *nitrides* tagged with either *emitting* or *luminescence* extracted from the Web of Knowledge database. Right: Publications on *nitrides* tagged with either *emitting* or *luminescence*, indicating the year of discovery for some selected efficient nitride phosphor materials colored according to their respective spectral emissions.

By now a multitude of efficient phosphor materials have been applied in highly energy efficient pc-LEDs replacing incandescent lamps and CFLs in the world market. Figure 1.3 indicates that trends in numbers of publications in nitrides and LEDs have independently been on the rise since the early 90s, while investigations on nitride and oxonitrides as phosphor materials gained in relevance from 2000 onwards. Further, discoveries of some key (oxo)nitride phosphor materials, some of which used for modern white light applications, are indicated. However, some challenges still remain in phosphor materials research, such as suitable narrow green phosphors for display applications, and tailored deep-red horticulture LEDs used to induce photosynthesis and plant growth through chlorophyll *a* and *b*, or germination by spectral stimuli in the infrared region.[69–73]

1.3.2 Ternary Nitrides for (Opto)electronic Applications

Oxide materials research has prevailed in solid-state science since the 1920s, partly due to their uncomplicated synthesis conditions and chemical stability. Hence, the major focus of optoelectronics research has thus, generally also been on oxide materials. Yet, with the overall increased interest in nitrides, for example as potential phosphor materials with wide band gaps, more investigations with regard to band gap tuning towards further (opto)electronic applications such as solar cells ensued accordingly as seen in Figure 1.4.

By now nitrides have gained their own *raison d'être* within the field of (opto)electronics apart from phosphor applications. Considering the dwindling reserves of resources like indium that is used in (Al,Ga,In)N solid solutions in commercial semiconductor devices such as transistor materials, ternary nitrides containing more earth-abundant elements are promising alternatives.[25,74,75] During heteroepitaxial growth of GaN on substrates like sapphire further challenges typical arise from a lattice mismatch of GaN and the substrate, which induces increased defect densities that negatively impact optoelectronic properties and can lead to device failure.[76,77]

In this regard, II-IV-N_2 materials prove promising as substrates for lattice matching to wutzite-type GaN in heteroepitaxy. That is because II-IV-N_2 materials often exhibit lattice parameters close to GaN and typically adopt either hexagonal, or orthorhombically distorted, structures related to wurtzite. For the above named reasons and their similar (opto)electronic properties to GaN, II-IV-N_2 materials have been investigated extensively both in theory and experiment in recent years.[74,75,78–84] For example, combinatory thin-film nanostructured growth and arrangement of heterostructure interfaces have been discussed from computational theory with regard to potential solar cell applications due to lowered interface gaps, where electrons in a proposed combination of ZnO/$ZnGeN_2$, GaN/$ZnGeN_2$ and ZnO/GaN would migrate from $ZnGeN_2$ to GaN to ZnO and holes from ZnO to $ZnGeN_2$, respectively.[83]

Many ternary nitrides can further be beneficial for photocatalytic water splitting applications. Here, nanostructured binary and ternary (transition-metal) nitrides are considered to offer more suitably confined band gaps between 0 and 3 eV in contrast to oxides, which often exhibit gaps beyond 3 eV.[4,85] Along with a high chemical stability, ternary nitrides such as $In_xGa_{1-x}N$ whose band gap can be tailored between 0.7 and 3.4 eV, were subsequently shown to provide high catalytic efficiencies in electrochemical water splitting reactions.[85–87] With regard to the ternary or even multinary nitride alternatives, potential for efficient photocatalytic water splitting was also reported for cation-disordered wurtzite-type $Zn_{1-x}Ge_{1-x}Ga_{2x}N_2$ ($x \leq 0.50$).[88] Apart from changes in the band gap by stoichiometric variations in the mixed occupancy sites, the role of disorder itself on the electronic structure is of interest for the design of materials. For $ZnSnN_2$, a material promising for photovoltaic applications, such effects have been studied by correlating experimental data from hard X-ray photoemission spectroscopy (HAXPES) of different $ZnSnN_2$ grown by epitaxy, to respective optical absorption measurements and DFT calculations on ordered and disordered supercell models. Accordingly, the band gaps were found to vary within a 1 eV range between fully disordered and fully ordered $ZnSnN_2$ variants.[89,90]

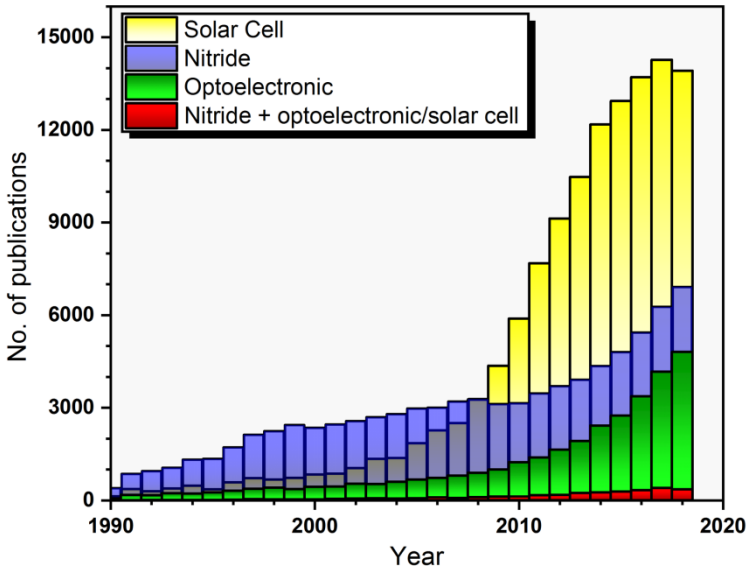

Figure 1.4 Number of publications within the chemistry, physics and materials science fields tagged under *solar cell, nitride*, *optoelectronic* and *nitrides* tagged with either *optoelectronic* or *solar cell,* extracted from the Web of Knowledge database.

Generally, however, there are not many systematic computational studies treating disorder effects, with most calculations usually approximating disordered structures from supercells. When chosen sufficiently large, supercells provide valid approximations to disorder, for calculations close to the stoichiometric equilibrium of 1:1. For larger unit cells or compositions with higher atomic concentration deviations such calculations, however, quickly become more costly.

As a consequence, the development of synthesis methods (*e. g.*: enhanced crystal growth by ammonothermal synthesis), for ternary and multinary nitride materials, along with the systematic treatment of their materials properties on a experimental or first principles basis are of great interest to semiconductor, physics and chemistry communities.

1.4 Phosphorus (Oxo)nitrides

Within the field of nitride chemistry phosphorus (oxo)nitride materials are of great interest to fundamental research due to their similarity to silicates. This similarity originates from the isoelectronic combination of "P/N" compared to "Si/O" and becomes strikingly evident for SiO_2 and PON. Within a certain temperature and pressure range SiO_2 and PON both form numerous polymorphs with isotypic structure each built from SiO_4 or $P(O/N)_4$ tetrahedra. More precisely at ambient conditions PON crystallizes in the β-cristobalite structure, while transforming to the α-quartz-type and moganite-type PON at high-pressure and temperature.[91–94] In addition with the high-pressure high-temperature synthesis of δ-PON a polymorph was found that so far was only topologically predicted for SiO_2.[95] Thus, exemplifying that PON polymorphs may not necessitate the existence of an analogous SiO_2 polymorph and could exhibit further structural diversity. At elevated pressures SiO_2 exhibits even further phase transitions to coesite,[96–98] rutil-type (stishovite),[99–101] $CaCl_2$-type,[102–104] seifertite (α-PbO_2),[105–107] and pyrite-type[108] SiO_2. Thus, with regard to the well studied high-pressure phase diagram of SiO_2 analogue phase transitions of PON at high pressures appear very likely. Especially the search for six-fold coordinated phosphorus $P(O,N)_6$ in nitride materials is of fundamental interest from a structural chemistry viewpoint but may in addition enable access to novel superhard materials.

1.5 (Oxo)Nitridophosphates

While phosphorus (oxo)nitrides constitute charge neutral P/O/N networks, the additional incorporation of electropositive elements allows for the creation of anionic (oxo)nitridophosphate network structures. Suitable elements to this regard comprise alkaline and alkaline earth cations, but also those of rare earth type. As anticipated their materials properties are similar to those of nitridosilicates as proven in recent years by numerous structurally diverse nitridophosphates. Examples thereof comprise luminescence in white emitting $Ba_3P_5N_{10}Br:Eu^{2+}$, orange, green and blue emitting $MP_2N_4:Eu^{2+}$ (Ca, Sr, Ba), or (para)magnetism in $Ho_3[PN_4]O$ and $M^{II}P_8N_{14}$ (M^{II} = Fe, Co, Ni).[109–112] Due to the thermodynamical stability of nitridophosphates, incorporation of lithium is of further interest with regard to the potential discovery and application as novel Li^+ ion conducting materials.

Ion conductivity (Li^+) has been investigated for the lithium (oxo)nitridophosphates Li_7PN_4, $LiPN_2$, LiPON as well as for more recent discoveries of $Li_{18}P_6N_{16}$, β-$Li_{10}P_4N_{10}$ and $Li_{13}P_4N_{10}X_3$ (X = Cl, Br), all of which typically exhibit conductivities in the magnitudes of 1×10^{-5}–10^{-6} $\Omega^{-1}cm^{-1}$.[113–116] Accordingly, the discovery of structurally diverse lithium nitridophosphates with voids or migration pathways for Li^+ is promising under the perspective of both fundamental research and applied science. With regard to the auspicious high-pressure investigations of P/N materials, high-pressure synthesis, can similarly be considered suitable for the discovery of equally diverse novel lithium nitridophosphates. Further investigations towards occurring high-pressure phase transitions involving experimental and computational approaches should yield promising insights with regard to thermodynamic properties and synthesis conditions of this materials class.

One of the aims of this thesis was focused on the discovery of novel (oxo)nitride phosphor materials. This involves explorative synthesis, the identification of novel luminescent phases and subsequent characterizations of materials properties together with synthesis optimization. The main objective of this thesis was however, aimed at theoretical density functional theory (DFT) characterizations of a selection of ternary and multinary nitride compounds. Herein, the efficient treatment and characterization of mixed occupancy in (oxo)nitride materials was of particular interest. As such, this thesis deals with different projects and contributions treating the overall electronic, optical, mechanical and structural properties of ternary and multinary nitrides. The efficient characterization by KKR for a variety of mixed-occupancy nitrides exhibiting a wide range of electronic band gaps is consequently shown by extensive investigations. Additionally, high-pressure phase transformations of ternary phosphorus oxonitride PON and lithium nitridophosphates are investigated.
Lastly, systematic *ab initio* calculations are employed allowing for the prediction of a series of novel nitridogermanates with promising material properties.

1.6 References

[1] M. S. Whittingham, Lithium Batteries and Cathode Materials, *Chem. Rev.* **2004**, *104*, 4271–4301.

[2] S. Luryi, J. Xu, A. Zaslavsky, *Future Trends in Microelectronics*, Dordrecht: Kluwer Academic, **1996**.

[3] H. Wong, Recent developments in silicon optoelectronic devices, *Microelectron. Reliab*. **2002**, *42*, 317–326.

[4] X. Yu, T. J. Marks, A. Facchetti, Metal oxides for optoelectronic applications, *Nat. Mater*. **2016**, *15*, 383–396.

[5] O. Ostroverkhova, Organic Optoelectronic Materials: Mechanisms and Applications, *Chem. Rev.* **2016**, *116*, 13279–13412.

[6] T. D Moustakas, R. Paiella, Optoelectronic device physics and technology of nitride semiconductors from the UV to the terahertz, *Rep. Prog. Phys*. **2017**, *80*, 106501.

[7] J. Liu, Z. Yang, B. Ye, Z. Zhao, Y. Ruan, T. Guo, X. Yu, G. Chena, S. Xua, A review of stability-enhanced luminescent materials: fabrication and optoelectronic applications, *J. Mater. Chem. C* **2019**, *7*, 4934–4955.

[8] G.-R. Walther, E. Post, P. Convey, A. Menzel, C. Parmesank, T. J. C. Beebee, J.-M. Fromentin, O. Hoegh-Guldberg, F. Bairlein, Ecological responses to recent climate change, *Nature* **2002**, *416*, 389–395.

[9] L. Pérez-Lombard, J. Ortiz, C. Pout, A review on buildings energy consumption information, *Energ. Buildings* **2008**, *40*, 394–398.

[10] R. H. Moss, J. A. Edmonds, K. A. Hibbard, M. R. Manning, S. K. Rose, D. P. van Vuuren, T. R. Carter, S. Emori, M. Kainuma, T. Kram, G. A. Meehl, J. F. B. Mitchell, N. Nakicenovic, K. Riahi, S. J. Smith, R. J. Stouffer, A. M. Thomson, J. P. Weyant, T. J. Wilbanks, The next generation of scenarios for climate change research and assessment, *Nature* **2010** *463*, 747–756.

[11] S. Randalls, History of the 2°C climate target, *Wiley Interdiscip. Rev.: Clim. Change* **2010**, 1, 598–605.

[12] N. L. Panwar, S. C. Kaushik, S. Kothari, Role of renewable energy sources in environmental protection: A review, *Renewable Sustainable Energy Rev.* **2011**, *15,* 1513–1524.

[13] E. Kriegler, K. Riahi, N. Bauer, V. J. Schwanitz, N. Petermann, V. Bosetti, A. Marcucci, S. Otto, L. Paroussos, S. Rao, T. A. Currás, S. Ashina, J. Bollen, J. Eom, M. Hamdi-Cherif, T. Longden, A. Kitous, A. Méjean, F. Sano, M. Schaeffer, K. Wada, P. Capros, D. P. van Vuuren, O. Edenhofer, Making or breaking climate targets: The AMPERE study on staged accession scenarios for climate policy, *Technol. Forecast. Soc. Change* **2015**, *90*, 24–44.

[14] *The Paris Protocol – A blueprint for tackling global climate change beyond 2020*, European Comission, Energy Union Package, Communication from the Commission to the European Parliament and the Council **2015.**

[15] S. I. Seneviratne, M. G. Donat, A. J. Pitman, R. Knutti, R. L. Wilby, Allowable CO_2 emissions based on regional and impact-related climate targets, *Nature* **2016**, *529*, 477–483.

[16] *Annual Energy Outlook 2018*, U.S. Energy Information Administration, Office of Energy Analysis, U.S. Department of Energy: Washington, DC, **2018**.

[17] J. Baxter, Z. Bian, G. Chen, D. Danielson, M. S. Dresselhaus, A. G. Fedorov, T. S. Fisher, C. W. Jones, E. Maginn, U. Kortshagen, A. Manthiram, A. Nozik, D. R. Rolison, T. Sands, L. Shi, D. Sholl, Y. Wu, Nanoscale design to enable the revolution in renewable energy, *Energy Environ. Sci.* **2009**, *2*, 559–588.

[18] *A Global Green New Deal for Climate, Energy, and Development*, United Nations Department of Economic and Social Affairs, Division for Sustainable Development, **2009**.

[19] Ş. Kılkış, G. Krajačić, N. Duić, M. A. Rosen, M. A. Al-Nimr, Advancements in sustainable development of energy, water and environment systems, *Energy Convers. Manag.* **2018,** *176*, 164–183.

[20] T. H. Kim, W. Wang, Q. Li, Advancement in materials for energy-saving lighting devices, *Front. Chem. Sci. Eng.* **2012**, *6*, 13–26.

[21] Navigant Consulting, *Energy Savings Forecast of Solid-State Lighting in General Illumination Applications*, Office of Energy Efficiency & Renewable Energy, U.S. Department of Energy: Washington, DC, **2016**.

[22] *Annual Energy Outlook 2018*, U.S. Energy Information Administration, Office of Energy Analysis, U.S. Department of Energy: Washington, DC, **2018**.

[23] J. Brodrick (ed.), DOE SSL Program, *2017 Suggested Research Topics Supplement: Technology and Market Context*, Office of Energy Efficiency & Renewable Energy, U.S. Department of Energy: Washington, DC, **2017**.

[24] IHS Markit, *IHS Markit Lighting Intelligence Service: Lighting,* **2017.**

[25] Y. Hinuma, T. Hatakeyama, Y. Kumagai, L. A. Burton, H. Sato, Y. Muraba, S. Iimura, H. Hiramatsu, I. Tanaka, H. Hosono, F. Oba, Discovery of earth-abundant nitride semiconductors by computational screening and high-pressure synthesis, *Nat. Commun.* **2016**, *7*, 11962.

[26] A. Aspecta, J. Villain, The birth of wave mechanics (1923–1926), *C. R. Physique* **2017**, *18*, 583–558.

[27] J. Reinhold, *Quantentheorie der Moleküle: Eine Einführung*, Springer, **2013.**

[28] J. Greeley, T. F. Jaramillo, J. Bonde, I. Chorkendorff, J. K. Nørskov, Computational high-throughput screening of electrocatalytic materials for hydrogen evolution, *Nat. Mater* **2006**, *5*, 909–913.

[29] A. Jain, G. Hautier, C. J. Moore, S. Ping Ong, C. C. Fischer, T. Mueller, K. A. Persson, G. Ced, A high-throughput infrastructure for density functional theory calculations, *Comput. Mater. Sci.* **2011**, *50*, 2295–2310.

[30] A. O. Lyakhov, A. R. Oganov, H. T. Stokes, Q. Zhu, New developments in evolutionary structure prediction algorithm USPEX, *Comput. Phys. Commun.* **2013**, *184*, 1172–1182.

[31] A. Bilić, J. D. Gale, M. A. Gibson, N. Wilson and K. McGregor, Prediction of novel alloy phases of Al with Sc or Ta, *Sci. Rep.* **2015**, *5*, 9909.

[32] Y. Zhuo, A. Mansouri Tehrani and J. Brgoch, Predicting the Band Gaps of Inorganic Solids by Machine Learning, *J. Phys. Chem. Lett.* **2018**, *9*, 1668–1673.

[33] Y. Zhuo, A. Mansouri Tehrani, A. O. Oliynyk, A. C. Duke, J. Brgoch, Identifying an efficient, thermally robust inorganic phosphor host via machine learning, *Nat. Commun.* **2018**, *9*, 4377.

[34] R. Sarmiento-Pérez, T. F. T. Cerqueira, S. Körbel, S. Botti and M. A. L. Marques, Prediction of Stable Nitride Perovskites, *Chem. Mater.* **2015**, *27*, 5957–5963.

[35] W. Sun, C. J. Bartel, E. Arca, S. R. Bauers, B. Matthews, B. Orvañanos, B.-R. Chen, M. F. Toney, L. T. Schelhas, W. Tumas, J. Tate, A. Zakutayev, S. Lany, A. M. Holder, G. Ceder, A map of the inorganic ternary metal nitrides, *Nat. Mater.* **2019**, *18*, 732–739.

[36] Y. Huang, C. Yu, W. Chen, Y. Liu, C. Li, C. Niu, F. Wang,Y. Jia, Band gap and band alignment prediction of nitride-based semiconductors using machine learning *J. Mater. Chem. C* **2019**, *7*, 3238–3245.

[37] Y. Wu, P. Lazic, G. Hautier, K. Persson, G. Ceder, First principles high throughput screening of oxynitrides for water-splitting photocatalysts, *Energy Environ. Sci*. **2013**, *6*, 157–168.

[38] N. Holonyak, S. F. Bevacqua, Coherent (visible) Light Emission from $Ga(As_{1-x}P_x)$ Junctions, *Appl. Phys. Lett.* **1962**, *1*, 82–83.

[39] D. A. Steigerwald, J. C. Bhat, D. Collins, R. M. Fletcher, M. O. Holcomb, M. J. Ludowise, P. S. Martin, S. L. Rudaz, Illumination With Solid State Lighting Technology, *IEEE J. Sel. Top. Quantum Electron.* **2002**, *8*, 310–320.

[40] J. I. Pankove, E. A. Miller, J. E. Berkeyheiser, GaN Electroluminescent Diodes, *RCA Rev.* **1971**, *32*, 383–392.

[41] H. P. Maruska, W. C. Rhines, D. A. Stevenson, Preparation of Mg-doped GaN diodes exhibiting violet electroluminescence, *Mater. Res. Bull.* **1972**, *7*, 777–781.

[42] H. P. Maruska, D. A. Stevenson, J. I. Pankove, Violet luminescence of Mg-doped GaN, *Appl. Phys. Lett.* **1973**, *22*, 303–305.

[43] H. P. Maruska, W. C. Rhines, A modern perspective on the history of semiconductor nitride blue light sources, *Solid State Electron*. **2015**, *111*, 32–41.

[44] H. Amano, N. Sawaki, I. Akasaki, Metalorganic vapor phase epitaxial growth of a high quality GaN film using an AlN buffer layer, *Appl. Phys. Lett.* **1986**, *48*, 353–355.

[45] C. P. Kuo, R. M. Fletcher, T. D. Osentowski, M. C. Lardizabal, M. G. Craford, High performance AlGaInP visible light-emitting diodes, *Appl. Phys. Lett.* **1990**, *57*, 2937–2939.

[46] S. Nakamura, GaN Growth Using GaN Buffer Layer, *Jpn. J. Appl. Phys*. **1991**, *30*, L1705–L1707.

[47] S. Nakamura, Highly P-Typed Mg-Doped GaN Films Grown with GaN Buffer Layers, *Jpn. J. Appl. Phys.* **1991**, *30*, L1708–L1711.

[48] F. G. McIntosh, K. S. Boutros, J. C. Roberts, S. M. Bedair, Growth and characterization of AlInGaN quaternary alloys, *Appl. Phys. Lett.* **1996**, *68*, 40–42.

[49] T. Mukai, H. Narimatsu, S. Nakamura, Amber InGaN-Based Light-Emitting Diodes Operable at High Ambient Temperatures, *Jpn. J. Appl. Phys.* **1998**, *37*, L479–L481.

[50] G. Tamulaitis, K. Kazlauskas, S. Juršenas, A. Žukauskas, Optical bandgap formation in AlInGaN alloys, *Appl. Phys. Lett.* **2000**, *77*, 2136–2138.

[51] J. Heber, Nobel Prize 2014: Akasaki, Amano & Nakamura, *Nat. Phys*. **2014**, *10*, 791.

[52] R. Mueller-Mach, G. O. Mueller, M. R. Krames, O. B. Shchekin, P. J. Schmidt, H. Bechtel, C.-H. Chen, O. Steigelmann, All-nitride monochromatic amber-emitting phosphor-converted light-emitting diodes, *Phys. Status Solidi RRL* **2009**, *3*, 215–217.

[53] Lumileds Holding B.V., Narrow Red Phosphor Technology, *White Papers* **2016**, WP32.

[54] G. Blasse, A. Bril, A New Phosphor for Flying-Spot Cathode-ray Tubes for Color Television: Yellow-Emitting $Y_3Al_5O_{12}$–Ce^{3+}, *Appl. Phys. Lett.* **1967**, *11*, 53–55.

[55] W. W. Holloway, M. Kestigian, Optical Properties of Cerium-Activated Garnet Crystals, *J. Opt. Soc. Am.* **1969**, *59*, 60–63.

[56] D. J. Robbins, B. Cockayne, J. L. Glasper, B. Lent, The Temperature Dependence of Rare-Earth Activated Garnet Phosphors, *J. Electrochem. Soc.* **1979**, *126*, 1221–1228.

[57] M. Batentschuk, B. Schmitt, J. Schneider, A. Winnacker, Color Engineering of Garnet Based Phosphors for Luminescence Conversion Light Emitting Diodes (Lucoleds), *MRS Proceedings*, **1999**, *560*, 215–220.

[58] Y. Shimizu, K. Sakano, Y. Noguchi, and T. Moriguchi, Light emitting device having a nitride compound semiconductor and a phosphor containing a garnet fluorescent material, U. S. Patent US5998925A, **1999**.

[59] J. Cho, J. H. Park, J. K. Kim, E. F. Schubert, White light-emitting diodes: History, progress, and future, Laser Photonics Rev. **2017**, *11*, 1600147.

[60] Lumileds, Personal Communication, **2019.**

[61] P. Dorenbos, A Review on How Lanthanide Impurity Levels Change with Chemistry and Structure of Inorganic Compounds, *ECS J. Solid State Sci. Technol.* **2013**, *2*, R3001–R3011.

[62] M. A. Reshchikov,H. Morkoç, Luminescence properties of defects in GaN, *J. Appl. Phys.* **2005**, *97*, 061301.

[63] P. Dorenbos, 5d-level energies of Ce^{3+} and the crystalline environment. I. Fluoride compounds, *Phys. Rev. B: Condens. Matter Mater. Phys.* **2000**, *62*, 15640–15649.

[64] P. Dorenbos, 5d-level energies of Ce^{3+} and the crystalline environment. III. Oxides containing ionic complexes, *Phys. Rev. B: Condens. Matter Mater. Phys.* **2001**, *64*, 125117.

[65] H. Huppertz, Strukturelle Erweiterung der Nitridosilicate, *Dissertation*, University of Bayreuth, **1997**.

[66] H. A. Höppe, H. Lutz, P. Morys, W. Schnick, A. Seilmeier, Luminescence in Eu^{2+}-doped $Ba_2Si_5N_8$: fluorescence, thermoluminescence, and upconversion, *J. Phys. Chem. Solids* **2000**, *61*, 2001–2006.

[67] J. W. H. van Krevel, On new rare-earth doped M-Si-Al-O-N materials: luminescence properties and oxidation resistance, *Dissertation*, Eindhoven University of Technology, **2000**.

[68] R. Mueller-Mach, G. Mueller, M. R. Krames, H. A. Höppe, F. Stadler, W. Schnick, T. Juestel, P. Schmidt, Highly efficient all-nitride phosphor-converted white light emitting diode, *Phys. Status Solidi A* **2005**, *202*, 1727–1732.

[69] L. Wang, X. Wang, T. Kohsei, K.-I. Yoshimura, M. Izumi, N. Hirosaki, R.-J. Xie, Highly efficient narrow-band green and red phosphors enabling wider color-gamut LED backlight for more brilliant displays, *Opt. Express* **2015**, *23*, 28707–28717.

[70] D. Singh, C. Basu, M. Meinhardt-Wollweber, B. Roth, LEDs for energy efficient greenhouse lighting, *Renew. Sust. Energ. Rev.* **2015**, *49*, 139–147.

[71] Lumileds Holding B.V., LUXEON SunPlus Series Lime LEDs Produce High Yield and Nutrition in Leafy Greens, *White Papers* **2017**, WP34.

[72] Lumileds Holding B.V., You make grow lights for horticulture, *APPLICATION SOLUTIONS BROCHURE* **2018**, BR28.

[73] M. Pattison, LEDs for Horticulture: More than meets the eye, *LD+A*, **2018**, 20–22.

[74] P. C. Quayle, K. He, J. Shan, K. Kash, Synthesis, lattice structure, and band gap of $ZnSnN_2$, *MRS Commun.* **2013**, *3*, 135–138.

[75] P. Narang, S. Chen, N. C. Coronel, S. Gul, J. Yano, L.-W. Wang, N. S. Lewis, H. A. Atwater, Bandgap Tunability in $Zn(Sn,Ge)N_2$ Semiconductor Alloys, *Adv. Mater.* **2014**, *26*, 1235–1241.

[76] F. K. Yam, L. L. Low, S. A. Oh, Z. Hassan, Gallium Nitride: An Overview of Structural Defects. In *Optoelectronics - Materials and Techniques*, InTech, **2011**.

[77] B. Kunert, Y. Mols, M. Baryshniskova, N. Waldron, A. Schulze, R. Langer, How to control defect formation in monolithic III/V hetero-epitaxy on (100) Si? A critical review on current approaches, *Semicond. Sci. Technol.* **2018**, *33*, 093002.

[78] A. D. Martinez, A. N. Fioretti, E. S. Toberer, A. C. Tamboli, Synthesis, structure, and optoelectronic properties of II–IV–V_2 materials, *J. Mater. Chem. A* **2017**, *5*, 11418–11435.

[79] L. D. Zhu, P.H. Maruska, P.E. Norris, P.W. Yip, L.O. Bouthillette, Epitaxial Growth and Structural Characterization of Single Crystalline $ZnGeN_2$, *MRS Internet J. Nitride Semicond. Res.* **1999**, *4*, 149–154.

[80] T. Cloitre, A. Sere, R. L. Aulombard, Epitaxial growth of $ZnSiN_2$ single-crystalline filmson sapphire substrates, *Superlattices Microstruct.* **2004**, *36*, 377–383.

[81] V. L. Shaposhnikov, A. V. Krivosheeva, F. Arnaud D'Avitaya, J.-L. Lazzari, V. E. Borisenko, Structural, electronic and optical properties of II–IV–N_2 compounds (II = Be, Zn; IV = Si, Ge), *Phys. Status Solidi B* **2008** *245*, 142–148.

[82] A. Punya, W. R. L. Lambrecht, M. van Schilfgaarde, Quasiparticle band structure of Zn-IV-N_2 compounds, *Phys. Rev. B: Condens. Matter Mater. Phys.* **2011**, *84*, 165204.

[83] A. Punya, W. R. L. Lambrecht, Band offsets between $ZnGeN_2$, GaN, ZnO, and $ZnSnN_2$ and their potential impact for solar cells, *Phys. Rev. B: Condens. Matter Mater. Phys.* **2013**, *88*, 075302.

[84] A. Punya, W. R. L. Lambrecht, Electronic band structure of Mg-IV-N_2 compounds in the quasiparticle-self-consistent GW approximation, *Phys. Rev. B* **2016**, *94*, 125201.

[85] N. Han, P. Liu, J. Jiang, S. Liu, Recent advances in nanostructured metal nitrides for water splitting, *J. Mater. Chem. A* **2018**, *6*, 19912–19933.

[86] J. Wu, W. Walukiewicz, K. M. Yu, W. Shan, J. W. Ager III, Superior radiation resistance of $In_{1-x}Ga_xN$ alloys: Full-solar-spectrum photovoltaic material system, *J. Appl. Phys.* **2003**, *94*, 6477–6482.

[87] J. Li, J. Y. Lin, H. X. Jiang, Direct hydrogen gas generation by using InGaN epilayers as working electrode, *Appl. Phys. Lett.* **2008** *93*, 162107

[88] T. Suehiro, M. Tansho, T. Shimizu, Quaternary Wurtzitic Nitrides in the System $ZnGeN_2$−GaN: Powder Synthesis, Characterization, and Potentiality as a Photocatalyst, *J. Phys. Chem. C* **2017**, *121*, 27590–27596.

[89] N. Feldberg, J. D. Aldous, W. M. Linhart, L. J. Phillips, K. Durose, P. A. Stampe, R. J. Kennedy, D. O. Scanlon, G. Vardar, R. L. Field III, T. Y. Jen, R. S. Goldman, T. D. Veal, S. M. Durbin, Growth, disorder, and physical properties of $ZnSnN_2$, *Appl. Phys. Lett.* **2013**, *103*, 042109.

[90] T. D. Veal, N. Feldberg, N. F. Quackenbush, W. M. Linhart, D. O. Scanlon, L. F. J. Piper, S. M. Durbin, Band Gap Dependence on Cation Disorder in $ZnSnN_2$ Solar Absorber, *Adv. Energy Mater.* **2015**, *5*, 1501462.

[91] V. P. Dmitriev, P. Tolédano, V. I. Torgashev, E. K. H. Salje, Theory of reconstructive phase transitions between SiO_2 polymorphs, *Phys. Rev. B: Condens. Matter Mater. Phys.* **1998**, *58*, 11911–11921.

[92] J. M. Léger, J. Haines, C. Chateau, G. Bocquillon, M. W. Schmidt, S. Hull, F. Gorelli, A. Lesauze, R. Marchand, Phosphorus oxynitride PON, a silica analogue: structure and compression of the cristobalite-like phase; *P–T* phase diagram, *Phys. Chem. Minerals* **2001**, *28*, 388–398.

[93] J. M. Léger, J. Haines, L. S. de Oliveira, C. Chateau, A. L. Sauze, R. Marchand, S. Hull, Crystal structure and high pressure behaviour of the quartz-type phase of phosphorus oxynitride PON, *J. Phys. Chem. Solids* **1999**, *60*, 145–152.

[94] J. Haines, C. Chateau, J. M. Léger, A. L. Sauze, N. Diot, R. Marchand, S. Hull, Crystal structure of moganite-type phosphorus oxynitride: relationship to other twinned-quartz-based structures, *Acta Crystallogr. Sect. B: Struct. Sci.* **1999**, *55*, 677–682.

[95] D. Baumann, S. J. Sedlmaier, W. Schnick, An Unprecedented AB2 Tetrahedra Network Structure Type in a High-Pressure Phase of Phosphorus Oxonitride PON, *Angew. Chem. Int. Ed.* **2012**, *51*, 4707–4709; *Angew. Chem.* **2012**, *124*, 4785–4787.

[96] L. Coes Jr., A New Dense Crystalline Silica, *Science* **1953**, *118*, 131–132.

[97] L. S. Ramsdell, The crystallography of "coesite", *Am. Mineral.* **1955**,*40*, 975–982.

[98] T. Zoltai, M. J. Buerger, The crystal structure of coesite, *Z. Kristallogr*. **1959,** *111*, 129–141.

[99] S. M. Stishov, S. V. Popova, A new dense modification of silica, *Geokhimiya* **1961**, *10*, 837-839.

[100] W. Sinclair, A. E. Ringwood, Single crystal analysis of the structure of stishovite, *Nature* **1978**, *272*, 714–715.

[101] R. J. Hill, M. D. Newton, G. V. Gibbs, A crystal chemical study of stishovite, *J. Solid State Chem.* **1983**,*47*, 185–200.

[102] Y. Tsuchida, T. Yagi, A new, post-stishovite highpressure polymorph of silica, *Nature* **1989**, *340*, 217–220.

[103] J. Kingma, R. E. Cohen, R. J. Hemley, H. K. Mao, Transformation of stishovite to a denser phase at lower-mantle pressures, *Nature* **1995**,*374*, 243–245.

[104] D. Andrault, R. J. Angel, J. L. Mosenfelder, T. Le Bihan, Equation of state of stishovite to lower mantle pressures, *Am. Mineral.* **2003**, *88*, 301–307.

[105] P. Dera, C. T. Prewitt, N. Z. Boctor, R. J. Hemley, Characterization of a high-pressure phase of silica from the Martian meteorite Shergotty, *Am. Mineral.* **2002**, *87*, 1018–1023.

[106] E. Goresy, P. Dera, T. G. Sharp, C. T. Prewitt, M. Chen, L. Dubrovinsky, B.Wopenka, N. Z. Boctor, R. J. Hemley, Seifertite, a dense orthorhombic polymorph of silica from the Martian meteorites Shergotty and Zagami, *Eur. J. Mineral.* **2008**, *20*, 523–528.

[107] M. Miyahara, S. Kaneko, E. Ohtani, T. Sakai, T. Nagase, M. Kayama, H. Nishido, N. Hirao, Discovery of seifertite in a shocked lunar meteorite, *Nat. Commun.* **2013**, *4*, 1737.

[108] Y. Kuwayama, K. Hirose, N. Sata, Y. Ohishi, The Pyrite-Type High-Pressure Form of Silica, *Science* **2005**, *309*, 923–925.

[109] A. Marchuk, W. Schnick, $Ba_3P_5N_{10}Br:Eu^{2+}$: A Natural-White-Light Single Emitter with Zeolite Structure Type, *Angew. Chem. Int. Ed.* **2015**, *54*, 2383–2387; *Angew. Chem.* **2015**, *127*, 2413–2417.

[110] F. J. Pucher, A. Marchuk, P. J. Schmidt, D. Wiechert, W. Schnick, Luminescent Nitridophosphates $CaP_2N_4:Eu^{2+}$, $SrP_2N_4:Eu^{2+}$, $BaP_2N_4:Eu^{2+}$, and $BaSr_2P_6N_{12}:Eu^{2+}$, *Chem .Eur. J.* **2015**, *21*, 6443–6448.

[111] S. D. Kloß, N. Weidmann, W. Schnick, Antiperovskite Nitridophosphate Oxide $Ho_3[PN_4]O$ by High-Pressure Metathesis, *Eur. J. Inorg. Chem.* **2017**, 1930–1937.

[112] S. D. Kloß, O. Janka, T. Block, R. Pöttgen, R. Glaum, W. Schnick, Open-shell 3d Transition Metal Nitridophosphates $M^{II}P_8N_{14}$(M^{II} = Fe, Co, Ni) by High-pressure Metathesis, *Angew. Chem. Int. Ed.* **2019**, *58*, 4685–4689; *Angew. Chem.* **2019**, *131*, 4733–4737.

[113] W. Schnick, J. Luecke, Lithium Ion Conductivity of $LiPN_2$ and Li_7PN_4, *Solid State Ionics* **1990**, *38*, 271–273.

[114] S. Zhao, Z. Fu, Q. Qin, A solid-state electrolyte lithium phosphorus oxynitride film prepared by pulsed laser deposition, Thin Solid Films **2002**, *415*, 108–113.

[115] E.-M. Bertschler, C. Dietrich, J. Janek, W. Schnick, $Li_{18}P_6N_{16}$ – A Lithium Nitridophosphate with Unprecedented Tricyclic $[P_6N_{16}]^{18-}$ Ions, *Chem .Eur. J.* **2017**, *23*, 2185–2191.

[116] E.-M. Bertschler, C. Dietrich, T. Leichtweiß, J. Janek, W. Schnick, Li^+ Ion Conductors with Adamantane-type Nitridophosphate Anions - β-$Li_{10}P_4N_{10}$ and $Li_{13}P_4N_{10}X_3$ with X = Cl, Br, *Chem. Eur. J.* **2018**, *24*, 196–205.

2 Computational Theory and Concepts

This chapter serves as superficial overview of the basic theoretical background and framework on the basis of which the results of this thesis were obtained. Further calculatory details can be found in the respective publications presented in this work.
The concepts and theory of this chapter are in its essence adapted from the respectively presented sources and recapitulate on history and theory without claiming intellectual property on the herein presented content.

2.1 Density Functional Theory

Unless indicated otherwise, the general subject matter of this section is, in its principal properties, adapted from references [1–5] which offer more in-depth theoretical treatments.

Since the fundamental proofs required for the emergence of modern density functional theory (DFT) was established by Hohenberg, Kohn and Sham around 1964–1965,[6,7] subsequent advances from around 1980–2010 led DFT to become a popular alternative to traditional *ab initio* methods.[8] A main reason for this can be attributed to its potent ratio between accuracy and requirements in computational effort.
The aim of density functional theory is in principle identical to the wavefunction approach, which is to provide an exact solution of the time independent many-body Schrödinger equation and to find the ground state properties of the calculated material according to

$$\hat{H}\Psi = E\Psi. \tag{1}$$

In consideration of the adiabatic approximation (Born-Oppenheimer approximation) in which the movement of the nuclei is considered as separated (static) due to the much faster movement of the electrons and their much lighter mass,[9] the complete dimensionless Hamiltonian (written in atomic units)[1]

$$\hat{H} = \underbrace{-\frac{1}{2}\sum_{i=1}^{N}\nabla_i^2}_{\hat{T}_e} \underbrace{-\frac{1}{2}\sum_{A=1}^{M}\frac{1}{M_A}\nabla_A^2}_{\hat{T}_N} \underbrace{-\sum_{i=1}^{N}\sum_{A=1}^{M}\frac{Z_A}{r_{iA}}}_{\hat{V}_{eN}} + \underbrace{\sum_{i=1}^{N}\sum_{j>i}^{N}\frac{1}{r_{ij}}}_{\hat{V}_{ee}} + \underbrace{\sum_{A=1}^{M}\sum_{B>A}^{M}\frac{Z_A Z_B}{R_{AB}}}_{\hat{V}_{NN}}, \tag{2}$$

can be reduced to the purely electronic Hamiltonian $\hat{H}_{el}$

$$\hat{H}_{el} = \underbrace{-\frac{1}{2}\sum_{i=1}^{N}\nabla_i^2}_{\hat{T}_e} \underbrace{-\sum_{i=1}^{N}\sum_{A=1}^{M}\frac{Z_A}{r_{iA}}}_{\hat{V}_{eN}} + \underbrace{\sum_{i=1}^{N}\sum_{j>i}^{N}\frac{1}{r_{ij}}}_{\hat{V}_{ee}}, \tag{3}$$

[1] $\hbar = m_e = e = 4\pi\varepsilon_0 = 1$.
$\hat{T}_e$ = kinetic energy of the electrons $\hat{T}_N$ = nuclear kinetic energy, $\hat{V}_{eN}$ = potential energy of the interaction between electrons and nuclei, $\hat{V}_{ee}$ = potential energy of the interaction between electrons, $\hat{V}_{NN}$ = potential energy between nuclei.

with the Laplacian $\nabla_k^2 = \frac{\partial^2}{\partial x_k^2} + \frac{\partial^2}{\partial y_k^2} + \frac{\partial^2}{\partial z_k^2}$. The positions of electrons and nuclei correspond to $\vec{r}_i$ and $\vec{r}_A$ with $r_{iA} = |\vec{r}_i - \vec{R}_A|$ and $r_{ij} = |\vec{r}_i - \vec{r}_j|$.

The central quintessence of DFT lies within the assumption that the ground state energy can be determined from the ground state electron density $\rho(\vec{r})$, without the foremost knowledge of the explicit ground state wave function. This dependence of the energy is expressed as a functional of the electron density via

$$E = E[\rho]. \tag{4}$$

And while the electronic wave function Ψ of a system with N electrons depends on 3 N variables[1]

$$\Psi = \Psi(\vec{r}_1, \dots \vec{r}_N), \tag{5}$$

the probability to find one single electron, only dependent on the 3 spatial coordinates $\vec{r}_1$, within a volume increment $d\vec{r}_1$ is

$$d\vec{r}_1 \int \Psi^* \Psi \, (d\vec{r}_2, \dots d\vec{r}_N). \tag{6}$$

The probability for all electrons N at $\vec{r}_1$ (i. e. the number of electrons per volume increment) is then obtained as the density

$$\rho(\vec{r}_1) = N \int \Psi^* \Psi \, (d\vec{r}_2, \dots d\vec{r}_N). \tag{7}$$

The total number N of electrons is then, generally obtained from integration over $\rho(\vec{r})$

$$\int \rho(\vec{r}) d\vec{r} = N \, . \tag{8}$$

Instead of calculating the wave function in order to obtain all observables, the ideological foundation of DFT can be represented by a scheme, where the specific external potential $\upsilon(\vec{r})$ is uniquely mapped from $\rho(\vec{r})$ in a reversed manner:

$$\rho(\vec{r}) \rightarrow \Psi(\vec{r}_1, \dots \vec{r}_N) \rightarrow \upsilon_{ext}(\vec{r}) \tag{9}$$

Following the electronic Hamiltonian the energy functional can thus, be written as

$$E[\rho] = E_{T_e}[\rho] + E_{V_{eN}}[\rho] + E_{V_{ee}}[\rho]. \tag{10}$$

With the famous Hohenberg-Kohn theorems in 1964, the groundwork for the practical applicability of DFT was derived. They proved, that the exact ground state in an external potential is accessible via the variational principle.[6]

[1] For simplicity the spin of the electrons is omitted.

2.1.1 The Kohn-Sham Equations

Soon after the work of Hohenberg and Kohn, in 1965 Kohn and Sham presented their work on the determination of the ground state electron density through an auxialliary system of non-interacting particles.[4,7] The leading thought is splitting the kinetic energy operator into a part containing the interaction of non-interacting particles $\hat{T}_S$ and a (not exactly defined) residual part $\hat{T}_C$ containing correlation effects[5]

$$\hat{T}[\rho] = \hat{T}_S + \hat{T}_C \tag{11}$$

with

$$\hat{T}_S = -\frac{1}{2}\sum_i^N \langle\varphi_i|\,\nabla^2\,|\varphi_i\rangle, \tag{12}$$

and the one-electron functions φ_i.

The idea is to determine the exact kinetic energy $\hat{T}[\rho]$ of the real interacting system (that is to be determined with the help of the auxiliary one), with the electron density $[\rho]$ of the auxiliary non-interacting system.
Finally, the energy functional of the real system $E[\rho]$ can be written as

$$E[\rho] = \hat{T}_S + E_J[\rho(\vec{r})] + E_{XC}[\rho(\vec{r})] + E_{V_{eN}}[\rho(\vec{r})]\,, \tag{13}$$

with the classical coulomb interaction $E_J[\rho]$ that contains the wrong electronic self-interaction

$$E_J[\rho] = \frac{1}{2}\int\int \frac{\rho(\vec{r}_1)\rho(\vec{r}_2)}{r_{12}}\,d\vec{r}_1 d\vec{r}_2\,, \tag{14}$$

and the potential energy $E_{V_{eN}}$

$$E_{V_{eN}}[\rho] = -\sum_{A=1}^{K} Z_A \int \frac{\rho(\vec{r})}{\vec{R}_A - \vec{r}}\,. \tag{15}$$

It is further true that

$$\hat{T}[\rho] > \hat{T}_S \tag{16}$$

Applying the variational principle with respect to φ_i then leads to

$$\left(-\tfrac{1}{2}\nabla^2 + \left[-\textstyle\sum_{A=1}^{K}\frac{Z_A}{r_{1A}} + \int\frac{\rho(\vec{r}_2)}{r_{12}}\mathrm{d}\vec{\mathrm{r}} + V_{XC}(\vec{r})\right]\right)\varphi_i = \left(-\tfrac{1}{2}\nabla^2 + V_{eff}(\vec{r}_1)\right)\varphi_i = \varepsilon_i\varphi_i \equiv \hat{f}^{KS}\varphi_i = \varepsilon_i\varphi_i. \tag{17}$$

Hence, the potential $V_{eff}(\vec{r})$ of the real system equates to $V_S(\vec{r})$ from the auxiliary system and the latter can thus, be calculated though minimization of φ_i in return yielding the exact ground state electron density $\rho^{\mathrm{GS}}(\vec{r})$. As such, DFT calculations are usually performed iteratively and self-consistently.

The important achievement of the Kohn-Sham approach is the access to a large part of the exact kinetic energy, which had until then been described insufficiently, while remaining in principle exact in its formalism. The unknown remaining exchange-correlation is thus, indirectly expressed as remainder of the other terms via

$$^{KS}E_{XC}[\rho] \equiv \left(\hat{T}[\rho] - \hat{T}_S[\rho]\right) + \left(E_{V_{ee}}[\rho] - J[\rho(\vec{r})]\right) = \hat{T}_C + {}^{HK}E_{XC}[\rho]\,, \qquad (18)$$

where $^{HK}E_{XC}[\rho]$ contains all non-classical terms of the electron exchange and correlation energy. The exact ground state energy can of course, only be calculated if the exchange-correlation part is known.

While until today no exact functional for the exchange-correlation terms has been found in DFT, significant advancements in the construction of suitable (partly semi-empirical) approximations for the exchange-correlation allow for a plurality of calculations accurate enough to offer descriptions and predictions of electronic properties for molecular or solid state properties in applied chemistry and physics with a good computationally cost-value ratio. Depending on which properties are calculated and which functional approximations are chosen for the exchange-correlation, DFT is able to provide excellent descriptions of electronic and materials properties.

2.1.2 The Local Density Approximation - LDA

The basic concept of the local density approximation (LDA) dates back to the Thomas-Fermi model of 1927 approximating the kinetic energy, which can be expressed exactly for a homogenous electron density, for a system with an inhomogeneous density instead. However, the resulting description of $\hat{T}_S^{LDA}$ already fails for simple molecules.

As the Kohn-Sham equations already provide a much superior treatment of $\hat{T}_S$ the true merit of the LDA became apparent with respect to approximating the exchange-correlation energy by the solution for the interacting homogenous electron gas.[10] The exchange part of LDA can be expressed as

$$E_X^{LDA}[\rho] = -\frac{3}{4}\left(\frac{3}{\pi}\right)^{\frac{1}{3}} \int \rho(\vec{r})^{\frac{4}{3}}\, d\vec{r}, \qquad (19)$$

while for the correlation part the situation is more complicated and values for E_C^{LDA} are nowadays typically parametrizations of Monte Carlo derived values.[5] While relatively simple the LDA describes inhomogeneous materials quite successfully, as it typically underestimates E_C and overestimates E_X resulting in systematic error cancelations.

2.1.3 The Generalized Gradient Approximation - GGA

Within the inhomogeneous electron density of a real system there are of course local changes in maxima and minima of the local density, i.e. density gradients, which are, however, unaccounted for within the simple homogenous LDA.

In order to improve upon the LDA attempts to implement the gradient of the electron density were considered. Early approximations started from a slowly varying uniform electron gas in a gradient expansion (GEA), which could however not account for the rapid changes in $\rho(\vec{r})$ present in real chemical systems

A more suitable solution came with the development of the generalized gradient approximation (GGA) for which $E_X^{GGA}[\rho(\vec{r})]$ takes the form[8,11,12]

$$E_X^{GGA}[\rho, \mathrm{x}] = \int \rho(\vec{r})^{\frac{4}{3}} F(x) d\vec{r}, \tag{20}$$

where *F(x)* has to be chosen appropriately.
While nowadays there exists a variety of exchange functionals of the GGA-type, E_X^{PBE} is one of the most widely spread and popular ones taking the form

$$E_X^{PBE} = \int \epsilon_X^{LDA}\big(\rho(\vec{r})\big) F_X\big(s(\vec{r})\big)\, d^3r \tag{21}$$

with the dimensionless reduced density gradient

$$s = \frac{|\nabla\rho(\vec{r})|}{2(3\pi^2)^{\frac{1}{3}}\rho(\vec{r})^{\frac{4}{3}}}, \tag{22}$$

$$\epsilon_X^{LDA} = -\frac{3}{4}\left(\frac{3}{\pi}\right)^{\frac{1}{3}} \rho(\vec{r})^{\frac{4}{3}}, \tag{23}$$

and the exchange enhancement factor

$$F_X = 1 + \kappa - \frac{\kappa}{\left(1+\frac{\mu s^2}{\kappa}\right)} \quad \text{with } \kappa = 0.804 \tag{24}$$

2.1.4 Hybrid and Meta-GGA Functionals

LDA and GGA based potentials are computationally cost-efficient and further improvement on the exchange correlation with more modern approaches has led to more costly hybrid functionals that improve upon E_{XC} by mixing in parts of the exchange or correlation from Hartree-Fock-type calculations. Prominent examples comprise for example the BLYP and B3LYP exchange functionals which have proved successful and popular in the chemistry community. Meta-GGAs on the other hand are less computationally demanding and only improve upon GGAs by further depending on the Kohn-Sham kinetic energy density $\tau(\vec{r})$ in order to satisfy further constrains on E_{XC}.[4,5]

2.1.4.1 The Modified Becke-Johnson Potential

With regard to an accurate description of the electronic band gap (E_g) the modified variant of the Becke-Johnson exchange potential has proved to yield accurate values of E_g for a vast number of semiconductors and insulators taking the form[13–15]

$$v_{x,\sigma}^{MBJ}(\vec{r}) = cv_{x,\sigma}^{BR}(\vec{r}) + (3c-2)\frac{1}{\pi}\sqrt{\frac{5}{12}}\sqrt{\frac{2\tau_\sigma(\vec{r})}{\rho_\sigma(\vec{r})}} \quad (25)$$

where $v_{x,\sigma}^{BR}(\vec{r})$ is the Becke-Roussel potential proposed to mimic the coulomb potential created by the exchange hole x_σ.[16] It is noteworthy that the modified Becke-Johnson (mBJ) potential is only designed to provide accurate single-particle energies of electron transitions between states and intended for the calculation of electronic properties only. It is not self-consistent with respect to the calculation of lattice relaxations, and is not suitable for such.

2.2 Band Structure Methods

Even with the average modern computational resources, the treatment of the complete electronic properties for systems with many atoms, which is especially true for solid-state materials, may still not be easily accomplished. Hence, nowadays many computational programs are available, some of which pursue different approaches, in order to treat the electronic properties within DFT as exact and cost-efficient as possible.
In the following a review of two band structure methods used in this thesis, namely the pseudopotential and KKR method will be reviewed.

2.2.1 Pseudopotentials and the Projector Augmented Wave Method

As the major chemical interactions take place between the outermost electron shells, the physical reasoning for the development of the pseudopotential approximation rests on the fact that the core wave functions of an atom are barely affected by the chemical environment.[17] Hence, the central idea is to approximate the Coulomb potential of the nuclei and the core electrons by an effective potential acting on the outer (valence) electrons, so that only the density of latter has to be calculated self consistently. As such the pseudopotentials are not uniquely determined leaving them open for different choices and optimizations. Additionally, pseudopotentials are typically described by a basis set of plane waves and designed to not show the strong oscillations that real radial atomic wave functions exhibit in their core-near region, which in turn reduces the necessary number of plane waves.[4,5]
The plurality of modern pseudopotentials are norm-conserving *ab initio* potentials, whereas the following requirements should by satisfied between the all-electron and the respective pseudo wave functions[4,18]

① Their *eigenvalues* agree for the chosen atomic reference configuration

② The wave functions agree beyond a chosen core radius r_c

③ Their logarithmic derivatives agree at $r > r_c$

④ Additionally, the first derivatives of their energies agree at $r > r_c$

⑤ The integrals from 0 to r of their charge densities agree for $r > r_c$ (norm conservation)

The assessment of how good a certain pseudopotential performs should further not be tied to its agreement with experimental data but rather to its reproduction of accurate all-electron calculations.[19] Plain norm-conserving pseudopotentials however still require core corrections in order to properly treat the interactions between core and valence charge densities. A deficiency that could be overcome by the development of the projector-augmented wave method.[19,20,21]

The projector augmented-wave (PAW) method established a generalization of the pseudopotential and linear augmented-plane-wave method. Unlike the pseudopotential method, which is not an all-electron method, the PAW method provides a way to reconstruct the all-electron valence wave function from pseudo wave functions according to

$$|\Psi_n^{AE}\rangle = |\Psi_n^{PS}\rangle + \sum_i \left(|\phi_i^{AE}\rangle - |\phi_i^{PS}\rangle\right)\langle p_i^{PS}|\Psi_n^{PS}\rangle \tag{26}$$

where Ψ_n^{AE} is the all-electron wave function (i.e. a full one-electron Kohn Sham wave function), Ψ_n^{PS}a pseudo wave function and ϕ_i the corresponding partial waves and p are projector functions (exactly one for each partial wave).
In a similar way to the wave function it can be shown that the charge density can likewise be decomposed. Lastly, the electronic total energy can be obtained as

$$E = E^{PS} - E^{PS,1} + E^{AE,1} \tag{27}$$

where $E^{PS,1}$ and $E^{AE,1}$ describe one-center contributions and each term comprises the contributions of kinetic, Hartree and exchange-correlation.[19,20] Strictly speaking the PAW method is not an all-electron method itself as it is based on the frozen core approximation, which is however legitimate for the plurality of properties in solids.[19]

It is due to this fact and the overall benefits PAWs provide computationally, that nowadays a plurality of quantum chemical programs utilize pseudopotentials along with the PAW method for the calculation of electronic and materials properties.

2.3 The Korringa-Kohn-Rostoker Green's Function Method

The Korringa-Kohn-Rostoker Green's function method (KKR-GF) is an alternative approach to solve the Kohn-Sham equation in terms of the single-particle Green Function, instead of conventional Kohn-Sham *eigenfunctions* and *eigenvalues*, in order to calculate the accurate ground state energy.[22,23] Its formalism is based on the multiple scattering theory (MST), drawing its name from Korringa, together with Kohn and Rostoker, who independently suggested the use of MST in 1947 and 1954.[24,25]
Instead of solving the Schrödinger equation the KKR-GF method aims at solving the Green's operator introduced as

$$G(z) = (z - H)^{-1}, \tag{28}$$

where $G(z)$ and H have the same *eigenfunctions* and the *eigenvalues* of H are the poles of $G(z)$, thus, solving for the latter will give the solutions for the Schrödinger equation.[22,23] The subsequent problem of $G(z)$ is, however, that it is not defined for the *eigenvalues* of H. Hence, in a redefinition of the Green's operator the *eigenvalues* of H are approached from above (+ solution) and from below (− solution)[23]

$$G^{\pm}(z) = \lim_{\varepsilon \to 0^{+}} (z - H \pm \varepsilon)^{-1}. \tag{29}$$

The propagation of the electron waves between the atomic potentials (scattering centers) is accordingly, described by the free-electron Green's functions $G^{0}(\vec{r}, \vec{r}', E)$.[22]
Using the *Dyson equation* within the KKR-GF method allows the treatment of the Green's function (GF) for a perturbed system in relation to an unperturbed reference system. As a result the KKR-GF method allows to treat systems without the restriction of Bloch symmetry such as two-dimensional periodic systems, impurity clusters or disordered systems.[22]

The central idea of MST lies in the decomposition of the electronic motion within a given system, for example in a solid material, into a scattering at atomic sites and regions of free-electron propagation in the interstitial regions. In a first step, the individual scattering processes can be expressed as single site scattering of an electron at a single spherical atomic potential V according to the reduced Schrödinger equation[23]

$$[k^2 + \nabla^2 - V(\vec{r})]\Psi_k = 0\,. \tag{30}$$

Considering the incoming electron wave function as a plane wave $\psi_{inc}(\vec{r}) = Ae^{ikr}$ scattered by the potential V and exiting as radial wave $\psi_{scatt}(\vec{r}) = f_k(\theta)\frac{e^{ikr}}{\vec{r}}$ the asymptotic form of Ψ_k can be expressed as

$$\psi_{inc}(\vec{r}) + \psi_{scatt}(\vec{r}) = \psi_k(\vec{r}) \xrightarrow[\vec{r} \to +\infty]{} A\left[e^{ikr} + f_{\vec{k}}(\theta)\frac{e^{ikr}}{\vec{r}}\right], \tag{31}$$

where $f_{\vec{k}}(\theta)$ is denoted as scattering amplitude or scattering factor.[23]
The numerically determined solutions of the radial Schrödinger equation in the atomic regions are dependent on the energy and angular momentum ℓ. This ℓ-dependence of the partial wave expansions for the radial wave function means that the KKR method is effectively a minimal basis-set method, depending on the chosen ℓ_{max}.[22] The central result of the single-site scattering process is the so called single-site scattering *t*-matrix $t_l(E)$ which, loosely speaking, represents the phase shift between $\psi_{inc}(\vec{r})$ and $\psi_{scatt}(\vec{r})$. Within MST the individual scattering processes, or their partial wave functions $R_l(r, E)$, can be effectively represented by a single-site scattering by *t*-matrix $t_l(E)$.[22]
After successfully solving the single-site scattering problem the inclusion of all scatterers (atoms in the solid) is done by MST, describing the full propagation of the electron movement throughout the crystal. This in turn represents the full solution of the Kohn-Sham equations. In practice modern KKR-GF methods solve of the *Dyson equation* with the help of

reformulations of an additional transition operator T representing the entire multiple scattering of all the single-site scattering processes $\bar{t}_i$. T is then best described using the scattering path operator τ^{ji} introduced by Györffy and Stott[22,26–28] which describes the possible travel paths of an electron from i to j, comprising corrections to distortions of $\bar{t}_i$ due to all atomic sites present in the system.

The solution of τ^{ji} can then be obtained by matrix inversion

$$\underline{\underline{\tau}}(E) = \underbrace{\left[\underline{\underline{t}}(E)^{-1} - \underline{\underline{G}}_0(E)\right]}_{\underline{\underline{M}}}^{-1}, \tag{32}$$

with $\underline{\underline{M}}$ as the real-space KKR matrix (restricted in size by the cut-off ℓ_{max}), the inversion of which is usually takes the most effort in the solution of the multiple scattering problem.[22]

In conclusion the part relating to multiple scattering within the modern KKR-GF approach can be comprised in the scheme:[23]

$$H \underset{Definition\ \ of\ G}{\Longleftrightarrow} G \underset{Dyson\ \ equation}{\Longleftrightarrow} T \underset{Definition\ \ of\ \tau^{ji}}{\Longleftrightarrow} \tau^{ji}$$

Beginning from the early non-relativistic treatment modern developments of the KKR-GF method have further led to various improvements up to the relativistic case.[23,29–37]

2.3.1 The Coherent Potential Approximation

In order to treat atomic (or analogues also magnetic) disorder effects in solids where crystallographic sites are statistically occupied by two (or more) elements, the coherent potential approximation (CPA) represents the most adequate theory among single-site alloy theories (ignoring short-range ordering). Many standard DFT programs, which utilize pseudopotentials for example, can typically only treat disorder by means of adequately sized supercells in order to approximate the statistical disorder observed from experimental X-ray diffraction. The KKR-GF together with the CPA on the other hand enables the treatment of disorder based on the normal sized unit cell in terms of a weighted configurational average over two hypothetically ordered mediums described by the scattering-path operator τ^{ji}. A hypothetical disordered binary solid A_xB_{1-x} is henceforth, described by the CPA condition determined by the CPAs scattering-path operator

$$\tau^{CPA} = x_A \tau^A + x_B \tau^B \tag{33}$$

with the site-diagonal component-projected scattering path operator τ^A (respectively τ^B)

$$\tau^A = \tau^{CPA}\left[1 + \left(t^{A^{-1}} - t^{CPA^{-1}}\right)\tau^{CPA}\right]^{-1}. \tag{34}$$

A simplified illustration of the CPA-scheme regarding is further given in Figure 2.1.

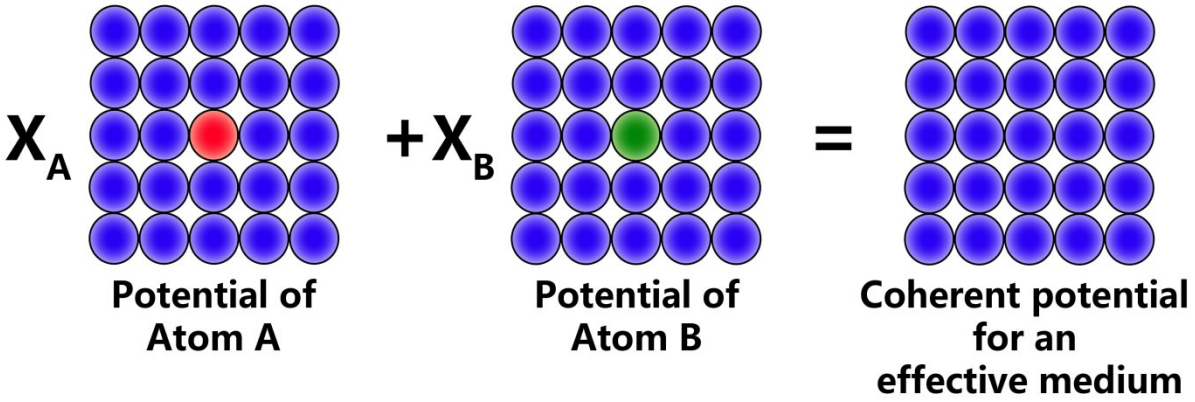

Figure 2.1 Illustration of the construction of the CPA potential. The real disordered alloy is represented by an effective coherent potential shown on the right. In this potential the statistically disordered atoms (red, green) are embedded assuming no induced changes in the surrounding potential (blue), hence ignoring local short-range disturbances. Illustration adapted from Ref. [23].

Both equations for τ^A and τ^{CPA} have to be solved iteratively and self-consistently together with the single-site t-matrices t^A and t^{CPA} where on usually starts from an initial starting guess for t^{CPA} in terms of weighted single-site t-matrices e.g. $t^{ATA} = x_A t^A + x_B t^B = t^{CPA}_{start}$.[22,23,38]

2.4 Theory of Elasticity

Unless indicated otherwise, in order to provide an understanding of the descriptions of elasticity in polycrystalline materials, this section provides a fundamental abridgment along with expressions given in reference [39] in which more detailed derivations and background information are presented.

In order to derive elastic constants and respective strain tensors the linear theory of elasticity is employed which only relies on small deformations within an isotropic material. This allows for dropping the distinction between undeformed and deformed configurations of a material, which would differ significantly for large deformations. A general deformation is thus, described by the respective displacement of two neighboring points P_0 and P_1. The displacement of each point is specified by two displacement vectors u_0 and u_1 respectively. The relative change in distance between P_0 and P_1 is then accounted by $\Delta r = r - r'$ where r and r′ denote the vectors connecting both Points before and after their respective displacements.

Since the components of r are small u can be expressed by a discontinued Taylor series around P_0 without accounting for higher-order terms, leading to the relation

$$\begin{aligned} u_1 &= u_0 + \frac{\partial u_1}{\partial x} r_x + \frac{\partial u_1}{\partial y} r_y + \frac{\partial u_1}{\partial z} r_z \\ v_1 &= v_0 + \frac{\partial v_1}{\partial x} r_x + \frac{\partial v_1}{\partial y} r_y + \frac{\partial v_1}{\partial z} r_z \\ w_1 &= w_0 + \frac{\partial w_1}{\partial x} r_x + \frac{\partial w_1}{\partial y} r_y + \frac{\partial w_1}{\partial z} r_z \end{aligned} \xrightarrow{\Delta r = r - r' = u_1 - u_0} \begin{aligned} \Delta r_x &= \frac{\partial u_1}{\partial x} r_x + \frac{\partial u_1}{\partial y} r_y + \frac{\partial u_1}{\partial z} r_z \\ \Delta r_y &= \frac{\partial v_1}{\partial x} r_x + \frac{\partial v_1}{\partial y} r_y + \frac{\partial v_1}{\partial z} r_z \\ \Delta r_z &= \frac{\partial w_1}{\partial x} r_x + \frac{\partial w_1}{\partial y} r_y + \frac{\partial w_1}{\partial z} r_z \end{aligned}$$

written as $\Delta r_i = u_{i,j} r_j$ in index notation where

$$u_{i,j} = \begin{bmatrix} \frac{\partial u}{\partial x} & \frac{\partial u}{\partial y} & \frac{\partial u}{\partial z} \\ \frac{\partial v}{\partial x} & \frac{\partial v}{\partial y} & \frac{\partial v}{\partial z} \\ \frac{\partial w}{\partial x} & \frac{\partial w}{\partial y} & \frac{\partial w}{\partial z} \end{bmatrix} \tag{35}$$

equals the displacement gradient tensor. The latter can further be split into its symmetric and anti-symmetric parts

$$u_{i,j} r_j = \varepsilon_{ij} + \Omega_{ij} = \underbrace{\frac{1}{2}\left(u_{i,j} + u_{j,i}\right)}_{\varepsilon_{ij}} + \underbrace{\frac{1}{2}\left(u_{i,j} - u_{j,i}\right)}_{\Omega_{ij}}, \tag{36}$$

where ε_{ij} denotes the symmetric strain tensor and Ω_{ij} the rotation tensor.

The symmetric second-order strain tensor $\varepsilon_{ij} = \varepsilon_{ji}$ is more commonly expressed in its matrix form

$$\varepsilon_{ij} = [\varepsilon] = \begin{bmatrix} \varepsilon_x & \varepsilon_{xy} & \varepsilon_{xz} \\ \varepsilon_{xy} & \varepsilon_y & \varepsilon_{yz} \\ \varepsilon_{xz} & \varepsilon_{yz} & \varepsilon_z \end{bmatrix}, \tag{37}$$

where $\varepsilon_x = \frac{\partial u}{\partial x}$, $\varepsilon_y = \frac{\partial v}{\partial y}$, $\varepsilon_z = \frac{\partial w}{\partial z}$, $\varepsilon_{yx} = \frac{1}{2}\left(\frac{\partial u}{\partial y} + \frac{\partial v}{\partial x}\right)$, $\varepsilon_{yz} = \frac{1}{2}\left(\frac{\partial v}{\partial z} + \frac{\partial w}{\partial y}\right)$, $\varepsilon_{xz} = \frac{1}{2}\left(\frac{\partial w}{\partial x} + \frac{\partial u}{\partial z}\right)$.

Strain as defined is however only a description for the different deformations while from a materials science point of view we are interested in the behavior of a material upon deformation, that is, upon exerting a force onto it.

Consequently, one can start so define a stress vector

$$\mathrm{T}^N(x, N) = \lim_{\Delta A \to 0} \frac{\Delta F}{\Delta A} \tag{38}$$

of the surface force ΔF acting on a small surface ΔA with normal vector *N*.

The stress vector can also be expressed for a three-dimensional object with unit vectors e_1, e_2, e_3 as

$$\begin{aligned} \mathrm{T}^N(x, N = e_1) &= \sigma_x e_1 + \tau_{xy} e_2 + \tau_{xz} e_3 \\ \mathrm{T}^N(x, N = e_2) &= \tau_{yx} e_1 + \sigma_y e_2 + \tau_{yx} e_3 \\ \mathrm{T}^N(x, N = e_1) &= \tau_{zx} e_1 + \tau_{zy} e_2 + \sigma_z e_3 \end{aligned} \tag{39}$$

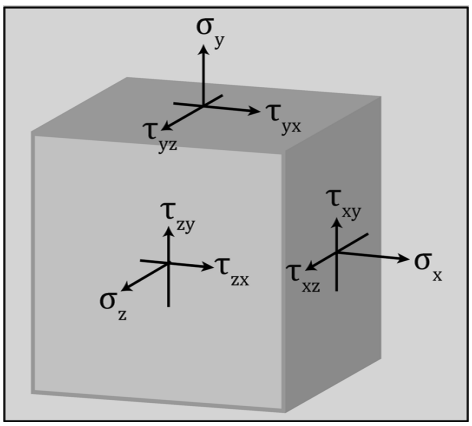

Figure 2.2 Illustrative stress components acting on a three-dimensional cubic body within a right-handed coordinate system, adapted from Ref. [39].

where σ and τ represent the 9 stress components (σ_{ij} normal stresses; τ_{ij} shearing stresses) as illustrated in Figure 2.2. In analogy to the strain tensor, the stress tensor comprising those components can be written as

$$\sigma_{ij} = [\sigma] = \begin{bmatrix} \sigma_x & \tau_{xy} & \tau_{xz} \\ \tau_{xy} & \sigma_y & \tau_{yz} \\ \tau_{xz} & \tau_{yz} & \sigma_z \end{bmatrix}. \tag{40}$$

2.4.1 Linear Elasticity

For the treatment of small deformations, a reasonable approximation to describe material behavior under stress is the assumption that the stress resulting from small deformations (one-dimensionally) behaves linearly according to

$$\sigma = \mathcal{L}\varepsilon\,, \tag{41}$$

with $\mathcal{L}$ denoting the linear strain-stress curve. Within such small deformations the material returns to its original shape after the force is removed and only after reaching its elastic limit non-elastic deformations begin.

Following the assumption of linear elasticity for the three-dimensional case, the stress components σ_{ij} can be connected to the strain components ε_{ij} as

$$\sigma_x = C_{11}\varepsilon_x + C_{12}\varepsilon_y + C_{13}\varepsilon_z + 2C_{14}\varepsilon_{xy} + 2C_{15}\varepsilon_{yz} + 2C_{16}\varepsilon_{zx}$$

$$\sigma_y = C_{21}\varepsilon_x + C_{22}\varepsilon_y + C_{23}\varepsilon_z + 2C_{24}\varepsilon_{xy} + 2C_{25}\varepsilon_{yz} + 2C_{26}\varepsilon_{zx}$$

$$\sigma_z = C_{31}\varepsilon_x + C_{32}\varepsilon_y + C_{33}\varepsilon_z + 2C_{34}\varepsilon_{xy} + 2C_{35}\varepsilon_{yz} + 2C_{36}\varepsilon_{zx}$$

$$\tau_{xy} = C_{41}\varepsilon_x + C_{42}\varepsilon_y + C_{43}\varepsilon_z + 2C_{44}\varepsilon_{xy} + 2C_{45}\varepsilon_{yz} + 2C_{46}\varepsilon_{zx}$$

$$\tau_{yz} = C_{51}\varepsilon_x + C_{52}\varepsilon_y + C_{53}\varepsilon_z + 2C_{54}\varepsilon_{xy} + 2C_{55}\varepsilon_{yz} + 2C_{56}\varepsilon_{zx}$$

$$\tau_{zx} = C_{61}\varepsilon_x + C_{62}\varepsilon_y + C_{63}\varepsilon_z + 2C_{64}\varepsilon_{xy} + 2C_{65}\varepsilon_{yz} + 2C_{66}\varepsilon_{zx}$$

which can be comprised in standard tensor notation corresponding to a generalization of Hooke's Law for linear elasticity[1,39]

$$\sigma_{ij} = C_{ijkl}\,\varepsilon_{kl}. \tag{42}$$

C_{ijkl} is a fourth-order elasticity tensor generally composed of 81 components. Due to the symmetry relations $C_{ijkl} = C_{jikl} = C_{ijlk}$ the number reduces to 36 components so that C_{ijkl} is typically, expressed as the elastic stiffness moduli C_{ij} via

$$C_{ijkl} = C_{ij} \tag{43}$$

where one associates[40]

$$xx \to 1;\ yy \to 2; zz \to 3; yz \to 4;\ zx \to 5; xy\ \to 6$$

to the indices, i.e. $C_{xxxx} \to C_{11}$ and so on.

Comprising the equations of the stress components using the symmetry relations in matrix format one arrives at

$$\begin{bmatrix} \sigma_x \\ \sigma_y \\ \sigma_z \\ \tau_{xy} \\ \tau_{yz} \\ \tau_{zx} \end{bmatrix} = \begin{bmatrix} C_{11} & C_{12} & & \cdots & & C_{16} \\ C_{21} & C_{22} & & & & \\ & & C_{33} & & & \vdots \\ \vdots & & & C_{44} & & \\ & & & & C_{55} & C_{56} \\ C_{61} & & & \cdots & C_{65} & C_{66} \end{bmatrix} \begin{bmatrix} \varepsilon_x \\ \varepsilon_y \\ \varepsilon_z \\ 2\varepsilon_{xy} \\ 2\varepsilon_{yz} \\ 2\varepsilon_{zx} \end{bmatrix}. \tag{44}$$

It can further be shown that $C_{ij} = C_{ji}$ thus, reducing the number of elements effectively needed to 21 independent elastic constants:

$$C_{ij} = \begin{bmatrix} C_{11} & C_{12} & C_{13} & C_{14} & C_{15} & C_{16} \\ & C_{22} & C_{23} & C_{24} & C_{25} & C_{26} \\ & & C_{33} & C_{34} & C_{35} & C_{36} \\ & & & C_{44} & C_{45} & C_{46} \\ & & & & C_{55} & C_{56} \\ & & & & & C_{66} \end{bmatrix}. \tag{45}$$

Depending on the symmetry of the crystal, it is further possible to reduce the number of independent constants as seen from Table 2.1.

A suitable approach to calculate the elastic constants at equilibrium volumes for single-crystals from *ab inito* DFT calculations, is thus to apply a set of strains, i.e. deformations, by introducing six finite distortions to the lattice. The elastic constants C_{ij} are subsequently derived from the corresponding stress-strain relationships.[41,42]

Table 2.1 Number of independent elastic constants C_{ij} according to Ref. [40]

Crystal System	Point Group	Elastic Constants
Triclinic	all	21
Monoclinic	all	13
Orthorhombic	all	9
Tetragonal	C_4, C_{4h}, S_4	7
	C_{4v}, D_4, D_{4h}, D_{2d}	6
Rhombohedral	C_3, S_6	7
	D_{3v}, D_3, D_{3d}	6
Hexagonal	all	5
Cubic	all	3

While single-crystals are per se anisotropic, and exhibit varying material properties along different directions, for the majority of polycrystalline macroscopic composites (with randomized crystal orientations) quasi-isotropic elastic behavior can be assumed. The elasticity of a macroscopic material is thus, typically expressed in terms of different material constants i.e. polycrystalline elastic moduli, such as the bulk modulus B (compressibility), the shear modulus G (rigidity) or Young's modulus Y (stiffness). In literature the latter are often also termed (k, μ and E). Further constants are Poisson's ratio ν and Lamé's constant λ.

Table 2.2 Elastic relations for isotropic materials: Y = Young's modulus, ν = Poisson's ratio, B = bulk modulus, G = shear modulus, λ = Lamé's constant. Adapted from Ref. [39]

	Y	ν	B	G	λ
Y, ν	Y	ν	$\frac{Y}{3(1-2\nu)}$	$\frac{Y}{2(1+\nu)}$	$\frac{Y\nu}{(1+\nu)(1-2\nu)}$
Y, B	Y	$\frac{3B-Y}{6B}$	B	$\frac{3BY}{9B-Y}$	$\frac{3B(3B-Y)}{9B-Y}$
Y, G	Y	$\frac{Y-2G}{2G}$	$\frac{GY}{3(3G-Y)}$	G	$\frac{G(Y-2G)}{3G-Y}$
Y, λ	Y	$\frac{2\lambda}{Y+\lambda+R}$	$\frac{Y+3\lambda+R}{6}$	$\frac{Y-3\lambda+R}{4}$	λ
ν, B	$3B(1-2\nu)$	ν	B	$\frac{3B(1-2\nu)}{2(1+\nu)}$	$\frac{3B\nu}{1+\nu}$
ν, G	$2G(1+\nu)$	ν	$\frac{2G(1+\nu)}{3(1-2\nu}$	G	$\frac{2G\nu}{1-2\nu}$
ν, λ	$\frac{\lambda(1+\nu)(1-2\nu)}{\nu}$	ν	$\frac{\lambda(1+\nu)}{3\nu}$	$\frac{\lambda(1-2\nu)}{2\nu}$	λ
B, G	$\frac{9BG}{3B+G}$	$\frac{3B-2G}{6B+2G}$	B	G	$B-\frac{3}{2}G$
B, λ	$\frac{9B(B-\lambda)}{3B-\lambda}$	$\frac{\lambda}{3B-\lambda}$	B	$\frac{3}{2}(B-\lambda)$	λ
G, λ	$\frac{G(3\lambda+2G)}{\lambda+G}$	$\frac{\lambda}{2(\lambda+G)}$	$\frac{3\lambda+2G}{3}$	G	λ

$R=\sqrt{Y^2+9\lambda^2+2Y\lambda}$

Assuming isotropic behavior only two constants are needed to express the others according to Table 2.2. In turn, the isotropic polycrystalline Bulk and Shear moduli, for example, can then be approximated from the anisotropic elastic constants C_{ij} of the single crystal. However, in a polycrystalline material the strain and stress may not be completely uniform. As a result B and G are found to lie in-between a lower bound, this is the Reuss approximation assuming uniform stress, and an upper bound derived from the Voigt approximation assuming uniform strain.[43,44]

Voigt calculates B and G accordingly from the elastic constants

$$B^V = \frac{(C_{11} + C_{22} + C_{33}) + 2(C_{12} + C_{23} + C_{31})}{9}$$

$$G^V = \frac{(C_{11} + C_{22} + C_{33}) - (C_{12} + C_{23} + C_{31}) + 3(C_{44} + C_{55} + C_{66})}{15}$$

and Reuss uses the compliance constants $S_{ijkl} = C_{ijkl}^{-1}$

$$B^R = \frac{1}{(S_{11} + S_{22} + S_{33}) + 2(S_{12} + S_{23} + S_{31})}$$

$$G^R = \frac{15}{4(S_{11} + S_{22} + S_{33}) - 4(S_{12} + S_{23} + S_{31}) + 3(S_{44} + S_{55} + S_{66})}.$$

Hill proved the validity of both approaches as the respective upper and lower bounds, and suggested to take the arithmetic mean of both approaches as means of an empirical approximation,[45] commonly termed the Voigt-Reuss-Hill approximation:

$$B^{VRH} = \frac{B^V + B^R}{2} \qquad G^{VRH} = \frac{G^V + G^R}{2}.$$

2.5 References

[1] G. Czycholl, *Theoretische Festkörperphysik: Von den klassischen Modellen zu modernen Forschungsthemen*, Springer-Lehrbuch, Springer **2007.**

[2] W. Koch, M. C. Holthausen, *Achemist's guide to density functional theory*, Wiley-VCH, **2002.**

[3] J. Reinhold, *Quantentheorie der Moleküle: Eine Einführung*, Springer, **2013.**

[4] R. M. Martin, *Electronic Structure: Basic Theory and Practical Methods*, Cambridge University Press, **2004.**

[5] K. Kapelle, A bird's-eye view of density-functional theory, *Braz. J. Phys.* **2006**, *36(4a*), 1318.

[6] P. Hohenberg, W. Kohn, Inhomogeneous Electron Gas, *Phys. Rev.* **1964**, *136*, B864–B871.

[7] W. Kohn, L. J. Sham, Self-Consistent Equations Including Exchange and Correlation Effects, *Phys. Rev.* **1965** *140*, A1133–A1138.

[8] A. D. Becke, Perspective: Fifty years of density-functional theory in chemical physics, *J. Chem. Phys.* **2014**, *140*, 18A301.

[9] M. Born, J. R. Oppenheimer, Zur Quantentheorie der Molekeln, *Ann. Phys.* **1927**, *84*, 457–484.

[10] M. Levy, J. P. Perdew, Hellmann-Feynman, virial, and scaling requisites for the exact universal density functionals. Shape of the correlation potential and diamagnetic susceptibility for atoms*, Phys. Rev. A: At., Mol., Opt. Phys.* **1985**, *32*, 2010–2021.

[11] J. P. Perdew, K. Burke, M. Ernzerhof, Generalized Gradient Approximation Made Simple, *Phys. Rev. Lett.* **1996**, *77*, 3865–3868.

[12] J. P. Perdew, K. Burke, M. Ernzerhof, Generalized Gradient Approximation Made Simple [*Phys. Rev. Lett.* **1996**, *77*, 3865], *Phys. Rev. Lett.* **1997**, *78*, 1396.

[13] A. D. Becke, E. R. Johnson, A simple effective potential for exchange, *J. Chem. Phys.* **2006**, *124*, 221101.

[14] F. Tran, P. Blaha, Accurate Band Gaps of Semiconductors and Insulators with a Semilocal Exchange-Correlation Potential, *Phys. Rev. Lett.* **2009**, *102*, 226401.

[15] J. A. Camargo-Martínez, R. Baquero, Performance of the modified Becke-Johnson potential for semiconductors, *Phys. Rev. B: Condens. Matter Mater. Phys.* **2012**, *86*, 195106.

[16] A. D. Becke, M. R. Roussel, Exchange holes in inhomogeneous systems: A coordinate-space model, *Phys. Rev. A* **1989**, *39*, 3761–3767.

[17] N. Troullier, J. L. Martins, Efficient pseudopotentials for plane-wave calculations, *Phys. Rev. B: Condens. Matter Mater. Phys.* **1991**, *43*, 1993–2006.

[18] D. R. Hamann, M. Schlüter, C. Chiang, Norm-Conserving Pseudopotentials, *Phys. Rev. Lett.* **1979**, *43*, 1494–1497.

[19] J. Hafner, *Ab-initio* simulations of materials using VASP: Density-functional theory and beyond, *J. Comput. Chem.* **2008**, *29*, 2044–2078.

[20] S. G. Louie, S. Froyen, M. L. Cohen, Nonlinear ionic pseudopotentials in spin-density-functional calculations, *Phys. Rev. B: Condens. Matter Mater. Phys.* **1982**, *26*, 1738–1742.

[21] P. E. Blöchl, Projector augmented-wave method, *Phys. Rev. B: Condens. Matter Mater. Phys.* **1994**, *50*, 17953–17979.

[22] H. Ebert, D. Koedderitzsch, J. Minár, Calculating condensed matter properties using the KKR-Green's function method–recent developments and applications, *Rep. Prog. Phys.* **2011**, *74*, 96501.

[23] D. Sébilleau, K. Hatada, H. Ebert, *Multiple Scattering Theory for Spectroscopies,* Springer, **2018**.

[24] J. Korringa, On the calculation of the energy of a Bloch wave in a metal, *Physica* **1947**, *13*, 392–400.

[25] W. Kohn, N. Rostoker, Solution of the Schrödinger Equation in Periodic Lattices with an Application to Metallic Lithium, *Phys. Rev.* **1954**, *94*, 1111–1120.

[26] B. L. Gyorffy, G. M. Stocks, Theory of Soft X-Ray Emission from Alloys, IN *Band Structure Spectroscopy of Metals and Alloys,* Academic Press London, **1973**.

[27] A. Gonis, W. H. Butler, *Multiple Scattering in Solids*, Springer; **1999**.

[28] J. Zabloudil, R. Hammerling, L. Szunyogh, P. Weinberger, *Electron Scattering in Solid Matter: A Theoretical and Computational Treatise*, Springer, **2005**.

[29] J. S. Faulkner, Scattering theory and cluster calculations, *J. Phys. C Solid State Phys.* **1977**,*10*, 4661–4670.

[30] J. S. Faulkner, Multiple-scattering approach to band theory, *Phys. Rev. B: Condens. Matter Mater. Phys.* **1979**, *19*, 6186–6206.

[31] J. S. Faulkner, G. M. Stocks, Calculating properties with the coherent-potential approximation, *Phys. Rev. B: Condens. Matter Mater. Phys.* **1980**, *21*, 3222–3244.

[32] B. L. Gyorffy, G. M. Stocks, Electronic States in Random Substitutional Alloys: The CPA and Beyond, IN *Electrons in Finite and Infinite Structures*, Plenum Press, **1976**.

[33] Y. Onodera, M. Okazaki, Relativistic Theory for Energy-Band Calculation, *J. Phys. Soc. Jpn.* **1966**, *21*, 1273–1281.

[34] P. Strange, H. Ebert, J. B. Staunton, B. L. Gyorffy, A relativistic spin-polarised multiple-scattering theory, with applications to the calculation of the electronic structure of condensed matter, *J. Phys. Condens. Matter* **1989**, *1*, 2959–2975.

[35] P. Weinberger*, Electron Scattering Theory for Ordered and Disordered Matter*, Oxford University Press, **1990**.

[36] P. Strange, *Relativistic Quantum Mechanics*, Cambridge University Press, **1998**.

[37] H. Ebert, *Electronic Structure and Physical Properties of Solids*, Springer, **2000**.

[38] J. Minár, L. Chioncel, A. Perlov, H. Ebert, M. I. Katsnelson, A. I. Lichtenstein, Multiple-scattering formalism for correlated systems: A KKR-DMFT approach, *Phys. Rev. B: Condens. Matter Mater. Phys.* **2005**, *72,* 045125.

[39] M. H. Sadd, *Elasticity theory, applications, and numerics*, Elsevier Butterworth Heinemann,**2005**.

[40] N. W. Ashcroft, N. D. Mermin, *Solid state physics,* Saunders college, **1976**.

[41] Y. Le Page, P. Saxe, Symmetry-general least-squares extraction of elastic data for strained materials from *ab initio* calculations of stress, *Phys. Rev. B: Condens. Matter Mater. Phys.* **2002**, *65*, 104104.

[42] S. L. Shang, Y. Wang, Z.K. Liu, First-principles elastic constants of α- and θ-Al_2O_3, *Appl. Phys. Lett.* **2007**, *90*, 101909.

[43] W. Voigt, *Lehrbuch der Kristallphysik (mit Ausschluss der Kristalloptik)*, B. G. Teubner, **1946**.

[44] A. Reuss, Berechnung der Fließgrenze von Mischkristallen auf Grund der Plastizitätsbedingung für Einkristalle, *Z. Angew. Math. Mech.* **1929**, *9*, 49–58.

[45] R. Hill, The Elastic Behaviour of a Crystalline Aggregate, *Proc. Phys. Soc. A* **1952**, *65*, 349–354.

3 Orange-Emitting $Li_4Sr_4[Si_4O_4N_6]O:Eu^{2+}$–a Layered Lithium Oxonitridosilicate Oxide

published in: *Inorg. Chem.* **2018**, *57*, 14304–14313.

authors: Robin Niklaus, Lukas Neudert, Juliane Stahl, Peter J. Schmidt and Wolfgang Schnick

DOI: 10.1021/acs.inorgchem.8b02391

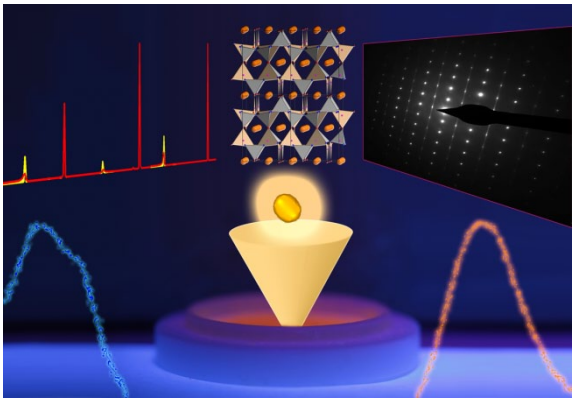

Abstract We report on the structure and properties of the lithium oxonitridosilicate oxide $Li_4Sr_4[Si_4O_4N_6]O:Eu^{2+}$ obtained from solid-state metathesis. The crystal structure was solved and refined from single-crystal X-ray data in the space group $P4_2/nmc$ (no. 137) [$Z = 2$, $a = 7.4833(6)$, $c = 9.8365(9)$ Å, and $R1(obs) = 0.0477$]. The structure of $Li_4Sr_4[Si_4O_4N_6]O:Eu^{2+}$ is built up from a layered 2D network of SiN_3O tetrahedra and exhibits stacking disorder. The results are supported by transmission electron microscopy and energy-dispersive X-ray spectroscopy as well as lattice energy, charge distribution, and density functional theory (DFT) calculations. Optical measurements suggest an indirect band gap of about 3.6 eV, while DFT calculations on a model free of stacking faults yield a theoretical electronic band gap of 4.4 eV. Samples doped with Eu^{2+} exhibit luminescence in the orange spectral range ($\lambda_{em} \approx 625$ nm; full width at half-maximum ≈ 4164 cm^{-1}; internal quantum efficiency at room temperature = 24%), extending the broad field of phosphor materials research toward the sparsely investigated materials class of lithium oxonitridosilicate oxides.

3.1 Introduction

The increase of the complexity with regard to the elemental and structural compositions of nitride phosphor materials has recently led to unexpected multinary phosphors like $Li_{38.7}RE_{3.3}Ca_{5.7}[Li_2Si_{30}N_{59}]O_2F:Ce^{3+}$ (*RE* = La, Ce, Y).[1] This process forebodes the importance of extending fundamental research toward similar complex systems by offering a number of tunable set screws in terms of composition and structural phenomena, which, in turn, can influence the materials properties. However, because of the difficulty of targeted synthesis toward phosphor materials from scratch, it ever so often resembles a roll of the dice. This is partly because of a number of competing reactions and possible thermodynamic sinks. This makes it difficult to control the synthesis and respective formation conditions of such multinary component systems, which often leads to microcrystalline samples. However, high-throughput

screening methods like single-particle diagnosis in combination with transmission electron microscopy (TEM) can help to facilitate the identification of novel compounds for which structure determination is not straightforward, such as $La_{24}Sr_{14-7x}[Si_{36}N_{72}](O_{1-x}F_x)_{14}$ (x = 0.489).[2,3] The subsequent migration into conventional synthetic optimization strategies, upon the identification of promising materials, can then be used to optimize bulk synthesis. With regard to maintaining at least a partially directed synthesis approach, phosphor host structures such as $Li_2Ca_2[Mg_2Si_2N_6]$, $Ca_3Mg[Li_2Si_2N_6]$, and $Ca_2Mg[Li_4Si_2N_6]$ exemplify that formal substitution of alkaline-earth metals by significantly smaller and lighter cations such as Li appears promising in order to increase the structural diversity, while maintaining fundamental structure motifs.[4–6] That is, these compounds can all be considered to be Ca-substituted variants of $Ca_5[Si_2N_6]$. Similar analogies are known from Li-substituted garnet-type materials, which have led to a number of suitable solid electrolytes.[7–9] This coincides with a general trend to incorporate Li into phosphor host structures because it may function both as a countercation like in $Li_2Ca_2[Mg_2Si_2N_6]$ and $Ca_{18.75}Li_{10.5}[Al_{39}N_{55}]$ and as part of the anionic network like in $Sr[LiAl_3N_4]$, $Sr_4[LiAl_{11}N_{14}]$, or $Ca_3Mg[Li_2Si_2N_6]$.[4,5,10–13] All of which exhibit interesting luminescence properties upon Eu^{2+} or Ce^{3+} doping with auxiliary examples such as $LiSi_2N_3:Eu^{2+}$, $Ba[Li_2(Al_2Si_2)N_6]:Eu^{2+}$, and $Ba_2LiSi_7AlN_{12}:Eu^{2+}$ at hand.[14–16] Undeniably, Li-containing nitridosilicates have attracted a lot of attention in recent years as novel phosphor materials.

With regard to the exploration of new and diverse anionic networks and frameworks, the extensive study of oxonitridosilicates has further promoted the synthesis of Eu-doped phosphor materials such as β-sialon, and the layered materials $(Sr,Ba)Si_2O_2N_2$ and $RE_{26}Ba_6[Si_{22}O_{19}N_{36}]O_{16}$ (*RE* = Y, Tb).[17–22] $M(Si_2O_2N_2)$ (*M* = Ca, Sr, Ba) represents an excellent example as to how the choice of the cation may further impact the structural properties. Alterations of layers and metal coordination are introduced upon going from $CaSi_2O_2N_2$ ($P2_1$) to $SrSi_2O_2N_2$ ($P1$) and $BaSi_2O_2N_2$ (*Pbcn*), impacting the luminescence properties upon Eu^{2+} doping. Concurrently, additional intergrowth occurs upon different mixed occupation ratios on the (Sr, Ba) site between the latter two.[21,23] Especially for such layered compounds, real structure phenomena such as stacking disorder and intergrowth can pose major obstructions upon structure determination in the absence of suitable single crystals or even in the attempted confirmation of bulk syntheses. Challenges can be successfully tackled by advanced analytical methods such as aberration-corrected TEM. Next to a detailed elucidation of the latter compounds by various TEM methods, applications comprise the elucidation of modulated structures and the differentiation of heavy cations with a roentgenographically similar Z-contrast.[3,20,24] In this contribution, we present the synthesis and characterization of the novel orange luminescent layered lithium oxonitridosilicate oxide $Li_4Sr_4[Si_4O_4N_6]O:Eu^{2+}$, extending the sparse field of lithium oxonitridosilicate compounds. The structure was solved by single-crystal X-ray diffraction (XRD). TEM investigations confirm the elemental composition and cell metrics while revealing low-level stacking disorder in the *ab* plane in both single crystals and bulk samples. Electronic and mechanical properties were calculated by subsidiary density functional theory (DFT) calculations. Our study combines different interlocking analytical methods that

together allow for concluding discussions on the possible impact of real-structure phenomena on the resulting luminescence properties relevant to future materials design considerations.

3.2 Experimental Section

3.2.1 Synthesis

All synthesis steps were performed in an argon-filled glovebox (Unilab, MBraun, Garching; O_2<1 ppm; H_2O<1 ppm) or in flame-dried glassware on a Schlenk line. The screening of different product mixtures yielded a minority phase of single crystals of $Li_4Sr_{3.62}Eu_{0.38}[Si_4O_4N_6]O$ from reacting a composite mixture of SrF_2 (0.17 mmol, 21.7 mg, Sigma-Aldrich, 99.99%), "$Si(NH)_2$" (0.18 mmol, 10.6 mg), LiN_3 (0.38 mmol, 19 mg), Mn (0.84 mmol, 46.4 mg, Alfa Aesar, 99.95%), and EuF_3 (0.009 mmol, 1.8 mg, Sigma-Aldrich, 99.99%).[25,26] The ground starting materials were placed in a Ta ampule, which was supposedly contaminated with traces of O during welding. The ampule was placed in a tube furnace under vacuum, heated to 950 °C at 5 K min^{-1}, and kept at 950 °C for 32 h before the furnace was turned off. The yellow-to-orange single crystals were identified out of the heterogeneous product by UV illumination. Following structure determination, the synthesis was optimized to obtain bulk samples of $Li_4Sr_4[Si_4O_4N_6]O:Eu^{2+}$. Powder samples of $Li_4Sr_4[Si_4O_4N_6]O$ were synthesized from SrF_2 (0.18 mmol, 22.2 mg; Sigma-Aldrich, 99.99%), SrH_2 (0.18 mmol, 15.9 mg; Materion, 99.7%), LiN_3 (0.363 mmol, 17.8 mg), $Li(NH_2)$ (0.206 mmol, 7.6 mg, Sigma-Aldrich, 95%), Li_2O (0.45 mmol, 13.56 mg, Schuchardt, 98%), and "$Si(NH)_2$" (0.36 mmol, 21.1 mg). CsI (0.2 mmol, 53 mg, Chempur, 99.9%) was used as a flux. The starting materials were thoroughly ground in an agate mortar and filled into a Nb ampule. The ampule was subsequently welded shut and placed in a tube furnace (type AXIO 10/450, Hüttinger Elektronik, Freiburg, Germany; maximal electrical output 10 kW), heated under vacuum to 900 °C for 3 h, maintained at that temperature for 32 h, and finally quenched to room temperature by switching off the furnace. The resulting product was washed with dry ethanol to remove excess CsI. The filter residue yielded a colorless mixture of variable amounts of LiF, Li_2SiN_2, and nanocrystalline $Li_4Sr_4[Si_4O_4N_6]O$ as the majority phase. The addition of EuF_3 during synthesis with a nominal concentration of 1 mol % Eu related to Sr yielded a powder of $Li_4Sr_4[Si_4O_4N_6]O:Eu^{2+}$ with yellow body color. All such samples show strong yellow-orange luminescence under irradiation with blue light. Doped and nondoped products are stable toward O_2 yet sensitive to the extended exposure of water.

3.2.2 Single-Crystal XRD

Single crystals of $Li_4Sr_4[Si_4O_4N_6]O:Eu^{2+}$ were isolated and mounted on MicroMounts (MiTeGen) with an aperture size of 20 µm. XRD data were measured with a Bruker D8 Venture diffractometer with a rotating anode (Mo Kα radiation). Absorption correction was performed using *SADABS*.[27] The crystal structure was solved using direct methods (*SHELXS*) and refined by a least-squares method (*SHELXL*).[28–30] Details on the crystal structure investigation can be obtained from the Cambridge Crystallographic Data Centre (CCDC) upon quoting the CCDC code 1862968.

3.2.3 Powder XRD (PXRD)

PXRD measurements were carried out on ground samples, which were loaded into silica glass capillaries of 0.2 mm diameter with a wall thickness of 0.01 mm (Hilgenberg GmbH, Malsfeld, Germany). Diffraction data were obtained using a STOE STADI P diffractometer [Cu $K\alpha_1$ radiation, Ge(111) monochromator, Mythen1K detector] in modified parafocusing Debye-Scherrer geometry. Rietveld refinements were carried out with TOPAS *Academic V4.1* software by applying the fundamental parameters approach (direct convolution of source emission profiles, axial instrument contributions, crystallite size, and microstrain effects).[31–34] Preferred orientation was taken into account by using fourth-order spherical harmonics, and anisotropic broadening of the reflection profiles was refined using the LeBail-Jouanneaux algorithm.[35] Absorption effects were corrected using the calculated absorption coefficient from XRD refinements.

3.2.4 UV/Vis Spectroscopy

A diffuse-reflectance spectrum of $Li_4Sr_4[Si_4O_4N_6]O$ was measured with a Jasco V-650 UV/vis spectrophotometer in the range of 240–800 nm with a 5 nm step size. The device is equipped with a deuterium/halogen lamp (Czerny-Turner monochromator with 1200 lines mm^{-1} concave grating, photomultiplier tube detector).

3.2.5 Fourier Transform Infrared (FTIR) Spectroscopy

FTIR spectroscopy on $Li_4Sr_4[Si_4O_4N_6]O:Eu^{2+}$ was carried out with a Perkin Elmer BXII spectrometer using the attenuated-total-reflectance (ATR) method.

3.2.6 Computational Details

The structural relaxation of $Li_4Sr_4[Si_4O_4N_6]O$ was performed with the Vienna ab initio simulation package (*VASP*).[36–38] The total energy of the unit cell was converged to 10^{-7} eV/atom with residual atomic forces below 5×10^{-3} eV $Å^{-1}$. The exchange correlation was treated within the generalized gradient approximation (GGA) of Perdew, Burke, and Ernzerhof and the projector-augmented-wave method.[39–42] A plane-wave cutoff of 535 eV was chosen for calculations with a Brillouin zone sampling on a *Γ*-centered *k*-mesh produced from the method of Monkhorst and Pack of $7 \times 7 \times 6$.[43] Additional calculations were performed with the modified Becke–Johnson formalism (GGA-mbj) to treat the electronic band gap.[44–46] In order to obtain elastic constants and moduli, calculations of the elastic tensors were conducted by deriving the stress–strain relationship from six finite lattice distortions of the crystal utilizing displacements of ±0.015 Å.[47]

3.2.7 Luminescence

Photoluminescence measurements were performed on nanocrystalline powder samples in poly(tetrafluoroethylene) sample holders using an in-house-built system based on a 5.3-in. integrating sphere and a spectrofluorimeter equipped with a 150 W Xe lamp and two 500 mm Czerny–Turner monochromators (1800 grooves mm^{-1} and 250/500 nm blaze gratings) with a

spectral range from 230 to 820 nm. The internal quantum efficiency (IQE) of the samples was determined by comparing integrated emission intensities and absorption at excitation wavelength with standard materials ($BaSO_4$, Merck, for white standard DIN 5033; commercial $(Sr,Ca)AlSiN_3:Eu^{2+}$, Mitsubishi Chemical, and $Y_3Al_5O_{12}:Ce^{3+}$, Philips) at room temperature. Thermal quenching of the emission was investigated with an AvaSpec-2048 spectrometer and a stabilized light-emitting-diode (LED) light source (450 nm) for sample excitation. Samples were measured in a temperature range from room temperature to 330 °C with a step size of ≈24 °C in Cu-plated sample holders that were temperature-controlled with an IR lamp. The cryospectroscopy setup covers the range from 300 to 6 K. The measurement was performed on a thick-bed powder layer of the specimen positioned in an evacuated cooling chamber. Cooling was done via a liquid-He compressor system from Advance Research System Inc. (ARS4HW).The samples were measured by a fiber-coupled spectroscopy system containing a thermally stabilized LED light source and a fiber-optic spectrometer from Ocean Optics (HR2000+ES).

3.2.8 TEM

The TEM investigations were done on crystallites originating from several samples of $Li_4Sr_4[Si_4O_4N_6]O:Eu^{2+}$. The crystals were crushed and suspended in ethanol and then drop-casted onto a Cu grid covered with a holey C film (PLANO GmbH, Wetzlar, Germany). TEM experiments were performed on a Titan Themis 60–300 microscope (FEI, Hillsboro, OR) operated at a 300 kV acceleration voltage and equipped with an X-FEG, monochromator, C_s corrector, and windowless four-quadrant Super-X EDX detector (acquisition time 45 s). The TEM images were recorded using a 4K × 4K Ceta CMOS camera (FEI, Hillsboro, OR). For data evaluation, the following software were used: *Digital Micrograph* and *ProcessDiffraction7* [geometric calculations for selected-area electron diffraction (SAED)], *JEMS* (SAED simulations), and *ES Vision* (evaluation of the EDX spectra).[48–51]

3.3 Results and Discussion

3.3.1 Synthesis and Chemical Analysis

For the synthesis of $Li_4Sr_4[Si_4O_4N_6]O:Eu^{2+}$, highly reactive starting materials such as SrF_2, "$Si(NH)_2$", SrH_2, and EuF_3 were used. The synthesis route yields typically nanocrystalline aggregates with single-crystal sizes of approximately 1 µm on average. A few crystals of larger size (≈10 µm) could be isolated for single-crystal analysis from a single reaction batch. The composition could be corroborated by TEM–EDX measurements on representative crystals of different batches (Table S3.1). ATR-IR spectroscopy further indicates the absence of N–H groups (Figure S3.1).

3.3.2 Crystal Structure

The crystal structure of $Li_4Sr_4[Si_4O_4N_6]O:Eu^{2+}$ was solved and refined in the space group $P4_2/nmc$ (no. 137). All atoms aside from Li were refined anisotropically. The crystallographic details are given in Table 3.1.

Table 3.1 Crystallographic data of the single-crystal structure determination of $Li_4Sr_{3.62(3)}Eu_{0.38(3)}[Si_4O_4N_6]O$

refined composition	$Li_4Sr_{3.62(3)}Eu_{0.38(3)}[Si_4O_4N_6]O$
formula mass [g·mol^{-1}]	679(2)
crystal system	tetragonal
space group	$P4_2/nmc$ (no. 137)
lattice parameters [Å]	a = 7.4833(6), c = 9.8365(9)
cell volume [Å^3]	550.84(10)
formula units / unit cell	2
X-ray density [g cm^{-3}]	4.096
abs. coefficient [μ mm^{-1}]	20.033
absorption correction	multiscan
diffractometer	Bruker D8 Venture
radiation [Å]	Mo-Kα (λ = 0.71073)
F(000)	623
θ range [°]	3.421 ≤ θ ≤ 30.497
independent reflections	475 [R_{int} = 0.0430]
refined parameters / restraints	35 / 0
GoF	1.094
$R1$ (all data/for $I > 2\sigma(I)$)	0.0477 / 0.0282
$wR2$ (all data/for $I > 2\sigma(I)$)	0.0633 / 0.0576
$\Delta\rho_{max}$ / $\Delta\rho_{min}$ (e Å^{-3})	0.59 / -0.75

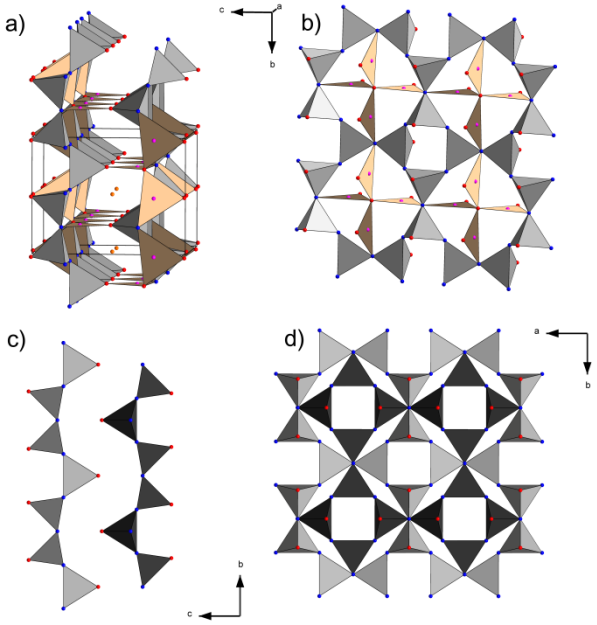

Figure 3.1 Different projections of the crystal structure of $Li_4Sr_4[Si_4O_4N_6]O:Eu^{2+}$ with SiN_3O tetrahedra (gray/black), N atoms (blue), O atoms (red), Li atoms (pink), and mixed Sr/Eu atoms (orange). (a) Projection along nearly [001] with the unit cell outlined in black. (b) Representation of a single layer forming *vierer* and *achter* rings enclosing trigonal-planar-coordinated Li. (c and d) Representation of SiN_3O layers along [100] (c) and [001] (d) illustrating the layered composition.

Additional crystallographic information is given in Tables S3.2–S3.4. The crystal structure within the unit cell and different structure motifs of $Li_4Sr_4[Si_4O_4N_6]O:Eu^{2+}$ are depicted in Figure 3.1a–d. The structure is composed of a layerlike network of doubly bridging Q^3-type SiN_3O tetrahedra stacked along [001].

The atomic ratio Si:(O/N) within the network is 2:5, which corresponds to the regular value found in single-layer silicates.[52] The crystal structure of $Li_4Sr_4[Si_4O_4N_6]O:Eu^{2+}$ exhibits motifs very similar to those of the previously reported nitridosilicate nitride $Li_2Sr_4[Si_2N_5]N$ (space group $I\bar{4}m2$).[53] Its structural relationship can be formally understood by the removal of half of the Sr atoms in the layered interspace of $Li_2Sr_4[Si_2N_5]N$ combined with a 180° twist of every second layer. In $Li_4Sr_4[Si_4O_4N_6]O:Eu^{2+}$, an additional isolated O atom is located centric of each *achter* ring. The cation coordination polyhedra are depicted in Figure 3.2. The Sr/Eu site is coordinated in the interspace of the layered network by O and N atoms of the SiN_3O tetrahedra, forming a distorted Johnson polyhedron (J_{49}). Li is coordinated trigonal-planar by the isolated O atom, and the N and terminal O atoms of two independent SiN_3O tetrahedra. The prolate nature of the O displacement ellipsoid of the isolated O2 is likely to originate from its higher degree of vibrational freedom compared to anions of the rigid and covalent oxonitridosilicate network. A possible split position and partial occupancy were further ruled out from difference Fourier mapping (Figure S3.2). CHARDI analysis further corroborates the cation assignment (Table S3.5).

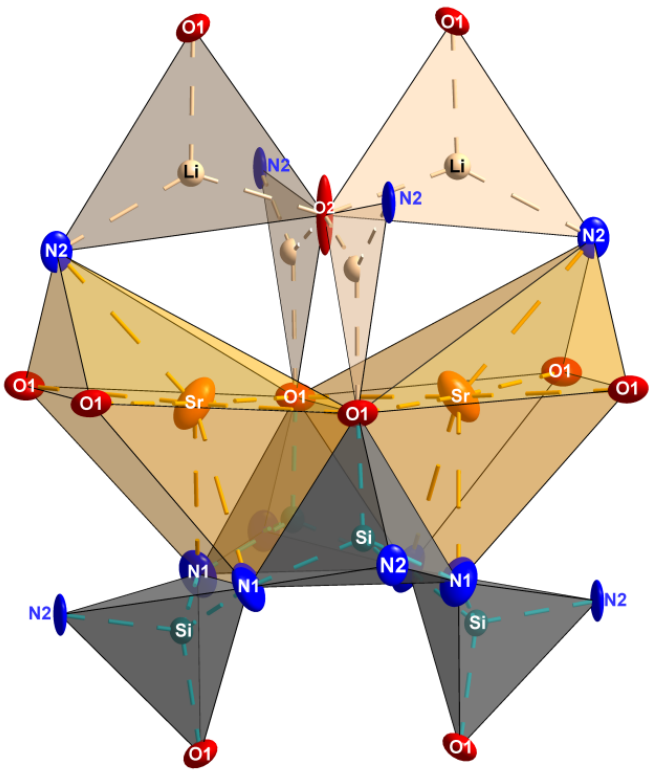

Figure 3.2 Coordination spheres of the Sr, Si, and Li atom sites in $Li_4Sr_4[Si_4O_4N_6]O:Eu^{2+}$. Displacement ellipsoids shown with 90% probability. Color code: Sr/Eu, orange; Si, turquoise; Li, ivory; O, red; N, blue.

The values for the tetrahedral bond lengths range from 1.692(3) Å (Si–O) to 1.708(2)–1.712(8) Å (Si–N), in good agreement with values found in comparable oxonitridosilicate compounds like $Ce_4[Si_4O_4N_6]O$ or $SrSi_2O_2N_2$.[52,54] The same applies for the Sr–O [2.580(2)–2.717(2) Å], Sr–N [2.833(4)–2.846(2) Å], Li–O [1.955(8)–1.967(8) Å], and Li–N [2.142(8) Å] interatomic distances.[53,55] In order to determine the composition of the samples, a Rietveld refinement has been carried out based on a PXRD pattern from an optimized synthesis bulk sample. A representative refinement is seen in Figure 3.3. It indicates $Li_4Sr_4[Si_4O_4N_6]O:Eu^{2+}$ as the majority phase (≈84%) next to small amounts of side phases like Li_2SiN_2 and LiF. A few minor unknown reflections were observed that could not be assigned or indexed. Furthermore, a broadening and intensity misfit for the reflections (011), (012), and (211) was observed. Hence, in order to corroborate the chemical composition, single-crystal unit-cell parameters, ruling out unidentified superstructures and in order to reveal further possible real-structure phenomena, TEM investigations were conducted. Investigations comprise different bulk samples along with the single crystals used for X-ray structure determination.

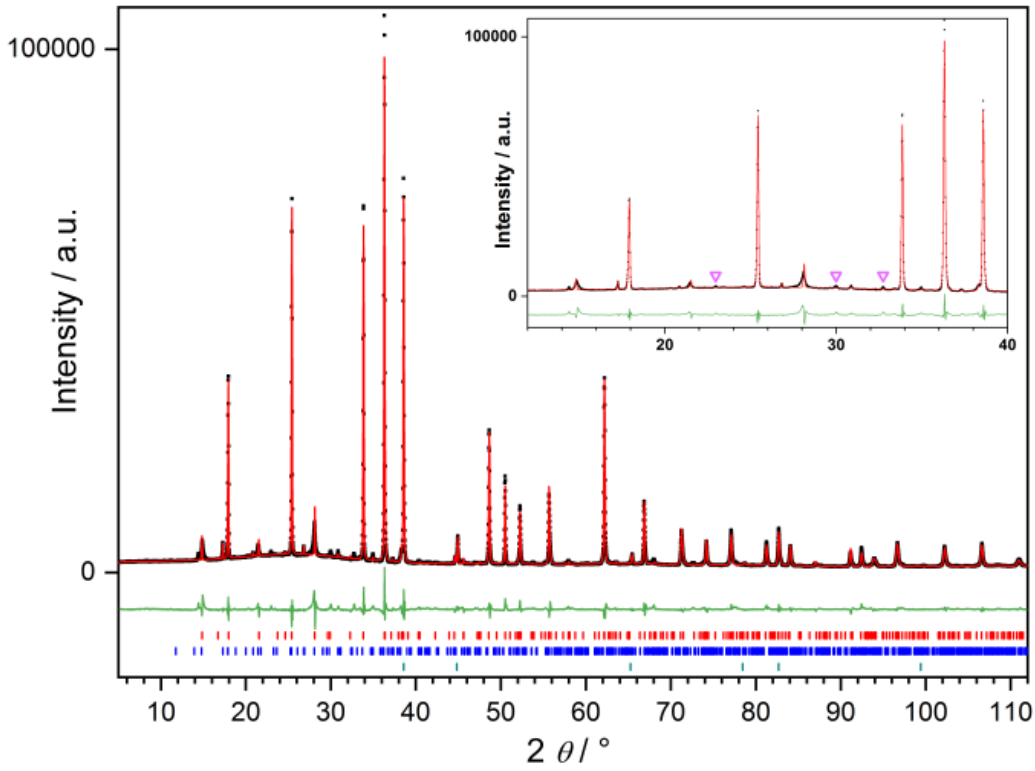

Figure 3.3 Rietveld refinement for a washed sample of $Li_4Sr_4(Si_4O_4N_6)O:Eu^{2+}$. Experimental data are in black, the Rietveld fit is the red line, and the difference plot is the green line. Minor unknown reflections (purple) are highlighted as triangles in the inset. Intensity misfits can be explained by stacking faults as observed by HRTEM investigations. Reflection positions for $Li_4Sr_4(Si_4O_4N_6)O:Eu^{2+}$ (red bars, 84 wt %), Li_2SiN_2 (blue bars, 5 wt%), and LiF (green bars, 11 wt%).

3.3.3 TEM and EDX

From a representative SAED tilt series of crystallites, as depicted in Figure 3.4, it was possible to determine the unit-cell parameters (tetragonal with a = 7.4 Å and c = 9.7 Å). They agree with the unit-cell parameters from X-ray structure determination. In accordance with Laue class 4/*mmm*, the SAED patterns along the zone axes [100], [110], and [011] show *mm*2 symmetry, and the reflection intensities approximately match those of the corresponding kinematical simulations (Figure 3.4, bottom). EDX measurements on several crystallites of $Li_4Sr_4[Si_4O_4N_6]O:Eu^{2+}$ further corroborate the chemical composition (Table S3.1).

Additional diffuse intensity along [001]* was observed in zone axes perpendicular to c like [100], [110], and [120]. It is likely that the diffuse intensity is caused by structural differences in the *ab* planes stacked along c. Figure 3.5 depicts HRTEM investigations on thicker crystallites of the sample from which the single crystal was taken and where the diffuse intensity is more visible. It could be shown that areas of approximately 100 nm^2 are enough to cause diffuse intensity in the corresponding Fourier transforms similar to SAED (see its magnification in Figure S3.3). This is in agreement with the fact that no diffuse intensities could be observed for such crystallites with very thin crystal areas (Figure S3.4).

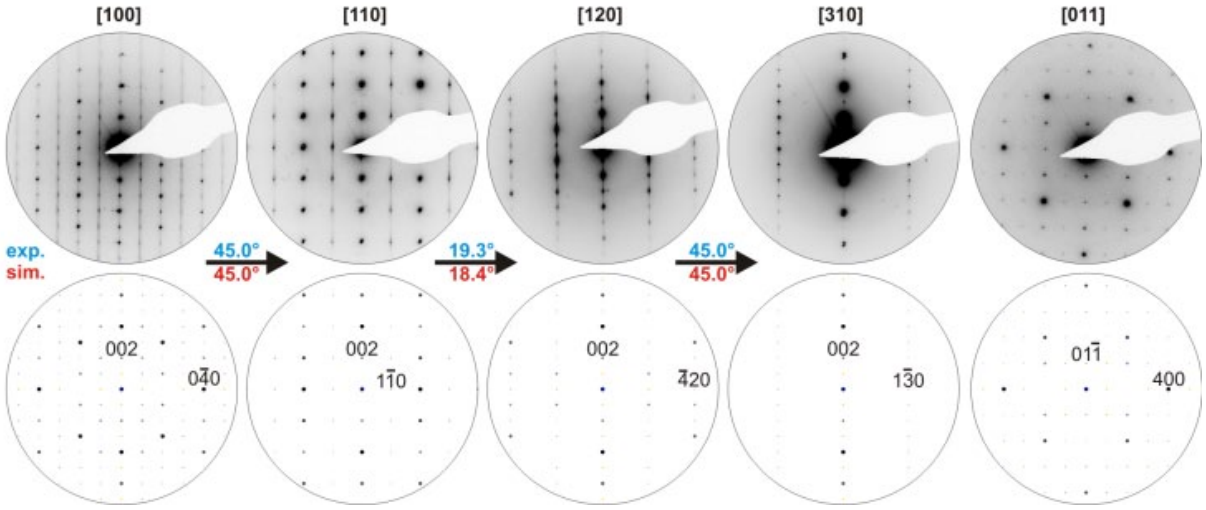

Figure 3.4 SAED tilt series of a representative crystallite of $Li_4Sr_4[Si_4O_4N_6]O:Eu^{2+}$ with experimental patterns (top) and tilt angles (blue) as well as simulated patterns (bottom) and tilt angles (red) based on the refined structure model from single-crystal X-ray data. Selected reflections are labeled with indices. Diffuse intensities are observed along [001].

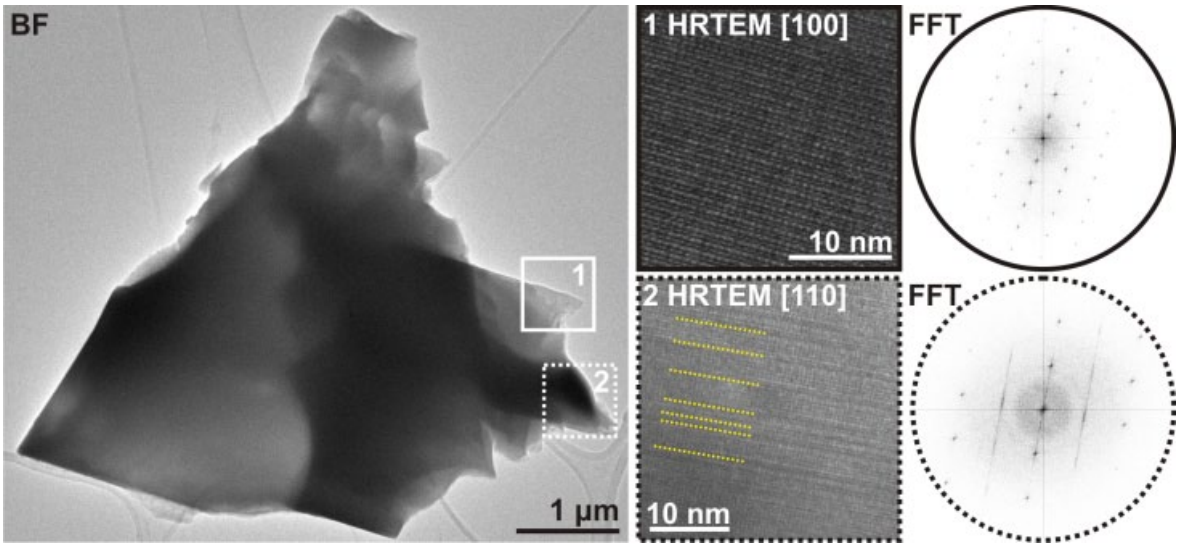

Figure 3.5 Bright-field image (left) and HRTEM images viewed along the [100] and [110] zone axes (middle) with corresponding Fourier transforms (right). Thin area 1 (highlighted by the solid line) shows no diffuse intensity in contrast to the thicker area 2 (highlighted by the dotted line). Contrast variations perpendicular to *c* possibly caused by defect layers are highlighted in yellow.

The observance of diffuse scattering can be in line with the broadening of reflections in the PXRD patterns and corroborates an assumed stacking disorder. Subsequently, this effect could be approximated by DIFFaX simulations by the introduction of stacking faults of about 2.5% impacting the reflections in question, as shown in Figure 3.6.[56] The chosen stacking variant along with the matrix–vector relationship to the original layer is found in Figure S3.5.

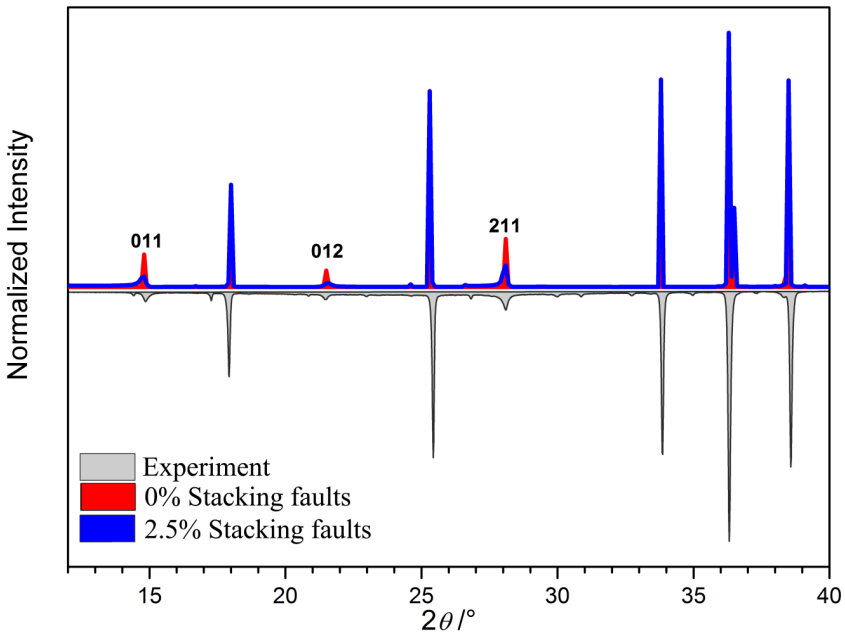

Figure 3.6 DIFFaX simulation of a possible stacking variant of $Li_4Sr_4[Si_4O_4N_6]O:Eu^{2+}$ indicating a broadening of selected reflections upon the introduction of low levels of stacking faults. Simulation based on a structure from single-crystal data.

3.3.4 MAPLE

The assignment of O and N from single-crystal refinement was further corroborated by calculations of the lattice energies by the MAPLE concept.[57–60] Results are shown in Table 3.2.

Table 3.2 Results of the MAPLE calculations [kJ/mol] for $Li_4Sr_4[Si_4O_4N_6]O$

	$Li_4Sr_4[Si_4O_4N_6]O$
Sr^{2+}	1666.653
Si^{4+}	9719.430
Li^{+}	864.558
$N1^{[2]}$	5464.986
$N2^{[2]}$	5401.430
$O1^{[1]}$	2469.910
$O2^{[0]}$	1550.042
Total MAPLE	93139 kJ/mol
$^4/_3$ Si_3N_4 + 4 SrO + Li_2O + $^2/_3$ Li_3N:	93479 kJ/mol

[a] Typical partial MAPLE values (kJ mol^{-1}): Sr^{2+}, 1500–2300; Si^{4+}, 9000–10200; $N^{[2]3-}$, 4600–6000; Li^{+}, 550–860; $O^{[1]2-}$, 2000–2800.

The total MAPLE value is in good agreement (Δ_E = 0.36%) with the one obtained by formation from binary compounds. Furthermore, partial MAPLE values of the different atoms are in the typical range of comparable compounds in the literature, confirming the chosen N, O, and Li assignments.[53,61] For $O2^{[0]}$, there is no corresponding range of MAPLE values, but lowered values with respect to O atoms of higher bridging degree have been observed for other oxonitridosilicate oxides before.[52,62,63] We therefore conclude that the lowered MAPLE value for O2 derives first from it not being incorporated into the rigid nitridosilicate network and second from its prolate displacement ellipsoid not being described accurately by point-charge approximations.

3.3.5 DFT Calculations

In order to calculate the electronic band gap and mechanical properties of $Li_4Sr_4[Si_4O_4N_6]O$, we performed additional DFT calculations.

3.3.5.1 Electronic Structure

Calculations of the electronic density of states for $Li_4Sr_4[Si_4O_4N_6]O$ are depicted in Figure 3.7. $Li_4Sr_4[Si_4O_4N_6]O$ exhibits insulating properties with an electronic band gap of about 4.4 eV. This increase compared to that of $Li_2Sr_4(Si_2N_5)N$, which was estimated to have an E_g of about 2.4 eV, can possibly be attributed to the removal of one Sr layer within $Li_4Sr_4[Si_4O_4N_6]O$. The elastic constants, resulting moduli, and Debye temperature (θ_D) are depicted in Table 3.3 and are obtained from common relations.[64–69] The calculations of elastic constants are in line with the layered structure of $Li_4Sr_4[Si_4O_4N_6]O$ because C_{11} and C_{22} (*a* and *b* directions) are significantly increased and less compressible with respect to C_{33} (*c* direction).

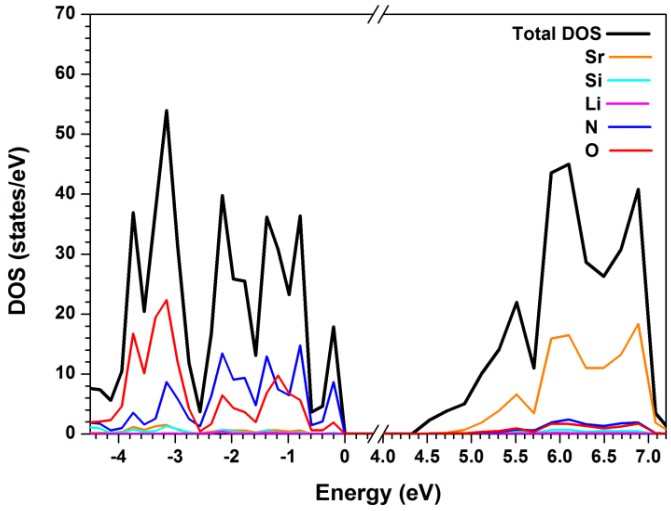

Figure 3.7 Density of states of $Li_4Sr_4(Si_4O_4N_6)O$ as calculated with the mBJ functional.

The Debye temperature (θ_D) is a prominent proxy for phosphor materials, denoting the rigidity of the crystal.[70–72] An increase in θ_D formally equates to an increase in rigidity and concomitantly energetically elevated lattice vibrations, which are harder to excite. Dopant atoms such as Eu^{2+} exhibiting transitions to protruding Eu 5*d* orbitals upon excitation should, therefore, be less likely affected by electron-phonon coupling effects with the host structure if embedded in a highly rigid network of anions. Compared to nitride compounds with higher condensation degrees such as $SrLiAl_3N_4$ (θ_D = 716 K) or $Sr_2Si_5N_8$ (θ_D = 702 K),[72] the lower θ_D value of 592 K for $Li_4Sr_4[Si_4O_4N_6]O:Eu^{2+}$, while reflecting both the low bulk and shear moduli in line with the layered nature of $Li_4Sr_4[Si_4O_4N_6]O:Eu^{2+}$, can possibly indicate an extenuated thermal quenching.

Table 3.3 Calculated elastic constants C_{nm}, bulk (B), shear (G) and Young's (Y) moduli in GPa, Debye temperature (θ_D) in K and Poisson's ratio (ν) for $Li_4Sr_4[Si_4O_4N_6]O$

Elastic Moduli		Elastic Constants	
B_V	114.8	C_{11}	230.4
B_R	107.4	C_{22}	230.4
B_{VRH}	111.1	C_{33}	174.4
G_V	70.0	C_{44}	47.8
G_R	62.0	C_{55}	47.8
G_{VRH}	65.9	C_{66}	108.8
Y_{VRH}	165.1	C_{12}	117.5
ν	0.25	C_{13}	40.6
θ_D	592.2	C_{23}	40.6

[a] Bulk and shear moduli according to the Voigt (B_V and G_V), Reuss (B_R and G_R), and Voigt–Reuss–Hill (B_{VRH} and G_{VRH}) approaches. The subscripts in C_{nm} were obtained from C_{ijkl} according to the Voigt notation $xx \rightarrow 1$, $yy \rightarrow 2$, $zz \rightarrow 3$, $yz \rightarrow 4$, $zx \rightarrow 5$, and $xy \rightarrow 6$.

3.3.6 UV/Vis Spectroscopy

The optical band gap was determined by UV/Vis spectroscopy on a non-doped sample of $Li_4Sr_4[Si_4O_4N_6]O$. The diffuse-reflectance spectrum is shown in Figure 3.8 together with insets of a pseudoabsorption spectrum obtained by transformation via the Kubelka–Munk formalism.[73–76] The diffuse-reflectance spectra show broad absorption ranging from 260 to 380 nm. The slight indent starting from 280 nm is attributed to natural defect states in the band gap possibly arising from the observed stacking faults. This is in line with the fact that dopant levels of about 1 mol% Eu in $Li_4Sr_4[Si_4O_4N_6]O$, resulting in distinct 4*f* and 5*d* states within the band gap, lead to a more pronounced effect in the same range of the spectrum (Figure S3.6). The optical band gap was subsequently derived by fitting the first ascent of the pseudoabsorption $[F(R)\ h\nu]^{1/n}$ and taking its inflection point with the energy scale. The resulting band gap of $Li_4Sr_4[Si_4O_4N_6]O$ is approximately 3.6 eV for indirect and 4.25 eV for direct transitions, agreeing well with band structure calculations favoring indirect transitions by about 0.6 eV (Figure S3.7). The value for direct transitions is in better correspondence with the obtained electronic band gap by DFT of approximately 4.4 eV. A higher value for the electronic band gap is to be expected because of the core–hole effect. Further, the stacking disorder in $Li_4Sr_4[Si_4O_4N_6]O$ might lower the band gap with regard to the fully ordered model from DFT calculations because of the possible introduction of defect states.

3.3.7 Luminescence

Luminescence measurements were performed on thick-bed powder samples of Eu^{2+}-doped $Li_4Sr_4[Si_4O_4N_6]O$ in air. Excitation of the samples with UV to blue light leads to a broad-band emission in the orange spectral range. The excitation and emission spectra of a sample with a nominal doping content of 1 mol % referred to Sr are shown in Figure 3.9. The excitation spectrum exhibits a broad band with a maximum at around 410–425 nm, enabling the phosphor to be efficiently excited by blue-emitting (In,Ga)N-LEDs.

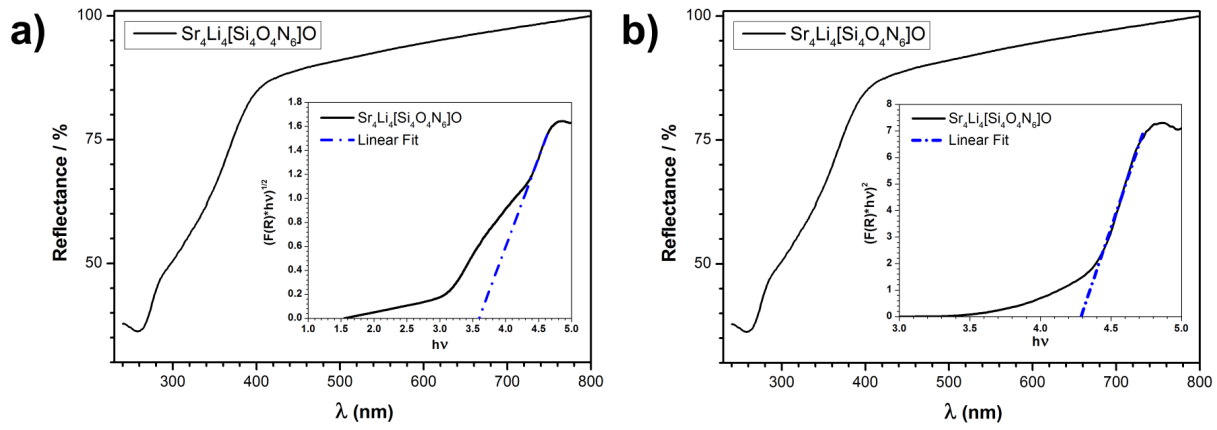

Figure 3.8 Diffuse-reflectance spectra of undoped $Li_4Sr_4[Si_4O_4N_6]O$ with insets of the respective Tauc plots $[F(R)\ h\nu]^{1/n}$ for (a) indirect (n = 2) and (b) direct (n = $^1/_2$) band gaps. Linear fit in order to determine E_g in blue.

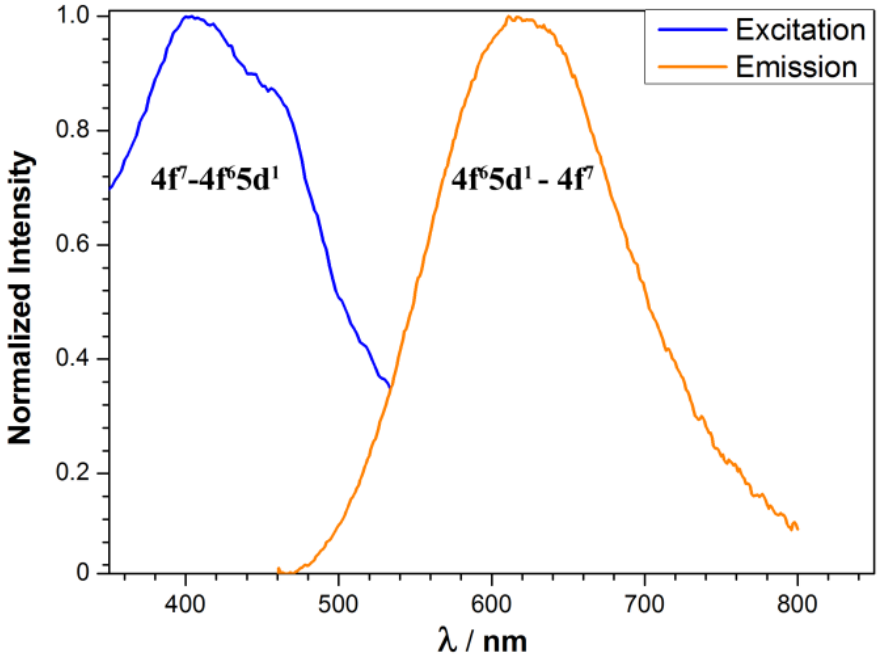

Figure 3.9 Excitation (blue) and emission (orange; λ_{exc} = 440 nm) spectra of bulk phase $Li_4Sr_4[Si_4O_4N_6]O:Eu^{2+}$ with a nominal dopant concentration of 1 mol %.

The emission spectrum peaks at 625 nm and exhibits a full width at half-maximum (fwhm) of 4164 cm^{-1} (160 nm), surpassing that of YAG:Ce^{3+} (fwhm ≈ 3700 cm^{-1}; 120 nm).[77]

A broad-band emission is observed for $Li_4Sr_4[Si_4O_4N_6]O:Eu^{2+}$, as seen from Figure 3.9, despite featuring only one crystallographic Sr/Eu site. A possible impact of side phases could be ruled out from single-crystal luminescence measurements showing identical emission behavior, as seen from Figure S3.8. A nearly Gaussian-shaped emission band on the energy scale is observed, which indicates a large Huang–Rhys parameter, corresponding to strong electron–phonon coupling.[78]

Figure 3.10 shows the rather asymmetric coordination of Sr by O and N ions paired with the relatively unidimensional Sr displacement ellipsoid toward the noncoordinating O2 ($d_{Sr\text{-}O2}$ = 3.11 A) position. The observed stacking disorder, observed from PXRD and TEM investigations, is likely to impact the local environment even further. Because the crystal field of the spacious 5d orbitals, involved in the electronic $4f^7$–$4f^65d^1$ transitions in Eu^{2+}, is prone to strong local distortions, an explanation for the observed broadening of emission, further enhanced by strong electron–phonon coupling, can hence be inferred. The color coordinates according to the CIE 1931 convention are x = 0.534 and y = 0.450 and are depicted in Figure 3.11.

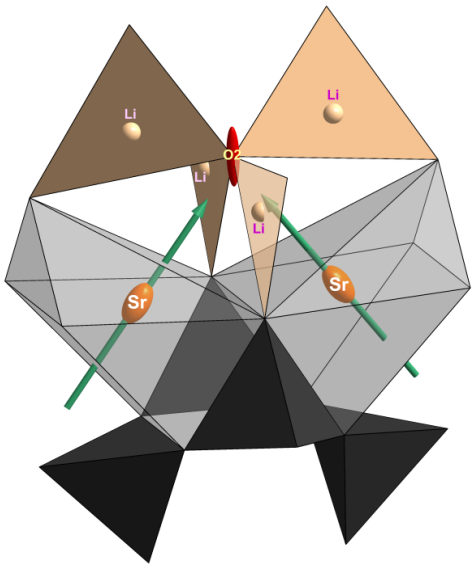

Figure 3.10 Coordination spheres of the Sr/Eu site (orange) in $Li_4Sr_4[Si_4O_4N_6]O$ with schematic displacement vectors (green arrows). Displacement ellipsoids are shown with 90% probability. Color code: SiN_3O tetrahedra, black; Sr/Eu coordination polyhedra, gray; Li, ivory; O, red.

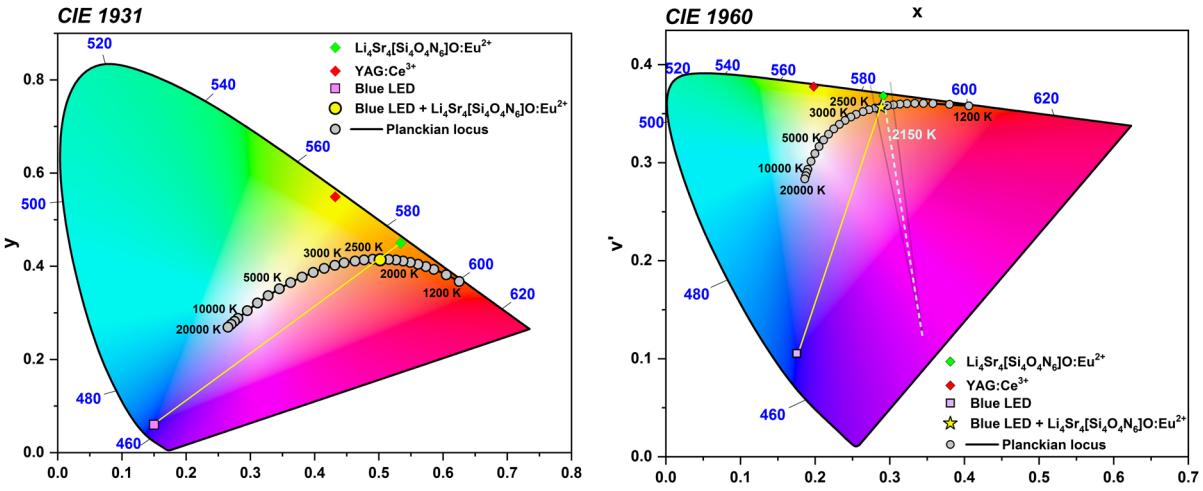

Figure 3.11 CIE 1931 (left) and CIE 1960 (right) color spaces showing the CIE coordinates of $Li_4Sr_4[Si_4O_4N_6]O:Eu^{2+}$ along with YAG:Ce^{3+}, a pure blue LED, and the those of an ideal blackbody radiator at different temperatures (K). CCT of a single-phosphor LED indicated as ☆ on the yellow conjugation line alongside a construction to determine the CCT of the phosphor material itself (dotted gray intersection of the planckian locus in CIE 1960).[79]

From Figure 3.11, it can be seen that the color point of $Li_4Sr_4[Si_4O_4N_6]O:Eu^{2+}$ lies in the orange spectral region close to the planckian locus. We estimated the correlated color temperature (CCT) of the phosphor to be around 2150 K from the CIE 1960 diagram according to

$$\mathrm{CCT} = \left(\frac{1}{T_i} + \frac{\theta_1}{\theta_2}\left(\frac{1}{T_{i+1}} - \frac{1}{T_i}\right)\right)^{-1},$$

where T_i and T_{i+1} correspond to the isothermals of the planckian CCT of the higher and lower isothermals and θ_1 to the angle between those isothermals. θ_2 corresponds to the angle between the higher CCT isothermal and the line drawn from the color point to the isothermal interception point.[79] The combination of a blue LED (λ_{em} = 450 nm) with $Li_4Sr_4[Si_4O_4N_6]O:Eu^{2+}$ would result in a CCT of ≈2200 K (candle light) and a CRI of 77.2 suitable for, e.g., decorative lighting applications.

3.3.8 Thermal Quenching

In order to determine the luminescence behavior of $Li_4Sr_4[Si_4O_4N_6]O:Eu^{2+}$, thermal quenching experiments were performed at low temperatures (6–300 K) and up to typical LED operating temperatures (around 100–200 °C) by measuring the luminescence intensity and performing integration at each step. The thermal quenching behavior is shown in Figure 3.12, together with the calculated thermal activation energy E_a obtained from an Arrhenius fit according to the equation

$$I = \frac{I_0}{1 + e^{\frac{E}{kT}}}$$

Here I_0 is the intensity at the beginning of measurement, k the Boltzmann constant (eV), T the temperature (K), and I the intensity at every following point of measurement.[80,81] E_a is then obtained as the slope of the plot $\ln[(I_0/I)-1]$ versus $1/kT$.

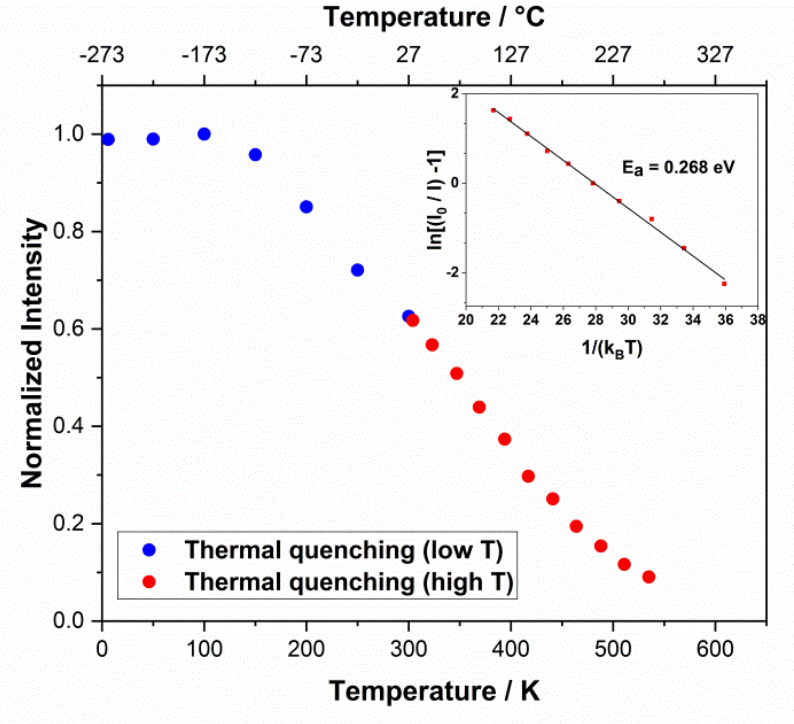

Figure 3.12 Thermal quenching measurements of $Li_4Sr_4[Si_4O_4N_6]O:Eu^{2+}$. The inset shows an Arrhenius plot of the thermal quenching data at elevated temperatures in order to determine the thermal activation energy E_a.

While the room temperature IQE was determined to be 24% (38% at 6 K), $Li_4Sr_4[Si_4O_4N_6]O:Eu^{2+}$ shows significant thermal quenching behavior at typical LED operating temperatures with E_a = 0.268 eV. This is subsequently significantly lower than that of commercial phosphors like $YAG:Ce^{3+}$ (0.81 eV).[82] The observed behavior is in line with the strong electron–phonon coupling, which could correspond to the 4f–5d crossing model with increasing nonradiative emissions possibly paired with thermal ionization to the conduction band.[81] The phosphor material is thus limited to a small application space of solid-state lighting, despite its attractive distribution of emission.

3.4 Conclusion

A suitable method for the discovery of novel materials is the screening of multicomponent mixtures. In this manner, the novel layered lithium oxonitridosilicate oxide $Li_4Sr_4[Si_4O_4N_6]O:Eu^{2+}$ has been obtained. Its structure formally derives from non-luminescent $Li_2Sr_4[Si_2N_5]N$ by means of O substitution and incorporation. The crystal structure was solved and refined from single-crystal X-ray data. Reproduction of the compound from optimized bulk syntheses was initially hindered by the occurrence of broadened reflections with low intensity. TEM investigations prove to be a suitable tool in overcoming such challenges, revealing stacking disorder as a real structure phenomenon of the layered compound while corroborating the cell metrics. As a result, the broadening of some reflections observed in the PXRD patterns was successfully modeled through the introduction of stacking faults. $Li_4Sr_4[Si_4O_4N_6]O:Eu^{2+}$ contributes to the sparsely investigated class of lithium oxonitridosilicate(oxides), exemplifying paths to the discovery of novel phosphor materials, highlighting the importance of continuous research for compounds in this materials class. $Li_4Sr_4[Si_4O_4N_6]O:Eu^{2+}$ shows emission in the yellow-to-orange spectral range featuring an indirect optical band gap of 3.6 eV. DFT calculations suggest an electronic band gap of about 4.4 eV for a model free from stacking faults. Calculations of the Debye temperature (592 K) reveal the highest mechanical compressibility along the [001] direction, in line with the layered structure of $Li_4Sr_4[Si_4O_4N_6]O$. The emission of $Li_4Sr_4[Si_4O_4N_6]O:Eu^{2+}$ is likely broadened because of large electron-phonon coupling and concomitant stacking faults between layers, as seen from the broadened Gaussian-shaped emission profile. This, in turn, corroborates the use of θ_D as a preliminary proxy when estimating the efficiency of a possible phosphor host material beforehand. The synthesis and subsidiary analytical approaches like TEM investigations of $Li_4Sr_4[Si_4O_4N_6]O:Eu^{2+}$ further exemplify how optimization, characterization, and in-depth illumination of real-structure phenomena can interlock and help to push the understanding of materials property relationships and phosphor materials research approaches in general.

3.5 Acknowledgements

We thank Dr. Peter Mayer for collecting single-crystal data (LMU). Dr. Constantin Hoch is thanked for valuable discussions regarding single-crystal analysis along with Christian Maak and Philipp Bielec (all at LMU) for constructive discussions. Detlef Wiechert and Volker Weiler (both at Lumileds Phosphor Center Aachen) are thanked for performing temperature-dependent luminescence measurements and data processing. Prof. Dr. Oliver Oeckler (Institute for Mineralogy, Crystallography and Materials Science, Leipzig University) is thanked for contributory annotations. Financial support by the Fonds der Chemischen Industrie is gratefully acknowledged.

3.6 References

[1] C. Maak, P. Strobel, V. Weiler, P. J. Schmidt, W. Schnick, Unprecedented Deep-Red Ce^{3+} Luminescence of the Nitridolithosilicates $Li_{38.7}RE_{3.3}Ca_{5.7}[Li_2Si_{30}N_{59}]O_2F$ (*RE* = La,Ce,Y), *Chem. Mater.* **2018**, *30*, 5500−5506.

[2] N. Hirosaki, T. Takeda, S. Funahashi, R.-J. Xie, Discovery of New Nitridosilicate Phosphors for Solid State Lighting by the Single-Particle-Diagnosis Approach, *Chem. Mater.* **2014**, *26*, 4280–4288.

[3] L. Neudert, D. Durach, F. Fahrnbauer, G. B. M. Vaughan, W. Schnick, O. Oeckler, Highly Symmetric AB2 Framework Related to Tridymite in the Disordered Nitridosilicate $La_{24}Sr_{14-7x}[Si_{36}N_{72}](O_{1-x}F_x)_{14}$ (x = 0.489), *Inorg. Chem.* **2017**, *56*, 13070–13077.

[4] P. Strobel, V. Weiler, C. Hecht, P. J. Schmidt, W. Schnick, Luminescence of the Narrow-Band Red Emitting Nitridomagnesosilicate $Li_2(Ca_{1-x}Sr_x)_2[Mg_2Si_2N_6]:Eu^{2+}$ (x = 0–0.06), *Chem. Mater.* **2017**, *29*, 1377–1383.

[5] C. Poesl, W. Schnick, Crystal Structure and Nontypical Deep-Red Luminescence of $Ca_3Mg[Li_2Si_2N_6]:Eu^{2+}$, *Chem. Mater.* **2017**, *29*, 3778–3784.

[6] S. Schmiechen, F. Nietschke, W. Schnick, Structural Relationship between the Mg-Containing Nitridosilicates $Ca_2Mg[Li_4Si_2N_6]$ and $Li_2Ca_2[Mg_2Si_2N_6]$, *Eur. J. Inorg. Chem.* **2015**, *2015*, 1592–1597.

[7] Y. Li, C.-A. Wang, H. Xie, J. Cheng, J. B. Goodenough, High lithium ion conduction in garnet-type $Li_6La_3ZrTaO_{12}$, *Electrochem. Commun.* **2011**, *13*, 1289–1292.

[8] R. Murugan, V. Thangadurai, W. Weppner, Fast Lithium Ion Conduction in Garnet-Type $Li_7La_3Zr_2O_{12}$, *Angew. Chem. Int. Ed.* **2007**, *6*, 7778–7781; *Angew. Chem.* **2007**, *119*, 7925–7928.

[9] J.-F. Wu, W. K. Pang, V. K. Peterson, L. Wei, X. Guo, Garnet-Type Fast Li-Ion Conductors with High Ionic Conductivities for All-Solid-State Batteries, *ACS Appl. Mater. Interfaces* **2017**, *9*, 12461–12468.

[10] S. Pagano, S. Lupart, S. Schmiechen, W. Schnick, $Li_4Ca_3Si_2N_6$ and $Li_4Sr_3Si_2N_6$ – Quaternary Lithium Nitridosilicates with Isolated $[Si_2N_6]^{10-}$ Ions, *Z. Anorg. Allg. Chem.* **2010**, *636*, 1907–1909.

[11] P. Wagatha, P. Pust, V. Weiler, A. S. Wochnik, P. J. Schmidt, C. Scheu, W. Schnick, $Ca_{18.75}Li_{10.5}[Al_{39}N_{55}]:Eu^{2+}$—Supertetrahedron Phosphor for Solid-State Lighting, *Chem. Mater.* **2016**, *28*, 1220–1226.

[12] P. Pust, V. Weiler, C. Hecht, A. Tücks, A. S. Wochnik, A.-K. Henß, D.Wiechert, C. Scheu, P. J. Schmidt, W. Schnick, Narrow-band red-emitting $Sr[LiAl_3N_4]:Eu^{2+}$ as a next-generation LED-phosphor material, *Nat. Mater.* **2014**, *13*, 891–896.

[13] D. Wilhelm, D. Baumann, M. Seibald, K. Wurst, G. Heymann, H. Huppertz, Narrow-Band Red Emission in the Nitridolithoaluminate $Sr_4[LiAl_{11}N_{14}]:Eu^{2+}$, *Chem. Mater.* **2017**, *29*, 1204–1209.

[14] Y. Q. Li, N. Hirosaki, R. J. Xie, T. Takeka, M. Mitomo, Crystal, electronic structures and photo-luminescence properties of rare-earth doped $LiSi_2N_3$, *J. Solid State Chem.* **2009**, *182*, 301–311.

[15] P. Strobel, S. Schmiechen, M. Siegert, A. Tücks, P. J. Schmidt, W. Schnick, Narrow-Band Green Emitting Nitridolithoalumosilicate $Ba[Li_2(Al_2Si_2)N_6]:Eu^{2+}$ with Framework Topology whj for LED/LCD-Backlighting Applications, *Chem. Mater.* **2015**, *27*, 6109–6115.

[16] T. Takeda, N. Hirosaki, S. Funahshi, R.-J. Xie, Narrow-Band Green-Emitting Phosphor $Ba_2LiSi_7AlN_{12}:Eu^{2+}$ with High Thermal Stability Discovered by a Single Particle Diagnosis Approach, *Chem. Mater.* **2015**, *27*, 5892–5898.

[17] R.-J. Xie, N. Hirosaki, H.-L- Li, Y. Q. Li, M. Mitomo, Synthesis and Photoluminescence Properties of β-sialon : Eu^{2+} ($Si_{6-z}Al_zOzN_{8-z}$: Eu^{2+}) : A Promising Green Oxynitride Phosphor for White Light-Emitting Diodes, *J. Electrochem. Soc.* **2007**, *154*, J314–J319.

[18] N. Hirosaki, R.-J. Xie, K. Kimoto, T. Sekiguchi, Y. Yamamoto, T. Suehiro, M. Mitomo, Characterization and properties of green-emitting β-SiAlON:Eu^{2+} powder phosphors for white light-emitting diodes, *Appl. Phys. Lett.* **2005**, *86*, 211905.

[19] S. Li, L. Wang, D. Tang, Y. Cho, X. Liu, X. Zhou, L. Lu, L. Zhang, T. Takeda, N. Hirosaki, R.-J. Xie, Achieving High Quantum Efficiency Narrow-Band β-Sialon:Eu^{2+} Phosphors for High-Brightness LCD Backlights by Reducing the Eu^{3+} Luminescence Killer, *Chem. Mater.* **2018**, *30*, 494–505.

[20] M. Seibald, O. Oeckler, V. R. Celinski, P. J. Schmidt, A. Tücks, W. Schnick, Real structure and diffuse scattering of $Sr_{0.5}Ba_{0.5}Si_2O_2N_2:Eu^{2+}$ - A highly efficient yellow phosphor for pc-LEDs. *Solid State Sci.* **2011**, *13*, 1769–1778.

[21] M. Seibald, T. Rosenthal, O. Oeckler, C. Maak, A. Tücks, P. J. Schmidt, D. Wiechert, W. Schnick, New Polymorph of the Highly Efficient LED-Phosphor $SrSi_2O_2N_2:Eu^{2+}$ – Polytypism of a Layered Oxonitridosilicate, *Chem. Mater.* **2013**, *25*, 1852–1857.

[22] C. Maak, C. Hoch, P. J. Schmidt, W. Schnick, Oxonitridosilicate Oxides $RE_{26}Ba_6[Si_{22}O_{19}N_{36}]O_{16}:Eu^{2+}$ (*RE* = Y, Tb) with a Unique Layered Structure and Orange-Red Luminescence for *RE* = Y, *Inorg. Chem.* **2018**, *57*, 2242–2248.

[23] M. Seibald, T. Rosenthal, O. Oeckler, W. Schnick, Highly Efficient pc-LED Phosphors $Sr_{1-x}Ba_xSi_2O_2N_2:Eu^{2+}$ (0 x 1) - Crystal Structures and Luminescence Properties Revisited, *Crit. Rev. Solid State Mater. Sci.* **2014**, *39*, 215–229.

[24] S. D. Kloß, L. Neudert, M. Döblinger, M. Nentwig, O. Oeckler, W. Schnick, Puzzling Intergrowth in Cerium Nitridophosphate Unraveled by Joint Venture of Aberration-Corrected Scanning Transmission Electron Microscopy and Synchrotron Diffraction, *J. Am. Chem. Soc.* **2017**, *139*, 12724–12735.

[25] H. Lange, G. Wötting, G. Winter, Silicon Nitride—From Powder Synthesis to Ceramic Materials, *Angew. Chem. Int. Ed.* **1991**, *30*, 1579–1597; *Angew. Chem.* **1991**, *103*, 1606–1625.

[26] N. Hofman-Bang, Preparation of Lithium Azide, *Acta Chem. Scand.* **1957**, *11*, 581–582.

[27] G. M. Sheldrick, *SADABS, v. 2: Multi-Scan Absorption Correction,* Bruker-AXS: Billerica, MA, **2012**.

[28] G. M. Sheldrick, *SHELXS-97: A Program for Crystal Structure Solution,* University of Göttingen: Göttingen, Germany, **1997**.

[29] G. M. Sheldrick, *SHELXL-97: A Program for Crystal Structure Refinement,* University of Göttingen: Göttingen, Germany, **1997**.

[30] G. M. Sheldrick, A short history of SHELX. *Acta Crystallogr, Sect. A: Found. Crystallogr.* **2008**, *64*, 112–122.

[31] H. M. Rietveld, A profile refinement method for nuclear and magnetic structures, *J. Appl. Crystallogr.* **1969**, *2*, 65–71.

[32] A. A. Coelho, *TOPAS, v. 4.1: A program for Rietveld refinement;* Coelho Software: Brisbane, Australia, **2007**.

[33] J. Bergmann, R. Kleeberg, A. Haase, B. Breidenstein, Advanced Fundamental Parameters Model for Improved Profile Analysis, *Mater. Sci. Forum* **2000**, *347–349*, 303–308.

[34] R. W. Cheary, A. A. Coelho, J. P. Cline, Fundamental Parameters Line Profile Fitting in Laboratory Diffractometers, *J. Res. Natl. Inst. Stand. Technol.* **2004**, *109*, 1–25.

[35] A. Le Bail, A. Jouanneaux, Qualitative Account for Anisotropic Broadening in Whole-Powder-Diffraction-Pattern Fitting by Second-Rank Tensors, *J. Appl. Crystallogr.* **1997**, *30*, 265–271.

[36] G. Kresse, J. Hafner, *Ab initio* molecular dynamics for liquid metals, *Phys. Rev. B: Condens. Matter Mater. Phys.* **1993**, *47*, 558–561.

[37] G. Kresse, J. Hafner, *Ab initio* molecular-dynamics simulation of the liquid-metal-amorphous-semiconductor transition in germanium, *Phys. Rev. B: Condens. Matter Mater. Phys.* **1994**, *49*, 14251–14269.

[38] G. Kresse, J. Furthmüller, Efficiency of ab-initio total energy calculations for metals and semiconductors using a plane-wave basis set, *Comput. Mater. Sci.* **1996**, *6*, 15–50.

[39] J. P. Perdew, K. Burke, M. Ernzerhof, Generalized Gradient Approximation Made Simple, *Phys. Rev. Lett.* **1996**, *77*, 3865–3868.

[40] J. P. Perdew, K. Burke, M. Ernzerhof, Generalized Gradient Approximation Made Simple [*Phys. Rev. Lett.* **1996**, *77*, 3865], *Phys. Rev. Lett.* **1997**, *78*, 1396.

[41] P. E. Blöchl, Projector augmented-wave method, *Phys. Rev. B: Condens. Matter Mater. Phys.* **1994**, *50*, 17953–17979.

[42] G. Kresse, D. Joubert, From ultrasoft pseudopotentials to the projector augmented-wave method, *Phys. Rev. B: Condens. Matter Mater. Phys.* **1999**, *59*, 1758–1775.

[43] H. J. Monkhorst, J. D. Pack, Special points for Brillouin-zone integrations, *Phys. Rev. B: Solid State* **1976**, *13*, 5188–5192.

[44] A. D. Becke, E. R. Johnson, A simple effective potential for exchange, *J. Chem. Phys.* **2006**, *124*, 221101.

[45] F. Tran, P. Blaha, Accurate Band Gaps of Semiconductors and Insulators with a Semilocal Exchange-Correlation Potential, *Phys. Rev. Lett.* **2009**, *102*, 226401.

[46] J. A. Camargo-Martínez, R. Baquero, Performance of the modified Becke-Johnson potential for semiconductors, *Phys. Rev. B: Condens. Matter Mater. Phys.* **2012**, *86*, 195106.

[47] Y. Le Page, P. Saxe, Symmetry-general least-squares extraction of elastic data for strained materials from *ab initio* calculations of stress, *Phys. Rev. B: Condens. Matter Mater. Phys.* **2002**, *65*, 104104.

[48] *Digital Micrograph, version 3.6.1,* Gatan, Warrendale, PA, **1999**.

[49] J. L. Lábár, Consistent indexing of a (set of) single crystal SAED pattern(s) with the ProcessDiffraction program, *Ultramicroscopy* **2005**, *103*, 237–249.

[50] P. A. Stadelmann, *JEMS, version 3.3425,* CIME–EPFL, Switzerland, **2008**.

[51] *ES Vision, version 4.0.164,* Emispec Systems Inc., USA, **2002**.

[52] E. Irran, K. Köllisch, S. Leoni, R. Nesper, F. H. Paul, T. W. Mark, W. Schnick, $Ce_4[Si_4O_4N_6]O$-A Hyperbolically Layered Oxonitridosilicate Oxide with an Ordered Distribution of Oxygen and Nitrogen, *Chem. Eur. J.* **2000**, *6*, 2714–2720.

[53] S. Lupart, S. Pagano, O. Oeckler, W. Schnick, $Li_2Sr_4[Si_2N_5]N$ – A Layered Lithium Nitridosilicate Nitride, *Eur. J. Inorg. Chem.* **2011**, *2011*, 2118–2123.

[54] O. Oeckler, F. Stadler, T. Rosenthal, W. Schnick, Real structure of $SrSi_2O_2N_2$, *Solid State Sci.* **2007**, *9*, 205–212.

[55] S. Pagano, S. Lupart, M. Zeuner, W. Schnick, Tuning the Dimensionality of Nitridosilicates in Lithium Melts, *Angew. Chem. Int. Ed.* **2009**, *48*, 6335–6338; *Angew. Chem.* **2009**, *121*, 6453–6456.

[56] M. M. J. Treacy, J. M. Newsam, M. W. Deem, A general recursion method for calculating diffracted intensities from crystals containing planar faults, *Proc. R. Soc. London, Ser. A* **1991**, *433*, 499–520.

[57] R. Shannon, Revised effective ionic radii and systematic studies of interatomic distances in halides and chalcogenides, *Acta Crystallogr. A* **1976**, *32*, 751–767.

[58] R. Hoppe, Madelung Constants, *Angew. Chem. Int. Ed. Engl.* **1966**, *5*, 95–106; *Angew. Chem.* **1966**, *78*, 52–63

[59] R. Hoppe, The Coordination Number – an ''Inorganic Chameleon'', *Angew. Chem. Int. Ed. Engl.* **1970**, *9*, 25–34; *Angew. Chem.* **1970**, *82*, 7–16.

[60] R. Hübenthal, *Maple, Program for the Calculation of MAPLE values*, version 4; University of Gießen: Gießen, Germany, **1993**.

[61] M. Zeuner, S. Pagano, W. Schnick, Nitridosilicates and Oxonitridosilicates: From Ceramic Materials to Structural and Functional Diversity, *Angew. Chem. Int. Ed.* **2011**, *50*, 7754–7775; *Angew. Chem.* **2011**, *123*, 7898–7920.

[62] J. A. Kechele, C. Schmolke, S. Lupart, W. Schnick, $Ln_3[SiON_3]O$ (Ln = La, Ce, Pr) – Three Oxonitridosilicate Oxides with Crystal Structures Derived from the Anti-Perovskite Structure Type, *Z. Anorg. Allg. Chem.* **2009**, *636*, 176–182.

[63] C. Maak, R. Niklaus, F. Friedrich, A. Mähringer, P. J. Schmidt, W. Schnick, W. Efficient Yellow–Orange Phosphor $Lu_4Ba_2[Si_9ON_{16}]O:Eu^{2+}$ and Orange–Red Emitting $Y_4Ba_2[Si_9ON_{16}]O:Eu^{2+}$: Two Oxonitridosilicate Oxides with Outstanding Structural Variety, *Chem. Mater.* **2017**, *29*, 8377–8384.

[64] N. W. Ashcroft, N. D. Mermin, *Solid state physics,* Saunders college, **1976**.

[65] R. Hill, The Elastic Behaviour of a Crystalline Aggregate, *Proc. Phys. Soc. A* **1952**, *65*, 349–354.

[66] C. Jiang, S. G. Srinivasan, A. Caro, S. A. Maloy, Structural, elastic, and electronic properties of Fe_3C from first principles, *J. Appl. Phys.* **2008**, *103*, 043502.

[67] E. Francisco, J. M. Recio, M. A. Blanco, A. M. Pendás, A. Costales, A. Quantum-Mechanical Study of Thermodynamic and Bonding Properties of MgF_2, *J. Phys. Chem. A* **1998**, *102*, 1595–1601.

[68] E. Francisco, M. A. Blanco, G. Sanjurjo, Atomistic simulation of SrF_2 polymorphs. *Phys. Rev. B: Condens. Matter Mater. Phys.* **2001**, *63*, 094107.

[69] J.-P. Poirier, *Introduction to the physics of the earth's interior*, Cambridge University Press, **1921**.

[70] J. Brgoch, S. P. DenBaars, R. Seshadri, Proxies from Ab Initio Calculations for Screening Efficient Ce^{3+} Phosphor Hosts, *J. Phys. Chem. C* **2013**, *117*, 17955–17959.

[71] K. A. Denault, J. Brgoch, S. D. Kloß, M. W. Gaultois, J. Siewenie, K. Page, R. Seshadri, Average and Local Structure, Debye Temperature, and Structural Rigidity in Some Oxide Compounds Related to Phosphor Hosts, *ACS Appl. Mater. Interfaces* **2015**, *7*, 7264–7272.

[72] Z. Wang, I.-H. Chu, F. Zhou, S. P. Ong, Electronic Structure Descriptor for the Discovery of Narrow-Band Red-Emitting Phosphors, *Chem. Mater.* **2016**, *28*, 4024–4031.

[73] P. Kubelka, F. Munk, Ein Beitrag Zur Optik Der Farbanstriche, *Z. Tech. Phys.* **1931**, *12*, 593–601.

[74] P. Kubelka, New Contributions to the Optics of Intensely Light-Scattering Materials. Part I, *J. Opt. Soc. Am.* **1948**, *38*, 448–457.

[75] J. Tauc, R. Grigorovici, A. Vancu, A. Optical Properties and Electronic Structure of Amorphous Germanium, *Phys. Status Solidi B* **1966**, *15*, 627–637.

[76] R. López, R. Gómez, Band-gap energy estimation from diffuse reflectance measurements on sol-gel and commercial TiO_2: a comparative study, *J. Sol-Gel Sci. Technol.* **2012**, *61*, 1–7.

[77] T. Moriguchi; Y. Noguchi; K. Sakanao; Y. Shimizu, Light emitting device having a nitride compound semiconductor and a phosphor containing a garnet fluorescent material, U. S. Patent US5998925A, **1997**.

[78] B. Henderson, G. Imbusch, *Optical Spectroscopy of Inorganic Solids*, Clarendon Press, **1989**.

[79] *Optical Testing for SuperFlux, SnapLED and LUXEON® Emitters,* PHILIPS LUMILEDS: *Application Brief*, AB08, **2006**.

[80] E. Pavitra; J. S. Yu, Luminescent properties of Gd^{3+} sensitized low-phonon energy $CaGd_4O_7:Tb^{3+}$ green emitting novel phosphors, *Ceram. Int.* **2013**, *39*, 1029–1036.

[81] X. Qin, X. Liu, W. Huang, M. Bettinelli, X. Liu, Lanthanide-Activated Phosphors Based on $4f$-$5d$ Optical Transitions: Theoretical and Experimental Aspects, *Chem. Rev.* **2017**, *117*, 4488–4527.

[82] J. Ueda, P. Dorenbos, A. J. J. Bos, K. Kuroishi, S. Tanabe, Control of electron transfer between Ce^{3+} and Cr^{3+} in the $Y_3Al_{5-x}Ga_xO_{12}$ host via conduction band engineering, *J. Mater. Chem. C* **2015**, *3*, 5642–5651.

3.7 Supporting Information

3.7.1 Infrared Spectroscopy

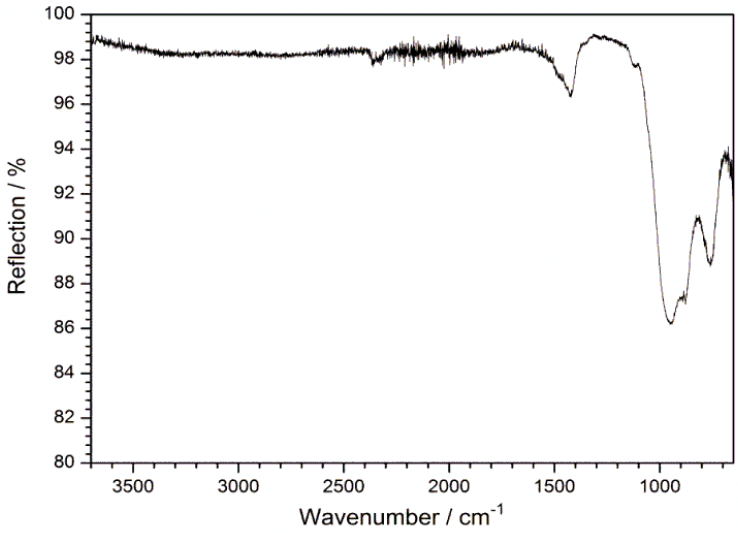

Figure S3.1 Infrared spectrum of $Li_4Sr_4[Si_4O_4N_6]O$ obtained in ATR geometry. No N–H or O–H bands are observed in the typical range of 3500–2500 cm^{-1}.

3.7.2 Electron Density Map

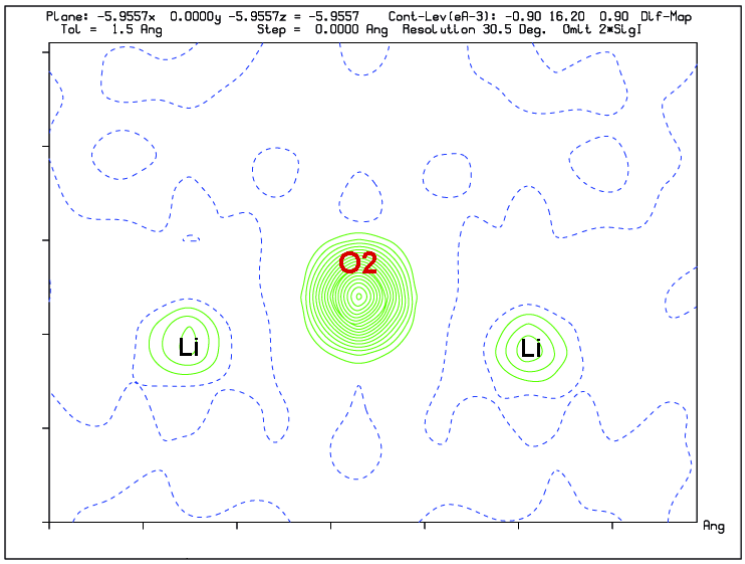

Figure S3.2 Plotted electron density at the crystallographic sites of O2 and Li within a difference Fourier map of $Li_4Sr_4[Si_4O_4N_6]O$. The uniform electron density of O2 and Li does not indicate any split positions or unusual phenomena.

3.7.3 EDX

Table S3.1 EDX analyses of representative $Li_4Sr_4[Si_4O_4N_6]O$ crystals, variance in parentheses

	1	2	3	4	5	6	7	mean value	calculated*
N(K)	22	21	22	21	22	24	20	22(1)	31
O(K)	26	27	27	28	24	25	20	26(3)	26
Si(K)	26	26	25	25	27	26	31	26(2)	21
Sr(L)	26	26	26	26	27	26	29	27(1)	21

* calculated for $Li_4Sr_4(Si_4O_4N_6)O$ without Li

3.7.4 Crystallographic Data

Table S3.2 Crystallographic data for the Rietveld refinement of $Li_4Sr_4(Si_4O_4N_6)O:Eu^{2+}$

Crystal Data	
Formula	$Li_4Sr_{3.9}Eu_{0.1}(Si_4O_4N_6)O$
Crystal system, space group	tetragonal, $P4_2/nmc$ (no. 137)
Lattice parameters / Å	a = 7.48088(11) c = 9.8781(2)
Cell volume / Å	552.81(2)
Formula units per cell	Z = 2
Data Collection	
Radiation	Cu
Monochromator	Ge(111)
Diffractometer	Stoe StadiP
Detector	MYTHEN 1K
2 θ-range / °	5-110
Temperature / K	297(2)
Data points	7001
Number of observed reflection	211
Refinement	
Number of parameters	64
Program used	TOPAS Academic V4.1
Structure refinement	Rietveld method
Profile function	fundamental parameters model
Background function	shifted Chebychev polynomial with 18 terms
R_{wp}	0.0772
R_{exp}	0.0194
R_p	0.0521
R_{Bragg}	0.0242

O and N positions were constrained to the same B_{iso} values for the refinement

Table S3.3 Atomic coordinates, isotropic displacement parameters [Å^2] and site occupancies of $Li_4Sr_{3.62(3)}Eu_{0.38(3)}[Si_4O_4N_6]O$, based on single-crystal analysis. Standard deviations in parentheses. Sr/Eu, occupy the same site

Atom		*x*	*y*	*z*	U_{eq}	s.o.f
Sr	8*g*	1/4	0.50390(6)	0.49519(5)	0.0140(17)	0.904(9)
Eu	8*g*	1/4	0.50390(6)	0.49519(5)	0.0140(17)	0.096(9)
Si	8*g*	1/4	0.02438(17)	0.18250(13)	0.0046(3)	1
Li	8*g*	1/4	0.5019(10)	0.8124(8)	0.0054(15)	1
O1	8*f*	1/4	0.9914 (4)	0.0123(3)	0.0090(7)	1
O2	2*b*	3/4	1/4	1/4	0.0175(17)	1
N1	8*f*	0.4457(4)	0.5543(4)	1/4	0.0122(8)	1
N2	4*d*	1/4	1/4	0.2089(6)	0.0073/11)	1

Table S3.4 Anisotropic displacement parameters of $Li_4Sr_{3.62(3)}Eu_{0.38(3)}[Si_4O_4N_6]O$, standard deviations in parentheses, based on single-crystal analysis

Atom	U_{11} /Å^2	U_{22} / Å^2	U_{33} / Å^2	U_{12} / Å^2	U_{13} / Å^2	U_{23} / Å^2
Sr/Eu	0.0085(3)	0.0134(3)	0.0200(2)	0	0	0.00815(19)
Si	0.0043(6)	0.0042(7)	0.0054(5)	0	0	0.0002(5)
O1	0.0125(17)	0.0084(16)	0.0061(14)	0	0	-0.0028(12)
O2	0.0021(18)	= U_{11}/	0.048(5)	0	0	-0.0047(13)
N1	0.095(11)	= U_{11}	0.0176(19)	-0.0025(16)	-0.0045(12)	= U_{13}
N2	0.008(3)	0.001(2)	0.013(3)	0	0	0

3.7.5 Charge Distribution (CHARDI) Calculations

CHARDI calculations were performed with VESTA, according to the theory of Hoppe et al.[1,2] The respective CHARDI values for each cation, Sr, Si, and Li are depicted in Table S3.5 corroborating the cation assignment.

Table S3.5 CHARDI values calculated for each of the cations. With Δq as the fraction of the charge received by the ion, Q the total charge received by the ion, and q the formal charge

Cation /Atom site	Δq	Q	q
Sr		1.888	2.0
Si		4.097	4
Li		1.015	1.0

3.7.6 TEM Investigations

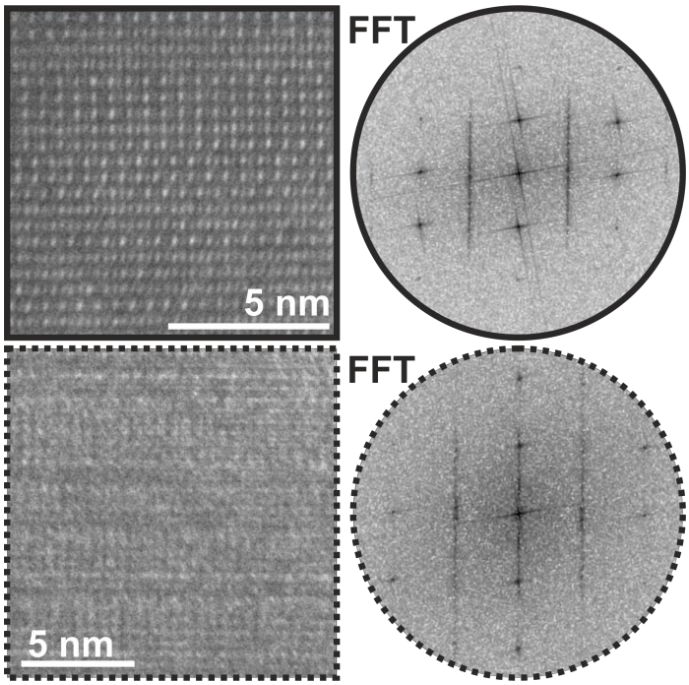

Figure S3.3 HRTEM images vied along [110] zone axis (left) showing contrast variations and defect layers perpendicular *c* causing stacking disorder along [001]. Corresponding Fourier transforms (right) show diffuse intensity along [001]*.

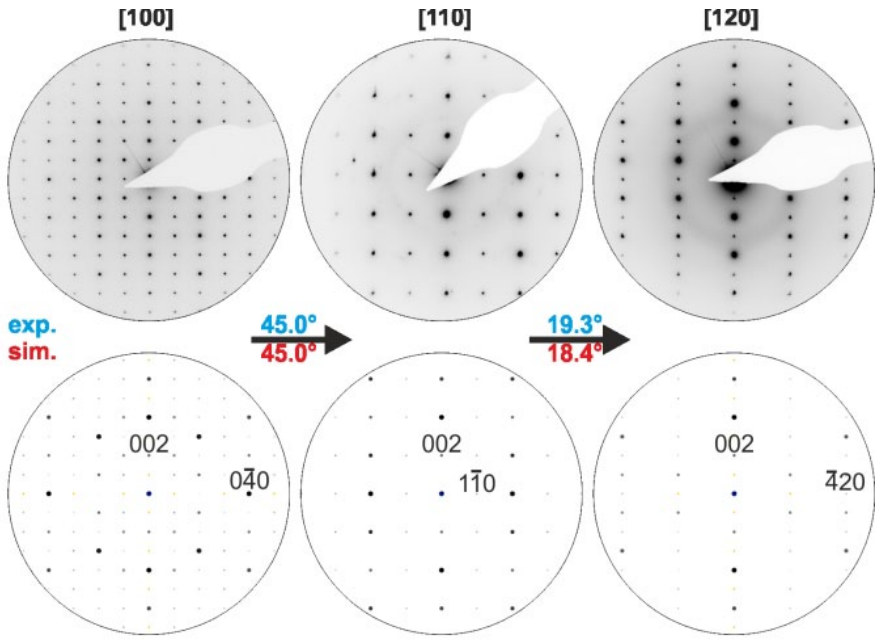

Figure S3.4 SAED tilt series of a very thin area of representative $Li_4Sr_4[Si_4O_4N_6]O:Eu^{2+}$ crystallites with experimental patterns (top) and tilt angles (blue) as well as simulated patterns (bottom) and tilt angles (red) based on the refined structure model from X-ray data. Selected reflections are labeled with indices. Compared to SAED images of thicker areas no diffuse intensities observed.

3.7.7 Stacking Disorder with DIFFaX

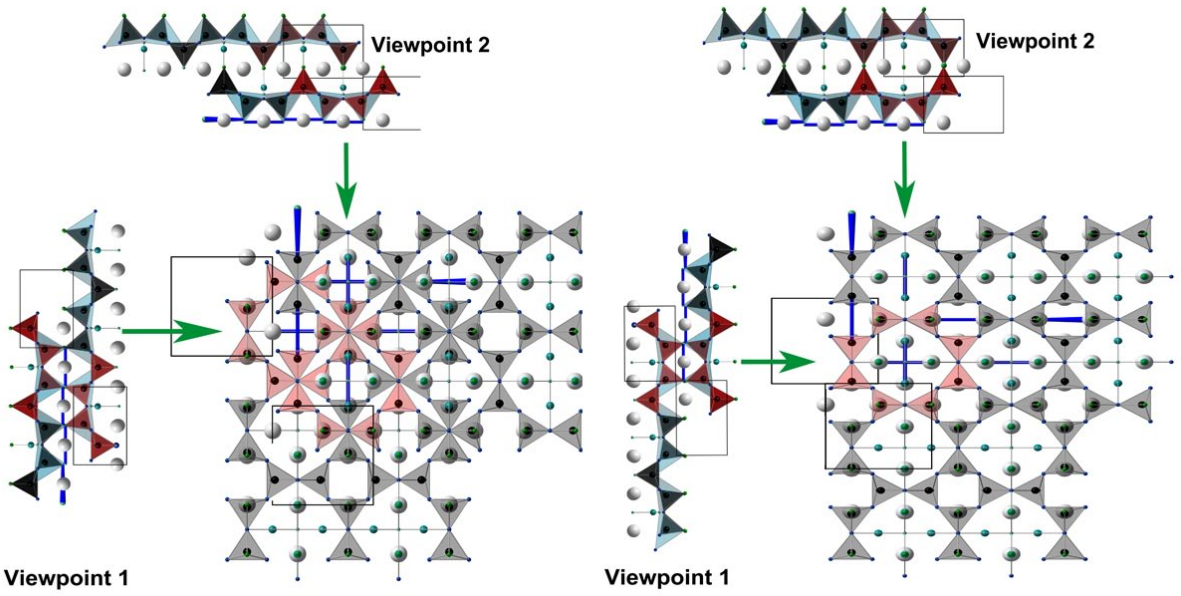

Figure S3.5 Left: Stacking of layers based on original single-crystal X-ray data. Right: Construction of a possible stacking variant of $Li_4Sr_4[Si_4O_4N_6]O$, resulting in broadening of selected reflections upon low-level stacking disorder after DIFFax simulation.[3] Layers shown consisting of SiN_3O-tetrahedra (gray) Sr atoms (white) and Li atoms (green), highlighted viewing directions in red.

The original and stacking fault variant shown in Figure S3.5 are obtained by taking one layer of the unit cell and stacking it via the matrix-vector relation

$$\begin{pmatrix} x' \\ y' \\ z' \end{pmatrix} = \begin{pmatrix} x \\ y \\ z \end{pmatrix} \begin{pmatrix} 0 & -1 & 0 \\ 1 & 0 & 0 \\ 0 & 0 & 1 \end{pmatrix} + \begin{pmatrix} 0.5 \\ 0 \\ 1 \end{pmatrix} \quad \text{(original)}, \qquad \begin{pmatrix} x' \\ y' \\ z' \end{pmatrix} = \begin{pmatrix} x \\ y \\ z \end{pmatrix} \begin{pmatrix} 0 & -1 & 0 \\ 1 & 0 & 0 \\ 0 & 0 & 1 \end{pmatrix} + \begin{pmatrix} 0 \\ 0.5 \\ 1 \end{pmatrix} \quad \text{(stacking)},$$

with x, y, z as the original atom coordinates of a single layer and x', y', z' as the resulting coordinates of the corresponding stacking variant.

3.7.8 UV/Vis

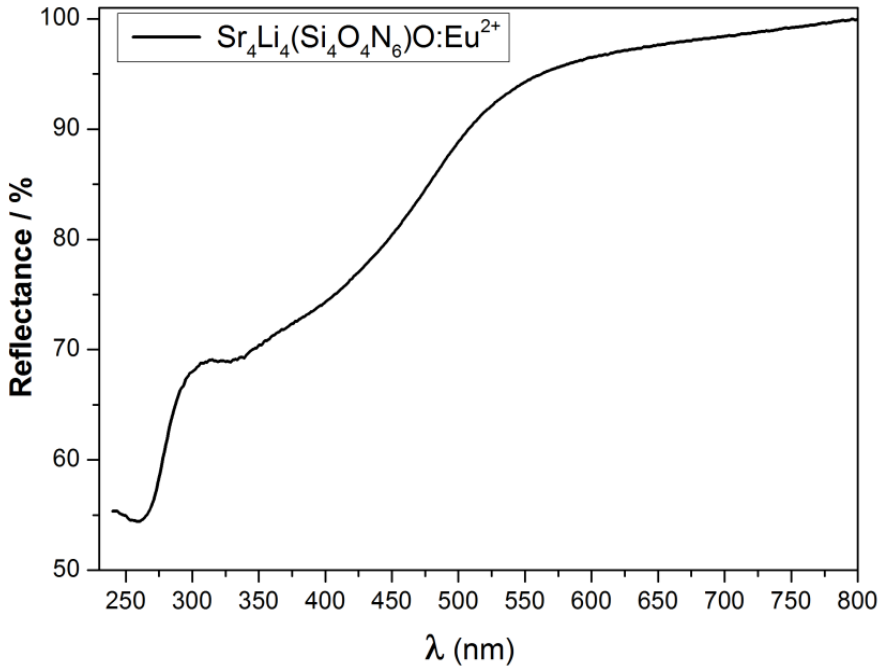

Figure S3.6 Diffuse reflectance spectrum of Eu-doped $Li_4Sr_4[Si_4O_4N_6]O$.

3.7.9 Band Structure

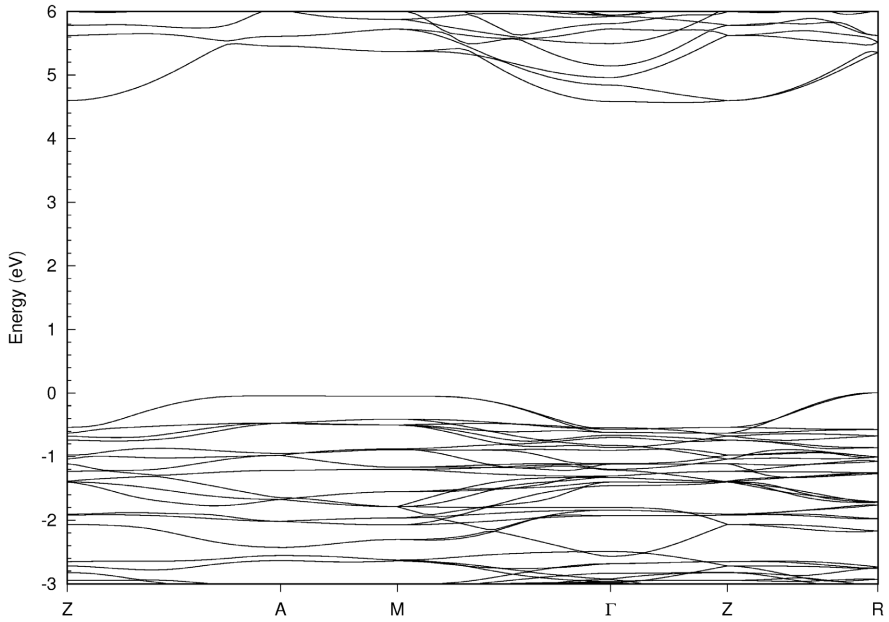

Figure S3.7 Band structure of $Li_4Sr_4[Si_4O_4N_6]O$ (space group no. 137) along high-symmetry directions in the first Brillouin zone as calculated from the mbj-PBE potential.

3.7.10 Single-crystal Luminescence

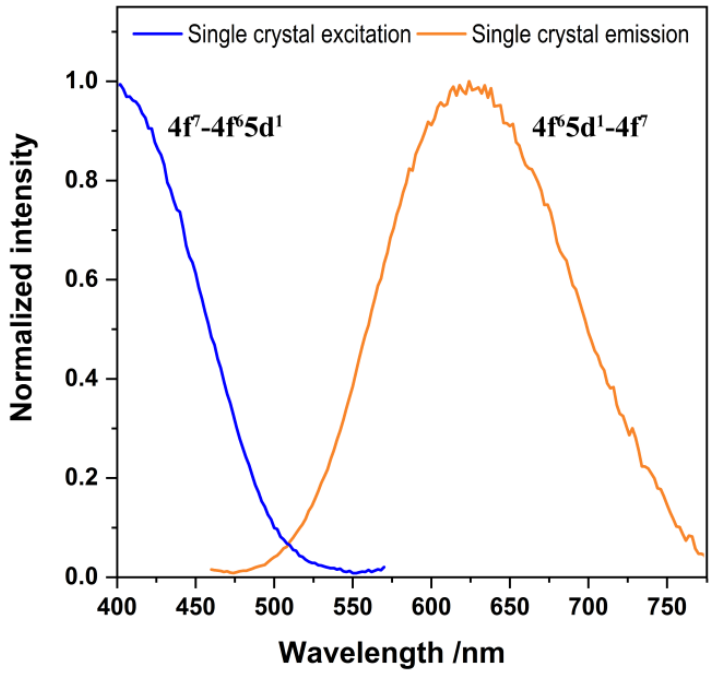

Figure S3.8 Single-crystal emission spectrum of $Li_4Sr_{3.62(3)}Eu_{0.38(3)}[Si_4O_4N_6]O$ λ_{em} = 624 nm.

3.7.11 References

[1] K. Momma, F. Izumi, VESTA: a three-dimensional visualization system for electronic and structural analysis, *J. Appl. Crystallogr.* **2008**, *41*, 653–658.

[2] R. Hoppe, S. Voigt, H. Glaum, J. Kissel, H. P. Müller, K. Bernet, A new route to charge distributions in ionic solids, *J. Less-Common Met.* **1989**, *156*, 105–122.

[3] M. M. J. Treacy, J. M. Newsam, M. W. Deem, A general recursion method for calculating diffracted intensities from crystals containing planar faults, *Proc. R. Soc. London, Ser. A* **1991**, *433*, 499–520.

4 First-principles and experimental characterization of the electronic properties of $CaGaSiN_3$ and $CaAlSiN_3$: the impact of chemical disorder

published in: *Phys. Chem. Chem. Phys.* **2017**, *19*, 9292–9299.

authors: Robin Niklaus, Ján Minár, Jonas Häusler and Wolfgang Schnick

DOI: 10.1039/C6CP08764G

Acknowledgment: Adapted from *Physical Chemistry Chemical Physics* with permission from the PCCP Owner Societies 2017. Copyright 2017 Royal Society of Chemistry.

Abstract We report a detailed investigation of the electronic, mechanical and optical properties of the recently discovered nitridogallosilicate $CaGaSiN_3$ which has potential as a LED-phosphor host material. We focus on chemical disorder effects, originating from the Ga/Si site, and compared them to those of isostructural $CaAlSiN_3$. We calculate the elastic moduli and the Debye temperature in terms of quasi-harmonic approximation. Spectral properties like the joint density of states (JDOS) are evaluated and the absorption, reflectance and energy loss function are obtained from the dielectric function. The optical band gap of $CaGaSiN_3$ from experiment is compared to the electronic band gap in terms of electronic DOS and band structure calculations. All properties are evaluated for different ordering models of Ga/Si while the experimentally observed substitutional disorder is accounted for by utilizing the Coherent Potential Approximation (CPA). We conclude a shrinking of the band gap for both $CaGaSiN_3$ and $CaAlSiN_3$ due to atomic disorder, which is unfavorable for potential phosphor applications. This study contributes to materials design considerations, and provides a close look on the electronic impact of substitutional disorder. Moreover, we open the scope for future investigations on solid solutions and phosphor host materials with low doping concentrations.

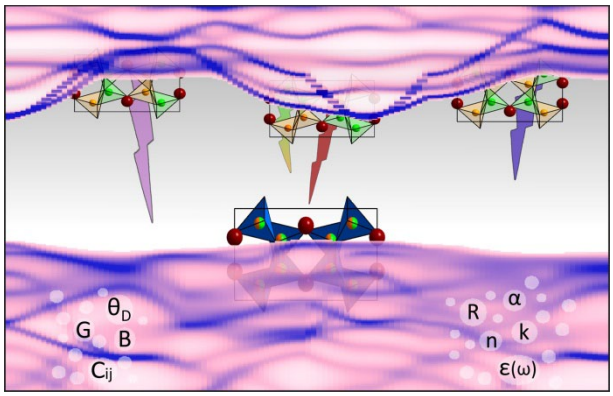

4.1 Introduction

Along with tackling the increasing global demand for electricity[1] with the phase out and replacement of incandescent light bulbs by solid-state LED lighting technology, there is a high demand for novel luminescent materials in phosphor-converted (pc)-LEDs that fulfill industrial standards for solid-state lighting.[2] $CaAlSiN_3$:Eu^{2+} represents a phosphor with efficient deep red luminescence. Partial substitution of Ca with Sr results in a shift of the emission maximum to

smaller wavelengths making (Ca,Sr)$AlSiN_3$:Eu^{2+} suitable for illumination grade lighting purposes.[3–6] While atomic substitution of Al by Ga has been achieved recently by ammonothermal synthesis of $CaGaSiN_3$,[7] effects of substitutional disorder itself for phosphor host materials are scarce. $CaGaSiN_3$ crystallizes in the same space group as $CaAlSiN_3$ and exhibits similar chemical disorder, showing red luminescence when doped with Eu^{2+}.[4,7] The electronic influence of the band gap (E_g) has been discussed extensively for phosphor materials. For instance, a small band gap can correspond to high thermal quenching at relatively low temperatures,[8] which can be attributed to exciton self-trapping effects in the conduction band.[9] There have also been attempts to connect the Debye temperature (θ_D), as an extent of the rigidity of the host lattice, to E_g and quantum efficiencies of luminescent materials.[10]

For $CaAlSiN_3$ there have already been extensive efforts to characterize the properties on a first-principles basis, such as the calculation of the band structure, and optical and mechanical properties.[11] However, the impact of Al/Si disorder has only been addressed implicitly. Mikami *et al*. performed calculations on the Al/Si disorder by means of the virtual crystal approach (VCA), yet the focus is mainly on the nature of the indirect band gap and the overall consistency of the band structure with that of the ordered Al/Si models.[12] Moreover, the used VCA only mimics a virtual atom from an averaged potential of the mixed occupancy site. Therefore, the VCA can describe only rigid shifts of the Fermi energy (E_f) and does not include lifetime broadening effects. In addition, this approximation is valid only for systems with small characteristic disorder and for atoms which have similar scattering properties. In this respect the VCA approximation is questionable for $CaGaSiN_3$ and similar compounds. In our work we utilize the more elaborate coherent potential approximation (CPA), within the Korringa–Kohn–Rostoker (KKR) Green function formalism, which includes a weighted site average derived from the scattering properties of the individual atoms to the crystal potential. In contrast to variational principle based DFT methods (like for example PAW), the use of the Green's function terminology allows one not to be limited to a purely 3D-periodical description when treating the electronic structure. Thus it is possible to treat chemical disorder within the KKR formalism. This formalism allows for a more dedicated approach to access the separated electronic properties of each atom on a mixed occupancy site. For future reference, this is particularly important if one is interested in considering the f-states of Eu on the Ca site, which would not be available from VCA. Limitations arise in the description of accurate band gap values due to exchange correlation as in any other DFT method. While values of E_g are accurately described relative to each other within the method itself, slight deviations may occur from the use of other DFT methods due to limitations of the KKR formalism in determining the Fermi energy.

A further widely used approach using an average from the ordered structures for a disordered system turns out to be a valid assumption to approximate mixed crystallographic occupancies. However, this usually requires a large number of structure models or the utilization of large supercells for heavily disordered systems ($A_xB_{1-x}C$ with $x < 0.5$).[13]
We therefore provide a detailed description of the mechanical, electronic and optical properties of recently discovered $CaGaSiN_3$ by performing state of the art calculations on ordered

structure models. We extend our analysis to the effects of chemical disorder in $CaGaSiN_3$ and conduct a comparison to $CaAlSiN_3$, which provides a suitable reference system due to its structural similarity and substantial characterization in the literature.[11,12,14,15]
Our work is an important contribution in terms of understanding the impact of substitutional disorder on the electronic structure of potential phosphor host materials and also on future work regarding calculations within the range of experimental doping in phosphor materials.

4.2 Computational Details

Along with the calculation of electronic band structures, DOS and optical properties, the structural relaxation of all internal cell parameters and internal coordinates was carried out for various ordering variants of $CaGaSiN_3$ within the Vienna *ab initio* simulation package (VASP).[16–18] Exchange correlation was described by utilizing the generalized gradient approximation (GGA) of Perdew, Burke, and Ernzerhof (PBE),[19,20] along with the projector-augmented-wave (PAW) method.[21,22] A plane-wave cut-off of 535 eV was chosen for the calculations and Brillouin zone sampling on a *Γ*-centered *k*-mesh (8 × 10 × 10) was done using the Monkhorst and Pack method.[23] To ensure high precision, the total energy of the unit cell was converged to 10^{-7} eV per atom with residual atomic forces below 3×10^{-4} eV $Å^{-1}$. The elastic tensors were derived from the stress–strain relationship by performing six finite lattice distortions of the crystal utilizing displacements of ±0.015 Å.[24] For band gap evaluation, additional calculations were performed using the modified Becke–Johnson formalism (GGA-mbj).[25,26] Comparative Bloch spectral functions and DOS calculations were further calculated from the VASP-optimized ordering models within the fully relativistic Korringa–Kohn–Rostoker (KKR) Green function method, while the disorder was treated by the CPA self-consistently and was fully relativistic within the four component Dirac formalism as implemented in the MUNICH SPR-KKR package.[27,28] In order to construct the different ordering variants depicted in Figure 4.1 for the disordered $CaGaSiN_3$ crystal, we considered a primitive

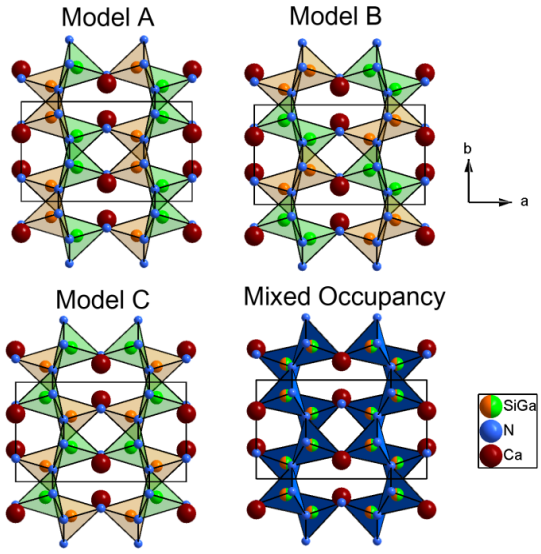

Figure 4.1 Different Si/Ga ordering variants (A–C) for orthorhombic $CaGaSiN_3$. Model for mixed Si/Ga occupation from experimental data. Structures illustrated by $(Si/Ga)N_4$ tetrahedra in the corresponding colors.

unit cell to arrive at the presented models in the same manner as Mikami *et al.*[12] Construction of a model with substitutional disorder was achieved by averaging over the relaxed cells and atomic positions and including symmetrization to the respective experimental space group $Cmc2_1$ (no. 36). Additionally, we conducted comparative CPA calculations for the disorder based on the Rietveld refinement of the experimental structure.[7]

4.3 Experimental Section

The ammonothermal synthesis of $CaGaSiN_3$ was carried out according to our recently reported procedure.[7] All working steps were conducted in an argon atmosphere employing flame-dried glassware connected to a vacuum line (≤0.1 Pa) or in Ar-filled glove boxes (Unilab, MBraun, Garching, O_2 <1 ppm, H_2O <1 ppm). The intermetallic precursor CaGaSi was synthesized by placing stoichiometric amounts of Ca (Sigma-Aldrich, 99.99%), Ga (smart elements, 99.999%) and Si (Alfa Aesar, 99.99%) in a tantalum ampule which was sealed in a water-cooled arc furnace under an argon atmosphere according to the procedure of Czybulka *et al.*[29] The doped sample was synthesized by adding 1% Eu as the dopant (smart elements, 99.99%). The ampule was transferred into a silica tube, which was evacuated and inserted in a tube furnace. The furnace was heated to 1300 K with 5 K min^{-1}, kept at 1300 K for 48 h and then cooled to room temperature with 0.5 K min^{-1}. CaGaSi (5 mmol) and NaN_3 (10 mmol, Sigma-Aldrich, 99.99%) were thoroughly ground in an agate mortar and transferred in a tantalum liner, which was then placed into an autoclave. The assembled autoclave was evacuated, cooled with ethanol/liquid nitrogen to 198 K and filled with ammonia (Air Liquide, 99.999%), which was passed through a gas purification cartridge (Micro Torr MC400–702FV, SAES Pure Gas Inc., San Luis Obispo, CA, USA; purity level <1 ppbV H_2O, O_2 and CO_2). Subsequently, the closed autoclave body was heated to 770 K with 3 K min^{-1}, kept at 770 K for 30 h, heated to 1073 K with 0.05 K min^{-1} and maintained at 1070 K for 10 h. The pressure was kept between 50 and 150 MPa during heating periods. The product was washed with 1 M HCl and dried at 350 K in air.

4.3.1 UV/Vis Spectroscopy

Reflectance spectra have been measured on a JASCO V-650 spectrometer with a He- and deuterium lamp. The measurements were done in the range of 200–800 nm with a step size of 1 nm and a bandwidth of 2 nm.

4.4 Results and Discussion

4.4.1 Mechanical Properties

The elastic constants for the $CaGaSiN_3$ and $CaAlSiN_3$ ordering variants are given in Table 4.1. All chosen models are stable with respect to the Born mechanical stability criteria for orthorhombic crystals.[30–32] The upper and lower bounds for the polycrystalline bulk (B) and shear (G) moduli are obtained within the isotropic approximations of Voigt and Reuss from the fourth-order elasticity tensors C_{ijkl} calculated by VASP.[33–36] They are expressed in terms of the abbreviated elastic constants C_{nm}.[37]

Table 4.1 Calculated elastic constants C_{nm} (GPa) in Voigt notation for the different $CaGaSiN_3$ and $CaAlSiN_3$ ordering variants

	$CaGaSiN_3$			**$CaAlSiN_3$**		
	A	**B**	**C**	**A**	**B**	**C**
C_{11}	295.7	290.6	294.6	329.2	324.8	329.4
C_{22}	269.7	268.2	270.1	287.9	288.2	290.8
C_{33}	300.9	299.5	283.4	324.9	323.7	316.2
C_{44}	103.2	101.1	94.7	111.2	110.5	104.7
C_{55}	74.4	77.4	71.7	83.4	84.7	81.8
C_{66}	58.5	60.8	61.6	67.7	68.5	69.7
C_{12}	129.6	131.6	122.1	116.6	118.1	116.8
C_{13}	79.9	82.4	87.2	68.8	71.9	73.7
C_{23}	95.6	92.1	95.9	100.1	98.3	95.6

Young's modulus (Y) and the Poisson ratio (ν) are obtained by common relations.[36] The Debye temperature θ_D is subsequently calculated within the quasi-harmonic approximation.[10,38–40]

The corresponding elastic bulk and shear moduli, Poissons's ratio, Young's modulus and Debye temperature (θ_D) are shown in Table 4.2. The Voigt–Reuss–Hill[35] bulk and shear moduli of models A and B are effectively the same while model C exhibits slightly smaller elastic moduli ($CaGaSiN_3$: Δ_B = 1.4 GPa and Δ_G = 2 GPa). The origin of this difference can be attributed to a strongly reduced C_{33} in model C, which is correlated with compressions along the c axis. In contrast to models A and B, the uniform arrangement of solely Ga and Si tetrahedra within the *ab*-plane in a layer-like manner allows for a stronger compression along the *c*-axis due to cation size differences. This effect has already been observed for $CaAlSiN_3$,[11] but appears to be more distinct in $CaGaSiN_3$ which we attribute to the smaller size difference of Al and Si.

Table 4.2 Calculated elastic bulk (B) shear (G) and Young's (Y) moduli in GPa, Debye temperature (θ_D) in K and Poisson's ratio (v) for $CaGaSiN_3$ and $CaAlSiN_3$

	$CaGaSiN_3$			**$CaAlSiN_3$**		
	A	**B**	**C**	**A**	**B**	**C**
B_V	163.5	163.4	162.1	168.2	168.2	167.6
B_R	163.1	163.2	161.7	167.9	168.1	167.4
B_{VRH}	163.3	163.3	161.9	168.0	168.1	167.5
G_V	84.9	84.7	81.8	96.2	96.0	94.6
G_R	79.8	80.0	78.8	91.2	91.3	90.7
G_{VRH}	82.35	82.35	80.3	93.8	93.6	92.7
Y_{VRH}	211.5	211.5	206.8	237.2	236.9	234.7
ν	0.28	0.28	0.29	0.26	0.27	0.27
θ_D	650.0	650.0	642.4	786.6	786.1	782.1

Calculation of the Debye temperature for $CaAlSiN_3$ yields values of $\theta_{D(A)}$ = 786.6 K, $\theta_{D(B)}$ = 786.1 K and $\theta_{D(C)}$ = 782.1 K, respectively. For $CaGaSiN_3$ the overall Debye temperature is decreased by approximately 125 K ($\theta_{D(A)}$ = 650 K, $\theta_{D(B)}$ = 650 K, $\theta_{D(C)}$ = 642.4 K), following its lowered elastic moduli and higher molar mass.

As the Debye temperature is the temperature at which all of the phonon frequencies in a material are excited, a high value of θ_D is correlated with vibrationally rigid structures.[10] Accordingly, one would expect a reasonable lower electron phonon coupling and possibly higher quantum efficiency for $CaAlSiN_3$. This concept should however be regarded with care due to the complexity of the luminescence process and can only be seen as a crude evaluation precept.

4.4.2 Electronic Properties

$CaGaSiN_3$: The overall band structures of the different ordering models as calculated from VASP shown in Figure 4.2(a–c) for the different models appear to be similar at first glance. They do however exhibit slightly different values for E_g of 3.235 eV (A), 3.10 eV (B) and 3.245 eV (C) for direct transitions at Γ. For model C an indirect transition occurs at (Z–T to Γ), which is energetically favored by 0.04 eV.

To account for the underestimation of the band gap within DFT we performed additional calculations using the modified Becke–Johnson exchange functional. The resulting band gaps yield values of 4.60, 4.40 and 4.50 eV for models A–C, respectively. The Fermi energy was set to the valence band edge. In terms of band dispersion the calculated Bloch spectral functions depicted in Figure 4.2(d–f) show good qualitative agreement with the standard GGA-PBE band structures calculated by VASP, showing larger deviations in the E_g values for direct transitions

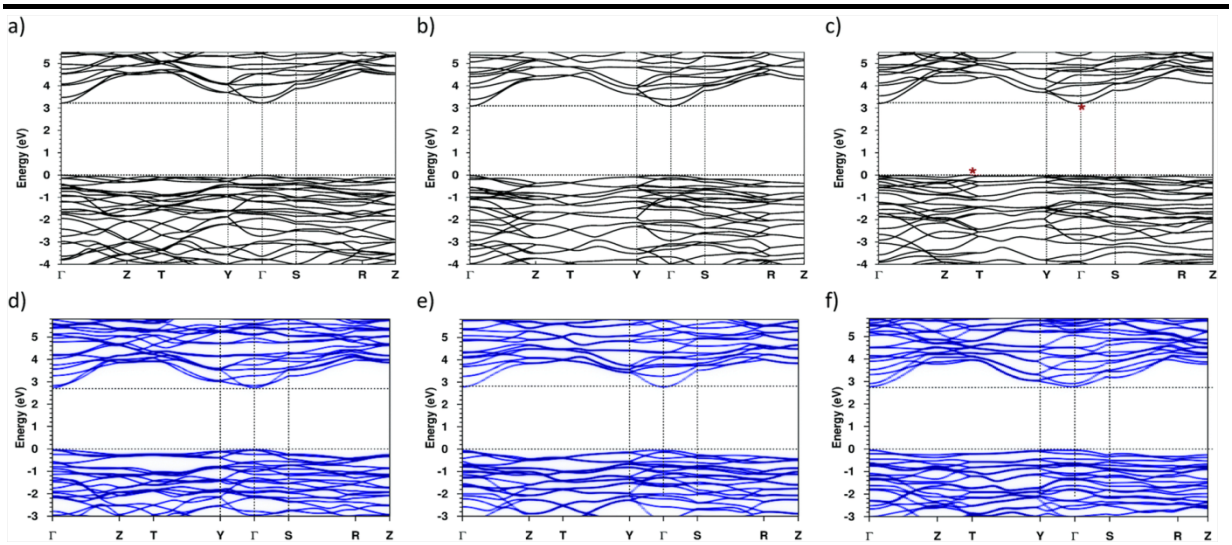

Figure 4.2 Band structure (a–c) and Bloch spectral function (d–f) calculated along high symmetry directions in the first Brillouin zone for the three $CaGaSiN_3$ ordering models within VASP (a–c) and the MUNICH SPR-KKR program package (d–f) from the relaxed VASP-models, where (a; d), (b; e) and (c; f) represent the Si/Ga-ordering variants A, B and C, respectively. The indirect transition of VASP relaxed model C is marked by a red asterisk.

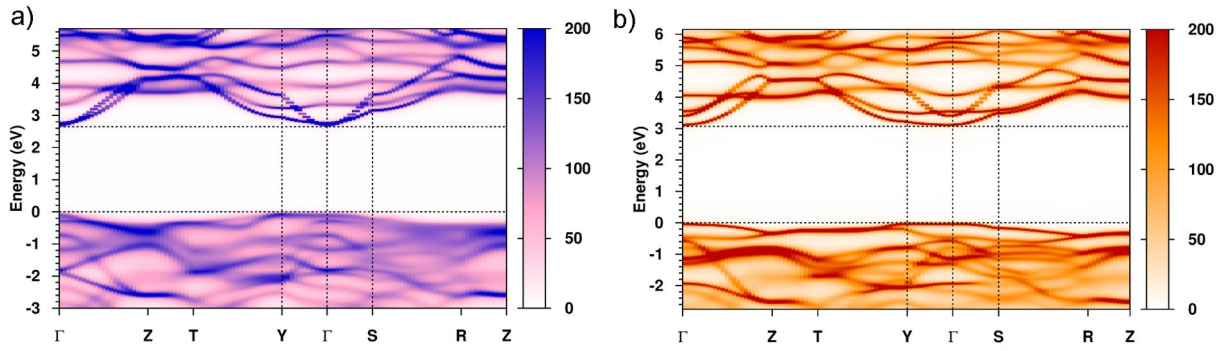

Figure 4.3 Bloch spectral function along high symmetry directions in the first Brillouin zone for the fully disordered structure of $CaGaSiN_3$ (a) and $CaAlSiN_3$ (b) obtained as symmetrized average of the relaxed ordering models and calculated within the KKR approach based on the CPA.

due to the nature of the KKR calculations resulting in the values for models A–C of 2.71 (*Γ*–*Γ*), 2.78 (*Γ* to *Γ*) and 2.75 eV (*Γ*–*Γ*). Both VASP and SPRKKR calculations indicate different magnitudes of the effective band gap for different Ga/Si ordering schemes in the unit cell. Relative differences in VASP and SPRKKR are mainly observed for ordering model B, with the smallest E_g value in VASP and the largest in KKR. Judging from careful convergence investigations with respect to internal parameters (such as the plane wave energy cutoff or l_{max}) this difference in E_g is attributed to the treatment of the basis set and the method of Bloch spectral calculation as such, since we observe the calculations of the DOS (see Figure 4.4) to be consistent for both methods identifying model B as the one with the smallest E_g.

The fully disordered model $CaGaSiN_3$, calculated within the CPA, is shown in Figure 4.3(a). As a result of the statistical Ga/Si distribution a smearing and general broadening of the Bloch spectral functions is observed. The disordered unit cell was obtained as an approximated average from the relaxed ordering models, symmetrized to *Cmc*2_1 (no. 36).

The disorder variant exhibits a direct band gap (*Γ* to *Γ*) of 2.65 eV and an equally large indirect band gap (*Y* to *Γ*), suggesting that the effective band gap of disordered $CaGaSiN_3$ is effectively limited with respect to the smallest band gap of the calculated ordering variants. This further holds true for calculations based on the non-relaxed experimental structure and ordering

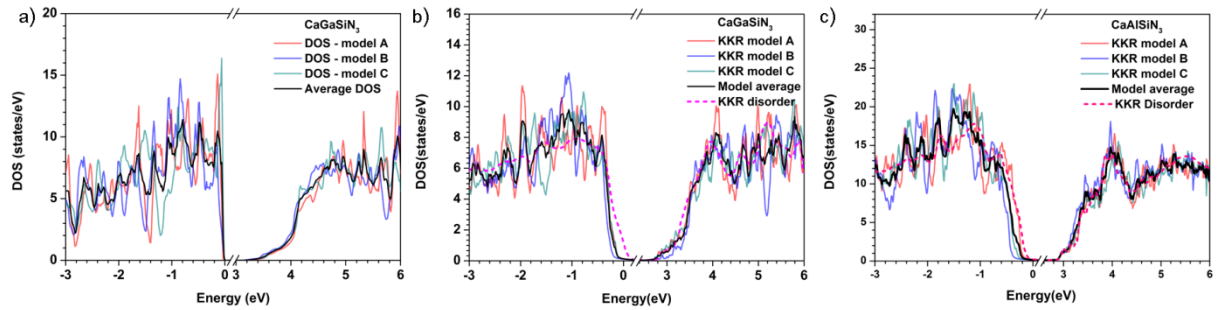

Figure 4.4 Total density of states near the valence and conduction band edge for the $CaGaSiN_3$ ordering models as calculated from VASP (a) and the SPRKKR-CPA approach for the relaxed models and disordered structures of $CaGaSiN_3$ (b) and $CaAlSiN_3$ (c). Averaged DOS for the three ordering models illustrated in black, respectively.

variants (see Figures S4.1–S4.3). Hence, the disorder results in a potentially smaller band gap, a process unfavorable for thermal quenching and excited-state trapping effects in general.[8,9] Figure 4.4 (a and b) depicts the total density of states (DOS) for the different ordering models according to VASP and SPRKKR including the Ga/Si disorder. The conduction band of the partial density of states (see Figure S4.4) has predominantly Ca 3d character followed by a mixture of Ga 3p/d, Si 3p and N 2p states. The valence band is strongly dominated by N 2p states followed by Ga 3d/3p/3s, Si 3p/3s and Ca 3d states. Figure 4.4(a) illustrates that the first maximum of the valence band DOS is situated closer to the absolute Fermi edge (E_f) for model C by about 0.13 eV respective to model A and 0.15 eV to model B. KKR calculations shown in Figure 4.4(b) suggest a similar optical behavior for models A and C, while the onset and maximum of the DOS of model B are shifted to lower energies in both VASP and KKR calculations. This can be interpreted in terms of a lower electronic transition probability from the valence to the conduction band for ordering model B at equal energies and, therefore, a larger optical band gap.

$CaAlSiN_3$: While extensive calculations on $CaAlSiN_3$ are already present in the literature,[11,12,14,15] our aim was set on comparative calculations to $CaGaSiN_3$ addressing the impact of disorder. KKR calculations for the respective ordering variants of $CaAlSiN_3$ reveal direct transitions at Γ with E_g values of 3.08, 3.23 and 3.11 eV for models A, B and C, respectively (see Figure S4.7 a–c). The Bloch spectral function depicted in Figure 4.3(b) for the chemically disordered variant of $CaAlSiN_3$ (Al : Si = 1 : 1) exhibits a band gap of 3.05 eV for both Γ–Γ and Y–Γ transitions. Just like in $CaGaSiN_3$ the band gap is similarly lowered by the disorder by about 0.05–0.18 eV compared to the ordered structures A, C and B. The principal effect that the disorder induces on an earlier ascent in the transition probability is also observed in the DOS (see in Figure 4.4(c)) and is in line with the effect observed in $CaGaSiN_3$.

The overall effect is however, less pronounced than in $CaGaSiN_3$. We attribute this effect to the higher chemical similarity of Al/Si compared to Ga/Si. Both SPRKKR and VASP values for the Band gap (E_g^{VASP} = 3.4 eV) show good agreement and an expectedly increased band gap of $CaAlSiN_3$ compared to $CaGaSiN_3$ by about 0.3 eV. The same holds true for the optical band gap from the calculated absorption spectra with an averaged optical band gap of about 4.0 eV (see Figure S4.9). Band gaps with GGA-mbj correction result in an electronic band gap of 4.5 eV which comes close to the optical band gap value of 5.0–5.3 eV as obtained by direct extrapolation from diffuse reflectance data.[4,41,42]

4.4.3 Optical Properties

To determine the experimental band gap of $CaGaSiN_3$, we conducted UV/Vis spectroscopy. Diffuse reflectance spectra (see Figure 4.5(a)) of undoped and Eu^{2+}-doped $CaGaSiN_3$ show a broad absorption band above 330 nm (3.75 eV). The undoped sample shows an additional absorption band (at around 270 nm) which is attributed to unknown amorphous contaminants from the ammonothermal synthesis. The band gap was determined using the Kubelka–Munk formalism for direct transitions,[43–45]

$$\alpha(h\nu) \approx B(h\nu - E_g)^n,$$

plotted as $(F(R)h\nu)^{1/n}$ in accordance with the calculated band structure of the disordered $CaGaSiN_3$. The experimental optical band gap was determined to be 3.20 and 3.37 eV for the undoped and doped samples, respectively (see Figure 4.5(b)). Close agreement with the calculated value for E_g of 3.10 eV appears counterintuitive as DFT is usually expected to underestimate the experimental band gap more severely. We conclude that the experimentally determined band gap is equally underestimated due to the broadened drop of reflectance (330–460 nm). The observed extensive Urbach tailing is ascribed to the statistical Ga/Si disorder and defects of the nanocrystallites.[46] The latter are strongly dependant on autoclave pressure variations and are attributed to slight band gap discrepancies of doped and undoped $CaGaSiN_3$. Direct extrapolation of the reflectivity as done for $CaAlSiN_3$[41,42] to the zero point of the x-abscissa of the diffuse reflectivity would result in a band gap of 4.4 eV for $CaGaSiN_3$ more closely in accordance with the GGA-mbj values. We believe the Tauc plot to be closer to reality which would also imply a smaller E_g value for $CaAlSiN_3$ and a similar overestimation by mbj-GGA.

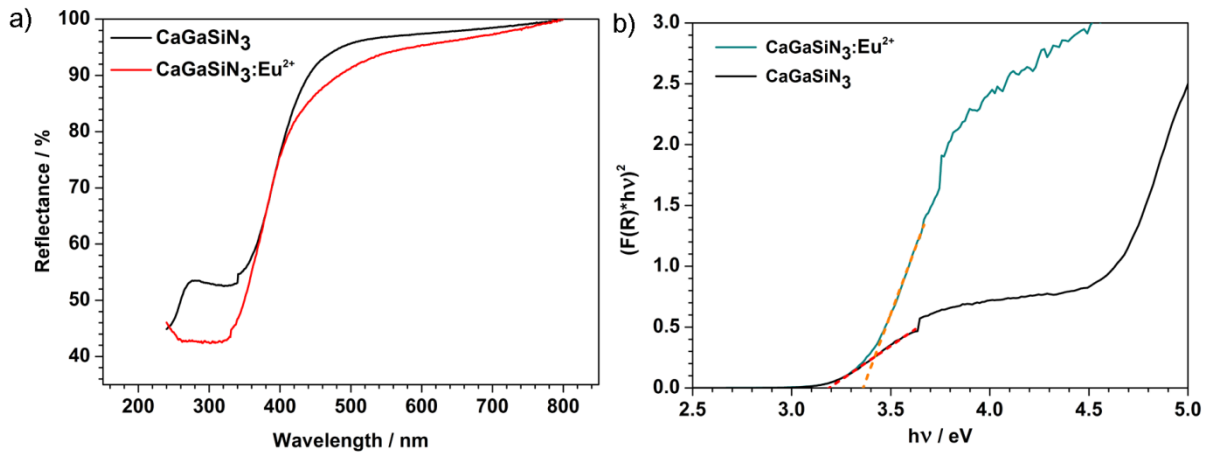

Figure 4.5 (a) Experimental normalized diffuse reflection spectrum of undoped (black) and Eu-doped (red) $CaGaSiN_3$. Intensity artifact at 330 nm due to a He to D-Lamp switch. (b) Tauc plot (n = 1/2) for Eu-doped (turquoise) and undoped (black) $CaGaSiN_3$. Dashed lines indicate a linear fit to determine E_g for the doped (orange) and undoped (red) sample, respectively.

In order to compare the experimental optical band gap we further determined the optical properties of $CaGaSiN_3$ from the calculated complex dielectric matrix:

$$\varepsilon = \varepsilon_1(\omega) + i\varepsilon_2(\omega),$$

where the imaginary part $\varepsilon_2(\omega)$ is obtained by summation over empty states and the real part $\varepsilon_1(\omega)$ follows from the Kramers–Kronig relation.[47] The optical properties such as extinction coefficient $k(\omega)$, refractive index $n(\omega)$, optical reflectivity $R(\omega)$ and absorption coefficient $\alpha(\omega)$ are obtained from the relations:[48]

$$k(\omega) = \sqrt{\frac{\sqrt{\varepsilon_1(\omega)^2 + \varepsilon_2(\omega)^2} - \varepsilon_1(\omega)}{2}},$$

$$n(\omega) = \sqrt{\frac{\sqrt{\varepsilon_1(\omega)^2 + \varepsilon_2(\omega)^2} + \varepsilon_1(\omega)}{2}},$$

$$R(\omega) = \frac{(n-1)^2 + k^2}{(n+1)^2 + k^2},$$

$$\alpha(\omega) = \frac{2k\omega}{c}$$

The calculated averaged absorption spectrum of $CaGaSiN_3$ is shown in Figure 4.6 (a). We estimate the optical band gaps for $CaGaSiN_3$ by extrapolation of the slopes to the energy axis from the calculated absorption spectra (Figure 4.6(b)).[45] In accordance to the calculated DOS, ordering model C shows an early onset of absorption, resulting in the smallest optical band gap of 3.72 eV, followed by model A with E_g = 3.90 eV and model B with E_g = 4.00 eV. The observed peaks of the averaged absorption spectrum can be approximately assigned to different electronic transitions with help of the partial DOS (see Figure S4.4). The first absorption peak at 6.3 eV can be assigned to N 2*p* to Ca 3*d* transitions, while the second peak at 8.7 eV appears

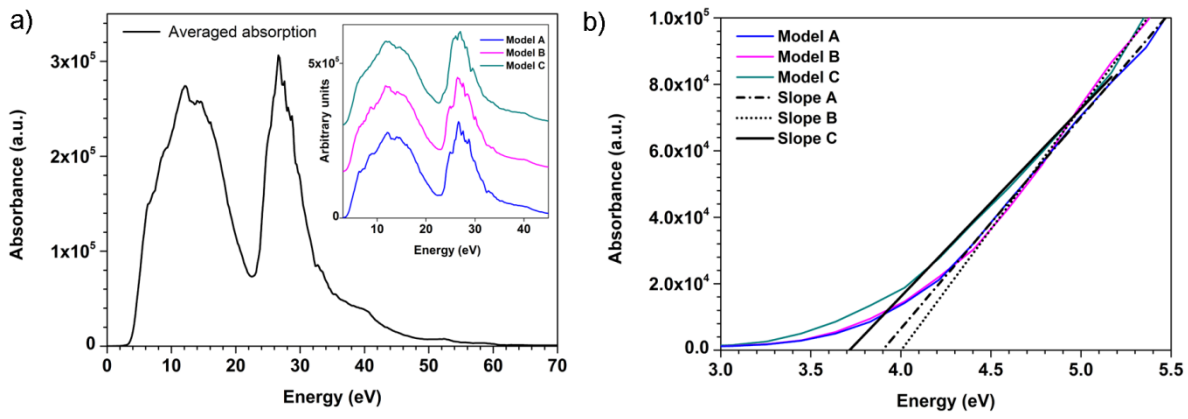

Figure 4.6 (a) Calculated absorption spectrum for $CaGaSiN_3$ as an average of the ordering models A, B and C calculated from VASP. The colored inset depicts the different contributions to the shape of the averaged spectrum. (b) Slopes of the first linear ascend in the absorption spectra.

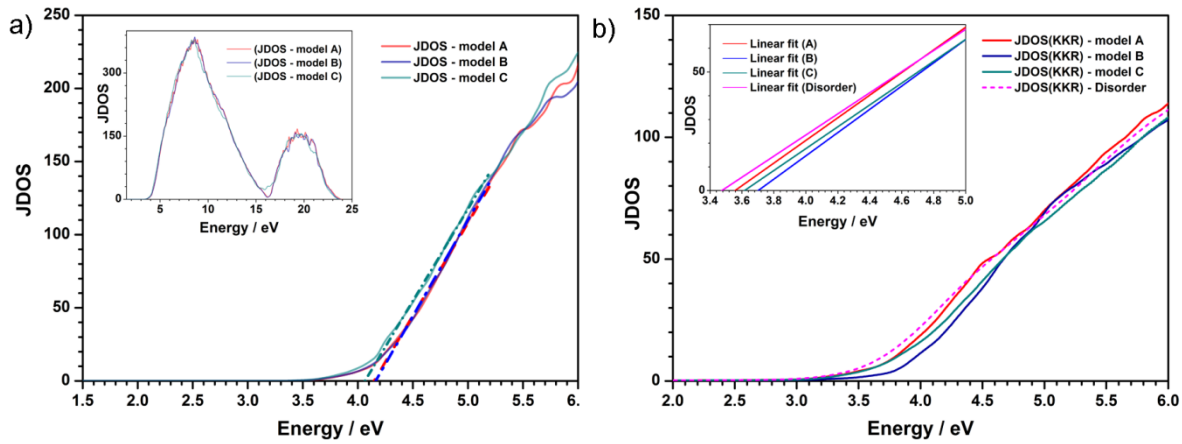

Figure 4.7 (a) Calculated joint DOS (JDOS) for the three ordering models A, B, C of $CaGaSiN_3$ as calculated with VASP with their corresponding extrapolated linear fits to evaluate E_g. (b) Calculated JDOS for ordered and disordered $CaGaSiN_3$ within the SPRKKR formalism. The inset displays the extrapolated linear fits to evaluate E_g.

ambiguously from most likely N 2*p* and Ga 3*p* to Ca 3*d* transitions. Note that this peak is not observed in model C. According to the selection rules the doublet at 12 eV can be attributed to Ga/Si 3*p* to Ca 3*d* and Si 3*s* to Ga/Si 3*p* transitions. The second absorption maximum peaking around 24–30 eV consists of different Ga, Si and N *s*/*p* state transitions to the conduction band. The evaluation of E_g was further conducted by calculations of the joint DOS depicted in Figure 4.7 (a and b), which is proportional to the measured absorption under the assumption of constant matrix elements, for both SPRKKR and VASP data. The determined band gap values from the VASP evaluated JDOS are slightly larger than those factoring the dielectric matrix elements (see Figure 4.6 (b)) but show an overall good agreement. The band gaps evaluated from the SPRKKR evaluated the JDOS range from 3.5 eV, for the disordered CPA calculation, to 3.7 eV for ordering model B. These results further corroborate the lowering of the electronic band gap with the introduced atomic disorder in $CaGaSiN_3$.

4.5 Conclusion

We report a detailed investigation and comparison of the electronic properties of $CaGaSiN_3$ and $CaAlSiN_3$ at a first-principles level. The effective band gap of the heavier homologue $CaGaSiN_3$ is expectedly reduced by about 0.3 eV. The diffuse reflectance spectra of $CaGaSiN_3$ suggest an optical band gap of 3.2–3.4 eV. By assuming different atomic ordering patterns for $CaGaSiN_3$, DFT predicts E_g to be 3.1–3.3 eV, while the utilization of GGA-mbj corrected electronic band gap values tends to overestimate the average band gap to 4.5 eV with regard to the experimental Tauc plot. Additional absorption spectra were calculated for different atomic ordering models of $CaGaSiN_3$ and $CaAlSiN_3$ with VASP and SPRKKR, respectively, resulting in optical band gaps of 3.6–4.0 eV ($CaGaSiN_3$) and 4.0 eV ($CaAlSiN_3$) on average.

In order to address the experimentally prevailing chemical disorder in both systems we employ the approach of SPRKKR + CPA, which to date has not been utilized extensively to study large band gap phosphor host materials. We show that for $CaGaSiN_3$ and $CaAlSiN_3$ the chemical

disorder impacts the electronic structure by diminishing the electronic and optical band gaps by about 0.1 eV on average with respect to chemically ordered structures. We thus provide insights into a better understanding of chemical disorder effects on the electronic structure at an *ab initio* level for the materials in question.

Our results might prove beneficial to future materials design considerations of phosphor materials under the presumption of being valid for a wider range of compounds. Most importantly the successful treatment of disorder with SPRKKR + CPA in this case study opens the scope to future investigations on related solid-solution materials and common nitride phosphor materials by addressing rare earth doping at an experimental level without the utilization of extensive super cell calculations.

4.6 Acknowledgements

This work was supported by the European Regional Development Fund (ERDF), project CEDAMNF, reg. no. CZ.02.1.01/0.0/0.0/15_003/0000358 and GACR (Proj. 17-14840S). Financial support by the Deutsche Forschungsgemeinschaft (DFG) within the research group "Chemistry and Technology of the Ammonothermal Synthesis of Nitrides" (FOR 1600), project SCHN377/16 and the Fonds der Chemischen Industrie (FCI) is gratefully acknowledged.

4.7 References

[1] IEA, *World Energy Outlook Special Report*, **2015**.

[2] ENERGY STAR® *Program Requirements for Integral LED Lamps,* **2011**.

[3] K. Uheda, N. Hirosaki, H. Yamamoto, Host lattice materials in the system Ca_3N_2–AlN–Si_3N_4 for white light emitting diode, *Phys. Status Solidi A* **2006**, *203*, 2712–2717.

[4] K. Uheda, N. Hirosaki, Y. Yamamoto, A. Naito, T. Nakajima, H. Yamamoto, Luminescence Properties of a Red Phosphor, $CaAlSiN_3:Eu^{2+}$, for White Light-Emitting Diodes, *Electrochem. Solid-State Lett.* **2006**, *9*, H22–H25.

[5] H. Watanabe, N. Kijima, Crystal structure and luminescence properties of $Sr_xCa_{1-x}AlSiN_3:Eu^{2+}$ mixed nitride phosphors, *J. Alloys Compd.* **2009**, *475*, 434–439.

[6] P. Pust, P. J. Schmidt, W. Schnick, A revolution in lighting, *Nat. Mater.* **2015**, *14*, 454–458.

[7] J. Häusler, L. Neudert, M. Mallmann, R. Niklaus, A.-C. L. Kimmel, N.S.A. Alt, E. Schlücker, O. Oeckler, W. Schnick, Ammonothermal Synthesis of Novel Nitrides: Case Study on $CaGaSiN_3$, *Chem. Eur. J.* **2017**, *23*, 2583–2590.

[8] S. Schmiechen, H. Schneider, P. Wagatha, C. Hecht, P. J. Schmidt, W. Schnick, Toward New Phosphors for Application in Illumination-Grade White pc-LEDs: The Nitridomagnesosilicates $Ca[Mg_3SiN_4]:Ce^{3+}$, $Sr[Mg_3SiN_4]:Eu^{2+}$, and $Eu[Mg_3SiN_4]$, *Chem. Mater.* **2014**, *26*, 2712–2719.

[9] P. Dorenbos, Thermal quenching of Eu^{2+} 5*d*–4*f* luminescence in inorganic compounds, *J. Phys.: Condens. Matter* **2005**, *17*, 8103.

[10] J. Brgoch, S. P. DenBaars, R. Seshadri, Proxies from Ab Initio Calculations for Screening Efficient Ce^{3+} Phosphor Hosts, *J. Phys. Chem. C* **2013**, *117*, 17955–17959.

[11] Z. Wang, B. Shen, F. Dong, S. Wang, W.-S. Su, A first-principles study of the electronic structure and mechanical and optical properties of $CaAlSiN_3$, *Phys. Chem. Chem. Phys.* **2015**, *17*, 15065–15070.

[12] M. Mikami, K. Uheda, N. Kijima, First-principles study of nitridoaluminosilicate $CaAlSiN_3$, *Phys. Status Solidi A* **2006**, *203*, 2705–2711.

[13] W. B. Park, S. U. Hong, S. P. Singh, M. Pyo, K.-S. Sohn, Systematic Approach To Calculate the Band Gap Energy of a Disordered Compound with a Low Symmetry and Large Cell Size via Density Functional Theory, *ACS Omega* **2016**, *1*, 483–490.

[14] M. Mikami, Computational Chemistry Approach for White LED (Oxy)Nitride Phosphors, *ECS J. Solid State Sci. Technol.* **2013**, *2*, R3048–R3058.

[15] L. Chen, M. Fei, Z. Zhang, Y. Jiang, S. Chen, Y. Dong, Z. Sun, Z. Zhao, Y. Fu, J. He, C. Li, Z. Jiang, Understanding the Local and Electronic Structures toward Enhanced Thermal Stable Luminescence of $CaAlSiN_3:Eu^{2+}$,*Chem. Mater.* **2016**, *28*, 5505–5515.

[16] G. Kresse, J. Hafner, Ab initio molecular dynamics for liquid metals, *Phys. Rev. B: Condens. Matter Mater. Phys.* **1993**, *47*, 558–561.

[17] G. Kresse, J. Hafner, Ab initio molecular-dynamics simulation of the liquid-metal-amorphous-semiconductor transition in germanium, *Phys. Rev. B: Condens. Matter Mater. Phys.* **1994**, *49*, 14251–14269.

[18] G. Kresse, J. Furthmüller, Efficiency of *ab-initio* total energy calculations for metals and semiconductors using a plane-wave basis set, *Comput. Mater. Sci.* **1996**, *6*, 15–50.

[19] J. P. Perdew, K. Burke, M. Ernzerhof, Generalized Gradient Approximation Made Simple, *Phys. Rev. Lett.* **1996**, *77*, 3865–3868.

[20] J. P. Perdew, K. Burke, M. Ernzerhof, Generalized Gradient Approximation Made Simple [*Phys. Rev. Lett.* **1996**, *77*, 3865], *Phys. Rev. Lett.* **1997**, *78*, 1396.

[21] P. E. Blöchl, Projector augmented-wave method, *Phys. Rev. B: Condens. Matter Mater. Phys.* **1994**, *50*, 17953–17979.

[22] G. Kresse, D. Joubert, From ultrasoft pseudopotentials to the projector augmented-wave method, *Phys. Rev. B: Condens. Matter Mater. Phys.* **1999**, *59*, 1758–1775.

[23] H. J. Monkhorst, J. D. Pack, Special points for Brillouin-zone integrations, *Phys. Rev. B: Solid State* **1976**, *13*, 5188–5192.

[24] Y. Le Page, P. Saxe, Symmetry-general least-squares extraction of elastic data for strained materials from *ab initio* calculations of stress, *Phys. Rev. B: Condens. Matter Mater. Phys.* **2002**, *65*, 104104.

[25] F. Tran, P. Blaha, Accurate Band Gaps of Semiconductors and Insulators with a Semilocal Exchange-Correlation Potential, *Phys. Rev. Lett.* **2009**, *102*, 226401.

[26] J. A. Camargo-Martínez, R. Baquero, Performance of the modified Becke-Johnson potential for semiconductors, *Phys. Rev. B: Condens. Matter Mater. Phys.* **2012**, *86*, 195106.

[27] H. Ebert, D. Ködderitzsch, J. Minár, Calculating condensed matter properties using the KKR-Green's function method—recent developments and applications, *Rep. Prog. Phys.* **2011**, *74*, 096501.

[28] H. Ebert et al., *The Munich SPR-KKR Package*, Version 6.3, http://olymp.cup.uni-muenchen.de/ak/ebert/SPRKKR, **2012**.

[29] A. Czybulka, B. Pinger, H.-U. Schuster, Neue Erdalkali-Gallium-Silicide, -Germanide und -Stannide mit vom AlB2-Typ abgeleiteten Strukturen, *Z. Anorg. Allg. Chem.* **1989**, *579*, 151–157.

[30] M. Born, On the stability of crystal lattices. I, *Math, Proc. Camb. Phil. Soc.* **1940**, *36*, 160–172.

[31] M. H. Sadd, *Elasticity theory, applications, and numerics*, Elsevier Butterworth Heinemann, **2005**.

[32] F. Mouhat, F.-X. Coudert, Necessary and sufficient elastic stability conditions in various crystal systems, *Phys. Rev. B: Condens. Matter Mater. Phys.* **2014**, *90*, 224104.

[33] W. Voigt, *Lehrbuch der Kristallphysik (mit Ausschluss der Kristalloptik)*, B. G. Teubner, **1946**.

[34] A. Reuss, Berechnung der Fließgrenze von Mischkristallen auf Grund der Plastizitätsbedingung für Einkristalle, *Z. Angew. Math. Mech.* **1929**, *9*, 49–58.

[35] R. Hill, The Elastic Behaviour of a Crystalline Aggregate, *Proc. Phys. Soc. A* **1952**, *65*, 349–354.

[36] C. Jiang, S. G. Srinivasan, A. Caro, S. A. Maloy, Structural, elastic, and electronic properties of Fe_3C from first principles, *J. Appl. Phys.* **2008**, *103*, 043502.

[37] N. W. Ashcroft, N. D. Mermin, *Solid state physics*, Saunders college, **1976**.

[38] E. Francisco, J. M. Recio, M. A. Blanco, A. M. Pendás, A. Costales, Quantum-Mechanical Study of Thermodynamic and Bonding Properties of MgF_2, *J. Phys. Chem. A* **1998**, *102*, 1595–1601.

[39] E. Francisco, M. A. Blanco, G. Sanjurjo, Atomistic simulation of SrF_2 polymorphs, *Phys. Rev. B: Condens. Matter Mater. Phys.* **2001**, *63*, 094107.

[40] J.-P. Poirier, *Introduction to the physics of the earth's interior*, Cambridge University Press, **1921**.

[41] Y. Q. Li, N. Hirosaki, R.-J. Xie, T. Takeda, M. Mitomo, Yellow-Orange-Emitting $CaAlSiN_3:Ce^{3+}$ Phosphor: Structure, Photoluminescence, and Application in White LEDs, *Chem. Mater.* **2008**, *20*, 6704–6714.

[42] Z. Zhang, O. M. ten Kate, A. C. A. Delsing, M. J. H. Stevens, J. Zhao, P. H. L. Notten, P. Dorenbos, H. T. Hintzen, Photoluminescence properties of Yb^{2+} in $CaAlSiN_3$ as a novel red-emitting phosphor for white LEDs, *J. Mater. Chem.* **2012**, *22*, 23871–23876.

[43] P. Kubelka, New Contributions to the Optics of Intensely Light-Scattering Materials. Part I, *J. Opt. Soc. Am.* **1948**, *38*, 448–457.

[44] P. Kubelka, F. Munk, Ein Beitrag Zur Optik Der Farbanstriche, *Z. Tech. Phys.* **1931**, *12*, 593–601.

[45] R. López, R. Gómez, Band-gap energy estimation from diffuse reflectance measurements on sol–gel and commercial TiO_2: a comparative study, *J. Sol-Gel Sci. Technol.* **2012**, *61*, 1–7.

[46] E. F. Schubert, *Light-Emitting Diodes*, Cambridge University Press, **2006**.

[47] M. Gajdoš, K. Hummer, G. Kresse, J. Furthmüller, F. Bechstedt, Linear optical properties in the projector-augmented wave methodology, *Phys. Rev. B: Condens. Matter Mater. Phys.* **2006**, *73*, 045112.

[48] F. Wooten, *Optical properties of solids*, Academic Press, **1972**.

4.8 Supporting Information

4.8.1 Formulas Used for the Calculation of Mechanical Properties

Stability criteria for orthorhombic crystals:

$$C_{11}C_{22} > C_{12}^2, C_{22}C_{33} > C_{23}^2, C_{11}C_{33} > C_{13}^2$$

$$C_{ii} > 0 \ (i\text{=}1; 4\text{–}6)$$

and $C_{11}C_{22}C_{33} + 2C_{12}C_{23}C_{13} - C_{11}C_{23}^2 - C_{22}C_{13}^2 - C_{33}C_{12}^2 > 0$

Bulk and shear modulus according to Voigt (B_V, G_V) and Reuss (B_R, G_R):(*,**)

$$B_V = \frac{C_{11} + C_{22} + C_{33} + 2(C_{12} + C_{23} + C_{31})}{9}$$

$$B_R = \frac{1}{S_{11} + S_{22} + S_{33} + 2(S_{12} + S_{23} + S_{31})}$$

$$G_V = \frac{(C_{11} + C_{22} + C_{33}) - (C_{12} + C_{23} + C_{31})}{15} + \frac{3(C_{44} + C_{55} + C_{66})}{15}$$

$$G_R = \frac{15}{4(S_{11} + S_{22} + S_{33} - S_{12} - S_{23} - S_{31} + 3(S_{44} + S_{55} + S_{66})}$$

* Subscripts C_{nm} obtained from C_{ijkl} according to the Voigt notation $xx \rightarrow 1$, $yy \rightarrow 2$, $zz \rightarrow 3$, $yz \rightarrow 4$, $zx \rightarrow 5$, $xy \rightarrow 6$.
** Compliance constants S_{nm} are obtained from the inversion of elastic constant matrix $S = C^{-1}$.

Voigt-Reuss-Hill approximation:

$$B_{VRH} = \frac{B_V + B_R}{2} \qquad G_{VRH} = \frac{G_V + G_R}{2}$$

Young's modulus (Y) and the Poisson ratio (ν) are obtained by the relations:

$$Y_{VRH} = \frac{9BG}{3B + G} \qquad \nu = \frac{3B - 2G}{6B + 2G}$$

Debye temperature:

$$\theta_D = \frac{\hbar}{k_B}\left[6\pi^2 V^{1/2} N\right]^{1/3} \Delta$$

with $\Delta = \sqrt{\frac{B}{M}}\left[3\left[2\left(\frac{2}{3}\frac{1+\nu}{1-2\nu}\right)^{3/2} + \left(\frac{1}{3}\frac{1+\nu}{1-\nu}\right)^{3/2}\right]^{-1}\right]^{1/3}$,

where, k_B and $\hbar$ are the Boltzmann and Plank's constant respectively, ν is the Poisson ratio, V[m^3] is the volume of the unit cell, N is the number of atoms in the cell. B [Pa] represents the bulk modulus and M [a.u.] the molar mass of the unit cell.

4.8.2 $CaGaSiN_3$

4.8.2.1 Band structure/DOS Calculations for the Unrelaxed Experimental Structure Models

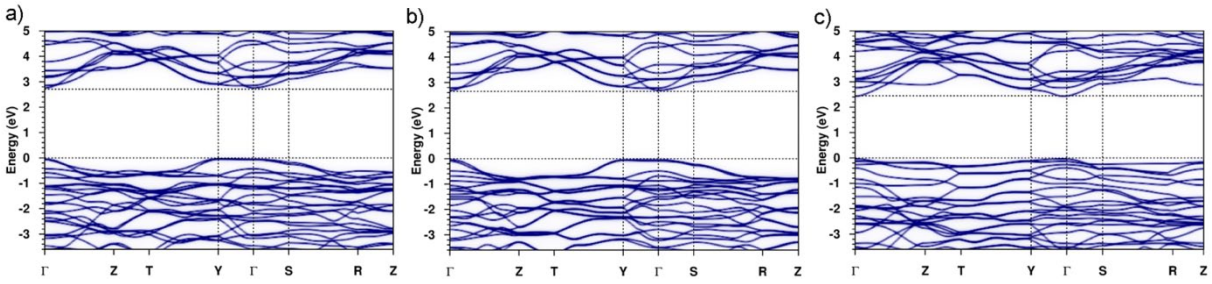

Figure S4.1 Bloch spectral functions (a-c) calculated along high symmetry directions in the first Brillouin zone within the MUNICH SPRKKR program package for the three $CaGaSiN_3$ ordering models based on the unrelaxed experimental crystal parameters where (a–c) represent the Si/Ga-ordering variants A, B and C, respectively.

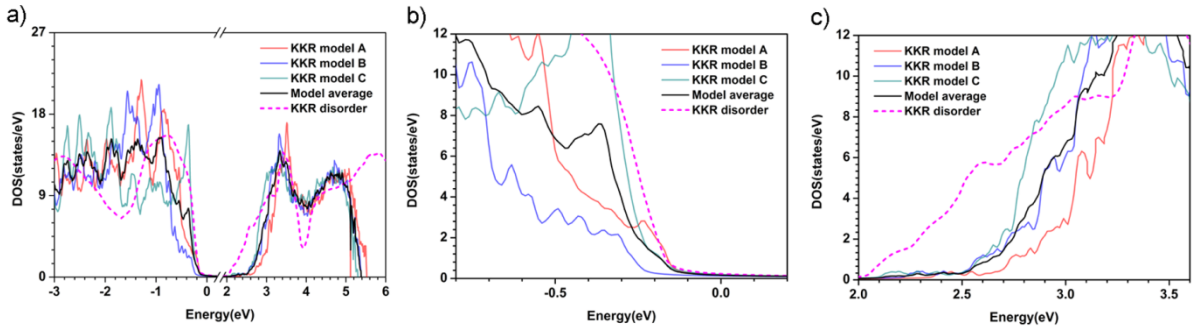

Figure S4.2 Colored: Interpolated total density of states near the valence and conduction band edge for the unrelaxed experimental $CaGaSiN_3$ ordering models as calculated from SPRKKR-CPA approach (a–c) including the Ga/Si disorder. Black: Average DOS of the three ordering models.

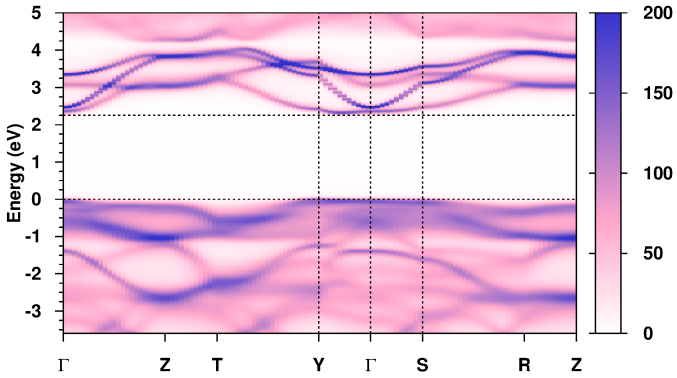

Figure S4.3 Bloch spectral functions along high symmetry directions in the first Brillouin zone for the fully disordered structure of $CaGaSiN_3$ as based on the experimental crystal structure refinement, calculated within the KKR approach based on the CPA.

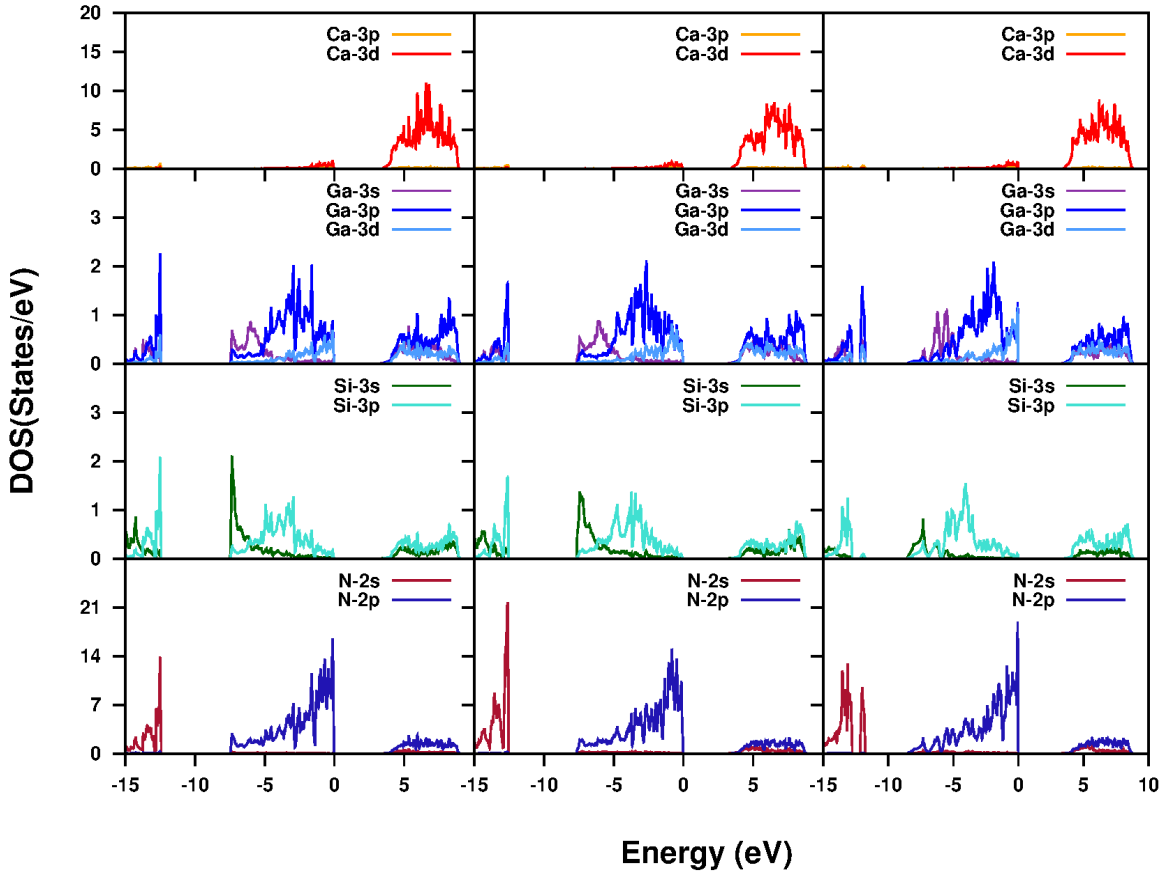

Figure S4.4 Partial density of states of the VASP relaxed ordering models of $CaGaSiN_3$. Left to Right: Ordering Models A, B and C.

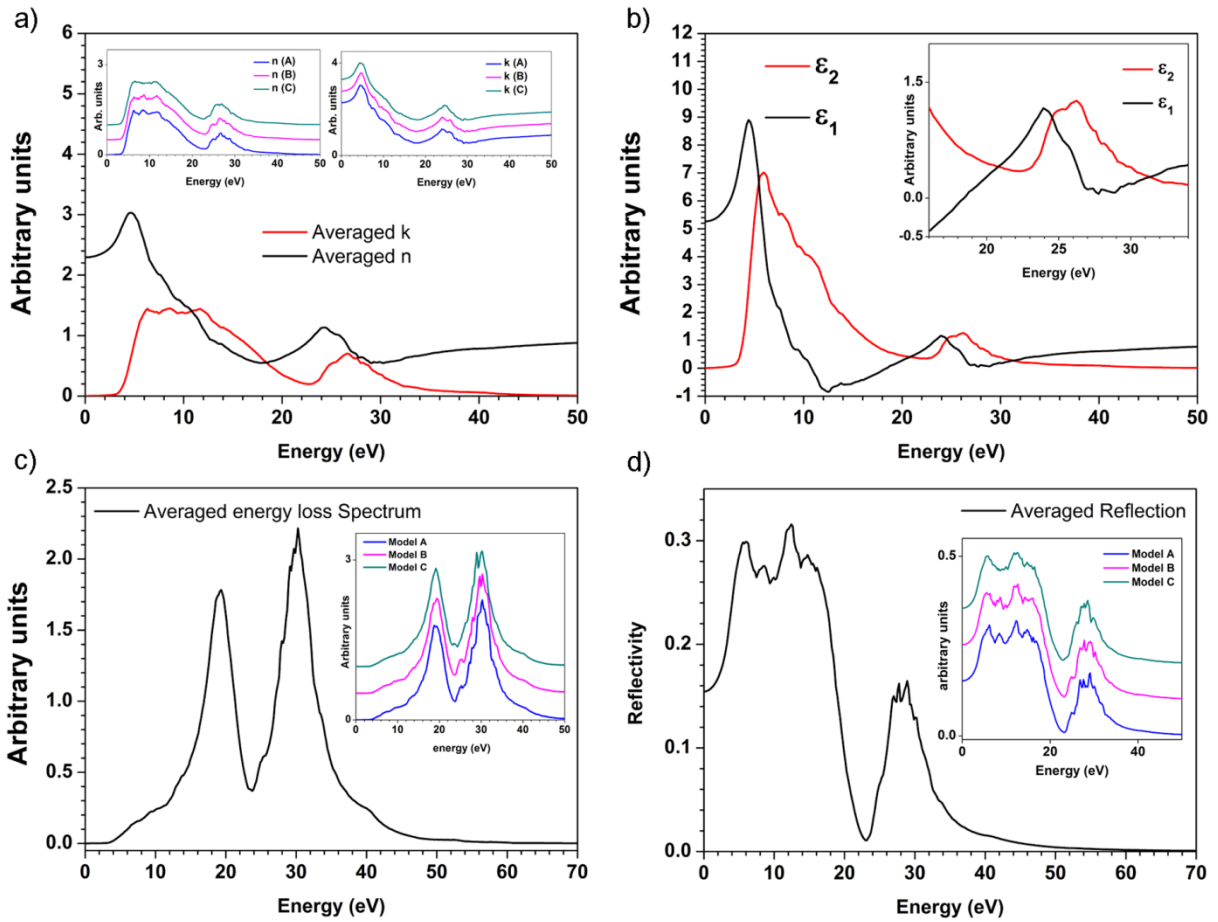

Figure S4.5 a) Calculated extinction coefficient k and refractive index *n*, b) imaginary (ε_2) and real (ε_1) part of the dielectric function, c) energy loss spectrum and d) reflectivity, for $CaGaSiN_3$ as an average of the ordering models A, B and C calculated from VASP. The differently colored inset (a, c, d) depicts the different contributions to the shape of the averaged spectrum.

The respective parts of the dielectric function ε, extinction coefficient *k*, refractive index *n*, reflectivity and energy loss spectra from the VASP calculations are depicted in Figure S4.5 (a–d). The static refractive index is found to be 2.29 and the overall refractive index reaches its maximum at 4.6 eV with a value of 3.03. The energy loss function is defined as

$$\mathrm{Im}\frac{1}{\varepsilon} = \frac{\epsilon_1^2}{\varepsilon_1^2 + \varepsilon_2^2 +}$$

taking large values for $\varepsilon_1 \rightarrow 0$ and $\varepsilon_2 < 1$.[1] The peaks of the plasma frequency can therefore, be identified as the maxima of the average energy loss function, with values of 19.5 and 30.25 eV, where ε_1 and ε_2 are sufficiently close to zero.

[1] R. E. Hummel, *Electronic Properties of Materials*, Springer, **2000**.

4.8.3 $CaAlSiN_3$

4.8.3.1 Total Energies (eV/Formula Unit) for the Relaxed Ordering Structures of $CaGaSiN_3$ and $CaAlSiN_3$

Table S4.1 Total energy after structural relaxation for both $CaAlSiN_3$ and $CaGaSiN_3$ in eV / formula unit as calculated by VASP

Ordering variant	A	B	C
Total energy (eV/f.u. of $CaAlSiN_3$)	−43.982	−43.980	−43.803
Total energy (eV/f.u. of $CaGaSiN_3$)	−41.132	−41.140	−40.885

4.8.3.2 DOS and Band Structure Calculations for Relaxed Structure Models

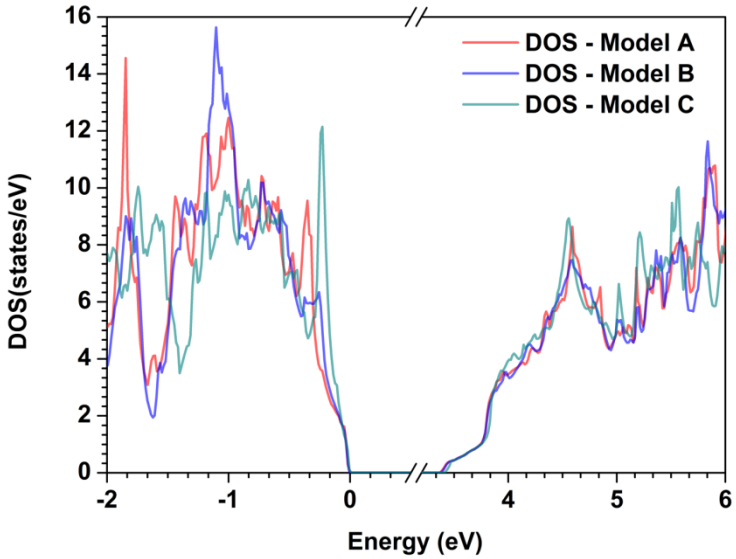

Figure S4.6 Density of states of $CaAlSiN_3$ for the relaxed $CaGaSiN_3$ analogue (Al/Si) ordering variants A, B and C as calculated by VASP.

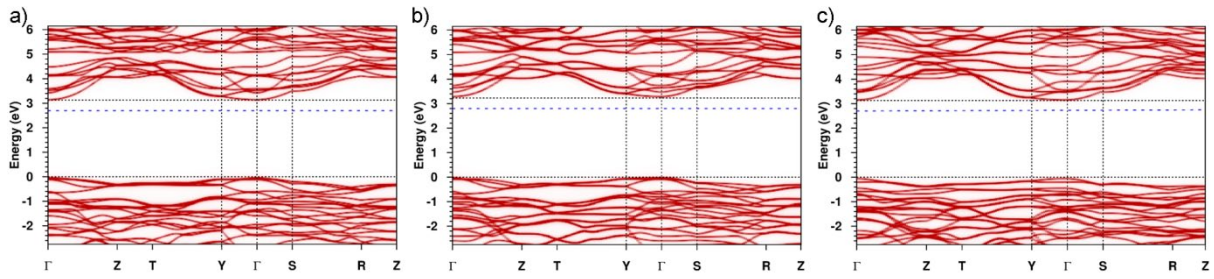

Figure S4.7 Bloch spectral function (a-c) calculated along high symmetry directions in the first Brillouin zone within the Munich SPRKKR program package for the three relaxed $CaAlSiN_3$ ordering models, where (a-c) represent the Si/Al-ordering variants A, B and C, respectively. Blue lines indicate the relative conduction band minimum for the calculations of the respective $CaGaSiN_3$ models.

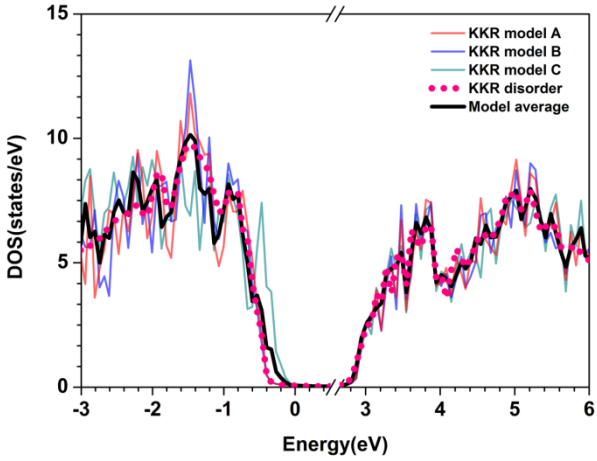

Figure S4.8 Unrelaxed calculated density of states of $CaAlSiN_3$ for the $CaGaSiN_3$ analogue (Al/Si) ordering variants A, B and C calculated with KKR. Black: Average Density of states of the combined models.

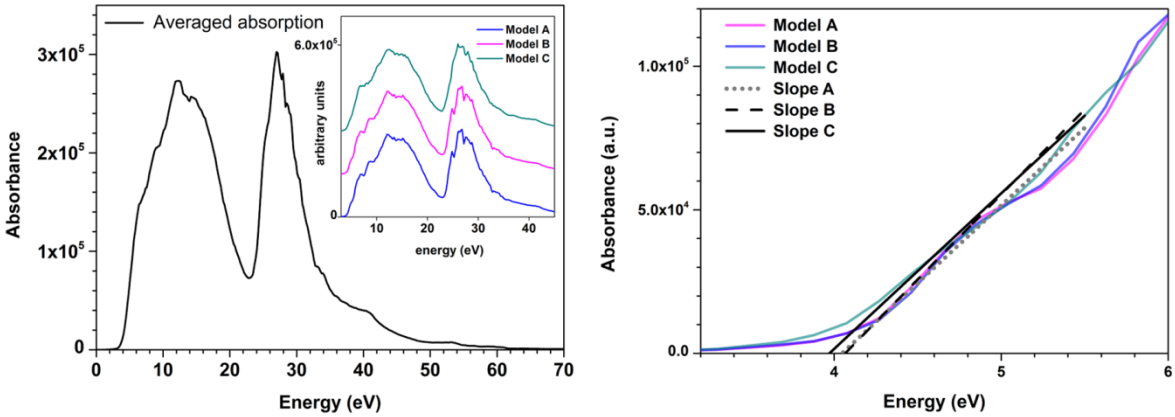

Figure S4.9 Calculated absorption (a) and intersecting slopes, corresponding to the optical band gap estimate, of the first steep ascend in absorption (b) for $CaAlSiN_3$ for the $CaGaSiN_3$ analogous (Al/Si) ordering variants A, B and C.

5 Ammonothermal Synthesis and Optical Properties of Ternary Nitride Semiconductors Mg-IV-N_2, Mn-IV-N_2 and Li-IV_2-N_3 (IV = Si, Ge)

published in: *Chem. Eur. J.* **2018**, *24*, 1686–1693.

authors: Jonas Häusler, Robin Niklaus, Ján Minár, and Wolfgang Schnick

DOI: 10.1002/chem.201704973

Abstract Grimm–Sommerfeld analogous nitrides $MgSiN_2$, $MgGeN_2$, $MnSiN_2$, $MnGeN_2$, $LiSi_2N_3$ and $LiGe_2N_3$ (generally classified as II-IV-N_2 and I-IV_2-N_3) are promising semiconductor materials with great potential for application in (opto)electronics or photovoltaics. A new synthetic approach for these nitride materials was developed using supercritical ammonia as both solvent and nitride-forming agent. Syntheses were conducted in custom-built high-pressure autoclaves with alkali metal amides $LiNH_2$, $NaNH_2$ or KNH_2 as ammonobasic mineralizers, which accomplish an adequate solubility of the starting materials and promote the formation of reactive intermediate species. The reactions were performed at temperatures between 870 and 1070 K and pressures up to 230 MPa. All studied compounds crystallize in wurtzite-derived superstructures with orthorhombic space groups *Pna*2_1 (II-IV-N_2) and *Cmc*2_1 (I-IV_2-N_3), respectively, which was confirmed by powder X-ray diffraction. Optical bandgaps were estimated from diffuse reflectance spectra using the Kubelka–Munk function ($MgSiN_2$: 4.8 eV, $MgGeN_2$: 3.2 eV, $MnSiN_2$: 3.5 eV, $MnGeN_2$: 2.5 eV, $LiSi_2N_3$: 4.4 eV, $LiGe_2N_3$: 3.9 eV). Complementary DFT calculations were carried out to gain insight into the electronic band structures of these materials and to corroborate the optical measurements.

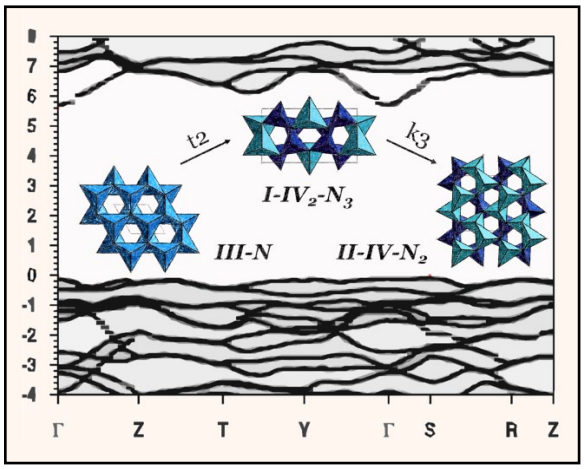

5.1 Introduction

Prospecting new semiconducting materials is an important issue in current research to meet the rapid development and high demands of modern electronic technologies. At present, gallium nitride and its solid solutions (Al,Ga,In)N (III-N) represent the most important nitride semiconductors for numerous applications, for example, light-emitting diodes, laser diodes or field-effect transistors.[1,2] In recent decades, a large number of new ternary nitrides were discovered, with many of them recently gaining increasing attention due to their promising optical and electronic properties.[3] In particular, ternary nitrides with structural relationships to group 13 nitrides are good candidates as next-generation semiconductor materials as they feature similar ranges of bandgaps and increased prospects for bandgap engineering. Furthermore, implied ternary nitrides are generally composed of earth-abundant elements, whereas metals like gallium or indium are becoming increasingly scarce. Zn-IV-nitrides (IV = Si, Ge, Sn) are currently the most prominent examples for such Grimm–Sommerfeld analogous compounds showing good bandgap tunability and small carrier effective masses.[3–6] Besides this, isotypic $MgSiN_2$ is also well-studied in terms of its electronic band structure, the photoluminescence of Mn^{2+} doped or rare earth doped materials as well as its ceramic properties.[7–10] On the other hand, further II-IV-N_2 compounds as well as wurtzite-related I-IV_2-N_3 nitrides have scarcely been investigated with regard to their optical and electronic properties so far. Previous experimental studies are mainly limited to the photoluminescence and ion conductivity of $LiSi_2N_3$, magnetic and optical properties of $MnSiN_2$ as well as the formation and optical tuning of $Mg_xMn_{1-x}SiN_2$ solid solutions.[11–16] Experimental analyses of optical parameters of the respective germanium compounds $MgGeN_2$, $MnGeN_2$ and $LiGe_2N_3$ have so far not been reported.

Common synthetic methods for Mg-IV-N_2, Mn-IV-N_2 and Li-IV_2-N_3 nitrides include high-temperature techniques under N_2 atmosphere, ammonolysis and vapor–liquid–solid (VLS) deposition.[15,17–19] In this contribution, we present an ammonothermal approach for bulk synthesis of these compounds using highly pressurized ammonia as the reaction medium. The ammonothermal technique is widely used for the crystal growth of binary nitrides like GaN,[20] whereas very few ternary nitrides were synthesized by this method so far. Recently, we described solution-based syntheses of $ZnSiN_2$ and $ZnGeN_2$ using ammonobasic supercritical ammonia.[21] In the present study, we report on synthesis and optical characterization of the ternary nitride semiconductors $MgSiN_2$, $MgGeN_2$, $MnSiN_2$, $MnGeN_2$, $LiSi_2N_3$ and $LiGe_2N_3$. The products were analyzed by powder X-ray diffraction, bandgaps were evaluated using diffuse reflectance spectroscopy and electronic structure was determined by DFT calculations based on the Korringa–Kohn–Rostoker (KKR) Green's function method.

5.2 Results and Discussion

5.2.1 Synthesis

The ternary nitrides $MgSiN_2$, $MgGeN_2$, $MnSiN_2$, $MnGeN_2$, $LiSi_2N_3$ and $LiGe_2N_3$ were synthesized by the ammonothermal method using custom-built high-pressure autoclaves. Ammonobasic mineralizers MNH_2 (M = Li, Na, K) were added to increase solubility of the starting materials. The alkali metal amides were obtained in situ starting from the azides because of the available purity and chemical stability of the latter. In analogy to the synthesis of Zn-IV-nitrides,[21] KNH_2 was preferred for syntheses of $MgSiN_2$ and $MnSiN_2$, while phase-pure samples of $MgGeN_2$ and $MnGeN_2$ were only obtained with $NaNH_2$ as the mineralizer. Mg/Mn were used in 20% excess and Li in 50% excess to facilitate complete conversion of the intermediates to the nitrides (see Experimental Section). Residual alkali or alkaline earth metal amides were easily washed out after the reactions (see below). The syntheses of II-IV-N_2 were carried out in two temperature steps, since intermediate species like amides or imides are preferentially formed at temperatures below 700 K.[22] In case of the Li-IV_2-N_3 compounds, the autoclaves were directly heated to the final desired temperature. Otherwise, a nearly complete transport of $LiNH_2$ into the colder peripheral parts of the vessels was observed. Lower heating rates were applied for the synthesis of $LiSi_2N_3$, taking the considerable decomposition of NH_3 at temperatures above 850 K into account.[23] All Si-containing products were synthesized at up to 1070 K with an autogenous pressure of 170 MPa. Phase-pure $LiSi_2N_3$ was obtained at 970 K, while Li_2SiN_2 was detected as a side-phase at 1070 K.[24] Besides, synthesis of $LiGe_2N_3$ was only successful starting from Ge_3N_4 instead of Ge. Since the Ge compounds are thermally less stable than the Si compounds, the former were synthesized at lower temperatures up to 900 K and a pressure of 230 MPa. Residual intermediates and mineralizer were dissolved in 5 M HCl ($MgSiN_2$, $MnSiN_2$, $LiSi_2N_3$), EtOH ($MgGeN_2$, $LiGe_2N_3$) or H_2O ($MnGeN_2$). The respective solvent was selected taking the chemical stability of the products and the formation of side-phases during the purification process into account. Crystal sizes of the obtained nitrides are in the range of 100 nm to 1 µm as shown in scanning electron microscopy (SEM) images (Figure S5.1).

5.2.2 Powder X-ray Diffraction and Crystal Structures

The purified products were analyzed by powder X-ray diffraction (see Figure 5.1). Wyckoff positions and atomic coordinates for Rietveld refinement were taken from literature.[17,25–27] The obtained crystallographic data are listed in Table 5.1, refined atomic coordinates and displacement parameters are given in Tables S5.1–S5.6 (see the Supporting Information). All referred compounds crystallize in orthorhombic symmetry. The crystal structures of both II-IV-N_2 and I-IV_2-N_3 can be derived from the wurtzite structure type (space group $P6_3mc$); ordering of the tetrahedrally coordinated cations results in space groups $Pna2_1$ and $Cmc2_1$, respectively.

Table 5.1 Crystallographic data of Mg-IV-N_2, Mn-IV-N_2 and Li-IV_2-N_3 (IV = Si, Ge) obtained by Rietveld refinement

Formula	**$MgSiN_2$**	**$MgGeN_2$**	**$MnSiN_2$**	**$MnGeN_2$**	**$LiSi_2N_3$**	**$LiGe_2N_3$**
Crystal system	orthorhombic					
Space group	*Pna*2$_1$	*Pna*2$_1$	*Pna*2$_1$	*Pna*2$_1$	*Cmc*2$_1$	*Cmc*2$_1$
a [Å]	5.2825(2)	5.5018(2)	5.2679(1)	5.4974(2)	9.2135(2)	9.5570(4)
b [Å]	6.4593(2)	6.6254(3)	6.5125(1)	6.6639(2)	5.2980(1)	5.5198(2)
c [Å]	4.9862(2)	5.1835(3)	5.0742(1)	5.2508(1)	4.7800(1)	5.0486(1)
Cell volume [Å^3]	170.132(9)	188.949(15)	174.082(6)	192.359(9)	233.324(9)	266.326(15)
Density [g·cm^{-3}]	3.1391	4.3916	4.2367	5.3715	2.9929	4.8429
Formula units [cell]	4					
T [K]	293(2)					
Diffractometer	STOE STADI P					
Radiation [Å]	Mo-Kα_1 (λ = 0.70930 Å)					
2θ range [°]	5.0 ≤ 2θ ≤ 50					
Profile function	fundamental parameters model					
Background function	Shifted Chebyshev					
Data points	3001					
Number of reflections	143	183	170	187	125	143
Refined parameters	56	50	35	51	33	54
R values	R_p = 0.0331 R_{wp} = 0.0417 R_{Bragg} = 0.0193	R_p = 0.0430 R_{wp} = 0.0578 R_{Bragg} = 0.0394	R_p = 0.0338 R_{wp} = 0.0434 R_{Bragg} = 0.0177	R_p = 0.0480 R_{wp} = 0.0632 R_{Bragg} = 0.0135	R_p = 0.0658 R_{wp} = 0.0877 R_{Bragg} = 0.0211	R_p = 0.0349 R_{wp} = 0.0453 R_{Bragg} = 0.0212
Goodness of fit	1.240	1.991	1.686	1.035	0.935	1.946

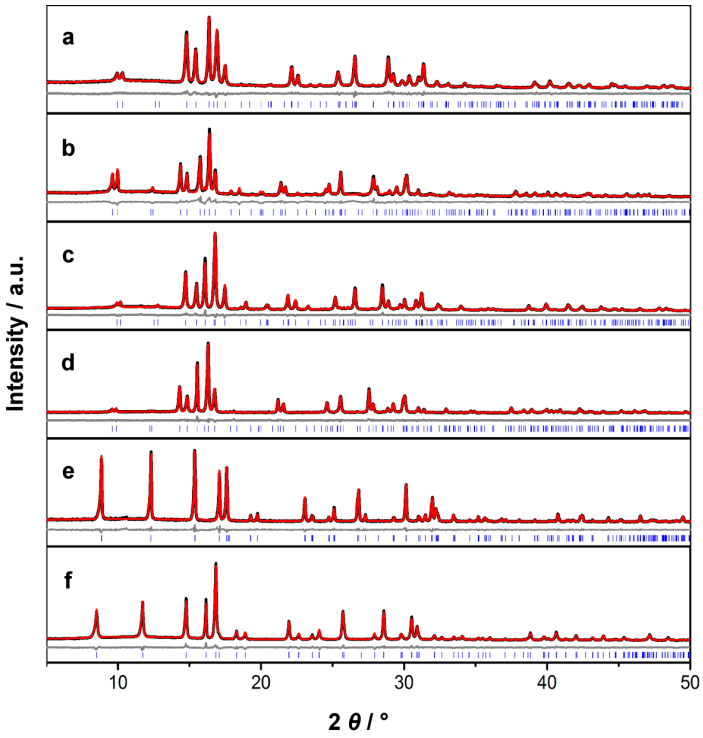

Figure 5.1 Rietveld refinements of $MgSiN_2$ (a), $MgGeN_2$ (b), $MnSiN_2$ (c), $MnGeN_2$ (d), $LiSi_2N_3$ (e) and $LiGe_2N_3$ (f) with experimental data (black lines, Mo-Kα_1 radiation, λ = 0.70930 Å), calculated patterns (red lines), difference profiles (gray lines) and positions of Bragg reflections (blue bars).

Crystal structures and group–subgroup relationships are illustrated in Figure 5.2. The three-dimensional networks are built up of corner-sharing cation-centered tetrahedra forming *sechser*-rings along [001].

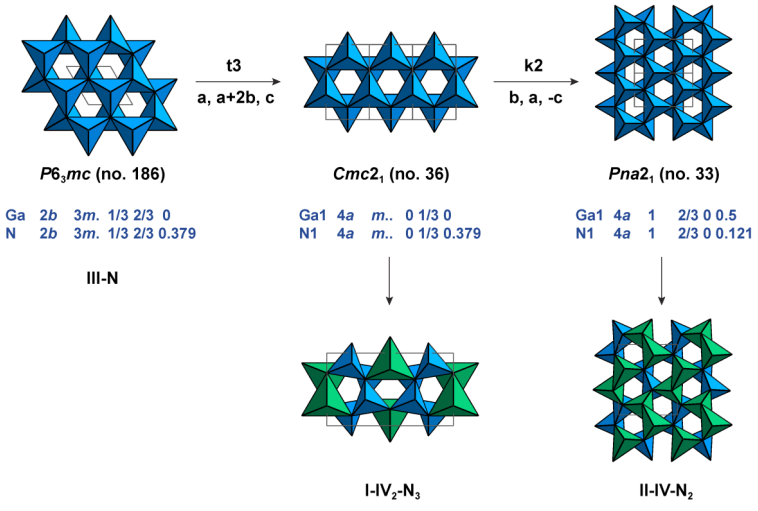

Figure 5.2 Group–subgroup relations of the wurtzite structure type ($P6_3mc$) and wurtzite superstructures of I-IV_2-N_3 ($Cmc2_1$) and II-IV-N_2 ($Pna2_1$) compounds viewed along [001]. GaN_4 (III-N) and MN_4 (M = Si, Ge in I-IV_2-N_3 and II-IV-N_2) tetrahedra are depicted in blue, $M'N_4$ tetrahedra (M' = Li, Mg or Mn) in green. Wyckoff positions of GaN were taken from literature.[28]

As expected, a slight tilting and distortion of the tetrahedra in II-IV-N_2 and I-IV_2-N_3 compared to the hypothetical superstructures based on III-N can be observed. Calculated lattice parameters and interatomic distances from Rietveld refinement are in the same range as earlier reported values.[17–25–27]

In addition, thermal stabilities of the synthesized nitrides were analyzed by temperature-programmed powder X-ray diffraction (TP-XRD). Degradation initiates at 770 K for $MgGeN_2$, 920 K for $MnSiN_2$ and between 1000–1200 K for the other nitrides as indicated by emerging reflections of the decomposition products (see Figure S5.2–S5.7 in the Supporting Information).

5.2.3 UV/Vis Reflectance Spectroscopy

Diffuse reflectance of the purified powder samples was measured to investigate the optical properties of the materials. The recorded spectra show broad absorption bands between 200–400 nm ($MgSiN_2$, $MnSiN_2$, $LiSi_2N_3$) and 300–500 nm ($MgGeN_2$, $MnGeN_2$, $LiGe_2N_3$), see Figure S5.8 in the Supporting Information. Pseudo-absorption spectra were calculated using the Kubelka–Munk function $F(R) = (1-R)^2/2\ R$ (R = reflectance).[29] The optical bandgaps were determined using Tauc plots $h\nu$ versus $(F(R)\cdot h\nu)^{1/n}$ with $n = 1/2$ for direct allowed transitions (Figure 5.3 and Table 5.2).[30] The observed absorption bands in the spectra were primarily attributed to direct transitions due to the similarity of direct and indirect bandgaps in the materials (section DFT calculations).

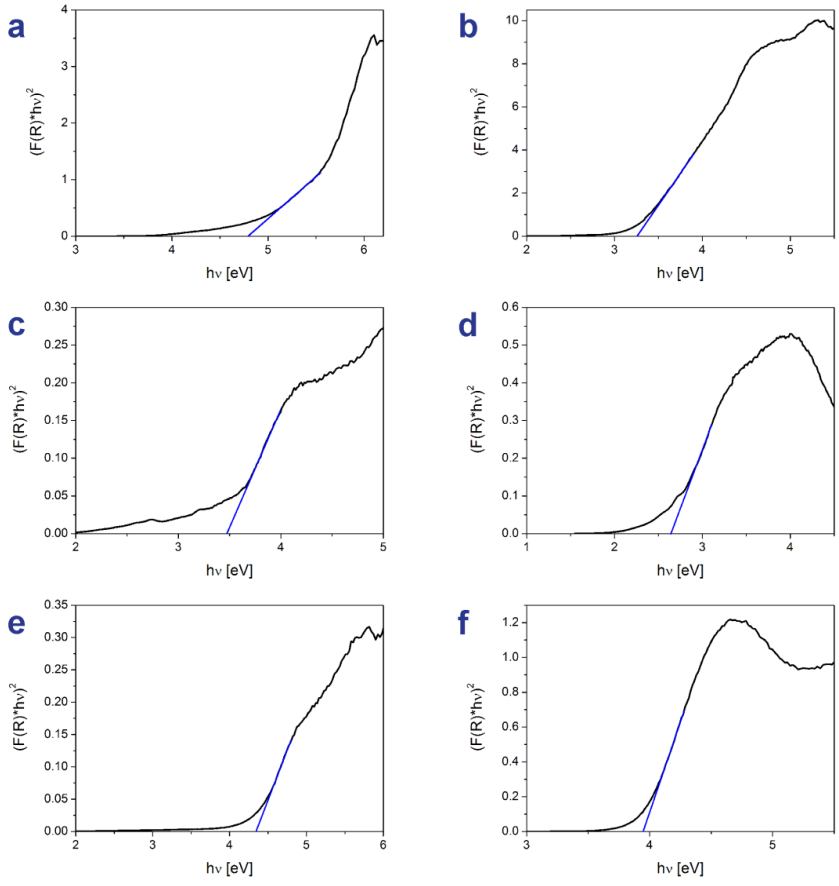

Figure 5.3 Tauc plots of $MgSiN_2$ (a), $MgGeN_2$ (b), $MnSiN_2$ (c), $MnGeN_2$ (d), $LiSi_2N_3$ (e) and $LiGe_2N_3$ (f).

Table 5.2 Evaluated optical bandgaps (eV) of Mg-IV-N_2, Mn-IV-N_2 and Li-IV_2-N_3 (IV = Si, Ge) from Tauc plots at room temperature

$MgSiN_2$	$MnSiN_2$	$LiSi_2N_3$	$MgGeN_2$	$MnGeN_2$	$LiGe_2N_3$
4.8	3.5	4.4	3.2	2.5	3.9

Apart from $MgSiN_2$, material properties of these nitrides have scarcely been investigated so far. Optical measurements were only reported for the respective Si nitrides $MgSiN_2$, $MnSiN_2$ and $LiSi_2N_3$. The evaluated bandgap of $MgSiN_2$ coincides well with previously determined values in the literature, ranging from 4.8 to 5.6 eV.[10,31] A deviation of ≈0.8 eV in comparison to other reported data was observed for $MnSiN_2$ and $LiSi_2N_3$ which can be attributed to different evaluation techniques for the bandgaps as well as different synthetic methods.[16,32] To some extent, variances can also arise from crystallographic defects within the materials. $MgGeN_2$, $MnGeN_2$ and $LiGe_2N_3$ exhibit smaller optical bandgaps in comparison to the respective Si nitrides, which is consistent with comparable systems.[3] Notably, sub-bandgap absorption was observed for $MnSiN_2$ and $MnGeN_2$ which was previously attributed to spin-forbidden d–d-transitions and associated selection rule relaxations.[15,16] This also explains the tails observed in the Tauc plots as well as the red and brown colors of the products (see Experimental section), which is in line with previous studies.[15,19]

5.2.4 DFT Calculations

In order to corroborate the experimental data, DFT calculations were carried out. Plots of the total and atom resolved density of states (DOS) are shown in Figure 5.4 for $MnSiN_2$ and $MnGeN_2$ (for specific bandgap region see Figure S5.9, supporting information) and in Figure S5.10 for Mg-IV-N_2 and Li-IV_2-N_3 (IV = Si, Ge). Excluding temperature effects, $MnSiN_2$ and $MnGeN_2$ exhibit spin polarization which is in agreement with previous calculations.[33] The spin polarization seen in Figure 5.4 a–b arises from the Mn atoms, in particular their 5d states. For Mn total magnetic moment values of 4.49 μB and 4.45 μB are obtained for $MnSiN_2$ and $MnGeN_2$, respectively.

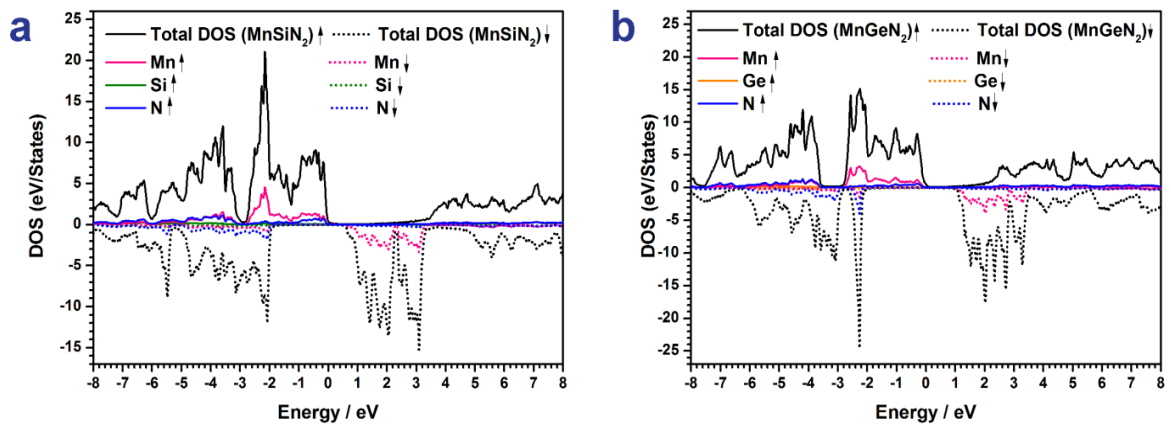

Figure 5.4 Total and atom resolved DOS of $MnSiN_2$ (a) and $MnGeN_2$ (b) within the SPRKKR formalism.

Table 5.3 Electronic (El.) and optical (Opt.) bandgaps (eV) for Mg-IV-N_2, Mn-IV-N_2 (spin up ↑ / spin down ↓) and Li-IV_2-N_3 (IV = Si, Ge) as calculated by SPRKKR formalism (EV-GGA)

	$MgSiN_2$	$MnSiN_2$	$LiSi_2N_3$	$MgGeN_2$	$MnGeN_2$	$LiGe_2N_3$
El.	4.2	0.6 ↑ 1.0 ↓	5.6	3.0	0.1 ↑ 1.0 ↓	3.6
Opt.	4.8	2.2 ↑ 2.8 ↓	4.9	3.6	1.4 ↑ 2.8 ↓	3.8

In order to estimate the optical absorption, the joint density of states (JDOS) was subsequently calculated for each compound as depicted in Figure 5.5 a–f in line with previous works[34] and was further validated by additional optical calculations within linear response formalism. E_g was then determined by means of a linear fit of the first steep ascend of the JDOS. Its values agree well with the evaluated optical bandgap from experimental data with merely minor deviations (Tables 5.2 and 5.3).

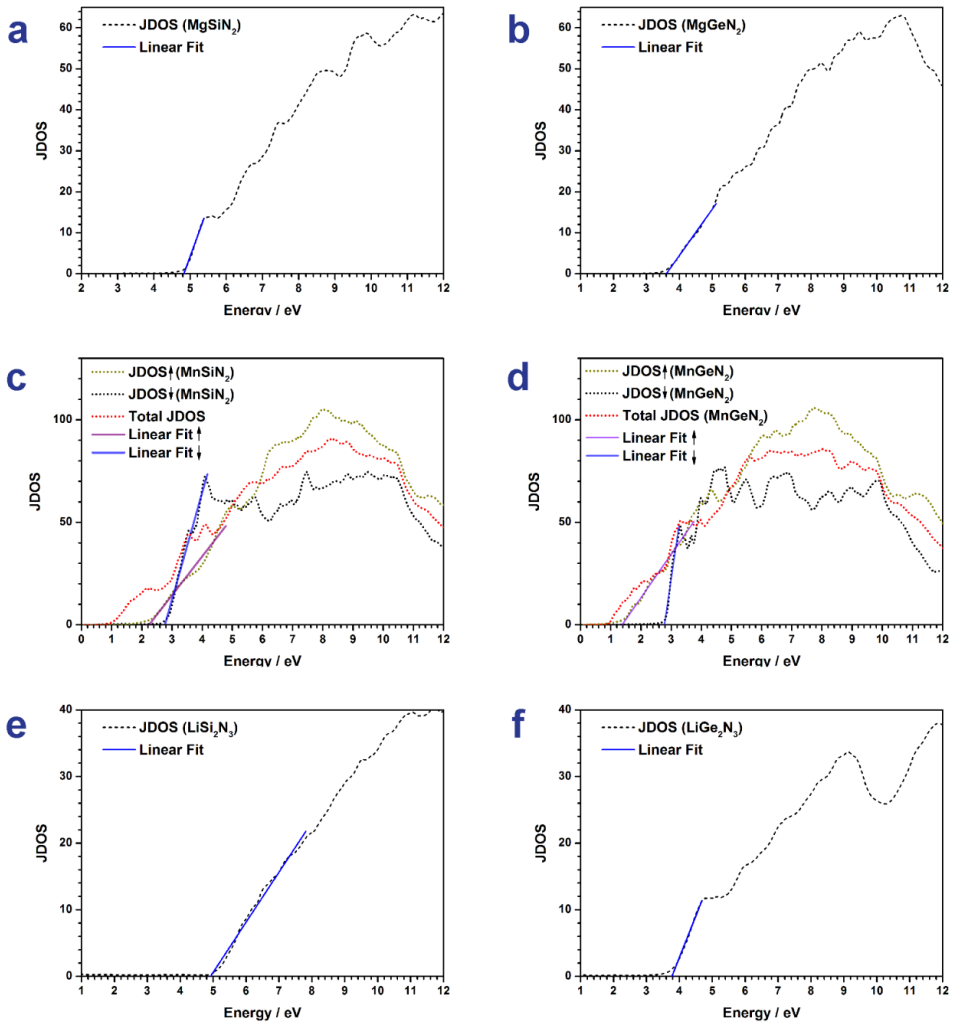

Figure 5.5 Calculated JDOS of $MgSiN_2$ (a), $MgGeN_2$ (b), $MnSiN_2$ (c), $MnGeN_2$ (d), $LiSi_2N_3$ (e) and $LiGe_2N_3$ (f) within the SPRKKR formalism. Extrapolated linear fits are used to evaluate E_g.

Due to the spin polarization of $MnSiN_2$ and $MnGeN_2$ their JDOS was calculated for both the spin up and spin down channel. Early absorption (1–2 eV) in the total JDOS would mainly represent Mn-3*d*–3*d* transitions that are deemed forbidden due to dipole selection rules. However, selection rule relaxations can induce absorption in this energy range to some extent.[15,16] Hence, E_g can be estimated from a mean value of the spin up and down JDOS. This appears to be a reasonable approximation for the optical bandgap in line with the experimental absorption starting at around 2 eV for both Mn compounds while the strong incline in absorption can likely be attributed to N 2*p* to Mn 3*d* transitions. Electronic bandgaps were determined from the Bloch spectral functions depicted in Figure 5.6 a–h. Mg-IV-N_2 and Li-IV_2-N_3 (IV = Si, Ge) exhibit direct and indirect bandgaps of very similar magnitude, while Mn-IV-N_2 reveal both direct and indirect gaps with respect to their spin channels.

Up to now, bandgap calculations referred to these nitrides were reported for $MgSiN_2$, $MgGeN_2$ and $LiSi_2N_3$. Estimated bandgaps range from 3.8 to 6.3 eV for $MgSiN_2$,[10,25,35–40] 2.9 to 5.4 eV for $MgGeN_2$[25,35–37,41] and 5.0 to 5.6 eV for $LiSi_2N_3$.[13,42]

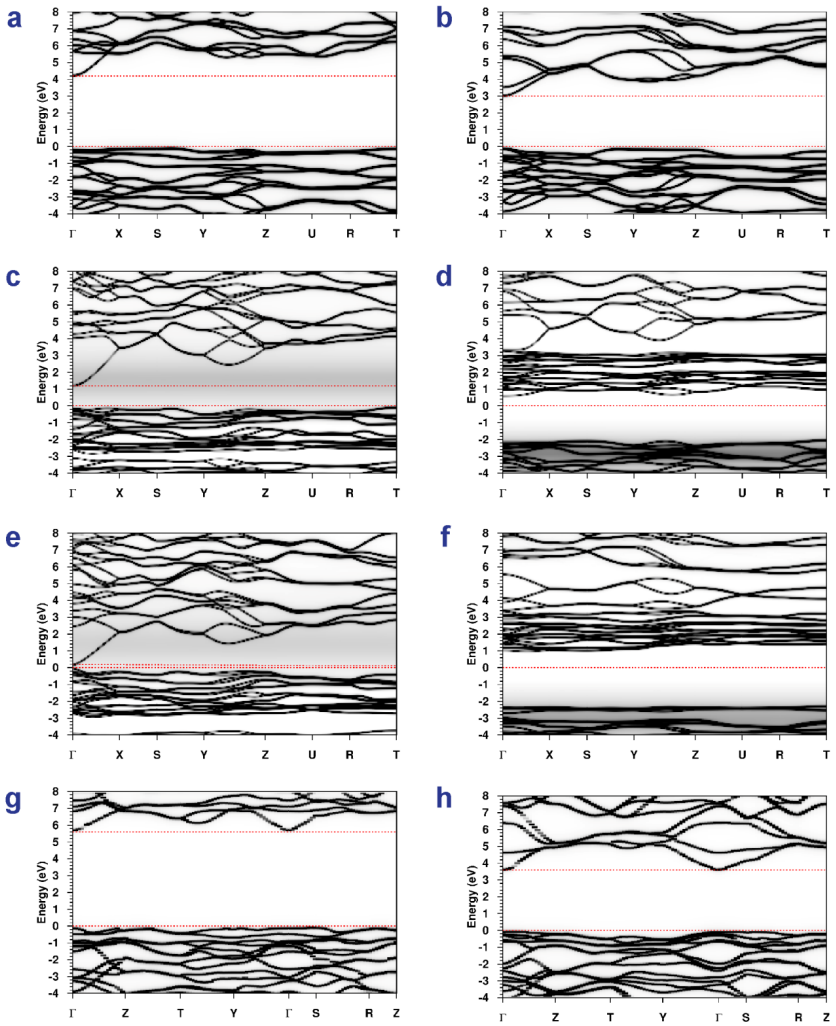

Figure 5.6 Bloch spectral functions of $MgSiN_2$ (a), $MgGeN_2$ (b), $MnSiN_2$ (↑c/↓d), $MnGeN_2$ (↑e/↓f), $LiSi_2N_3$ (g) and $LiGe_2N_3$ (h) as calculated by SPRKKR formalism (EV-GGA). ↑ and ↓ indicate spin up and down channels, respectively.

The large discrepancies result from different calculation methods which can lead to a significant under- or overestimation of the bandgaps. In general, the applied SPRKKR formalism seems to provide reasonable values with regard to the experimental data.

5.3 Conclusions

We developed a new synthetic approach for the ternary nitrides Mg-IV-N_2, Mn-IV-N_2 and Li-IV_2-N_3 (IV = Si, Ge) implementing solutions of supercritical ammonia (p_{crit} = 11.3 MPa, T_{crit} = 405.5 K)[43] with alkali metal amides as ammonobasic mineralizers. Custom-built high-pressure autoclaves made of nickel-based superalloys Inconel 718 (max. 900 K, 300 MPa) and Haynes alloy 282 (max. 1100 K, 170 MPa) provided the required temperature and pressure for the formation of these materials. Evaluation of observed absorption bands in diffuse reflectance spectra resulted in a range of bandgaps between 2.5 eV ($MnGeN_2$) and 4.8 eV ($MgSiN_2$). Band structures and the type of band transitions were calculated by DFT, which corroborated the estimated optical bandgaps, further providing new insights into electronic and optical properties of the materials in question. Calculated Bloch spectral functions show bandgaps similar in magnitude to the optical bandgaps with direct bandgaps for the majority of discussed compounds. $MnSiN_2$ and $MnGeN_2$ exhibit much lower electronic bandgaps than estimated from experimental and calculated optical bandgaps however with low transition probabilities as indicated by DOS and JDOS calculations.

Up to now, only few reports on ammonothermal synthesis of ternary and multinary nitrides can be found in literature. Syntheses in supercritical ammonia are still challenging due to the high demands on autoclave materials and high-pressure facilities. However, recent achievements in this research field are very intriguing for future studies.[21,34,44,45]

With regard to the structural relationship of III-N, II-IV-N_2 and I-IV_2-N_3 nitrides, bandgap engineering and further tuning of optical properties by formation of solid solutions is very promising. Even more attainable compositions for wurtzite-derived superstructures have been proposed by Parthé and Baur.[46–48] For instance, the thermodynamic stability of wurtzite-related quaternary nitride semiconductors like $LiAlGe_2N_4$ and $LiGaGe_2N_4$ was recently predicted as well.[49] On the basis of our latest studies, the ammonothermal approach is thus very promising for the discovery and design of novel and innovative next-generation semiconductors.

5.4 Experimental Section

The autoclaves were loaded and sealed in Ar-filled glove boxes (Unilab, MBraun, Garching, O_2<1 ppm, H_2O<1 ppm) to avoid oxygen and moisture contamination of the starting materials. A vacuum line (≤0.1 Pa) with connected argon and ammonia supply was used for the condensation procedure. Ar (Air Liquide, 99.999%) and NH_3 (Air Liquide, 99.999%) were passed through gas purification cartridges (Micro torr FT400-902 and MC400-702FV, SAES Pure Gas Inc., San Luis Obispo, CA, USA) providing a purity level of <1 ppbV H_2O, O_2 and CO_2.

Custom-built autoclaves manufactured from nickel-based superalloys Inconel 718 (max. 900 K, 300 MPa, 10 mL/97 mL) or Haynes 282 (max. 1100 K, 170 MPa, 10 mL) were used for ammonothermal syntheses. The autoclave body and lid is sealed via flange joints using silver-

coated Inconel 718 metal-C-rings (GFD seals) as sealing gaskets. The hand valve (SITEC), pressure transmitter (HBM P2VA1/5000 bar) and safety head with integrated bursting disc (SITEC) are connected to the autoclave lid via 3/8'' high-pressure tubing connections.

5.4.1 Synthesis of $MgSiN_2$, $MnSiN_2$ and $LiSi_2N_3$

To facilitate a complete conversion to intermediate compounds, Si (Alfa Aesar, 99.9%) was ball-milled under argon for 10 h using a planetary ball mill (Retsch PM 400). Mg (10 mmol, Alfa Aesar, 99.8%), Si (8 mmol) and KN_3 (25 mmol, Sigma–Aldrich, 99.9%), Mn (10 mmol, Alfa Aesar, 99.95%), Si (8 mmol) and KN_3 (25 mmol) or LiN_3 (5 mmol, synthesized according to the procedure of Fair *et al.*)[50] and Si (5 mmol) were placed in Mo liners, respectively. The Mo liners were transferred into Haynes 282 autoclaves. The autoclaves were closed under argon, evacuated and cooled with ethanol/liquid nitrogen to 198 K. Ammonia was condensed into the autoclaves via a pressure regulating valve. For the synthesis of $MgSiN_2$ and $MnSiN_2$, the autoclave body was heated in a custom-built vertical tube furnace (Loba, HTM Reetz) to 570 K with a rate of 3 K min^{-1}, held at this temperature for 15 h, heated to 1070 K with a rate of 1 K min^{-1} and held for further 100 h. For the synthesis of $LiSi_2N_3$, the autoclave body was heated to 970 K with a rate of 1.5 K min^{-1} and maintained at this temperature for 100 h. The pressure was kept between 100 MPa and 170 MPa during the heating periods and was appropriately reduced if necessary. The autoclaves were cooled down to room temperature by switching off the furnace. The products were washed with H_2O and 5 M HCl to remove the residual mineralizer and intermediates and dried at 350 K in air. $MgSiN_2$ and $LiSi_2N_3$ where obtained as white powders and $MnSiN_2$ as red powder, respectively.

5.4.2 Synthesis of $MgGeN_2$, $MnGeN_2$ and $LiGe_2N_3$

Ge (smart-elements, 99.99%) was ground for 15 min with an oscillating mixer mill (Specac Specamill) prior to the syntheses. Mg (20 mmol, Alfa Aesar, 99.8%), Ge (16 mmol) and NaN_3 (50 mmol, Sigma–Aldrich, 99.5%), Mn (20 mmol, Alfa Aesar, 99.95%), Ge (16 mmol) and NaN_3 (50 mmol) or Li (25 mmol, Alfa Aesar, 99%) and Ge_3N_4 (3 mmol, ABCR, 99.9%) were directly placed into Inconel 718 autoclaves, respectively. The autoclaves were closed under argon, evacuated and cooled with ethanol/liquid nitrogen to 198 K. Ammonia was condensed into the autoclaves via a pressure regulating valve. For the synthesis of $MgGeN_2$ and $MnGeN_2$, the autoclave body (97 mL internal volume) was heated in a custom-built vertical tube furnace (Loba, HTM Reetz) to 670 K with a rate of 3 K min^{-1}, kept at this temperature for 15 h, heated to 870 K with a rate of 2 K min^{-1} and held for further 100 h. For the synthesis of $LiGe_2N_3$, the autoclave body (10 mL internal volume) was heated to 900 K with a rate of 3 K min^{-1} and maintained at this temperature for 100 h. The pressure was kept between 150 MPa and 230 MPa during the heating periods and was appropriately reduced if necessary. The autoclaves were cooled down to room temperature by switching off the furnace. The products were washed with EtOH ($MgGeN_2$, $LiGe_2N_3$) or H_2O ($MnGeN_2$) to remove the residual mineralizer and intermediates and dried at 350 K in air. $MgGeN_2$, $MnGeN_2$ and $LiGe_2N_3$ where obtained as beige, light brown and white powders, respectively.

5.4.3 Powder X-ray Diffraction

The products were finely ground and loaded in glass capillaries (0.3 mm diameter, 0.01 mm wall thickness, Hilgenberg GmbH). XRD measurements were performed using a Stoe STADI P diffractometer (Mo $K\alpha_1$, λ = 0.70930 Å, Ge(111) monochromator, Mythen 1 K detector) in modified Debye–Scherrer geometry. Temperature-programmed powder X-ray diffraction was conducted on a Stoe STADI P diffractometer (Mo $K\alpha_1$, λ = 0.70930 Å, Ge(111) monochromator, image plate position sensitive detector) which is equipped with a high-temperature graphite furnace. The diffraction patterns were recorded in segments of 50 K up to 1270 K with a heating rate of 5 K min^{-1}. TOPAS-Academic Software was used for Rietveld refinement applying the fundamental parameters model with direct convolution of source emission profiles, axial instrument contributions, crystallite size and microstrain effects for the peak shape function.[51,52] Capillary absorption correction (inner diameter 0.28 mm) was performed with the calculated absorption coefficient. Further details on the crystal structure investigations may be obtained from the Fachinformationszentrum Karlsruhe, 76344 Eggenstein-Leopoldshafen, Germany (E-mail: crysdata@fiz-karlsruhe.de), on quoting the depository numbers CSD-433631 ($MgSiN_2$), CSD-433632 ($MgGeN_2$), CSD-433633 ($MnSiN_2$), CSD-433634 ($MnGeN_2$), CSD-433635 ($LiSi_2N_3$) and CSD-433636 ($LiGe_2N_3$).

5.4.4 Scanning Electron Microscopy (SEM)

The crystal morphology of the products was investigated using a FEI Helios G3 UC scanning electron microscope (SEM; field emission gun, acceleration voltage 30 kV). The purified products were placed on an adhesive carbon pad and subsequently coated with a conductive carbon film using a high-vacuum sputtercoater (BAL-TEC MED 020, Bal Tec AG).

5.4.5 UV/Vis Spectroscopy

A Jasco V-650 UV/Vis spectrophotometer equipped with Czerny–Turner mount, photomultiplier tube detector and deuterium (190–350 nm)/halogen (330–900 nm) lamps as light sources was used for diffuse reflectance measurements. The intensity artifacts at 330 nm arising from the deuterium—halogen lamp switch were corrected for a reliable determination of the bandgap.

5.4.6 DFT Calculations

Bloch spectral functions and DOS calculations were conducted based on Rietveld refinements of the experimental structures as shown in Table 5.2 within the fully relativistic Korringa–Kohn–Rostoker (KKR) Green's function method as implemented in the Munich SPRKKR package.[53,54] The Brillouin zone was sampled with *k*-meshes of 12 × 10 × 13 (II-IV-N_2) and 12 × 12 × 11 (Li-IV_2-N_3) respectively. An angular momentum expansion of l = 3 was used for all calculations. Electronic convergence was achieved based on the local density approximation (LDA) of Vosko, Wilk, and Nusair and further by the EV-GGA (Engel Vosko) in order to compare the electronic bandgaps to the experimental measurements.[55,56] For the Li-IV_2-N_3 phases *k*-dependent convergence parameters for the structure constant matrix had to be set manually to values of ETA = 2.0, RMAX = 2.5 and GMAX = 2.5 in order to achieve reasonable results.

5.5 References

[1] S. P. DenBaars, D. Feezell, K. Kelchner, S. Pimputkar, C.-C. Pan, C.-C. Yen, S. Tanaka, Y. Zhao, N. Pfaff, R. Farrell, M. Iza, S. Keller, U. Mishra, J. S. Speck, S. Nakamura, Development of gallium-nitride-based light-emitting diodes (LEDs) and laser diodes for energy-efficient lighting and displays, *Acta Mater.* **2013**, *61*, 945–951.

[2] K. Shinohara, D. C. Regan, Y. Tang, A. L. Corrion, D. F. Brown, J. C. Wong, J. F. Robinson, H. H. Fung, A. Schmitz, T. C. Oh, S. J. Kim, P. S. Chen, R. G. Nagele, A. D. Margomenos, M. Micovic, Scaling of GaN HEMTs and Schottky Diodes for Submillimeter-Wave MMIC Applications, *IEEE Trans. Electron Dev.* **2013**, *60*, 2982–2996.

[3] Y. Hinuma, T. Hatakeyama, Y. Kumagai, L. A. Burton, H. Sato, Y. Muraba, S. Iimura, H. Hiramatsu, I. Tanaka, H. Hosono, F. Oba, Discovery of earth-abundant nitride semiconductors by computational screening and high-pressure synthesis, *Nat. Commun.* **2016**, *7,* 11962.

[4] P. Narang, S. Chen, N. C. Coronel, S. Gul, J. Yano, L.-W. Wang, N. S. Lewis, H. A. Atwater, Bandgap tunability in Zn(Sn,Ge)N_2 semiconductor alloys, *Adv. Mater.* **2014**, *26*, 1235–1241.

[5] P. C. Quayle, K. He, J. Shan, K. Kash, Synthesis, lattice structure, and band gap of $ZnSnN_2$, *MRS Commun.* **2013**, *3*, 135–138.

[6] A. D. Martinez, A. N. Fioretti, E. S. Toberer, A. C. Tamboli, Synthesis, structure, and optoelectronic properties of II–IV–V_2 materials, *J. Mater. Chem. A* **2017**, *5*, 11418–11435.

[7] R. J. Bruls, A. A. Kudyba-Jansen, P. Gerharts, H. T. Hintzen, R. Metselaar, Preparation, characterization and properties of $MgSiN_2$ ceramics, *J. Mater. Sci. Mater. Electron.* **2002**, *13*, 63–75.

[8] C. Kulshreshtha, J. H. Kwak, Y.-J. Park, K.-S. Sohn, Photoluminescent and decay behaviors of Mn^{2+} and Ce^{3+} coactivated $MgSiN_2$ phosphors for use in light-emitting-diode applications, *Opt. Lett.* **2009**, *34*, 794–796.

[9] J. B. Quirk, M. Råsander, C. M. McGilvery, R. Palgrave, M. A. Moram, Band gap and electronic structure of $MgSiN_2$, *Appl. Phys. Lett.* **2014**, *105*, 112108.

[10] T. de Boer, T. D. Boyko, C. Braun, W. Schnick, A. Moewes, Band gap and electronic structure of $MgSiN_2$ determined using soft X-ray spectroscopy and density functional theory, *Phys. Status Solidi RRL* **2015**, *9*, 250–254.

[11] H. Yamane, S. Kikkawa, M. Koizumi, Preparation of lithium silicon nitrides and their lithium ion conductivity, *Solid State Ion.* **1987**, *25*, 183–191.

[12] E. Narimatsu, Y. Yamamoto, T. Nishimura, N. Hirosaki, Effect of sintering temperature and sintering additiveson ionic conductivity of $LiSi_2N_3$, *J. Ceram. Soc. Jpn.* **2010**, *118*, 837–841.

[13] Y. Q. Li, N. Hirosaki, R.-J. Xie, T. Takeka, M. Mitomo, Crystal, electronic structures and photoluminescence properties of rare-earth doped $LiSi_2N_3$, *J. Solid State Chem.* **2009**, *182*, 301–311.

[14] Q. Wu, Y. Li, X. Wang, Z. Zhao, C. Wang, H. Li, A. Mao, Y. Wang, Novel optical characteristics of Eu^{2+} doped and Eu^{2+}, Ce^{3+} co-doped $LiSi_2N_3$ phosphors by gas-pressed sintering, *RSC Adv.* **2014**, *4*, 39030–39036.

[15] S. Esmaeilzadeh, U. Hålenius, M. Valldor, Crystal Growth, Magnetic, and Optical Properties of the Ternary Nitride $MnSiN_2$, *Chem. Mater.* **2006**, *18*, 2713–2718.

[16] C. J. Duan, A. C. A. Delsing, H. T. Hintzen, Red emission from Mn^{2+} on a tetrahedral site in $MgSiN_2$, *J. Lumin.* **2009**, *129*, 645–649.

[17] M. Orth, W. Schnick, Zur Kenntnis von $LiSi_2N_3$: Synthese und Verfeinerung der Kristallstruktur, *Z. Anorg. Allg. Chem.* **1999**, *625*, 1426–1428.

[18] Z. Lenčéš, K. Hirao, Y. Yamauchi, S. Kanzaki, Reaction Synthesis of Magnesium Silicon Nitride Powder, *J. Am. Ceram. Soc.* **2003**, *86*, 1088–1093.

[19] J. Guyader, M. Maunaye, J. Lang, Sur la préparation d'un nitrure double de germanium et manganèse, *C. R. Acad. Sci. Paris, Ser. C* **1971**, *272*, 311–313.

[20] G. Dhanaraj, K. Byrappa, V. Prasad, M. Dudley, *Springer Handbook of Crystal Growth* **2010**, Springer Berlin Heidelberg, Germany.

[21] J. Häusler, S. Schimmel, P. Wellmann, W. Schnick, Ammonothermal Synthesis of Earth-Abundant Nitride Semiconductors $ZnSiN_2$ and $ZnGeN_2$ and Dissolution Monitoring by In Situ X-ray Imaging *Chem. Eur. J.* **2017**, *23*, 12275–12282.

[22] T. Richter, R. Niewa, Chemistry of Ammonothermal Synthesis, *Inorganics* **2014**, *2*, 29–78.

[23] S. Pimputkar, S. Nakamura, Decomposition of supercritical ammonia and modeling of supercritical ammonia–nitrogen–hydrogen solutions with applicability toward ammonothermal conditions, *J. Supercrit. Fluids* **2016**, *107*, 17–30.

[24] S. Pagano, M. Zeuner, S. Hug, W. Schnick, Single-Crystal Structure Determination and Solid-State NMR Investigations of Lithium Nitridosilicate Li_2SiN_2 Synthesized by a Precursor Approach Employing Amorphous "$Si(CN_2)_2$", *Eur. J. Inorg. Chem.* **2009**, *2009*, 1579–1584.

[25] Y. H. Jung, L. C. Tang, M. H. Lee, *Ab initio* study of the structural and optical properties of orthorhombic ternary nitride crystals, *J. Phys.: Condens. Matter* **2001**, *13*, 10417.

[26] M. Maunaye, R. Marchand, J. Guyader, Y. Laurent, J. Lang, Structure de $MnSiN_2$ et $MnGeN_2$, *Bull. Soc. Fr. Miner. Cristallogr.* **1971**, *94*, 561–564.

[27] J. David, J. P. Charlot, J. Lang, Les nitrures doubles de lithium et de germanium, *Rev. Chim. Miner.* **1974**, *11*, 405–413.

[28] W. Paszkowicz, S. Podsiadło, R. Minikayev, Rietveld-refinement study of aluminium and gallium nitrides, *J. Alloys Compd.* **2004**, *382*, 100–106.

[29] R. López, R. Gómez, Band-gap energy estimation from diffuse reflectance measurements on sol–gel and commercial TiO_2: a comparative study, *J. Sol-Gel Sci. Technol.* **2012**, *61*, 1–7.

[30] J. Tauc, R. Grigorovici, A. Vancu, Optical Properties and Electronic Structure of Amorphous Germanium, *Phys. Status Solidi B* **1966**, *15*, 627–637.

[31] C. M. Fang, R. A. d. Groot, R. J. Bruls, H. T. Hintzen, G. d. With, Ab initio band structure calculations of Mg_3N_2 and $MgSiN_2$, *J. Phys.: Condens. Matter* **1999**, *11*, 4833–4842.

[32] F. Liang, L. Tian, H. Zhang, F. Liang, S. Liu, R. Cheng, S. Zhang, Low temperature synthesis of $LiSi_2N_3$ nanobelts via molten salt nitridation and their photoluminescence properties, *RSC Adv.* **2016**, *6*, 68615–68618.

[33] D. Naveh, L. Kronik, Spin-polarized electronic structure of Mn–IV–V_2 chalcopyrites, *Phys. Status Solidi B* **2006**, *243*, 2159–2163.

[34] R. Niklaus, J. Minar, J. Häusler, W. Schnick, First-principles and experimental characterization of the electronic properties of $CaGaSiN_3$ and $CaAlSiN_3$: the impact of chemical disorder, *Phys. Chem. Chem. Phys.* **2017**, *19*, 9292–9299.

[35] A. P. Jaroenjittichai, W. R. L. Lambrecht, Electronic band structure of Mg−IV−N_2 compounds in the quasiparticle-self-consistent GW approximation, *Phys. Rev. B* **2016**, *94*, 125201.

[36] Y. M. Basalaev, P. V. Demushin, Energy band genesis from sublattice states in $MgSiN_2$ and $MgGeN_2$ crystals, *J. Struct. Chem.* **2010**, *51*, 1191–1194.

[37] T. Misaki, X. Wu, A. Wakahara, A. Yoshida, Theoretical Analysis of Multinary Nitride Semiconductors by Density Functional Theory, *Proc. Int. Workshop on Nitride Semiconductors, IPAP Conf. Series 1* **2000**, 685–688.

[38] M. Råsander, M. A. Moram, Electronic structure of the high and low pressure polymorphs of $MgSiN_2$, *Mater. Res. Express* **2016**, *3*, 085902.

[39] C. M. Fang, H. T. Hintzen, G. de With, High-pressure phases of $MgSiN_2$ from first-principles calculations, *Appl. Phys. A* **2004**, *78*, 717–719.

[40] H. M. Huang, S. J. Luo, K. L. Yao, First Principles Study of Half-Metallic and Magnetic Properties of V Doped $MgSiN_2$ Chalcopyrite, *J. Supercond. Nov. Magn.* **2014**, *27*, 257–261.

[41] L. C. Tang, Y. C. Chang, J. Y. Huang, C. S. Chang, *Proc. SPIE Vol. 7056, Photonic Fiber and Crystal Devices: Advances in Materials and Innovations in Device Applications II* **2008**, *7056*, 705605.

[42] H. Zhang, J. Ren, L. Wu, J. Zhang, Ionic ASi_2N_3 (*A*=Li, Na, K and Rb) stabilized by the covalent Si–N bonding: First-principles calculations, *J. Solid State Chem.* **2017**, *245*, 184–189.

[43] E. Brunner, Fluid mixtures at high pressures VI. Phase separation and critical phenomena in 18 (*n*-alkane + ammonia) and 4 (*n*-alkane + methanol) mixtures, *J. Chem. Thermodyn.* **1988**, *20*, 273–297.

[44] J. Häusler, L. Neudert, M. Mallmann, R. Niklaus, A.-C. L. Kimmel, N. S. A. Alt, E. Schlücker, O. Oeckler, W. Schnick, Ammonothermal Synthesis of Novel Nitrides: Case Study on $CaGaSiN_3$, *Chem. Eur. J.* **2017**, *23*, 2583–2590.

[45] N. Cordes, W. Schnick, Ammonothermal Synthesis of Crystalline Oxonitride Perovskites $LnTaON_2$ (Ln=La, Ce, Pr, Nd, Sm, Gd), *Chem. Eur. J.* **2017**, *23*, 11410–11415.

[46] E. Parthé, Contributions to the crystal chemistry of normal and defect tetrahedral structures, *Z. Kristallogr. Cryst. Mater.* **1964**, *119*, 204–225.

[47] T. J. McLarnan, W. H. Baur, Enumeration of wurtzite derivatives and related dipolar tetrahedral structures, *J. Solid State Chem.* **1982**, *42*, 283–299.

[48] W. H. Baur, T. J. McLarnan, Observed wurtzite derivatives and related dipolar tetrahedral structures, *J. Solid State Chem.* **1982**, *42*, 300–321.

[49] Z.-H. Cai, P. Narang, H. A. Atwater, S. Chen, C.-G. Duan, Z.-Q. Zhu, J.-H. Chu, Cation-Mutation Design of Quaternary Nitride Semiconductors Lattice-Matched to GaN, *Chem. Mater.* **2015**, *27*, 7757–7764.

[50] H. D. Fair, R. F. Walker, *Energetic Materials, Physics and Chemistry of Inorganic Azides, 1st ed.*, Springer, **1977**.

[51] A. Coelho, *TOPAS Academic*, *Version 4.1*, Coelho Software, Brisbane (Australia), **2007**.

[52] R. W. Cheary, A. A. Coelho, J. P. Cline, Fundamental Parameters Line Profile Fitting in Laboratory Diffractometers, *J. Res. Natl. Inst. Stand. Technol.* **2004**, *109*, 1–25.

[53] H. Ebert, D. Ködderitzsch, J. Minár, Calculating condensed matter properties using the KKR-Green's function method—recent developments and applications, *Rep. Prog. Phys.* **2011**, *74*, 096501.

[54] H. Ebert et al., *The Munich SPR-KKR Package, Version 7.7*, http://olymp.cup.uni-muenchen.de/ak/ebert/SPRKKR, **2012**.

[55] S. H. Vosko, L. Wilk, M. Nusair, Accurate spin-dependent electron liquid correlation energies for local spin density calculations: a critical analysis, *Can. J. Phys.* **1980**, *58*, 1200–1211.

[56] E. Engel, S. H. Vosko, Exact exchange-only potentials and the virial relation as microscopic criteria for generalized gradient approximations, *Phys. Rev. B: Condens. Matter Mater. Phys.* **1993**, *47*, 13164–13174.

5.6 Supporting Information

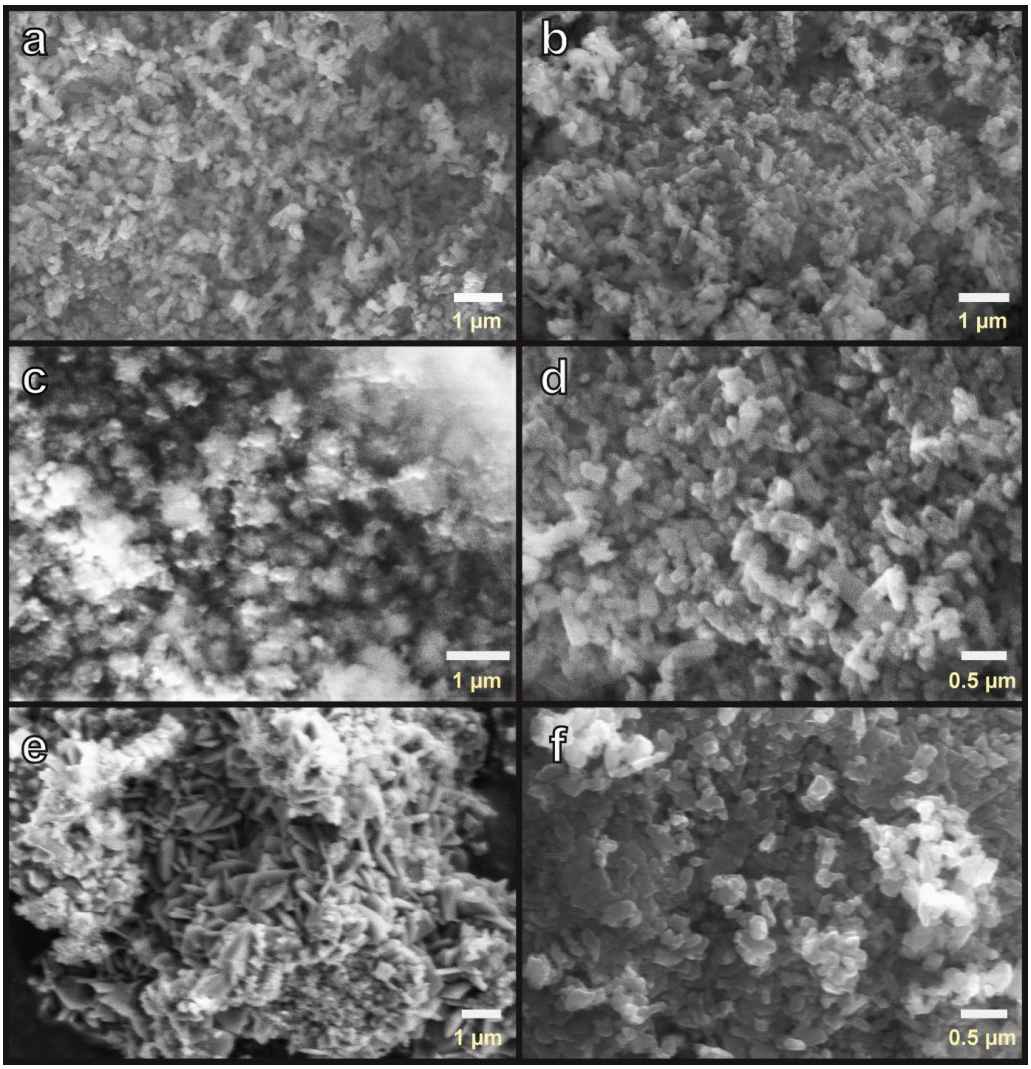

Figure S5.1 Scanning electron microscopy (SEM) images of $MgSiN_2$ (a), $MgGeN_2$ (b), $MnSiN_2$ (c), $MnGeN_2$ (d), $LiSi_2N_3$ (e) and $LiGe_2N_3$ (f).

Table S5.1 Wyckoff positions and atomic coordinates of $MgSiN_2$ obtained from Rietveld refinement, standard deviations in parentheses

Atom	Wyckoff	*x*	*y*	*z*	SOF	U_{iso} (Å^2)
Mg	4*a*	0.0861(5)	0.6192(7)	0.9945(13)	1	0.0061(3)
Si	4*a*	0.0689(4)	0.1246(6)	0.0063(11)	1	0.0061(3)
N1	4*a*	0.0530(15)	0.0894(12)	0.3634(18)	1	0.0061(3)
N2	4*a*	0.1059(12)	0.6581(10)	0.4213(18)	1	0.0061(3)

Table S5.2 Wyckoff positions and atomic coordinates of $MgGeN_2$ obtained from Rietveld refinement, standard deviations in parentheses

Atom	Wyckoff	*x*	*y*	*z*	SOF	U_{iso} (Å^2)
Mg	4*a*	0.0781(10)	0.6238(21)	0.0061(70)	1	0.0130(4)
Ge	4*a*	0.0745(3)	0.1255(7)	0.0063(25)	1	0.0130(4)
N1	4*a*	0.0860(25)	0.1462(23)	0.3917(29)	1	0.0130(4)
N2	4*a*	0.0849(26)	0.6521(23)	0.3988(18)	1	0.0130(4)

Table S5.3 Wyckoff positions and atomic coordinates of $MnSiN_2$ obtained from Rietveld refinement, standard deviations in parentheses

Atom	Wyckoff	*x*	*y*	*z*	SOF	U_{iso} (Å^2)
Mn	4*a*	0.0767(2)	0.6233(4)	0.9966(8)	1	0.0027(2)
Si	4*a*	0.0686(4)	0.1235(8)	0.9949(15)	1	0.0027(2)
N1	4*a*	0.1151(8)	0.6600(10)	0.4165(13)	1	0.0027(2)
N2	4*a*	0.0526(10)	0.0885(11)	0.3489(8)	1	0.0027(2)

Table S5.4 Wyckoff positions and atomic coordinates of $MnGeN_2$ obtained from Rietveld refinement, standard deviations in parentheses

Atom	Wyckoff	*x*	*y*	*z*	SOF	U_{iso} (Å^2)
Mn	4*a*	0.0786(6)	0.6245(16)	0.9867(24)	1	0.0101(3)
Ge	4*a*	0.0721(4)	0.1255(11)	0.9889(26)	1	0.0101(3)
N1	4*a*	0.0628(25)	0.1031(31)	0.3529(37)	1	0.0101(3)
N2	4*a*	0.1064(22)	0.6258(38)	0.3933(24)	1	0.0101(3)

Table S5.5 Wyckoff positions and atomic coordinates of $LiSi_2N_3$ obtained from Rietveld refinement, standard deviations in parentheses

Atom	Wyckoff	*x*	*y*	*z*	SOF	U_{iso} (Å²)
Li	4*a*	0	0.3500(31)	0.9945(29)	1	0.0037(3)
Si	8*b*	0.1662(2)	0.8369(4)	0.0251(36)	1	0.0037(3)
N1	8*b*	0.1978(5)	0.8617(12)	0.3899(6)	1	0.0037(3)
N2	4*a*	0	0.2743(11)	0.4488(11)	1	0.0037(3)

Table S5.6 Wyckoff positions and atomic coordinates of $LiGe_2N_3$ obtained from Rietveld refinement, standard deviations in parentheses

Atom	Wyckoff	*x*	*y*	*z*	SOF	U_{iso} (Å²)
Li	4*a*	0	0.336(9)	0.979(32)	1	0.0087(3)
Ge	8*b*	0.1657(3)	0.8280(5)	0.9795(1)	1	0.0087(3)
N1	8*b*	0.1883(13)	0.8216(33)	0.3452(14)	1	0.0087(3)
N2	4*a*	0	0.2940(30)	0.3873(18)	1	0.0087(3)

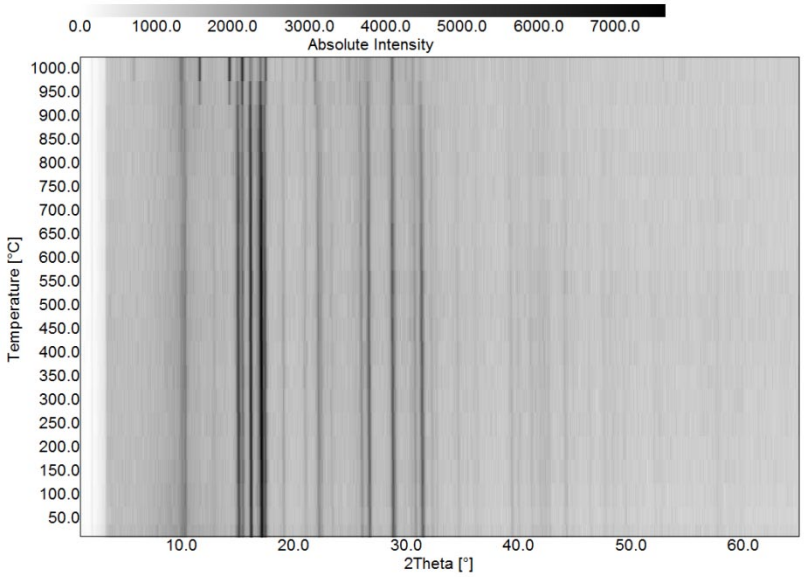

Figure S5.2 Temperature-programmed powder X-ray diffraction pattern of $MgSiN_2$.

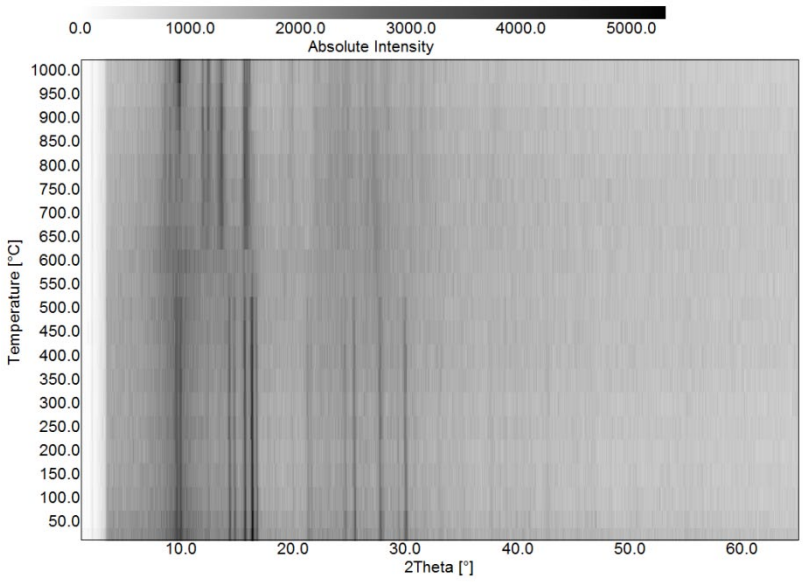

Figure S5.3 Temperature-programmed powder X-ray diffraction pattern of $MgGeN_2$.

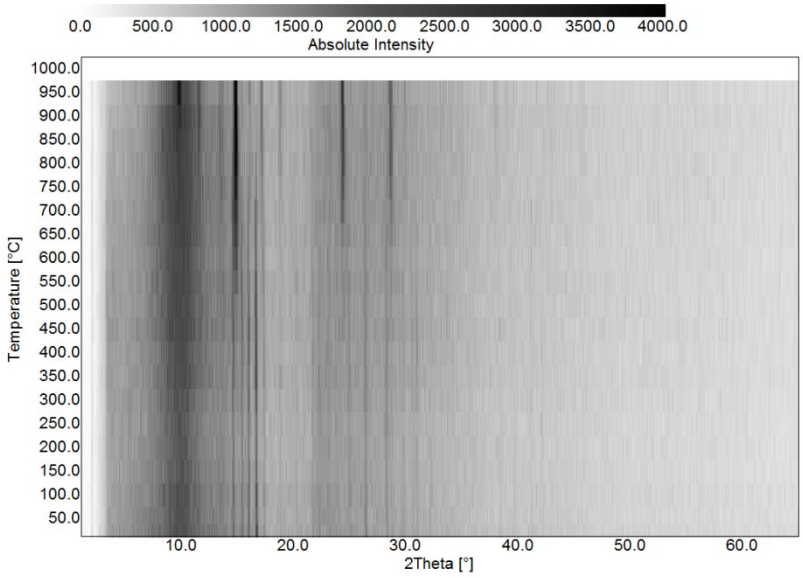

Figure S5.4 Temperature-programmed powder X-ray diffraction pattern of $MnSiN_2$.

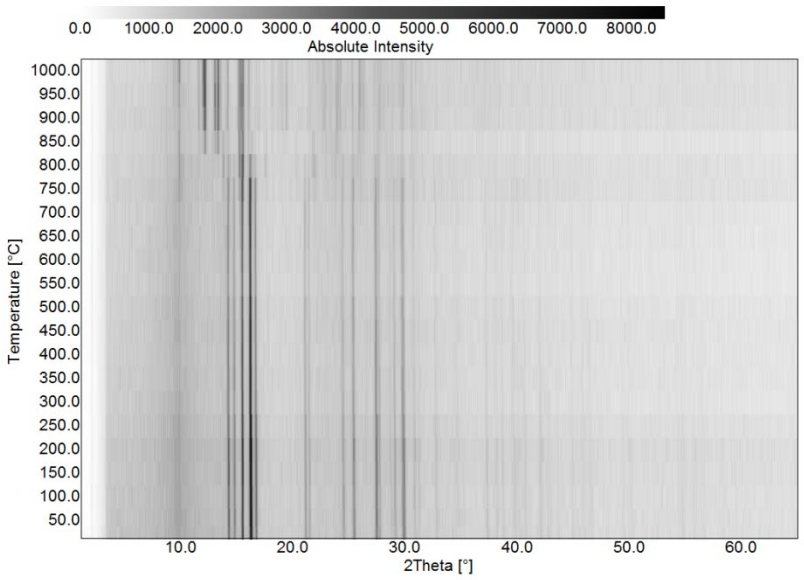

Figure S5.5 Temperature-programmed powder X-ray diffraction pattern of $MnGeN_2$.

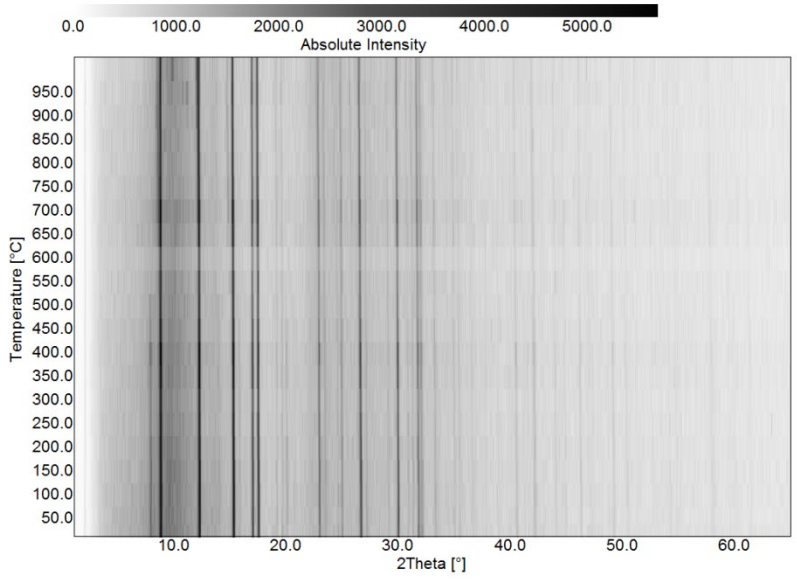

Figure S5.6 Temperature-programmed powder X-ray diffraction pattern of $LiSi_2N_3$.

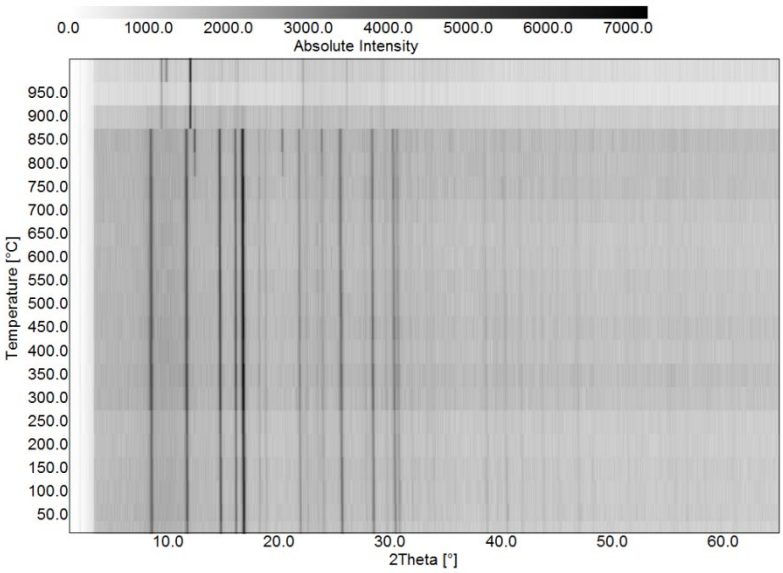

Figure S5.7 Temperature-programmed powder X-ray diffraction pattern of $LiGe_2N_3$.

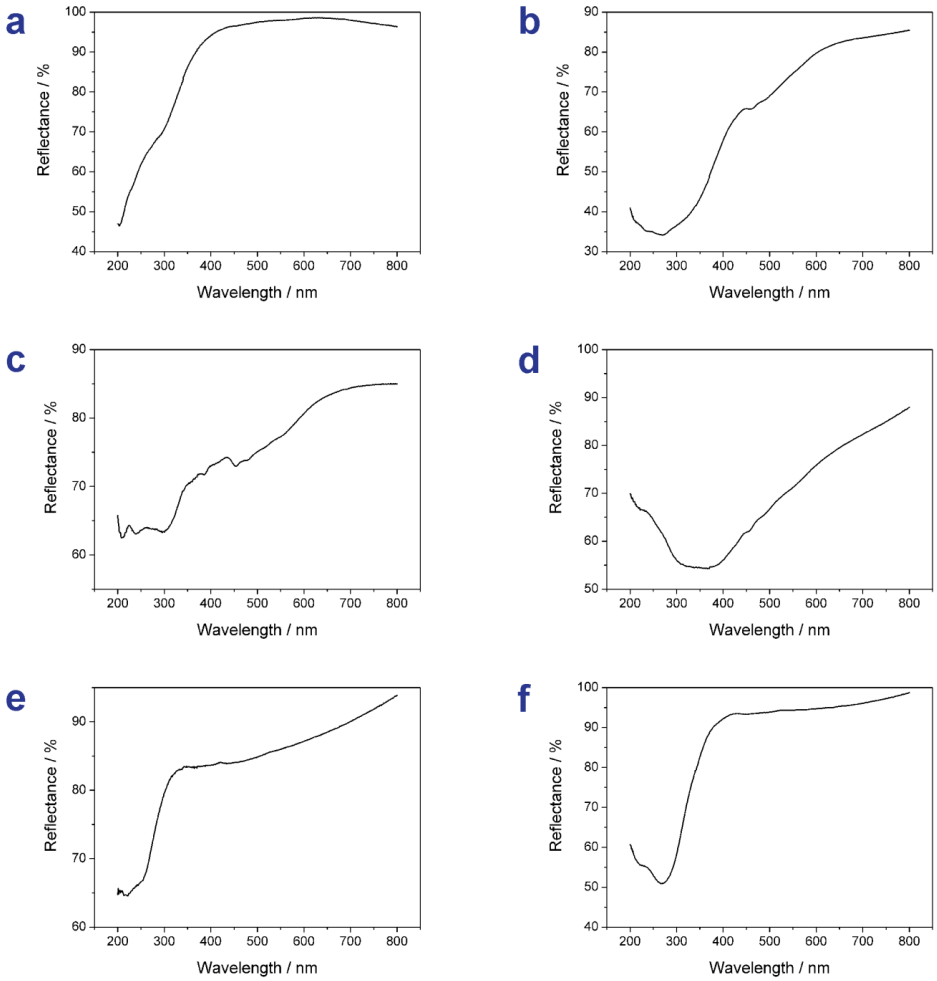

Figure S5.8 Diffuse reflectance spectra of $MgSiN_2$ (a), $MgGeN_2$ (b), $MnSiN_2$ (c), $MnGeN_2$ (d), $LiSi_2N_3$ (e) and $LiGe_2N_3$ (f).

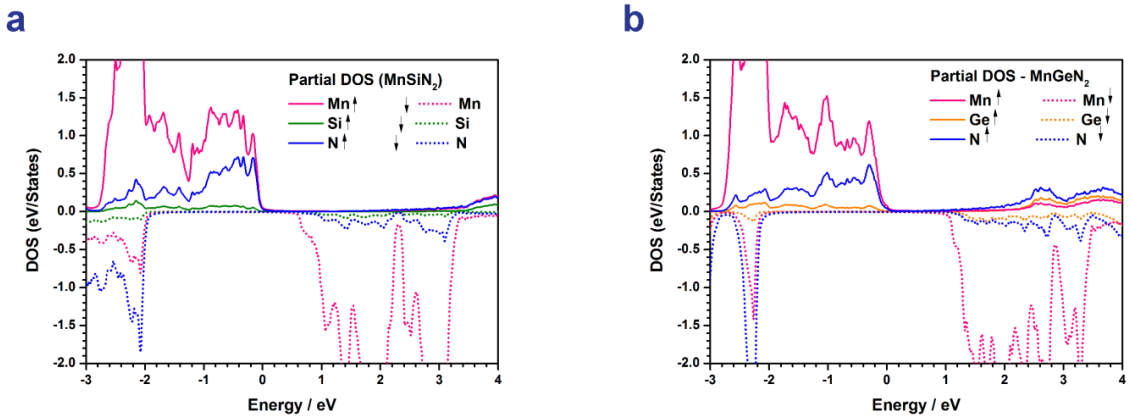

Figure S5.9 Enlarged section of total and atom resolved DOS of $MnSiN_2$ (a) and $MnGeN_2$ (b) within the SPRKKR formalism.

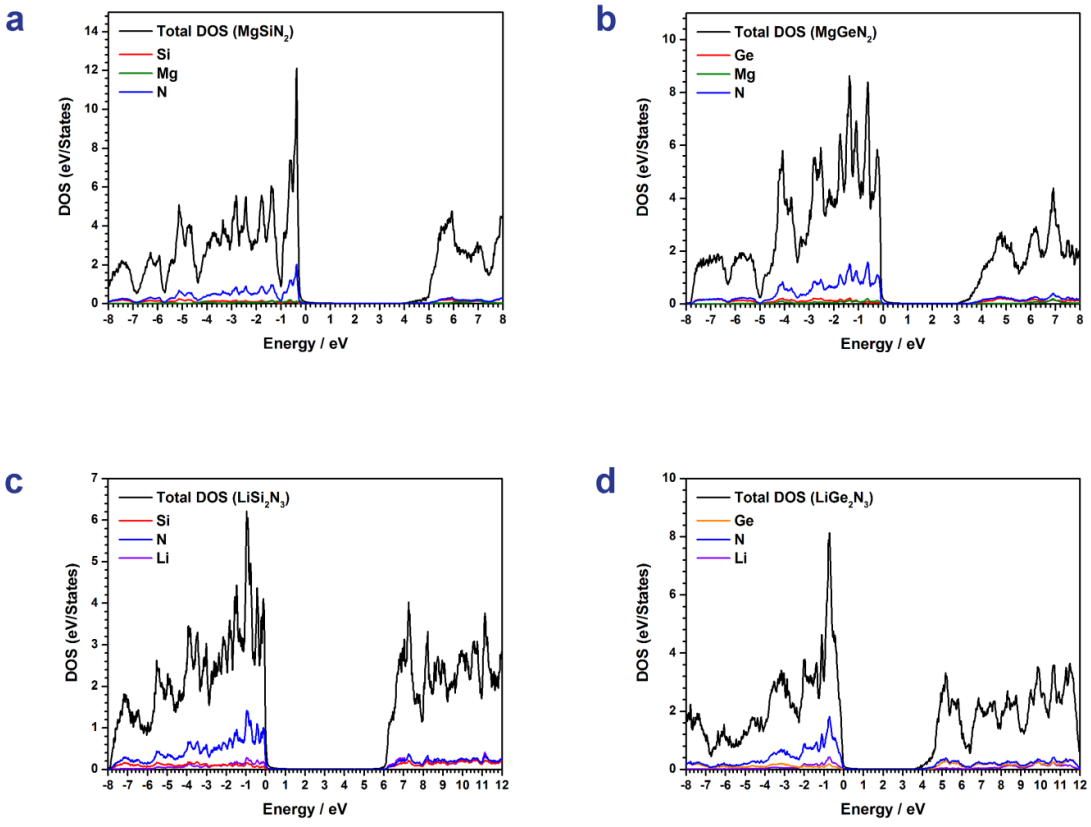

Figure S5.10 Total and atom resolved DOS of $MgSiN_2$ (a), $MgGeN_2$ (b), $LiSi_2N_3$ (c) and $LiGe_2N_3$ (d) within the SPRKKR formalism.

6 Solid Solutions of Grimm-Sommerfeld Analogous Nitride Semiconductors II-IV-N_2 with II = Mg, Mn, Zn; IV = Si, Ge – Ammonothermal Synthesis and DFT Calculations

published in: *Chem. Eur. J.* **2019**, *10.1002/chem.201903897*.

authors: Mathias Mallmann, Robin Niklaus, Tobias Rackl, Maximilian Benz, Thanh G. Chau, Dirk Johrendt, Ján Minár and Wolfgang Schnick

DOI: 10.1002/chem.201903897

Acknowledgment: Adapted from *Chemistry – A European Journal*, with permission from WILEY-VCH Verlag GmbH & Co. KGaA, Weinheim.

Abstract Grimm-Sommerfeld analogous II-IV-N_2 nitrides like $ZnSiN_2$, $ZnGeN_2$ or $MgGeN_2$ are promising semiconductor materials for substitution of commonly used (Al,Ga,In)N. In this contribution, we present a combined study on the ammonothermal synthesis of solid solutions of II-IV-N_2 compounds (II = Mg, Mn, Zn and IV = Si, Ge), having the general formula $(II^a_{1-x}II^b_x)$-IV-N_2 with x ≈ 0.5 and *ab initio* DFT calculations of their electronic and optical properties are presented. The ammonothermal reactions were conducted in custom-built high-temperature, high-pressure autoclaves by using the corresponding elements as starting materials. $NaNH_2$ and KNH_2 act as ammonobasic mineralizers, that increase the solubility of the reactants in supercritical ammonia. Temperatures between 870 and 1070 K and pressures up to 200 MPa were chosen as reaction conditions. All solid solutions crystallize in wurtzite-type superstructures with space group *Pna*2_1 (no. 33), confirmed by powder X-ray diffraction. The chemical compositions were analyzed by energy-dispersive X-ray spectroscopy. Diffuse reflectance spectroscopy was used for estimation of optical bandgaps of all compounds, which ranged from 2.6 to 3.5 eV (Ge-compounds) and 3.6 to 4.4 eV (Si-compounds), and thus demonstrated bandgap tunability between the respective boundary phases. Experimental findings were corroborated by DFT calculations of the electronic structure of pseudorelaxed mixed-occupancy structures by using the KKR+CPA approach.

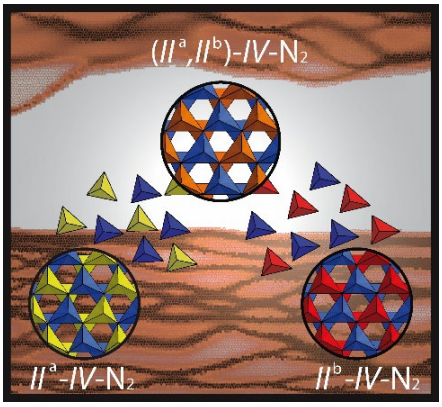

6.1 Introduction

The investigation of new semiconducting materials is of essential importance due to the increasing demand and the large number of possible applications. At present, GaN and solid solutions of group 13 nitrides (Al,Ga,In)N are the most important (opto)electronic

semiconductors with different application fields in modern electronic technologies. These include areas such as light-emitting diodes (LEDs), field-effect transistors or laser diodes.[1–2]

By using solid solutions of group 13 nitrides, a large bandgap range from around 0.7 to 6.2 eV can be covered.[3] However, the major problem of these compounds arises from the limited availability of the constitutent elements. Ga and In only arise as byproducts during the production of copper, aluminum, lead or zinc and are therefore difficult to access. In contrast, the natural abundance of elements such as Zn or Si is considerably higher. Therefore, one goal of modern semiconductor research is to synthesize compounds composed of earth-abundant elements. Recently, DFT calculations indicated various zinc nitrides such as Grimm-Sommerfeld analogous Zn(Si,Ge,Sn)N_2 compounds as possible next-generation semiconductors.[4] These materials exhibit similar electronic and optical properties compared to GaN, including high carrier mobility and small carrier effective masses, as well as high chemical stability and dopability. Additionally, such II-IV-N_2 compounds show lattice parameters similar to (Al,Ga,In)N, which enable the formation of hybrid structures or epitaxial growth on group 13 nitrides. In the last few years, different studies examined the synthesis and properties of II-IV-N_2 compounds.[5–10] However, the bulk synthesis of these materials is still challenging. Recently, we employed the ammonothermal method as a suitable synthesis approach to Zn-IV-N_2 compounds (IV = Si, Ge), as well as other Grimm-Sommerfeld analogous nitrides such as II-IV-N_2 (II = Mg, Mn; IV = Si, Ge), II_2-P-N_3 (II = Mg, Zn), $CaGaSiN_3$ or $Ca_{1-x}Li_xAl_{1-x}Ge_{1+x}N_3$ ($x \approx 0.2$).[11–15] By employing this method, we were able to synthesize crystalline $ZnSiN_2$ and $ZnGeN_2$ with crystal sizes of several micrometers and, for the first time, single crystals of Mg_2PN_3 with lengths of up to 30 µm. Furthermore, well defined crystallites of InN were obtained ammonothermally quite recently, indicating the ammonothermal process as an auspicious method for synthesis and crystal growth of semiconducting nitrides.[16]
Herein, we present the synthesis of the solid solutions $Mg_{1-x}Mn_xSiN_2$, $Mg_{1-x}Zn_xSiN_2$, $Mn_{1-x}Zn_xSiN_2$, $Mg_{1-x}Mn_xGeN_2$, $Mg_{1-x}Zn_xGeN_2$ and $Mn_{1-x}Zn_xGeN_2$ ($x \approx 0.5$) under ammonothermal conditions. The Si-compounds were synthesized at 1070 K and pressures up to 150 MPa, whereas the Ge-compounds already decompose at such high temperatures and were therefore synthesized at 870 K and maximum pressures of up to 200 MPa. The products were analyzed by powder X-ray diffraction and energy dispersive X-ray spectroscopy (EDX). Diffuse reflectance spectroscopy and DFT calculations were used for evaluation of optical and electronic properties. Due to the mixed occupancy sites in solid solutions, DFT calculations are challenging without relying on extensive supercell calculations. Previous works on mixed occupancy materials $CaMSiN_3$ (M = Al, Ga) and fully ordered II-IV-N_2 materials were successfully used to describe the electronic structure in the Korringa–Kohn–Rostoker (KKR) Green's function method together with bandgap corrections by the Engel Vosko formalism.[12,17] Here we advance the described method to show successful application to solid solutions of these nitride materials. The presented results again demonstrate the great potential of the ammonothermal approach for synthesis of semiconducting materials and mark another step of II-IV-N_2 compounds towards next-generation semiconductors as alternatives for commonly used group 13 nitrides.

6.2 Results and Discussion

6.2.1 Synthesis

The solid solutions of II-IV-N_2 compounds $Mg_{1-x}Mn_xSiN_2$, $Mg_{1-x}Zn_xSiN_2$, $Mn_{1-x}Zn_xSiN_2$, $Mg_{1-x}Mn_xGeN_2$, $Mg_{1-x}Zn_xGeN_2$ and $Mn_{1-x}Zn_xGeN_2$ ($x \approx 0.5$) were synthesized using supercritical ammonia as solvent in custom-built high-pressure, high-temperature autoclaves. The respective elements (Mg, Mn, Zn, Ge and Si) were used as starting materials. NaN_3 (Ge-compounds) and KN_3 (Si-compounds) were added to the reaction mixture. They decompose during the reaction and form the corresponding amides ($NaNH_2$ and KNH_2), acting as ammonobasic mineralizers. The azides were used instead of metals or amides because of their high purity and chemical stability toward hydrolysis. The mineralizers increase the solubility of the other starting materials in supercritical ammonia by formation of soluble intermediates (e.g. $K_2[Zn(NH_2)_4]$).[18–19] In the case of the Si-compounds, the use of KNH_2 instead of $NaNH_2$ resulted in products with higher crystallinity. These findings are consistent with previous results, where $MgSiN_2$ and $MnSiN_2$ were synthesized with KNH_2, and $MgGeN_2$ and $MnGeN_2$ with $NaNH_2$.[12] Due to the preferred formation of intermediates around 700 K and the following transformation into the nitrides at higher temperatures, the syntheses were conducted in two temperature steps (see Experimental Section). Whereas all Si-compounds were synthesized at 1070 K with an autogenous pressure of around 150 MPa, Ge containing compounds are thermally less stable and already decompose at these temperatures. Therefore, $Mg_{1-x}Mn_xGeN_2$, $Mg_{1-x}Zn_xGeN_2$ and $Mn_{1-x}Zn_xGeN_2$ ($x \approx 0.5$) were synthesized at 870 K reaching maximum pressures of about 200 MPa. To prevent uncontrolled diffusion of the starting materials through the autoclave, the reaction mixtures were contained in closed Ta-liners. The lids of the liners contain a small hole to ensure the filling with ammonia. After reaction, residual amides and other impurity phases were removed as far as possible (see below) by washing the products with ethanol and acetic acid. Optical micrographs of the obtained products are shown in Figure 6.1.

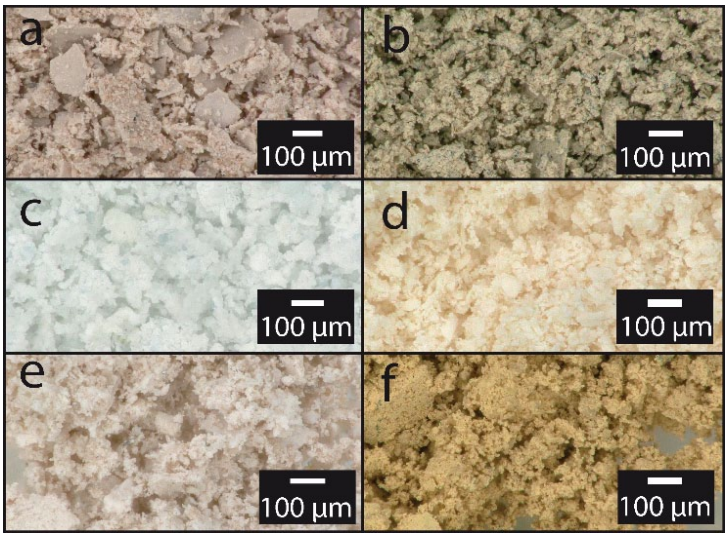

Figure 6.1 Optical micrographs of $Mg_{1-x}Mn_xSiN_2$ (a), $Mg_{1-x}Mn_xGeN_2$ (b), $Mg_{1-x}Zn_xSiN_2$ (c), $Mg_{1-x}Zn_xGeN_2$ (d), $Mn_{1-x}Zn_xSiN_2$ (e), and $Mn_{1-x}Zn_xGeN_2$ (f) with $x \approx 0.5$.

6.3 Crystal Structure

The purified compounds were analyzed by PXRD. Rietveld plots of all products are shown in Figure 6.2. Wyckoff positions, atomic coordinates and lattice parameters as starting values for the refinement were taken from ammonothermally synthesized II-IV-N_2 phases in the literature.[11–12] Obtained crystallographic data are summarized in Table 6.1, and refined atomic coordinates and displacement parameters in Tables S6.1–S6.2 in the Supporting Information. All compounds crystallize in orthorhombic space group *Pna*2_1 (no. 33) and can be derived from the wurtzite structure type (*P*6_3*mc*, no. 186) by ordering of tetrahedrally coordinated divalent and tetravalent cations, to form *sechser*-rings along [001] (Figure 6.3).[20] The ordering can be verified by the expected (011) and (110) superstructure reflections for the orthorhombic structure,[21] which occur as the first two reflections of the target phases in the powder patterns. Further ordering of the different divalent cations in the solid solutions (e.g. Mg^{2+} and Zn^{2+} in $Mg_{1-x}Zn_xGeN_2$) could not be detected by PXRD. The occupation of the divalent cation positions were refined and slightly deviate from 0.5 for each divalent cation (see Supporting Information Tables S6.1–S6.6). The largest deviation is found in $Mg_{0.375}Mn_{0.625}GeN_2$, whereas the deviations of all other compounds are in the range of ± 0.05. The chemical compositions of the products were verified by elemental analysis (see below). Cell volumes of the solid solutions are within the range of the respective boundary phases reported in literature.[11–12]

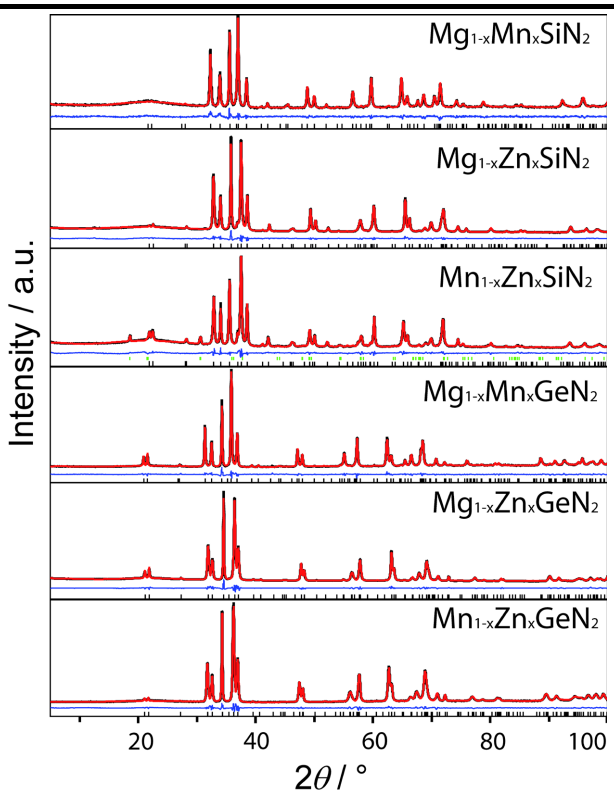

Figure 6.2 Rietveld refinement of PXRD pattern of solid solutions of II-IV-N_2 compounds (II = Mg, Mn, Zn; IV = Si, Ge) with experimental data (black lines), calculated data (red lines), difference profiles (blue lines), and reflection positions (black bars). Green bars indicate reflection position of K_3MnO_4 side phase.

Table 6.1 Crystallographic data of $Mg_{1-x}Mn_xSiN_2$, $Mg_{1-x}Mn_xGeN_2$, $Mg_{1-x}Zn_xSiN_2$, $Mg_{1-x}Zn_xGeN_2$, $Mn_{1-x}Zn_xSiN_2$ and $Mn_{1-x}Zn_xGeN_2$ ($x \approx 0.5$) obtained by Rietveld refinement

formula		$Mg_{1-x}Mn_xSiN_2$ (x = 0.543)	$Mg_{1-x}Mn_xGeN_2$ (x = 0.625)	$Mg_{1-x}Zn_xSiN_2$ (x = 0.515)	$Mg_{1-x}Zn_xGeN_2$ (x = 0.545)	$Mn_{1-x}Zn_xSiN_2$ (x = 0.53)	$Mn_{1-x}Zn_xGeN_2$ (x = 0.55)
crystal system		orthorhombic					
space group		$Pna2_1$ (33)					
lattice parameters / Å	*a*	5.27579(12)	5.50086(8)	5.26264(8)	5.48149(8)	5.26071(10)	5.48798(9)
	b	6.49871(17)	6.65560(11)	6.36667(11)	6.51446(11)	6.35726(15)	6.54510(13)
	c	5.03780(13)	5.22654(8)	5.00805(7)	5.18384(7)	5.04257(11)	5.22186(9)
cell volume / Å^3		172.725(7)	191.352(5)	167.797(5)	185.110(5)	168.642(6)	187.566(6)
Density / g·cm^{-3}		3.732	5.001	3.972	5.286	4.592	5.676
formula units / cell		4					
T / K		293(2)					
diffractometer		STOE STADI P					
radiation / Å		Cu-Kα_1 (λ = 1.5406)					
2θ range / °		5.0 ≤ 2θ ≤ 100					
profile function		fundamental parameters model					
background function		Shifted Chebyshev					
data points		6365	6365	6365	6365	6365	6365
number of reflections		104	116	100	111	101	114
refined parameters		56	51	50	56	64	52
R values		R_p = 0.0266	R_p = 0.0342	R_p = 0.0395	R_p = 0.0413	R_p = 0.0339	R_p = 0.0368
		R_{wp} = 0.0340	R_{wp} = 0.0452	R_{wp} = 0.0490	R_{wp} = 0.0575	R_{wp} = 0.0419	R_{wp} = 0.0491
		R_{Bragg} = 0.0191	R_{Bragg} = 0.0134	R_{Bragg} = 0.0146	R_{Bragg} = 0.0158	R_{Bragg} = 0.0114	R_{Bragg} = 0.0105
Goodness of fit		2.08	2.47	3.07	3.54	2.60	2.47

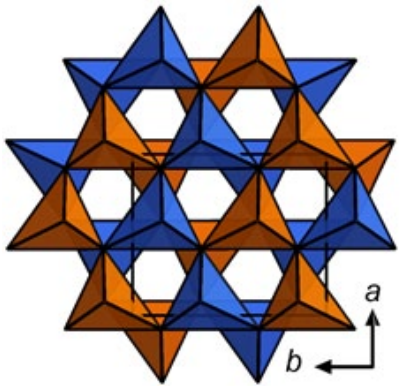

Figure 6.3 Crystal structure of solid solutions of II-IV-N_2 compounds (II = Mg, Mn, Zn; IV = Si, Ge) along [001]. Mixed occupied II-N_4-tetrahedra are depicted in blue, IV-N_4-tetrahedra in orange.

However, the values of the solid solution deviate slightly from those expected from Vegard's rule (see Supporting Information Figure S.6.1).[22] Possible explanations for this slight divergence could be a certain heterogeneous phase width of the solid solutions, which could also explain slight reflection broadening effects in the PXRD patterns of the solid solutions compared to the boundary phases, vacancies within the crystal structure, and as measuring inaccuracies.

To show that, in principle, solid solutions with other compositions are possible, $Mg_{1-x}Zn_xGeN_2$ with $x \approx 0.8$ was synthesized. The Rietveld plot, atomic coordinates, and crystallographic data are given in the Supporting Information (Figure S6.2, Tables S6.7 and S6.8).

6.4 Scanning Electron Microscopy

SEM was conducted for verification of the chemical composition of the solid solutions as well as for examination of crystallite size and morphology. EDX values are summarized in Tables S6.9 and S6.10 in the Supporting Information. The slightly differing compositions measured at different measuring points suggest a phase width. A possible explanation could be the different solubilities of the starting materials (Mg, Mn and Zn) in supercritical ammonia, resulting in a varying transport through the autoclave, which could not be prevented completely by the use of Ta liners. Nevertheless, based on the obtained values, it can be assumed that the solid solutions have an atomic ratio of the divalent cations close to 1 : 1, which is consistent with the findings received from Rietveld refinement. Exemplarily, SEM images of $Mn_{1-x}Zn_xSiN_2$ and $Mn_{1-x}Zn_xGeN_2$ (Figure S6.3 in the Supporting Information) show crystallites with sizes up to several micrometers. The sizes and well-defined crystal faces suggest a solution based growth mechanism, as already reported for $ZnGeN_2$.[11] SEM images of the Mg-containing compounds only show nanocrystalline products and were therefore not presented in the Supporting Information.

6.5 UV/Vis Spectroscopy

The optical properties of the solid solutions were investigated by diffuse reflectance spectroscopy. Whereas the Si-compounds show absorption bands in the region between 200 and 350 nm, the absorption bands of the Ge-compounds are shifted to higher wavelengths between 300 and 500 nm (see Figure S6.4 in the Supporting Information). In the case of Mn-containing compounds, sub-bandgap absorption was observed. These absorption bands can be attributed to the absorption of Mn^{2+} [transition of the ground state $^6A_1(^6S)$ to the excited states $^4T_1(^4G)$, $^4T_2(^4G)$, $^4A_1$,$^4E(^4G)$, $^4T_2(^4D)$ and $^4E(^4D)$] according to literature.[8,23] In the case of the germanium compounds, these absorption bands are partially overlaid by the bandgap absorption. The Kubelka-Munk function $F(R) = (1-R)^2/2R$, where R is reflectance, was used to calculate pseudo-absorption spectra.[24] Figure 6.4 shows Tauc plots, which were used for evaluation of the bandgaps E_g, whereby the energy $h\nu$ was plotted against $[F(R)\cdot h\nu]^{1/n}$ with $n = 1/2$ for direct bandgaps.[25] Direct transitions were assumed according to DFT calculations (see below). Table 6.2 summarizes the measured bandgaps. The evaluated bandgaps are in similar ranges to those already described in literature for the boundary phases.[9,11–12,26–31]

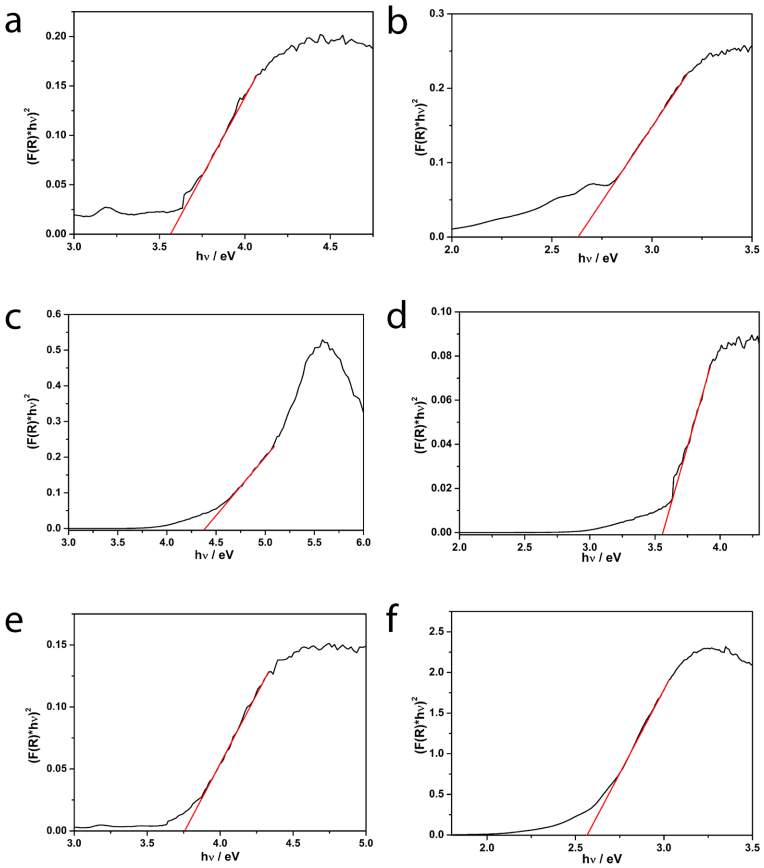

Figure 6.4 Tauc plots of $Mg_{1-x}Mn_xSiN_2$ (a), $Mg_{1-x}Mn_xGeN_2$ (b), $Mg_{1-x}Zn_xSiN_2$ (c), $Mg_{1-x}Zn_xGeN_2$ (d), $Mn_{1-x}Zn_xSiN_2$ (e) and $Mn_{1-x}Zn_xGeN_2$ (f) with $x \approx 0.5$. Red lines indicate tangents at the inflection points.

Table 6.2 Evaluated optical bandgaps (E_g^{exp}) of the the mixed occupancy ($II^a_{1-x}II^b_x$)-IV-N_2 ($x \approx 0.5$) compound series from Tauc plots at room temperature.

$Mg_{1-x}Mn_xSiN_2$	$Mg_{1-x}Mn_xGeN_2$	$Mg_{1-x}Zn_xSiN_2$	$Mg_{1-x}Zn_xGeN_2$	$Mn_{1-x}Zn_xSiN_2$	$Mn_{1-x}Zn_xGeN_2$
3.6 eV	2.7 eV	4.4 eV	3.5 eV	3.8eV	2.6 eV

Compared with the boundary phases prepared from ammonothermal syntheses (Figure S6.5 in the Supporting Information), the measured E_g of the mixed phases do not exactly match the mean values of their constituent boundary phases. This is in line with the aforementioned minor deviations and possible measuring inaccuracies of lattice parameters observed from structure refinement. Considering the extensive Urbach tailing observed in the diffuse reflectance spectra (see Figure S6.4 in the Supporting Information), such deviations might well be explained by slight variations in the occupation of the divalent cation sites, possible defect sites, or resulting increased phonon-assisted absorption in the nanocrystallites obtained from ammonothermal synthesis.[17,32] In the case of $Mg_{1-x}Zn_xGeN_2$ the evaluated bandgap (3.5 eV) is larger than those of the corresponding boundary phases (both 3.2 eV). On the basis of numerous theoretical calculations, it can be assumed that the bandgap of $MgGeN_2$ should actually be larger (around 4 eV) than previously estimated (3.2 eV).[12,33]

6.6 DFT Calculations

To validate and investigate the observed trends of the experimentally deduced bandgap behavior of the examined solid solutions, DFT calculations were carried out for all boundary phases and the solid solutions $Mg_{0.5}Mn_{0.5}SiN_2$, $Mg_{0.5}Zn_{0.5}SiN_2$ and $Mn_{0.5}Zn_{0.5}SiN_2$, as well as the isotypical Ge series $Mg_{0.5}Mn_{0.5}GeN_2$, $Mg_{0.5}Zn_{0.5}GeN_2$ and $Mn_{0.5}Zn_{0.5}GeN_2$, in which the mixed occupancy was fixed at 0.5 for the sake of consistency. Each mixed occupancy model was constructed from a symmetrized average of three VASP-relaxed orderings with regard to atomic position and lattice parameters (for models, see Figure S6.6 in the Supporting Information). These pseudorelaxed models were used as starting points for electronic structure calculations of the mixed-occupancy models $(II^a_{0.5}II^b_{0.5})$-IV-N_2 by means of the MUNICH SPRKKR package, which has been shown to be a sensible approach according to our previous work.[17] Figure 6.5 depicts the calculated plots for the density of states (DOS) for each material.

Excluding temperature effects, all $(Mn_{0.5}II_{0.5})$-IV-N_2 (II = Mg, Zn / IV = Si, Ge) compounds (Figure 6.5 a, b, e, f) exhibit spin polarization with values of total magnetic moments ranging between 4.17 – 4.23 μ_B. The obtained electronic bandgaps for the calculated solid solutions lie in-between the calculated values of the respective boundary phases for all compounds calculated within the framework of the used code. These obtained E_g values for purely

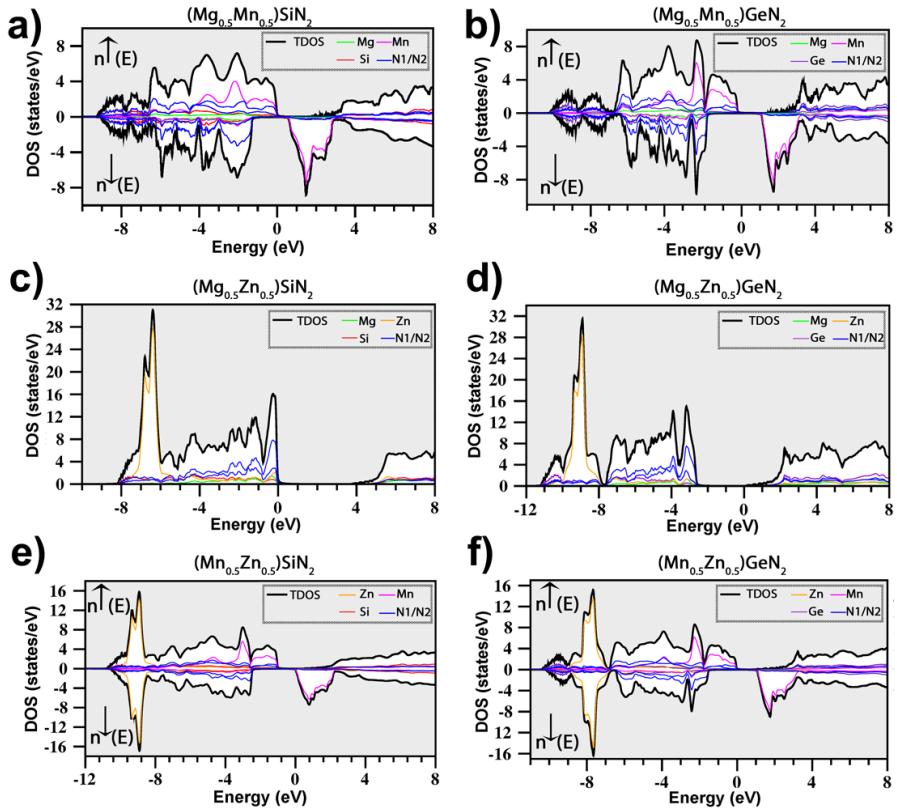

Figure 6.5 Density of states (DOS) as calculated by the KKR formalism with the coherent potential approximation and Engel Vosko exchange correlation (EV-GGA) for the mixed occupancy $(II^a_{0.5}II^b_{0.5})$-IV-N_2 compound series. $(Mg_{0.5}Mn_{0.5})SiN_2$ (a), $(Mg_{0.5}Mn_{0.5})GeN_2$ (b), $(Mg_{0.5}Zn_{0.5})SiN_2$ (c), $(Mg_{0.5}Zn_{0.5})GeN_2$ (d), $(Mn_{0.5}Zn_{0.5})SiN_2$ (e) and $(Mn_{0.5}Zn_{0.5})GeN_2$ (f).

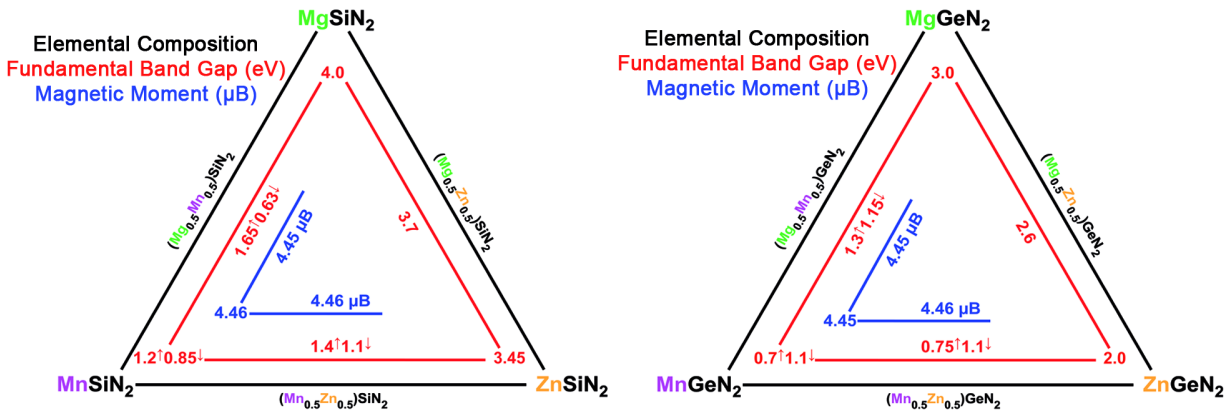

Figure 6.6 Electronic and magnetic properties as calculated by the KKR formalism with the coherent potential approximation and Engel-Vosko exchange correlation (EV-GGA) for the mixed occupancy ($II^a_{0.5}II^b_{0.5}$)-IV-N_2 compound series. Left: Si-series, Right: Ge-series. Arrows indicate direct electronic gaps for up and down spin channels.

electronic transitions are estimated from the respective Bloch spectral functions (see Figures S6.7 and S6.8 in the Supporting Information) and are summarized in Figure 6.6. For spin-polarized Mn-compounds E_g is given in terms of the respective spin-up and spin-down channels along values of magnetic moments. Owing to the underestimation of the exchange-correlation by PBE we utilize the EV-PBE functional implemented in SPRKKR to correct the exchange-correlation and increase the bandgap accordingly. For a variety of materials including group 13 nitrides, EV-GGA has been shown to provide accurate band dispersion with gaps lying somewhere between those of LDA/GGA and those from the modified Becke Johnson potential (mBJ), the latter of which is widely considered to reproduce gaps with good accuracy.[34–40] Due to the smearing of the bands introduced by the mixed-occupancy disorder and the induced smearing of the Bloch spectral functions, together with the relatively flat progression of the valence states, the assignment of the transition types for the solid solutions is not without ambiguity. For better analysis we performed subsequent calculations on the respective ordering models within VASP and the therein-available mBJ potential. For all ordered compounds $Mg_{0.5}Zn_{0.5}SiN_2$, $Mn_{0.5}Zn_{0.5}SiN_2$ and $Mn_{0.5}Mg_{0.5}SiN_2$, the ordered models suggest that indirect transitions are slightly favored over direct transitions, whereas for $Mn_{0.5}Zn_{0.5}GeN_2$ and $Mn_{0.5}Mg_{0.5}GeN_2$ direct and indirect transitions arise depending on the cation ordering with only $Mg_{0.5}Zn_{0.5}GeN_2$ showing consistent direct transitions. From the respective KKR calculations of the solid solutions indirect transitions are found for the ($II^a_{0.5}II^b_{0.5}$)-Si-N_2 compounds, albeit with only about 0.05 eV difference to direct transitions. For the ($II^a_{0.5}II^b_{0.5}$)-Ge-N_2 compound series direct and indirect transitions are found to be energetically identical.

As both types of transitions are found for the ordering models, KKR+CPA calculations appear to consistently describe the solid solution for statistical mixed occupancy. With regard to the minimal difference in direct and indirect transitions, we estimate that optically allowed direct transitions are more likely to be occur and thus best described with the Kubelka-Munk formalism for direct transitions, as chosen accordingly for the experimental evaluation by

UV/Vis spectroscopy. With regard to the bandgap the ordered mBJ calculations on average further increase the bandgaps from EV-PBE by about 1 eV. Lambrecht *et al.* have further published a number of computationally dedicated bandgap estimates from QSGW calculations for $MgSiN_2$, $ZnSiN_2$, $MgGeN_2$ and $ZnGeN_2$. For $MgSiN_2$ and $ZnSiN_2$ indirect transitions of 5.84 and 5.44 eV are reported, whereas for $MgGeN_2$ and $ZnGeN_2$ direct transitions of 5.14 and 3.42 eV in magnitude were obtained from the QSGW calculations, respectively, while more recent calculations that explicitly correct the influence of semicore *d* states suggest a corrected bandgap of 4.11 eV for $MgGeN_2$.[33,41,42]

Although our bandgap determined for $MgGeN_2$ from EV-GGA appears to still underestimate E_g, it seems to be a reasonable cost-efficient correction for the exchange correlation compared to PBE while qualitatively describing the trend in gap progression between the II-IV-N_2 boundary phases correctly. Hence, we assume that the fundamental electronic bandgaps of both $(II^a_{0.5}II^b_{0.5})$-Si-N_2 and $(II^a_{0.5}II^b_{0.5})$-Ge-N_2 should be increased by approximately 1 eV, which would place them closer to QSGW calculations.[33,41,42] A summary of our bandgap determinations, along with experimental and QSGW evaluations from literature where available, is given in Tables S6.11 and S6.12 of the Supporting Information. Figure 6.5 shows that the edges of the conduction bands (CBs) for the majority spin channels are characterized by a slow ascent for all II-IV-N_2 compounds. This is due to the limited number of states originating from a single band (conduction band minimum at the *Γ* point, see also Figure S6.7 in the Supporting Information), which is mostly characterized by mixed N and M^{2+} states with s character. In turn this implies reduced optical transition probabilities for the optical absorption, as can be seen from calculations of the joint DOS shown in Figure 6.7. These calculations are in good agreement with the experimentally determined pseudo-absorption spectra from Kubelka-Munk theory, even in terms of analogous bandgap estimates, as shown in Table 6.3. Whereas the experimentally determined bandgaps may be lowered due to defects introduced during synthesis and Urbach tail absorptions, the herein estimated bandgaps from the JDOS are expected to overestimate the fundamental bandgap due to the decreased transition probability of the CB edges.

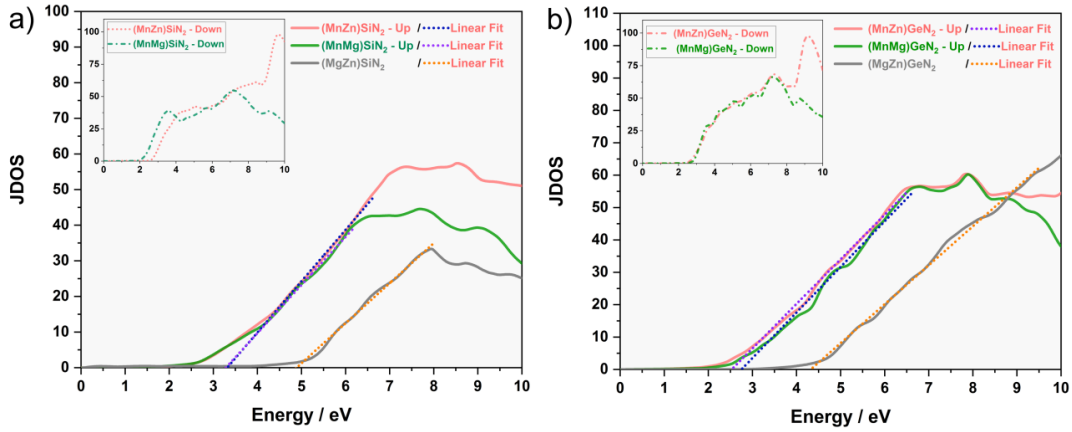

Figure 6.7 JDOS calculations for $(II^a_{0.5}II^b_{0.5})$-Si-N_2 (a) and $(II^a_{0.5}II^b_{0.5})$-Ge-N_2-compounds (b) within the KKR formalism. Extrapolated linear fits (dotted lines) were used for the estimation of optical bandgaps. Inset: JDOS of spin down channels.

Table 6.3 Optical bandgaps E_g^{JD} (eV) of the the mixed occupancy ($II^a_{0.5}II^b_{0.5}$)-IV-N_2 compound series from joint DOS calculations based on the EV-PBE functional within the MUNICH SPRKKR program package.

$Mg_{0.5}Mn_{0.5}SiN_2$	$Mg_{0.5}Mn_{0.5}GeN_2$	$Mg_{0.5}Zn_{0.5}SiN_2$	$Mg_{0.5}Zn_{0.5}GeN_2$	$Mn_{0.5}Zn_{0.5}SiN_2$	$Mn_{0.5}Zn_{0.5}GeN_2$
3.4 eV	2.8 eV	4.9 eV	4.3 eV	3.4 eV	2.5 eV

This effect is, however, likely compensated by underestimations for E_g from DFT. The low-energy transitions to CB at the Γ point seen from the JDOS might also further influence the broad absorption tails observed in the diffuse reflectance spectra. Accordingly, advanced experimental measurement techniques to determine the fundamental bandgaps with more accuracy such as XAS-XES might prove promising for future investigations of this materials class, which are so far only available for $MgSiN_2$ (XANES-XES: 5.6 eV).[31]

6.7 Magnetic Measurements

Magnetic measurements were performed to investigate the magnetic behavior of the Mn-containing solid-solutions. However, due to paramagnetic impurities, a precise statement on the magnetic properties is difficult. A corresponding discussion together with detailed information on the magnetic measurements is presented in the Supporting Information

6.8 Conclusions

Herein we report on the synthesis of the solid solutions $Mg_{1-x}Mn_xSiN_2$, $Mg_{1-x}Zn_xSiN_2$, $Mn_{1-x}Zn_xSiN_2$, $Mg_{1-x}Mn_xGeN_2$, $Mg_{1-x}Zn_xGeN_2$ and $Mn_{1-x}Zn_xGeN_2$ ($x \approx 0.5$) using supercritical ammonia (T_{crit} = 405.5 K, p_{crit} = 11.3 MPa) as reaction media and alkali metal amides as mineralizers.[19] Special autoclaves constructed of nickel-based superalloys (Inconel 718 and Haynes alloy 282) were used for the syntheses. All six compounds crystallize in a wurtzite-type superstructure in space group $Pna2_1$. The measured optical bandgaps range from 2.6 to 3.5 eV (Ge compounds) and 3.6 to 4.4 eV (Si compounds). Additionally, DFT calculations of ($II^a_{0.5}II^b_{0.5}$)-IV-N_2 (II = Mg, Mn, Zn; IV = Si, Ge) provide detailed insights into the electronic structures, electronic and optical bandgaps, and type of band transitions. The resulting values for the electronic bandgaps as well as the values for the optical transitions obtained by JDOS calculations are of the same order of magnitude as the measured ones and thus corroborate the validity of our approach to calculate both solid solutions and boundary phases of II-IV-N_2 semiconductors.

Although the ammonothermal synthesis of ternary and higher (oxide) nitrides is still challenging and only a small number of synthesized compounds are known from literature, these studies once again demonstrate the great potential of this method.[11–15,43–46] Furthermore, it could be shown within the scope of this work that bandgap tunability is possible in this system, paving the way for possible future applications of bandgap engineering. With regard to the semiconducting properties of II-IV-N_2 and their potential as alternatives to commonly used group 13 nitride semiconductors, the crystal growth and further characterization of materials

properties of these solid solutions, for example electronic band structure measurements by means of XES-XAS measurements, is the next step in the exploration and contribution to a better understanding of II-IV-N_2 compounds.

6.9 Experimental Section

The autoclaves were loaded in an Ar-filled glovebox (Unilab, MBraun, Garching, O2 < 1 ppm, H2O < 1 ppm) to prevent oxygen or moisture contamination. Ammonia was condensed into the autoclaves by using a vacuum line (≤ 0.1 Pa) with argon and ammonia (both: Air Liquide, 99.999%) supply. Gas purification cartridges (Micro Torr FT400-902 (for Ar) and MC400-702FV (for NH_3), SAES Pure Gas Inc., San Luis Obispo, CA, USA) were used for further purification, providing a purity level of < 1 ppbV H_2O, O_2 and CO_2.

6.9.1 Ammonothermal Synthesis of $Mg_{1-x}Mn_xGeN_2$, $Mg_{1-x}Zn_xGeN_2$, $Mn_{1-x}Zn_xGeN_2$

$Mg_{1-x}Mn_xGeN_2$, $Mg_{1-x}Zn_xGeN_2$ and $Mn_{1-x}Zn_xGeN_2$ ($x \approx 0.5$) as well as $Mg_{1-x}Zn_xGeN_2$ ($x \approx 0.8$) were synthesized under ammonothermal conditions starting from the corresponding metals [Mg (1.5 mmol, 36.5 mg, Alfa Aesar, 99.8%), Mn (1.5 mmol, 82.4 mg, Alfa Aesar, 99.95%) and Zn (1.5 mmol, 98.1 mg, Alfa Aesar, 99.9 %)], Ge (3 mmol, 217.9 mg, smart-elements, 99.99%) and NaN_3 (7.5 mmol, 487.5 mg, Sigma-Aldrich, 99.5%) as mineralizer for $x \approx 0.5$ and Mg (0.75 mmol, 18.2 mg, Alfa Aesar, 99.8%), Zn (2.25 mmol, 147.2 mg, Alfa Aesar, 99.9 %), Ge (3 mmol, 217.9 mg, smart-elements, 99.99%) and NaN_3 (7.5 mmol, 487.5 mg, Sigma-Aldrich, 99.5%) for $x \approx 0.8$. The starting materials were mixed and transferred in a Ta liner, to protect the mixture against contamination by the autoclave material. The liners were closed by means of a Ta lid with a small hole. Afterwards, the liner was placed in the autoclave (Inconel® 718, max. 900 K, 300 MPa, 10 mL), which was sealed with a lid via flange joints using a sealing gasket (silver coated Inconel® 718 ring, GFD seals). The autoclave body is connected via an Inconel® 718 high pressure tube to the upper part, consisting of a hand valve (SITEC), a pressure transmitter (HBM P2VA1/5000 bar), and a bursting disc (SITEC). After closing under argon, the autoclave was evacuated and cooled with an ethanol/liquid nitrogen mixture to 198 K. Subsequently, ammonia (≈ 7 mL) was directly condensed into the autoclave via a pressure regulating valve. The amount of NH_3 was determined by means of a mass flow meter (D-6320-DR, Bronkhorst, Ruurlo, Netherlands). The autoclave was heated to 670 K within 2 h, held at this temperature for 16 h, heated to 870 K within 2 h, and kept at this temperature for 96 h, reaching pressures around 200 MPa. After cooling, residual ammonia was removed and the products were separated in air, washed with EtOH and acetic acid and dried at 350 K. $Mg_{1-x}Mn_xGeN_2$, $Mg_{1-x}Zn_xGeN_2$ and $Mn_{1-x}Zn_xGeN_2$ ($x \approx 0.5$) were obtained as light brown, beige and ocher powders, respectively.

6.9.2 Ammonothermal Synthesis of $Mg_{1-x}Mn_xSiN_2$, $Mg_{1-x}Zn_xSiN_2$ and $Mn_{1-x}Zn_xSiN_2$

The ammonothermal method was used for synthesis of the solid solutions $Mg_{1-x}Mn_xSiN_2$, $Mg_{1-x}Zn_xSiN_2$ and $Mn_{1-x}Zn_xSiN_2$ ($x \approx 0.5$). The corresponding metals [Mg (1.5 mmol, 36.5 mg, Alfa Aesar, 99.8%), Mn (1.5 mmol, 82.4 mg, Alfa Aesar, 99.95%) and Zn (1.5 mmol, 98.1 mg, Alfa

Aesar, 99.9 %)], Si (3 mmol, 84.3 mg, Alfa Aesar, 99.9%) and KN_3 (7.5 mmol, 608.4 mg, Sigma-Aldrich, 99.9%) as mineralizer were used as starting material. Si was ball-milled under argon for 10 h in a planetary ball mill (Retsch PM 400) to support reaction in supercritical ammonia. The reactants were mixed and placed in a Ta liner. The liners were closed by means of a Ta lid with a small hole. Subsequently, the liner was transferred into the autoclave (Haynes® 282®, max. 1100 K, 170 MPa, 10 mL), which was closed under argon. The autoclave setup is similar to the above mentioned one. After evacuating and cooling the reactor to 198 K, NH_3 (≈ 4.5 mL) was condensed into the autoclave. The amount of NH_3 was determined by means of a mass flow meter (D-6320-DR, Bronkhorst, Ruurlo, Netherlands). The autoclave was heated to 670 K within 2 h, held for 16 h, heated to 1070 K within 3 h and kept at this temperature for 96 h, resulting in maximum pressures of up to 150 MPa. After cooling to room temperature and removing residual ammonia, the samples were extracted from the liners and washed with ethanol and acetic acid. $Mg_{1-x}Mn_xSiN_2$ ($x \approx 0.5$) was obtained as white powder, and $Mg_{1-x}Zn_xSiN_2$ and $Mn_{1-x}Zn_xSiN_2$ ($x \approx 0.5$) were obtained as brown powders.

6.9.3 Digital Microscope

Optical micrographs of the obtained powders were recorded with a digital microscope (VHX-5000, Keyence) under white light irradiation. All sample images were collected with a magnification of 200.

6.9.4 Powder X-ray Diffraction

The products were ground and filled in glass capillaries (0.3 mm diameter, 0.01 mm wall thickness, Hilgenberg GmbH). The data were collected with a Stoe STADI P diffractometer with Cu-$K_{\alpha1}$ radiation (λ = 1.5406 Å), Ge(111) monochromator and Mythen 1K detector in Debye-Scherrer geometry. TOPAS was used for Rietveld refinement.[47]
CCDC 1903084 ($Mg_{0.375}Mn_{0.625}GeN_2$), CCDC 1903085 ($Mg_{0.455}Zn_{0.545}GeN_2$ CCDC 1903088 ($Mn_{0.55}Zn_{0.45}GeN_2$), CCDC 1903087 ($Mg_{0.457}Mn_{0.543}SiN_2$), CCDC 1903086 ($Mg_{0.515}Zn_{0.485}SiN_2$) and CCDC 1903089 ($Mn_{0.47}Zn_{0.53}SiN_2$) contain the supplementary crystallographic data for this paper. The data are provided free of charge from The Cambridge Crystallographic Data Centre.

6.9.5 Scanning Electron Microscopy

A Dualbeam Helios Nanolab G3 UC (FEI) scanning electron microscope, equipped with an EDX detector (X-Max 80 SDD, Oxford instruments) was used for determination of crystal morphologies and their chemical composition. The samples were placed on an adhesive carbon pad and coated with a conductive carbon film by using a high-vacuum sputter coater (BAL-TEC MED 020, Bal Tec A).

6.9.6 UV/Vis Spectroscopy

For determination of the optical bandgaps, diffuse reflectance measurements of the samples at room temperature were recorded using a Jasco V-650 UV/Vis spectrophotometer equipped with Czerny-Turner mount, photomultiplier tube detector and deuterium (190 – 350 nm) / halogen (330 – 900 nm) lamps as light sources.

6.9.7 Computational Details

Initial structural relaxations for the ordered models for all ($II^a_{0.5}II^b_{0.5}$)-IV-N_2 compounds were performed by means of the VASP program package with the implemented projector augmented wave (PAW) method.[48–52] The generalized gradient approximation (GGA) functional of Perdew, Burke and Ernzerhof (PBE) was used to model the exchange-correlation.[53,54] A plane-wave cutoff energy of 535 eV was used for all calculations together with a Brillouin zone sampling on dense gamma centered Monkhorst-Pack meshes of 10 x 8 x 10. Electronic and structural convergence criteria of 10^{-8} and 10^{-7} eV were set in order to ensure precision of total energies. For the respective ordering models the exchange-correlation was further corrected with the modified Becke–Johnson formalism (mBJ -GGA) in order to estimate the bandgaps more accurately.[40,55,56] Subsequently, in order to accurately estimate the electronic properties of the experimental solid solution the relaxed structures were averaged, symmetrized and converted with the CIF2Cell program[57] to formats compatible with the MUNICH SPRKKR program package.[58,59] The electronic structure was further converged to values of 10^{-5} eV utilizing the implemented fully relativistic Korringa–Kohn–Rostoker (KKR) Green's function method with the PBE functional.[53,54] Owing to the currently missing implementation of the mBJ-GGA potential the EV-GGA (Engel Vosko) formalism was used to obtain more reliable bandgaps by calculating the respective Bloch spectral functions and DOS.[60] The chemical disorder was treated by the coherent potential approximation (CPA) self consistently and fully relativistic within the four component Dirac formalism. For all calculations an angular momentum expansion of $l = 3$ was used.

6.9.8 Acknowledgements

The project was funded by the Deutsche Forschungsgemeinschaft (DFG, German Research Foundation) under Germany's Excellence Strategy – EXC 2089/1 – 390776260 and within the research group "Chemistry and Technology of the Ammonothermal Synthesis of Nitrides" (FOR 1600), project SCHN377/16-2, by the European Regional Development Fund (ERDF), project CEDAMNF, reg. no. CZ.02.1.01/0.0/0.0/15_003/0000358 and the Czech Science Foundation (GACR), Proj. 17-14840S. The authors gratefully acknowledge the group of Prof. Dr. E. Schlücker (Anna Kimmel and Thomas Steigerwald) for fabrication and maintenance of the autoclaves (FAU Erlangen-Nürnberg). In addition, we want to thank Lisa Gamperl for SEM/EDX measurements and Dr. C. Hoch for digital microscopy pictures (all at Department of Chemistry, LMU Munich).

6.10 References

[1] S. P. DenBaars, D. Feezell, K. Kelchner, S. Pimputkar, C.-C. Pan, C.-C. Yen, S. Tanaka, Y. Zhao, N. Pfaff, R. Farrell, M. Iza, S. Keller, U. Mishra, J. S. Speck, S. Nakamura, Development of gallium-nitride-based light-emitting diodes (LEDs) and laser diodes for energy-efficient lighting and displays, *Acta Mater.* **2013**, *61*, 945–951.

[2] K. Shinohara, D. C. Regan, Y. Tang, A. L. Corrion, D. F. Brown, J. C. Wong, J. F. Robinson, H. H. Fung, A. Schmitz, T. C. Oh, S. J. Kim, P. S. Chen, R. G. Nagele, A. D. Margomenos, M. Micovic, Scaling of GaN HEMTs and Schottky Diodes for Submillimeter-Wave MMIC Applications, *IEEE Trans. Electron Devices* **2013**, *60*, 2982–2996.

[3] J. Wu, W. Walukiewicz, Band gaps of InN and group III nitride alloys, *Superlattices Microstruct.* **2003**, *34*, 63–75.

[4] Y. Hinuma, T. Hatakeyama, Y. Kumagai, L. A. Burton, H. Sato, Y. Muraba, S. Iimura, H. Hiramatsu, I. Tanaka, H. Hosono, F. Oba, Discovery of earth-abundant nitride semiconductors by computational screening and high-pressure synthesism *Nat. Commun.* **2016**, *7*, 11962.

[5] P. C. Quayle, K. He, J. Shan, K. Kash, Synthesis, lattice structure, and band gap of $ZnSnN_2$, *MRS Commun.* **2013**, *3*, 135–138.

[6] A. D. Martinez, A. N. Fioretti, E. S. Toberer, A. C. Tamboli, Synthesis, structure, and optoelectronic properties of II-IV-V_2 materials, *J. Mater. Chem.* **2017**, *5*, 11418–11435.

[7] P. Narang, S. Chen, N. C. Coronel, S. Gul, J. Yano, L. W. Wang, N. S. Lewis, H. A. Atwater, Bandgap Tunability in Zn(Sn,Ge)N_2 Semiconductor Alloys, *Adv. Mater.* **2014**, *26*, 1235–1241.

[8] S. Esmaeilzadeh, U. Hålenius, M. Valldor, Crystal Growth, Magnetic, and Optical Properties of the Ternary Nitride $MnSiN_2$, *Chem. Mater.* **2006**, *18*, 2713–2718.

[9] C. J. Duan, A. C. A. Delsing, H. T. Hintzen, Red emission from Mn^{2+} on a tetrahedral site in $MgSiN_2$, *J. Lumin.* **2009**, *129*, 645–649.

[10] M. Råsander, J. B. Quirk, T. Wang, S. Mathew, R. Davies, R. G. Palgrave, M. A. Moram, Structure and lattice dynamics of the wide band gap semiconductors $MgSiN_2$ and $MgGeN_2$, *J. Appl. Phys.* **2017**, *122*, 085705.

[11] J. Häusler, S. Schimmel, P. Wellmann, W. Schnick, Ammonothermal Synthesis of Earth-Abundant Nitride Semiconductors $ZnSiN_2$ and $ZnGeN_2$ and Dissolution Monitoring by In Situ X-ray Imaging, *Chem. Eur. J.* **2017**, *23*, 12275–12282.

[12] J. Häusler, R. Niklaus, J. Minár, W. Schnick, Ammonothermal Synthesis and Optical Properties of Ternary Nitride Semiconductors Mg-IV-N_2, Mn-IV-N_2 and Li-IV_2-N_3 (IV = Si, Ge), *Chem. Eur. J.* **2018**, *24*, 1686–1693.

[13] M. Mallmann, C. Maak, R. Niklaus, W. Schnick, Ammonothermal Synthesis, Optical Properties, and DFT Calculations of Mg_2PN_3 and Zn_2PN_3, *Chem. Eur. J.* **2018**, *24*, 13963–13970.

[14] J. Häusler, L. Neudert, M. Mallmann, R. Niklaus, A.-C. L. Kimmel, N. S. A. Alt, E. Schlücker, O. Oeckler, W. Schnick, Ammonothermal Synthesis of Novel Nitrides: Case Study on $CaGaSiN_3$, *Chem. Eur. J.* **2017**, *23*, 2583–2590.

[15] J. Häusler, L. Eisenburger, O. Oeckler, W. Schnick, Ammonothermal Synthesis and Crystal Structure of the Nitridoalumogermanate $Ca_{1-x}Li_xAl_{1-x}Ge_{1+x}N_3$ ($x \approx 0.2$), *Eur. J. Inorg. Chem.* **2018**, 759–764.

[16] J. Hertrampf, P. Becker, M. Widenmeyer, A. Weidenkaff, E. Schlücker, R. Niewa, Ammonothermal Crystal Growth of Indium Nitride, *Cryst. Growth Des.* **2018**, *18*, 2365–2369.

[17] R. Niklaus, J. Minár, J. Häusler, W. Schnick, First-principles and experimental characterization of the electronic properties of $CaGaSiN_3$ and $CaAlSiN_3$: the impact of chemical disorder, *Phys. Chem. Chem. Phys.* **2017**, *19*, 9292–9299.

[18] J. Häusler, W. Schnick, Ammonothermal Synthesis of Nitrides: Recent Developments and Future Perspectives, *Chem. Eur. J.* **2018**, *24*, 11864–11879.

[19] T. Richter, R. Niewa, Chemistry of Ammonothermal Synthesis, *Inorganics* **2014**, *2*, 29–78.

[20] The term sechser ring was coined by Liebau and is derived from the German word "sechser"; a sechser ring comprises six tetrahedra centers.

[21] E. W. Blanton, K. He, J. Shan, K. Kash, Characterization and control of $ZnGeN_2$ cation lattice ordering, *J. Cryst. Growth* **2017**, *461*, 38–45.

[22] A. R. Denton, N. W. Ashcroft, Vegard's law, *Phys. Rev. A: At., Mol., Opt. Phys.* **1991**, *43*, 3161–3164.

[23] Y. Tanabe, S. Sugano, On the Absorption Spectra of Complex Ions. I, *J. Phys. Soc. Jpn.* **1954**, *9*, 753–766.

[24] R. López, R. Gómez, Band-gap energy estimation from diffuse reflectance measurements on sol–gel and commercial TiO_2: a comparative study, *J. Sol-Gel Sci. Technol.* **2012**, *61*, 1–7.

[25] J. Tauc, R. Grigorovici, A. Vancu, Optical Properties and Electronic Structure of Amorphous Germanium, *Phys. Status Solidi B* **1966**, *15*, 627–637.

[26] C. M. Fang, R. A. d. Groot, R. J. Bruls, H. T. Hintzen, G. d. With, *Ab initio* band structure calculations of Mg_3N_2 and $MgSiN_2$, *J. Phys.: Condens. Matter* **1999**, *11*, 4833–4842.

[27] T. Endo, Y. Sato, H. Takizawa, M. Shimada, High-pressure synthesis of new compounds, $ZnSiN_2$ and $ZnGeN_2$ with distorted wurtzite structure, *J. Mater. Sci. Lett.* **1992**, *11*, 424–426.

[28] W. L. Larson, H. P. Maruska, D. A. Stevenson, Synthesis and Properties of $ZnGeN_2$, *J. Electrochem. Soc.* **1974**, *121*, 1673–1674.

[29] T. Misaki, A. Wakahara, H. Okada, A. Yoshida, Optical properties of $ZnGeN_2$ epitaxial layer, *Phys. Status Solidi C* **2003**, *0*, 2890–2893.

[30] M. Shang, J. Wang, J. Fan, H. Lian, Y. Zhang, J. Lin, $ZnGeN_2$ and $ZnGeN_2$:Mn^{2+} phosphors: hydrothermal-ammonolysis synthesis, structure and luminescence properties, *J. Mater. Chem. C* **2015**, *3*, 9306–9317.

[31] T. de Boer, T. D. Boyko, C. Braun, W. Schnick, A. Moewes, Band gap and electronic structure of $MgSiN_2$ determined using soft X-ray spectroscopy and density functional theory, *Phys. Status Solidi RRL* **2015**, *9*, 250–254.

[32] E. F. Schubert, *Light-Emitting Diodes*, Cambridge University Press **2006**.

[33] S. Lyu, W. R. L. Lambrecht, Quasiparticle self-consistent GW band structures of Mg-IV-N_2 compounds: The role of semicore *d* states, *Solid State Commun.* **2019**, *https://doi.org/10.1016/j.ssc.2019.113664*.

[34] M. Bilal, I. Ahmad, H. A. Rahnamaye Aliabad, S. J. Asadabadi, Detailed DFT studies of the band profiles and optical properties of antiperovskites $SbNCa_3$ and $BiNCa_3$, *Comput. Mater. Sci.* **2014**, *85*, 310–315.

[35] R. Ali, S. Mohammad, H. Ullah, S. A. Khan, H. Uddin, M. Khan, N. U. Khan, The structural, electronic and optical response of IIA–VIA compounds through the modified Becke–Johnson potential, *Physica B* **2013**, *410*, 93–98.

[36] A. Reshak, First Principle Calculations of Transition Metal Oxide, $AgAlO_2$, as Active Photocatalyst: Sustainable Alternative Sources of Energy, *Int. J. Electrochem. Sci.* **2013**, *8*, 9371–9383.

[37] R. Ahmed, S. J. Hashemifar, H. Akbarzadeh, M. Ahmed, F. Aleem, Ab initio study of structural and electronic properties of III-arsenide binary compounds, *Comput. Mater. Sci.* **2007**, *39*, 580–586.

[38] R. Ahmed, H. Akbarzadeh, Fazal-e-Aleem, A first principle study of band structure of III-nitride compounds, *Physica B* **2005**, *370*, 52–60.

[39] M. I. Ziane, Z. Bensaad, T. Ouahrani, B. Labdelli, H. B. Nacer, H. Abid, First-principles prediction of the structural and electronic properties of zinc blende GaN_xAs_{1-x} alloys, *Mater. Sci. Semicond. Process.* **2013**, *16*, 1138–1147.

[40] J. A. Camargo-Martínez, R. Baquero, Performance of the modified Becke-Johnson potential for semiconductors, *Phys. Rev. B: Condens. Matter Mater. Phys.* **2012**, *86*, 195106.

[41] A. Punya, W. R. L. Lambrecht, M. van Schilfgaarde, Quasiparticle band structure of Zn-IV-N_2 compounds, *Phys. Rev. B: Condens. Matter Mater. Phys.* **2011**, *84*, 165204.

[42] A. P. Jaroenjittichai, W. R. L. Lambrecht, Electronic band structure of MgIV$-N_2$ compounds in the quasiparticle-self-consistent GW approximation *Phys. Rev. B* **2016**, *94*, 125201.

[43] N. Cordes, W. Schnick, Ammonothermal Synthesis of Crystalline Oxonitride Perovskites $LnTaON_2$ (Ln=La, Ce, Pr, Nd, Sm, Gd), *Chem. Eur. J.* **2017**, *23*, 11410–11415.

[44] J. Li, T. Watanabe, H. Wada, T. Setoyama, M. Yoshimura, Low-Temperature Crystallization of Eu-Doped Red-Emitting $CaAlSiN_3$ from Alloy-Derived Ammonometallates, *Chem. Mater.* **2007**, *19*, 3592–3594.

[45] T. Watanabe, K. Nonaka, J. Li, K. Kishida, M. Yoshimura, Low temperature ammonothermal synthesis of europium-doped $SrAlSiN_3$ for a nitride red phosphor, *J. Ceram. Soc. Jpn.* **2012**, *120*, 500–502.

[46] T. Toshima, K. Kishida, Y. Maruyama, T. Watanabe, Low-temperature synthesis of $BaTaO_2N$ by an ammonothermal method, *J. Ceram. Soc. Jpn.* **2017**, *125*, 643–647.

[47] A. Coelho, *TOPAS Academic, Version 6*, Coelho Software, Brisbane (Australia), **2016**.

[48] G. Kresse, J. Hafner, Ab initio molecular dynamics for liquid metals, *Phys. Rev. B: Condens. Matter Mater. Phys.* **1993**, *47*, 558–561.

[49] G. Kresse, J. Hafner, Ab initio molecular-dynamics simulation of the liquid-metal–amorphous-semiconductor transition in germanium, *Phys. Rev. B: Condens. Matter Mater. Phys.* **1994**, *49*, 14251–14269.

[50] G. Kresse, J. Furthmüller, Efficiency of ab-initio total energy calculations for metals and semiconductors using a plane-wave basis set, *Comput. Mater. Sci.* **1996**, *6*, 15–50.

[51] G. Kresse, D. Joubert, From ultrasoft pseudopotentials to the projector augmented-wave method, *Phys. Rev. B: Condens. Matter Mater. Phys.* **1999**, *59*, 1758–1775.

[52] P. E. Blöchl, Projector augmented-wave method, *Phys. Rev. B: Condens. Matter Mater. Phys.* **1994**, *50*, 17953–17979.

[53] J. P. Perdew, K. Burke, M. Ernzerhof, Generalized Gradient Approximation Made Simple, *Phys. Rev. Lett.* **1996**, *77*, 3865–3868.

[54] J. P. Perdew, K. Burke, M. Ernzerhof, Generalized Gradient Approximation Made Simple [*Phys. Rev. Lett.* **1996**, *77*, 3865], *Phys. Rev. Lett.* **1997**, *78*, 1396.

[55] A. D. Becke, E. R. Johnson, A simple effective potential for exchange, *J. Chem. Phys.* **2006**, *124*, 221101.

[56] F. Tran, P. Blaha, Accurate Band Gaps of Semiconductors and Insulators with a Semilocal Exchange-Correlation Potential, *Phys. Rev. Lett.* **2009**, *102*, 226401.

[57] T. Björkman, Generating geometries for electronic structure programs, *Comput. Phys. Commun.* **2011**, *182*, 1183–1186.

[58] H. Ebert et al., *The Munich SPR-KKR Package*, Version 7.7, http://olymp.cup.uni-muenchen.de/ak/ebert/SPRKKR, 2012.

[59] H. Ebert, D. Ködderitzsch, J. Minár, Calculating condensed matter properties using the KKR-Green's function method—recent developments and applications, *Rep. Prog. Phys.* **2011**, *74*, 096501.

[60] E. Engel, S. H. Vosko, Exact exchange-only potentials and the virial relation as microscopic criteria for generalized gradient approximations, *Phys. Rev. B: Condens. Matter Mater. Phys.* **1993**, *47*, 13164–13174.

6.11 Supporting Information

6.11.1 Additional Crystallographic Data

Table S6.1 Wyckoff positions and atomic coordinates of $Mg_{1-x}Mn_xSiN_2$ ($x \approx 0.543$) obtained from powder X-ray diffraction, standard deviations in parentheses

Atom	Wyckoff	*x*	*y*	*z*	SOF	U_{iso}
Mg_1	4*a*	0.0810(4)	0.6251(6)	-0.0116(5)	0.457(12)	0.0127
Mn_1	4*a*	0.0810(4)	0.6251(6)	-0.0116(5)	0.543(12)	0.0127
Si_1	4*a*	0.0646(5)	0.1356(6)	0.0082(7)	1	0.0127
N_1	4*a*	0.0468(12)	0.0799(15)	0.3611(11)	1	0.0127
N_2	4*a*	0.1235(9)	0.6388(17)	0.4167(12)	1	0.0127

Table S6.2 Wyckoff positions and atomic coordinates of $Mg_{1-x}Zn_xSiN_2$ ($x \approx 0.515$) obtained from powder X-ray diffraction, standard deviations in parentheses

Atom	Wyckoff	*x*	*y*	*z*	SOF	U_{iso}
Mg_1	4*a*	0.08133(16)	0.6226(3)	0.0043(3)	0.485(3)	0.0127
Zn_1	4*a*	0.08133(16)	0.6226(3)	0.0043(3)	0.515(3)	0.0127
Si_1	4*a*	0.0742(3)	0.1225(5)	0.0048(7)	1	0.0214(5)
N_1	4*a*	0.0560(7)	0.1010(11)	0.3610(5)	1	0.0127
N_2	4*a*	0.1086(6)	0.6528(10)	0.4168(5)	1	0.0127

Table S6.3 Wyckoff positions and atomic coordinates of $Mn_{1-x}Zn_xSiN_2$ ($x \approx 0.53$) obtained from powder X-ray diffraction, standard deviations in parentheses

Atom	Wyckoff	*x*	*y*	*z*	SOF	U_{iso}
Mn_1	4*a*	0.08166(18)	0.6227(4)	0.9652(5)	0.47(2)	0.0127
Zn_1	4*a*	0.08166(18)	0.6227(4)	0.9652(5)	0.53(2)	0.0127
Si_1	4*a*	0.0709(4)	0.1213(9)	0.9672(17)	1	0.0171(1)
N_1	4*a*	0.1097(12)	0.6601(15)	0.3690(8)	1	0.0127
N_2	4*a*	0.0397(14)	0.1082(19)	0.3118(8)	1	0.0127

Table S6.4 Wyckoff positions and atomic coordinates of $Mg_{1-x}Mn_xGeN_2$ ($x \approx 0.625$) obtained from powder X-ray diffraction, standard deviations in parentheses

Atom	Wyckoff	*x*	*y*	*z*	SOF	U_{iso}
Mg_1	4*a*	0.0827(3)	0.6217(7)	0.0880(10)	0.375(6)	0.0127
Mn_1	4*a*	0.0827(3)	0.6217(7)	0.0880(10)	0.625(6)	0.0127
Ge_1	4*a*	0.0711(2)	0.1267(4)	0.0814(6)	1	0.0265(4)
N_1	4*a*	-0.0621(14)	-0.0877(12)	-0.0476(12)	1	0.0127
N_2	4*a*	0.1065(11)	0.6248(18)	0.4827(11)	1	0.0127

Table S6.5. Wyckoff positions and atomic coordinates of $Mg_{1-x}Zn_xGeN_2$ ($x \approx 0.545$) obtained from powder X-ray diffraction, standard deviations in parentheses

Atom	Wyckoff	*x*	*y*	*z*	SOF	U_{iso}
Mg_1	4*a*	0.0843(3)	0.6251(7)	0.9629(7)	0.455(4)	0.0127
Zn_1	4*a*	0.0843(3)	0.6251(7)	0.9629(7)	0.545(4)	0.0127
Ge_1	4*a*	0.07434(19)	0.1261(5)	0.9691(4)	1	0.0203(3)
N_1	4*a*	0.0745(14)	0.125(2)	0.3342(9)	1	0.0127
N_2	4*a*	0.0954(13)	0.6515(14)	0.3697(9	1	0.0127

Table S6.6. Wyckoff positions and atomic coordinates of $Mn_{1-x}Zn_xGeN_2$ ($x \approx 0.45$) obtained from powder X-ray diffraction, standard deviations in parentheses

Atom	Wyckoff	*x*	*y*	*z*	SOF	U_{iso}
Mn_1	4*a*	0.0839(3)	0.6255(10)	0.9900(11)	0.55(2)	0.0127
Zn_1	4*a*	0.0839(3)	0.6255(10)	0.9900(11)	0.45(2)	0.0127
Ge_1	4*a*	0.0733(3)	0.1277(9)	0.9922(8)	1	0.0137(1)
N_1	4*a*	0.0743(19)	0.117(5)	0.3587(19)	1	0.0127
N_2	4*a*	0.0998(18)	0.652(3)	0.3886(19)	1	0.0127

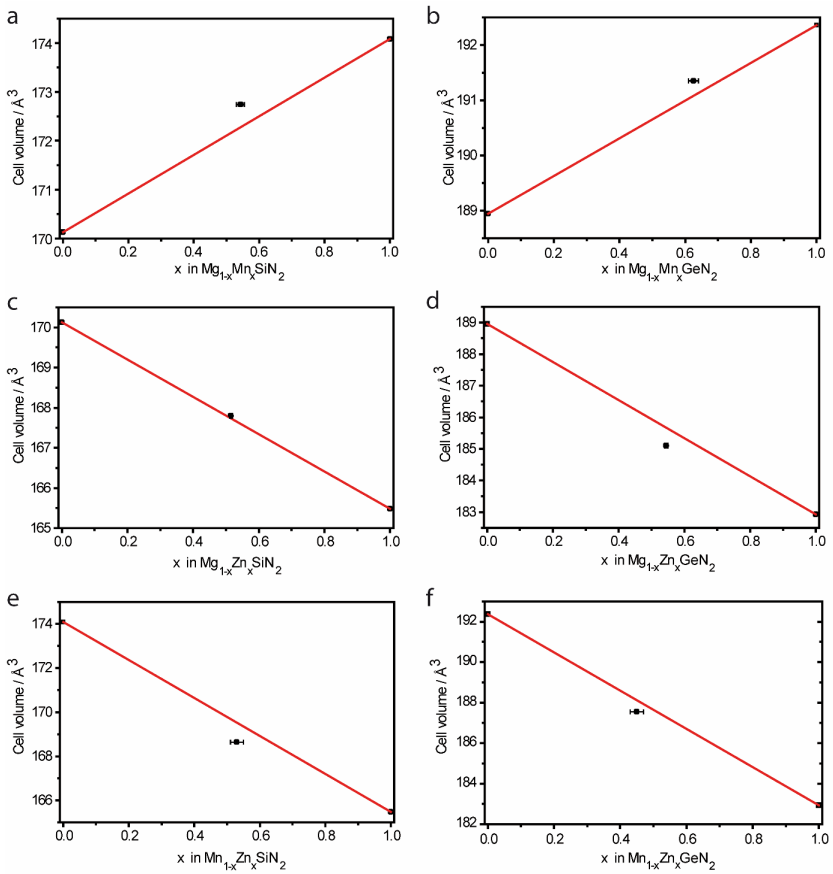

Figure S6.1 Comparison of the cell volumes of the solid solutions $Mg_{1-x}Mn_xSiN_2$ (a), $Mg_{1-x}Mn_xGeN_2$ (b), $Mg_{1-x}Zn_xSiN_2$ (c), $Mg_{1-x}Zn_xGeN_2$ (d), $Mn_{1-x}Zn_xSiN_2$ (e) and $Mn_{1-x}Zn_xGeN_2$ (f) with the cell volumes of their corresponding edge phases.[1-2] Error bars represent the standard deviations obtained from rietveld refinement. The red lines were extrapolated using Vegard's rule.

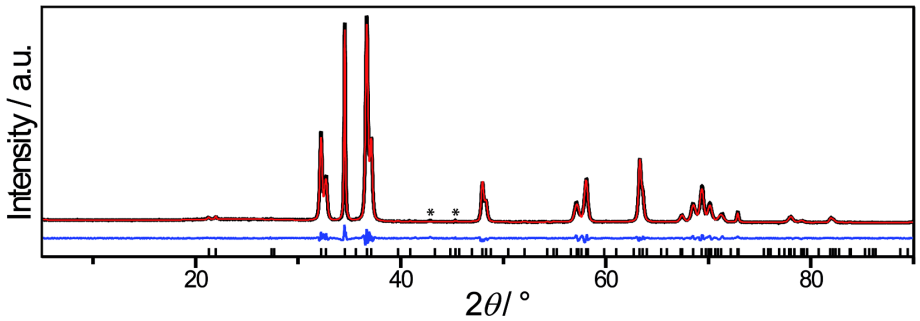

Figure S6.2 Rietveld refinement of PXRD pattern (Cu-Kα_1) of solid solution of $Mg_{1-x}Zn_xGeN_2$ ($x \approx 0.826$) with experimental data (black line), calculated data (red line), difference profile (blue lines), and reflection positions (black bars). Asterisks mark unknown reflections.

Table S6.7 Wyckoff positions and atomic coordinates of $Mn_{1-x}Zn_xGeN_2$ ($x \approx 0.826$) obtained from powder X-ray diffraction, standard deviations in parentheses

Atom	Wyckoff	*x*	*y*	*z*	SOF	U_{iso}
Mg_1	4*a*	0.0785(4)	0.6273(7)	0.9696(6)	0.174(6)	0.0127
Zn_1	4*a*	0.0785(4)	0.6273(7)	0.9696(6)	0.826(6)	0.0127
Ge_1	4*a*	0.0802(4)	0.1249(7)	0.9719(7)	1	0.0528(5)
N_1	4*a*	0.1161(12)	0.093(2)	0.3733(13)	1	0.0127
N_2	4*a*	0.0567(15)	0.645(3)	0.3334(13)	1	0.0127

Table S6.8 Crystallographic data of $Mg_{1-x}Zn_xGeN_2$ ($x = 0.826$) obtained by Rietveld refinement

formula		$Mg_{0.174}Zn_{0.826}GeN_2$
crystal system		orthorhombic
space group		$Pna2_1$ (33)
lattice parameters / Å	*a*	5.47260(10)
	b	6.44130(13)
	c	5.18932(10)
cell volume / Å^3		182.927(6)
Density / g·cm^{-3}		5.766(6)
formula units / cell		4
T / K		293(2)
diffractometer		STOE STADI P
radiation / Å		Cu-Kα1 (λ = 1.5406)
2θ range /°		$5.0 \leq 2\theta \leq 90$
profile function		fundamental parameters model
background function		Shifted Chebyshev
data points		5668
number of reflections		89
refined parameters		56
R values		R_p = 0.0539
		R_{wp} = 0.0699
		R_{Bragg} = 0.0161
Goodness of fit		1.52

6.11.2 Details on Scanning Electron Microscopy

All EDX measurements showed small amounts of impurities like Na, K and O which originate from residual mineralizer as well as washing steps with ethanol and acetic acid. For the quantification of the composition of the compounds, the peaks of Na, K and O were deconvoluted.

Table S6.9 SEM EDX measurements of Si-compounds

$Mg_{1-x}Mn_xSiN_2$	Mg	Mn	Si	N
measurement 1:	11.3	10.6	23.7	54.4
measurement 2:	11.8	12.0	25.7	50.5
measurement 3:	11.9	12.1	25.7	50.3
measurement 4:	11.3	11.8	24.3	52.6
Ø	**11.6**	**11.6**	**24.9**	**51.9**

$Mg_{1-x}Zn_xSiN_2$	Mg	Zn	Si	N
measurement 1:	13.1	14.9	26.9	45.1
measurement 2:	11.4	13.2	27.1	48.3
measurement 3:	14.4	11.3	28.1	46.2
measurement 4:	12.4	10.4	27.0	50.2
Ø	**12.8**	**12.5**	**27.3**	**47.4**

$Mn_{1-x}Zn_xSiN_2$	Mn	Zn	Si	N
measurement 1:	12.6	12.4	27.9	47.1
measurement 2:	12.6	12.4	28.0	47.0
measurement 3:	11.5	11.3	25.9	51.3
measurement 4:	12.0	9.4	26.6	52.0
Ø	**12.2**	**11.4**	**27.1**	**49.3**

Table S6.10 SEM EDX measurements of Ge-compounds

$Mg_{1-x}Mn_xGeN_2$	Mg	Mn	Ge	N
measurement 1:	12.5	11.8	22.7	53.0
measurement 2:	12.2	11.2	21.8	54.8
measurement 3:	12.8	12.8	23.8	50.6
measurement 4:	13.6	12.9	24.3	49.2
Ø	**12.8**	**12.2**	**23.1**	**51.9**

$Mg_{1-x}Zn_xGeN_2$	Mg	Zn	Ge	N
measurement 1:	14.6	13.0	22.7	49.7
measurement 2:	14.6	14.8	25.5	45.1
measurement 3:	13.6	13.8	24.8	47.8
measurement 4:	13.3	13.9	27.1	45.7
Ø	**14.0**	**13.9**	**25.0**	**47.1**

$Mn_{1-x}Zn_xGeN_2$	Mn	Zn	Ge	N
measurement 1:	10.8	11.2	25.4	52.6
measurement 2:	13.3	12.5	25.6	48.6
measurement 3:	14.2	12.8	28.8	44.2
measurement 4:	10.9	10.4	23.0	55.7
Ø	**12.3**	**11.7**	**25.7**	**50.3**

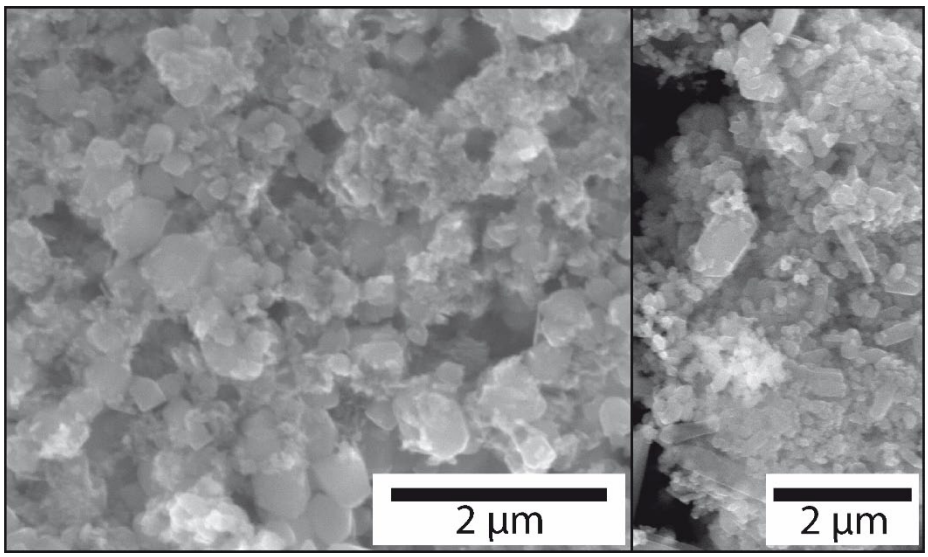

Figure S6.3 SEM images of $Mn_{1-x}Zn_xSiN_2$ (left) and $Mn_{1-x}Zn_xGeN_2$ (right).

6.11.3 Details on UV/Vis Reflectance Spectroscopy

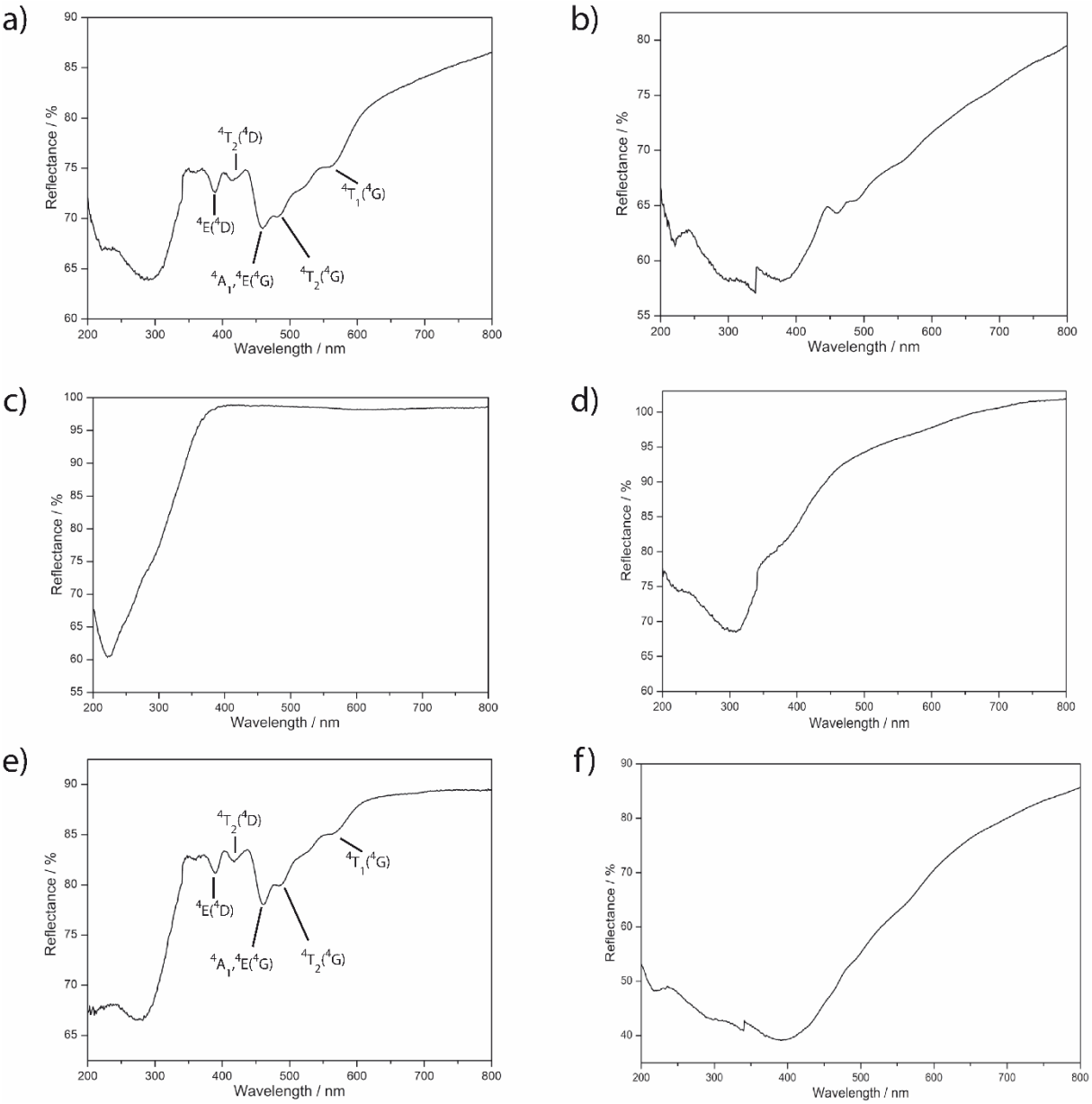

Figure S6.4 Diffuse reflectance spectra of $Mg_{1-x}Mn_xSiN_2$ (a), $Mg_{1-x}Mn_xGeN_2$ (b), $Mg_{1-x}Zn_xSiN_2$ (c), $Mg_{1-x}Zn_xGeN_2$ (d), $Mn_{1-x}Zn_xSiN_2$ (e) and $Mn_{1-x}Zn_xGeN_2$ (f). Sub-bandgap absorption bands in the case of $Mg_{1-x}Mn_xSiN_2$ (a) and $Mn_{1-x}Zn_xSiN_2$ (e) can be attributed to the absorption of Mn^{2+} (transition of the ground state $^6A_1(^6S)$ to the excited states $^4T_1(^4G)$, $^4T_2(^4G)$, $^4A_1$, $^4E(^4G)$, $^4T_2(^4D)$ and $^4E(^4D)$ according to literature.[3]

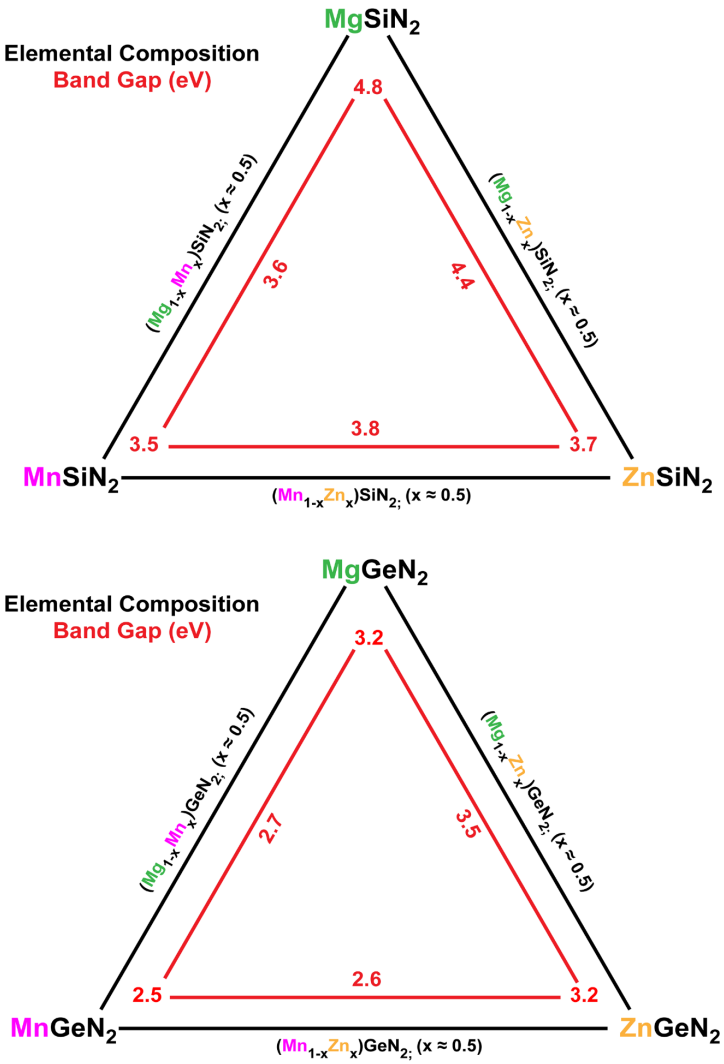

Figure S6.5 Evaluated bandgaps (E_g^{exp}) of the mixed occupancy ($II^a_{1-x}II^b_x$)-IV-N_2 compound series. Top: Si-series, bottom Ge-series. Band gaps of edge phases were taken from literature.[1-2]

6.11.4 Additional Data of DFT Calculations

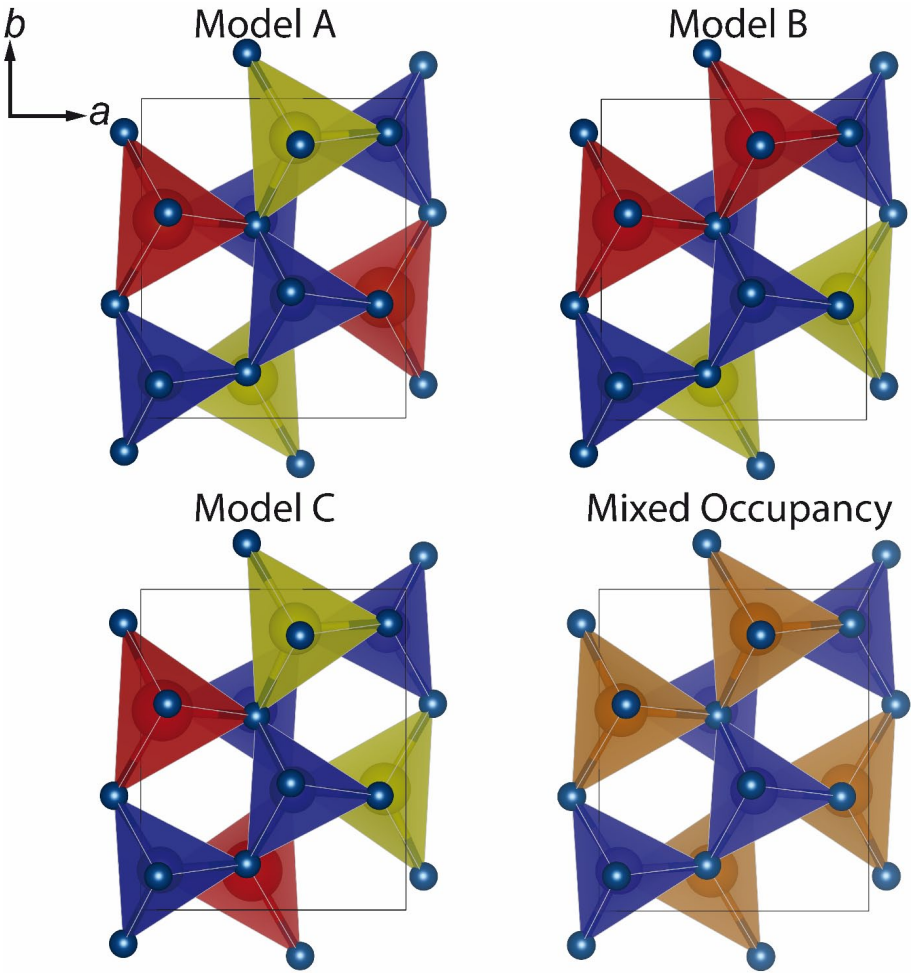

Figure S6.6 Different ordering variants (A-C) and model for mixed occupation of divalent cations in ($II^{a}_{1-x}II^{b}_{x}$)-IV-N_2 (x = 0.5). II^{a}-N_4 tetrahedra are depicted in red, II^{b}-N_4 tetrahedra in yellow, IV-N_4 in blue and mixed occupied $II^{a/b}$-N_4 tetrahedra in orange.

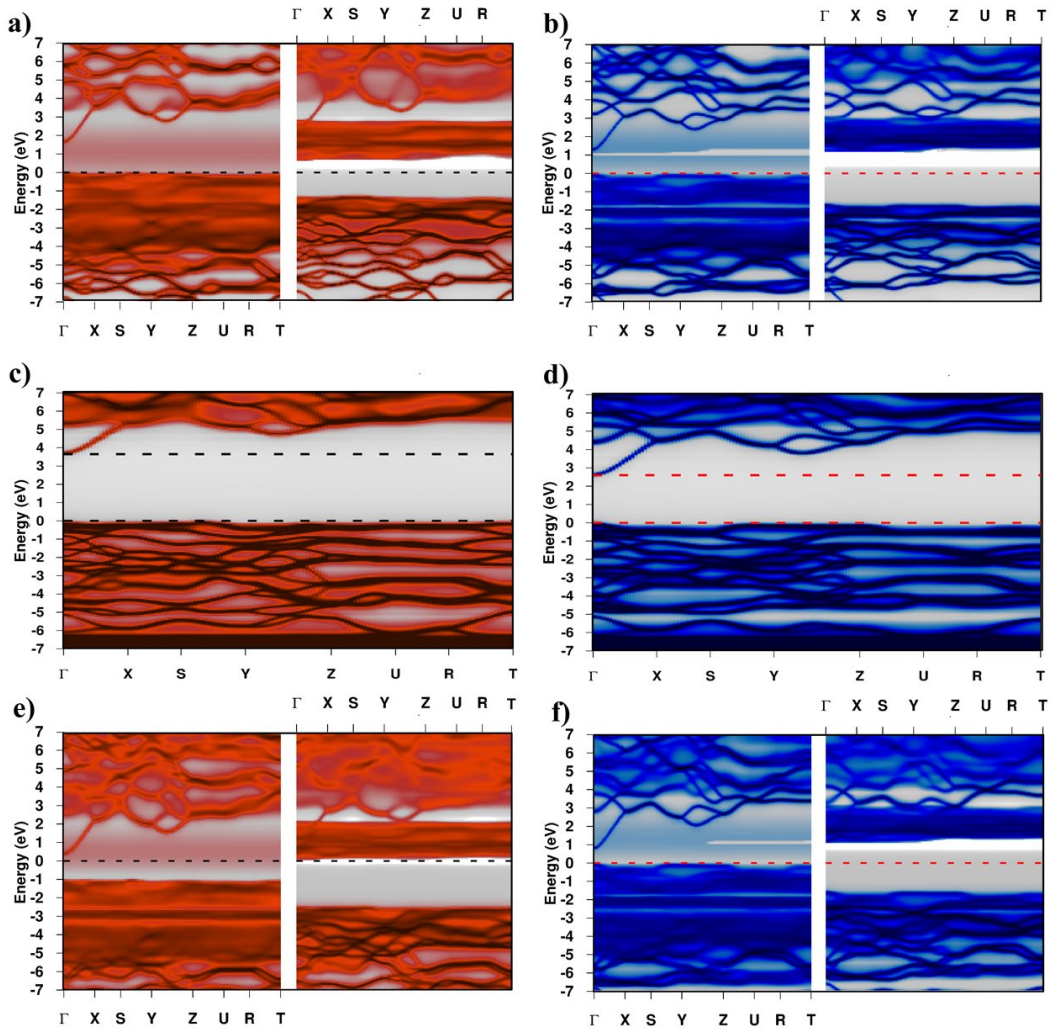

Figure S6.7 Bloch spectral functions as calculated by the SPRKKR formalism (EV-GGA) of $(Mg_{0.5}Mn_{0.5})SiN_2$ (a) (left: ↑/right: ↓), $(Mg_{0.5}Mn_{0.5})GeN_2$ (b) (left: ↑/right: ↓), $(Mg_{0.5}Zn_{0.5})SiN_2$ (c), $(Mg_{0.5}Zn_{0.5})GeN_2$ (d), $(Mn_{0.5}Zn_{0.5})SiN_2$ (e) (left: ↑/right: ↓) and $(Mn_{0.5}Zn_{0.5})GeN_2$ (f) (left: ↑/right: ↓).

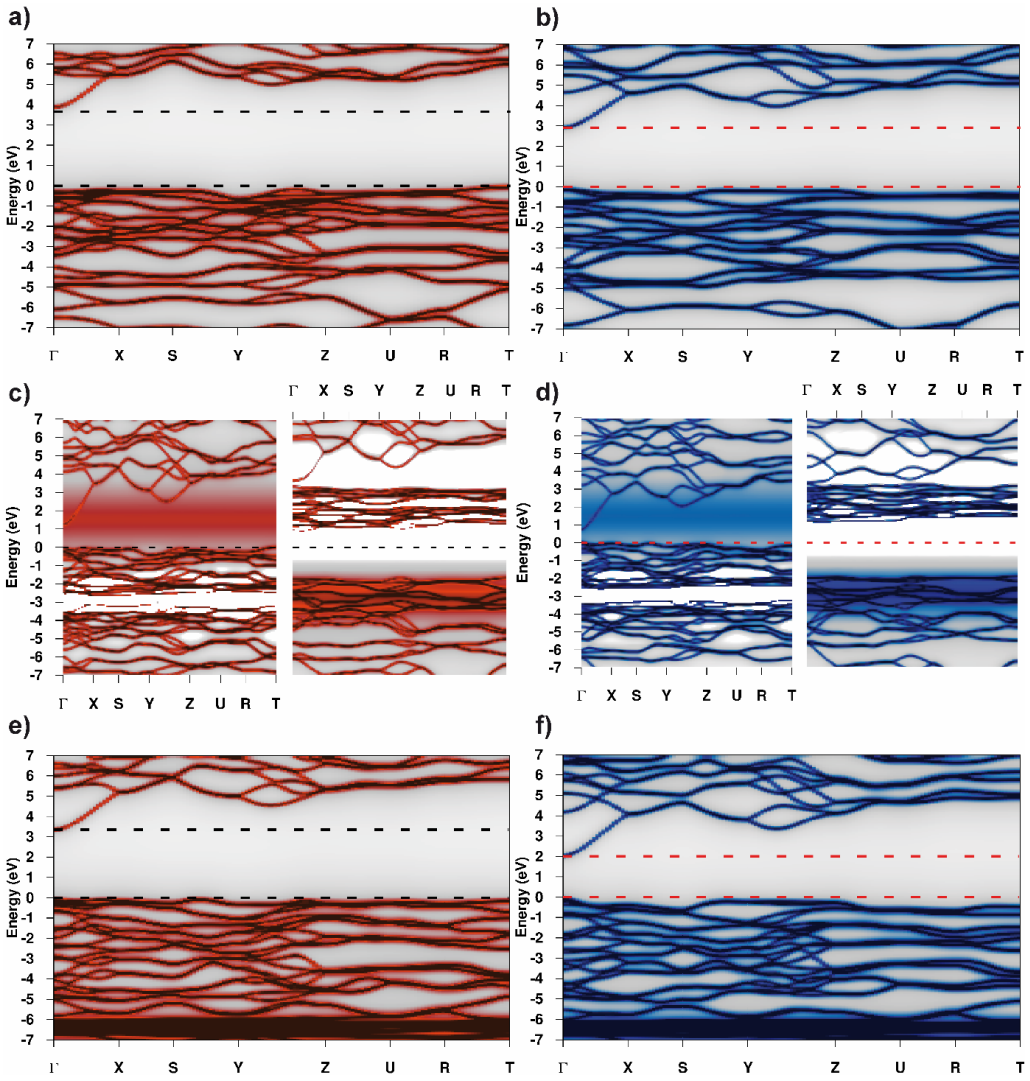

Figure S6.8 Bloch spectral functions as calculated by the SPRKKR formalism (EV-GGA) of $MgSiN_2$ (a), $MgGeN_2$ (b), $MnSiN_2$ (c) (left: ↑/right: ↓), $MnGeN_2$ (d) (left: ↑/right: ↓), $ZnSiN_2$ (e) and $ZnGeN_2$ (f).

Table S6.11 Bandgap values [eV] for the different $(II^a_{1-x}II^b_x)$-Si-N_2 compounds from experiment and theory in comparison to values of the preceding literature

	[a)]mBJ-GGA $Ø^{A+B+C}$		[a)]KKR^{EV-GGA}		QSGW $0.8\sum + \Delta_0$ (+ E_{xb})		EXP.
Transition	↑ to ↑	↑ to ↓	↑ to ↑	↑ to ↓	direct	indirect	
	direct ≈ indirect		direct ≈ indirect				
$MgSiN_2$			4.1		6.28[4]	5.84[4]	4.8–5.6[2,5–6]
$Mg_{0.5}Mn_{0.5}SiN_2$	2.78	2.28	1.65	0.63			[a)]3.6
$MnSiN_2$			1.2	0.85			3.5–4.3[2,7]
$Mn_{0.5}Zn_{0.5}SiN_2$	2.44	2.4	1.4	1.1			[a)]3.8
$ZnSiN_2$			3.45		5.66[8]	5.44[8]	3.7–4.4[1,9–11]
$Mg_{0.5}Zn_{0.5}SiN_2$	4.55		3.7				[a)]4.4
$MgSiN_2$			4.1		6.28[4]	5.84[4]	4.8–5.6[2,5–6]

[a)] Bandgap values from this work

Table S6.12 Bandgap values [eV] for the different $(II^a_{1-x}II^b_x)$-Ge-N_2 compounds from experiment and theory in comparison to values of the preceding literature

	[a)]mBJ-GGA $Ø^{A+B+C}$		[a)]KKR^{EV-GGA}		QSGW $0.8\sum + \Delta_0$ (+ E_{xb})	EXP.
Transition	↑ to ↑	↑ to ↓	↑ to ↑	↑ to ↓	direct	
	direct ≈ indirect		direct ≈ indirect			
$MgGeN_2$			3.1		5.14[4]	3.2[2]
$Mg_{0.5}Mn_{0.5}GeN_2$	1.42	1.8	1.3	1.15		[a)]2.7
$MnGeN_2$			0.7	1.1		2.5[2]
$Mn_{0.5}Zn_{0.5}GeN_2$	1.09	1.43	0.75	1.1		[a)]2.6
$ZnGeN_2$			2.0		3.42[8]	3.1–3.5[1,10–13]
$Mg_{0.5}Zn_{0.5}GeN_2$	3.14		2.6			[a)]3.5
$MgGeN_2$			3.1		5.14[4]	3.2[2]

[a)] Bandgap values from this work

6.11.5 Magnetic Measurements

Experimental

Magnetic measurements were performed with a Quantum Design PPMS-9. The magnetic properties were determined using the vibrating sample magnetometer (VSM) option. Temperature dependent magnetization measurements were carried out between 2 and 400 K with an applied field of 0.01 T and 3 T. The isothermal magnetization was determined at 2 and 400 K with variable fields of $B = \pm 5$ T.

Results and Discussion

The magnetic properties of $MnSiN_2$ and $MnGeN_2$ are well known from literature. Both The magnetic properties of $MnSiN_2$ and $MnGeN_2$ have been reported in literature. Both compounds order anti-ferromagnetically with Néel temperatures of T_N = 453 K ($MnSiN_2$) and T_N = 448 K ($MnGeN_2$).[14–15] The magnetic structure of $MnSiN_2$ was determined from neutron powder diffraction and magnetization data. Above 500 K the nitride appeared to be paramagnetic with strong antiferromagnetic fluctuations. Antiferromagnetic order occurs below 490 K, which changes into a capped antiferromagnetic state with spin tilting disorder at 442 K.[16]

We first reinvestigated the magnetic behavior of $MnSiN_2$ synthesized via solid state methods or via ammonothermal reactions with and without mineralizer, according to literature.[2,16] In the range between 300 and 400 K, we find linearly decreasing susceptibility for $MnSiN_2$ from solid state and ammonothermal synthesis without mineralizer, both in agreement with the antiferromagnetic state reported in literature [16] (Figures S6.9, S6.10). The upturn at lower temperatures is probably caused by paramagnetic impurities. Samples prepared with KNH_2 in the ammonothermal reaction reveal increasing paramagnetic susceptibility over the whole temperature range. This is probably caused by higher amounts of paramagnetic impurities like K_3MnO_4 (see Figure 6.2), which has an effective moment of 2.80μ_B.[17] It is also possible that the samples contain amorphous proportions of potassium manganites. Thus the magnetic measurements of all samples synthesized with mineralizer are mainly affected by impurity phases and therefore of limited significance.

The solid solutions $Mg_{1-x}Mn_xSiN_2$, $Mn_{1-x}Zn_xSiN_2$, $Mg_{1-x}Mn_xGeN_2$ and $Mn_{1-x}Zn_xGeN_2$ ($x \approx 0.5$) were synthesized using a mineralizer. The susceptibility data are similar to those of magnetic $MnSiN_2$ synthesized via the same synthetic method. Consequently, the magnetism of the solid solutions are also mainly affected by paramagnetic impurity phases (see Figure S6.12–S6.15), which impedes a reliable determination of the intrinsic magnetic properties. However, the data shown in Figures S6.12–S6.15 are compatible with antiferromagnetism in the solid solutions similar to the boundary phases $MnSiN_2$ and $MnGeN_2$.

$MnSiN_2$ (solid state reaction)

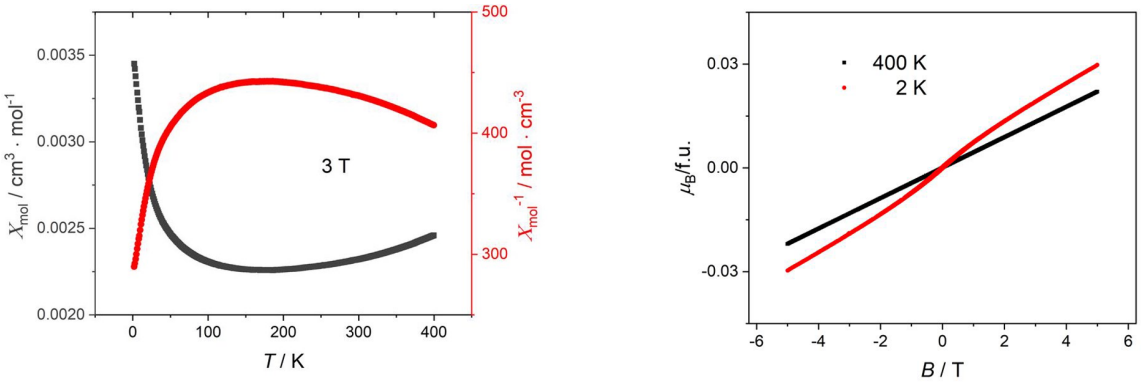

Figure S6.9 Magnetic measurements of $MnSiN_2$. **Left:** Susceptibility and inverted susceptibility (red) at 3 T in the temperature range of 2 – 400 K. **Right:** Magnetization isotherms at 2 K (red) and 400 K (black).

$MnSiN_2$ (Ammonothermal without mineralizer)

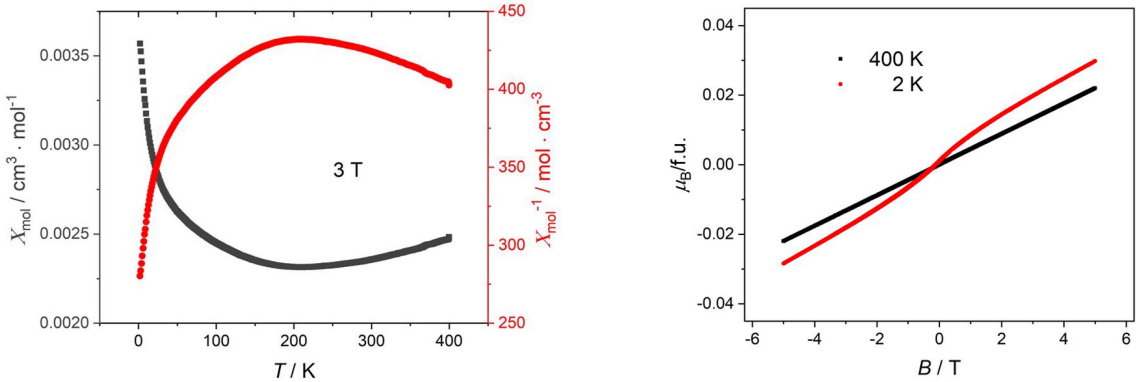

Figure S6.10 Magnetic measurements of $MnSiN_2$. **Left:** Susceptibility and inverted susceptibility (red) at 3 T in the temperature range of 2 – 400 K. **Right:** Magnetization isotherms at 2 K (red) and 400 K (black).

$MnSiN_2$ (Ammonothermal with mineralizer)

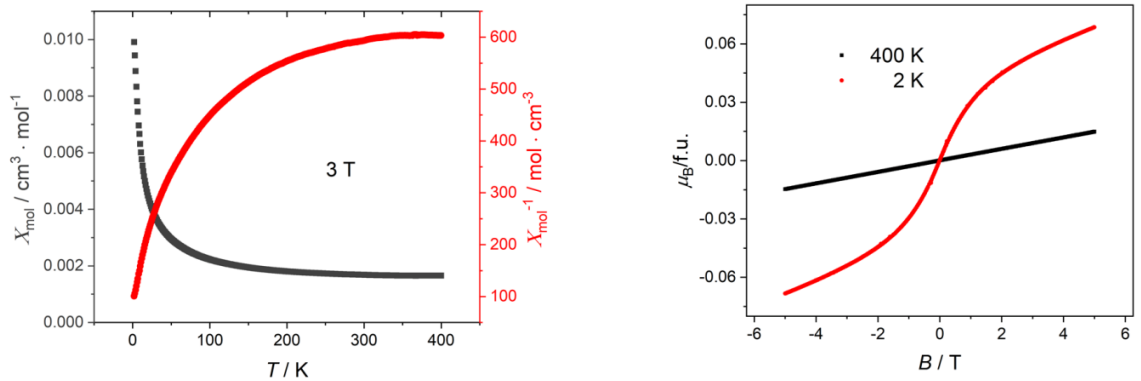

Figure S6.11 Magnetic measurements of $MnSiN_2$. **Left:** Susceptibility and inverted susceptibility (red) at 3 T in the temperature range of 2 – 400 K. **Right:** Magnetization isotherms at 2 K (red) and 400 K (black).

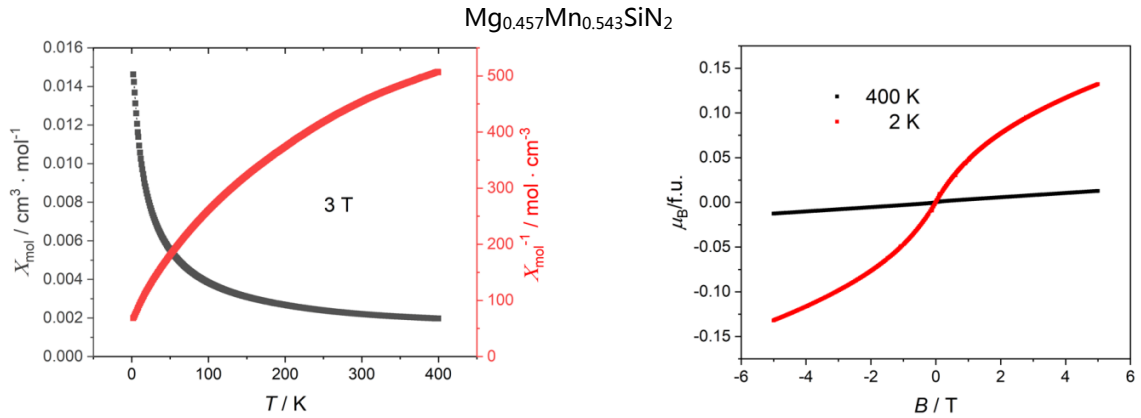

Figure S6.12 Magnetic measurements of $Mg_{0.457}Mn_{0.543}SiN_2$. **Left:** Susceptibility and inverted susceptibility (red) at 3 T in the temperature range of 2 – 400 K. **Right:** Magnetization isotherms at 2 K (red) and 400 K (black).

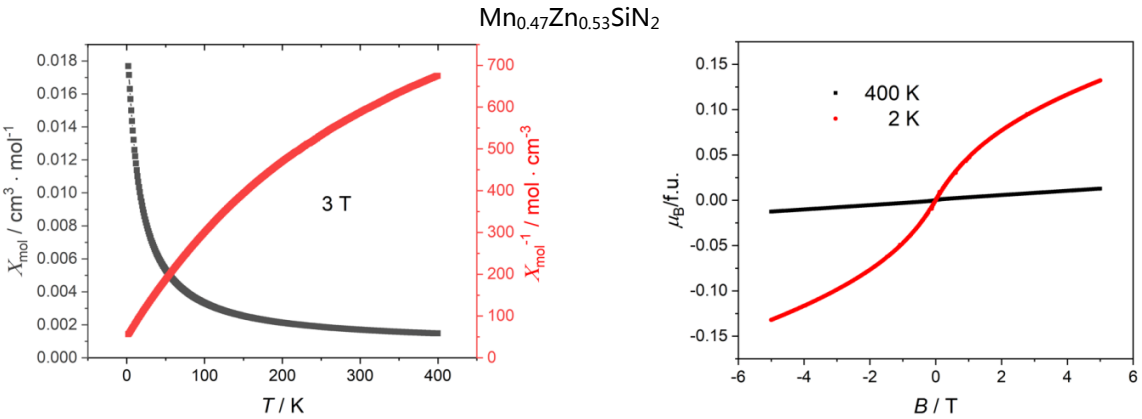

Figure S6.13 Magnetic measurements of $Mn_{0.47}Zn_{0.53}SiN_2$. **Left:** Susceptibility and inverted susceptibility (red) at 3 T in the temperature range of 2 – 400 K. **Right:** Magnetization isotherms at 2 K (red) and 400 K (black).

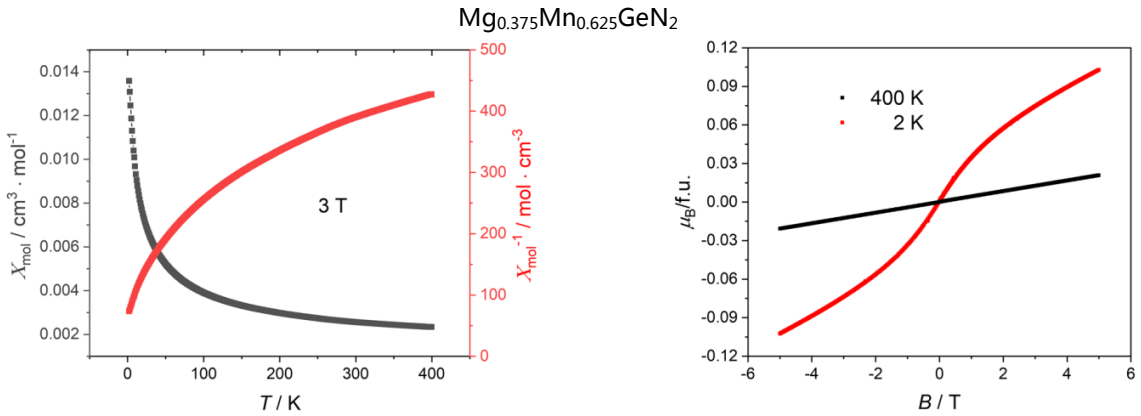

Figure S6.14 Magnetic measurements of $Mg_{0.375}Mn_{0.625}GeN_2$. **Left:** Susceptibility and inverted susceptibility (red) at 3 T in the temperature range of 2 – 400 K. **Right:** Magnetization isotherms at 2 K (red) and 400 K (black).

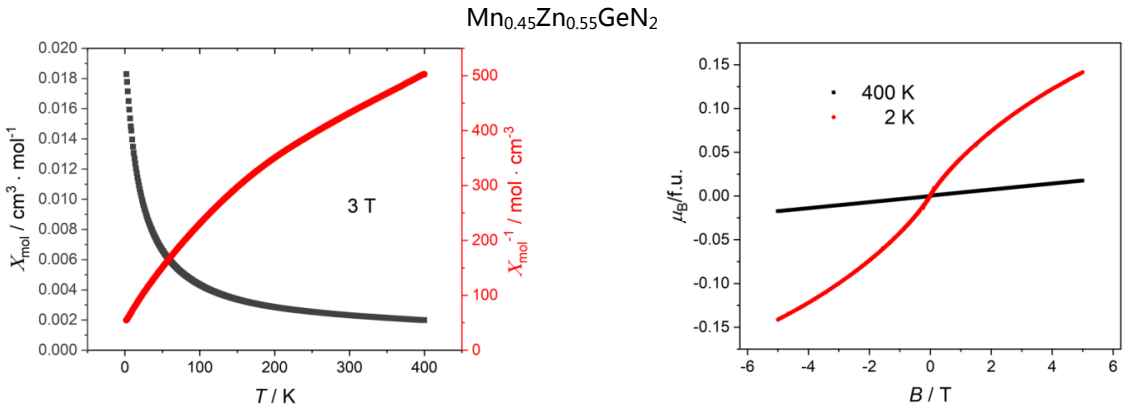

Figure S6.15 Magnetic measurements of $Mn_{0.45}Zn_{0.55}GeN_2$. **Left** Susceptibility and inverted susceptibility (red) at 3 T in the temperature range of 2 – 400 K. **Right:** Magnetization isotherms at 2 K (red) and 400 K (black).

6.11.6 References

[1] J. Häusler, S. Schimmel, P. Wellmann, W. Schnick, Ammonothermal Synthesis of Earth-Abundant Nitride Semiconductors $ZnSiN_2$ and $ZnGeN_2$ and Dissolution Monitoring by In Situ X-ray Imaging, *Chem. Eur. J.* **2017**, *23*, 12275–12282.

[2] J. Häusler, R. Niklaus, J. Minár, W. Schnick, Ammonothermal Synthesis and Optical Properties of Ternary Nitride Semiconductors Mg-IV-N_2, Mn-IV-N_2 and Li-IV_2-N_3 (IV=Si, Ge), *Chem. Eur. J.* **2018**, *24*, 1686–1693.

[3] Y. Tanabe, S. Sugano, On the Absorption Spectra of Complex Ions. I., *J. Phys. Soc. Jpn.* **1954**, *9*, 753–766.

[4] A. P. Jaroenjittichai, W. R. L. Lambrecht, Electronic band structure of Mg–IV–N_2 compounds in the quasiparticle-self-consistent GW approximation, *Phys. Rev. B* **2016**, *94*, 125201.

[5] C. M. Fang, R. A. d. Groot, R. J. Bruls, H. T. Hintzen, G. d. With, *Ab initio* band structure calculations of Mg_3N_2 and $MgSiN_2$, *J. Phys.: Condens. Matter* **1999**, *11*, 4833–4842.

[6] T. de Boer, T. D. Boyko, C. Braun, W. Schnick, A. Moewes, Band gap and electronic structure of $MgSiN_2$ determined using soft X-ray spectroscopy and density functional theory, *Phys. Status Solidi RRL* **2015**, *9*, 250–254.

[7] C. J. Duan, A. C. A. Delsing, H. T. Hintzen, Red emission from Mn^{2+} on a tetrahedral site in $MgSiN_2$, *J. Lumin.* **2009**, *129*, 645–649.

[8] A. Punya, W. R. L. Lambrecht, M. van Schilfgaarde, Quasiparticle band structure of Zn-IV-N_2 compounds *Phys. Rev. B: Condens. Matter Mater. Phys.* **2011**, *84*, 165204.

[9] T. Endo, Y. Sato, H. Takizawa, M. Shimada, High-pressure synthesis of new compounds, $ZnSiN_2$ and $ZnGeN_2$ with distorted wurtzite structure, *J. Mater. Sci. Lett.* **1992**, *11*, 424–426.

[10] A. Osinsky, V. Fuflyigin, L. D. Zhu, A. B. Goulakov, J. W. Graff, E. F. Schubert, IN *Proc. 2000 IEEE/ Cornell Conference on High Performance Devices*, New concepts and preliminary results for SiC bipolar transistors: $ZnSiN_2$and $ZnGeN_2$ heterojunction emitters **2000**; 168−172.

[11] J. Muth, A. Cai, A. Osinsky, H. Everitt, B. Cook, I. Avrutsky, Optical Properties of II-IV-N_2 Semiconductors, *Mater. Res. Soc. Symp. Proc.* **2005**, *831*, E11.45.11−15.

[12] T. Misaki, A. Wakahara, H. Okada, A. Yoshida, Optical properties of $ZnGeN_2$ epitaxial layer, *Phys. Status Solidi C* **2003**, *0*, 2890−2893.

[13] M. Shang, J. Wang, J. Fan, H. Lian, Y. Zhang, J. Lin, $ZnGeN_2$ and $ZnGeN_2$:Mn^{2+} phosphors: hydrothermal-ammonolysis synthesis, structure and luminescence properties, *J. Mater. Chem. C* **2015**, *3*, 9306−9317.

[14] M. Wintenberger, J. Guyader, M. Maunaye, Etude cristallographique et magnetique de $MnGeN_2$ par diffraction neutronique, *Solid State Commun.* **1972**, *11*, 1485–1488.

[15] M. Wintenberger, R. Marchand, M. Maunaye, Etude cristallographique et magnetique de $MnSiN_2$ par diffraction des neutrons, *Solid State Commun.* **1977**, *21*, 733–735.

[16] S. Esmaeilzadeh, U. Hålenius, M. Valldor, Crystal Growth, Magnetic, and Optical Properties of the Ternary Nitride $MnSiN_2$, *Chem. Mater.* **2006**, *18*, 2713–2718.

[17] R. Olazcuaga, J.-M. Reau, G. Leflem, P. Hagenmuller, Préparation, Proprietés Cristallographiques et Magnétiques des Phases K_3XO_4 (X=V, Cr, Mn), *Z. Anorg. Allg. Chem.* **1975**, *412*, 271–280.

7 A High-Pressure Polymorph of Phosphorus Oxonitride with the Coesite Structure

published in: *Angew. Chem. Int. Ed.* **2015**, *54,* 4388–4391;
Angew. Chem. **2015**, *127,* 4463–4466.

authors: Dominik Baumann, Robin Niklaus, Wolfgang Schnick

DOI: 10.1002/anie.201410526

Abstract The chemical and physical properties of phosphorus oxonitride (PON) closely resemble those of silica, to which it is isosteric. A new high-pressure phase of PON is reported herein. This polymorph, synthesized by using the multianvil technique, crystallizes in the coesite structure. This represents the first occurrence of this very dense network structure outside of SiO_2. Phase-pure coesite PON (coe-PON) can be synthesized in bulk at pressures above 15 GPa. This compound was thoroughly characterized by means of powder X-ray diffraction, DFT calculations, and FTIR and MAS NMR spectroscopy, as well as temperature-dependent diffraction. These results represent a major step towards the exploration of the phase diagram of PON at very high pressures and the possibly synthesis of a stishovite-type PON containing hexacoordinate phosphorus.

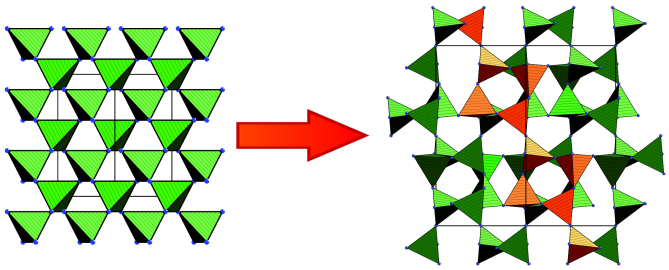

7.1 Introduction with Results and Discussion

Owing to its unique properties, silica (SiO_2) has been of great interest for physicists, chemists, and geoscientists for many decades. This is partly due to its properties and the resultant applications, such as nonlinear optical properties[1]or piezoelectricity,[2] but it is also to a large extent due to the wide variety of crystal structures found for this material.[3] With SiO_2 being the parent compound of the major components of the crust and mantle of the Earth,[4–6] precise knowledge of the phase diagram of silica leads to a detailed understanding of many geological processes. The high-pressure polymorph coesite was artificially synthesized[7] and studied in detail[8,9] before it was first discovered in nature as a product of meteorite impacts.[10] Subsequent investigations showed that the presence of coesite in rocks can serve as an indicator of the material having undergone ultrahigh-pressure metamorphism.[11–13] This enables a detailed understanding of the geological history of these rocks.

Similarly, the polymorphs stable at even higher pressures, namely stishovite[14,15] and seifertite,[16,17] can be used as indicators of previous impact events. Stishovite has additionally drawn particular interest because of remarkable mechanical properties. It held the record for the hardest oxide[18] until it was surpassed by cotunnite-type TiO_2 in 2001.[19]

In order to gain a more detailed understanding of the high-pressure behavior of silica related phases we have investigated the phase diagram of phosphorus oxonitride PON, which is isosteric to SiO_2[20] and its analogues PN(NH)[21] and $AlPO_4$.[22] Owing to the similar ionic radii (Si^{4+}: 26 pm, P^{5+}: 17 pm; O^{2-}: 135 pm, N^{3-}: 146 pm)[23] some of the polymorphs exhibited by silica can also be found in PON. At ambient pressure PON adopts a β-cristobalite-type structure and has no known high-temperature polymorphs.[24] The high-pressure phases include quartz-[25] and moganite-type polymorphs.[26] In the case of silica, moganite has only been found in microscopic quantities in nature, whereas it is synthetically accessible in bulk quantities for PON. Recently, we were able to synthesize another polymorph of phosphorus oxonitride that crystallizes in a unique structure type that had not been observed in any other compound before.[27] This indicates that the diversity of possible structure types for PON could possibly even exceed that for SiO_2. A particular factor that could extend the range of possible AB_2-structures in PON is the fact that the nitride ion is able to connect more than two neighboring $P(O,N)_4$ tetrahedra.[28] Notable examples that contain triply bridging nitrogen are α- and β-HP_4N_7,[29–31] P_4N_6O[32] as well as the layered oxonitrido phosphate $Sr_3P_6O_6N_8$.[33]
Herein, we report the discovery of a new polymorph of PON that crystallizes in the coesite structure type, for which we propose the name coesite PON or *coe*-PON. This high-pressure phase was synthesized in a modified Walker-type multianvil assembly. The starting material cristobalite-type PON was treated at 15.5 GPa and approximately 1300 °C for 60 min.

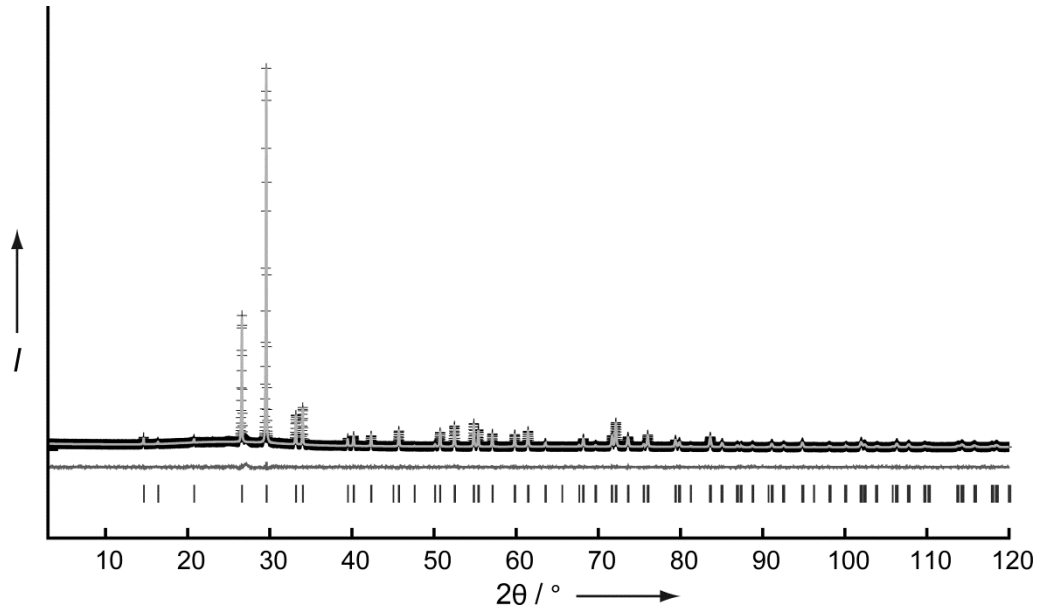

Figure 7.1 Observed (crosses) and calculated (light gray line) powder diffraction pattern of *coe*-PON as well as difference profile (dark gray line). Black vertical bars represent the positions of Bragg reflections.

The product could then be isolated as a colorless crystalline solid. Energy-dispersive X-ray (EDX) spectroscopy was used to establish the absence of any elements other than P, O, and N. The crystal structure was elucidated from powder X-ray diffraction data.[34] Structure solution was performed by using the charge-flipping algorithm.[35–37] Both structure solution and Rietveld refinement were carried out by using TOPAS-Academic 4.1.[38] Rietveld refinement also showed no signs of any amorphous or crystalline side phases (Figure 7.1). The unit cell of *coe*-PON (a = 6.95903(8), b = 12.0610(2), c = 6.96821(8) Å, β = 120.0348(7)°) displays remarkable lattice pseudosymmetry, appearing hexagonal at first glance. The symmetry of the structure itself, however, is monoclinic, a fact that has similarly been observed for coesite SiO_2.[9] The crystal structure (Figure 7.2) closely resembles that of coesite. The compound is composed of a three-dimensional network of all-side vertex-sharing $P(O,N)_4$ tetrahedra. As with the other known polymorphs of PON, there was no indication of any ordering of the anion positions. We thus assume a statistical disorder of the anions. In the case of cristobalite PON, this was confirmed by neutron diffraction experiments.[39] The topological identity of the networks of coesite SiO_2 and PON is also illustrated by topological analysis with TOPOS.[40,41] Both compounds are described by the point symbol $(4^2.6.8^2.9)(4^2.6^3.8)$.

According to the nomenclature established by Liebau, the crystal structure of *coe*-PON can be described as loop-branched *dreier* single chains that are interconnected to form a three-dimensional network. This leads to a loop-branched *dreier* framework $\{IB,^3_\infty\}[^3P_4(O,N)_8]$ similar to that found in feldspars.[42] The P–(O,N) bond lengths are in the range of 154 to 164 pm (Figure 7.3). A similarly large variance in the interatomic distances has been observed in δ-PON.[27] The $P(O,N)_4$ tetrahedra are slightly distorted, but to a lesser degree than those in δ-PON. The P–(O,N)–P angles around most of the anion sites range from 137 to 147° and are therefore very similar to those found in coesite SiO_2. The angle P1–(O,N)1–P1, however, exhibits an intriguing value of 180°.

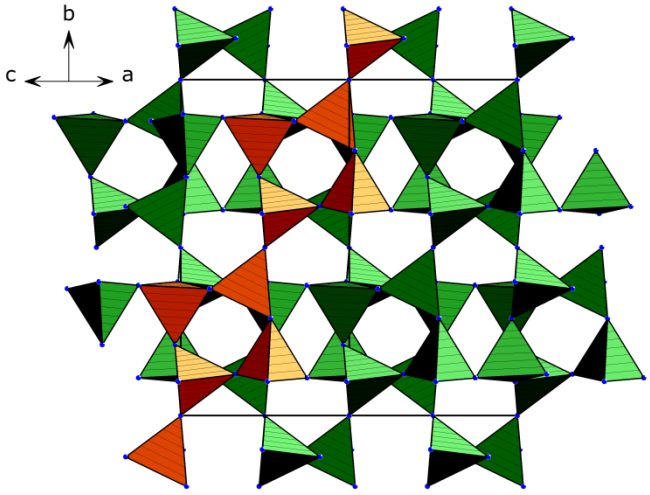

Figure 7.2 Crystal structure of *coe*-PON in polyhedral representation. View along [101]. One fundamental chain is highlighted in orange.

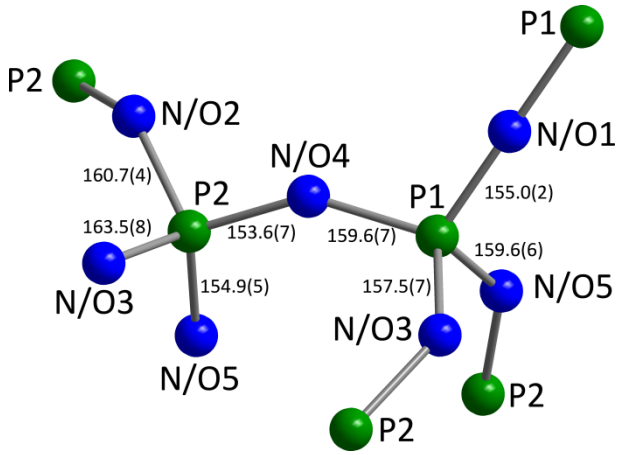

Figure 7.3 Atomic arrangement and bond lengths in coe-PON. Bond lengths are denoted in pm.

Since this same angle occurs in coesite SiO_2 as well and differs greatly from the value of 140° for a strain-free Si–O–Si bond, it has been discussed in detail by Liebau.[42] He came to the conclusion that this angle is not an artifact caused by the fact that the bridging atom resides on an inversion center but is intrinsic to the crystal structure. In order to show the same for *coe*-PON, we also performed the structure solution in the non-centrosymmetric space group *Cc*. This did not lead to a significant deviation of this angle from 180°, thus indicating that the structural model in space group *C*2/*c* is correct. Another possible cause of an apparent angle of 180° could be static or dynamic disorder of the bridging atom around the crystallographic site. Such an effect, which can also be described as a coupled rotation of the involved tetrahedra, has been discussed for β-cristobalite.[43] This would, however, lead to a significantly increased displacement parameter for the anion site. Since the B_{eq} value for (O,N)1 is similar to those of the other anion sites, this phenomenon is unlikely for *coe*-PON.

In order to quantify the similarity between the crystal structures of coesite SiO_2 and coesite PON, the two were compared by using the COMPSTRU program of the Bilbao Crystallographic Server.[44] The calculated arithmetic mean of the distance between equivalent atomic sites amounts to just 4.4 pm. This leads to a measure of similarity[45] (Δ) of 0.014, thus indicating that the two crystal structures are in fact very closely related.DFT calculations were employed to validate our experimental findings. Owing to the statistical O/N disorder, energy-volume curves were calculated for all six chemically reasonable arrangements of O and N. For comparison, the energy-volume curves for cristobalite PON with the lowest energy O/N arrangements were also determined. Details of the calculations and ordered structural models can be found in the Supporting Information. The corresponding enthalpy–pressure diagram (Figure S7.7 in the Supporting Information) shows that coesite PON is expected to be more stable than the ambient pressure polymorph above 7.5–10.5 GPa, which is in good agreement with the pressure of 15.5 GPa used in the synthesis. The predicted bulk modulus for *coe*-PON is in the range of 151 to 170 GPa.

The high-pressure high-temperature conditions used for the synthesis, combined knowledge of the phase diagram of closely related SiO_2, strongly suggest that *coe*-PON is a high-pressure phase of phosphorus oxonitride and therefore metastable at ambient pressure. In order to

corroborate this hypothesis, we performed temperature-dependent powder X-ray diffraction up to 1000 °C. The results (Figure S7.4) show that at ambient pressures, *coe*-PON transforms back into the cristobalite polymorph above 750 °C. This result indicates that temperatures above 700 °C are needed to initiate reconstructive transformations in phosphorus oxonitride, which is consistent with our laboratory experience. At 975 °C, the first signs of thermal decomposition can be observed. In order to corroborate the results of the structure solution, a ^{31}P MAS NMR spectrum was acquired (Figure S7.1). The spectrum shows two rather broad peaks at −48 and −66 ppm that can be attributed to the two crystallographic P sites. The broad signals can be explained by statistical O/N disorder. This leads to a range of distinct local environments around the P nuclei. Since the NMR signal is an average over all of the P sites in the sample, this leads to a broadening of the NMR signals. A similar effect has been observed in the case of δ-PON.[27] In order to rule out the presence of NH groups in the sample, which could in theory replace the isoelectronic O^{2-}, an FTIR spectrum of the sample was collected (Figure S7.2). It showed no signs of the characteristic N–H vibrations around 3000 cm^{-1}, which is a strong indication of the absence of hydrogen in the sample. The discovery of *coe*-PON provides new insight into the high-pressure chemistry of phosphorus oxonitride. Previous investigations up to a pressure of 70 GPa with diamond anvil cells at room temperature showed no reconstructive transformations to new high-pressure phases,[46] while experiments in laser-heated diamond anvil cells at 20 GPa led to the formation of the already known moganite PON. The new results presented herein show that it is indeed possible to obtain further high-pressure phases of PON through a combined high-temperature high-pressure approach by using the multianvil technique. The formation of a coesite-type phase shows that the similarity between SiO_2 and PON extends to higher pressures. However, the pressure needed for the transformation of PON (15.5 GPa) is significantly higher than that for SiO_2 (3.5 GPa).[7] It is plausible that this similarity could extend to the extreme pressure phases known for silica. Stishovite-type PON containing hexacoordinate phosphorus might thus be accessible, albeit at even higher pressures than for stishovite SiO_2. The possibility of synthesizing and recovering compounds containing pentacoordinate phosphorus has already been shown for the closely related systems P_3N_5[47,48] and $P_4N_6(NH)$.[49]

7.2 References

[1] P. A. Franken, A. E. Hill, C. W. Peters, G. Weinreich, Generation of Optical Harmonics, *Phys. Rev. Lett.* **1961**, *7*, 118–119.

[2] G. W. Pierce, Piezoelectric Crystal Resonators and Crystal Oscillators Applied to the Precision Calibration of Wavemeters, *Proc. Am. Acad. Arts Sci.* **1923**, *59*, 81–106.

[3] N. R. Keskar, J. R. Chelikowsky, Structural properties of nine silica polymorphs, *Phys. Rev. B: Condens. Matter Mater. Phys.* **1992**, *46*, 1–13.

[4] D. L. Anderson, Composition of the Earth, *Science* **1989**, *243*, 367–370.

[5] W. F. McDonough, S.-S. Sun, The composition of the Earth, *Chem. Geol.* **1995**, *120*, 223–253.

[6] C. J. Allègre, J.-P. Poirier, E. Humler, A. W. Hofmann, The chemical composition of the Earth, *Earth Planet. Sci. Lett.* **1995**, *134*, 515–526.

[7] L. Coes Jr., A New Dense Crystalline Silica, *Science* **1953**, *118*, 131–132.

[8] L. S. Ramsdell, The crystallography of "coesite", *Am. Mineral.* **1955**, *40*, 975–982.

[9] T. Zoltai, M. J. Buerger, The crystal structure of coesite, the dense, high-pressure form of silica, *Z. Kristallogr.* **1959**, *111*, 129–141.

[10] E. C. T. Chao, E. M. Shoemaker, B. M. Madsen, First Natural Occurrence of Coesite, *Science* **1960**, *132*, 220–220.

[11] D. C. Smith, Coesite in clinopyroxene in the Caledonides and its implications for geodynamics, *Nature* **1984**, *310*, 641–644.

[12] C. Chopin, Coesite and pure pyrope in high-grade blueschists of the Western Alps: a first record and some consequences, *Contrib. Mineral. Petrol.* **1984**, 86, 107–118.

[13] S. R. Bohlen, D. H. Lindsley, Thermometry and Barometry of Igneous and Metamorphic Rocks, *Ann. Rev. Earth Planet. Sci.* **1987**, *15*, 397–420.

[14] W. Sinclair, A. E. Ringwood, Single crystal analysis of the structure of stishovite, *Nature* **1978**, *272*, 714–715.

[15] R. J. Hill, M. D. Newton, G. V. Gibbs, A crystal chemical study of stishovite, *J. Solid State Chem.* **1983**, *47*, 185–200.

[16] P. Dera, C. T. Prewitt, N. Z. Boctor, R. J. Hemley, Characterization of a high-pressure phase of silica from the Martian meteorite Shergotty, *Am. Mineral.* **2002**, *87*, 1018–1023.

[17] A. E. Goresy, P. Dera, T. G. Sharp, C. T. Prewitt, M. Chen, L. Dubrovinsky, B. Wopenka, N. Z. Boctor, R. J. Hemley, Seifertite, a dense orthorhombic polymorph of silica from the Martian meteorites Shergotty and Zagami, *Eur. J. Mineral.* **2008**, *20*, 523–528.

[18] J. M. Léger, J. Haines, M. Schmidt, J. P. Petitet, A. S. Pereira, J. A. H. da Jornada, Discovery of hardest known oxide, *Nature* **1996**, *383*, 401.

[19] L. S. Dubrovinsky, N. A. Dubrovinskaia, V. Swamy, J. Muscat, N. M. Harrison, R. Ahuja, B. Holm, B. Johansson, Materials science. The hardest known oxide, *Nature* **2001**, *410*, 653–654.

[20] A. L. Sauze, J. Haines, C. Chateac, J. M. Leger, R. Marchand, Phosphorus Oxynitride PON: A New Silica, *Mater. Sci. Forum* **2000**, *325–326*, 77–82.

[21] J. Liebig, F. Wöhler, Nachtrag der Redaction, Liebigs *Ann. Chem.* **1834**, *11*, 139–150.

[22] A. F. Wright, A. J. Leadbetter, The structures of the β-cristobalite phases of SiO_2 and $AlPO_4$, *Philos. Mag.* **1975**, *31*, 1391–1401.

[23] R. D. Shannon, Revised effective ionic radii and systematic studies of interatomic distances in halides and chalcogenides, *Acta Crystallogr. Sect. A: Cryst. Phys. Diffr. Theor. Gen. Crystallogr.* **1976**, *32*, 751–767.

[24] J. M. Léger, J. Haines, C. Chateau, G. Bocquillon, M. W. Schmidt, S. Hull, F. Gorelli, A. Lesauze, R. Marchand, Phosphorus oxynitride PON, a silica analogue: structure and compression of the cristobalite-like phase; *P–T* phase diagram, *Phys. Chem. Minerals* **2001**, *28*, 388–398.

[25] J. M. Léger, J. Haines, L. S. de Oliveira, C. Chateau, A. L. Sauze, R. Marchand, S. Hull, Crystal structure and high pressure behaviour of the quartz-type phase of phosphorus oxynitride PON, *J. Phys. Chem. Solids* **1999**, *60*, 145–152.

[26] J. Haines, C. Chateau, J. M. Léger, A. L. Sauze, N. Diot, R. Marchand, S. Hull, Crystal structure of moganite-type phosphorus oxynitride: relationship to other twinned-quartz-based structures, *Acta Crystallogr. Sect. B: Struct. Sci.* **1999**, *55*, 677–682.

[27] D. Baumann, S. J. Sedlmaier, W. Schnick, An Unprecedented AB2 Tetrahedra Network Structure Type in a High-Pressure Phase of Phosphorus Oxonitride PON, *Angew. Chem. Int. Ed.* **2012**, *51*, 4707–4709; *Angew. Chem.* **2012**, *124*, 4785–4787.

[28] W. Schnick, Solid-State Chemistry with Nonmetal Nitrides, *Angew. Chem. Int. Ed. Engl.* **1993**, *32*, 806–818; *Angew. Chem.* **1993**, *105*, 846–858.

[29] S. Horstmann, E. Irran, W. Schnick, Phosphorus(V) Nitride Imide HP_4N_7: Synthesis from a Molecular Precursor and Structure Determination with Synchrotron Powder Diffraction, *Angew. Chem. Int. Ed. Engl.* **1997**, *36*, 1992–1994; *Angew. Chem.* **1997**, *109*, 2085–2087.

[30] S. Horstmann, E. Irran, W. Schnick, Synthese, Kristallstruktur und Eigenschaften von Phosphor(V)-nitridimid HP_4N_7, *Z. Anorg. Allg. Chem.* **1998**, *624*, 221–227.

[31] D. Baumann, W. Schnick, High-Pressure Polymorph of Phosphorus Nitride Imide HP_4N_7 Representing a New Framework Topology, *Inorg. Chem.* **2014**, *53*, 7977–7982.

[32] J. Ronis, B. Bondars, A. Vitola, T. Millers, J. Schneider, F. Frey, Crystal Structure of the Phosphorus Oxynitride P_4ON_6, *J. Solid State Chem.* **1995**, *115*, 265–269.

[33] S. Sedlmaier, J. S. auf der Günne, W. Schnick, $Sr_3P_6O_6N_8$—a highly condensed layered phosphate, *Dalton Trans.* **2009**, 4081–4084.

[34] Crystal data for *coe*-PON: a = 6.95903(8), b = 12.0610(2), c = 6.96821(8) Å, β = 120.0348(7)°, V = 506.33(2) Å^3, space group $C2/c$ (no. 15), Z = 16; Stoe StadiP powder diffractometer with MYTHEN 1K Si strip detector, Cu-$K_{\alpha1}$ radiation (λ = 1.54059 Å, Ge(111) monochromated), T = 298(2) K, 7800 data points, 385 measured reflections, 65 parameters, peak shape modelled by fundamental parameters approach,[50, 51] background function: shifted Chebychev (21 coefficients), χ^2 = 2.111, R_{wp} = 0.04069, R_{exp} = 0.01927, R_{Bragg} = 0.00657; Further details of the crystal structure investigation can be obtained from the Fachinformations-Zentrum Karlsruhe, 76344 Eggenstein-Leopoldshafen, Germany (fax: (+49)7247-808-666; email: crysdata@fiz-karlsruhe.de) on quoting the depository number CSD-428382.

[35] G. Oszlányi, A. Sütő, *Ab initio* structure solution by charge flipping, *Acta Crystallogr. Sect. A: Found. Crystallogr.* **2004**, *60*, 134–141.

[36] G. Oszlányi, A. Sütő, The charge flipping algorithm, *Acta Crystallogr. Sect. A: Found. Crystallogr.* **2008**, *64*, 123–134.

[37] A. A. Coelho, A charge-flipping algorithm incorporating the tangent formula for solving difficult structures, *Acta Crystallogr. Sect. A: Found. Crystallogr.* **2007**, *63*, 400–406.

[38] A. Coelho, *TOPAS-Academic Version 4.1*, Coelho Software: Brisbane, **2007**.

[39] L. Boukbir, R. Marchand, Y. Laurent, P. Bacher, G. Roult, Preparation and time-of-flight neutron diffraction study of the cristobalite-type PON phosphorus oxynitride, *Ann. Chim. Fr.* **1989**, *14*, 475–481.

[40] V. A. Blatov, M. O'Keeffe, D. M. Proserpio, Vertex-, face-, point-, Schläfli-, and Delaney-symbols in nets, polyhedra and tilings: recommended terminology, *CrystEngComm* **2010**, *12*, 44–48.

[41] V. Blatov, A. Shevchenko, D. Proserpio, Applied Topological Analysis of Crystal Structures with the Program Package ToposPro, *Cryst. Growth Des.* **2014**, *14*, 3576–3586.

[42] F. Liebau, *Structural Chemistry of Silicates*, Springer, Berlin, **1985**.

[43] T. R. Welberry, L. Hua, R. L. Withers, An optical transform and Monte Carlo study of the disorder in β-cristobalite SiO_2, *J. Appl. Crystallogr.* **1989**, *22*, 87–95.

[44] E. Tasci, G. de la Flor, D. Orobengoa, C. Capillas, J. Perez-Mato, M. Aroyo, An introduction to the tools hosted in the Bilbao Crystallographic Server, *EPJ Web Conf.* **2012**, *22*, 00009.

[45] G. Bergerhoff, M. Berndt, K. Brandenburg, T. Degen, Concerning inorganic crystal structure types, *Acta Crystallogr. Sect. B: Struct. Sci.* **1999**, *55*, 147–156.

[46] K. J. Kingma, R. E. Gerald Pacalo, P. F. McMillan, IN *Properties of Earth and Planetary Materials at High Pressure and Temperature*, (Eds.: M. H. Manghnani, T. Yagi), American Geophysical Union, **1998**, 105–119.

[47] K. Landskron, H. Huppertz, J. Senker, W. Schnick, High-Pressure Synthesis of γ-P_3N_5 at 11 GPa and 1500 °C in a Multianvil Assembly: A Binary Phosphorus(V) Nitride with a Three-Dimensional Network Structure from PN_4 Tetrahedra and Tetragonal PN_5 Pyramids, *Angew. Chem. Int. Ed.* **2001**, *40*, 2643–2645; *Angew. Chem.* **2001**, *113*, 2713–2716.

[48] K. Landskron, H. Huppertz, J. Senker, W. Schnick, Multianvil-Synthese, Pulver-Röntgenstrukturanalyse, ^{31}P-MAS-NMR- und FTIR-Spektroskopie sowie Materialeigenschaften von γ-P_3N_5, einer Hochdruckphase von binärem Phosphor(V)nitrid mit verzerrt quadrat ischen PN_5-Pyramiden und PN_4-Tetraedern *Z. Anorg. Allg. Chem.* **2002**, *628*, 1465–1471.

[49] D. Baumann, W. Schnick, Pentacoordinate Phosphorus in a High-Pressure Polymorph of Phosphorus Nitride Imide $P_4N_6(NH)$, *Angew. Chem. Int. Ed.* **2014**, *53*, 14490–14493; *Angew. Chem.* **2014**, *126*, 14718–14721.

[50] R. W. Cheary, A. Coelho, A fundamental parameters approach to X-ray line-profile fitting, *J. Appl. Crystallogr.* **1992**, *25*, 109–121.

[51] R. W. Cheary, A. A. Coelho, J. P. Cline, Fundamental Parameters Line Profile Fitting in Laboratory Diffractometers, *J. Res. Natl. Inst. Stand. Technol.* **2004**, *109*, 1–25.

7.3 Supporting Information

7.3.1 Experimental Details of the HP/HT-Synthesis of *coe*-PON

The starting material cristobalite PON was synthesized by a two-step condensation of phosphoric triamide. A mixture of $PO(NH_2)_3$ and NH_4Cl, obtained by reacting $POCl_3$ (99%, Sigma Aldrich) with liquid NH_3 (5.0, Air Liquide) as described in the literature,[1] was heated to 620 °C for 5 h in a stream of dry ammonia. The resulting amorphous condensation product was crystallized for 7 days at 750 °C in evacuated fused quartz ampoules yielding pure cristobalite-type PON. *coe*-PON was synthesized by a high-pressure high-temperature reaction using a modified Walker-type multianvil assembly. The starting material cristobalite PON was tightly packed in a BN crucible which was in turn placed in a MgO octahedron (Ceramic Substrates & Components, Isle of Wight, UK) with an edge length of 10 mm. More details about the assembly can be found in the literature.[2–6] The sample was compressed to 15.5 GPa between eight truncated tungsten carbide cubes (Hawedia, Marklkofen, Germany) using a 1000 t hydraulic press (Voggenreiter, Mainleus, Germany). The temperature was raised to 1300 °C within 15 min and held for 60 min. After quenching and decompression the sample was mechanically isolated and ground in an agate mortar.

7.3.2 Information on Data Collection and Structure Elucidation of *coe*-PON

X-ray powder diffraction measurements were conducted in parafocusing Debye-Scherrer geometry using a StadiP-diffractometer (Stoe & Cie, Darmstadt, Germany) using Ge(111) monochromated Cu-Kα_1-radiation and a MYTHEN 1K Si-strip detector (Dectris, Baden, Switzerland). Structure elucidation was performed using TOPAS Academic 4.1.[7] The powder pattern was indexed using the SVD-algorithm[8] and the reflection intensities extracted with the Pawley-method. Structure solution was carried out with the charge-flipping algorithm.[9] Final refinement was carried out using the Rietveld method, peak shapes being modelled by the fundamental parameters approach (direct convolution of source emission profiles, axial instrument contributions and crystallite size and microstrain effects).[10,11] The anion positions were occupied equally with 0.5 for both O and N applying a common atomic displacement parameter. Capillary absorption correction (inner diameter 0.28 mm) was carried out using the calculated absorption coefficient. Preferred orientation was corrected using spherical harmonics functions of the 4th order.[12] Temperature dependent X-ray powder diffraction measurements were carried out on a Stoe StadiP diffractometer that was equipped with a high-temperature graphite furnace using Ge(111) monochromated Mo-Kα_1 radiation (λ = 0.70930) and an image plate position sensitive detector. The sample was heated with a rate of 10 °C/min between measurements. The temperature was held constant for each 15 min measurement. The FTIR spectrum was collected on a Spectrum BX II-spectrometer (Perkin Elmer, Waltham MA, USA) in ATR geometry. The ^{31}P-NMR spectrum was collected on a Bruker Avance III spectrometer, using a 11.7T magnet and a 1.3 mm MAS probe. The sample was spun at a MAS rate of 50 KHz. The spectrum was acquired using a 90° pulse using a long recycle delay with T_1 estimated to be >30 min. The chemical shift values are referenced to 0.1% TMS in $CDCl_3$ (Sigma-Aldrich) as an

external reference. Energy dispersive X-ray analyses were performed using a JSM 6500F scanning electron microscope (Jeol, Tokyo, Japan) with an Oxford Instruments 7418 X-ray detector.

7.3.3 Additional Crystallographic Data for *coe*-PON

Table S7.1 Fractional atomic coordinates, isotropic thermal displacement parameters, and site occupancies for *coe*-PON

Atom	Wyckoff Position	*x*	*y*	*z*	U_{eq} / Å^2	occupancy
P1	8*f*	0.1434(4)	0.1066(2)	0.0753(4)	0.0193(6)	1
P2	8*f*	0.5037(5)	0.1613(2)	0.5376(3)	0.0132(4)	1
O1	4*a*	0	0	0	0.024(2)	0.5
N1	4*a*	0	0	0	0.024(2)	0.5
O2	4*e*	1/2	0.1121(7)	3/4	0.024(2)	0.5
N2	4*e*	1/2	0.1121(7)	3/4	0.024(2)	0.5
O3	8*f*	0.257(1)	0.1229(4)	0.9300(7)	0.012(2)	0.5
N3	8*f*	0.257(1)	0.1229(4)	0.9300(7)	0.012(2)	0.5
O4	8*f*	0.319(1)	0.1014(5)	0.334(1)	0.031(2)	0.5
N4	8*f*	0.319(1)	0.1014(5)	0.334(1)	0.031(2)	0.5
O5	8*f*	0.0178(8)	0.2109(4)	0.4831(7)	0.018(2)	0.5
N5	8*f*	0.0178(8)	0.2109(4)	0.4831(7)	0.018(2)	0.5

Table S7.2 Interatomic distances / pm for *coe*-PON

P1–O1/N1	155.0(2)	P2–O2/N2	160.7(4)
P1–O3/N3	157.5(7)	P2–O3/N3	163.5(8)
P1–O4/N4	159.6(7)	P2–O4/N4	153.6(7)
P1–O5/N5	159.6(6)	P2–O5/N5	154.9(5)

Table S7.3 Bond angles / ° for *coe*-PON

O1/N1–P1–O3/N3	109.3(2)	O5/N5–P2–O2/N2	114.1(4)
O1/N1–P1–O4/N4	110.4(3)	O5/N5–P2–O3/N3	109.8(3)
O1/N1–P1–O5/N5	108.4(3)	O2/N2–P2–O3/N3	104.7(2)
O3/N3–P1–O4/N4	112.7(4)	P1–O1/N1–P1	180
O3/N3–P1–O5/N5	104.6(3)	P2–O2/N2–P2	136.6(6)
O4/N4–P1–O5/N5	111.3(3)	P1–O3/N3–P2	138.6(3)
O4/N4–P2–O5/N5	112.7(3)	P2–O4/N4–P1	147.0(5)
O4/N4–P2–O2/N2	106.5(4)	P2–O5/N5–P1	137.5(4)
O4/N4–P2–O3/N3	108.6(4)		

7.3.4 Details of the Rietveld Refinement

Table S7.4 Crystal details for *coe*-PON

formula	PON
formula mass / g · mol^{-1}	60.98
crystal system / space group	monoclinic, *C*2/*c* (no. 15)
lattice parameters / Å, °	*a* = 6.95903(8)
	b = 12.0610(2)
	c = 6.96821(8)
	β = 120.0348(7)
cell volume / Å^3	506.33(2)
formula units per cell Z	16
X-ray density / g · cm^{-3}	3.200
linear absorption coefficient / cm^{-1}	138.23
radiation	Cu-Kα_1 (λ = 154.059 pm)
monochromator	Ge(111)
diffractometer	Stoe StadiP
detector	MYTHEN 1K
2θ-range / °	3–119.985
temperature / K	298 (2)
data points	7800
number of observed reflections	385
number of parameters	65
constraints	0
program used	TOPAS Academic
structure solution	charge-flipping
structure refinement	Rietveld-Method
profile function	fundamental parameters model
background function	shifted Chebychev
R_{wp}	0.04069
R_{exp}	0.01927
R_p	0.02716
R_{Bragg}	0.00657
χ^2	2.111

7.3.5 Comparison of coesite SiO_2 and PON

Table S7.5 Comparison of the atomic coordinates of coesite SiO_2 and PON. |u| is the absolute distance between the equivalent atomic sites

Wyckoff position	Atom (SiO_2)[a]	*x* (SiO_2)	*y* (SiO_2)	*z* (SiO_2)	Atom (PON)[b]	*x* (PON)	*y* (PON)	*z* (PON)	|u| / pm
8*f*	Si1	0.1403	0.1084	0.0723	P1	0.1434	0.1066	0.0753	3.07
8*f*	Si2	0.5066	0.1580	0.5405	P2	0.5037	0.1613	0.5376	4.64
4*a*	O1	0	0	0	(O,N)1	0	0	0	0
4*e*	O2	1/2	0.1161	3/4	(O,N)2	1/2	0.1121	3/4	4.87
8*f*	O3	0.2660	0.1232	0.9400	(O,N)3	0.2565	0.1229	0.9300	6.95
8*f*	O4	0.3110	0.1037	0.3280	(O,N)4	0.3191	0.1014	0.3342	5.95
8*f*	O5	0.0177	0.2119	0.4784	(O,N)5	0.0178	0.2109	0.4831	3.56

a) lattice parameters: a = 7.17, b = 7.17, c = 12.38 Å, β = 120.0°;[13] b) lattice parameters: a = 6.95903, b = 12.0610, c = 6.96821 Å, β = 120.0348°

7.3.6 Solid-state-NMR and FTIR spectra

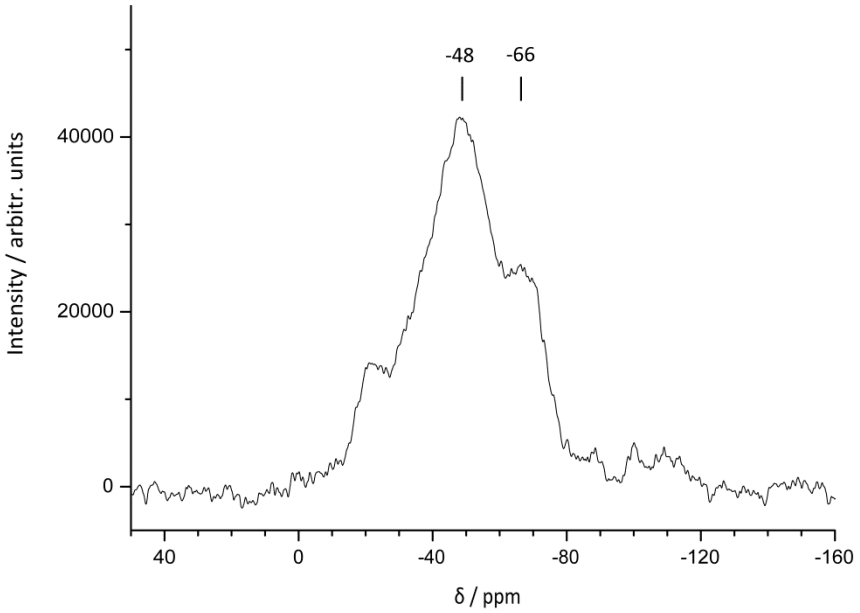

Figure S7.1 ^{31}P-solid-state NMR spectrum of *coe*-PON. The signals at -20 and -100 ppm may be caused by small amounts of a high-pressure polymorph of P_4N_6O with γ-HP_4N_7-structure present in the sample used for the measurement.[14]

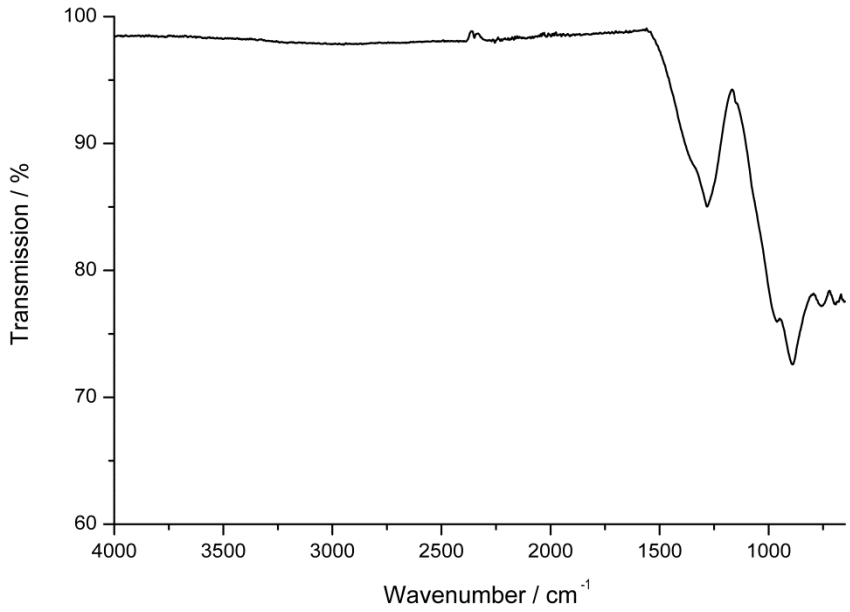

Figure S7.2 FTIR spectrum of *coe*-PON.

7.3.7 Detailed Rietveld Plot

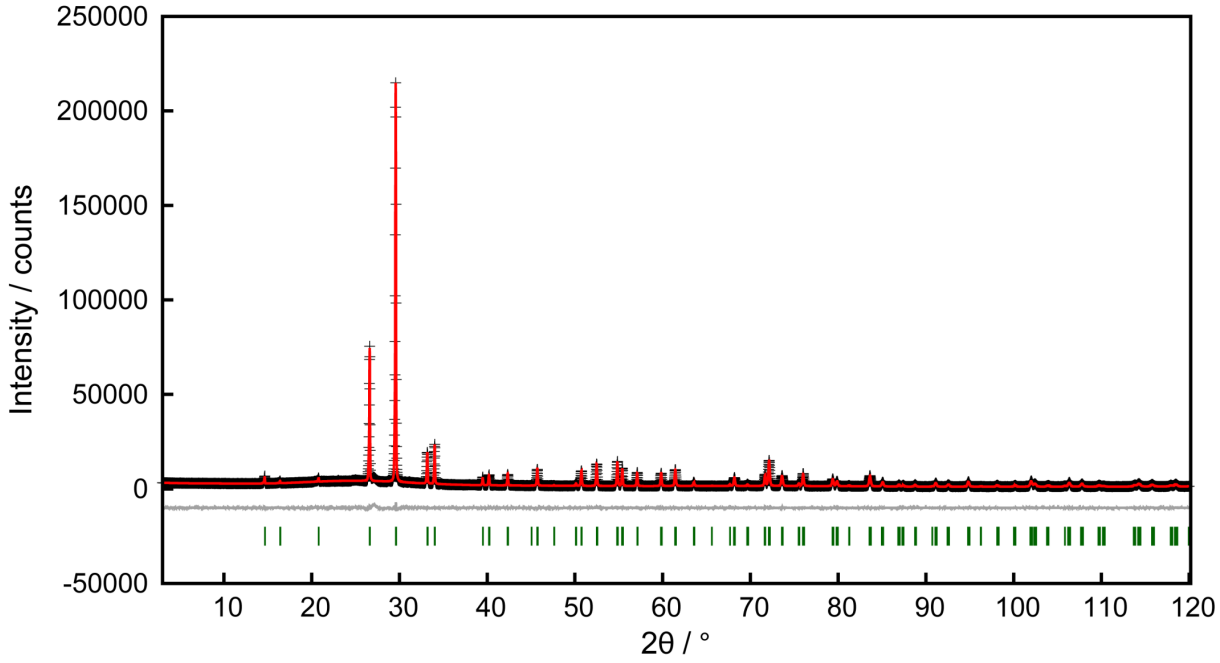

Figure S7.3 Observed (crosses) and calculated (red line) powder diffraction pattern of *coe*-PON as well as positions of Bragg reflections (green) and difference profile (gray line).

7.3.8 Temperature Dependent Powder X-ray Diffraction

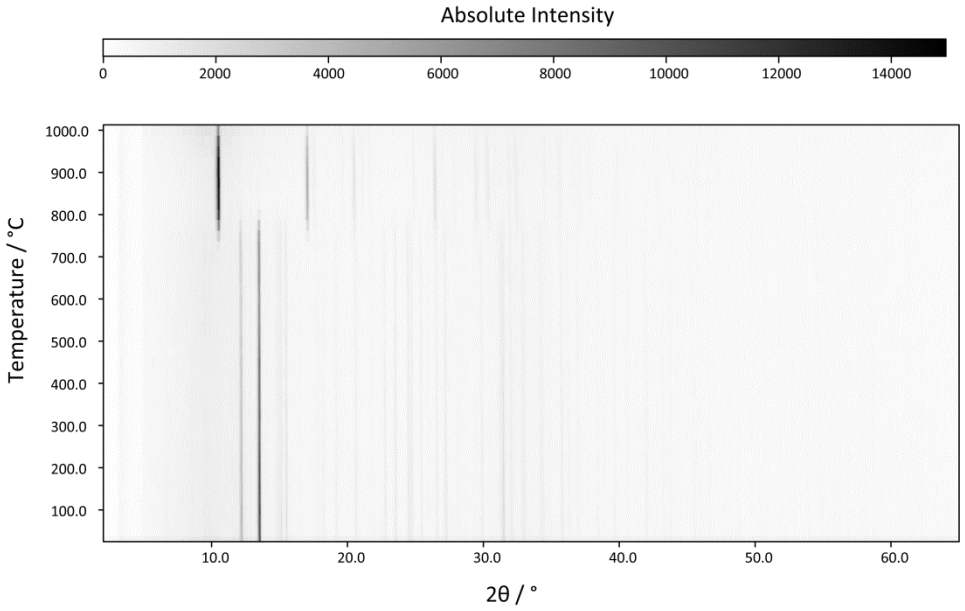

Figure S7.4 Temperature dependent powder X-ray diffraction for *coe*-PON.

7.3.9 Details on the DFT Calculations

To corroborate the observed high pressure phase transition from β-cristobalite to coesite-type for PON, ab initio calculations were performed for a variety of O/N ordering models of both structure types. Ordering models in *P1* were considered, since it is not easily feasible to perform structure optimizations for statistical atom occupation, as has been proven to be the case for the O/N site of cristobalite PON, and which is also observed for the high-pressure coesite phase. Hence, to examine the trend in transition pressure, chemically reasonable ordering models, each containing PON tetrahedra with 2 O and 2 N atoms respectively, were created for both phases of PON. The different ordering variants for cristobalite and *coe*-PON are depicted in Figure S7.5.

We calculated the total energies and atomic structures using density functional theory in the generalized gradient approximation (GGA) of Perdew, Burke, and Ernzerhof (PBE),[15,16] together with the projector-augmented-wave (PAW) method,[17,18] as implemented in the Vienna *ab initio* simulation package (VASP).[19–21] The GGA was chosen over the LDA as it is typically superior in reproducing the transition pressures in solid-state materials.[22,23] The structures of all PON models, were completely optimized by relaxing all internal coordinates and cell parameters, while using a plane-wave cut-off of 535 eV. The Brillouin zone was sampled on a dense gamma centered *k*-mesh (cristobalite PON: 10 x 10 x 7, *coe*-PON: 8 x 5 x 9) produced from the method of *Monkhorst* and *Pack* [24] to ensure high precision. The energy convergence criterion was set to 1×10^{-8} eV per unit cell to ensure accurate electronic convergence, while the residual atomic forces were converged below values of 2×10^{-3} eV/Å.

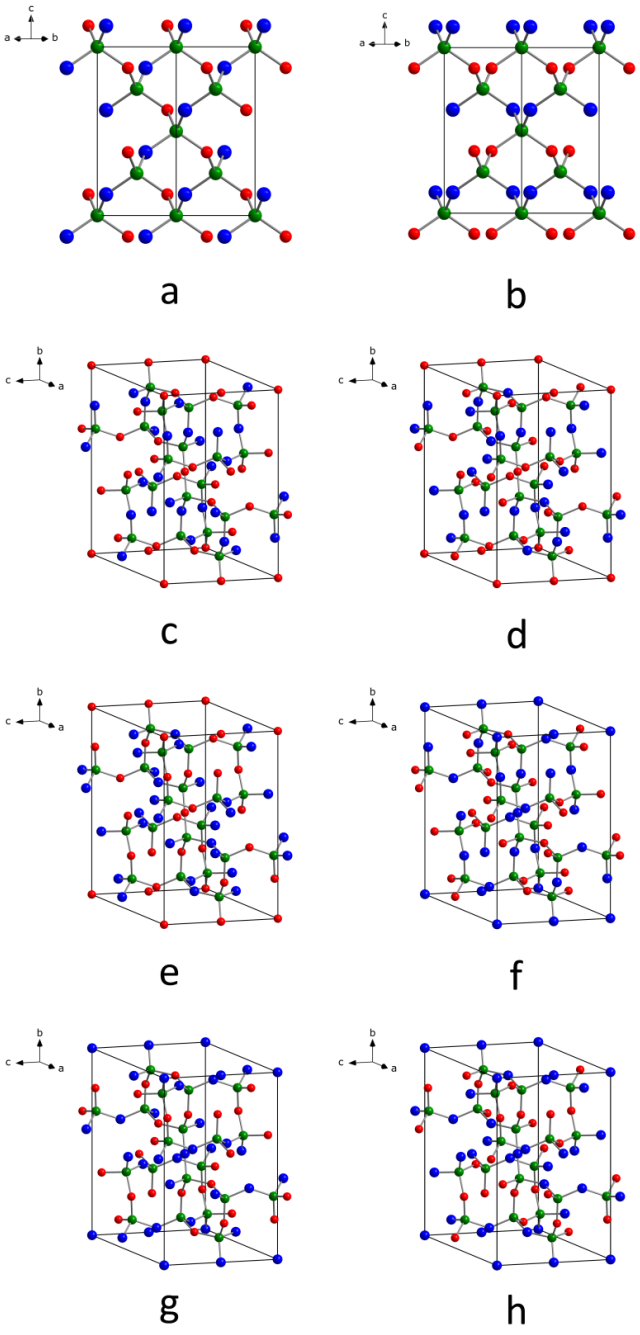

Figure S7.5 Different O/N arrangements used for the DFT calculations. a) cristobalite PON – N1N2O3O4N5N6O7O8 b) cristobalite PON N1O2N3O4O5N6N7O8. c–h) models used for *coe*-PON: c) O1O2O3N4N5, d) O1O2N3O4N5, e) O1O2N3N4O5, f) N1N2O3O4N5, g) N1N2O3N4O5, h) N1N2N3O4O5. Numbers reference the anion positions according to Table S7.1.

The total energies were calculated for all chosen ordering variants of cristobalite and *coe*-PON as depicted in Table S7.6. As expected the difference in total energy between the ordering models is small and partly identical for cristobalite PON which is in agreement with the observed statistical ordering of N and O determined by neutron diffraction.[25]

Table S7.6 Total energies per formula unit of PON for the chosen ordering models of cristobalite and *coe*-PON within the GGA

Cristobalite-PON		*coe*-PON	
Ordering variant	Total energy (eV) / PON	Ordering variant	Total energy (eV) / PON
N1N2O3O4N5N6O7O8	−22.08301681	O1O2O3N4N5	−21.76608136
N1O2N3O4N5O6N7O8	−22.07427969	O1O2N3O4N5	−21.76171247
N1O2N3O4N5O6O7N8	−22.06690326	O1O2N3N4O5	−21.78091168
N1O2N3O4O5N6N7O8	−22.08155875	N1N2O3O4N5	−21.86939451
N1O2N3O4O5N6O7N8	−22.07427969	N1N2O3N4O5	−21.87634218
N1O2O3N4N5O6N7O8	−22.06690326	N1N2N3O4O5	−21.86940664
N1O2O3N4N5O6O7N8	−22.07427969		
N1O2O3N4O5N6N7O8	−22.07427969		
N1O2O3N4O5N6O7N8	−22.08155874		

To study the structural behavior at high pressures, the total energies were (re)calculated at constant volume for a uniform expansion of the lattice parameters to simulate an expansion and compression of volume between 103% and 96% (respectively 91% for cristobalite PON) of the originally relaxed structure, resulting in pressures up to 20 GPa. This was done only for the two energetically lowest ordering modifications of cristobalite PON, for we consider them the most fitting representation of the ambient pressure modification of cristobalite PON from which the transition is initiated in the experiment. For *coe*-PON on the other hand, all ordering variants were taken into account as the high pressure and temperature of the reaction might shift the relative stability of the ordering variants. The resulting energy-volume(E-V) curves are depicted in Figure S7.6 and demonstrate further that cristobalite PON is energetically favored

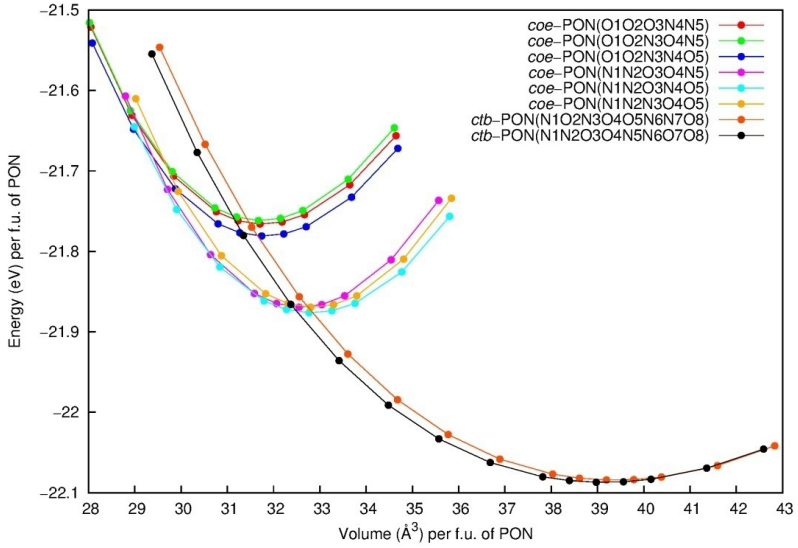

Figure S7.6 Energy -volume diagram for anion ordering of the energetically lowest models of cristobalite(*ctb*)-PON and the different coesite (*coe*)-PON models. The results were obtained with GGA. Each point represents one structural optimization at constant volume. Energy and volume are given per formula unit (f.u.) of PON.

Table S7.7 Results of the Murnaghan-EOS fit for the chosen ordering models of *coe*-PON.[a]

coe-PON (GGA)							
Model	O1O2O3 N4N5	O1O2N3 O4N5	O1O2N3 N4O5	N1N2O3 O4N5	N1N2O3 N4O5	N1N2N3 O4O5	$\bar{x}$
E_0	−21.76	−21.76	−21.78	−21.86	−21.87	−21.86	
V_0	31.70	31.67	31.74	32.55	32.76	32.80	
B_0	151.5	156.3	149.4	169.4	150.5	168.8	157.7
B'	3.3	2.7	3.1	1.9	1.5	1.7	

by about 0.2 eV compared to *coe*-PON and that a phase transition at higher pressure can be predicted. The fact that two sets of the ordering variants of *coe*-PON differ by 0.088 eV can possibly be explained by the fact that within the three energetically lower ordering variants the (O,N)1 position, which is part of the 180° bond, is occupied by N instead of O.

By fitting the total energies of the resulting E-V diagram with the Murnaghan equation of state (EOS)[26] it is possible to obtain the bulk modulus B_0 as depicted in Table S7.7 for the different coesite-PON models, and subsequently to create enthalpy-pressure diagrams. Phase changes are dependent on the free energy $G = E + pV - TS$, where ΔG constitutes the driving force between the occurring transition. Due to the small difference in entropy between the crystal structures of two solid-state materials, this part of ΔG is usually neglected, reducing ΔG to ΔH, where $H = E + pV$, permitting for accurate estimations, depending only on the energy, volume and pressure of the system. By variation of the volume, the pressure can be extracted from the resulting E-V diagram by a simple numerical differentiation: $p = -\partial E/\partial V$. The enthalpy difference ΔH between two phases can, subsequently, be plotted in reference to the phase of interest, in this case with respect to cristobalite PON.

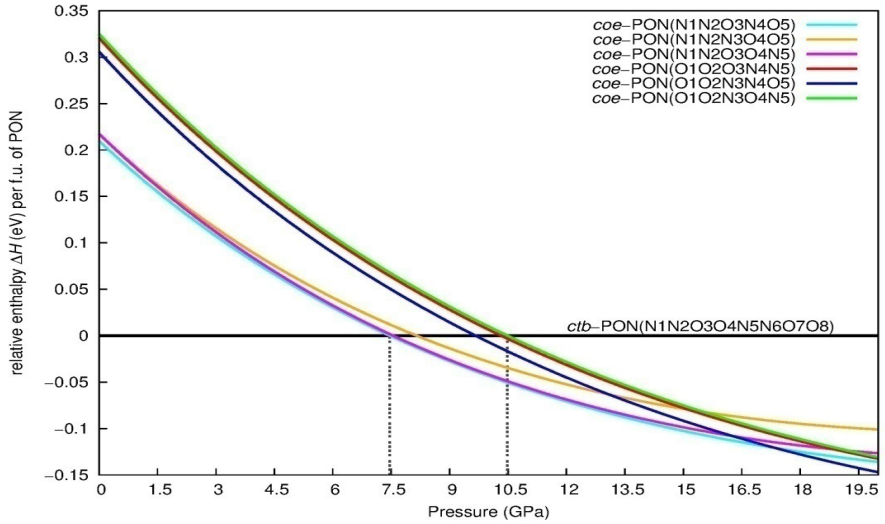

Figure S7.7 Enthalpy-pressure diagram for the high pressure phase transition of PON from the energetically most stable cristobalite (*ctb*) model to the different coesite (*coe*) models as obtained by fitting the Murnaghan equation of state from the energy-volume diagram. The enthalpy is given per formula unit of PON relative to the *ctb* modification of PON. The approximate range of pressure for the transitions is indicated by the dotted lines.

The enthalpy-pressure diagram is depicted in Figure S7.7. The points of intersection for the different *coe*-PON curves with the chosen cristobalite PON curve indicate the pressure at which the free energy and enthalpy is identical for both phases and beyond which the phase transition to *coe*-PON becomes thermodynamically favored.
From Figure S7.7 a transition pressure for PON of about 7.5 GPa can be extracted for the transition of the energetically lowest cristobalite model to the energetically lowest coesite model, while the highest possible pressure is determined to about 10.5 GPa for the transition to the energetically most unfavorable coesite model. While we cannot guarantee having examined every possible modification for the ordering variants of coesite and cristobalite, the broad variety of chosen PO_2N_2-tetrahedron-models are all in good agreement with the experimental observation on the formation of coesite-like PON at pressures of 15 GPa. The enthalpy curves of all models of *coe*-PON are energetically very close in terms of enthalpy, and do intersect each other beyond pressures of 12.5 GPa, further corroborating the observed statistical contribution of the O and N positions in *coe*-PON.

7.3.10 References

[1] R. Klement, O. Koch, Phosphoroxy-triamid und Phosphorthio-triamid, *Chem. Ber.* **1954**, *87*, 333–340.

[2] N. Kawai, S. Endo, The Generation of Ultrahigh Hydrostatic Pressures by a Split Sphere Apparatus, *Rev. Sci. Instrum.* **1970**, *41*, 1178–1181.

[3] D. Walker, M. A. Carpenter, C. M. Hitch, Some simplifications to multianvil devices for high pressure experiments, *Am. Mineral.* **1990**, *75*, 1020–1028.

[4] D. Walker, Lubrication, gasketing, and precision in multianvil experiments, *Am. Mineral.* **1991**, *76*, 1092–1100.

[5] D. C. Rubie, Characterising the sample environment in multianvil high-pressure experiments, *Phase Transitions* **1999**, *68*, 431–451.

[6] H. Huppertz, Multianvil high-pressure / high-temperature synthesis in solid state chemistry, *Z. Kristallogr.* **2004**, *219*, 330–338.

[7] A. A. Coelho, *TOPAS-Academic*, Version 4.1, Coelho Software, Brisbane (Australia), **2007**.

[8] A. A. Coelho, Indexing of powder diffraction patterns by iterative use of singular value decomposition, *J. Appl. Crystallogr.* **2003**, *36*, 86–95.

[9] a) G. Oszlányi, A. Sütő, *Ab initio* structure solution by charge flipping, *Acta Crystallogr., Sect. A: Found. Crystallogr.* **2004**, *60*, 134–141; b) G. Oszlányi, A. Sütő, The charge flipping algorithm, *Acta Crystallogr., Sect. A: Found. Crystallogr.* **2008**, *64*, 123–134; c) A. A. Coelho, A charge-flipping algorithm incorporating the tangent formula for solving difficult structures, *Acta Crystallogr., Sect. A: Found. Crystallogr.* **2007**, *63*, 400–406.

[10] R. W. Cheary, A. Coelho, A fundamental parameters approach to X-ray line-profile fitting, *J. Appl. Crystallogr.* **1992**, *25*, 109–121.

[11] R. W. Cheary, A. A. Coelho, J. P Cline, Fundamental Parameters Line Profile Fitting in Laboratory Diffractometers, *J. Res. Natl. Inst. Stand.Technol.* **2004**, *109*, 1–25.

[12] M. Järvinen, Application of symmetrized harmonics expansion to correction of the preferred orientation effect, *J. Appl. Crystallogr.* **1993**, *26*, 525–531.

[13] G. V. Gibbs, C.T. Prewitt, K.J. Baldwin, A study of the structural chemistry of coesite, *Z. Kristallogr., Kristallgeom., Kristallphys., Kristallchem.* **1977**, *145*, 108–123.

[14] D. Baumann, W. Schnick, Pentacoordinate Phosphorus in a High-Pressure Polymorph of Phosphorus Nitride Imide $P_4N_6(NH)$, *Angew. Chem. Int. Ed.* **2014**, *53*, 14490–14493; *Angew. Chem.* **2014**, *126*, 14718–14721.

[15] J. P. Perdew, K. Burke, M. Ernzerhof, Generalized Gradient Approximation Made Simple, *Phys. Rev. Lett.* **1996**, *77*, 3865–3868.

[16] J. P. Perdew, K. Burke, M. Ernzerhof, Generalized Gradient Approximation Made Simple [*Phys. Rev. Lett.* **1996**, *77*, 3865], *Phys. Rev. Lett.* **1997**, *78*, 1396.

[17] P. E. Blöchl, Projector augmented-wave method, *Phys. Rev. B: Condens. Matter Mater. Phys.* **1994**, *50*, 17953–17979.

[18] G. Kresse, D. Joubert, From ultrasoft pseudopotentials to the projector augmented-wave method, *Phys. Rev. B: Condens. Matter Mater. Phys.* **1999**, *59*, 1758–1775.

[19] G. Kresse, J. Hafner, *Ab initio* molecular dynamics for liquid metals, *Phys. Rev. B: Condens. Matter Mater. Phys.* **1993**, *47*, 558–561.

[20] G. Kresse, J. Hafner, *Ab initio* molecular-dynamics simulation of the liquid-metal-amorphous-semiconductor transition in germanium, *Phys. Rev. B: Condens. Matter Mater. Phys.* **1994**, *49*, 14251–14269.

[21] G. Kresse, J. Furthmüller, Efficiency of *ab-initio* total energy calculations for metals and semiconductors using a plane-wave basis set, *Comput. Mater. Sci.* **1996**, *6*, 15–50.

[22] J. E. Jaffe, J. A. Snyder, Z. Lin, A. C. Hess, LDA and GGA calculations for high-pressure phase transitions in ZnO and MgO, *Phys. Rev. B: Condens. Matter Mater. Phys.* **2000**, *62*, 1660–1665.

[23] P. Kroll, W. Schnick, A Density Functional Study of Phosphorus Nitride P_3N_5: Refined Geometries, Properties, and Relative Stability of α-P_3N_5 and γ-P_3N_5 and a Further Possible High-Pressure Phase δ-P_3N_5 with Kyanite-Type Structure, *Chem. Eur. J.* **2002**, *8*, 3530–3537.

[24] H. J. Monkhorst, J. D. Pack, Special points for Brillouin-zone integrations, *Phys. Rev. B: Solid State* **1976**, *13*, 5188–5192.

[25] L. Boukbir, R. Marchand, Y. Laurent, P. Bacher, G. Roult, Preparation and time-of-flight neutron diffraction study of the cristobalite-type PON phosphorus oxynitride, *Ann. Chim. Fr.* **1989**, *14*, 475–481.

[26] F. D. Murnaghan, The Compressibility of Media under Extreme Pressures, *Proc. Natl. Acad. Sci. USA* **1944**, *30*, 244–247.

8 Stishovite's Relative: A Post-Coesite Form of Phosphorus Oxonitride

published in: *Angew. Chem. Int. Ed.* **2018**, *57*, 6691–6695; *Angew. Chem.* **2018**, *130*, 6801–6805.

authors: Sebastian Vogel, Dominik Baumann, Robin Niklaus, Elena Bykova, Maxim Bykov, Natalia Dubrovinskaia, Leonid Dubrovinsky and Wolfgang Schnick

DOI: 10.1002/anie.201803610

Acknowledgment: Reprinted (adapted) with permission from *Angewandte Chemie*.

Abstract Phosphorus oxonitride (PON) is isoelectronic with SiO_2 and may exhibit a similar broad spectrum of intriguing properties as silica. However, PON has only been sparsely investigated under high-pressure conditions and there has been no evidence on a PON polymorph with a coordination number of P greater than 4. Herein, we report a post-coesite (pc) PON polymorph exhibiting a stishovite-related structure with P in a (5+1) coordination. The *pc*-PON was synthesized using the multianvil technique and characterized by powder X-ray diffraction, solid-state NMR spectroscopy, TEM measurements and in situ synchrotron X-ray diffraction in diamond anvil cells. The structure model was verified by single-crystal X-ray diffraction at 1.8 GPa and the isothermal bulk modulus of *pc*-PON was determined to K_0=163(2) GPa. Moreover, an orthorhombic PON polymorph (*o*-PON) was observed under high-pressure conditions and corroborated as the stable modification at pressures above 17 GPa by DFT calculations.

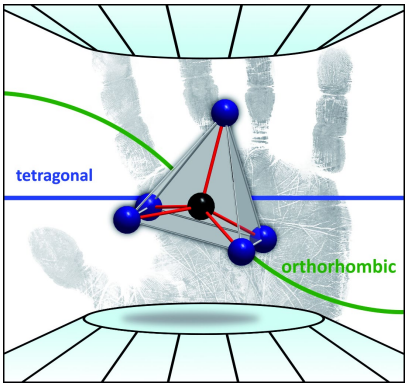

8.1 Introduction with Results and Discussion

The pressure-coordination rule, stating that the coordination number increases with an increase of pressure,[1] has already been verified for fundamental inorganic nitrides and oxides such as BN,[2] Si_3N_4,[3] P_3N_5,[4] CO_2[5–8] and SiO_2.[9–15] Respective high-pressure polymorphs show intriguing properties, such as increased incompressibility, high density or changes in types of chemical bonding. For instance, rutile-type SiO_2 (stishovite), with Si situated in an octahedral six-fold coordination by O, is one of the hardest oxides known.[9,16,17] Extensive in situ investigations in diamond anvil cells revealed post-stishovite SiO_2 polymorphs with $CaCl_2$-, α-PbO_2- and high-pressure PdF_2-type structures, which all have the motif of SiO_6 octahedra in common.[10–15] Phosphorus oxonitride PON is isoelectronic with silica and adopts cristobalite-, moganite- and quartz-type structures, which are isotypic with the eponymous SiO_2 forms.[18–20] Furthermore, an additional δ-PON modification with a unique structure related to a

theoretically predicted SiO_2 polymorph has been synthesized at 12 GPa while at 15.5 GPa a coesite-type (coe) PON form has been prepared, which hitherto represents the top end of the PON phase diagram.[21,22] PON polymorphs with an increased coordination number of P, however, seem to be feasible, considering findings from fundamental structural research on solid-state P–N and P–O compounds. Square pyramidal and trigonal bipyramidal PN_5 units have been reported in the high-pressure phases γ-P_3N_5 and γ-HP_4N_7 and six-fold coordinated P has been predicted for the high-pressure phases δ-P_3N_5 and spinel-type BeP_2N_4.[4,23–26] Recently, five- and six-fold O-coordinated P has been reported for $TiPO_4$-V and a distorted $CaCl_2$-related form of $AlPO_4$, respectively.[27,28] In contrast, high-pressure polymorphs of PON with an increased coordination number of P (CN >4), are still unknown. Considering the kinship of PON and SiO_2, a stishovite-type PON polymorph with a six-fold coordination of P may be plausible and is considered the missing link in fundamental structural research on phosphorus (oxo)nitrides.

Herein, we report on a stishovite-related post-coesite (pc) form of PON with a (5+1) coordination of P, which was prepared from cristobalite-type (cri) PON at 20 GPa using a 1000 t hydraulic press and the multianvil technique based on a modified Walker-type setup.[29,30] Energy dispersive X-ray (EDX) spectroscopy showed no other elements than P, O and N in the sample and any presence of N–H or O–H functionality was ruled out by FTIR spectroscopy. The *pc*-PON structure was solved and refined from powder X-ray diffraction (PXRD) pattern ($P4_2/mnm$ (no. 136), a = 4.6184(2), c = 2.45536(9) Å, Z = 2, R_{Bragg} = 0.021) and cell metrics were confirmed by selected area electron diffraction (SAED) tilting series.[31] *pc*-PON adopts a stishovite-related structure with one P site located in an octahedral coordination sphere of O and N (Figure 8.1a). The refined coordinates of P are close to Wyckoff position 2*a* (*m.mm*), but refinement indicated a significant displacement. Thus, P was refined at Wyckoff position 4*f* (*m.2m*), which results in a split position of P (site occupation factor (*s.o.f.*) = 0.5) with a

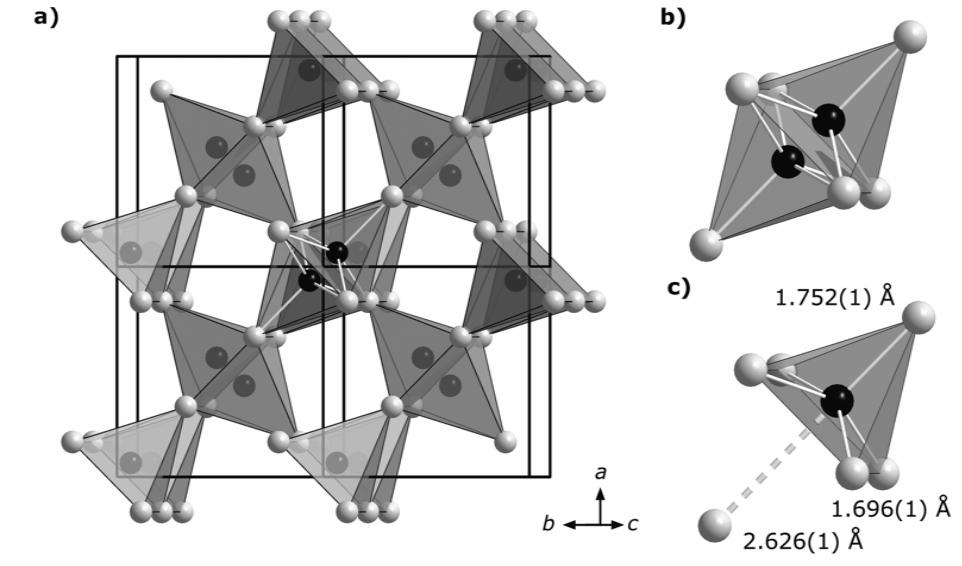

Figure 8.1 The crystal structure of pc-PON (a) shows a split position for P located in octahedral coordination by O and N (b). An occupation of 0.5 of the P position leads to a (5+1) coordination with distorted square pyramidal geometry (c). P: black, N/O: gray.

0.874(1) Å distance between the two electron density maxima (Figure 8.1b). There is, however, no evidence for any superstructure caused by a systematically ordering of P in *pc*-PON, as there were no additional reflections observed during PXRD, TEM measurements or single-crystal XRD presented below. Considering the split position, P is in a (5+1) coordination by O and N with distorted square pyramidal geometry for the first coordination sphere (Figure 8.1c). The $P(N,O)_5$ pyramids share common edges along *c* and common vertices along ⟨110⟩. The interatomic distances between P and (N,O) are 1.696(1) Å for equatorial and 1.752(1) Å for axial position, which is in good agreement with the five-fold coordinated P positions in γ-HP_4N_7 and γ−P_3N_5.[4,23] The P–(N,O) distance of the second axial (N,O) position in *pc*-PON is 2.626(1) Å corresponding to minor interactions only and thus, this (N,O) position is assigned to the second coordination sphere. The ^{31}P solid-state MAS NMR spectrum of *pc*-PON shows one broadened signal at δ = −86.9 ppm (FWHM = 20 ppm), in line with one crystallographic position of P in the *pc*-PON structure. Peak broadening may be caused by varying local N/O coordination of P and has been observed in other PON modifications before.[21,22] Moreover, statistic occupation of the split position of P can enhance peak broadening in this case.

A simplified description of the *pc*-PON structure may be revealed by reducing the split position of P to its center of gravity, resulting in an octahedral coordination of P by N and O atoms. This simplified structure model would be isotypic with stishovite (rutile-type SiO_2) as the P(4*f, m.2m*) site (*s.o.f.* = 0.5) would be transformed into a P(2*a, m.mm*) site (*s.o.f.* = 1). Thus, *pc*-PON may be understood as the analog of stishovite in the phase diagram of PON and represents the first phosphorus oxonitride with exclusively five-fold coordination of P. More detailed information on the synthesis of *pc*-PON and its characterization by PXRD, TEM, EDX, NMR and FTIR is provided in the Supporting Information.
In order to investigate *pc*-PON on its elastic properties, in situ XRD measurements with synchrotron radiation in diamond anvil cells (DAC) were performed. At an initial pressure of 1.8 GPa a single-crystal data set was collected, which verifies the structure model presented above.[32] Owing to the measuring geometry of DACs the single-crystal (SC) XRD data set is incomplete (77 %). A comparison of the electron density maps and respective standard deviations, however, indicate that PXRD and SC-XRD refinements are tantamount in quality and accuracy, as presented in the Supporting Information.

Subsequently, 16 PXRD patterns up to a maximum pressure of almost 40 GPa were collected in which the PXRD pattern of *pc*-PON is preserved up to a pressure of approximately 20 GPa. At pressures exceeding 20 GPa, however, a new phase is observed, as reflections in the region 10.0° < 2θ < 11.5° change significantly (Figure 8.2). The coexistence of both phases at 19.6 GPa is a strong indication for a second order phase transition, which was described by a *translationengleiche* symmetry reduction (*t*2) to the orthorhombic crystal system ($P4_2/mnm$ (no. 136) → *Pnnm* (no. 58)). In order to gain further information on the nature of the tetragonal → orthorhombic phase transition, the recovered sample was re-measured at ambient conditions, showing tetragonal symmetry again. Thus, the orthorhombic (o) PON phase is solely stabilized at high pressures and may be the initial product of the multianvil

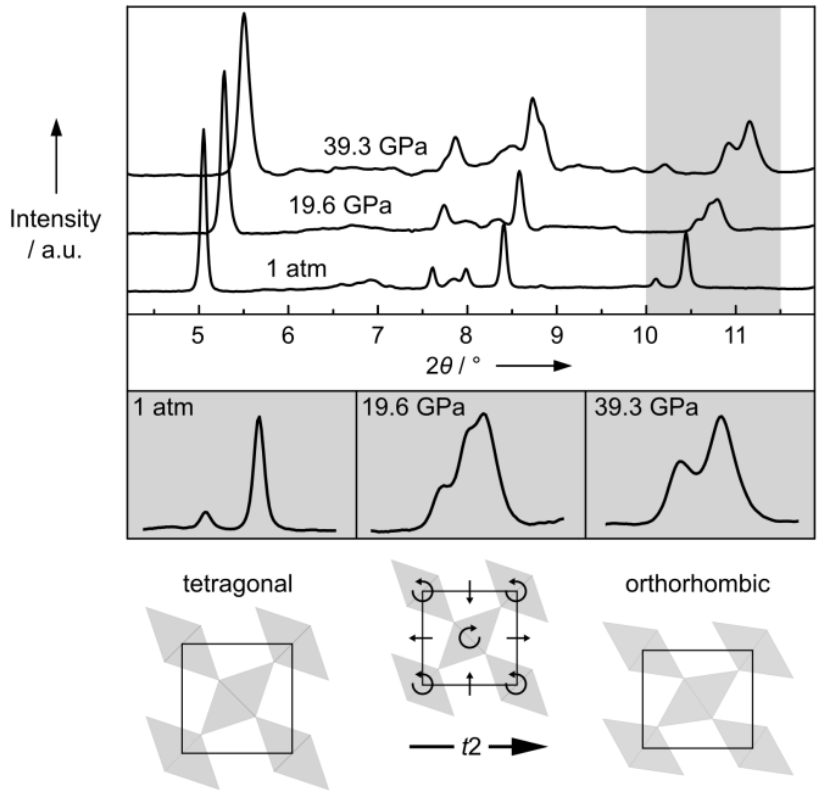

Figure 8.2 Exemplary PXRD patterns from synchrotron measurements at high-pressure conditions (λ = 0.28874 Å) with enlarged regions of interest and a schematic illustration of the tetragonal → orthorhombic phase transition assumed for PON.

synthesis at 20 GPa, while the tetragonal *pc*-PON phase might form upon pressure quenching. In turn, *pc*-PON is unstable at ambient conditions as well, but kinetically inert towards transformation to *cri*-PON, as indicated by temperature-dependent PXRD.

This reversible tetragonal → orthorhombic phase transition of PON is of remarkable similarity to the stishovite ($P4_2/mnm$) → $CaCl_2$-type SiO_2 (*Pnnm*) phase transition of silica, which is characterized by an alternating tilting of the SiO_6 octahedra in the *a*-*b* plane with increasing pressure.[10,33] Considering a spontaneous strain analysis of *pc*- and *o*-PON, the phase transition in PON appears to proceed in a similar way, suggesting an alternating tilting of the P coordination polyhedra and a $CaCl_2$-related structure for *o*-PON (Figure 8.2).[33] More detailed information on the experimental setup and the synchrotron measurements as well as on the spontaneous strain formalism is provided in the Supporting Information.

Lattice parameters of *pc*- and *o*-PON were refined from PXRD data with the method of Le Bail using tetragonal ($P4_2/mnm$, $p < 20$ GPa) and orthorhombic (*Pnnm*, $p > 20$ GPa) metrics, respectively (Figure 8.3). Subsequently, the isothermal bulk modulus K_0 of *pc*-PON was determined to 163(2) GPa from equation of state and with that, *pc*-PON exhibits a twice as high bulk modulus than cri-PON ($K_0 \approx 80$ GPa).[34] However, *pc*-PON seems to be significantly more compressible than stishovite ($K_0 \approx 310$ GPa), which may be due to the (5+1) coordination polyhedra of P being less rigid than the SiO_6 octahedra.[33]

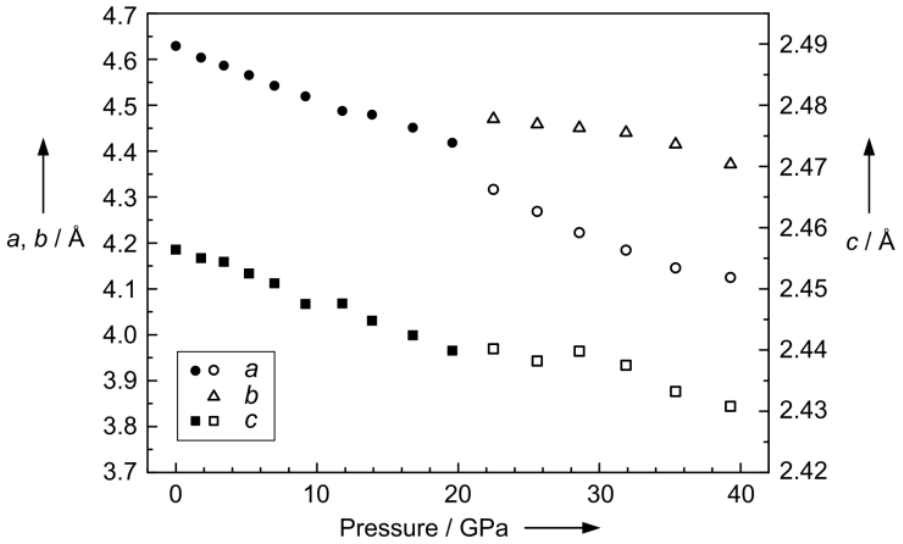

Figure 8.3 Refined lattice parameters of pc- and o-PON as a function of pressure.

Furthermore, the lattice parameter *a* was found to be notably more compressible than *c* ($K_0(a^3)$ = 109(2) GPa, $K_0(c^3)$ = 927(35) GPa), which may be an effect of the $P(N,O)_5$ pyramids sharing common vertices along ⟨110⟩, but common edges along *c*. Thus, a decrease in volume upon compression in *pc*-PON is mostly effected by a contraction of the cell along *a*, which in turn corresponds to an axial compression of the $P(N,O)_{5+1}$ polyhedra and a decrease of the axial P–(O,N) interatomic distances. Consequently, a hitherto unreported regular six-fold coordination of P in phosphorus (oxo)nitrides might be plausible for PON at sufficiently high pressure and may lead to a significant increase of its incompressibility and bulk modulus. More detailed information on the elastic properties of *pc*-PON is provided in the Supporting Information.

To confirm the experimental findings and to corroborate *o*-PON as the high-pressure polymorph, DFT calculations within the generalized gradient approximation (GGA) were performed. Accounting for the split position of P a 2 × 2 × 2 supercell was constructed with P at the center of the N/O octahedra and different charge neutral N/O-ordering models were constructed to approximate statistical N/O-disorder. Disregarding unreasonable or computationally collapsing structures, relaxation of the supercell resulted in an alternating displacement of P atoms from the center of the $P(N/O)_6$ octahedra, in line with the experimental findings of the split position of P (Figure 8.4a). This systematic ordering of P appears as a coupled feature of the introduced N/O-ordering, as the displacement of each P site is systematically directed towards an axial N position. As a result N and O are found exclusively in three- and two-fold coordination, respectively, as expressed by the Niggli formula $^{3}_{\infty}[P^{[5]}O^{[2]}N^{[3]}]$.[35] Thus, the axial P–N interaction seems to be more favorable than the axial P–O interaction. Concerning the experimental data presented above, there are, however, no indications of a superstructure caused by a systematic ordering of P. Considering the favored axial P–N interaction this random distribution of P may be correlated with a N/O-disorder in *pc*-PON.

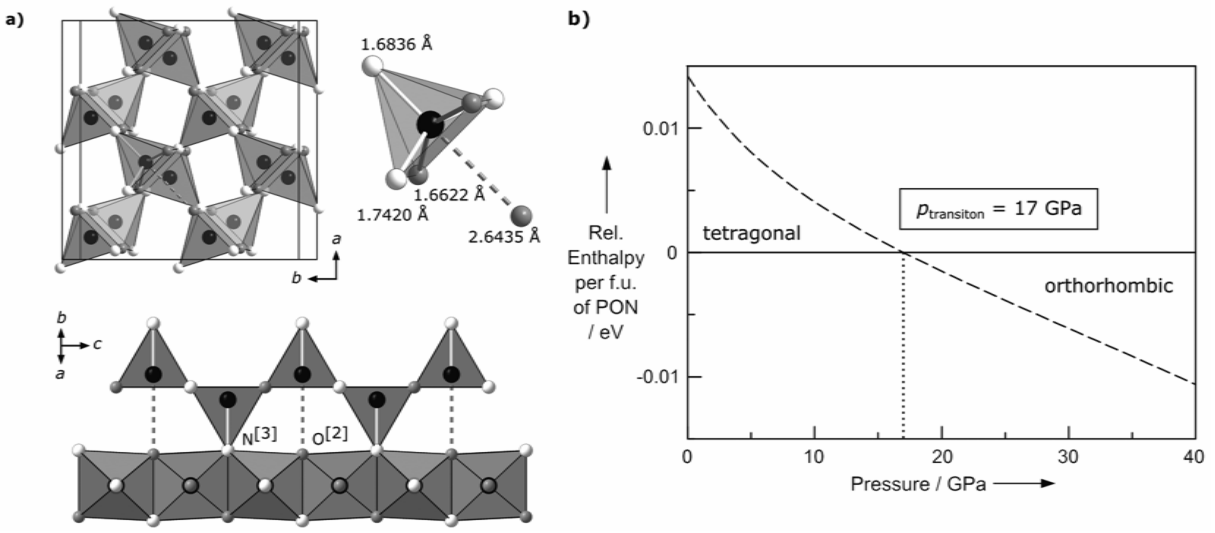

Figure 8.4 Approximated structure model of pc-PON from structure relaxation with N/O-order used for DFT calculations (a). P: black, O: gray, N: white. Relative enthalpy plot with transition pressure of 17 GPa derived from calculated *E*-*V* data of *pc*- and *o*-PON (b).

The tetragonal structure model was used for construction of an orthorhombic model and subsequent energy-volume calculations of both cells. The respective total energies of both phases corroborate *o*-PON the stable modification above 17 GPa. The transition pressure was determined from the relative enthalpy plot (Figure 8.4b) and is in accordance with the experimental findings, considering the approximated structure model used for the DFT calculations. More detailed information on the theoretical study of both PON polymorphs is provided in the Supporting Information.

Recapitulating, the phase diagram of PON is extended by two high-pressure polymorphs. *pc*-PON adopts a stishovite-related structure with a split position of P in a (5+1) coordination and has been considered the missing link in fundamental structural research on phosphorus (oxo)nitrides, previously. In addition, *o*-PON is found to be the stable polymorph at pressures >20 GPa, which has been proven by ab initio calculations, as well. In turn, P is just on the brink of a regular six-fold coordination in PON polymorphs and its experimental evidence will be the great goal of future high-pressure investigations.

8.2 References

[1] A. Neuhaus, Synthesis, Structural Behavior, and Valence State of Inorganic Matter in the Realm of Higher and Highest Pressure, *Chimia* **1964**, *18*, 93–103.

[2] R. H. Wentorf, Cubic Form of Boron Nitride, *J. Chem. Phys.* **1957**, *26*, 956–957.

[3] A. Zerr, R. Riedel, G. Miehe, G. Serghiou, M. Schwarz, E. Kroke, H. Fueß, P. Kroll, R. Boehler, Synthesis of cubic silicon nitride, *Nature* **1999**, *400*, 340–342.

[4] K. Landskron, H. Huppertz, J. Senker, W. Schnick, High-Pressure Synthesis of γ-P_3N_5 at 11 GPa and 1500 °C in a Multianvil Assembly: A Binary Phosphorus(V) Nitride with a Three-Dimensional Network Structure from PN_4 Tetrahedra and Tetragonal PN_5 Pyramids, *Angew. Chem. Int. Ed.* **2001**, *40*, 2643–2645; *Angew. Chem.* **2001**, *113*, 2713–2716.

[5] F. Datchi, B. Mallick, A. Salamat, S. Ninet, Structure of Polymeric Carbon Dioxide CO_2−V, *Phys. Rev. Lett.* **2012**, *108*, 125701.

[6] V. Iota, C. S. Yoo, H. Cynn, Quartzlike Carbon Dioxide: An Optically Nonlinear Extended Solid at High Pressures and Temperatures, *Science* **1999**, *283*, 1510–1513.

[7] A. Sengupta, C.-S. Yoo, Coesite-like CO_2: An analog to SiO_2, *Phys. Rev. B: Condens. Matter Mater. Phys.* **2010**, 82, 012105.

[8] V. Iota, C.-S. Yoo, J.-H. Klepeis, Z. Jenei, W. Evans, H. Cynn, Six-fold coordinated carbon dioxide VI, *Nat. Mater.* **2007**, *6*, 34–38.

[9] S. M. Stishov, S. V. Popova, A new dense modification of silica, *Geokhimiya* **1961**, *10*, 837-839.

[10] Y. Tsuchida, T. Yagi, A new, post-stishovite highpressure polymorph of silica, *Nature* **1989**, *340*, 217–220.

[11] L. S. Dubrovinsky, S. K. Saxena, P. Lazor, R. Ahuja, O. Eriksson, J. M. Wills, B. Johansson, Experimental and theoretical identification of a new high-pressure phase of silica, *Nature* **1997**, *388*, 362–365.

[12] N. A. Dubrovinskaia, L. S. Dubrovinsky, S. K. Saxena, F. Tutti, S. Rekhi, T. Le Bihan, Direct transition from cristobalite to post-stishovite α-PbO_2-like silica phase, *Eur. J. Mineral.* **2001**, *13*, 479–483.

[13] L. S. Dubrovinsky, N. A. Dubrovinskaia, S. Saxena, F. Tutti, S. Rekhi, T. Le Bihan, G. Shen, J. Hu, Pressure-induced transformations of cristobalite, *Chem. Phys. Lett.* **2001**, *333*, 264–270.

[14] P. Dera, C. T. Prewitt, N. Z. Boctor, R. J. Hemley, Characterization of a high-pressure phase of silica from the Martian meteorite Shergotty, *Am. Mineral.* **2002**, *87*, 1018–1023.

[15] Y. Kuwayama, K. Hirose, N. Sata, Y. Ohishi, The Pyrite-Type High-Pressure Form of Silica, *Science* **2005**, *309*, 923–925.

[16] J.-M. Léger, J. Haines, M. Schmidt, J. P. Petitet, A. S. Pereira, J. A. H. da Jornada, Discovery of hardest known oxide, *Nature* **1996**, *383*, 401.

[17] L. S. Dubrovinsky, N. A. Dubrovinskaia, V. Swamy, J. Muscat, N. M. Harrison, R. Ahuja, B. Holm, B. Johansson, The hardest known oxide, *Nature* **2001**, *410*, 653–654.

[18] L. Boukbir, R. Marchand, Y. Laurent, P. Bacher, G. Roult, Preparation and time-of-flight neutron diffraction study of the cristobalite-type PON phosphorus oxynitride, *Ann. Chim. Fr.* **1989**, *14*, 475–481.

[19] J. Haines, C. Chateau, J. M. Léger, A. L. Sauze, N. Diot, R. Marchand, S. Hull, Crystal structure of moganite-type phosphorus oxynitride: relationship to other twinned-quartz-based structures, *Acta Crystallogr. Sect. B: Struct. Sci.* **1999**, *55*, 677–682.

[20] J. M. Léger, J. Haines, L. S. de Oliveira, C. Chateau, A. L. Sauze, R. Marchand, S. Hull, Crystal structure and high pressure behaviour of the quartz-type phase of phosphorus oxynitride PON, *J. Phys. Chem. Solids* **1999**, *60*, 145–152.

[21] D. Baumann, S. J. Sedlmaier, W. Schnick, An Unprecedented AB2 Tetrahedra Network Structure Type in a High-Pressure Phase of Phosphorus Oxonitride PON, *Angew. Chem. Int. Ed.* **2012**, *51*, 4707–4709; *Angew. Chem.* **2012**, *124*, 4785–4787.

[22] D. Baumann, R. Niklaus, W. Schnick, A High-Pressure Polymorph of Phosphorus Oxonitride with the Coesite Structure, *Angew. Chem. Int. Ed.* **2015**, *54*, 4388–4391; *Angew. Chem.* **2015**, *127*, 4463–4466.

[23] D. Baumann, W. Schnick, Pentacoordinate Phosphorus in a High-Pressure Polymorph of Phosphorus Nitride Imide $P_4N_6(NH)$, *Angew. Chem. Int. Ed.* **2014**, *53*, 14490–14493; *Angew. Chem.* **2014**, *126*, 14718–14721.

[24] P. Kroll, W. Schnick, A Density Functional Study of Phosphorus Nitride P_3N_5: Refined Geometries, Properties, and Relative Stability of α-P_3N_5 and γ-P_3N_5 and a Further Possible High-Pressure Phase δ-P_3N_5 with Kyanite-Type Structure, *Chem. Eur. J.* **2002**, *8*, 3530–3537.

[25] F. J. Pucher, S. R. Römer, F. W. Karau, W. Schnick, Phenakite-Type BeP_2N_4—A Possible Precursor for a New Hard Spinel-Type Material, *Chem. Eur. J.* **2010**, *16*, 7208–7214.

[26] W. Y. Ching, S. Aryal, P. Rulis, W. Schnick, Electronic structure and physical properties of the spinel-type phase of BeP_2N_4 from all-electron density functional calculations, *Phys. Rev. B: Condens. Matter Mater. Phys.* **2011**, *83*, 155109.

[27] M. Bykov, E. Bykova, M. Hanfland, H.-P. Liermann, R. K. Kremer, R. Glaum, L. S. Dubrovinsky, S. van Smaalen, High-Pressure Phase Transformations in $TiPO_4$: A Route to Pentacoordinated Phosphorus, *Angew. Chem. Int. Ed.* **2016**, *55*, 15053–15057; *Angew. Chem.* **2016**, *128*, 15277–15281.

[28] J. Pellicer-Porres, A. M. Saitta, A. Polian, J. P. Itie, M. Hanfland, Six-fold-coordinated phosphorus by oxygen in $AlPO_4$ quartz homeotype under high pressure, *Nat. Mater.* **2007**, *6*, 698–702.

[29] D. Walker, Lubrication, gasketing, and precision in multianvil experiments, *Am. Mineral.* **1991**, *76*, 1092–1100.

[30] H. Huppertz, Multianvil high-pressure / high-temperature synthesis in solid state chemistry, *Z. Kristallogr.* **2004**, *219*, 330–338.

[31] Crystal data of *pc*-PON from PXRD refinement (p = 1 atm): M = 60.98 g·mol^{-1}, tetragonal, $P4_2/mnm$ (no. 136), a = 4.6184(2) and c = 2.45536(9) Å, V = 52.694(4) Å^3, Z = 2, ρ = 3.843 g·cm^{-3}, μ = 17.54 cm^{-1}, Mo-$K_{\alpha1}$-radiation (λ = 0.71073 Å), T = 293 K, 97 measured reflections, 34 parameters, Stoe StadiP powder diffractometer with MYTHEN 1K Si strip detector and Ge(111) monochromator, peak shape modelled by fundamental parameters approach,[36,37] background function: shifted Chebychev (19 parameters), R_{Bragg} = 0.02108, R_p = 0.03484, R_{wp} = 0.04621, R_{exp} = 0.03484, *GoF* = 1.327. Further information on the crystal structure of *pc*-PON may be obtained from the Fachinformationszentrum Karlsruhe, 76344 Eggenstein-Leopoldshafen, Germany (fax: (+49)7247-808-666; e-mail: crysdata@fiz-karlsruhe.de) on quoting the deposition number CSD-433717.

[32] Crystal data of *pc*-PON from single-crystal XRD refinement (p = 1.8 GPa): M = 60.98 g·mol^{-1}, tetragonal, $P4_2/mnm$ (no. 136), a = 4.6027(3) and c = 2.4560(3) Å, V = 52.030(9) Å^3, Z = 2, ρ = 3.892 g·cm^{-3}, μ = 1.8 cm^{-1}, synchrotron radiation (PETRAIII, DESY, Hamburg, Germany, λ = 0.28874 Å), T = 293 K, 244 observed reflections, 113 independent reflections, 9 parameters, R_{int} = 0.0463, R_σ = 0.0513, R_1 = 0.0513, wR_2 = 0.1110, *GoF* = 1.343, residual electron density 0.602, −0.601 *e*·Å^{-3}. Further information on the crystal structure of *pc*-PON may be obtained from the Fachinformationszentrum Karlsruhe, 76344 Eggenstein-Leopoldshafen, Germany (fax: (+49)7247-808-666; e-mail: crysdata@fiz-karlsruhe.de) on quoting the deposition number CSD-434035.

[33] D. Andrault, R. J. Angel, J. L. Mosenfelder, T. Le Bihan, Equation of state of stishovite to lower mantle pressures, *Am. Mineral.* **2003**, *88*, 301–307.

[34] K. J. Kingma, R. E. G. Pacalo, P. F. McMillan, High-pressure stability of the cristobalite framework in PON and PN(NH), *Eur. J. Solid State Inorg. Chem.* **1997**, *34*, 679–692.

[35] U. Müller, *Anorganische Strukturchemie*, *6th Ed.*, Vieweg + Teubner, **2008**, p. 246.

[36] R. W. Cheary, A. Coelho, A fundamental parameters approach to X-ray line-profile fitting, *J. Appl. Crystallogr.* **1992**, *25*, 109–121.

[37] R. W. Cheary, A. A. Coelho, J. P Cline, Fundamental Parameters Line Profile Fitting in Laboratory Diffractometers, *J. Res. Natl. Inst. Stand.Technol.* **2004**, *109*, 1–25.

8.3 Supporting Information

Experimental Procedures

8.3.1 Preparation of Starting Materials

P_3N_5 was prepared according to Stock and Hoffmann from P_4S_{10} (Acros Organics, >98%) in a continuous flow of dry ammonia (5.0, Air Liquide).[1] P_4S_{10} was loaded in a fused silica boat and saturated by a continuous flow of dry ammonia at 298 K for 4 h before it was heated at 1123 K for another 4 h. The product was washed with concentrated HCl, de-ionized water, and ethanol then dried in vacuum to yield an orange powder. Phase purity was confirmed by PXRD and FTIR spectroscopy. cri-PON was prepared according to a modified literature protocol by heating stoichiometric amounts of P_3N_5 and P_4O_{10} in a corundum crucible for 48 h at 1053 K in a sealed silica ampoule filled with argon.[2] Phase purity was confirmed by PXRD and FTIR spectroscopy.

8.3.2 High-Pressure High-Temperature Synthesis

pc-PON was prepared in a high-pressure high-temperature procedure using a 1000 t hydraulic press (Voggenreiter, Mainleus, Germany) and the multianvil technique based on a modified Walker-type setup.[3,4] As a starting material cri-PON was ground, packed in a capsule and sealed with a cap both consisting of hexagonal boron nitride (Henze, Kempten, Germany). The capsule was placed in the center of two graphite tubes using two MgO spacers (Cesima Caramics, Wust-Fischbach, Germany). The assembly was put in the center of an Cr_2O_3 doped MgO octahedron (5% Cr_2O_3, edge length 10 mm, Ceramic Substrates & Components Ltd, Isle of Wight, United Kingdom) equipped with a sleeve of ZrO_2 (Cesima Ceramics, Wust-Fischbach, Germany) acting as a thermal insulator. To enable electric contact between the surrounding anvils and the graphite tubes two molybdenum plates were used. The as-prepared octahedron was compressed between eight truncated cubes of cobalt doped tungsten carbide (6% Co, truncated edge length 5 mm, Hawedia, Marklkofen, Germany) and the sample was heated by an electric resistance heating with a maximal power of 3000 W. The assembly was compressed to 20 GPa within 11 h and than heated up to 1500 K within 10 min. The temperature was kept for another 15 min before the heating was turned off and the sample was slowly decompressed within 33 h. *pc*-PON was isolated as an air- and moisture-stable gray crystalline powder.

8.3.3 Powder X-ray Diffraction (PXRD)

Powder X-ray diffraction measurements were performed on a STOE STADI P powder diffractometer (STOE & Cie GmbH, Darmstadt, Germany; Mo-$K_{\alpha1}$-radiation, λ = 0.71073 Å) equipped with a Ge(111) monochromator and MYTHEN 1K Si-strip detector (Dectrics, Baden-Daettwil, Switzerland) in modified Debye-Scherrer geometry. For measurements the sample was loaded into tube capillaries (Hilgenberg, Malsfeld, Germany) with an outer diameter of 0.2 mm. Indexing, structure solution and refinement from the PXRD pattern was performed using the TOPAS-Academic V4.1 software.[5] Indexing was achieved with the SVD-algorithm and intensities were extracted with the Pawley-method.[6,7] The charge-flipping algorithm was used

for structure solution and the *pc*-PON structure model was subsequently refined with the Rietveld method.[8–11] Peak profiles were modeled using the fundamental parameters approach and a possible preferred orientation of crystals was accounted for with a spherical harmonics function of fourth order.[12] The background was described using a shifted Chebyshev polynomial. Absorption was treated with a capillary absorption correction. Temperature-dependent PXRD data were collected on a STOE STADI P powder diffractometer (STOE & Cie GmbH, Darmstadt, Germany; Mo-$K_{\alpha1}$-radiation, λ = 0.71073 Å) equipped with a Ge(111) monochromator, a STOE resistance graphite furnace and an IP-PSD detector. The sample was loaded in a fused silica capillary (Hilgenberg, Malsfeld, Germany) with an outer diameter of 0.5 mm and heated from 298 to 1073 K in steps of 20 K with a rate of 5 K·min^{-1} under Ar atmosphere. The temperature was held constant for data collection.

8.3.4 Transmission Electron Microscopy (TEM)

TEM experiments were performed on a Titan 80–300 (FEI, USA) with a field emission gun operated at 300 kV. EDX spectra were recorded on a TOPS 30 EDX spectrometer (EDAX, Germany). Bright field images as well as selected area electron diffraction (SAED) patterns were recorded using an UltraScan 1000 camera (Gatan, USA, resolution: 2k×2k). Corresponding data were processed and evaluated with the software ES Vision and Digital Micrograph.[13,14] The PON crystals were ground in absolute ethanol and drop-casted on copper TEM grids coated with a holey carbon film (S160, Plano GmbH, Germany) and further fixed on a double-tilt holder.

8.3.5 Computational Details

Density functional theory (DFT) calculations were conducted for both, the *pc*- and the *o*-PON phase. The structural relaxation of *pc*-PON was performed with the Vienna ab initio simulation package (VASP).[15–17] Total energies of the unit cells were converged to 10^{-6} eV/atom with residual atomic forces below 10^{-4} eV·Å^{-1}. The exchange correlation was treated within the generalized gradient approximation (GGA) of Perdew, Burke, and Ernzerhof (PBE) and the projector-augmented-wave (PAW) method.[18–21] For all calculations a plane-wave cut-off of 535 eV was used. The Brillouin zone was sampled on a *Γ*-centered *k*-mesh produced from the method of Monkhorst and Pack of 6 × 6 × 12.[22] *E*–*V* data were obtained from structural relaxations at a range of constant volumes (86 to 107%) corresponding to compression and expansion of the unit cells. A variation in lattice parameters *a* and *b* was introduced manually in order to converge tetragonal to orthorhombic PON at constant volume owing to its marginal difference in total energy. Due to the close similarity of the *E*–*V* curves, the step size in volume compression was 0.25% below 15 GPa and subsequently increased to 1% with increasing pressure. The enthalpy difference ΔH was derived from $H = E + pV$ in the volume region between 32 and 54 Å^3, with the pressure p obtained from the numerical differentiation of $p = \partial E/\partial V$.

8.3.6 Solid-State MAS NMR Spectroscopy

A ^{31}P solid-state MAS NMR spectrum was collected using a DSX Advance III 500 spectrometer (Bruker, Karlsruhe, Germany) with a magnetic field of 11.7 T, corresponding to a Larmor frequency of ν(^{31}P) = 202.5 MHz. The sample was placed in a ZrO_2 rotor of 1.3 mm in outer diameter, which was mounted in a commercial pneumatic MAS probe (Bruker, Karlsruhe, Germany) and spun at rotation frequency of ν_{rot} = 50 kHz. Experimental data were analyzed with device-specific software.

8.3.7 Fourier Transform Infrared Spectroscopy (FTIR)

The FTIR spectrum was collected on a Spectrum BX II spectrometer with DuraSampler ATR-device (Perkin Elmer) at ambient conditions.

8.3.8 Diamond Anvil Cell (DAC)

For in situ high-pressure investigations up to a maximum pressure of almost 40 GPa a BX90 diamond anvil cell (DAC) was used.[23] The DAC was equipped with Boehler-Almax type diamond anvils with 350 µm diameter culets and a rhenium gasket, which was pre-indented to a thickness of 35 µm and drilled to an inner diameter of 160 µm. Neon was used as pressure-transmitting medium and ruby spheres served as a pressure standard. The DAC was loaded with a polycrystalline particle of *pc*-PON and compressed to an initial pressure of 1.8 GPa after neon pressure-loading.

8.3.9 Synchrotron Measurements

In situ XRD experiments were performed at the extreme-conditions beamline P02.2 of PETRAIII (DESY, Hamburg, Germany).[24] The X-ray beam with a wavelength of 0.28874 Å was focused by a Kirkpatrick-Baez mirror system to a size of 1.8×1.9 µm^2 (V×H) and diffraction intensities were collected on a PerkinElmer XRD 1621 flat-panel detector. At 1.8 GPa a single-crystal data set was collected by an ω scan (ω_{max} = ±38°; $\Delta\omega$ = 0.5°; $t_{exposure}$ = 10 s). Indexing and integration of the reflection intensities were performed using CrysAlisPro software.[25] A single crystal of an orthoenstatite ($(Mg_{1.93},Fe_{0.06})(Si_{1.93},Al_{0.06})O_6$, *Pbca*, a = 8.8117(2), b = 5.18320(10), c = 18.2391(3) Å), was used to calibrate instrument model of CrysAlisPro software (sample-to-detector distance, the detector' s origin, offsets of the goniometer angles and rotation of the X-ray beam and the detector around the instrument axis). The structure was solved with SHELXT and refined in anisotropic approximation against F^2 on all data by full-matrix least squares with SHELXL.[26,27] In order to examine the behavior of *pc*-PON under high-pressure conditions a series of 16 wide scans (ω_{max} = ±20°; $\Delta\omega$ = 1°; $t_{exposure}$ = 40 s) up to a maximum pressure of almost 40 GPa were collected. Respective pressure values were determined by the ruby fluorescence method.[28,29] Powder X-ray diffraction patterns were revealed by masking single-crystal reflections from diamond and neon followed by subsequent integration using the Dioptas software.[30] Lattice parameters were determined by Le Bail refinements with Jana2006 using a pseudo-Voigt function and a manually adjusted background for profile fitting.[31]

8.3.10 Equation of State

For a quantitative evaluation of the elastic properties of *pc*-PON the *p*-*V* data were fitted by the second order Birch-Murnaghan equation (Equation 1) using the EoSFit7 software.[32–34] Herein, *V* is the volume of the unit cell at the pressure *p*, V_0 corresponds to the cell volume at a theoretical pressure of zero, and K_0 is the isothermal bulk modulus.

$$p(V) = \frac{3}{2} K_0 \left[\left(\frac{V}{V_0} \right)^{-\frac{7}{3}} - \left(\frac{V}{V_0} \right)^{-\frac{5}{3}} \right] \quad (1)$$

Results and Discussion

8.3.11 Crystal Structure of *pc*-PON from PXRD at 1 atm

Indexing of the PXRD pattern suggested tetragonal symmetry with lattice parameters *a* = 4.6184(2) and *c* = 2.45536(9) Å. Analysis of systematically absent reflections indicated space group $P4_2/mnm$ (no. 136) in which charge flipping led to identification of all atom positions, refined by a subsequent Rietveld refinement (Figure S8.1). A minor amount of γ-HP_4N_7 was not refined.[35] The increased background in the region 5°< 2θ <20° can be assigned to non-crystalline material, formed by amorphization at high-pressure conditions during synthesis. All atoms are situated on 4*f* sites with *m*.2*m* site symmetry and thus, respective *x* and *y* coordinates were constrained to one common parameter. The refined coordinates of P are close to Wyckoff position 2*a* but refinement indicated a significant displacement, which results

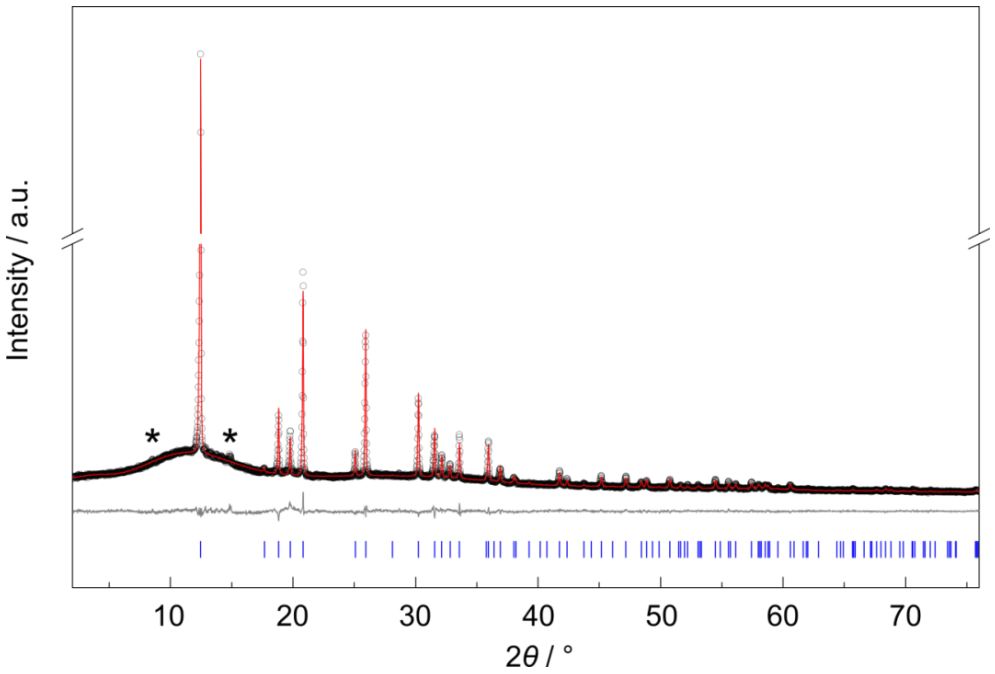

Figure S8.1 Observed (black circles) and calculated (red line) PXRD pattern (Mo-Kα_1-radiation, λ = 0.71073 Å) and difference profile (gray) from Rietveld refinement of *pc*-PON. Peak positions are marked by vertical blue lines. Tagged reflections (*) can be assigned to γ-HP_4N_7 as minor side phase.[35]

in a split position of P with a 0.874(1) Å distance between the two electron density maxima. Thus, the site occupation factor of P was set to 0.5. Accounting for the mixed anion position of N and O the isotropic atomic displacement parameters were constrained to one common parameter and the respective site occupation factors were set to 0.5 (Table S8.2).

Table S8.1 Crystallographic data on *pc*-PON based on Rietveld refinement (p = 1 atm)

Formula	**PON**
Crystal system	tetragonal
Space group (no.)	$P4_2/mnm$ (136)
Lattice parameters / Å	a = 4.62782(10)
	c = 2.46042(4)
Cell volume / Å^3	V = 52.694(4)
Formula units per cell	2
Calculated X-ray density / g·cm^{-3}	3.843
Linear absorption coefficient / cm^{-1}	17.54
Radiation	Mo-Kα_1 (λ = 0.71073 Å)
θ-range / °	1.000–38.177
Temperature / K	293
Data points	4958
Number of observed reflections	97
Number of parameters (thereof background)	34 (19)
R indices	R_{Bragg} = 0.02108
	R_p = 0.03535
	R_{wp} = 0.04621
	R_{exp} = 0.03484
Goodness of fit	1.327

Table S8.2 Refined atomic coordinates, isotropic displacement parameters and site occupation factors (*s.o.f.*) in *pc*-PON based on PXRD refinement (p = 1 atm)[a]

	x	***y***	***z***	**U_{iso} / Å^2**	**s.o.f.**
P1 (4f)	0.0668(2)	0.0668(2)	0	0.0070(3)	0.5
O1 (4f)	0.3345(2)	0.3345(2)	0	0.0045(4)	0.5
N1 (4f)	0.3345(2)	0.3345(2)	0	0.0045(4)	0.5

[a] The site occupation factors for all atoms were set to 0.5 accounting for the split position of P and the mixed anion position of N and O, respectively.

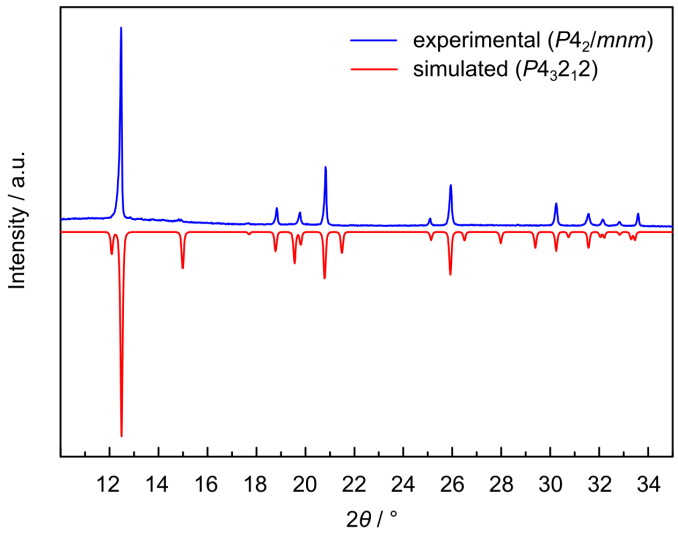

Figure S8.2 Experimental PXRD of *pc*-PON (blue) and a simulated PXRD using the modified DFT structure model presented below with a crystallographic ordering of P (red). As the simulated PXRD pattern does not match the experimental one, there is no indication for any long-range ordering of P in *pc*-PON.

A crystallographic ordering of P at its split position as suggested from DFT calculations presented below was simulated using the modified DFT structure model (Figure S8.2). The simulated PXRD pattern shows additional reflections and thus does not match the experimental one. Moreover, no superstructure reflections were observed during single-crystal XRD and TEM measurements. Thus, there is no evidence for any superstructure caused by a systematically ordering of P in *pc*-PON. Owing to a marginal X-ray scattering contrast of O and N no indications for any crystallographic N/O-ordering in *pc*-PON are obtained from PXRD measurements. Previous investigations by neutron diffraction have indicated similarly a random N/O-disorder in cri-PON, which was used as a starting material for *pc*-PON.[36] Due to small sample quantities (<15 mg per batch) additional investigations by neutron diffraction are, however, not feasible for *pc*-PON.

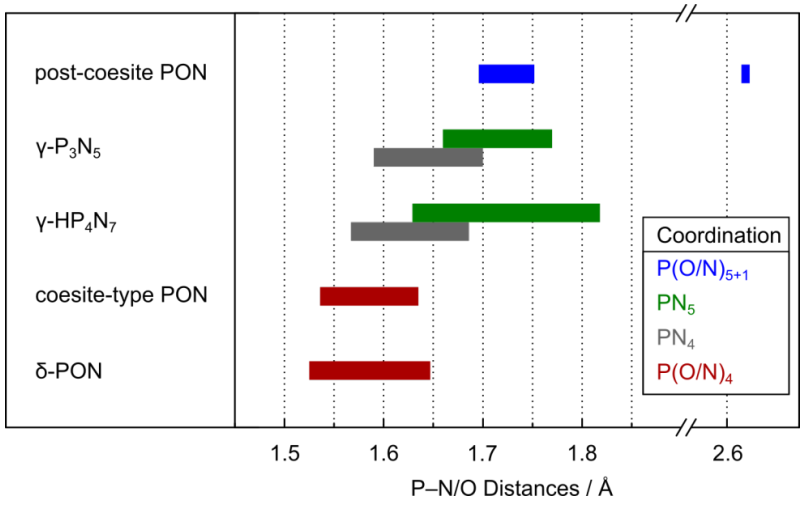

Figure S8.3 Bar chart of interatomic distances between P and N/O in *pc*-PON and related compounds.[35–39]

Table S8.3 Interatomic distances (Å) and angles (°) of *pc*-PON based on Rietveld refinement (p = 1 atm)

P1–N1	1.6964(8)	N1–P1–N1	79.36(5)
P1–N1	1.7521(12)	N1–P1–N1	104.93(5)
P1–N1	2.6263(12)	N1–P1–N1	180

Table S8.4 Calculated X-ray densities of selected SiO_2 and PON phases. The calculated X-ray density of *pc*-PON was determined to 3.843 g·cm^{-3} corresponding to an increase of 20.1% relative to *coe*-PON and 42.2% to *cri*-PON, thus, *pc*-PON represents the densest PON phase so far.[36,38] However, the increase in density upon transition is less than reported for the respective SiO_2 phases (48.2 and 85.1%), which may be attributable to the six-fold coordination of Si in stishovite, resulting in a significant higher density[40–42]

	Cristobalite	**Coesite**	**Stishovite**	***cri*-PON**	***coe*-PON**	***pc*-PON**
Density / g·cm^{-3}	2.318	2.896	4.291	2.702	3.200	3.843
Ref.	(40)	(41)	(42)	(36)	(38)	this work

8.3.12 TEM and EDX Measurements

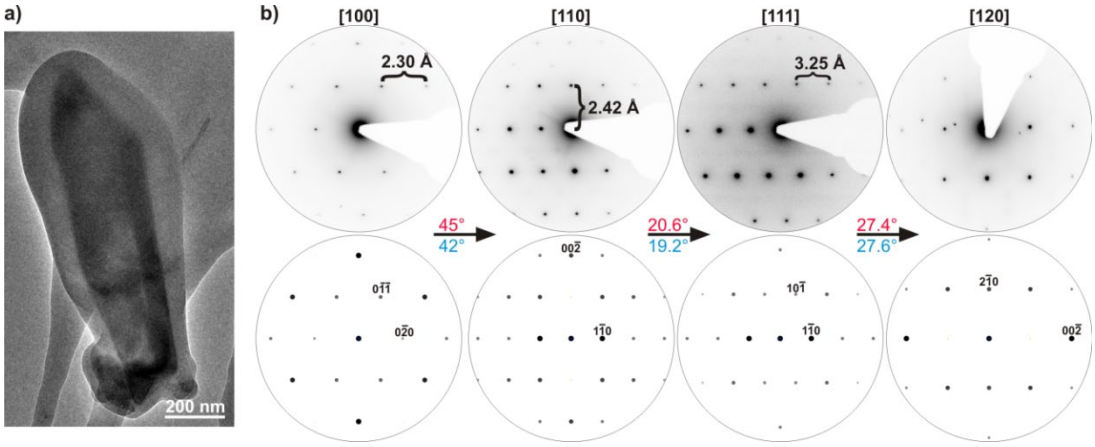

Figure S8.4 Bright-field image of *pc*-PON crystallite (a). SAED-tilting series (b, top) with corresponding simulations (b, bottom) with tilting angles (experimental blue, simulated red) and exemplarily indexed reflections. Simulations based on structural data, obtained from PXRD refinement (structure model in space group $P4_2/mnm$ with a = 4.62782(10) Å, c = 2.46042(4) Å). D-values directly measured from SAED patterns: d_{020} = 2.30 Å, d_{001} = 2.42 Å and d_{110} = 3.25 Å.

Table S8.5 TEM-EDX measurements (300 kV) of *pc*-PON in atom percent, showing no other elements than P, O and N in the sample. The measured atomic ratio, within the standard deviations and the precision of the methods for light elements, is close to P : O : N = 1 : 1 : 1

	1	2	3	4	5	6	7	mean value	ideal value
P	43.1	41.0	41.6	42.7	35.5	40.2	42.2	40.9(26)	33.0
O	30.8	31.7	31.0	32.2	29.8	31.7	31.2	31.0(9)	33.0
N	26.1	27.3	27.4	25.1	34.7	28.1	27.6	28.0(31)	33.0

8.3.13 ^{31}P Solid-State NMR and FTIR Measurements of *pc*-PON

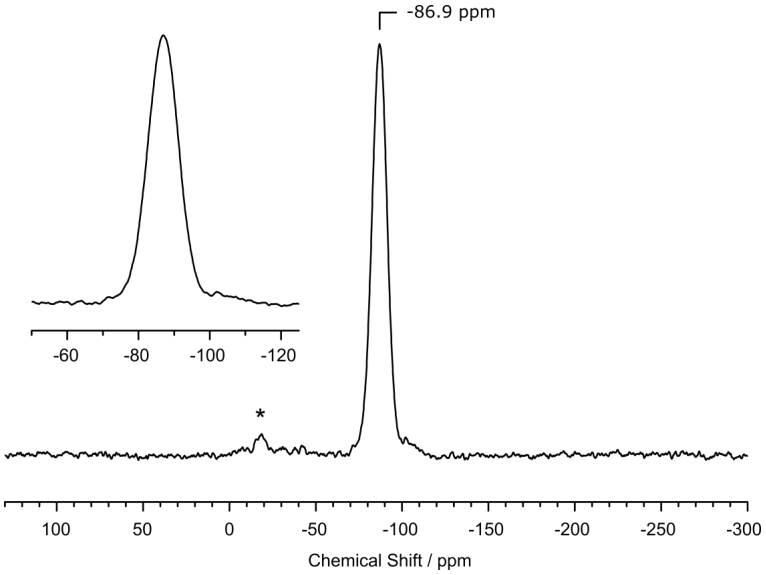

Figure S8.5 ^{31}P solid-state MAS NMR spectrum of *pc*-PON (B_0 = 11.7 T, $\nu(^{31}P)$ = 202.5 MHz, ν_{rot} = 50 kHz) showing one broadened signal at δ = −86.9 ppm ($\Delta\nu_{FWHM}$ = 20 ppm), which can be assigned to the one crystallographic position of P in the *pc*-PON structure. Peak broadening can be caused by varying local N/O coordination of P and has been observed in other PON modifications as well.[38,39] A statistic occupation of the split position of P may enhance peak broadening in this case. The marked signal at δ = −17 ppm (*) can be assigned to a minor contamination of γ-HP_4N_7.[35]

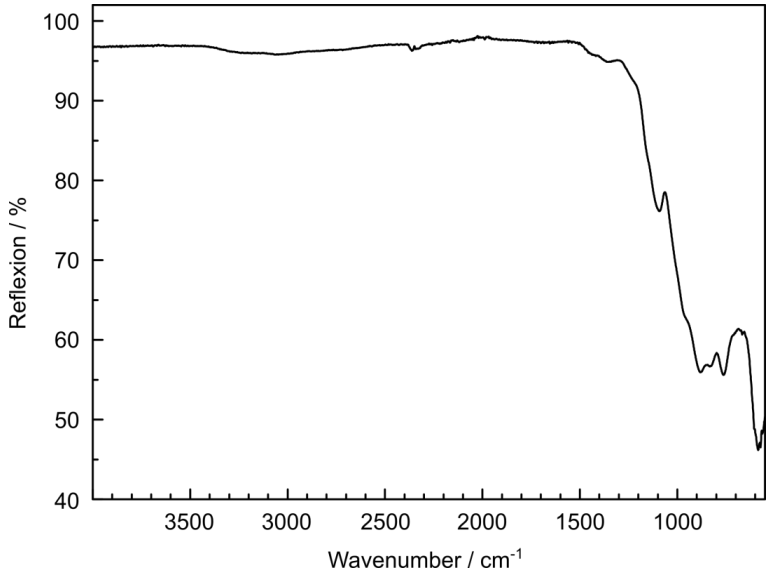

Figure S8.6 FTIR spectra of *pc*-PON (ATR). In contrast to H–P–N compounds (e.g. HPN_2, HP_4N_7) *pc*-PON does not show any significant signals in the region 2300–3300 cm^{-1}, which indicates the absence of N–H and O–H bonds in the PON sample.[35,43–47]

8.3.14 Crystal Structure of *pc*-PON from Single-crystal XRD at 1.8 GPa

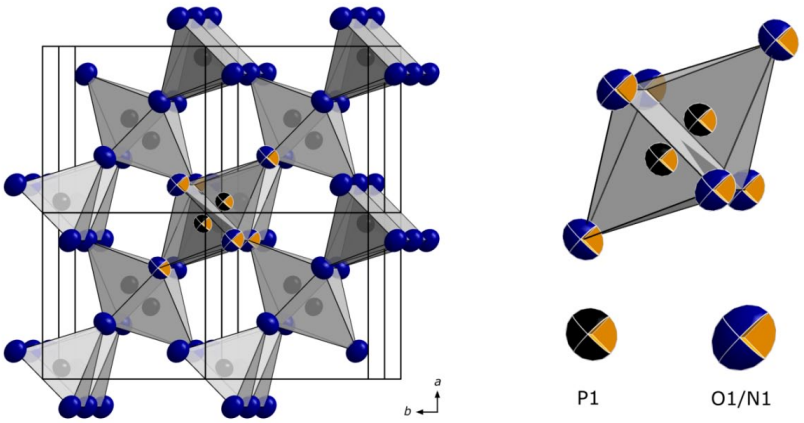

Figure S8.7 Crystal structure of *pc*-PON from single-crystal structure refinement. Ellipsoids are displayed at 90% probability level. P: black, N,O: blue.

Table S8.6 Crystallographic data on *pc*-PON based on single-crystal refinement (p = 1.8 GPa)

Formula	**PON**
Crystal system	tetragonal
Space group (no.)	$P4_2/mnm$ (136)
Lattice parameters / Å	a = 4.6027(3)
	c = 2.4560(3)
Cell volume / Å^3	V = 52.030(9)
Formula units per cell	2
Calculated X-ray density / g·cm^{-3}	3.892
Linear absorption coefficient / cm^{-1}	1.8
Device	PETRA III, DESY
Radiation	Synchrotron (λ = 0.28874 Å)
θ-range / °	2.542–17.163
Temperature / K	293
Number of observed reflections	244
Independent reflections (> 2σ)	113 (100)
Number of parameters	9
F(000)	60
Residual electron density / e·Å^{-3}	0.602; −0.601
R indices	R_{int} = 0.0463;
	R_σ = 0.0513;
	R_1 = 0.0513 (> 2σ);
	wR_2 = 0.1110 (> 2σ);
	R_1 = 0.0577 (all data);
	wR_2 = 0.1169 (all data);
Goodness of fit	1.343

Table S8.7 Refined atomic coordinates, isotropic displacement parameters and site occupation factors (*s.o.f.*) in *pc*-PON based on single-crystal refinement (p = 1.8 GPa)

	x	y	z	U_{eq} / Å^2	*s.o.f.*
P1 (4*f*)	0.0661(2)	0.0661(2)	0	0.0094(3)	0.5
O1 (4*f*)	0.3325(3)	0.3325(3)	0	0.0139(4)	0.5
N1 (4*f*)	0.3325(3)	0.3325(3)	0	0.0139(4)	0.5

Table S8.8 Anisotropic displacement parameters (Å^2) of *pc*-PON based on single-crystal refinement (p = 1.8 GPa)

	U_{11}	U_{22}	U_{33}	U_{23}	U_{13}	U_{12}
P1 (4*f*)	0.0105(4)	0.0105(4)	0.0072(5)	0	0	−0.0008(3)
O1 (4*f*)	0.0164(6)	0.0164(6)	0.0089(7)	0	0	−0.0027(6)
N1 (4*f*)	0.0164(6)	0.0164(6)	0.0089(7)	0	0	−0.0027(6)

Table S8.9 Interatomic distances (Å) and angles (°) of *pc*-PON based on single-crystal refinement (p = 1.8 GPa)

P1–N1	1.6976(14)	N1–P1–N1	79.92(8)
P1–N1	1.7341(21)	N1–P1–N1	104.68(8)
P1–N1	2.5946(21)	N1–P1–N1	180

8.3.15 Comparison of Crystallographic Data of *pc*-PON

Table S8.10 Comparison of crystallographic data of pc-PON from powder and single-crystal X-ray refinements

Formula	**PON**	
Crystal system	tetragonal	
Space group (no.)	$P4_2/mnm$ (136)	
Lattice parameters / Å	a = 4.62782(10) c = 2.46042(4)	a = 4.6027(3) c = 2.4560(3)
Cell volume / Å^3	V = 52.694(4)	V = 52.030(9)
Z	2	
Sample	Powder	Single-crystal
Radiation source	Mo-Kα_1	Synchrotron
Wavelength / Å	0.71073	0.28874
Obs. indep. reflections	97	113
θ-range / °	1.000–38.177	2.542–17.163
Resolution / Å	0.57	0.49
Temperature / K	293	293
Pressure / GPa	10^{-4}	1.8
Goodness of fit	1.327	1.343
CSD deposition number	433717	434035

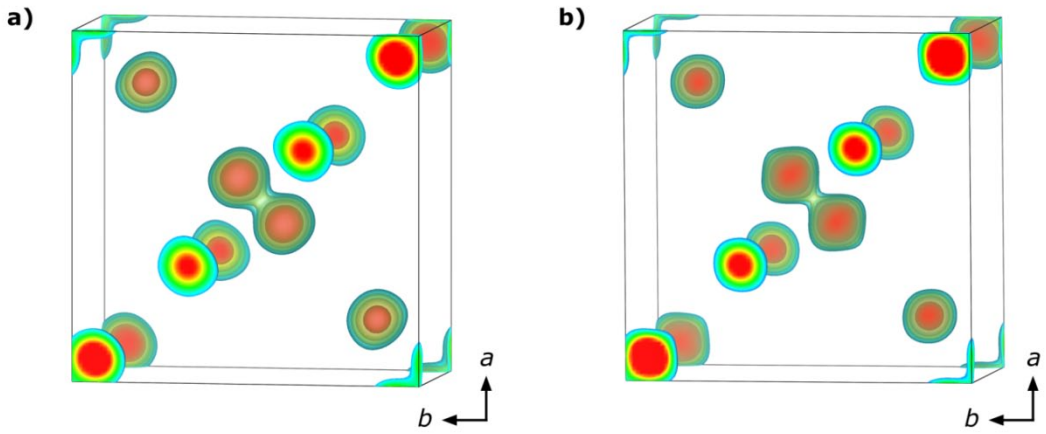

Figure S8.8 Isosurfaces of the electron density for *pc*-PON based on PXRD (a) and single-crystal XRD refinement (b), indicating that both refinements are tantamount in quality and accuracy. Isosurface levels are 20, 13, 9, and 6 electrons·a_0^{-3}, respectively (a_0 = Bohr radius).

8.3.16 High-Pressure PXRD Patterns of *pc*- and *o*-PON from Synchrotron Measurements

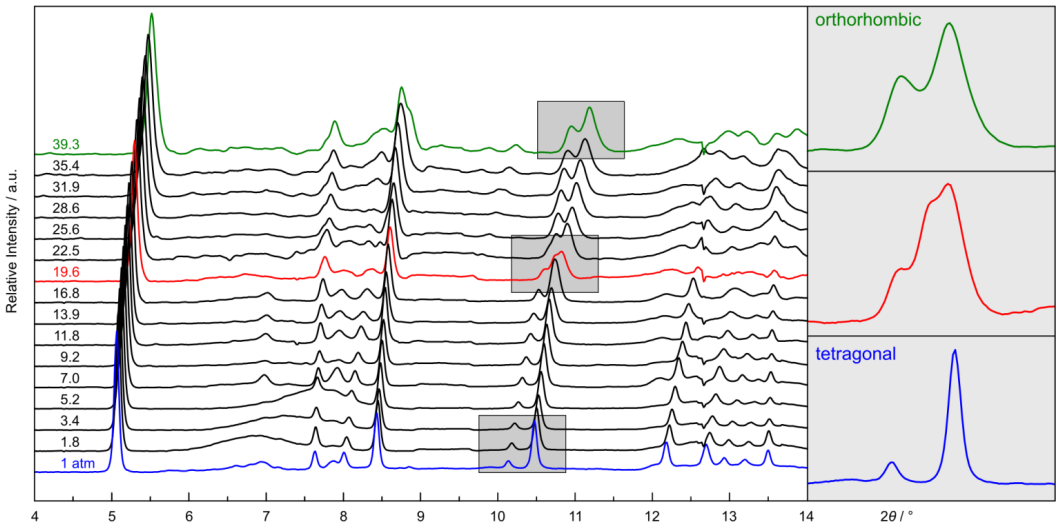

Figure S8.9 Pressure-dependent powder X-ray diffraction patterns from synchrotron measurements (λ = 0.28874 Å) showing two different types of pattern. Corresponding pressures (GPa) are given on the left side. The *pc*-PON structure (blue pattern) seems to be preserved up to ca. 20 GPa. At higher pressures, however, a new phase is observed (green pattern), as the reflections in the region 10.0°<2θ<11.5° change significantly. At 19.6 GPa the phases coexist, as both types of pattern superpose (red pattern). The regions of interest are highlighted and enlarged on the right side. The broad signals in the range 6°<2θ<9° up to 5.2 GPa can be assigned to a liquid neon phase in the DAC.

8.3.17 Temperature-Dependent PXRD of *pc*-PON

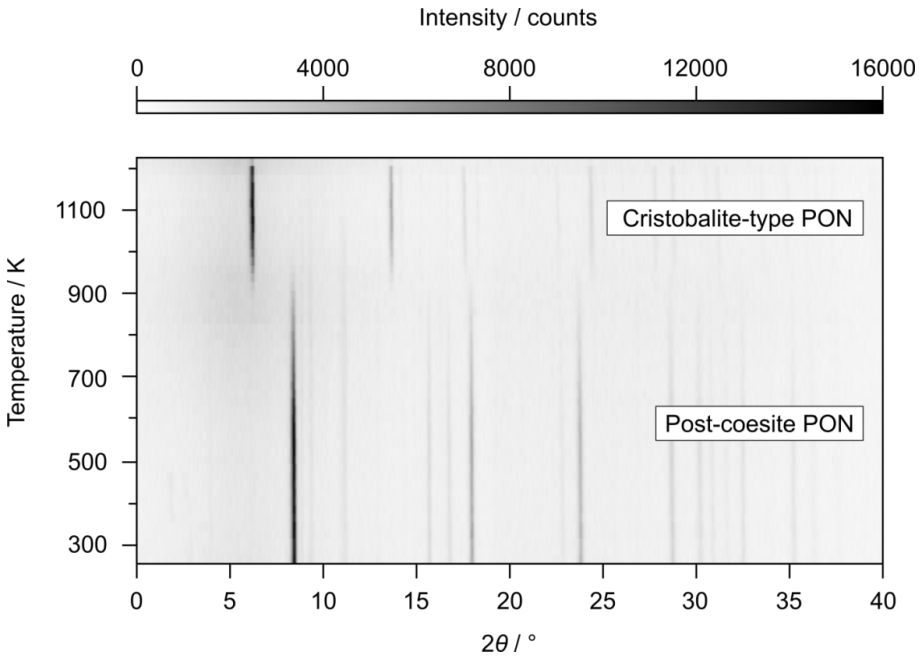

Figure S8.10 Temperature-dependent X-ray diffraction patterns from *pc*-PON (Mo-Kα_1, λ = 0.71073 Å) collected in steps of 20 K. At ca. 900 K phase transition to *cri*-PON is observed, proving *pc*-PON to be metastable at ambient conditions.

8.3.18 Tetragonal to Orthorhombic Phase Transition in PON, Spontaneous Strain Formalism

To compare the nature of the phase transition from tetragonal to orthorhombic symmetry in PON to SiO_2, it is described in terms of spontaneous strains as reported in former works for SiO_2.[48] Therefore, the lattice parameters of the *pc*-PON ($P4_2/mnm$, high-symmetry phase) are extrapolated into the pressure regime of *o*-PON (*Pnnm*, low-symmetry phase). Hereby, *symmetry-breaking* (*sb*) and *non-symmetry-breaking* (*nsb*) elements of the spontaneous strain are distinguished.[49,50] The respective non-zero components ε_{11sb}, ε_{22sb}, ε_{11nsb}, ε_{22nsb}, ε_{33nsb} and V_S are calculated according to equations 2–5, where a_0, c_0 and V_0 corresponds to the extrapolated parameters of the tetragonal phase and a, b, c and V to those of the orthorhombic one.

$$\varepsilon_{11sb} = -\varepsilon_{22sb} = (a - b)/2a_0 \quad (2)$$

$$\varepsilon_{11nsb} = \varepsilon_{22nsb} = (a + b)/2a_0 - 1 \quad (3)$$

$$\varepsilon_{33nsb} = c/c_0 - 1 \quad (4)$$

$$V_S = V/V_0 - 1 \quad (5)$$

Figure S8.11 illustrates the calculated spontaneous strain components and the volume strain V_S. An evaluation of the observed phase transition in terms of spontaneous strain is justified as the relation $V_S = 2\varepsilon_{11nsb} + \varepsilon_{33nsb}$ is almost preserved in the whole pressure range.

The non-symmetry-breaking elements of the spontaneous strain ε_{11nsb}, ε_{22nsb}, ε_{33nsb} as well as the volume strain V_S remain small in the whole pressure range. The symmetry-breaking components ε_{11sb} and ε_{22sb}, however, show the largest magnitude by far. Almost identical results were obtained for rutile-type ($P4_2/mnm$) → $CaCl_2$-type ($Pnnm$) phase transition in SiO_2 corroborating the kinship of both compounds. Although, we were not able to extract any structural information on *o*-PON, the mechanism of phase transition seems to be similar to the one observed in SiO_2. Thus, one would expect a tilting of the P coordination polyhedra in the *a*-*b* plane with increasing pressure and a $CaCl_2$-related structure for *o*-PON.

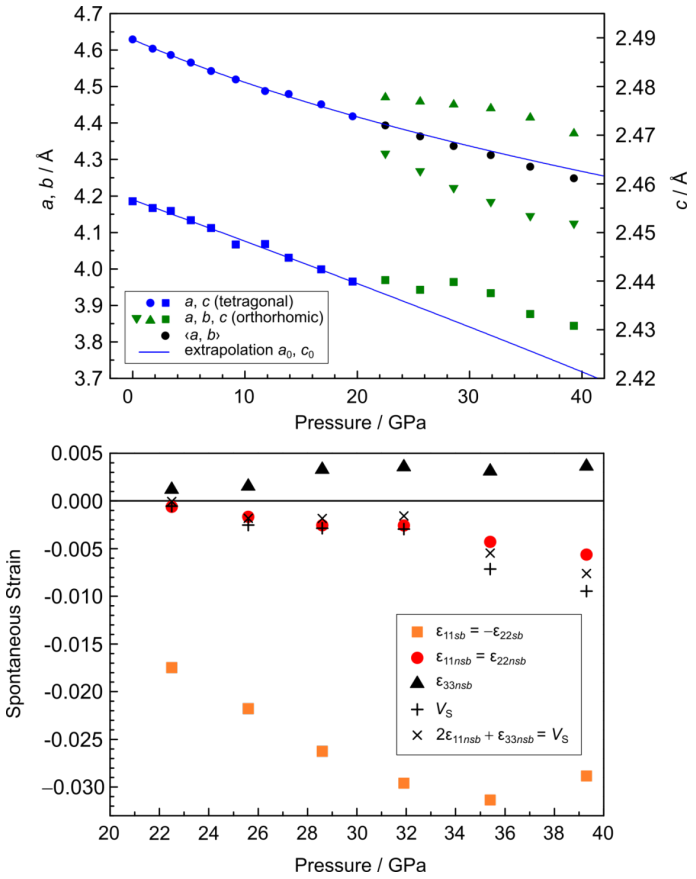

Figure S8.11 Evolution of the lattice parameters with pressure (top) and calculated s*ymmetry-breaking* (*sb*) and *non-symmetry-breaking* (*nsb*) components of spontaneous strain as a function of pressure with ε_{11sb} (orange) appearing the largest component (bottom).

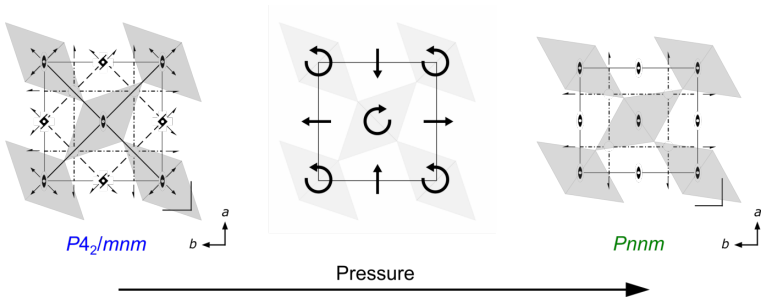

Figure S8.12 Schematic illustration of the stishovite → $CaCl_2$-type SiO_2 phase transition, which is characterized by an alternating tilting of the SiO_6 octahedra in the *a*-*b* plane. A similar mechanism is assumed for the tetragonal → orthorhombic phase transition in PON, considering reduction of symmetry and findings from spontaneous strain formalism.

8.3.19 Equation of States and Elastic Properties of *pc*-PON

In order to classify *pc*-PON on its elastic properties, equations of state were fitted using a second order Birch-Murnaghan equation with V_0 = 52.64(2) Å^3 and K_0 = 163(2) GPa. Corresponding parameters refined from the calculated *p*-*V* data obtained from DFT calculations were determined to be V_0 = 53.8(2) Å^3 and K_0 = 164(9) GPa. Keeping in mind that GGA based calculations typically show a systematic overestimation of the cell volume, the calculated data are in very good agreement with the experimental ones. A corresponding refinement of *o*-PON was not possible. Due to softening effects up to 30 GPa there are not enough reliable pressure points. Therefore, the as refined equations of state of *pc*-PON are extrapolated to the pressure regime of *o*-PON (blue lines, Figure S8.13). By analogy with stishovite and $CaCl_2$-type SiO_2 the orthorhombic phase (*o*-PON) appears slightly more compressible than the tetragonal one (*pc*-PON).[48] However, as only small deviations from the extrapolated equations of state are observed, one would expect a minor change of the bulk modulus upon transition.

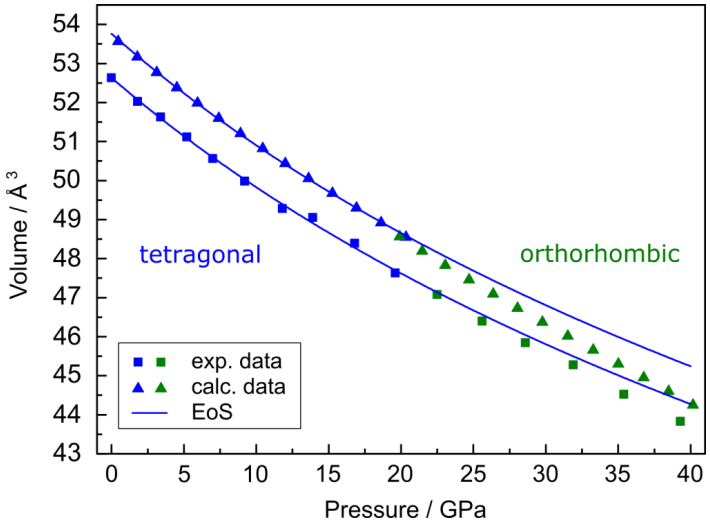

Figure S8.13 Experimental and calculated pressure points of tetragonal (blue) and o-PON (green) and extrapolated equations of state of *pc*-PON (blue lines).

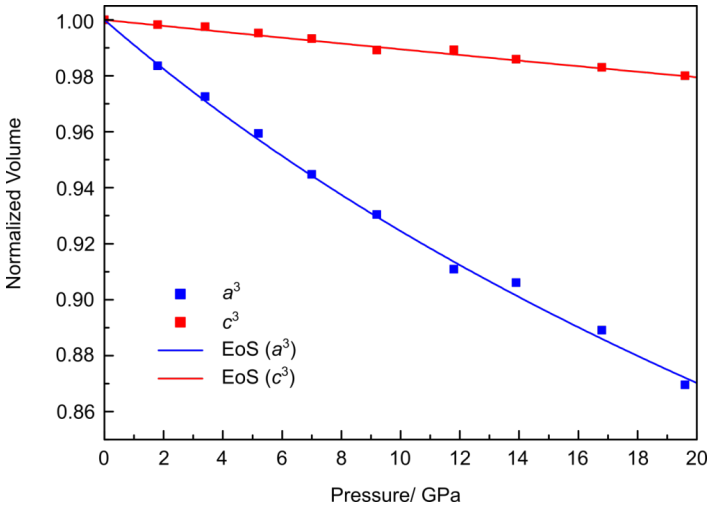

Figure S8.14 Pressure evolution of a^3 and c^3 in *pc*-PON and refined equations of state (second order Birch-Murnaghan) with $K_0(a^3)$ = 109(2) GPa and $K_0(c^3)$ = 927(35) GPa, respectively.

8.3.20 DFT Calculations

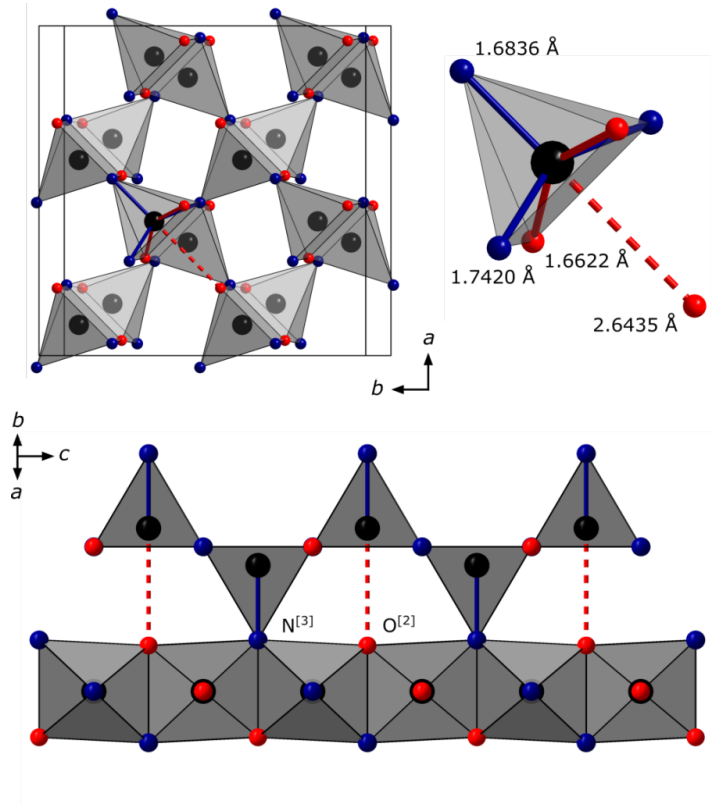

Figure S8.15 Structure model of *pc*-PON from structure relaxation with N/O-order used for DFT calculations (top). The alternating displacement of the P atoms appears as a coupled feature of the introduced N/O-ordering model resulting in $N^{[3]}$ and $O^{[2]}$, which are bound to three and two P atoms, respectively (bottom). P: black, O: red, N: blue.

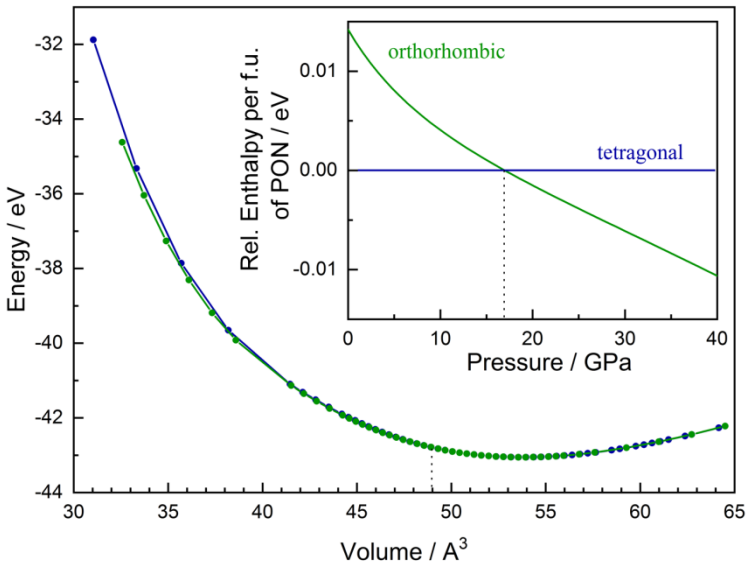

Figure S8.16 E-V curves of *pc*- (blue) and *o*-PON (green) from DFT calculations for two formulas of PON and relative enthalpy per formula unit of PON as a function of pressure with transition pressure of 17 GPa (inlay).

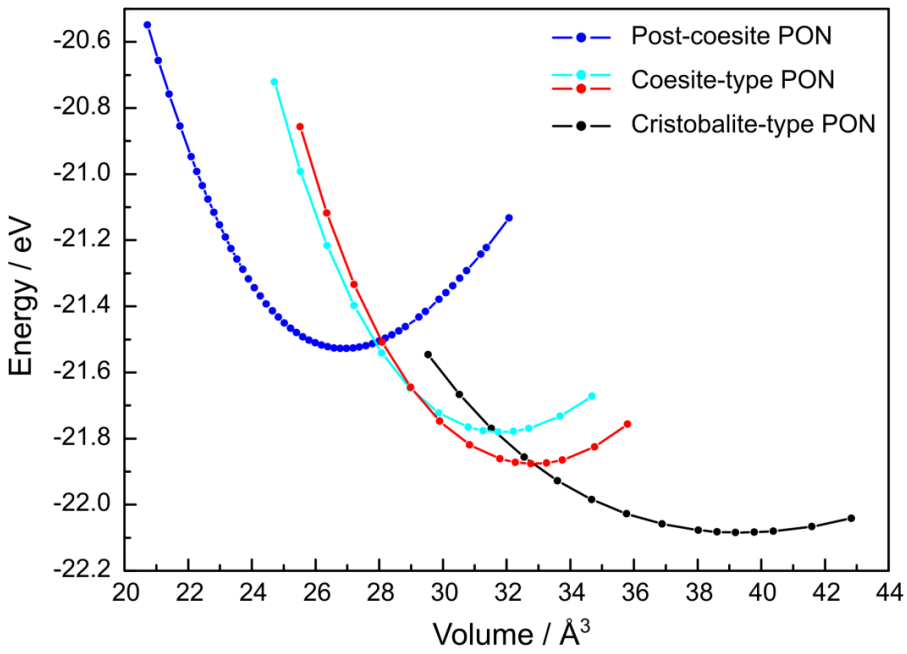

Figure S8.17 *E-V* curves of *cri*-, *coe*- and *pc*-PON from DFT calculations for one formula of PON.[38] The two curves of *coe*-PON correspond to two different N/O ordering models.

8.3.21 References

[1] A. Stock, B. Hoffmann, Die Einwirkung von Ammoniak auf Phosphorpentasulfid und der Phosphorstickstoff, P_3N_5, *Ber. Dtsch. Chem. Ges.* **1903**, *36*, 314–319.

[2] K. J. Kingma, R. E. G. Pacalo, P. F. McMillan, High-pressure stability of the cristobalite framework in PON and PN(NH), *Eur. J. Solid State Inorg. Chem.* **1997**, *34*, 679–692.

[3] D. Walker, Lubrication, gasketing, and precision in multianvil experiments, *Am. Mineral.* **1991**, *76*, 1092–1100.

[4] H. Huppertz, Multianvil high-pressure / high-temperature synthesis in solid state chemistry, *Z. Kristallogr.* **2004**, *219*, 330–338.

[5] A. A. Coelho, TOPAS-Academic v4.1, Brisbane, **2007**.

[6] A. A. Coelho, Indexing of powder diffraction patterns by iterative use of singular value decomposition, *J. Appl. Crystallogr.* **2003**, *36*, 86–95.

[7] G. S. Pawley, Unit-cell refinement from powder diffraction scans, *J. Appl. Crystallogr.* **1981**, *14*, 357–361.

[8] G. Oszlányi, A. Sütő, The charge flipping algorithm, *Acta Crystallogr. Sect. A: Found. Crystallogr.* **2008**, *64*, 123–134.

[9] G. Oszlányi, A. Sütő, Ab initio structure solution by charge flipping. II. Use of weak reflections, *Acta Crystallogr. Sect. A: Found. Crystallogr.* **2005**, 61, 147–152.

[10] G. Oszlányi, A. Sütő, *Ab initio* structure solution by charge flipping, *Acta Crystallogr. Sect. A: Found. Crystallogr.* **2004**, *60*, 134–141.

[11] H. M. Rietveld, A profile refinement method for nuclear and magnetic structures, *J. Appl. Crystallogr.* **1969**, *2*, 65–71.

[12] R. W. Cheary, A. A. Coelho, J. P. Cline, Fundamental Parameters Line Profile Fitting in Laboratory Diffractometers, *J. Res. Natl. Inst. Stand. Technol.* **2004**, *109*, 1–25.

[13] ES Vision, v4.0.164, Emispec Systems Inc., Tempe, USA, **1994–2002**.

[14] Digital Micrograph, v3.6.1, Gatan Software Team, Pleasanton, USA, **1999**.

[15] G. Kresse, J. Hafner, *Ab initio* molecular dynamics for liquid metals, *Phys. Rev. B: Condens. Matter Mater. Phys.* **1993**, *47*, 558–561.

[16] G. Kresse, J. Hafner, *Ab initio* molecular-dynamics simulation of the liquid-metal-amorphous-semiconductor transition in germanium, *Phys. Rev. B: Condens. Matter Mater. Phys.* **1994**, *49*, 14251–14269.

[17] G. Kresse, J. Furthmüller, Efficiency of ab-initio total energy calculations for metals and semiconductors using a plane-wave basis set, *Comput. Mater. Sci.* **1996**, *6*, 15–50.

[18] J. P. Perdew, K. Burke, M. Ernzerhof, Generalized Gradient Approximation Made Simple, *Phys. Rev. Lett.* **1996**, *77*, 3865–3868.

[19] J. P. Perdew, K. Burke, M. Ernzerhof, Generalized Gradient Approximation Made Simple [*Phys. Rev. Lett.* **1996**, *77*, 3865], *Phys. Rev. Lett.* **1997**, *78*, 1396.

[20] P. E. Blöchl, Projector augmented-wave method, *Phys. Rev. B: Condens. Matter Mater. Phys.* **1994**, *50*, 17953–17979.

[21] G. Kresse, D. Joubert, From ultrasoft pseudopotentials to the projector augmented-wave method, *Phys. Rev. B: Condens. Matter Mater. Phys.* **1999**, *59*, 1758–1775.

[22] H. J. Monkhorst, J. D. Pack, Special points for Brillouin-zone integrations, *Phys. Rev. B: Solid State* **1976**, *13*, 5188–5192.

[23] I. Kantor, V. Prakapenka, A. Kantor, P. Dera, A. Kurnosov, S. Sinogeikin, N. Dubrovinskaia, L. Dubrovinsky, BX90: A new diamond anvil cell design for X-ray diffraction and optical measurements, *Rev. Sci. Instrum.* **2012**, *83*, 125102.

[24] H. P. Liermann, Z. Konôpková, W. Morgenroth, K. Glazyrin, J. Bednarčik, E. E. McBride, S. Petitgirard, J. T. Delitz, M. Wendt, Y. Bican, A. Ehnes, I. Schwark, A. Rothkirch, M. Tischer, J. Heuer, H. Schulte-Schrepping, T. Kracht, H. Franz, The Extreme Conditions Beamline P02.2 and the Extreme Conditions Science Infrastructure at PETRA III, *J. Synchrotron Radiat.* **2015**, *22*, 908–924.

[25] Rigaku Oxford Diffraction, CrysAlisPro Software system, version 1.171.37.35, Rigaku Corporation, Oxford, UK, **2014**.

[26] G. M. Sheldrick, SHELXT - Integrated space-group and crystal-structure determination, *Acta Crystallogr. Sect. A Found. Crystallogr.* **2015**, *71*, 3–8.

[27] G. M. Sheldrick, A short history of SHELX, *Acta Crystallogr. Sect. A Found. Crystallogr.* **2008**, *64*, 112–122.

[28] H. K. Mao, J. Xu, P. M. Bell, Calibration of the ruby pressure gauge to 800 kbar under quasi-hydrostatic conditions, *J. Geophys. Res.* **1986**, *91*, 4673–4676.

[29] A. Dewaele, M. Torrent, P. Loubeyre, M. Mezouar, Compression curves of transition metals in the Mbar range: Experiments and projector augmented-wave calculations, *Phys. Rev. B: Condens. Matter Mater. Phys.* **2008**, *78*, 104102.

[30] C. Prescher, V. B. Prakapenka, DIOPTAS: a program for reduction of two-dimensional X-ray diffraction data and dataexploration, *High Pressure Res.* **2015**, *35*, 223–230.

[31] V. Petříček, M. Dušek, L. Palatinus, Crystallographic Computing System JANA2006: General features, *Z. Kristallogr. – Cryst. Mater.* **2014**, *229*, 345–352.

[32] F. D. Murnaghan, The Compressibility of Media under Extreme Pressures, *Proc. Natl. Acad. Sci. USA.* **1944**, *30*, 244–247.

[33] F. Birch, Finite Elastic Strain of Cubic Crystals, *Phys. Rev.* **1947**, *71*, 809–824.

[34] J. Gonzalez-Platas, M. Alvaro, F. Nestola, R. Angel, EosFit7-GUI: a new graphical user interface for equation of state calculations, analyses and teaching, *J. Appl. Crystallogr.* **2016**, *49*, 1377–1382.

[35] D. Baumann, W. Schnick, Pentacoordinate Phosphorus in a High-Pressure Polymorph of Phosphorus Nitride Imide $P_4N_6(NH)$, *Angew. Chem. Int. Ed.* **2014**, *53*, 14490–14493; *Angew. Chem.* **2014**, *126*, 14718–14721.

[36] L. Boukbir, R. Marchand, Y. Laurent, P. Bacher, G. Roult, Preparation and time-of-flight neutron diffraction study of the cristobalite-type PON phosphorus oxynitride, *Ann. Chim. Fr.* **1989**, *14*, 475–481.

[37] K. Landskron, H. Huppertz, J. Senker, W. Schnick, High-Pressure Synthesis of γ-P_3N_5 at 11 GPa and 1500 °C in a Multianvil Assembly: A Binary Phosphorus(V) Nitride with a Three-Dimensional Network Structure from PN_4 Tetrahedra and Tetragonal PN_5 Pyramids, *Angew. Chem. Int. Ed.* **2001**, *40*, 2643–2645; *Angew. Chem.* **2001**, *113*, 2713–2716.

[38] D. Baumann, R. Niklaus, W. Schnick, A High-Pressure Polymorph of Phosphorus Oxonitride with the Coesite Structure, *Angew. Chem. Int. Ed.* **2015**, *54*, 4388–4391; *Angew. Chem.* **2015**, *127*, 4463–4466.

[39] D. Baumann, S. J. Sedlmaier, W. Schnick, An Unprecedented AB2 Tetrahedra Network Structure Type in a High-Pressure Phase of Phosphorus Oxonitride PON, *Angew. Chem. Int. Ed.* **2012**, *51*, 4707–4709; *Angew. Chem.* **2012**, *124*, 4785–4787.

[40] T. Zoltai, M. J. Buerger, The crystal structure of coesite, the dense, high-pressure form of silica, *Z. Kristallogr*. **1959**, *111*, 129–141.

[41] H. Jacobs, R. Nymwegen, S. Doyle, T. Wroblewski, W. Kockelmann, Kristallines Phoshor(V)-nitrid-imid, HPN_2 bzw. DPN_2 – Strukturbestimmung mit Rontgen-, Synchrotron- und Neutronenstrahlung, *Z. Anorg. Allg. Chem.* **1997**, *623*, 1467–1474.

[42] W. Sinclair, A. E. Ringwood, Single crystal analysis of the structure of stishovite, *Nature* **1978**, *272*, 714–715.

[43] H. Jacobs, R. Nymwegen, S. Doyle, T. Wroblewski, W. Kockelmann, Kristallines Phoshor(V)-nitrid-imid, HPN_2 bzw. DPN_2 – Strukturbestimmung mit Rontgen-, Synchrotron- und Neutronenstrahlung, *Z. Anorg. Allg. Chem.* **1997**, *623*, 1467–1474.

[44] W. Schnick, J. Lücke, Darstellung, Kristallstruktur und IR-spektroskopische Untersuchung von Phosphor(V)-nitrid-imid, HPN_2, *Z. Anorg. Allg. Chem.* **1992**, *610*, 121–126.

[45] S. Horstmann, E. Irran, W. Schnick, Synthese, Kristallstruktur und Eigenschaften von Phosphor(V)-nitridimid HP_4N_7, *Z. Anorg. Allg. Chem.* **1998**, *624*, 221–227.

[46] S. Horstmann, E. Irran, W. Schnick, Phosphorus(V) Nitride Imide HP_4N_7: Synthesis from a Molecular Precursor and Structure Determination with Synchrotron Powder Diffraction, *Angew. Chem. Int. Ed. Engl.* **1997**, *36*, 1992–1994; *Angew. Chem.* **1997**, *109*, 2085–2087.

[47] D. Baumann, W. Schnick, High-Pressure Polymorph of Phosphorus Nitride Imide HP_4N_7 Representing a New Framework Topology, *Inorg. Chem.* **2014**, *53*, 7977–7982.

[48] D. Andrault, R. J. Angel, J. L. Mosenfelder, T. Le Bihan, Equation of state of stishovite to lower mantle pressures, *Am. Mineral.* **2003**, *88*, 301–307.

[49] M. A. Carpenter, E. K. Salje, Elastic anomalies in minerals due to structural phase transitions, *Eur. J. Mineral.* **1998**, *10*, 693–812.

[50] M. A. Carpenter, R. J. Hemley, H.-k. Mao, High-pressure elasticity of stishovite and the $P4_2/mnm \rightleftharpoons$ Pnnm phase transition, *J. Geophys. Res.: Solid Earth* **2000**, *105*, 10807–10816.

9 $Li_{12}P_3N_9$ with Non-Condensed $[P_3N_9]^{12-}$ Rings and its High-Pressure Polymorph Li_4PN_3 with Infinite Chains of PN_4-Tetrahedra

published in: *Chem. Eur. J.* **2017**, *23*, 9592-9599.

authors: Eva-Maria Bertschler, Robin Niklaus, Wolfgang Schnick

DOI: 10.1002/chem.201700979

Abstract $Li_{12}P_3N_9$ was synthesized by solid-state reaction of Li_3N and P_3N_5 at 790 °C. It is made up of non-condensed $[P_3N_9]^{12-}$ *dreier*-rings of PN_4-tetrahedra. The corresponding high-pressure polymorph, Li_4PN_3, was synthesized under high-pressure/high-temperature conditions from $Li_{12}P_3N_9$ or $LiPN_2$ and Li_7PN_4 at 6 or 7 GPa, respectively, using the multianvil technique. Li_4PN_3 is the first lithium *catena*-nitridophosphate and contains PN_3 *zweier*-chains of corner sharing PN_4-tetrahedra. To confirm the structure elucidated from single-crystal X-ray data, Rietveld refinement, ^6Li, ^7Li, and ^{31}P solid-state NMR spectroscopy, FTIR spectroscopy and EDX measurements were carried out. To examine the phase transition of $Li_{12}P_3N_9$ to Li_4PN_3 at 6 GPa and to corroborate the latter as the corresponding high-pressure polymorph, DFT calculations were conducted. Electronic band gap and electron localization function (ELF) calculations were carried out to elucidate the electronic properties and bonding behavior of both polymorphs.

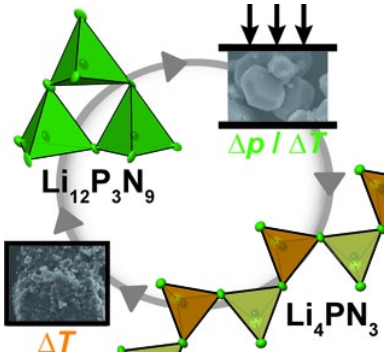

9.1 Introduction

PN_4-tetrahedra are the characteristic structural motif of nitridophosphates.[1,2] Due to the ability to form framework structures, from networks of corner- and/or edge-sharing tetrahedra, these compounds are of high interest concerning their structural variety and their technical applicability.[2–6] Prominent examples of such materials include optical materials for example, $Ba_3P_5N_{10}Br:Eu^{2+}$,[7] a promising white-light-emitting luminescent material, (oxo)nitridophosphate zeolites,[8-10] or lithium ion conductors (e.g., in materials like "*LiPON*").[11–14] High hardness was observed in *γ*-P_3N_5, where besides PN_4-tetrahedra, square PN_5-pyramids occur as well.[15,16] Accordingly, exploration of new structures with new topologies or new compositions leads to interesting new materials.[5]

In lithium nitridophosphates different linking patterns of corner-sharing PN_4-tetrahedra occur, surrounded by a matrix of Li^+ ions.[1] Yet, only five ternary lithium nitridophosphates were described in literature. Li_7PN_4 has the lowest atomic ratio P/N and contains non-condensed

$[PN_4]^{7-}$ ions.[17] Preliminary investigations assumed that the PN_4-tetrahedra in $Li_{12}P_3N_9$ form non-condensed *dreier*-rings[18,19] isoelectronic to $[Si_3O_9]^{6-}$, but until now no complete structural analysis has been published.[1,20] In $Li_{18}P_6N_{16}$ the $[P_6N_{16}]^{18-}$ tricyclic ring structure is composed of one *vierer*-ring with two annulated *dreier*-rings.[14] A cage like structure occurs in $Li_{10}P_4N_{10}$ with adamantane like $[P_4N_{10}]^{10-}$ ions, isoelectronic to $[P_4O_{10}]$.[21] $LiPN_2$ has the lowest Li content and is made up of a three-dimensional network-structure with corner sharing PN_4-tetrahedra that is isoelectronic to SiO_2.[22] All of these lithium nitridophosphates, except $Li_{18}P_6N_{16}$, can be synthesized from Li_3N and P_3N_5 below 850 °C in Ta or W crucibles. Higher reaction temperatures lead to decomposition of P_3N_5, due to its limited thermal stability.[1] To prevent decomposition, high-pressure/high-temperature synthesis emerged as a powerful tool to obtain new lithium nitridophosphates with the Li_3N self-flux method. $Li_{18}P_6N_{16}$ is the first lithium nitridophosphate synthesized by high-pressure/high-temperature technique.[14]

Recently, a number of intriguing P/N-networks, with high degrees of condensation, were synthesized by this high-pressure/high-temperature approach, for example, β-cristobalite-type PN(NH),[23,24] and β-PN(NH);[25] α-P_4N_6(NH),[6,26] β-P_4N_6(NH),[5] and γ-P_4N_6(NH).[27]

In this contribution we report on synthesis and structural investigation of $Li_{12}P_3N_9$ (="3 Li_4PN_3") and its high-pressure polymorph Li_4PN_3. We were able to grow single crystals of both polymorphs, enabling structure determination on the basis of single-crystal X-ray diffraction data. DFT calculations corroborate the observed high-pressure phase transition.

9.2 Results and Discussion

9.2.1 Synthesis

$Li_{12}P_3N_9$ and Li_4PN_3 were synthesized by different approaches after empirical optimization [Equations (1) to (5)]. $Li_{12}P_3N_9$ was obtained at high-temperatures and normal pressure, while Li_4PN_3 is accessible at high-temperature and high-pressure conditions. To avoid hydrolysis, all compounds were handled under inert conditions.

$$4\ Li_3N + P_3N_5 \xrightarrow{\Delta T} Li_{12}P_3N_9 \quad (1)$$

$$3\ LiPN_2 + 3\ Li_3N \xrightarrow{\Delta T} Li_{12}P_3N_9 \quad (2)$$

$$2\ LiPN_2 + Li_7PN_4 + Li_3N \xrightarrow{\Delta T} Li_{12}P_3N_9 \quad (3)$$

$$Li_{12}P_3N_9 \xrightarrow{\Delta T,\ \Delta p} 3\ Li_4PN_3 \quad (4)$$

$$LiPN_2 + Li_7PN_4 \xrightarrow{\Delta T,\ \Delta p} 2\ Li_4PN_3 \quad (5)$$

According to Equations (1), (2), and (3), different amounts of $Li_{12}P_3N_9$ were obtained together with Li_3P, Li_7PN_4, $Li_{10}P_4N_{10}$, or $LiPN_2$ as side phases depending on initial weight ratio and reaction temperature. For all routes we used a Li_3N flux method, in open Ta-crucibles sealed in silica ampoules under nitrogen atmosphere, with different amounts of Li_3N excess. The high-pressure polymorph Li_4PN_3 was synthesized according to two different routes. According to Equation (4) Li_4PN_3 was made from $Li_{12}P_3N_9$ at 6 GPa and 820 °C using a Walker-type multianvil assembly.[28-32] Products with smaller amounts of side products were obtained by reaction from non-equimolar amounts of $LiPN_2$ and Li_7PN_4 (molar ratio 1:2.25). The significant excess of Li_7PN_4 leads to an in situ formation of Li_3N (self-flux), as described in previous work.[14] According to this route, 9 GPa and 1200 °C seemed to be favorable. Due to the better crystal quality after synthesis according to Equation (1) and (5), single-crystals of these approaches were used for structure analysis. Detailed information on the synthesis of the two polymorphs is given in the Experimental section.

9.2.2 Crystal Structure

The crystal structures of both polymorphs were solved and refined from single-crystal X-ray diffraction data. $Li_{12}P_3N_9$ crystallizes in monoclinic space group *Cc* (no. 9) with four formula units per unit cell (Table 9.1).

The reflection conditions *hkl* for $h+k=2n$ and *h*0*l* for $l = 2n$ are in accordance with space groups *Cc* or *C*2/*c*. The E-value statistics suggest a non-centrosymmetric space group. Furthermore, the orthorhombic space group $Cmc2_1$ exhibits significant higher *R* values, especially for wR_2 (R_{int} is twice as high). Thus, $Li_{12}P_3N_9$ was refined in *Cc* as a pseudo-orthorhombic twin with a two-fold axis (100 0-10 00−1). All P and N positions were determined during structure solution and were refined anisotropically. The Li atom positions were localized during structure refinement from difference Fourier maps. The P/N substructure of $Li_{12}P_3N_9$ is made up of three corner sharing PN_4-tetrahedra forming *dreier*-rings in chair conformation, analogously to the cyclo-trisilicate $[Si_3O_9]^{6-}$ (Figure 9.1).[33]

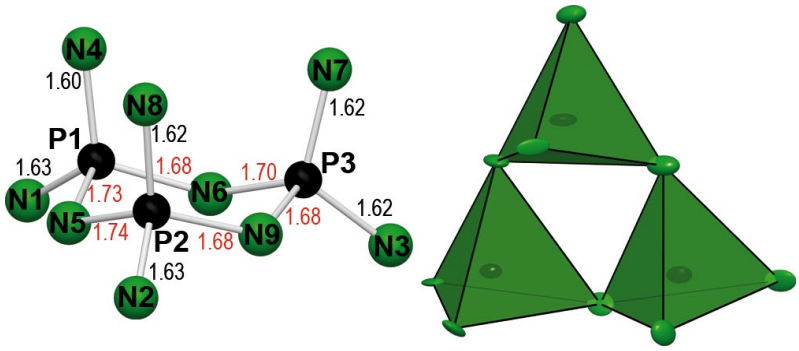

Figure 9.1 Left: $[P_3N_9]^{12-}$ anion in chair conformation with P–N distances. Right: $[P_3N_9]^{12-}$ anion with PN_4 tetrahedra of the P/N-framework in green. The thermal ellipsoids are depicted at 90% probability level. (P: black, N: green).

Table 9.1 Crystallographic data of $Li_{12}P_3N_9$ and Li_4PN_3

Formula	$Li_{12}P_3N_9$	Li_4PN_3
crystal size [mm³]	0.01 x 0.01 x 0.01	0.01 x 0.01 x 0.01
formula mass [g mol⁻¹]	302.28	100.76
crystal system	monoclinic	orthorhombic
space group	Cc (no. 9)	Pccn (no. 56)
twin	100 $0\bar{1}0$ $00\bar{1}$	
BASF	0.203(7)	
cell parameters/ Å,°	a = 12.094(5)	a = 9.6597(4)
	b = 7.649(3)	b = 11.8392(6)
	c = 9.711(4)	c = 4.8674(2)
	β = 90.53(2)	
cell volume/ Å³	898.3(6)	556.65(4)
formula units/ cell	4	8
calculated density/ g · cm⁻³	2.235	2.405
F(000)	576	384
diffractometer	Bruker D8 Venture	
temperature/ °C	−173	25
radiation, monochromator	Mo-K_α (λ = 0.71073 Å), Goebel mirror	
absorption correction	multi scan	
θ range/ °	2.10-30.53	2.72-28.30
number of collected data	5897	6353
number of unique data	2625	698
number of unique data with $I \geq 2\sigma(I)$	2298	597
refined parameters	158	61
GooF	1.093	1.116
R indices [$F_0^2 \geq 2\sigma(F_0^2)$]	R_1 = 0.0442, wR_2 = 0.0942[a]	R_1 = 0.0388, wR_2 = 0.0844[b]
R indices (all data)	R_1 = 0.0554, wR_2 = 0.0994[a]	R_1 = 0.0497, wR_2 = 0.0982[b]
max/min res. electron density/ eÅ⁻³	0.50/ −0.42	0.79/−0.62
R_{int}/ R_σ	0.0595/0.0869	0.0560/0.0317

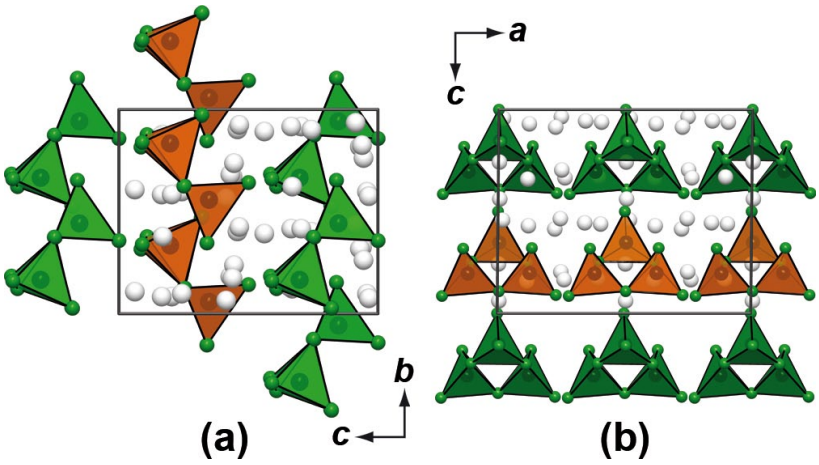

Figure 9.2 Packing of $Li_{12}P_3N_9$: viewed along *a* (a) and viewed along *b* (b). (P: black, N: green; Li: gray; PN_4 tetrahedra: green or orange depending on the orientation).

These *dreier*-rings are not further condensed and form two types of layers (Figure 9.2: orange and green). Within one layer all $[P_3N_9]^{12-}$ units are orientated equally. In every other layer the *dreier*-rings are orientated differently, but also equally within the layer.

The high-pressure polymorph Li_4PN_3 crystallizes in the centrosymmetric orthorhombic space group *Pccn* (no. 56). Analogously to $Li_{12}P_3N_9$, all P and N positions were determined during structure solution and were refined anisotropically. The Li atom positions were localized from difference Fourier maps. Li_4PN_3 is made of infinite *zweier*-chains of corner sharing PN_4-tetrahedra $^{3}_{\infty}[PN_2N_{2/2}]^{4-}$, running along *c* (shortest lattice parameter). The *catena*-nitridophosphate chains have a stretching factor of f_s = 0.923 and a chain periodicity of P = 2 ($f_s = I_{chain}/(I_T \times P) = 4.855/(2.627 \times 2)$. For definitions of I_{chain} and I_T see Figure 9.3 a.

Liebau introduced f_s for the classification of chain and layer silicates and this formalism can also be adapted to nitridophosphates. This value is a measure of infinitely extended chains.[18]

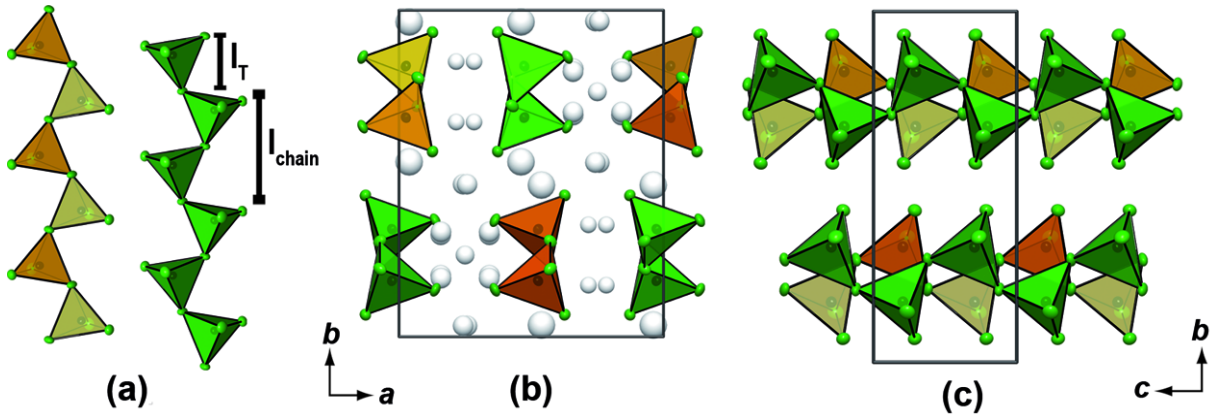

Figure 9.3 (a) *Zweier*-chains in Li_4PN_3. (b) Li_4PN_3 viewed along *c*. (c) Li_4PN_3 viewed along *a*. The thermal ellipsoids are depicted at 90% probability level in (a), (b), and (c). (P: black, N: green; Li: gray; PN_4 tetrahedra: green or orange depending on the orientation).

Maximal stretched chains (f_s = 1) occur in for example, Ca_2PN_3.[34,35] Less stretched chains of corner sharing PN_4-tetrahedra have been reported for Mg_2PN_3[34] and Zn_2PN_3 (f_s=0.88).[36] Li_4PN_3 contains four infinite chains per unit cell with two different orientations (Figure 9.3, orange and green). The P−N distances for $Li_{12}P_3N_9$ vary from 1.60 to 1.73 Å and for Li_4PN_3 from 1.61 to 1.73 Å. Analogously to other nitridophosphates the values for P−N bond lengths to terminal nitrogen atoms of PN_4-tetrahedra are shorter than those to bridging ones.[14,37] These values are in accordance with other nitridophosphates.[14,21]

The $[P_3N_9]^{12-}$ and $[PN_3]^{4-}$ anions are surrounded by Li^+ ions. The latter were not refined anisotropically, due to their low scattering intensity. In $Li_{12}P_3N_9$ the Li^+ ions are coordinated by N with coordination numbers 3, 4, and 5 sharing edges or corners of resulting polyhedra. The shortest Li–Li distance is 2.31 Å, which is comparable to Li−Li distances in other multinary lithium compounds (e.g., $LiCa_3Si_2N_5$).[38] In the high-pressure polymorph Li_4PN_3 there are only $[LiN_4]$ and $[LiN_5]$ polyhedra. A free refinement of the occupation factors of the Li atoms showed partial occupation for three Li sites (Li4 (8*e*): 50%, Li5 (8*e*): 30%, Li6 (4*c*): 40%). Involving the partially occupation, the shortest Li−Li distance is between Li2 and Li5 with 2.14 Å, which also corresponds with other Li containing compounds.[38]

9.2.3 Structural Snalysis of Possible Lithium Migration Pathways

Calculating Voronoi–Dirichlet polyhedra with TOPOS yields the possible voids and migration pathways for Li^+.[39–42] $Li_{12}P_3N_9$ shows a possible movement of the Li^+ ions in three different directions in space (Supporting Information Figure S9.15). In Li_4PN_3 Li4, Li5, and Li6 indicate possible movement between each other in contrast to Li1, which shows no movement. The possible migration pathways of Li2 and Li3 build chains along *a* (Figure 9.4).

According to these calculations both polymorphs seem to be promising candidates for lithium ion conductivity. Measurements of other lithium nitridophosphates show lithium ion conductivity in the range of 10^{-5} Ω^{-1} cm^{-1} at 127 °C, which we also expect for $Li_{12}P_3N_9$ and Li_4PN_3.[12,14]

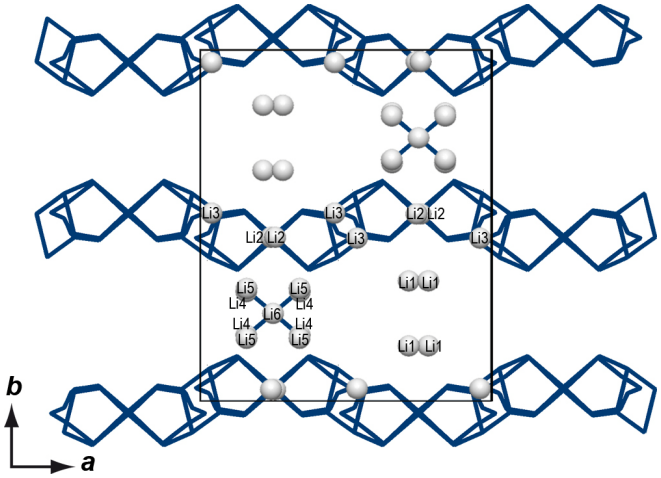

Figure 9.4 Calculated possible Li^+ pathways (blue) according to the voids in the structure and unit cell of Li_4PN_3 viewed along *c*. (Li: gray).

9.2.4 Solid State NMR-Spectroscopy

^{31}P, ^{6}Li, and ^{7}Li solid-state MAS NMR spectroscopy was performed to corroborate the crystal structure models of $Li_{12}P_3N_9$ and Li_4PN_3 (Supporting Information, Figures S9.5–S9.10). The ^{31}P NMR spectrum of $Li_{12}P_3N_9$ shows two strong resonances at 22.76 and 15.08 ppm together with the resonances for Li_7PN_4 (50.23 ppm) and Li_3P (–274.5 ppm). Integration of the two strong signals of $Li_{12}P_3N_9$ results in a ratio of 2:1, which is in accordance with three crystallographically independent P sites, two of which exhibit the same chemical shift (22.76 ppm). This corresponds to P1 and P2, which exhibit nearly the same bonding lengths to N. P3 has one shorter distance to N6 and corresponds to the signal at 15.08 ppm (Figure 9.1).

The ^{6}Li solid-state MAS NMR spectrum shows four strong resonances in the range of 5.2 to 1.9 ppm; they all exhibit shoulders. The ^{7}Li solid-state MAS spectrum shows one broad signal at 4.87 ppm (with Li_7PN_4 and Li_3P as side phase). Due to the small chemical shift differences of the Li signals of $Li_{12}P_3N_9$ and the side phases, no differentiation of the phases and the crystallographically independent sites can be observed in the Li spectra.

The ^{31}P solid-state MAS NMR spectrum of Li_4PN_3 shows one strong resonance at 21.58 ppm, corresponding to one crystallographically independent P site. The ^{31}P MAS NMR signals of both polymorphs are similar with other nitridophosphates (Zn_2PN_3: 42.8 ppm; $Li_{18}P_6N_{16}$: 22.24 to 5.51 ppm).[14,36] The ^{6}Li and ^{7}Li solid-state MAS NMR spectra show one strong signal each (2.41 and 2.59 ppm, respectively). The values found for both compounds are similar to those of other ternary nitridophosphates or lithium nitridophosphates/silicates for ^{7}Li (0.3 for $LiLa_5Si_4N_{10}O$ to 2.8 ppm for $LiCa_3Si_2N_5$; $Li_{18}P_6N_{16}$: 1.6 ppm; Li_7PN_4 (with Li_3P as side phase): 3.33 ppm).[14,38,43]

9.2.5 Chemical Analysis (EDX, IR, Powder Diffraction)

To determine the elemental composition, EDX measurements were carried out. Besides phosphorus and nitrogen, only traces of oxygen were found, which can be explained by the hydrolysis of the compounds during contact with air (Supporting Information, Table S9.10 and S9.11). The determined atomic ratio P/N is in agreement with the results from the crystal structure analysis ($Li_{12}P_3N_9$: P/N=0.32; Li_4PN_3: P/ N=0.33).
FTIR spectroscopy of both compounds was performed to prove the absence of hydrogen (Supporting Information, Figure S9.13 and S9.14). Both spectra show significant vibrations between 600 and 1500 cm^{-1} and no marked signals in the region around 3000 cm^{-1} (N-H). A weak signal can be explained by surface hydrolysis of the sample.

To determine phase purity of the samples a powder diffraction pattern was collected (Supporting Information, Figure S9.3 and S9.4). Rietveld refinement confirms the structure determined by single-crystal structure analysis.

9.2.6 Thermal Stability

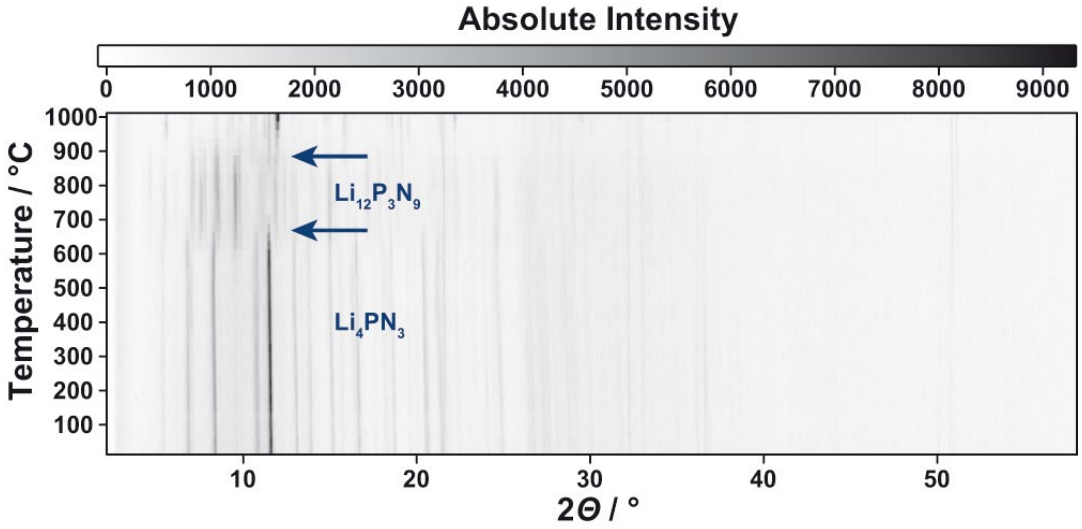

Figure 9.5 Temperature-dependent powder X-ray diffraction data for Li_4PN_3 under ambient pressure. The transformation to $Li_{12}P_3N_9$ starts at 650 °C.

In order to corroborate that Li_4PN_3 is a high-pressure polymorph of $Li_{12}P_3N_9$, a temperature-dependent powder X-ray diffraction pattern was recorded between room temperature and 1000 °C. The results (Figure 9.5) show that at ambient pressure, Li_4PN_3 transforms back into the ambient pressure polymorph $Li_{12}P_3N_9$ at 650 °C. At 880 °C the first indications of further decomposition can be observed.

9.2.7 Comparison of Density

The density of Li_4PN_3 (ρ = 2.405 g cm^{-3}) is 7% higher than that of $Li_{12}P_3N_9$ (ρ = 2.235 g cm^{-3}), which is in accordance with the principle of Le Chatelier and suggests that Li_4PN_3 is a high-pressure polymorph of $Li_{12}P_3N_9$. A density difference in this range is also observed in $P_4N_6(NH)$ with 5 and 16% (α-$P_4N_6(NH)$: 2.88,[26] β-$P_4N_6(NH)$: 3.037,[5] γ-$P_4N_6(NH)$: 3.613 g cm^{-3}).[27] A smaller difference is observed in PN(NH) with 2% (β-cristobalite-type PN(NH): 2.66,[23] β-PN(NH): 2.71 g cm^{-3})[25] and a higher in P_3N_5 with 32% (α-P_3N_5: 2.77, γ-P_3N_5: 3.65 g cm^{-3}).[15]

9.2.8 Density Functional Theory Calculations

9.2.8.1 Volume Pressure Calculations

Due to different observed partial occupancies of three Li sites in Li_4PN_3 we constructed a charge neutral model for Li_4PN_3 with full Li occupancies. Due to different observed partial occupancies of three Li sites in Li_4PN_3 we constructed a charge neutral model for Li_4PN_3 with full Li occupancies. This was done by removing the Li6-Wyckoff site (40% occupation) and subsequently converting half of the partially occupied Li4 (50%) and Li5 (30%) sites into new fully ordered Li sites for our calculations (Figure 9.6).

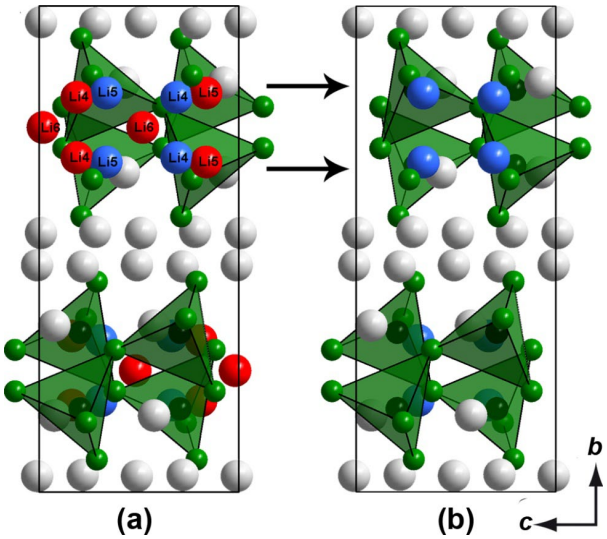

Figure 9.6 (a) Unit cell of Li_4PN_3 with partially occupied Li positions (Li4: 50%, Li5: 30%, Li6: 40%). (b) Ordering model of Li_4PN_3 with fully occupied Li atoms. Red: Li positions which were removed; blue: Li positions which were retained and adjusted to 100% occupancy. (P: black, N: green; Li: gray; PN_4 tetrahedra: green).

Experimental synthesis pressures were covered by structural relaxations for a variety of constant volume compressions and expansions (91% to 105% with 19 steps for both compounds) of the respective unit cells, maintaining the space group. The resulting energy-volume (EV) curves are shown in Figure 9.7a. $Li_{12}P_3N_9$ is energetically favored by 0.217 eV (20.94 kJ mol^{-1}) at ambient pressure. By fitting the EV curves according to the Murnaghan equation of state[44] we obtained the bulk modulus (B = 83.8 for $Li_{12}P_3N_9$ and B=87.4 GPa for Li_4PN_3) and calculated the enthalpy difference ΔH from the equation $H = E + pV$, while pressure p is obtained by a numerical differentiation of $p = \partial E/\partial V$. Figure 9.7b depicts the relative enthalpy with respect to the presumed low pressure polymorph $Li_{12}P_3N_9$.

Without accounting for temperature, the transition pressure from $Li_{12}P_3N_9$ to Li_4PN_3 can be estimated to 6.55 GPa, evidently corroborating Li_4PN_3 as high-pressure polymorph of $Li_{12}P_3N_9$, being in line with the observed synthesis pressure of 6 GPa.

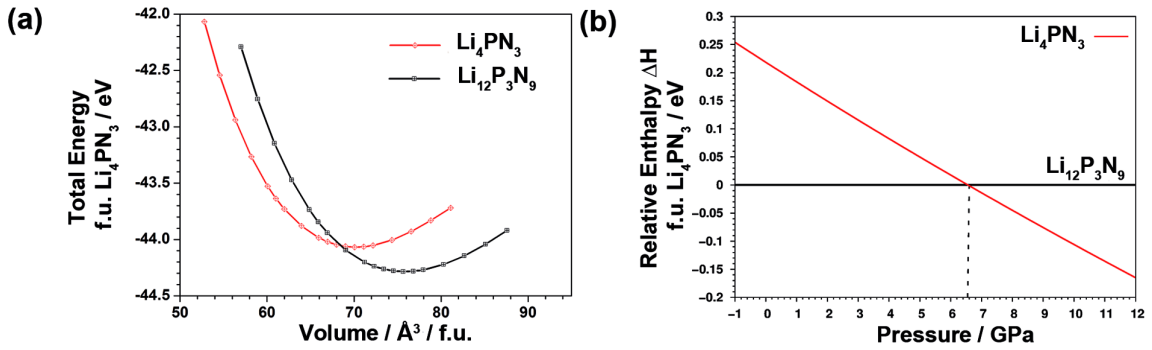

Figure 9.7 (a) Energy–volume diagram for $Li_{12}P_3N_9$ and Li_4PN_3. Each point constitutes one structural optimization at constant volume. Energy and Volume are given per formula unit (f.u.) of Li_4PN_3. (b) Enthalpy–pressure diagram for the high-pressure phase transition of $Li_{12}P_3N_9$ to Li_4PN_3, obtained from a fit of the Murnaghan equation of state to the energy-volume diagram. The enthalpy is given per formula unit of Li_4PN_3 relative to $Li_{12}P_3N_9$.

9.2.8.2 Electronic Band Structure

In Figure 9.8 it can be seen that both Li/P/N polymorphs are electronically insulating materials with a wide electronic indirect band-gap of 5 eV for $Li_{12}P_3N_9$ (*Y* to *Γ*) and an increased direct band gap of 6.1 eV for the high-pressure polymorph Li_4PN_3 (*Γ* to *Γ*).

The value found for $Li_{12}P_3N_9$ is in approximately the same range as in the case of α-P_3N_5 (indirect band gap of 5.21 eV).[45] In comparison, the Si_3N_4 and Ge_3N_4 spinels have direct band gaps and the values are decreasing with increasing pressure (α-Si_3N_4: 5.3, β-Si_3N_4: 5.18, γ-Si_3N_4: 3.45 eV; α-Ge_3N_4: 3.18, β-Ge_3N_4: 3.10, γ-Ge_3N_4: 2.22 eV).[46] Horvath-Bordon *et al.* report that band gaps in high-pressure phases of some nitrides are reduced while the elastic moduli are increased compared to the values found for ambient pressure polymorphs.[46] In contrast Li_3N and BN behave inversely, not moving the system towards a metallic system (α-Li_3N: 1.25, α'-Li_3N: 1.3, β-Li_3N: 1.5, γ-Li_3N: 6 eV; *h*-BN: 3.81–4.10, *c*-BN: 4.20–5.18, *w*-BN: 4.90–5.81 eV).[47,48]

9.2.8.3 Electronic Localization Function

In order to analyze the chemical bonding in both polymorphs we calculated the electron localization function (ELF), constituting the probability of finding an electron of opposed spin within the proximity of another, effectively revealing positions of chemical bonds or electron lone pairs.[49] No indication of covalent bonds between Li and N can be found, corroborating chemical intuition of a strong ionic character. The P-N bonding situation for an ELF isovalue $\eta = 0.83$ reveals strong covalency within the $[P_3N_9]^{12-}$ and $^3_\infty[PN_2N_{2/2}]^{4-}$units (Supporting Information, Figures S9.16 to S9.18). The P-N bonds show strong N-polarization and free electron pairs of N^{3-} are found at terminal and bridging N atoms, as expected from VSEPR considerations.

Recently, highly polarized (almost ionic) P−N bonds have been discussed in $(PNCl_2)_3$. Analysis of the density distribution showed that the rings can be separated into Cl_2PN units that indicate perfect transferability between the different rings, which excludes the presence of aromatic delocalization in the planar P_3N_3 ring of $(PNCl_2)_3$.[50]

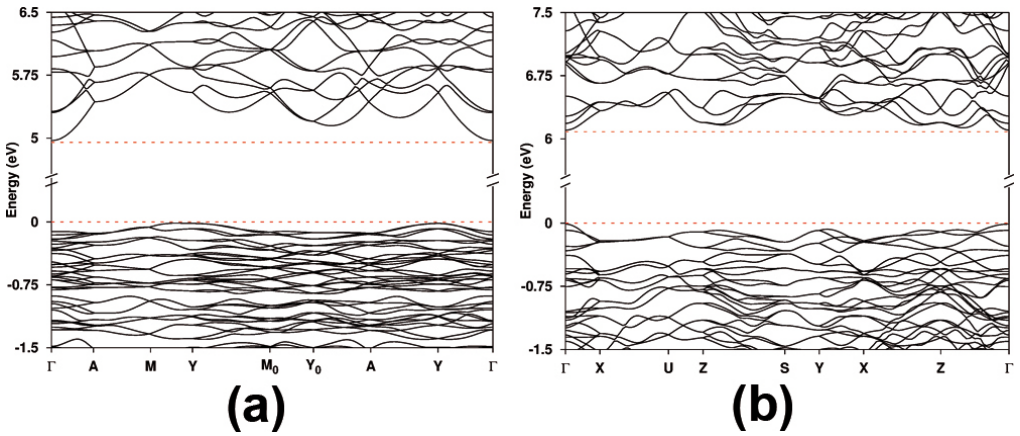

Figure 9.8 Electronic band structure along high-symmetry directions in the first Brillouin zone for (a) $Li_{12}P_3N_9$ and (b) Li_4PN_3.

9.3 Conclusion

Herein we report on synthesis and full characterization of two lithium nitridophosphate polymorphs, namely $Li_{12}P_3N_9$ and Li_4PN_3. The ambient pressure polymorph $Li_{12}P_3N_9$ was prepared in ampoules and the high-pressure polymorph Li_4PN_3 by solid-state high-pressure synthesis. We showed that Li_4PN_3 is a reconstructive high-pressure polymorph of $Li_{12}P_3N_9$. This phase relation was deduced from experimental data as well as temperature-dependent powder X-ray diffraction and DFT calculations. $Li_{12}P_3N_9$ is made of *dreier*-rings, which are not further condensed, surrounded by a matrix of Li^+ ions. The new lithium *catena*-nitridophosphate with infinite chains of corner sharing PN_4-tetrahedra has a stretching factor of f_s = 0.923 and a chain periodicity P = 2. Li_4PN_3 reveals that high-pressure synthesis gives an important boost to nitridophosphate chemistry by realizing compounds that were not accessible before. Furthermore, it shows that this approach is a powerful technique to obtain novel lithium nitridophosphates with unprecedented structures and interesting properties. In addition, this finding could indicate that even ternary lithium nitridophosphates with layered structures could be accessible using multianvil techniques.

9.4 Experimental Section

9.4.1 Synthesis of Starting Materials

P_3N_5[51] was synthesized by reaction of P_4S_{10} (8 g, Sigma–Aldrich, 99%) in a constant flow of ammonia (Air-Liquide, 99.999%). After saturation for 4 h with NH_3, the silica tube was heated to 1123 K with 5 K min^{-1} and kept at this temperature for an additional 4 h. It was subsequently cooled down to room temperature with 5 K min^{-1}. To eliminate side products, the orange product was washed with water, ethanol, and acetone. Powder X-ray diffraction and FTIR spectroscopy confirmed phase purity of P_3N_5. All further steps were performed with strict exclusion of oxygen and moisture in an argon filled glove box (Unilab, MBraun, Garching, O_2<1 ppm, H_2O<0.1 ppm). $LiPN_2$[22] and Li_7PN_4[17] were synthesized by reaction of Li_3N (Rockwood Lithium, 95%) and P_3N_5 ($LiPN_2$: molar ratio 1.2:1; Li_7PN_4: 7.2:1) in sealed silica ampoules under N_2 atmosphere. After grinding the starting materials they were transferred into a Ta-crucible, which was placed in a dried silica tube. The sealed silica ampoule was heated for 90 h in a tube furnace at 1073 or 893 K, respectively. To eliminate side products, $LiPN_2$ was washed with diluted hydrochloric acid, water, and ethanol. Li_7PN_4 was not washed. Powder X-ray diffraction and FTIR spectroscopy confirmed phase purity of the starting materials.

9.4.2 Synthesis of $Li_{12}P_3N_9$

$Li_{12}P_3N_9$ can be synthesized according to three different routes in sealed silica ampoules under Ar atmosphere. For synthesis according to Equation (1) Li_3N (Rockwood Lithium, 95%) and P_3N_5 were mixed with a molar ratio of 4.2:1 (Equation (2): $LiPN_2$ and Li_3N with a molar ratio of 1:1.2; Equation (3): $LiPN_2$, Li_7PN_4 and Li_3N with a molar ratio of 2:1 : 1.1). After grinding the starting materials in an agate mortar, the mixture was transferred into a tantalum crucible, which was placed in a dried silica tube. The ampoules were heated for 120 h in a tube furnace at 790 °C

(Equation (2): 680 °C; Equation (3): 650 °C). All syntheses yielded a colorless powder containing dark traces (Li_3P) and single crystals of $Li_{12}P_3N_9$. The product was sensitive to traces of air and moisture.

9.4.3 High-Pressure Synthesis of Li_4PN_3

Li_4PN_3 can be synthesized according to two different routes at high-pressure/high-temperature conditions with a modified Walker–type multianvil module in combination with a 1000 t press (Voggenreiter, Mainleus, Germany).[28–32] After mixing the starting materials, they were ground under argon atmosphere and compactly packed in a *h*-BN crucible (Henze BNP GmbH, Kempten, Germany). The *h*-BN crucible was transferred into the specially prepared pressure medium (Cr_2O_3 doped (5%) MgO-octahedra (Ceramic Substrates & Components, Isle of Wight, UK); edge length 18 mm [Eq. (4)] or 14 mm [Eq. (5)]). Then the octahedron was placed centrically in eight truncated WC cubes (Hawedia, Marklkofen, Germany, truncation length 11 mm [Eq. (4)] or 8 mm [Eq. (5)]) separated by pyrophyllite gaskets. Detailed information describing the complete setup can be found in the literature.[29, 30, 32] According to Equation (4) (Equation (5)) the assembly was compressed to 6 GPa (9 GPa) at room temperature within 2.6 h (4 h) and then heated to about 820 °C (1200 °C) within 1 h (1 h). Under these conditions, the sample was treated for 1.6 h (1 h) and cooled down to room temperature within 1.6 h (1 h). Subsequently, the sample was decompressed in 8 h (12.5 h). Both syntheses yielded a colorless powder containing single crystals. The product is sensitive to traces of air and moisture.

9.4.4 Single-crystal X-ray Analysis

Single-crystal X-ray diffraction was performed with a D8 Venture diffractometer (Bruker, Billerica MA, USA) using $Mo_{K\alpha}$ radiation from a rotating anode source. The collected data were averaged with Xprep[52] and the program package WinGX (SHELXS-97, SHELXL-97, PLATON)[40, 53-55] was used for structure solution by direct methods and refinement (see Table 9.1).[56] All P and N atoms were refined anisotropically. The crystal structure was visualized using DIAMOND.[57]

9.4.5 Powder X-ray Diffraction

To check phase purity of the products, X-ray powder diffraction was carried out with a STOE StadiP diffractometer (Stoe & Cie, Darmstadt, Germany) in parafocusing Debye–Scherrer geometry. With a Ge(111) single-crystal monochromator the $Cu_{K\alpha1}$ radiation was selected. A Mythen 1 K Si-strip detector (Dectris, Baden, Switzerland) was used for detection of the diffracted radiation. For measurement the samples were enclosed in glass capillaries with 0.5 mm diameter (Hilgenberg, Malsfeld, Germany) under inert gas. Rietveld refinement was carried out using the program package TOPAS-Academic v4.1.[58] The background was handled with a shifted Chebychev function and the peak shapes were described using the fundamental parameters approach.[59, 60]

Temperature-dependent powder X-ray diffraction data were recorded on a STOE StadiP diffractometer equipped with a graphite furnace with $Mo_{K\alpha1}$ radiation (λ = 0.70930 Å) in

Debye-Scherrer geometry, an image plate position sensitive detector and a Ge(111) monochromator. Data were collected every 25 °C, starting from room temperature up to 1000 °C, with a heating rate of 5 °C min^{-1}.

9.4.6 Solid-State NMR MAS (Magic Angle Spinning) NMR Methods

^{6}Li, ^{7}Li, and ^{31}P solid-state MAS NMR spectra of both polymorphs were recorded on a DSX Avance spectrometer (Bruker) with a magnetic field of 11.7 T. The sample was transferred into a ZrO_2 rotor, with an outer diameter of 2.5 mm, which was mounted in a commercial MAS probe (Bruker) under inert conditions. The rotor was spun at rotation frequency of 20 kHz. The experimental data were analyzed by device-specific software.

9.4.7 EDX Measurements

The atomic ratio P/N of the samples was analyzed by energy-dispersive X-ray spectroscopy. A carbon-coated sample was examined with a scanning electron microscope (SEM) JSM-6500F (Joel, Tokyo, Japan, maximum acceleration voltage 30 kV). Qualitative and semiquantitative elemental analyses were executed by an energy dispersive spectrometer (Model 7418, Oxford Instruments, Abington, United Kingdom) and analyzed by INCA.[61]

9.4.8 Fourier-transformed Infrared (FTIR) Spectroscopy

Infrared spectroscopy measurements were carried out on a Bruker FTIR-IFS 66v/S spectrometer. Before measurement in the range of 400–4000 cm^{-1} the sample was mixed with KBr in a glove box and cold-pressed into a pellet (Ø = 12 mm). The data were evaluated by OPUS.[62]

9.4.9 Computational Details

The structural relaxation of both of $Li_{12}P_3N_9$ and Li_4PN_3 were carried out with the Vienna ab initio simulation package (VASP).[63–65] Total energies of the unit cell were converged to 10^{-7} eV $atom^{-1}$ with residual atomic forces below 5×10^{-3} eV $Å^{-1}$. The exchange correlation was treated within the generalized gradient approximation (GGA) of Perdew, Burke, and Ernzerhof (PBE)[66, 67] and the projector-augmented-wave (PAW) method.[68,69] A plane-wave cut-off of 535 eV was chosen for the calculations with a Brillouin zone sampling on a *Γ*-centered *k*-mesh, produced from the method of Monkhorst and Pack,[70] of 5 × 7 × 6 ($Li_{12}P_3N_9$) and 6 × 5 × 11 (Li_4PN_3) respectively. Additional calculations were performed with the modified Becke-Johnson formalism (GGA-mbj)[71,72] to treat the electronic band gaps.

9.5 Acknowledgements

We would like to thank Dr. Peter Mayer for single-crystal X-ray measurements, Thomas Miller for high-temperature powder diffraction measurements, Christian Minke for EDX, SEM, and solid-state MAS NMR measurements, Marion Sokoll for IR measurements, and Dr. Constantin Hoch for helpful discussions concerning the structural analysis (all at Department of Chemistry of LMU Munich). We gratefully acknowledge financial support and granted by the Fonds der Chemischen Industrie (FCI), the Deutsche Forschungsgemeinschaft (DFG).

9.6 References

[1] W. Schnick, Solid-State Chemistry with Nonmetal Nitrides, *Angew. Chem. Int. Ed. Engl.* **1993**, *32*, 806–818; *Angew. Chem.* **1993**, *105*, 846–858.

[2] W. Schnick, J. Lücke, F. Krumeich, Phosphorus Nitride P_3N_5: Synthesis, Spectroscopic, and Electron Microscopic Investigations *Chem. Mater.* **1996**, *8*, 281–286.

[3] S. Horstmann, E. Irran, W. Schnick, Synthesis and Crystal Structure of Phosphorus(V) Nitride α-P_3N_5, *Angew. Chem. Int. Ed. Engl.* **1997**, *36*, 1873–1875; *Angew. Chem.* **1997**, *109*, 1938–1940.

[4] W. Schnick, J. Lücke, $Zn_7[P_{12}N_{24}]Cl_2$ – A Sodalite with a Phosphorus Nitrogen Framework, *Angew. Chem. Int. Ed. Engl.* **1992**, *31*, 213–215; *Angew. Chem.* **1992**, *104*, 208–209.

[5] D. Baumann, W. Schnick, High-Pressure Polymorph of Phosphorus Nitride Imide HP_4N_7 Representing a New Framework Topology, *Inorg. Chem.* **2014**, *53*, 7977–7982.

[6] S. Horstmann, E. Irran, W. Schnick, Phosphorus(V) Nitride Imide HP_4N_7: Synthesis from a Molecular Precursor and Structure Determination with Synchrotron Powder Diffraction, *Angew. Chem. Int. Ed. Engl.* **1997**, *36*, 1992–1994; *Angew. Chem.* **1997**, *109*, 2085–2087.

[7] A. Marchuk, W. Schnick, $Ba_3P_5N_{10}Br:Eu^{2+}$: A Natural-White-Light Single Emitter with Zeolite Structure Type, *Angew. Chem. Int. Ed.* **2015**, *54*, 2383–2387; *Angew. Chem.* **2015**, *127*, 2413–2417.

[8] S. J. Sedlmaier, M. Döblinger, O. Oeckler, J. Weber, J. Schmedt auf der Günne, W. Schnick, Unprecedented Zeolite-Like Framework Topology Constructed from Cages with 3-Rings in a Barium Oxonitridophosphate, *J. Am. Chem. Soc.* **2011**, *133*, 12069–12078.

[9] S. Correll, O. Oeckler, N. Stock, W. Schnick, $Li_xH_{12-x-y+z}[P_{12}O_yN_{24-y}]Cl_z$ – An Oxonitridophosphate with a Zeolitelike Framework Structure Composed of 3-Rings, *Angew. Chem. Int. Ed.* **2003**, *42*, 3549–3552; *Angew. Chem.* **2003**, *115*, 3674–3677.

[10] S. Correll, N. Stock, O. Oeckler, J. Senker, T. Nilges, W. Schnick, $Li_xH_{12-x-y+z}[P_{12}O_yN_{24-y}]X_z$ (*X* = Cl, Br) - Oxonitridophosphate mit NPO-Zeolithstruktur, *Z. Anorg. Allg. Chem.* **2004**, *630*, 2205–2217.

[11] S. Zhao, Z. Fu, Q. Qin, A solid-state electrolyte lithium phosphorus oxynitride film prepared by pulsed laser deposition, *Thin Solid Films* **2002**, *415*, 108–113.

[12] W. Schnick, J. Lücke, Lithium Ion Conductivity of $LiPN_2$ and Li_7PN_4, *Solid State Ionics* **1990**, *38*, 271–273.

[13] S. Correll, N. Stock, W. Schnick, Synthesis, crystal structures and properties of the *bis*-(trimetaphosphimato)-metallates $Na_4\{Co[(PO_2NH)_3]_2\}\cdot 12H_2O$ and $Na_4\{Ni[(PO_2NH)_3]_2\}\cdot 12H_2O$, *Solid State Sci.* **2004**, *6*, 953–965.

[14] E.-M. Bertschler, C. Dietrich, J. Janek, W. Schnick, $Li_{18}P_6N_{16}$ – A Lithium Nitridophosphate with Unprecedented Tricyclic $[P_6N_{16}]^{18-}$ Ions *Chem. Eur. J.* **2017**, *23*, 2185–2191.

[15] K. Landskron, H. Huppertz, J. Senker, W. Schnick, High-Pressure Synthesis of γ-P_3N_5 at 11 GPa and 1500 °C in a Multianvil Assembly: A Binary Phosphorus(V) Nitride with a Three-Dimensional Network Structure from PN_4 Tetrahedra and Tetragonal PN_5 Pyramids, *Angew. Chem. Int. Ed.* **2001**, *40*, 2643–2645; *Angew. Chem.* **2001**, *113*, 2713–2716.

[16] K. Landskron, H. Huppertz, J. Senker, W. Schnick, Multianvil-Synthese, Pulver-Röntgenstrukturanalyse, ^{31}P-MAS-NMR- und FTIR-Spektroskopie sowie Materialeigenschaften von γ-P_3N_5, einer Hochdruckphase von binäremPhosphor(V)-nitrid mit verzerrt quadratischen PN_5-Pyramiden und PN_4-Tetraedern, *Z. Anorg. Allg. Chem.* **2002**, *628*, 1465–1471.

[17] W. Schnick, J. Lücke, Synthesis and Crystal Structure of Lithium Phosphorus Nitride Li_7PN_4: The First Compound Containing Isolated PN_4-Tetrahedra, *J. Solid State Chem.* **1990**, *87*, 101–106.

[18] F. Liebau, *Structural Chemistry of Silicates*, Springer, **1985**.

[19] The term dreier (vierer) ring was coined by Liebau and is derived from the German word "drei" ("vier"). A dreier (vierer) ring comprised three (four) tetrahera centers.

[20] W. Schnick, Darstellung, Charakterisierung und festkörperchemische Umsetzungen von Phosphor(V)-nitrid, *habilitation treatise*, University of Bonn, **1992**.

[21] U. Berger, W. Schnick, $Li_{10}P_4N_{10}$ - A Lithium Phosphorus(V) Nitride with the Novel Complex Anion $P_4N_{10}^{10-}$, *Angew. Chem. Int. Ed. Engl.* **1991**, *30*, 830–831; *Angew. Chem.* **1991**, *103*, 857–858.

[22] W. Schnick, J. Lücke, Zur Kenntnis von Lithium-phosphor(V)-nitrid. Reindarstellung und Verfeinerung der Kristallstruktur von $LiPN_2$, *Z. Anorg. Allg. Chem.* **1990**, *588*, 19–25.

[23] W. Schnick, J. Lücke, Darstellung, Kristallstruktur und IR-spektroskopische Untersuchung von Phosphor(V)-nitrid-imid, HPN_2, *Z. Anorg. Allg. Chem.* **1992**, *610*, 121–126.

[24] R. Nymwegen, S. Doyle, T. Wroblewski, W. Kockelmann, H. Jacobs, Kristallines Phoshor(V)-nitrid-imid, HPN_2 bzw. DPN_2 – Strukturbestimmung mit Röntgen-, Synchrotron- und Neutronenstrahlung, *Z. Anorg. Allg. Chem.* **1997**, *623*, 1467–1474.

[25] A. Marchuk, F. J. Pucher, F. W. Karau, W. Schnick, A High-Pressure Polymorph of Phosphorus Nitride Imide, *Angew. Chem. Int. Ed.* **2014**, *53*, 2469–2472*, Angew. Chem.* **2014**, *126*, 2501–2504.

[26] S. Horstmann, E. Irran, W. Schnick, Synthese, Kristallstruktur und Eigenschaften von Phosphor(V)-nitridimid HP_4N_7, *Z. Anorg. Allg. Chem.* **1998**, *624*, 221–227.

[27] D. Baumann, W. Schnick, Pentacoordinate Phosphorus in a High-Pressure Polymorph of Phosphorus Nitride Imide $P_4N_6(NH)$, *Angew. Chem. Int. Ed.* **2014**, *53*, 14490–14493; *Angew. Chem.* **2014**, *126*, 14718–14721.

[28] N. Kawai, S. Endo, The Generation of Ultrahigh Hydrostatic Pressures by a Split Sphere Apparatus, *Rev. Sci. Instrum.* **1970**, *41*, 1178–1181.

[29] D. Walker, M. A. Carpenter, C. M. Hitch, Some simplifications to multianvil devices for high pressure experiments, *Am. Mineral.* **1990**, *75*, 1020–1028.

[30] D. Walker, Lubrication, gasketing, and precision in multianvil experiments, *Am. Mineral.* **1991**, *76*, 1092–1100.

[31] D. C. Rubie, Characterising the sample environment in multianvil high-pressure experiments, *Phase Transitions* **1999**, *68*, 431–451.

[32] H. Huppertz, Multianvil high-pressure / high-temperature synthesis in solid state chemistry, *Z. Kristallogr.* **2004**, *219*, 330–338.

[33] W. Schnick, Phosphorus(V) Nitrides: Preparation, Properties, and Possible Applications of New Solid State Materials with Structural Analogies to Phosphates and Silicates, *Phosphorus. Sulfur. Silicon Relat. Elem.* **1993**, *76*, 183–186.

[34] V. Schultz-Coulon, W. Schnick, Mg_2PN_3 und Ca_2PN_3 - Phosphor(V)-nitride mit eindimensional unendlichen Ketten eckenverknüpfter PN_4-Tetraeder *Z. Anorg. Allg. Chem.* **1997**, *623*, 69–74.

[35] V. Schulz-Coulon, W. Schnick, Ca_2PN_3 – A Novel Phosphorus(V) Nitride with One-Dimensional Infinite Chains of Corner-Sharing PN_4 Tetrahedra, *Angew. Chem. Int. Ed. Engl.* **1993**, *32*, 280–281; *Angew. Chem.* **1993**, *108*, 308–309.

[36] S. J. Sedlmaier, M. Eberspächer, W. Schnick, High-Pressure Synthesis, Crystal Structure, and Characterization of Zn_2PN_3 – A New *catena*-Polynitridophosphate, *Z. Anorg. Allg. Chem.* **2011**, *637*, 362–367.

[37] A. Durif, *Crystal Chemistry of Condensed Phosphates*, Springer, Berlin, **1995**.

[38] S. Lupart, W. Schnick, $LiCa_3Si_2N_5$ – A Lithium Nitridosilicate with a $[Si_2N_5]^{7-}$ Double-Chain, *Z. Anorg. Allg. Chem.* **2012**, *638*, 2015–2019.

[39] V. A. Blatov, Voronoi–dirichlet polyhedra in crystal chemistry: theory and applications, *Cryst. Rev.* **2004**, *10*, 249–318.

[40] G. M. Sheldrick, *SHELXS*, University of Göttingen, **1997**.

[41] N. A. Anurova, V. A. Blatov, G. D. Ilyushin, O. A. Blatova, A. K. Ivanov-Schitz, L. N. Dem'yanets, Migration maps of Li^+ cations in oxygen-containing compounds, *Solid State Ionics* **2008**, *179*, 2248–2254.

[42] V. A. Blatov, A. P. Shevchenko, V. N. Serezhkin, TOPOS3.1 – program package for multipurpose geometrical and topological analysis of crystal structures, *J. Appl. Cryst.* **1999**, *32*, 377–377.

[43] S. Lupart, W. Schnick, $LiLa_5Si_4N_{10}O$ and $LiPr_5Si_4N_{10}O$ – Chain-Type Oxonitridosilicates, *Z. Anorg. Allg. Chem.* **2012**, *638*, 94–97.

[44] F. D. Murnaghan, The Compressibility of Media under Extreme Pressures, *Proc. Natl. Acad. Sci. USA* **1944**, *30*, 244–247.

[45] T. M. Tolhurst, C. Braun, T. D. Boyko, W. Schnick, A. Moewes, Experiment-Driven Modeling of Crystalline Phosphorus Nitride P_3N_5: Wide-Ranging Implications from a Unique Structure, *Chem. Eur. J.* **2016**, *22*, 10475–10483.

[46] E. Horvath-Bordon, R. Riedel, A. Zerr, P. F. McMillan, G. Auffermann, Y. Prots, W. Bronger, R. Kniep, P. Kroll, High-pressure chemistry of nitride-based materials, *Chem. Soc. Rev.* **2006**, *35*, 987–1014.

[47] Y. Yan, J. Y. Zhang, T. Cui, Y. Li, Y. M. Ma, J. Gong, Z. G. Zong, G. T. Zou, First-principles study of high pressure phase transformations in Li_3N, *Eur. Phys. J. B* **2008**, *61*, 397–403.

[48] C. E. Dreyer, J. L. Lyons, A. Janotti, C. G. Van De Walle, Band alignments and polarization properties of BN polymorphs, *Appl. Phys. Express* **2014**, *7*, 31001.

[49] A. D. Becke, K. E. Edgecombe, A simple measure of electron localization in atomic and molecular systems, *J. Chem. Phys.* **1990**, *92*, 5397–5403.

[50] V. Jancik, F. Cortés-Guzmán, R. Herbst-Irmer, D. Martínez-Otero, Is Hexachloro-cyclo-triphosphazene Aromatic? Evidence from Experimental Charge Density Analysis, *Chem. Eur. J.* **2017**, *23*, 6964–6968.

[51] A. Stock, H. Grüneberg, Über den Phosphorstickstoff, *Ber. Dtsch. Chem. Ges.* **1907**, *40*, 2573–2578.

[52] XPREP Reciprocal Space Exploration*, Vers. 6.12*, Bruker-AXS, Karlsruhe, **2001**.

[53] G. M. Sheldrick, A short history of SHELX, *Acta Crystallogr. Sect. A* **2008**, *64*, 112–122.

[54] L. J. Farrugia, WinGX suite for small-molecule single-crystal crystallography, *J. Appl. Crystallogr.* **1999**, *32*, 837–838.

[55] L. J. Farrugia, *PLATON, Vers. 1.16*, University of Glasgow, **1995**.

[56] Further details of the crystal structure investiation can be obatined from the Fachinformations-Zentrum Karlsruhe, 76344 Eggenstein- Leopoldshafen, Germany (Fax: (+49)7247-808-666; E-Mail: Crysdata@fiz-Karlsruhe.de) on Quoting the Depository Number CSD- 432590 ($Li_{12}P_3N_9$) and CSD-432591 (Li_4PN_3).

[57] K. Brandenburg, Crystal Impact GbR: Bonn **2005**.

[58] A. Coelho, *TOPAS-Academic* **2007**.

[59] R. W. Cheary, A. Coelho, A fundamental parameters approach to X-ray line-profile fitting, *J. Appl. Crystallogr.* **1992**, *25*, 109–121.

[60] R. W. Cheary, A. A. Coelho, J. P. Cline, Fundamental Parameters Line Profile Fitting in Laboratory Diffractometers, *J. Res. Natl. Inst. Stand. Technol.* **2004**, *109*, 1–25.

[61] *INCA, Version 4.02*, OXFORD Instruments.

[62] *OPUS/IR*, Bruker Analytik GmbH, **2000**.

[63] G. Kresse, J. Hafner, *Ab initio* molecular dynamics for liquid metals, *Phys. Rev. B: Condens. Matter Mater. Phys.* **1993**, *47*, 558–561.

[64] G. Kresse, J. Hafner, *Ab initio* molecular-dynamics simulation of the liquid-metal-amorphous-semiconductor transition in germanium, *Phys. Rev. B: Condens. Matter Mater. Phys.* **1994**, *49*, 14251–14269.

[65] G. Kresse, J. Furthmüller, Efficiency of *ab-initio* total energy calculations for metals and semiconductors using a plane-wave basis set, *Comput. Mater. Sci.* **1996**, *6*, 15–50.

[66] J. P. Perdew, K. Burke, M. Ernzerhof, Generalized Gradient Approximation Made Simple, *Phys. Rev. Lett.* **1996**, *77*, 3865–3868.

[67] J. P. Perdew, K. Burke, M. Ernzerhof, Generalized Gradient Approximation Made Simple [*Phys. Rev. Lett.* **1996**, *77*, 3865], *Phys. Rev. Lett.* **1997**, *78*, 1396.

[68] P. E. Blöchl, Projector augmented-wave method, *Phys. Rev. B: Condens. Matter Mater. Phys.* **1994**, *50*, 17953–17979.

[69] G. Kresse, D. Joubert, From ultrasoft pseudopotentials to the projector augmented-wave method, *Phys. Rev. B: Condens. Matter Mater. Phys.* **1999**, *59*, 1758–1775.

[70] H. J. Monkhorst, J. D. Pack, Special points for Brillouin-zone integrations, *Phys. Rev. B: Solid State* **1976**, *13*, 5188–5192.

[71] F. Tran, P. Blaha, Accurate Band Gaps of Semiconductors and Insulators with a Semilocal Exchange-Correlation Potential, *Phys. Rev. Lett.* **2009**, *102*, 226401.

[72] J. A. Camargo-Martínez, R. Baquero, Performance of the modified Becke-Johnson potential for semiconductors, *Phys. Rev. B: Condens. Matter Mater. Phys.* **2012**, *86*, 195106.

9.7 Supporting Information

9.7.1 Additional Crystallographic Data for $Li_{12}P_3N_9$

Table S9.1 Fractional atomic coordinates, isotropic thermal displacement parameters, and site occupancies for $Li_{12}P_3N_9$

Atom	Wyckoff symbol	*x*	*y*	*z*	U_{iso} / Å^2	Occupancy
P1	4*a*	0.12676(11)	0.1655(2)	0.3023(2)	0.0033(3)	1
P2	4*a*	0.38275(12)	0.6692(2)	0.3047(2)	0.0040(3)	1
P3	4*a*	0.0060(2)	0.4422(2)	0.1523(2)	0.0038(2)	1
N1	4*a*	0.2309(4)	0.1604(7)	0.4098(6)	0.0044(10)	1
N2	4*a*	0.2818(4)	0.6837(7)	0.4147(5)	0.0051(10)	1
N3	4*a*	0.5082(6)	0.1534(5)	0.1603(5)	0.0055(8)	1
N4	4*a*	0.1347(4)	0.0265(7)	0.1793(6)	0.0043(10)	1
N5	4*a*	0.0061(5)	0.1228(5)	0.3914(4)	0.0049(8)	1
N6	4*a*	0.1157(5)	0.3748(7)	0.2494(5)	0.0044(10)	1
N7	4*a*	0.0000(5)	0.3578(5)	0.0000(4)	0.0045(8)	1
N8	4*a*	0.3638(4)	0.5300(7)	0.1821(6)	0.0056(10)	1
N9	4*a*	0.3978(5)	0.1256(7)	0.7459(5)	0.0060(11)	1
Li1	4*a*	0.2626(10)	0.416(2)	0.3351(13)	0.008(2)	1
Li2	4*a*	0.2497(9)	0.083(2)	0.7963(11)	0.008(2)	1
Li3	4*a*	0.5037(12)	0.4019(12)	0.2575(9)	0.010(2)	1
Li4	4*a*	0.1202(9)	0.1816(14)	0.5701(11)	0.006(2)	1
Li5	4*a*	0.0063(12)	0.3923(12)	0.4387(10)	0.007(2)	1
Li6	4*a*	0.6158(10)	0.131(2)	0.3412(13)	0.010(2)	1
Li7	4*a*	0.2242(9)	0.4352(13)	0.0861(11)	0.007(2)	1
Li8	4*a*	0.4048(10)	0.325(2)	0.0617(12)	0.011(2)	1
Li9	4*a*	0.2459(10)	0.075(2)	0.0354(12)	0.013(2)	1
Li10	4*a*	0.3957(9)	0.122(2)	0.3309(12)	0.009(2)	1
Li11	4*a*	0.0181(10)	0.0974(12)	0.0425(10)	0.009(2)	1
Li12	4*a*	0.3419(9)	0.2376(14)	0.5558(11)	0.011(2)	1

Table S9.2 Anisotropic displacement parameters occurring in $Li_{12}P_3N_9$

Atom	U_{11} / Å^2	U_{22} / Å^2	U_{33} / Å^2	U_{12} / Å^2	U_{13} / Å^2	U_{23} / Å^2
P1	0.0049(8)	0.0021(7)	0.0031(8)	-0.0001(6)	0.0002(5)	-0.0001(5)
P2	0.0064(8)	0.0026(7)	0.0030(8)	-0.0004(6)	-0.0001(5)	-0.0006(6)
P3	0.0065(5)	0.0016(5)	0.0034(5)	-0.0004(7)	-0.0012(6)	0.0004(5)
N1	0.006(2)	0.001(2)	0.006(2)	0.000(2)	0.002 (2)	0.002(2)
N2	0.010(3)	0.004(2)	0.002(2)	-0.000(2)	0.000(2)	-0.002(2)
N3	0.009(2)	0.003(2)	0.005(2)	-0.001(3)	0.001(2)	0.000(2)
N4	0.004(2)	0.002(2)	0.007(2)	0.002(2)	-0.002(2)	-0.001 (2)
N5	0.008(2)	0.005 (2)	0.001(2)	0.001(2)	0.001(2)	0.001(2)
N6	0.007(3)	0.002(2)	0.004(2)	0.001(2)	0.001(2)	0.001(2)
N7	0.008(2)	0.003(2)	0.003(2)	-0.002(2)	-0.004(2)	0.0001(14)
N8	0.004(2)	0.006(3)	0.006(2)	0.000(2)	-0.002(2)	-0.001(2)
N9	0.011(3)	0.004(3)	0.004(3)	0.000(2)	0.001(2)	-0.000(2)

Table S9.3 List of interatomic distances / Å for $Li_{12}P_3N_9$

P1—N4	1.603(5)	P2—N8	1.612(6)	P3—N7	1.616(4)
P1—N1	1.628(6)	P2—N2	1.633(5)	P3—N3^{vi}	1.617(4)
P1—N6	1.686(5)	P2—N9^{iii}	1.681(6)	P3—N9^{vii}	1.683(6)
P1—N5	1.734(6)	P2—N5^{iv}	1.742(6)	P3—N6	1.700(6)
N1—Li12	2.032(12)	N1—Li4	2.069(12)	N1—Li1	2.127(13)
N1—Li10	2.162(13)	N1—Li2^{i}	2.180(12)	N1—Li9^{viii}	2.183(13)
N2—Li7^{v}	2.026(12)	N2—Li2^{iii}	2.153(12)	N2—Li1	2.195(13)
N2—Li8^{v}	2.054(13)	N2—Li6^{vi}	2.161(14)	N2—Li9^{v}	2.230(13)
N3—Li8	2.049(13)	N3—Li3	2.123(10)	N3—Li5^{x}	2.180(11)
N3—Li4^{x}	2.054(12)	N3—Li10	2.166(13)	N3—Li6	2.183(14)
N4—Li4^{i}	1.919(12)	N4—Li9	1.984(13)	N4—Li3^{ii}	2.00(2)
N4—Li2^{i}	1.976(12)	N4—Li11	2.003(12)	N5—Li8^{xi}	2.104(12)
N5—Li5	2.113(10)	N5—Li3^{ii}	2.132(10)	N5—Li11^{viii}	2.238(10)
N5—Li4	2.253(12)	N6—Li1	1.982(13)	N6—Li7	2.119(11)
N6—Li6^{vi}	2.159(13)	N6—Li5	2.278(12)	N7—Li5^{iii}	2.003(10)
N7—Li11	2.046(10)	N7—Li6^{vii}	2.094(14)	N7—Li12^{vii}	2.121(13)
N7—Li10^{vii}	2.067(12)	N8—Li8	2.015(13)	N8—Li7	2.052(12)
N8—Li3	2.08(2)	N8—Li12^{iii}	2.175(12)	N8—Li11^{iv}	2.374(12)
N8—Li1	2.119(13)	N9—Li2	1.888(12)	N9—Li10^{viii}	2.067(13)
N9—Li12	2.139(12)	N9—Li5^{xii}	2.281(13)		

(i) x, -y, -0.5+z; (ii) -0.5+x, -0.5+y, z; (iii) x, 1-y, -0.5+z; (iv) 0.5+x, 0.5+y, z;
(v) x, 1-y, 0.5+z; (vi) -0.5+x, 0.5+y, z; (vii) -0.5+x, 0.5-y, -0.5+z; (viii) x, -y, 0.5+z;
(ix) 0.5+x, -0.5+y, z; (x) 0.5+x, 0.5-y, -0.5+z; (xi) -0.5+x, 0.5-y, 0.5+z; (xii) 0.5+x, 0.5-y, 0.5+z;
(xiii) x, y, 1+z; (xiv) x, y, -1+z.

Table S9.4 List of bond angles / ° for $Li_{12}P_3N_9$

N–P–N					
N4—P1—N1	114.2(3)	N8—P2—N2	115.2(3)	N9^{vii}—P3—N6	102.3(2)
N4—P1—N6	114.0(3)	N8—P2—N9^{iii}	112.4(3)	N7—P3—N3^{vi}	116.3(2)
N1—P1—N6	106.1(3)	N2—P2—N9^{iii}	104.0(3)	N7—P3—N9^{vii}	110.0(3)
N4—P1—N5	107.6(3)	N8—P2—N5^{iv}	109.7(3)	N3^{vi}—P3—N9^{vii}	107.1(3)
N1—P1—N5	109.0(3)	N2—P2—N5^{iv}	109.9(3)	N7—P3—N6	114.5(3)
N6—P1—N5	105.4(3)	N9^{iii}—P2—N5^{iv}	105.0(3)	N3^{vi}—P3—N6	105.3(3)
P–N–P					
P1—N5—P2^{ii}	116.2(2)	P1—N6—P3	121.1(3)		

(i) x, -y, -0.5+z; (ii) -0.5+x, -0.5+y, z; (iii) x, 1-y, -0.5+z; (iv) 0.5+x, 0.5+y, z;
(v) x, 1-y, 0.5+z; (vi) -0.5+x, 0.5+y, z; (vii) -0.5+x, 0.5-y, -0.5+z; (viii) x, -y, 0.5+z;
(ix) 0.5+x, -0.5+y, z; (x) 0.5+x, 0.5-y, -0.5+z; (xi) -0.5+x, 0.5-y, 0.5+z; (xii) 0.5+x, 0.5-y, 0.5+z;
(xiii) x, y, 1+z; (xiv) x, y, -1+z.

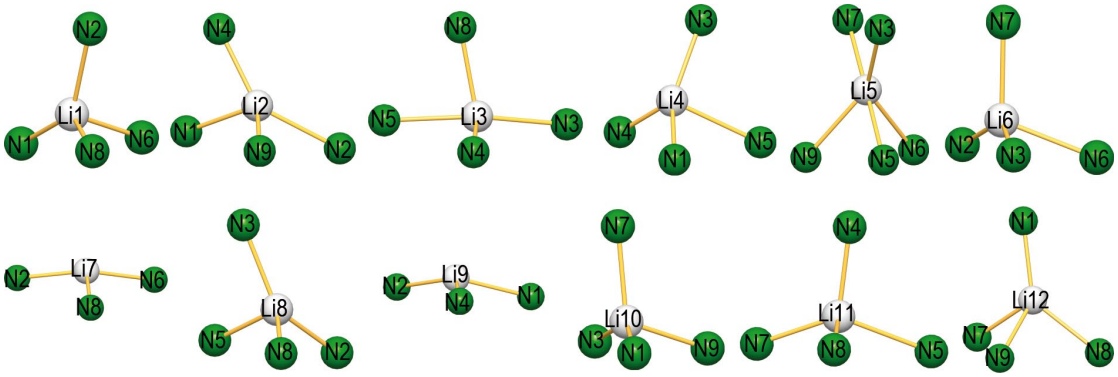

Figure S9.1 Coordination spheres of the Li^+ sites. Bond length up to 2.88 Å are shown by a orange line. Gray: Li, Green: N.

9.7.2 Additional Crystallographic Data for Li_4PN_3

Table S9.5 Fractional atomic coordinates, isotropic thermal displacement parameters, and site occupancies for Li_4PN_3

Atom	Wyckoff symbol	*x*	*y*	*z*	U_{iso} / Å²	Occupancy
P1	8*e*	0.52591(8)	0.17130(6)	0.2950(2)	0.0058(2)	1
N1	8*e*	0.6270(3)	0.0671(2)	0.2115(5)	0.0076(5)	1
N2	8*e*	0.5721(3)	0.2926(2)	0.1210(5)	0.0075(5)	1
N3	8*e*	0.1370(3)	0.3567(2)	0.2652(6)	0.0093(5)	1
Li1	8*e*	0.2162(6)	0.6574(5)	0.0754(12)	0.0148(12)	1
Li2	8*e*	0.2425(8)	0.0332(5)	0.0097(14)	0.0226(13)	1
Li3	8*e*	0.0387(9)	0.5356(7)	0.219(2)	0.041(2)	1
Li4	8*e*	0.1580(14)	0.1880(12)	0.189(3)	0.023(3)	0.494
Li5	8*e*	0.159(2)	0.179(2)	0.336(6)	0.023(3)	0.29
Li6	4*c*	1/4	1/4	0.019(4)	0.019(6)	0.43

Table S9.6 Anisotropic displacement parameters occurring in Li_4PN_3

Atom	U_{11} / Å²	U_{22} / Å²	U_{33} / Å²	U_{12} / Å²	U_{13} / Å²	U_{23} / Å²
P1	0.0056(4)	0.0062(3)	0.0056(3)	-0.0006(3)	-0.0005(3)	-0.0001(3)
N1	0.0068(11)	0.0072(11)	0.0088(12)	0.0005(9)	0.000(1)	-0.0006(10)
N2	0.0092(11)	0.0085(11)	0.0048(10)	-0.0017(10)	-0.0015(10)	0.0009(10)
N3	0.0061(12)	0.0096(12)	0.0123(13)	-0.0026(9)	-0.0004(10)	-0.0009(10)

Table S9.7 List of interatomic distances / Å for Li_4PN_3

P1—N3^{i}	1.614(3)	P1—N1	1.625(3)	P1—N2^{ii}	1.703(3)
P1—N2	1.725(3)	N1—Li1^{iv}	1.959(6)	N1—Li2^{viii}	2.039(7)
N1—Li1^{iii}	2.124(6)	N1—Li3^{i}	2.010(9)	N1—Li2^{ix}	2.120(7)
N1—Li3^{iv}	2.292(9)	N2—Li1^{vi}	2.115(6)	N2—Li4^{i}	2.259(14)
N2—Li1^{xi}	2.334(6)	N2—Li3^{vi}	2.203(9)	N2—Li1^{iv}	2.327(6)
N2—Li5^{i}	2.49(2)	N3—Li2^{ii}	2.038(7)	N3—Li4	2.041(14)
N3—Li6^{ii}	2.076(13)	N3—Li5^{i}	2.04(2)	N3—Li6	2.056(12)
N3—Li4^{i}	2.083(14)	N3—Li4^{ii}	2.14(2)	N3—Li5	2.14(2)
N3—Li2^{i}	2.145(7)	N3—Li3	2.332(9)		

(i) 0.5-x, 0.5-y, z; (ii) x, 0.5-y, 0.5+z; (iii) 1-x, -0.5+y, 0.5-z; (iv) 0.5+x, -0.5+y, -z;
(v) 0.5-x, y, 0.5+z; (vi) 0.5+x, 1-y, 0.5-z; (vii) 0.5+x, -0.5+y, 1-z; (viii) 1-x, -y, -z;
(ix) 0.5+x, -y, 0.5-z; (x) x, 0.5-y, -0.5+z; (xi) 1-x, 1-y, -z; (xii) -0.5+x, 0.5+y, -z;
(xiii) -0.5+x, 1-y, 0.5-z; (xiv) 1-x, 0.5+y, 0.5-z; (xv) 0.5-x, 1.5-y, z; (xvi) 0.5-x, y, -0.5+z;
(xvii) -0.5+x, -y, 0.5-z; (xviii) -x, 1-y, -z; (xix) -x, 0.5+y, 0.5-z; (xx) -0.5+x, 0.5+y, 1-z.

Table S9.8 List of bond angles / ° for Li_4PN_3

N–P–N					
$N3^{i}$—P1—N1	114.05(14)	$N3^{i}$—P1—$N2^{ii}$	112.98(14)	N1—P1—$N2^{ii}$	105.44(14)
$N3^{i}$—P1—N2	112.24(13)	N1—P1—N2	110.71(13)	$N2^{ii}$—P1—N2	100.41(9)
P–N–P					
$P1^{x}$—N2—P1	126.8(2)				

(i) 0.5-x, 0.5-y, z; (ii) x, 0.5-y, 0.5+z; (iii) 1-x, -0.5+y, 0.5-z; (iv) 0.5+x, -0.5+y, -z;
(v) 0.5-x, y, 0.5+z; (vi) 0.5+x, 1-y, 0.5-z; (vii) 0.5+x, -0.5+y, 1-z; (viii) 1-x, -y, -z;
(ix) 0.5+x, -y, 0.5-z; (x) x, 0.5-y, -0.5+z; (xi) 1-x, 1-y, -z; (xii) -0.5+x, 0.5+y, -z;
(xiii) -0.5+x, 1-y, 0.5-z; (xiv) 1-x, 0.5+y, 0.5-z; (xv) 0.5-x, 1.5-y, z; (xvi) 0.5-x, y, -0.5+z;
(xvii) -0.5+x, -y, 0.5-z; (xviii) -x, 1-y, -z; (xix) -x, 0.5+y, 0.5-z; (xx) -0.5+x, 0.5+y, 1-z.

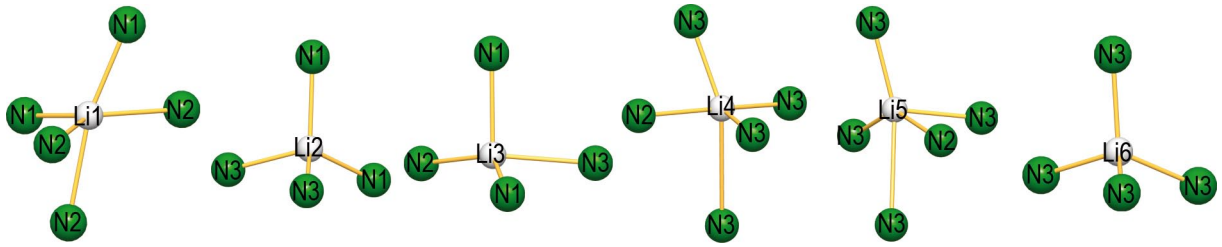

Figure S9.2. Coordination spheres of the Li^+ sites. Distances up to 2.88 Å are shown by orange lines. Gray: Li, green: N.

9.7.3 Details of the Rietveld Refinement

Table S9.9 Details of the Rietveld refinement of $Li_{12}P_3N_9$ and Li_4PN_3

formula	**$Li_{12}P_3N_9$**	**Li_4PN_3**
formula mass / g · mol^{-1}	534.9	100.8
crystal system / space group	monoclinic *Cc* (no. 9)	orthorhombic *Pccn* (no. 56)
lattice parameters / Å, °	*a* = 12.1088(3)	*a* = 9.6497(2)
	b = 7.6588(2)	*b* = 11.8299(3)
	c = 9.7215(2)	*c* = 4.8677(1)
	β = 90.899(2)	
cell volume / Å^3	901.45(3)	555.67(2)
formula units per cell *Z*	4	8
X-ray density / g · cm^{-3}	2.22726(9)	2.40867(10)
linear absorption coefficient / cm^{-1}	73.79	
radiation	Cu-$K_{\alpha1}$ (λ = 1.540596 Å)	
monochromator	Ge(111)	
diffractometer	Stoe StadiP	
detector	linear PSD	
2θ-range / °	5.0-92.0	5.0-113.1
temperature / K	298 (2)	
data points	5800	7208
number of observed reflections	393	373
number of parameters	86	75
program used	TOPAS Academic	
structure refinement	Rietveld method	
profile function	fundamental parameters model	
background function	shifted Chebyshev	
R_{wp}	16.122	8.631
R_{exp}	6.569	2.066
R_p	10.524	5.768
R_{Bragg}	3.836	1.882
χ^2	2.454	4.177

9.7.4 Detailed Rietveld Plots

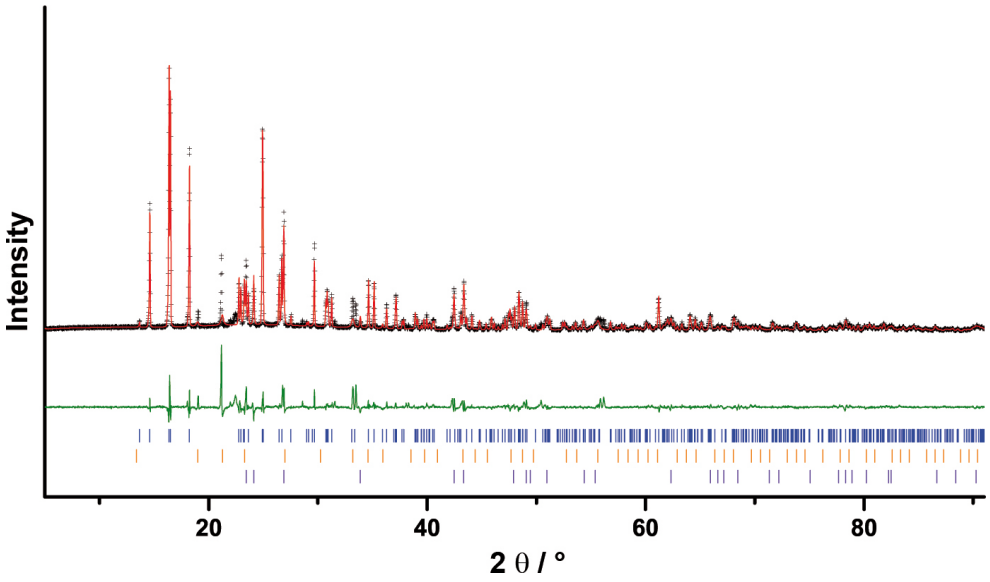

Figure S9.3 $Li_{12}P_3N_9$: Observed (black crosses) and calculated (red line) powder diffraction pattern as well as difference profile (green) of the Rietveld refinement. Reflex positions are marked by vertical blue bars. Peak positions of side phases are marked by vertical orange (Li_7PN_4 9.83%) and violet (Li_3P 4.69%) bars.

The difference of the peace profile of some peak positions is due to a further side phase, which could not be analyzed in detail.

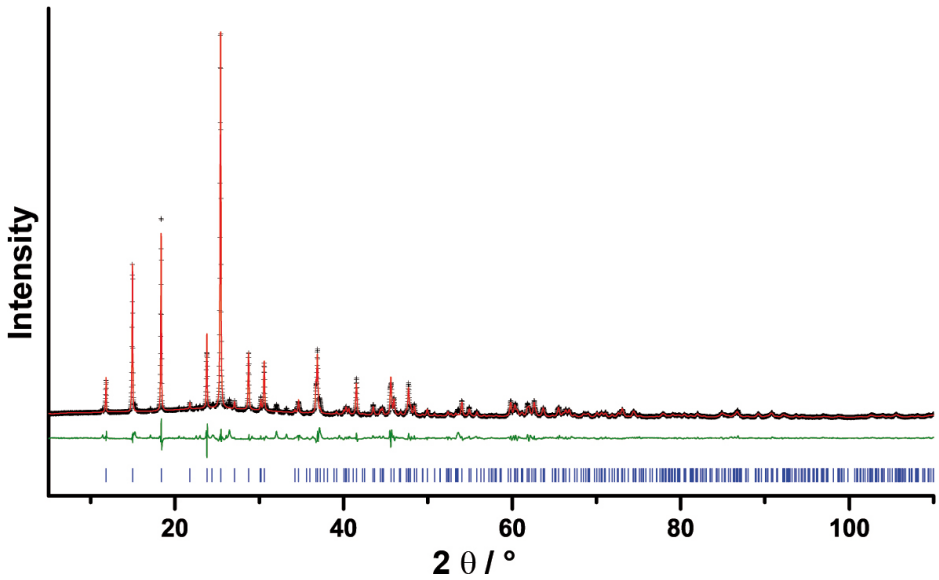

Figure S9.4 Li_4PN_3: Observed (black crosses) and calculated (red line) powder diffraction pattern as well as difference profile (green) of the Rietveld refinement. Reflex positions are marked by vertical blue bars.

9.7.5 ^{31}P, ^{6}Li and ^{7}Li Solid-State MAS NMR Spectroscopy

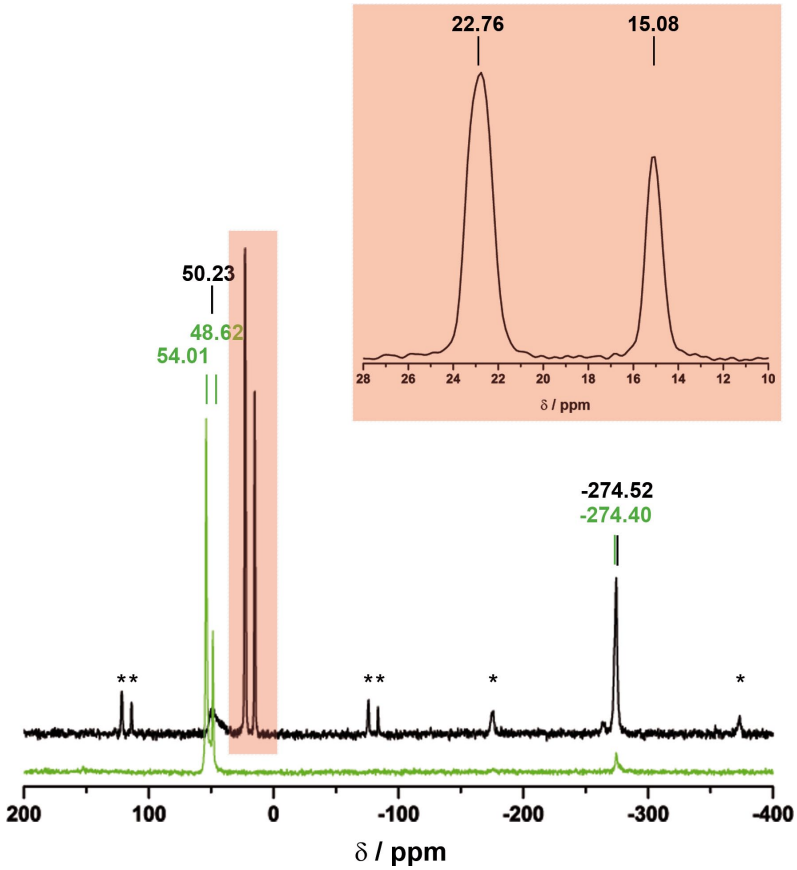

Figure S9.5 ^{31}P MAS NMR spectrum of $Li_{12}P_3N_9$ in black and the side phases Li_7PN_4 and Li_3P in green. Rotational sidebands are marked with asterisks.

The ^{31}P MAS NMR spectrum of $Li_{12}P_3N_9$ is shown in black and shows strong resonances at 15.08 and 22.76 ppm at a ratio of 2 to 1, which correspond to three crystallographically independent P sites (black). The ^{31}P MAS NMR-spectrum of Li_7PN_4 and Li_3P is shown in green (Li_7PN_4 with a little amount of Li_3P). The resonances at 48.62 and 54.01 ppm correspond to two crystallographically independent P sites of Li_7PN_4 (Wyck. 2*a* and 6*c* in $P\bar{4}3n$). The resonance at -274.40 ppm corresponds to Li_3P, which has one crystallographically independent site. The values for $Li_{12}P_3N_9$ correspond with those of other ternary nitridophosphates.[1]

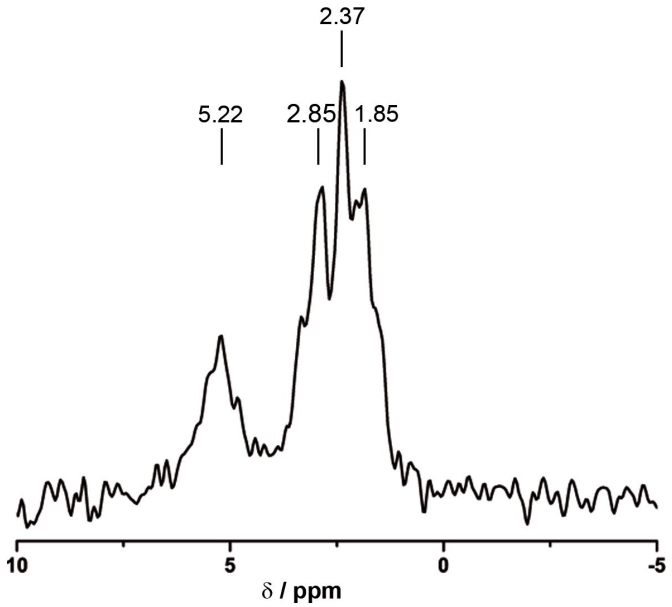

Figure S9.6 ^{6}Li MAS NMR spectrum of $Li_{12}P_3N_9$.

The ^{6}Li MAS NMR spectrum shows strong resonances between 5.22 and 1.85 ppm. Due to the small chemical shift differences of the signals, the differentiation of the 12 crystallographically independent sites cannot be observed in the spectrum.

The ^{7}Li MAS NMR spectrum shows one strong resonances at 4.87 ppm. Due to the small chemical shift differences of the signals, no differentiation of the crystallographically independent sites can be observed in the spectrum. ^{7}Li MAS NMR spectra of different lithium nitridophosphates or silicates normally show one resonance in this range.[2–5]

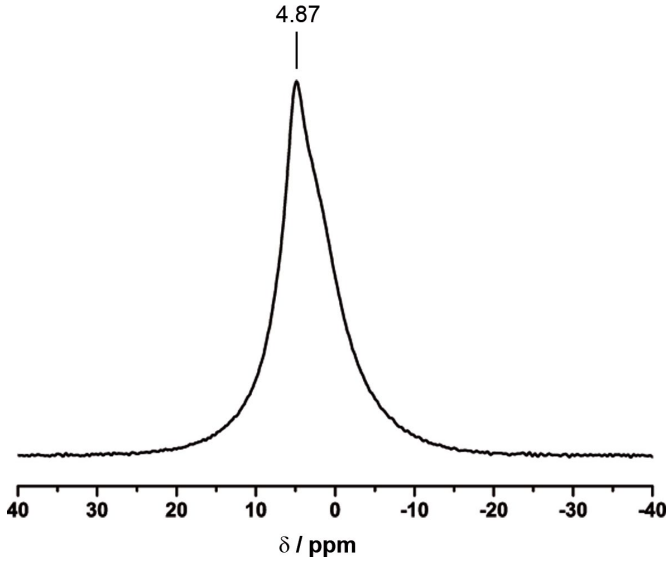

Figure S9.7 ^{7}Li MAS NMR spectrum of $Li_{12}P_3N_9$.

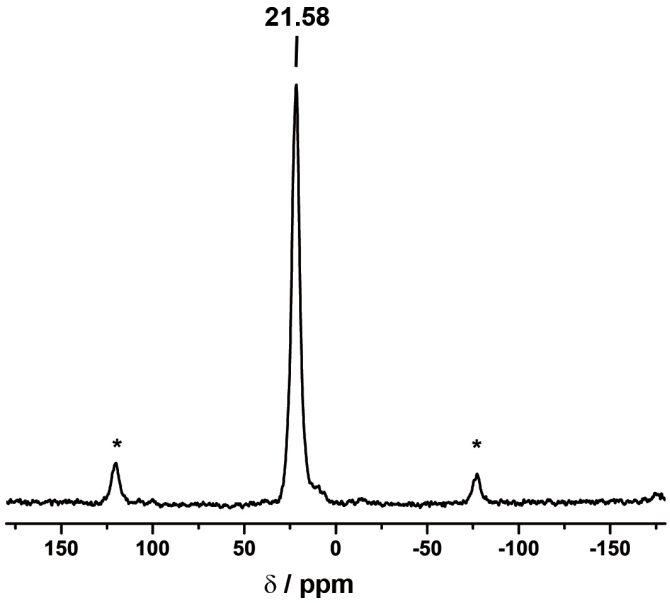

Figure S9.8 ^{31}P MAS NMR spectrum of Li_4PN_3. Rotational sidebands are marked with asterisks.

The ^{31}P MAS NMR spectrum shows one strong resonances at 21.58 ppm, which corresponds to one crystallographically independent P site. These values correspond with those of other ternary nitridophosphates.[1]

The ^{6}Li MAS NMR spectrum shows one strong resonances at 2.41 ppm. Due to the small chemical shift differences of the signals, no differentiation of the crystallographically independent sites can be observed in the spectrum.

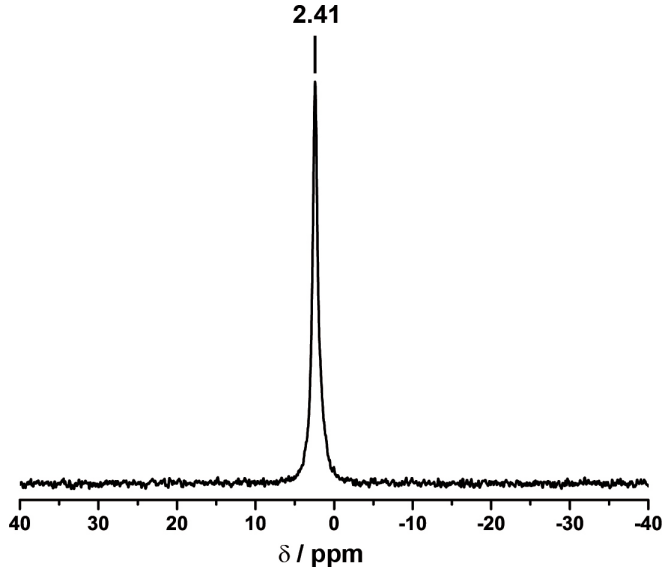

Figure S9.9 ^{6}Li MAS NMR spectrum of Li_4PN_3.

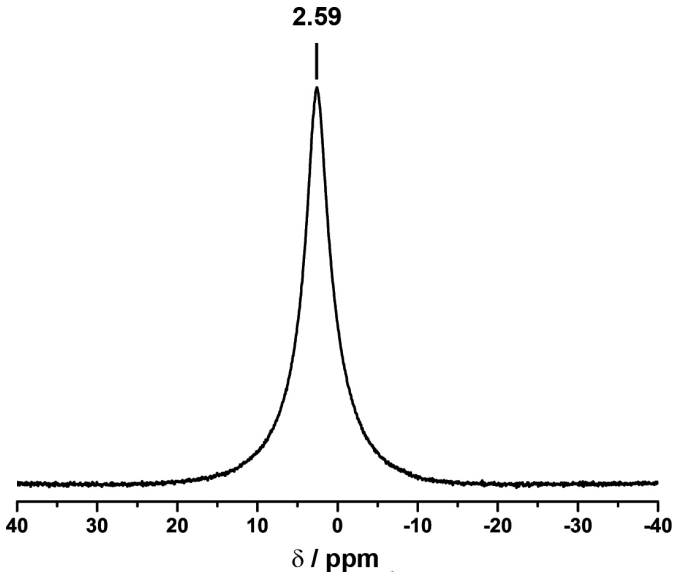

Figure S9.10 ^{7}Li MAS NMR spectrum of Li_4PN_3.

The ^{7}Li MAS NMR spectrum shows one strong resonances at 2.59 ppm. Due to the small chemical shift differences of the signals, no differentiation of the crystallographically independent sites can be observed in the spectrum. ^{7}Li MAS NMR spectra of different lithium nitridophosphates or silicates normally show one resonance in this range.[2–5]

9.7.6 Details of Scanning Electron Microscopy

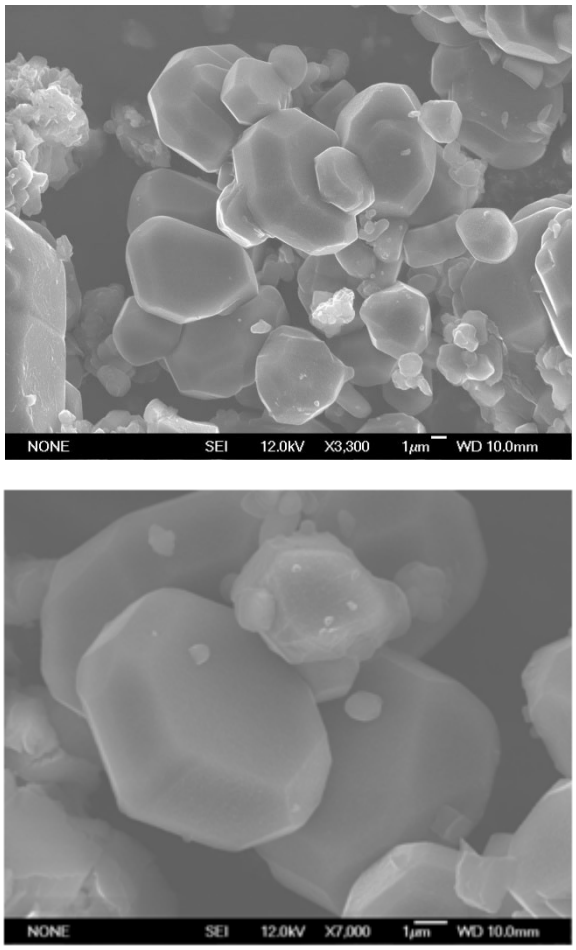

Figure S9.11 Scanning electron micrographs of $Li_{12}P_3N_9$.

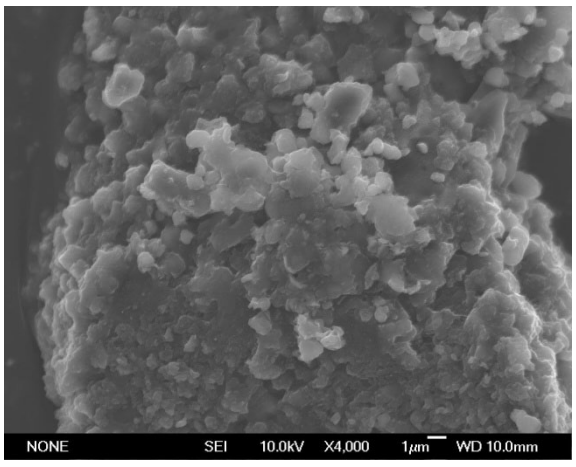

Figure S9.12 Scanning electron micrograph of Li_4PN_3.

9.7.7 FTIR Spectrum

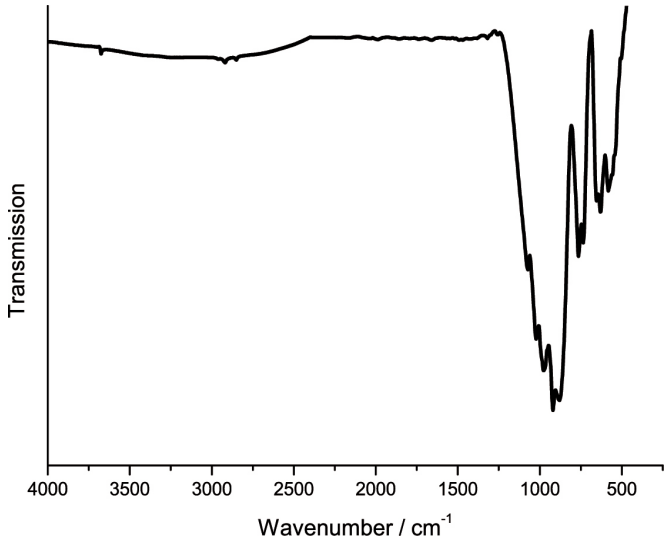

Figure S9.13 FTIR spectrum of $Li_{12}P_3N_9$.

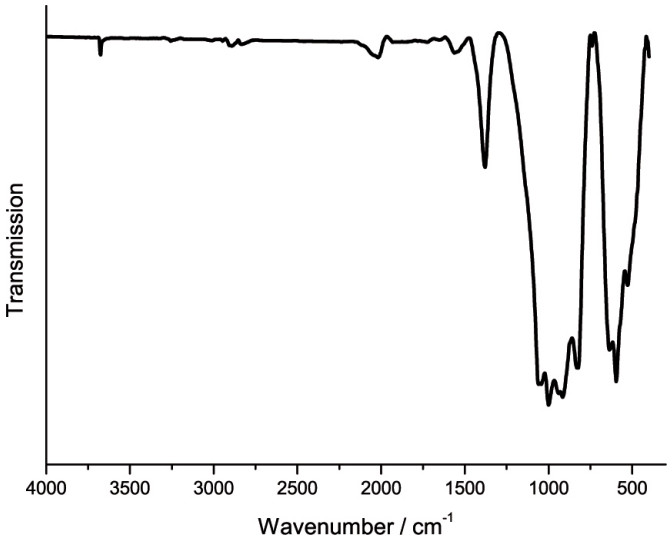

Figure S9.14 FTIR spectrum of Li_4PN_3.

Infrared spectroscopy measurements were performed on a Bruker FTIR-IFS 66v/S spectrometer. Before measurement in the range of 400–4000 cm^{-1} the sample was mixed with KBr in a glove box and cold-pressed into a pellet (Ø = 12 mm).The spectrum shows no significant valence vibrations in the region of 3000 cm^{-1}, where N–H vibrations are expected. A weak signal in that region can be explained by surface hydrolysis of the sample. Thus, the incorporation of stoichiometric amounts of hydrogen seems unlikely. Much more significant are the characteristic PN framework vibrations between 600 and 1500 cm^{-1}.

9.7.8 Structural Analysis of Possible Lithium Migration Pathways

Possible voids and migration pathways in $Li_{12}P_3N_9$ and Li_4PN_3 were analyzed with TOPOS.[6–9]

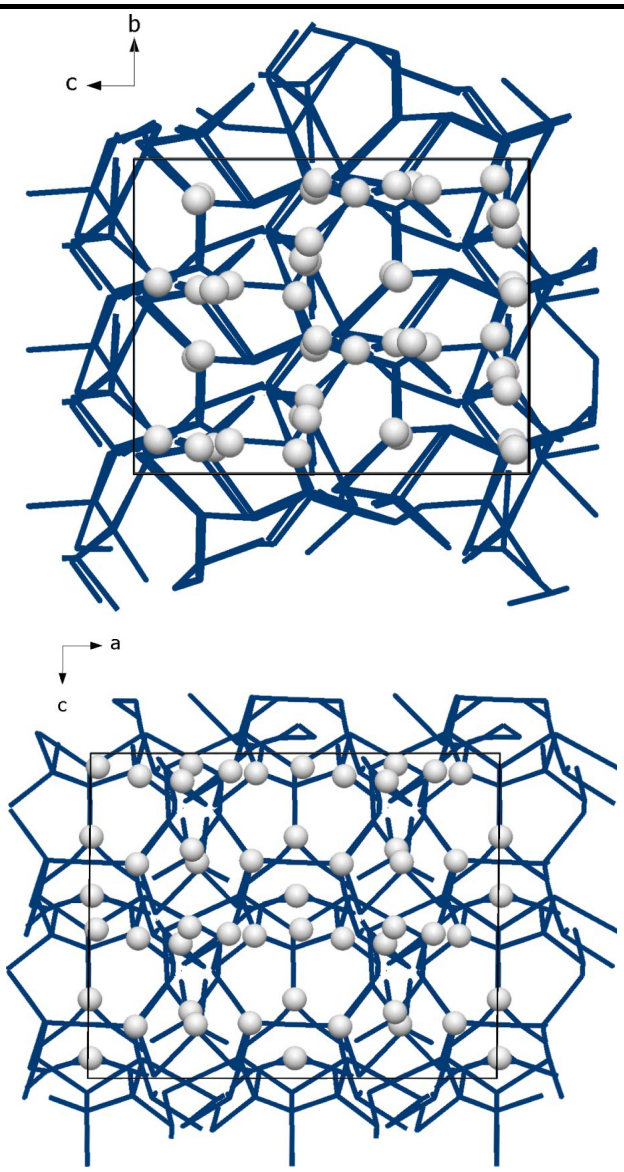

Figure S9.15 Calculated possible Li^+ pathways (blue) according to the voids in the structure and unit cell of $Li_{12}P_3N_9$.

9.7.9 Electron Localization Function

In order to analyze the chemical bonding with both compounds we calculated the electron localization function (ELF), constituting the probability of finding an electron of opposed spin within the proximity of another, effectively revealing positions of chemical bonds or electron lone pairs.[10] ELF is defined between 0 and 1, where 0 constitutes no localization, and a value of 0.5 being equivalent to a homogenous electron distribution as typically found in metals. Values close to 1 correspond to strong localization as found in covalent bonds.

Figure S9.16 illustrates designated lattice planes of ELF intersecting the Li positions in both $Li_{12}P_3N_9$ and Li_4PN_3. The electron pair probability in terms of the ELF can be seen to be strongly localized solely around the Li atoms with no indication of contributions to covalent bonds between Li and N, corroborating chemical intuition of a strong ionic character. The P–N bonding situation for an ELF isovalue η = 0.83 reveals strong covalency within the $P_3N_9^{12-}$ and $PN_{2(2/2)}^{4-}$ units (Figure S9.17 and S9.18). The P–N bonds show strong N-polarization and free electron pairs of N^{3-} are found at terminal and bridging N atoms as expected from VSEPR considerations.

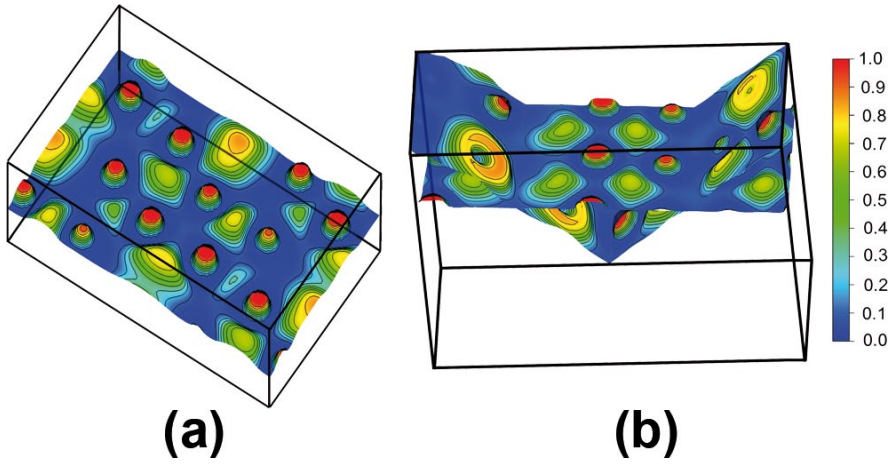

Figure S9.16 ELF contour plot with 0.15 increments, intersecting the Li atoms (seen as highly localized regions in red) within a chosen section of the unit cell of (a) $Li_{12}P_3N_9$ and (b) Li_4PN_3.

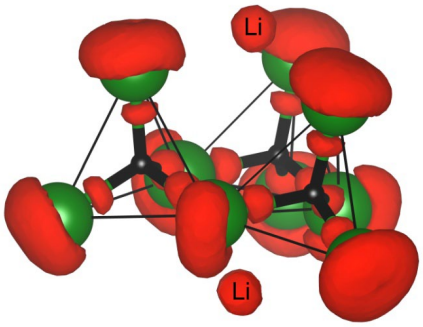

Figure S9.17 Isosurface of ELF (η = 0.83) for $Li_{12}P_3N_9$ in red. P: black; N: green; Li: gray.

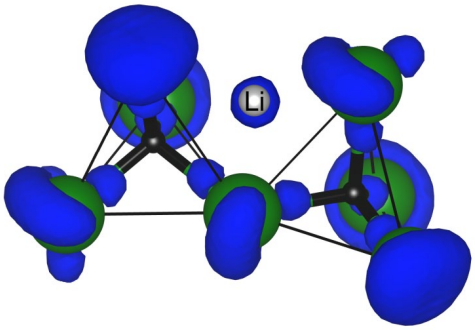

Figure S9.18 Isosurface of ELF (η = 0.83) for Li_4PN_3 in blue. P: black; N: green; Li: gray.

9.7.10 References

[1] K. Landskron, Phosphor(V)-nitride durch Hochdruck-Hochtemperatur-Synthese, *Doctoral Thesis*, Universtiy of Munich, **2001**.

[2] S. Pagano, M. Zeuner, S. Hug, W. Schnick, Single-Crystal Structure Determination and Solid-State NMR Investigations of Lithium Nitridosilicate Li_2SiN_2 Synthesized by a Precursor Approach Employing Amorphous "$Si(CN_2)_2$", *Eur. J. Inorg. Chem.* **2009**, *2009*, 1579–1584.

[3] S. Lupart, W. Schnick, $LiCa_3Si_2N_5$ – A Lithium Nitridosilicate with a $[Si_2N_5]^{7-}$ Double-Chain, *Z. Anorg. Allg. Chem.* **2012**, *638*, 2015–2019.

[4] S. Pagano, S. Lupart, S. Schmiechen, W. Schnick, $Li_4Ca_3Si_2N_6$ and $Li_4Sr_3Si_2N_6$ - Quaternary Lithium Nitridosilicates with Isolated $[Si_2N_6]^{10-}$ Ions, *Z. Anorg. Allg. Chem.* **2010**, *636*, 1907–1909.

[5] M. Orth, W. Schnick, Zur Kenntnis von $LiSi_2N_3$: Synthese und Verfeinerung der Kristallstruktur, *Z. Anorg. Allg. Chem.* **1999**, *625*, 1426–1428.

[6] V. A. Blatov, Multipurpose crystallochemical analysis with the program package TOPOS, *IUCr CompComm Newsl.* **2006**, *7*, 4–38.

[7] V. A. Blatov, Voronoi–dirichlet polyhedra in crystal chemistry: theory and applications, *Crystallogr. Rev.* **2004**, *10*, 249–318.

[8] N. A. Anurova, V. A. Blatov, G. D. Ilyushin, O. A. Blatova, A. K. Ivanov-Schitz, L. N. Dem'yanets, Migration maps of Li^+ cations in oxygen-containing compounds, *Solid State Ionics* **2008**, *179*, 2248–2254.

[9] V. A. Blatov, A. P. Shevchenko, V. N. Serezhkin, TOPOS3.1 – program package for multipurpose geometrical and topological analysis of crystal structures, *J. Appl. Cryst.* **1999**, *32*, 377–377.

[10] A. D. Becke, K. E. Edgecombe, A simple measure of electron localization in atomic and molecular systems, *J. Chem. Phys.* **1990**, *92*, 5397–5403.

10 Reversible Polymerization of Adamantane-type $[P_4N_{10}]^{10-}$ Anions to Honeycomb-type $[P_2N_5]^{5-}$ Layers under High-Pressure

published in: *Chem. Eur. J.* **2018**, *24*, 736–742.

authors: Eva-Maria Bertschler, Robin Niklaus, Wolfgang Schnick

DOI: 10.1002/chem.201704975

Acknowledgment: Reprinted (adapted) with permission from *Chemistry – A European Journal*. Copyright 2018 John Wiley and Sons.

Abstract The high-pressure polymorph $Li_5P_2N_5$ of $Li_{10}P_4N_{10}$ (= "2 $Li_5P_2N_5$") was synthesized by high-pressure/high-temperature reaction of $LiPN_2$ and Li_7PN_4 or β-$Li_{10}P_4N_{10}$ at 9 GPa, using the Li_3N self-flux method in a Walker-type multianvil assembly. $Li_5P_2N_5$ is the first lithium nitridophosphate with a layered structure and is made up of corner sharing PN_4 tetrahedra forming a corrugated honeycomb-type layer of linked *sechser*-rings in chair conformation. The arrangement of the P atoms is analogous to that of black phosphorus. The structure was elucidated from single-crystal X-ray data. To confirm the structure Rietveld refinement, ^6Li, ^7Li and ^{31}P solid-state NMR spectroscopy were conducted. To corroborate $Li_5P_2N_5$ as the corresponding high-pressure polymorph of β-$Li_{10}P_4N_{10}$ DFT calculations and temperature dependent X-ray powder diffraction were carried out. DFT calculations estimated the transition pressure to 6.5 GPa (without accounting for temperature), which is in line with the synthesis pressure.

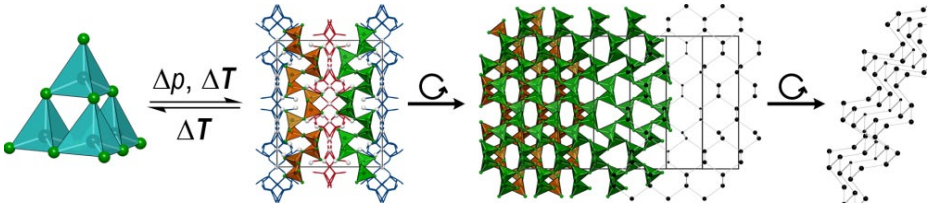

10.1 Introduction

Nitridophosphates are closely related to silicates, but they offer a broader structural diversity, due to the possibility of triply bridging N atoms.[1–4] The tetrahedral PN_4 group, the primary building unit of nitridophosphates, allows various linking patterns and leads to an intriguing structural variability and interesting properties.[5] Representatives in this compound class include nitridic zeolites (NPO, NPT),[6–8] clathrates ($P_4N_4(HN)_4(NH_3)$),[9] glassy compounds (Li–Ca–P–N),[10,11] luminescent materials ($Ba_3P_5N_{10}X$:Eu^{2+} (X = Cl, Br, I) or MP_2N_4:Eu^{2+} (M = Ca, Sr, Ba)),[12–14] or lithium ion conductors ("*LiPON*").[15]

The discovery of new nitridophosphates was in particular facilitated by the use of high-pressure techniques.[16] For example the high-pressure polymorph γ-P_3N_5, where remarkable hardness was observed, is made up of square PN_5 pyramids beside PN_4 tetrahedra.[17,18]

Furthermore different polymorphs of silica analogous PON and isoelectronic PN(HN) were characterized.[19–25] Recently, we established different approaches to obtain sufficiently large crystals for structure determination. By addition of the mineralizer NH_4Cl, the crystallinity of nitridophosphates increases and compounds like β- and γ-$P_4N_6(NH)$[16,26] have been structurally elucidated.[25] To gain access to rare earth-metal nitridophosphates high-pressure metathesis was established.[27] A third approach to grow single crystals by application of high-pressure is the Li_3N flux/self-flux method.[28] By this method we were able to structurally characterize lithium nitridophosphates with unprecedented topologies. Recently, we described different linking patterns of corner sharing PN_4 tetrahedra which form various P/N anions (Figure 10.1) in a matrix of Li^+ ions. Yet, lithium nitridophosphates with non-condensed PN_4 tetrahedra (a), rings (b), annelated ring-systems (c), cages (d), chains (e), or even three-dimensional network structures have been found (f).

Li_7PN_4 has the lowest atomic ratio P/N (Figure 10.1 a).[29] In $Li_{12}P_3N_9$ $[P_3N_9]^{12-}$ units form *dreier*-rings of PN_4 tetrahedra (Figure 10.1 b).[30,34,35] $Li_{18}P_6N_{16}$ is composed of one *vierer*-ring with two annelated *dreier*-rings (Figure 10.1 c).[28] In *α*- and β-$Li_{10}P_4N_{10}$ a cage like structure occurs with adamantane like $[P_4N_{10}]^{10-}$ T2 supertetrahedra, which are isoelectronic to $[P_4O_{10}]$ (Figure 10.1 d). β-$Li_{10}P_4N_{10}$ transforms reversibly to the *α*-polymorph at about 80 °C and irreversibly at about 600 °C. Both polymorphs differ in distortion of the polyhedra.[31,32] Li_4PN_3 is the high-pressure polymorph of $Li_{12}P_3N_9$ (6 GPa and 820 °C) and represents the first chain like structure in lithium nitridophosphates. It transforms back to $Li_{12}P_3N_9$ at 650 °C (Figure 10.1 e).[30] $LiPN_2$ is made up of a three-dimensional network structure with corner sharing PN_4 tetrahedra isoelectronic to SiO_2 (Figure 10.1 f).[33] In this work we report on synthesis and structural investigation of the high-pressure polymorph $Li_5P_2N_5$, which represents the first layered structure in lithium nitridophosphates. With the Li_3N self-flux method we were able to grow crystals that were sufficiently large for single-crystal structure determination. Furthermore DFT calculations were performed to corroborate the observed high-pressure phase transition.

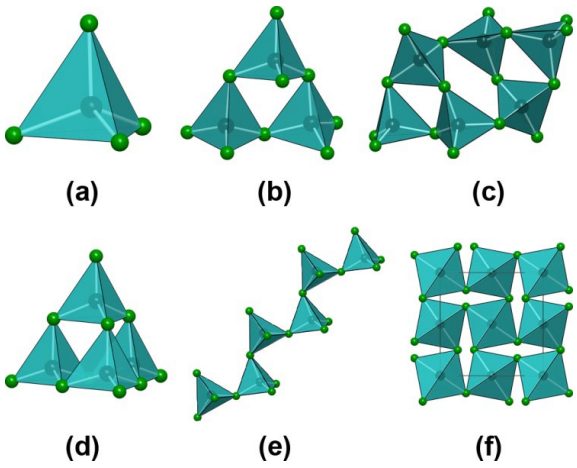

Figure 10.1 Known linking patterns of PN_4 tetrahedra in lithium nitridophosphates. (a) Isolated PN_4 tetrahedra in Li_7PN_4. (b) *Dreier*-rings in $Li_{12}P_3N_9$. (c) An annulated ring-system in $Li_{18}P_6N_{16}$. (d) A cage like structure in α- and β-$Li_{10}P_4N_{10}$. (e) *Zweier*-chains in Li_4PN_3. (f) A three-dimensional network structure in $LiPN_2$.[5,28-33] (P: black, N: green).

10.2 Results and Discussion

10.2.1 Synthesis

According to Equation (1) and Equation (2) $Li_5P_2N_5$ was synthesized by the Li_3N self-flux method[28] under high-pressure/high-temperature conditions. All compounds were handled under argon atmosphere to avoid hydrolysis.

$$\beta\text{-}Li_{10}P_4N_{10} \rightarrow 2\ Li_5P_2N_5 \quad (1)$$

$$3\ LiPN_2 + Li_7PN_4 \rightarrow 2\ Li_5P_2N_5 \quad (2)$$

According to Equation (1) $Li_5P_2N_5$ was made from the low temperature polymorph β-$Li_{10}P_4N_{10}$ at 9 GPa and 1000 °C using a Walker-type multianvil assembly.[36–40] $Li_5P_2N_5$ was obtained together with $LiPN_2$ and unknown side-phases. Synthesis at 7 or 8 GPa and 800 °C leads to higher amount of unknown side phases. Reaction of equimolar amounts of $LiPN_2$ and Li_7PN_4 (excess of Li_7PN_4) at 9 GPa and 1000 °C leads to in situ formation of Li_3N (self-flux), which is beneficial for the growth of single crystals. Due to the better crystal quality resulting from this treatment, a single-crystal of this approach was used for structure analysis. $Li_5P_2N_5$ was obtained together with Li_4PN_3 and unknown side phases. As we described in previous work, the in situ formed Li_3N may evaporate later on, or may react with the *h*-BN crucible.[28] Detailed information on the synthesis is given in the Experimental section.

10.2.2 Crystal Structure

The crystal structure of $Li_5P_2N_5$ was solved and refined from single-crystal X-ray diffraction data. $Li_5P_2N_5$ crystallizes as colorless platelets in monoclinic space group *C*2/*c* (no. 15) with 12 formula units per unit cell (Table 10.1).[41]

It was refined as a two component twin with a translation matrix of [1 $\overline{1}$ 0.33 / 0 $\overline{1}$ 0 / 0 0 $\overline{1}$]. The relatively high residual electron density of 1.53 e Å^{-3} is due to the mobility and disorder of the Li^+ ions. The Fourier map shows clearly that the Li^+ ions appear as smeared and are not localized on discrete sites (Supporting Information, Figure S10.2). An anisotropic refinement of the Li positions leads to rather large ellipsoids, which also indicates a lack of localization.

Table 10.1 Crystallographic Data of $Li_5P_2N_5$.

	$Li_5P_2N_5$
crystal size [mm^3]	0.01× 0.03× 0.03
formula mass [g mol^{-1}]	166.69
crystal system, space group	monoclinic, $C2/c$ (no. 15)
twin	two component twin [1 $\bar{1}$ 0.33 / 0 $\bar{1}$ 0 / 0 0 $\bar{1}$]
BASF	0.479(4)
a [Å]	14.770(3)
b [Å]	17.850(4)
c [Å]	4.8600(10)
β [°]	93.11(3)
cell volume [$Å^3$]	1279.4(5)
formula units/ cell	12
calculated density [g cm^{-3}]	2.596
F(000)	960
diffractometer	Bruker D8 Venture
temperature [°C]	293(2)
radiation, monochromator	$Mo_{K\alpha}$ (λ=0.71073 Å), Goebel mirror
absorption correction	multi scan
θ range [°]	2.28–27.46
number of collected data	7667
number of unique data	2864
number of unique data with $I \geq 2\sigma(I)$	2320
refined parameters	127
GooF	1.057
R indices [$F_0^2 \geq 2\sigma(F_0^2)$]	R_1 = 0.0547, wR_2 = 0.1280
R indices (all data)	R_1 = 0.0705, wR_2 = 0.1369
max/min res. electron density [e $Å^{-3}$]	1.53/−0.81
R_{int}/ R_σ for component 1	0.0252/0.0318
R_σ (both components)	0.0423

w=1/[$\sigma^2(F_o^2)$+(0.0513P)^2+10.9661P] where P=(F_o^2+2F_c^2)/3.

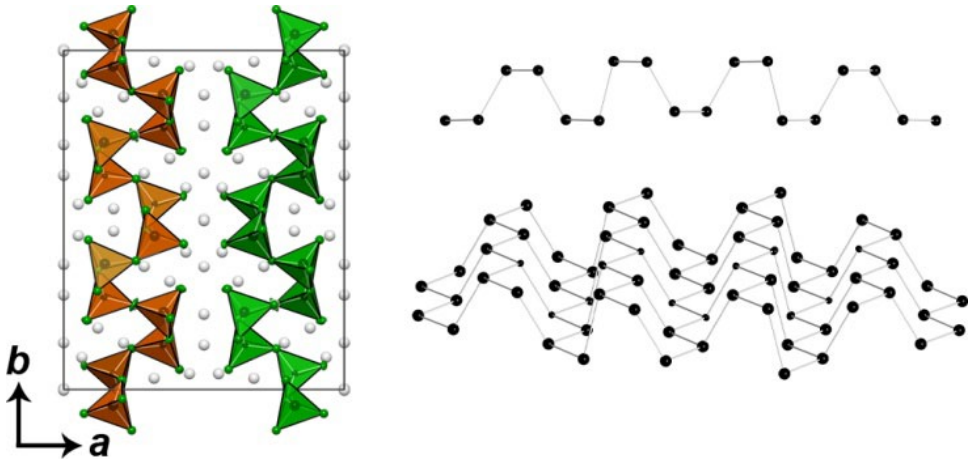

Figure 10.2 Left: Unit cell of $Li_5P_2N_5$, view along *c*. The anisotropic displacement ellipsoids are depicted at 90 % probability. Right top: P atoms of layer 1 (green) viewing along *c*. Right bottom: P atoms of layer 1 viewing along *hkl* = (5 0 9). (P: black, N: green, Li: gray).

The P/N substructure is made up of corner sharing PN_4 tetrahedra forming a corrugated layer of linked *sechser*-rings in chair conformation (Figure 10.2). The arrangement of the P atoms is analogous to that of black phosphorus.[42] The unit cell is made up of two layers (layer 1 (green) and 2 (orange)) perpendicular to *a*. Both layers can be transformed into each other by rotation around 180°. The framework anion topology was determined by the TOPOS software. It is represented by the point symbol 6^3. Thus, the network can be described as an uninodal three-connected net with the *hcb* (honeycomb) topology (Shubnikov hexagonal plane), which is shown in Figure 10.3.[43–45]

A related polymerization from an adamantane-type structure (P_4O_{10})[46] to layers (*o*'-P_2O_5)[47] was observed in phosphorous(V) oxide at 360 °C (2–3 weeks). The layers in *o*'-P_2O_5 are made up of corner sharing PO_4 tetrahedra forming a corrugated layer of linked *sechser*-rings in boat conformation with *hcb* topology as well.[47]

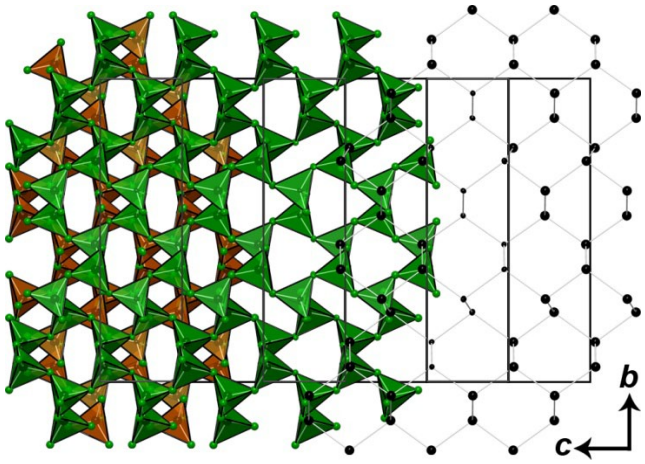

Figure 10.3 Unit cell of $Li_5P_2N_5$ viewing along *a*. Li is omitted for clarity. The anisotropic displacement ellipsoids are depicted at 90% probability. From left to right: Layer 1 (green) and 2 (orange); Layer 1 (green); P atoms of layer 1. (P: black, N: green).

Hence, the polymerization products $Li_5P_2N_5$ and *o'*-P_2O_5 only differ by the conformation (chair/boat) of the *sechser*-rings.

10.2.3 Structural Analysis of Possible Lithium Migration Pathways

To confirm the possible movement of the Li^+ ions, possible voids and migration pathways were analyzed with TOPOS.[50–52] Calculating the Voronoi–Dirichlet polyhedra leads to possible migration pathways. The migration pathways of the Li positions build two different layers along *c* (Figure 10.4: red and blue). Both layers can be transformed into each other by a shift along *b*. According to these calculations $Li_5P_2N_5$ seems to be a promising candidate for Li^+ ion conductivity, due to the defined layers in which the Li^+ ions can migrate.
Figure 10.4 (left, top) shows that there is one Li position (Li10) which indicates no movement. Li10 is placed in the middle of a *sechser*-ring and is coordinated by 6 N atoms building an octahedron (Figure 10.5).

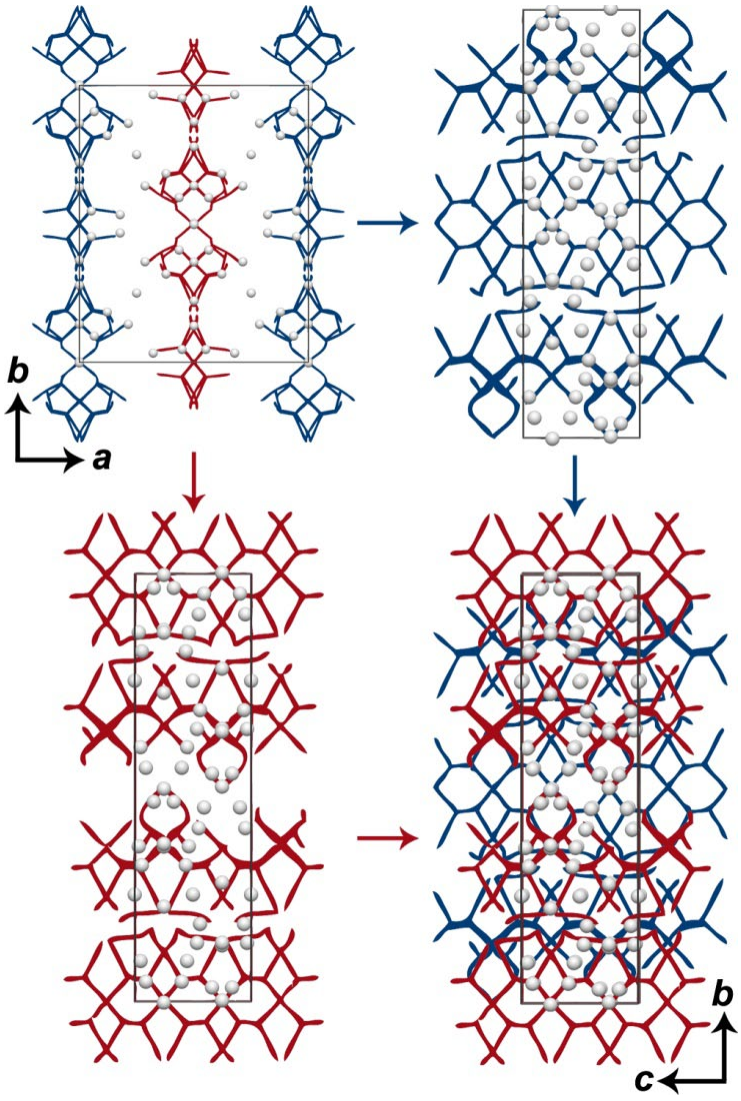

Figure 10.4 Calculated possible Li^+ pathways of different layers (red and blue) according to the voids in the structure and unit cell of $Li_5P_2N_5$. (Li: gray).

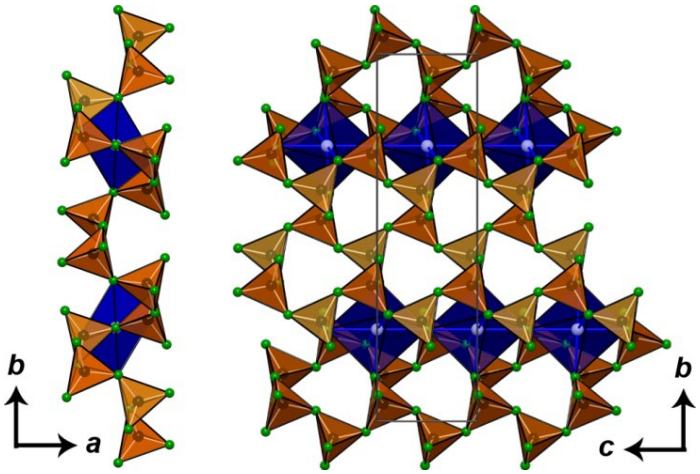

Figure 10.5 Layer 2 of $Li_5P_2N_5$ together with the Li position Li10, which forms an octahedron (blue) in the middle *sechser*-rings. (P: black, N: green, Li: gray).

10.2.4 Solid-state NMR Spectroscopy

^{31}P, ^{7}Li, and ^{6}Li NMR spectroscopy of $Li_5P_2N_5$ were performed to corroborate the crystal structure model (Supporting Information, Figure S10.4–S10.6). The ^{31}P spectrum shows one strong narrow resonance at 5.22 ppm and four smaller and broader ones at 19.42, 8.98, −7.55, and −14.36 ppm, which we assign to side phases. $Li_5P_2N_5$ has three crystallographically independent P sites, which all exhibit very similar bonding lengths to N (Supporting Information, Table S10.3) and therefore the same chemical shift at 5.22 ppm. This effect was already observed in $Li_{12}P_3N_9$.[30] The side phase $LiPN_2$ exhibits one strong resonance at 5.68 ppm, which corresponds to one crystallographically independent P site. The ^{6}Li NMR spectrum shows two strong resonances at 5.43 and 1.87 ppm. The resonance at 1.87 ppm exhibits a shoulder. Due to the small shift differences of the signals, no differentiation of the 9 crystallographically independent sites can be achieved. But the three signals (including the shoulder) can be assigned to the three different coordination numbers of Li that occur in $Li_5P_2N_5$. The side phase $LiPN_2$ shows one resonance at 1.64 ppm. The ^{7}Li NMR spectrum shows two overlapping signals at 4.9 and 1.7 ppm. Due to the small chemical differences of the Li signals and the side phases (among others $LiPN_2$: 1.66 ppm), no differentiation of the phases and the crystallographically independent sites can be achieved.

10.2.5 Chemical Analysis (EDX) FTIR-Spectroscopy, Powder Diffraction

EDX measurements were carried out to determine the elemental composition of the product. Besides P and N only traces of O were found, which can be explained by surface hydrolysis of the sample during contact with air (Supporting Information, Table S10.6). The determined atomic ratio P/N is in agreement with the results from the crystal structure analysis ($Li_5P_2N_5$: P/N = 0.4). To prove the absence of hydrogen FTIR spectroscopy (cold-pressed KBr pellet) was performed (Supporting Information, Figure S10.8). The spectrum shows the characteristic PN framework vibrations between 400 and 1500 cm^{-1}. A weak signal in the region around 3000 cm^{-1} (N−H) can be explained by slight hydrolysis of the sample during preparation.

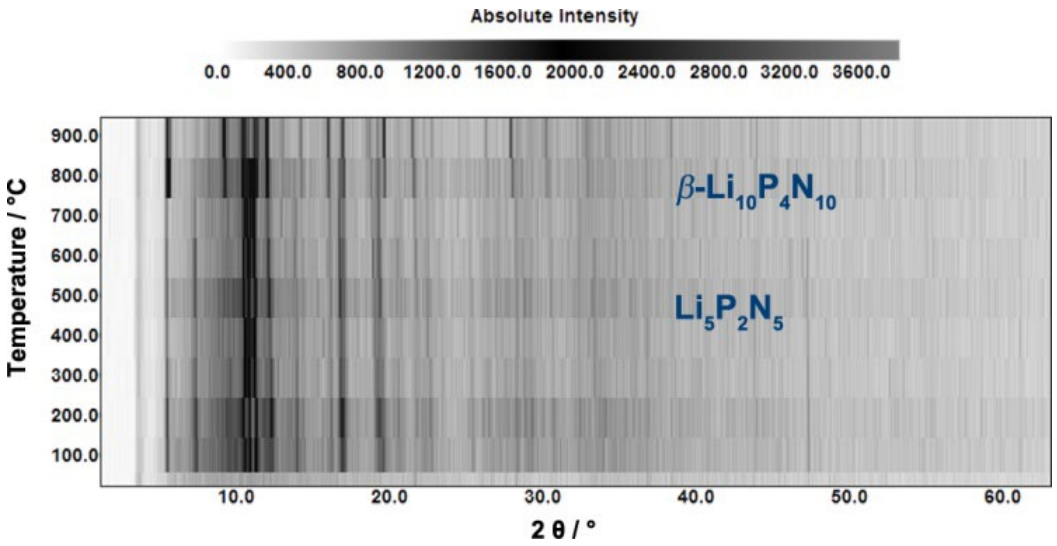

Figure 10.6 Temperature-dependent powder X-ray diffraction data for $Li_5P_2N_5$ under ambient pressure.

Phase purity of the product was determined by powder diffraction (Supporting Information, Figure S10.3). Beside the main phase $Li_5P_2N_5$, $LiPN_2$, and *h*-BN (crucible) were detected, together with further unknown side phases. Rietveld refinement confirms the determined crystal structure (Supporting Information, Table S10.5).

10.2.6 Thermal Stability

Temperature dependent powder X-ray diffraction patterns were recorded between room temperature and 900 °C to corroborate that $Li_5P_2N_5$ is a high-pressure polymorph of β-$Li_{10}P_4N_{10}$. Figure 10.6 shows that, at ambient pressure, $Li_5P_2N_5$ transforms back to the ambient pressure polymorph at 700 °C.

10.2.7 Comparison of the Density

According to Le Chatelier, the density for high-pressure polymorphs is higher than that of the corresponding low-pressure polymorphs. This principle is also adaptable to lithium nitridophosphates. The calculated density of $Li_5P_2N_5$ (2.596 g cm^{-3}) is about 9.5% higher than that of β-$Li_{10}P_4N_{10}$ (2.350 g cm^{-3}). In $Li_{12}P_3N_9$ the polymerization of *dreier*-rings to chains leads to a decrease of density of about 7%. For this reaction a lower synthesis pressure (6 GPa) was necessary.[30] Both differences in density are similar to other high-pressure transformations of nitridophosphates, for example, $P_4N_6(NH)$ with 5 (*α* to *β*) and 16% (*β* to *γ*).[16,26,53] In comparison the calculated density of *σ*'-P_2O_5 (2.928 g cm^{-3}) is about 22% higher than that of *h*-P_2O_5 (2.276 g cm^{-3}).[46,47]

10.2.8 Density functional theory calculations

10.2.8.1Volume pressure calculations

Due to the observed partial occupancy of one Li site (occupancy of 2/3) in β-$Li_{10}P_4N_{10}$ we constructed a charge neutral model with full Li occupancies (Supporting Information, Figure S10.10).

By means of structural relaxations for a variety of constant volume compressions and expansions (92% to 105% with 1% steps (0.5% steps around equilibrium); β-$Li_{10}P_4N_{10}$: 17 steps, $Li_5P_2N_5$: 18 steps) of the respective unit cells (maintaining the space group), experimental synthesis pressures were covered.

Figure 10.7 (top) shows the resulting energy–volume (EV) curves. β-$Li_{10}P_4N_{10}$ is energetically favored by 0.87 eV (84 kJ mol^{-1}) at ambient pressure. By fitting the EV curves according to the Murnaghan equation of state,[54] we obtained a bulk modulus of B = 84.0 for β-$Li_{10}P_4N_{10}$ and B = 96.4 GPa for $Li_5P_2N_5$. We calculated the enthalpy difference ΔH from the equation $H = E + pV$, while pressure p is obtained by a numerical differentiation of $p = \partial E/\partial V$.

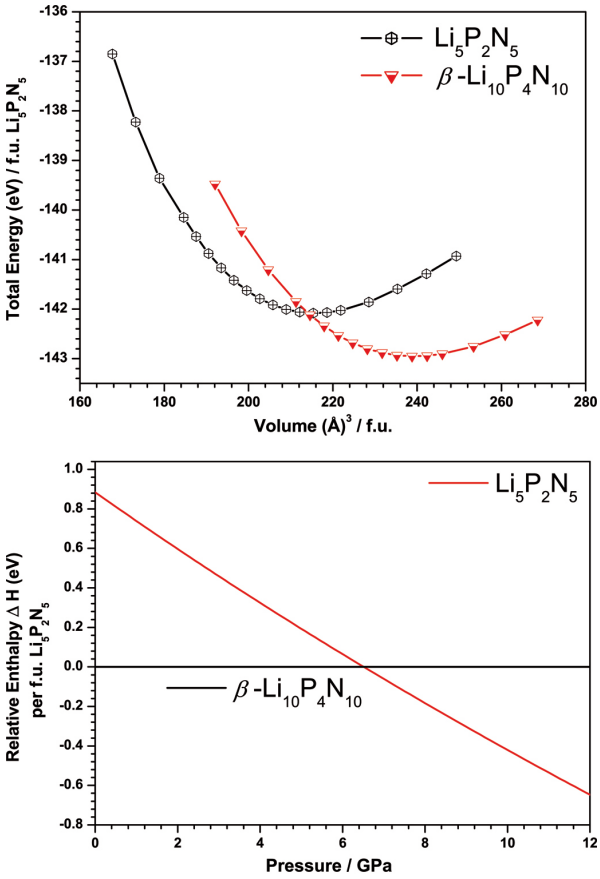

Figure 10.7 Top: Energy–volume diagram of β-$Li_{10}P_4N_{10}$ and $Li_5P_2N_5$. Each point constitutes one structural optimization at constant volume. Energy and volume are given per formula unit (f.u.) of $Li_5P_2N_5$. Bottom: Enthalpy–pressure diagram for the high-pressure phase transition of β-$Li_{10}P_4N_{10}$ to $Li_5P_2N_5$, obtained from a fit of the Murnaghan equation of state to the energy-volume diagram. The enthalpy is given per formula unit of $Li_5P_2N_5$ relative to β-$Li_{10}P_4N_{10}$.

Figure 10.7 (bottom) shows the relative enthalpy with respect to the presumed low pressure polymorph β-$Li_{10}P_4N_{10}$. The transition pressure from β-$Li_{10}P_4N_{10}$ to $Li_5P_2N_5$ can be estimated as 6.5 GPa without accounting for temperature (0 K). Consequently $Li_5P_2N_5$ is corroborated as high-pressure polymorph of β-$Li_{10}P_4N_{10}$. The observed synthesis pressure of 8 GPa is slightly increased with respect to the calculated reaction pressure, but $Li_5P_2N_5$ was also obtained as a side phase (small percentages) at reaction pressure of about 7 GPa.
The densities of β-$Li_{10}P_4N_{10}$ and $Li_5P_2N_5$ were calculated from the volume at the equilibrium (Figure 10.7 top) with respect to one formula unit of $Li_{10}P_4N_{10}$ (= "$2Li_5P_2N_5$"). The calculated densities (DFT) show a difference of about 10% (β-$Li_{10}P_4N_{10}$: ρ = 2.32 g cm^{-3}; $Li_5P_2N_5$: ρ = 2.58 g cm^{-3}), which is in line with the densities calculated from X-ray measurements. These results corroborate $Li_5P_2N_5$ as the high-pressure polymorph.

10.2.8.2 Electronic Band Structure

$Li_5P_2N_5$ is an electronically insulating material with a wide electronic direct band-gap of 5.6 eV (at *Γ*) (Supporting Information, Figure S10.11). The band-gap for the low pressure polymorph β-$Li_{10}P_4N_{10}$ was estimated to 3.5 eV (Supporting Information, Figure S10.12). This trend was also found for $Li_{12}P_3N_9$ (indirect band-gap of 5 eV from *Y* to *Γ*) and its high-pressure polymorph Li_4PN_3 (direct band-gap of 6.1 eV at *Γ*).[30]

10.3 Conclusions

Herein we report on synthesis and thorough characterization of the first layered lithium nitridophosphate, namely $Li_5P_2N_5$. The high-pressure polymorph $Li_5P_2N_5$ can be prepared by solid-state reaction of $LiPN_2$ and Li_7PN_4 with the Li_3N self-flux method, or directly starting from the low pressure polymorph β-$Li_{10}P_4N_{10}$. By temperature dependent X-ray powder diffraction we showed that $Li_5P_2N_5$ is a high-pressure polymorph of β-$Li_{10}P_4N_{10}$, because it transforms back at about 700 °C. This result was also confirmed by DFT calculations. The adamantane like T2 supertetrahedra in β-$Li_{10}P_4N_{10}$ polymerizes to corrugated layers of corner sharing PN_4 tetrahedra, forming *sechser*-rings in chair conformation under high-pressure/high-temperature conditions. The framework topology can be described as a honeycomb-type (*hcb*) net.

Together with the recently published polymerization from *dreier*-rings in $Li_{12}P_3N_9$ to chains in Li_4PN_3, this shows that high-pressure/high-temperature synthesis is a powerful technique to obtain lithium nitridophosphates with unprecedented structures, which range from isolated ions (rings, ring-systems, cages) to chains, layers, and nets of corner-sharing PN_4 tetrahedra. With our work we are aiming for a better understanding of the synthesis conditions of these compounds, which will help to optimize materials with regard to their properties. Higher pressures could also make structures accessible with additional edge-sharing tetrahedra, PN_5 square-pyramids, or even PN_6 octahedra, which will lead to a plethora of yet unexplored structures and unexpected properties as well.

10.4 Experimental Section

10.4.1 Synthesis of Starting Materials

P_3N_5[1] was synthesized by reaction of P_4S_{10} (8 g, Sigma – Aldrich, 99%) in a constant flow of ammonia (Air-Liquide, 99.999%) at 850 °C (4 h). Before heating, the silica tube was saturated for 4 h with NH_3. By washing with water, ethanol, and acetone, any side products were eliminated. Powder X-ray diffraction and FTIR spectroscopy confirmed the phase purity of P_3N_5. All further steps were performed with strict exclusion of oxygen and moisture in an argon filled glove box (Unilab, MBraun, Garching, O_2<1 ppm, H_2O<0.1 ppm).

$LiPN_2$,[22] Li_7PN_4,[52] and β-$Li_{10}P_4N_{10}$[32] were synthesized by reaction of Li_3N (Rockwood Lithium, 94%) and P_3N_5 ($LiPN_2$: molar ratio 1.2:1; Li_7PN_4: 7.2:1; β-$Li_{10}P_4N_{10}$: 2.8:1) in sealed silica ampoules under Ar atmosphere. The starting materials were ground and transferred into a Ta-crucible, which was placed in a dried silica tube. The sealed silica ampoule was heated for 90 h or 120 h in a tube furnace at 800, 600, or 680 °C. To eliminate side products, $LiPN_2$ was washed with diluted hydrochloric acid, water, and ethanol. Li_7PN_4 was not washed and was used with Li_3P as side phase. β-$Li_{10}P_4N_{10}$ was washed with dry ethanol to eliminate Li_3P as side phase. Powder X-ray diffraction and FTIR spectroscopy confirmed phase purity of the starting materials.

10.4.2 High-Pressure Synthesis of $Li_5P_2N_5$

$Li_5P_2N_5$ can be synthesized according to two different routes at high-pressure/high-temperature conditions, with a modified Walker-type multianvil module in combination with a 1000 t press (Voggenreiter, Mainleus, Germany).[36–40] The starting materials were ground under argon atmosphere and compactly packed in an *h*-BN crucible (Henze BNP GmbH, Kempten, Germany). The *h*-BN crucible was transferred into the specially prepared pressure medium (Cr_2O_3 doped (5%) MgO-octahedra (Ceramic Substrates & Components, Isle of Wight, UK); edge length 18 mm (Eq. 4) or 14 mm (Eq. 5)). Then the octahedron was placed centrically in eight truncated WC cubes (Hawedia, Marklkofen, Germany, truncation length 11 mm (Eq. 1) or 8 mm (Eq. 2)) separated by pyrophyllite gaskets. Detailed information describing the complete setup is given in literature.[37,38,40] The assembly was compressed to 9 GPa at room temperature and then heated to about 1000 °C within 60 min (30 min for Eq. 2). Under these conditions, the sample was treated for 60 min and cooled down to room temperature within 60 min (200 min) and then decompressed. Both syntheses yielded a powder containing colorless single crystals. The product is sensitive to traces of air and moisture.

10.4.3 Single-Crystal X-ray Analysis

With a D8 Venture diffractometer, single-crystal X-ray diffraction was performed (Bruker, Billerica MA, USA) using $Mo_{K\alpha}$ radiation from a rotating anode source. During collection of the data two twin components were identified and indexed with CELL_NOW.[55] After integration with the Bruker SAINT Software package[56,57] the final cell constants were calculated and the intensity data were corrected for absorption with TWINABS.[57,58] Both twin components can be transformed into each other by [1 $\bar{1}$ 0.33 / 0 $\bar{1}$ 0 / 0 0 $\bar{1}$]. The data of component 1 (HKLF4) were

averaged with Xprep[59] and the program package WinGX (SHELXS-97, SHELXL-97, PLATON)[59-63] was used for structure solution by direct methods, and refinement (see Table 10.1). For final structure refinement the refined structure of component 1 was handled taking to account both twin components (HKLF5). All P and N atoms were refined anisotropically. The Li atom positions were determined during structure refinement from difference Fourier maps. The crystal structure was visualized using DIAMOND.[64]

10.4.4 Powder X-ray Diffraction

X-ray powder diffraction was carried out with a STOE StadiP diffractometer (Stoe & Cie, Darmstadt, Germany) in parafocusing Debye–Scherrer geometry, to prove phase purity of the products. A Ge(111) single-crystal monochromator was used to select $Cu_{K\alpha 1}$ radiation. A Mythen 1 K Si-strip detector (Dectris, Baden, Switzerland) was used for detection of the diffracted radiation. For measurement the samples were enclosed in glass capillaries with 0.5 mm diameter (Hilgenberg, Malsfeld, Germany) under inert gas. Rietveld refinement was carried out using the program package TOPAS-Academic v4.1.[65] The background was handled with a shifted Chebychev function and the peak shapes were described using the fundamental parameters approach.[66,67]

Temperature dependent powder X-ray diffraction data were recorded on a STOE StadiP diffractometer equipped with a graphite furnace using $Mo_{K\alpha 1}$ radiation (λ = 0.70930 Å) in Debye–Scherrer geometry, an image plate position sensitive detector, and a Ge(111) monochromator. Data were collected every 25 °C starting from room temperature, up to 900 °C, with a heating rate of 5 °C min^{-1}.

10.4.5 Solid-State MAS (Magic Angle Spinning) NMR (Nuclear Magnetic Resonance) Methods

^{6}Li, ^{7}Li, and ^{31}P solid-state MAS NMR spectra of both polymorphs were recorded on a DSX Avance spectrometer (Bruker) with a magnetic field of 11.7 T. The sample was transferred into a ZrO_2 rotor with outer diameter of 2.5 mm ($LiPN_2$) and 1.3 mm ($Li_5P_2N_5$), which was mounted in a commercial MAS probe (Bruker) under inert conditions. The rotor was spun at a rotation frequency of 20 or 50 kHz, respectively. The experimental data were analyzed by device-specific software.

10.4.6 EDX Measurements

The atomic ratio P/N of the samples was analyzed by energy-dispersive X-ray spectroscopy. A carbon coated sample (BAL-TEC MED 020, Bal Tec AG) was examined with a FEI Helios G3 UC scanning electron microscope (SEM, field emission gun, acceleration voltage 30 kV). Qualitative and semiquantitative elemental analyses were executed by an energy dispersive spectrometer and analyzed by INCA.[68]

10.4.7 Fourier Transform Infrared (FTIR) Spectroscopy

Infrared spectroscopy measurements were carried out on a Bruker FTIR-IFS 66v/S spectrometer. Before measurement in the range of 400–4000 cm^{-1} the sample was mixed with KBr in a glove box and cold-pressed into a pellet (Ø = 12 mm). The data were evaluated with OPUS.[69]

10.4.8 Computational Details

The structural relaxation of both of polymorphs were carried out with the Vienna ab initio simulation package (VASP).[70–72] Total energies of the unit cell were converged to 10^{-7} eV $atom^{-1}$ with residual atomic forces below 5×10^{-3} eV $Å^{-1}$. The exchange correlation was treated within the generalized gradient approximation (GGA) of Perdew, Burke, and Ernzerhof (PBE)[73,74] and the projector-augmented-wave (PAW) method.[75,76] A plane-wave cut-off of 535 eV was chosen for the calculations with a Brillouin zone sampling on a *Γ*-centered *k*-mesh of 6 × 6 × 3 (β-$Li_{10}P_4N_{10}$) and 4 × 4 × 11 ($Li_5P_2N_5$) respectively, produced from the method of Monkhorst and Pack.[77] Additional calculations were performed with the modified Becke-Johnson formalism (GGA-mbj)[78,79] to treat the electronic band gaps.

10.5 Acknowledgements

We would like to thank Dr. Peter Mayer for single-crystal X-ray measurements, Thomas Miller for high-temperature powder diffraction measurements, Christian Minke for EDX, SEM, and solid-state MAS NMR measurements, Marion Sokoll for IR measurements, and Dr. Constantin Hoch for helpful discussion concerning the twinning of the single-crystal (all Department of Chemistry of LMU Munich). We gratefully acknowledge financial support granted by the Fonds der Chemischen Industrie (FCI), and the Deutsche Forschungsgemeinschaft (DFG), project SCHN377/18.

10.6 References

[1] A. Stock, H. Grüneberg, Über den Phosphorstickstoff, *Ber. Dtsch. Chem. Ges.* **1907**, *40*, 2573–2578.

[2] S. Horstmann, E. Irran, W. Schnick, Synthesis and Crystal Structure of Phosphorus(V) Nitride α-P_3N_5, *Angew. Chem. Int. Ed. Engl.* **1997**, *36*, 1873–1875; *Angew. Chem.* **1997**, *109*, 1938–1940.

[3] S. Horstmann, E. Irran, W. Schnick, Phosphor(V)-nitrid α-P_3N_5: Synthese ausgehend von Tetraaminophosphoniumiodid und Kristallstrukturaufklärung mittels Synchrotron-Pulver-Röntgenbeugung, *Z. Anorg. Allg. Chem.* **1998**, *624*, 620–628.

[4] S. Horstmann, E. Irran, W. Schnick, Phosphorus(V) Nitride Imide HP_4N_7: Synthesis from a Molecular Precursor and Structure Determination with Synchrotron Powder Diffraction, *Angew. Chem. Int. Ed. Engl.* **1997**, *36*, 1992–1994; *Angew. Chem.* **1997**, *109*, 2085–2087.

[5] W. Schnick, Solid-State Chemistry with Nonmetal Nitrides, *Angew. Chem. Int. Ed. Engl.* **1993**, *32*, 806–818; *Angew. Chem.* **1993**, *105*, 846–858.

[6] S. Correll, O. Oeckler, N. Stock, W. Schnick, $Li_xH_{12-x-y+z}[P_{12}O_yN_{24-y}]Cl_z$ – An Oxonitridophosphate with a Zeolitelike Framework Structure Composed of 3-Rings, *Angew. Chem. Int. Ed.* **2003**, *42*, 3549–3552; *Angew. Chem.* **2003**, *115*, 3674–3677.

[7] S. Correll, N. Stock, O. Oeckler, J. Senker, T. Nilges, W. Schnick, $Li_xH_{12-x-y+z}[P_{12}O_yN_{24-y}]X_z$ (*X* = Cl, Br) - Oxonitridophosphate mit NPO-Zeolithstruktur, *Z. Anorg. Allg. Chem.* **2004**, *630*, 2205–2217.

[8] S. J. Sedlmaier, M. Döblinger, O. Oeckler, J. Weber, J. Schmedt auf der Günne, W. Schnick, Unprecedented Zeolite-Like Framework Topology Constructed from Cages with 3-Rings in a Barium Oxonitridophosphate, *J. Am. Chem. Soc.* **2011**, *133*, 12069–12078.

[9] F. Karau, W. Schnick, A Nitridic Clathrate: $P_4N_4(NH)_4(NH_3)$, *Angew. Chem. Int. Ed.* **2006**, *45*, 4505–4508; *Angew. Chem.* **2006**, *118*, 4617–4620.

[10] T. Grande, S. Jacob, J. R. Holloway, P. F. McMillan, C. A. Angell, High-pressure synthesis of nitride glasses, *J. Non-Cryst. Solids* **1995**, *184*, 151–154.

[11] E. Horvath-Bordon, R. Riedel, A. Zerr, P. F. McMillan, G. Auffermann, Y. Prots, W. Bronger, R. Kniep, P. Kroll, High-pressure chemistry of nitride-based materials, *Chem. Soc. Rev.* **2006**, *35*, 987–1014.

[12] A. Marchuk, W. Schnick, $Ba_3P_5N_{10}Br:Eu^{2+}$: A Natural-White-Light Single Emitter with Zeolite Structure Type, *Angew. Chem. Int. Ed.* **2015**, *54*, 2383–2387; *Angew. Chem.* **2015**, *127*, 2413–2417.

[13] A. Marchuk, S. Wendl, N. Imamovic, F. Tambornino, D. Wiechert, P. J. Schmidt, W. Schnick, Nontypical Luminescence Properties and Structural Relation of $Ba_3P_5N_{10}X:Eu^{2+}$ (*X* = Cl, I): Nitridophosphate Halides with Zeolite-like Structure, *Chem. Mater.* **2015**, *27*, 6432–6441.

[14] F. J. Pucher, A. Marchuk, P. J. Schmidt, D. Wiechert, W. Schnick, Luminescent Nitridophosphates $CaP_2N_4:Eu^{2+}$, $SrP_2N_4:Eu^{2+}$, $BaP_2N_4:Eu^{2+}$, and $BaSr_2P_6N_{12}:Eu^{2+}$, *Chem. Eur. J.* **2015**, *21*, 6443–6448.

[15] S. Zhao, Z. Fu, Q. Qin, A solid-state electrolyte lithium phosphorus oxynitride film prepared by pulsed laser deposition, *Thin Solid Films* **2002**, *415*, 108–113.

[16] D. Baumann, W. Schnick, High-Pressure Polymorph of Phosphorus Nitride Imide HP_4N_7 Representing a New Framework Topology, *Inorg. Chem.* **2014**, *53*, 7977–7982.

[17] K. Landskron, H. Huppertz, J. Senker, W. Schnick, High-Pressure Synthesis of γ-P_3N_5 at 11 GPa and 1500 °C in a Multianvil Assembly: A Binary Phosphorus(V) Nitride with a Three-Dimensional Network Structure from PN_4 Tetrahedra and Tetragonal PN_5 Pyramids, *Angew. Chem. Int. Ed.* **2001**, *40*, 2643–2645; *Angew. Chem.* **2001**, *113*, 2713–2716.

[18] K. Landskron, H. Huppertz, J. Senker, W. Schnick, Multianvil-Synthese, Pulver-Röntgenstrukturanalyse, ^{31}P-MAS-NMR- und FTIR-Spektroskopie sowie Materialeigenschaften von γ-P_3N_5, einer Hochdruckphase von binärem Phosphor(V)-nitrid mit verzerrt quadratischen PN_5-Pyramiden und PN_4-Tetraedern *Z. Anorg. Allg. Chem.* **2002**, *628*, 1465–1471.

[19] J. M. Léger, J. Haines, C. Chateau, G. Bocquillon, M. W. Schmidt, S. Hull, F. Gorelli, A. Lesauze, R. Marchand, Phosphorus oxynitride PON, a silica analogue: structure and compression of the cristobalite-like phase; *P–T* phase diagram, *Phys. Chem. Minerals* **2001**, *28*, 388–398.

[20] J. M. Léger, J. Haines, L. S. de Oliveira, C. Chateau, A. L. Sauze, R. Marchand, S. Hull, Crystal structure and high pressure behaviour of the quartz-type phase of phosphorus oxynitride PON, *J. Phys. Chem. Solids* **1999**, *60*, 145–152.

[21] J. Haines, C. Chateau, J. M. Léger, A. L. Sauze, N. Diot, R. Marchand, S. Hull, Crystal structure of moganite-type phosphorus oxynitride: relationship to other twinned-quartz-based structures, *Acta Crystallogr. Sect. B: Struct. Sci.* **1999**, *55*, 677–682.

[22] D. Baumann, R. Niklaus, W. Schnick, A High-Pressure Polymorph of Phosphorus Oxonitride with the Coesite Structure, *Angew. Chem. Int. Ed.* **2015**, *54*, 4388-4391; *Angew. Chem.* **2015**, *127*, 4463-4466.

[23] W. Schnick, J. Lücke, Darstellung, Kristallstruktur und IR-spektroskopische Untersuchung von Phosphor(V)-nitrid-imid, HPN_2, *Z. Anorg. Allg. Chem.* **1992**, *610*, 121–126.

[24] H. Jacobs, R. Nymwegen, S. Doyle, T. Wroblewski, W. Kockelmann, Kristallines Phoshor(V)-nitrid-imid, HPN_2 bzw. DPN_2 – Strukturbestimmung mit Rontgen-, Synchrotron- und Neutronenstrahlung, *Z. Anorg. Allg. Chem.* **1997**, *623*, 1467–1474.

[25] A. Marchuk, F. J. Pucher, F. W. Karau, W. Schnick, A High-Pressure Polymorph of Phosphorus Nitride Imide, *Angew. Chem. Int. Ed.* **2014**, *53*, 2469–2472*, Angew. Chem.* **2014**, *126*, 2501–2504.

[26] D. Baumann, W. Schnick, Pentacoordinate Phosphorus in a High-Pressure Polymorph of Phosphorus Nitride Imide $P_4N_6(NH)$, *Angew. Chem. Int. Ed.* **2014**, *53*, 14490–14493; *Angew. Chem.* **2014**, *126*, 14718–14721.

[27] S. D. Kloß, W. Schnick, Rare-Earth-Metal Nitridophosphates through High-Pressure Metathesis, *Angew. Chem. Int. Ed.* **2015**, *54*, 11250–11253: *Angew. Chem.* **2015**, *127*, 11402–11405.

[28] E.-M. Bertschler, C. Dietrich, J. Janek, W. Schnick, $Li_{18}P_6N_{16}$ – A Lithium Nitridophosphate with Unprecedented Tricyclic $[P_6N_{16}]^{18-}$ Ions *Chem. Eur. J.* **2017**, *23*, 2185–2191.

[29] W. Schnick, J. Lücke, Synthesis and Crystal Structure of Lithium Phosphorus Nitride Li_7PN_4: The First Compound Containing Isolated PN_4-Tetrahedra, *J. Solid State Chem.* **1990**, *87*, 101–106.

[30] E.-M. Bertschler, R. Niklaus, W. Schnick, $Li_{12}P_3N_9$ with Non-Condensed $[P_3N_9]^{12-}$-Rings and its High-Pressure Polymorph Li_4PN_3 with Infinite Chains of PN_4-Tetrahedra, *Chem. Eur. J.* **2017**, *23*, 9592–9599.

[31] W. Schnick, U. Berger, $Li_{10}P_4N_{10}$ - A Lithium Phosphorus(V) Nitride with the Novel Complex Anion $P_4N_{10}^{10-}$, *Angew. Chem. Int. Ed. Engl.* **1991**, *30*, 830–831; *Angew. Chem.* **1991**, *103*, 857–858.

[32] E.-M. Bertschler, C. Dietrich, T. Leichtweiss, J. Janek, W. Schnick, Li^+ Ion Conductors with Adamantane-Type Nitridophosphate Anions β-$Li_{10}P_4N_{10}$ and $Li_{13}P_4N_{10}X_3$ with X = Cl, Br, *Chem. Eur. J.* **2017**, *24*, 196–205.

[33] W. Schnick, J. Lücke, Zur Kenntnis von Lithium-phosphor(V)-nitrid. Reindarstellung und Verfeinerung der Kristallstruktur von $LiPN_2$, *Z. Anorg. Allg. Chem.* **1990**, *588*, 19–25.

[34] F. Liebau, *Structural Chemistry of Silicates*, Springer, **1985**.

[35] The term *dreier (vierer, sechser)* ring was coined by Liebau and is derived from the German word "drei" ("vier", "sechs"). A *dreier (vierer, sechser)* ring is comprised of three (four, six) tetrahedra centers.

[36] N. Kawai, S. Endo, The Generation of Ultrahigh Hydrostatic Pressures by a Split Sphere Apparatus, *Rev. Sci. Instrum.* **1970**, *41*, 1178–1181.

[37] D. Walker, M. A. Carpenter, C. M. Hitch, Some simplifications to multianvil devices for high pressure experiments, *Am. Mineral.* **1990**, *75*, 1020–1028.

[38] D. Walker, Lubrication, gasketing, and precision in multianvil experiments, *Am. Mineral.* **1991**, *76*, 1092–1100.

[39] D. C. Rubie, Characterising the sample environment in multianvil high-pressure experiments, *Phase Transitions* **1999**, *68*, 431–451.

[40] H. Huppertz, Multianvil high-pressure / high-temperature synthesis in solid state chemistry, *Z. Kristallogr.* **2004**, *219*, 330–338.

[41] Further details of the crystal structure investigation can be obtained from the Fachinformations-Zentrum Karlsruhe, 76344 Eggenstein- Leopoldshafen, Germany (fax: (+49)7247-808-666; e-Mail: crysdata@fiz-Karlsruhe.de) on quoting the deposition number CSD-433592.

[42] L. Cartz, S. R. Srinivasa, R. J. Riedner, J. D. Jorgensen, T. G. Worlton, Effect of pressure on bonding in black phosphorus, *J. Chem. Phys.* **1979**, *71*, 1718–1721.

[43] V. A. Blatov, Multipurpose crystallochemical analysis with the program package TOPOS, *IUCr CompComm Newsl.* **2006**, *7*, 4–38.

[44] V. A. Blatov, M. O'Keeffe, D. M. Proserpio, Vertex-, face-, point-, Schläfli-, and Delaney-symbols in nets, polyhedra and tilings: recommended terminology, *CrystEngComm* **2010**, *12*, 44–48.

[45] T. G. Mitina, V. A. Blatov, Topology of 2-Periodic Coordination Networks: Toward Expert Systems in Crystal Design, *Cryst. Growth Des.* **2013**, *13*, 1655–1664.

[46] M. Jansen, Lüer Burkhard, Refinement of the crystal structure of tetraphosphorus decaoxide, *Z. Kristallogr.* **1986**, *177*, 149–151.

[47] D. Stachel, I. Svoboda, H. Fuess, Phosphorus Pentoxide at 233 K, *Acta Crystallogr. Sect. C* **1995**, *51*, 1049–1050.

[48] A. Durif, *Crystal Chemistry of Condensed Phosphates*, Springer, **1995**.

[49] S. Lupart, W. Schnick, $LiCa_3Si_2N_5$ – A Lithium Nitridosilicate with a $[Si_2N_5]^{7-}$ Double-Chain, *Z. Anorg. Allg. Chem.* **2012**, *638*, 2015–2019.

[50] V. A. Blatov, Voronoi–dirichlet polyhedra in crystal chemistry: theory and applications, *Crystallogr. Rev.* **2004**, *10*, 249–318.

[51] N. A. Anurova, V. A. Blatov, G. D. Ilyushin, O. A. Blatova, A. K. Ivanov-Schitz, L. N. Dem'yanets, Migration maps of Li^+ cations in oxygen-containing compounds, *Solid State Ionics* **2008**, *179*, 2248–2254.

[52] V. A. Blatov, A. P. Shevchenko, V. N. Serezhkin, TOPOS3.1 - program package for multipurpose geometrical and topological analysis of crystal structures, *J. Appl. Crystallogr.* **1999**, *32*, 377.

[53] S. Horstmann, E. Irran, W. Schnick, Synthese, Kristallstruktur und Eigenschaften von Phosphor(V)-nitridimid HP_4N_7, *Z. Anorg. Allg. Chem.* **1998**, *624*, 221–227.

[54] F. D. Murnaghan, The Compressibility of Media under Extreme Pressures, *Proc. Natl. Acad. Sci. USA* **1944**, *30*, 244–247.

[55] G. M. Sheldrick, *Cell_NOW, Version 2008/4*, Georg-August-Universtiät Göttingen, Göttingen, Germany, **2008**.

[56] *SAINT, Data Integration Software*, Madison, Wisconsin, USA, **1997**.

[57] *APEX 3 v 2016.5-0*, Bruker-AXS, **2016**.

[58] G. M. Sheldrick, *TWINABS*, Universtiy Of Göttingen, Göttingen, Germany.

[59] *XPREP Reciprocal Space Exploration, Vers. 6.12*, Bruker-AXS, Karlsruhe, **2001**.

[60] G. M. Sheldrick, *SHELXS*, University of Göttingen, **1997**.

[61] G. M. Sheldrick, *Acta Crystallogr., Sect. A Found. Crystallogr.* **2008**, *64*, 112–122.

[62] L. J. Farrugia, WinGX suite for small-molecule single-crystal crystallography, *J. Appl. Crystallogr.* **1999**, *32*, 837–838.

[63] L. J. Farrugia, *PLATON, Vers. 1.16*, University of Glasgow, **1995**.

[64] K. Brandenburg, H. Putz, *Diamond - Crystal and Molecular Structure Visualization*, Crystal Impact, Bonn, Germany.

[65] A. Coelho, *TOPAS-Academic* **2007**.

[66] R. W. Cheary, A. Coelho, A fundamental parameters approach to X-ray line-profile fitting, *J. Appl. Crystallogr.* **1992**, *25*, 109–121.

[67] R. W. Cheary, A. A. Coelho, J. P Cline, Fundamental Parameters Line Profile Fitting in Laboratory Diffractometers, *J. Res. Natl. Inst. Stand.Technol.* **2004**, *109*, 1–25.

[68] *INCA, Version 4.02*, OXFORD Instruments.

[69] *OPUS/IR*, Bruker Analytik GmbH, **2000**.

[70] G. Kresse, J. Hafner, *Ab initio* molecular dynamics for liquid metals, *Phys. Rev. B: Condens. Matter Mater. Phys.* **1993**, *47*, 558–561.

[71] G. Kresse, J. Hafner, *Ab initio* molecular-dynamics simulation of the liquid-metal-amorphous-semiconductor transition in germanium, *Phys. Rev. B: Condens. Matter Mater. Phys.* **1994**, *49*, 14251–14269.

[72] G. Kresse, J. Furthmüller, Efficiency of *ab-initio* total energy calculations for metals and semiconductors using a plane-wave basis set, *Comput. Mater. Sci.* **1996**, *6*, 15–50.

[73] J. P. Perdew, K. Burke, M. Ernzerhof, Generalized Gradient Approximation Made Simple, *Phys. Rev. Lett.* **1996**, *77*, 3865–3868.

[74] J. P. Perdew, K. Burke, M. Ernzerhof, Generalized Gradient Approximation Made Simple [*Phys. Rev. Lett.* **1996**, *77*, 3865], *Phys. Rev. Lett.* **1997**, *78*, 1396.

[75] P. E. Blöchl, Projector augmented-wave method, *Phys. Rev. B: Condens. Matter Mater. Phys.* **1994**, *50*, 17953–17979.

[76] G. Kresse, D. Joubert, From ultrasoft pseudopotentials to the projector augmented-wave method, *Phys. Rev. B: Condens. Matter Mater. Phys.* **1999**, *59*, 1758–1775.

[77] H. J. Monkhorst, J. D. Pack, Special points for Brillouin-zone integrations, *Phys. Rev. B: Solid State* **1976**, *13*, 5188–5192.

[78] F. Tran, P. Blaha, Accurate Band Gaps of Semiconductors and Insulators with a Semilocal Exchange-Correlation Potential, *Phys. Rev. Lett.* **2009**, *102*, 226401.

[79] J. A. Camargo-Martínez, R. Baquero, Performance of the modified Becke-Johnson potential for semiconductors, *Phys. Rev. B: Condens. Matter Mater. Phys.* **2012**, *86*, 195106.

10.7 Supporting Information

10.7.1 Additional Crystallographic Data for $Li_5P_2N_5$

Table S10.1 Fractional atomic coordinates, isotropic thermal displacement parameters, and site occupancies for $Li_5P_2N_5$

Atom	Wyck. symbol	*x*	*y*	*z*	U_{iso} / Å^2	Occupancy
P1	8*f*	0.35644(7)	0.22823(6)	0.0530(2)		1
P2	8*f*	0.17597(7)	0.04753(6)	0.5596(2)		1
P3	8*f*	0.14635(7)	0.37020(6)	0.4444(2)		1
N1	8*f*	0.0875(2)	0.55895(19)	0.0212(8)		1
N2	8*f*	0.2422(2)	0.12046(19)	0.4786(8)		1
N3	4*c*	1/4	1/4	0		1
N4	8*f*	0.3798(2)	0.2097(2)	0.3892(8)		1
N5	8*f*	0.1228(2)	0.3518(2)	0.1089(8)		1
N6	8*f*	0.2917(2)	0.4714(2)	0.1122(8)		1
N7	8*f*	0.0726(2)	0.0710(2)	0.5086(8)		1
N8	8*f*	0.0820(3)	0.2035(2)	0.0332(8)		1
Li1	8*f*	0.0520(7)	0.4536(5)	0.096(2)	0.026(2)	1
Li2	4*e*	0	0.6312(9)	1/4	0.033(4)	1
Li3	8*f*	0.1216(10)	0.1813(8)	0.439(3)	0.058(4)	1
Li4	8*f*	0.2133(7)	0.1371(6)	0.035(2)	0.031(2)	1
Li5	8*f*	0.3221(7)	0.0330(6)	0.164(2)	0.025(2)	1
Li6	4*e*	0	0.2782(8)	1/4	0.022(3)	1
Li7	4*e*	0	0.0025(9)	1/4	0.021(2)	1
Li8	4*e*	0	0.1377(14)	1/4	0.066(6)	1
Li9	8*f*	0.4353(15)	0.4053(12)	0.050(5)	0.090(6)	1
Li10	4*d*	1/4	1/4	1/2	0.061(5)	1

Table S10.2 Anisotropic displacement parameters occurring in $Li_5P_2N_5$

Atom	U_{11} / Å^2	U_{22} / Å^2	U_{33} / Å^2	U_{12} / Å^2	U_{13} / Å^2	U_{23} / Å^2
P1	0.0064(5)	0.0063(5)	0.0052(5)	0.0010(4)	0.0017(4)	0.0004(4)
P2	0.0051(5)	0.0046(5)	0.0042(5)	-0.0005(4)	-0.0003(4)	0.0002(4)
P3	0.0047(5)	0.0044(5)	0.0050(5)	0.0000(4)	0.0004(4)	0.0006(4)
N1	0.0075(16)	0.0074(16)	0.0104(19)	-0.0016(13)	0.0002(15)	-0.0011(15)
N2	0.0045(15)	0.0051(16)	0.0095(19)	-0.0004(12)	0.0001(14)	0.0002(15)
N3	0.009(2)	0.021(3)	0.020(3)	0.010(2)	-0.002(2)	0.000(3)
N4	0.0063(16)	0.0068(16)	0.0064(17)	-0.0017(13)	-0.0015(14)	0.0004(14)
N5	0.0096(17)	0.0084(17)	0.0053(17)	0.0029(14)	0.0004(14)	-0.0007(15)
N6	0.0098(17)	0.0067(15)	0.0054(17)	-0.0018(14)	0.0003(14)	0.0004(14)
N7	0.0054(15)	0.0111(17)	0.0114(19)	-0.0005(13)	-0.0017(15)	0.0028(16)
N8	0.0133(18)	0.0069(17)	0.013(2)	-0.0018(14)	0.0047(16)	0.0011(16)

Table S10.3 List of interatomic distances / Å for $Li_5P_2N_5$

P1—N8^{i}	1.589(4)	P2—N7	1.589(4)	P3—N1^{ix}	1.591(4)
P1—N3	1.6263(11)	P2—N6^{iii}	1.675(4)	P3—N2^{iii}	1.677(4)
P1—N5^{i}	1.667(4)	P2—N6^{v}	1.678(4)	P3—N5	1.681(4)
P1—N4	1.684(4)	P2—N2	1.687(4)	P3—N4^{iii}	1.695(4)
Li1—N1^{ix}	2.116(11)	Li5—N6^{v}	2.327(11)	Li8—N8^{xv}	2.024(15)
Li2—N1^{xv}	2.174(10)	Li5—N1^{i}	2.329(11)	Li9—Li8^{i}	1.95(2)
Li2—N4^{xi}	2.389(10)	Li5—N5^{i}	2.602(11)	Li9—N8^{i}	2.00(2)
Li2—N5^{ix}	2.466(4)	Li6—N8^{xv}	2.120(9)	Li9—N7^{xxi}	2.09(2)
Li3—N4^{iii}	2.117(15)	Li6—N5^{xv}	2.371(8)	Li9—N7^{iii}	2.19(2)
Li4—N6^{i}	2.066(11)	Li6—N4^{iii}	2.436(4)	Li10—N4^{iii}	2.143(4)
Li4—N5^{i}	2.564(11)	Li7—N7^{xv}	2.020(11)	Li10—N2^{iii}	2.317(3)
Li5—N1^{v}	2.028(11)	Li7—N7^{xvii}	2.094(11)	Li10—N3^{vii}	2.4300(5)
Li5—N6^{i}	2.096(11)				

(i) 0.5-x, 0.5-y, -z; (ii) 0.5+x, -0.5+y, z; (iii) 0.5-x, 0.5-y, 1-z; (iv) x, y, -1+z; (v) 0.5-x, -0.5+y, 0.5-z; (vi) x, -y, 0.5+z; (vii) x, y, 1+z; (viii) -x, -y, 1-z; (ix) x, 1-y, 0.5+z; (x) -x, 1-y, 1-z; (xi) 0.5-x, 0.5+y, 0.5-z; (xii) x, 1-y, -0.5+z; (xiii) -x, 1-y, -z; (xiv) -0.5+x, 0.5-y, 0.5+z; (xv) -x, y, 0.5-z; (xvi) -0.5+x, 0.5+y, z; (xvii) x, -y, -0.5+z; (xviii) -0.5+x, 0.5-y, -0.5+z; (xix) -0.5+x, -0.5+y, z; (xx) -x, -y, -z; (xxi) 0.5+x, 0.5-y, -0.5+z; (xxii) 0.5+x, 0.5+y, z; (xxiii) 1-x, y, 0.5-z.

Table S10.4 List of bond angles / ° for $Li_5P_2N_5$

N–P–N					
N8^{i}—P1—N3	109.69(15)	N7—P2—N6^{iii}	115.0(2)	N1^{ix}—P3—N2^{iii}	114.28(18)
N8^{i}—P1—N5^{i}	114.2(2)	N7—P2—N6^{v}	115.6(2)	N1^{ix}—P3—N5	107.2(2)
N3—P1—N5^{i}	109.32(14)	N6^{iii}—P2—N6^{v}	103.69(14)	N2^{iii}—P3—N5	112.6(2)
N8^{i}—P1—N4	108.4(2)	N7—P2—N2	108.89(18)	N1^{ix}—P3—N4^{iii}	114.57(19)
N3—P1—N4	110.22(14)	N6^{iii}—P2—N2	103.83(19)	N2^{iii}—P3—N4^{iii}	102.91(18)
N5^{i}—P1—N4	104.87(19)	N6^{v}—P2—N2	108.97(19)	N5—P3—N4^{iii}	104.94(18)
P–N–P					
P3^{iii}—N2—P2	126.8(2)	P1—N4—P3^{iii}	126.0(2)	P1^{i}—N5—P3	126.3(2)

(i) 0.5-x, 0.5-y, -z; (ii) 0.5+x, -0.5+y, z; (iii) 0.5-x, 0.5-y, 1-z; (iv) x, y, -1+z; (v) 0.5-x, -0.5+y, 0.5-z; (vi) x, -y, 0.5+z; (vii) x, y, 1+z; (viii) -x, -y, 1-z; (ix) x, 1-y, 0.5+z; (x) -x, 1-y, 1-z; (xi) 0.5-x, 0.5+y, 0.5-z; (xii) x, 1-y, -0.5+z; (xiii) -x, 1-y, -z; (xiv) -0.5+x, 0.5-y, 0.5+z; (xv) -x, y, 0.5-z; (xvi) -0.5+x, 0.5+y, z; (xvii) x, -y, -0.5+z; (xviii) -0.5+x, 0.5-y, -0.5+z; (xix) -0.5+x, -0.5+y, z; (xx) -x, -y, -z; (xxi) 0.5+x, 0.5-y, -0.5+z; (xxii) 0.5+x, 0.5+y, z; (xxiii) 1-x, y, 0.5-z.

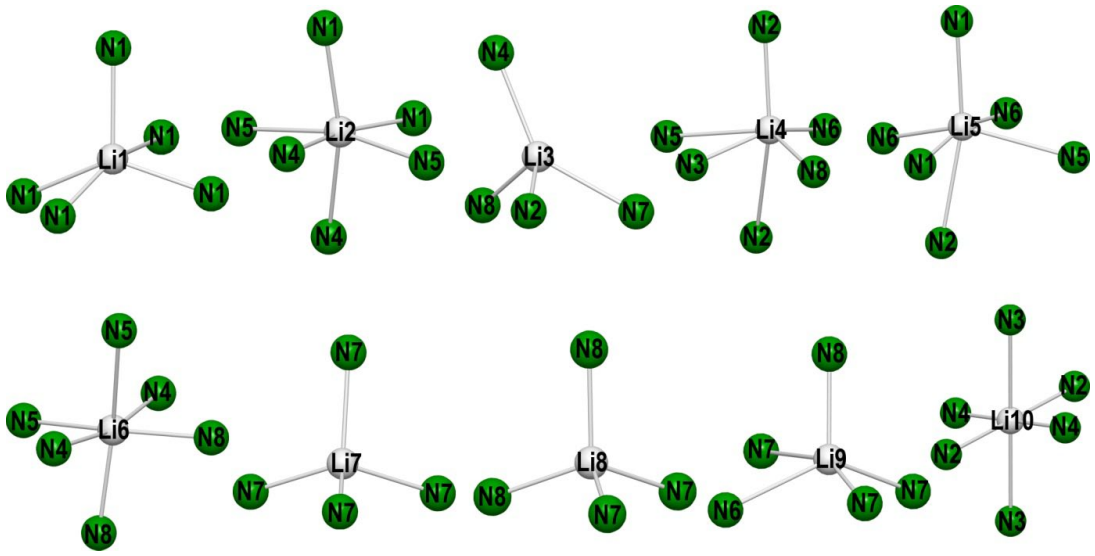

Figure S10.1 Coordination spheres of the Li^+ sites. Bond length up to 2.88 Å are shown by a gray line. Gray: Li, Green: N.

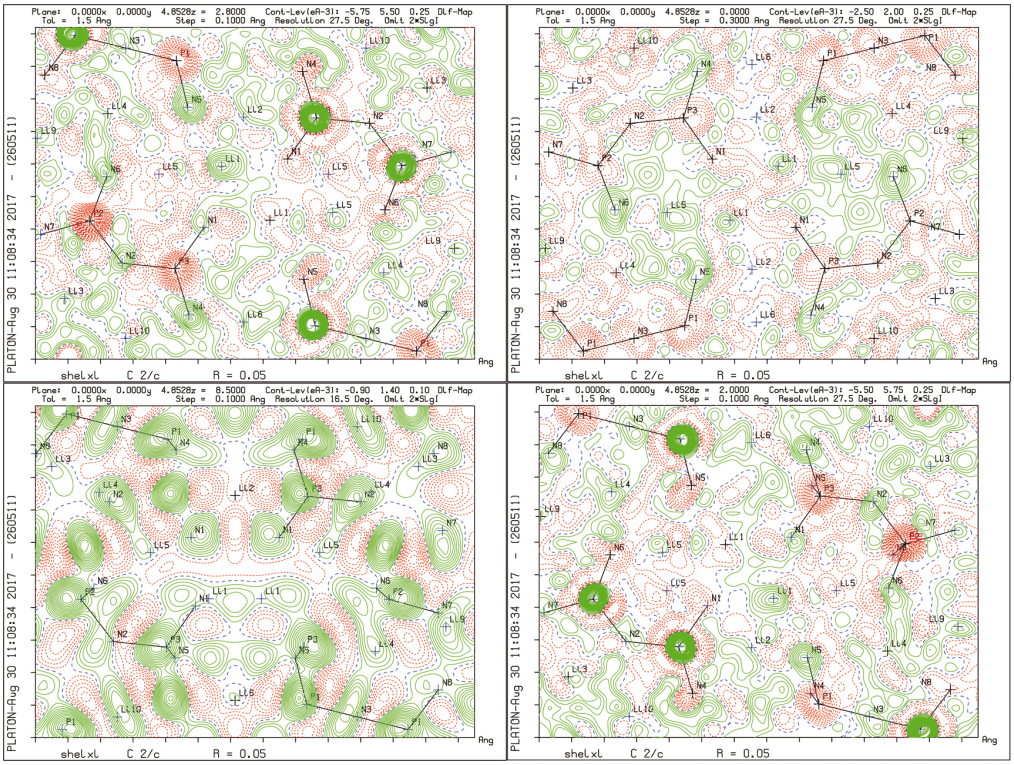

Figure S10.2 Different Difference Fourier maps of $Li_5P_2N_5$.

10.7.2 Details of the Rietveld Refinement

Table S10.5 Details of the Rietveld refinement of $Li_5P_2N_5$

formula	**$Li_5P_2N_5$**
formula mass / g · mol^{-1}	534.9
crystal system / space group	monoclinic *C* 2/*c* (no. 15)
lattice parameters / Å, °	*a* = 14.752(2)
	b = 17.802(2)
	c = 4.8479(5)
	β = 93.196(8)
cell volume / Å^3	1271.1(2)
formula units per cell *Z*	12
X-ray density / g · cm^{-3}	2.61305(49)
linear absorption coefficient / cm^{-1}	82.02(2)
radiation	Cu-$K_{\alpha1}$ (λ = 1.540596 Å)
monochromator	Ge(111)
diffractometer	Stoe StadiP
detector	linear PSD
2*θ*-range / °	5.0-112.1
temperature / K	298 (2)
data points	7144
number of observed reflections	845
number of parameters	72
program used	TOPAS Academic
structure refinement	Rietveld method
profile function	fundamental parameters model
background function	shifted Chebyshev with 24 terms
R_{wp}	11.310
R_{exp}	2.041
R_p	7.614
R_{Bragg}	6.008
χ^2	5.542

10.7.3 Detailed Rietveld Plot

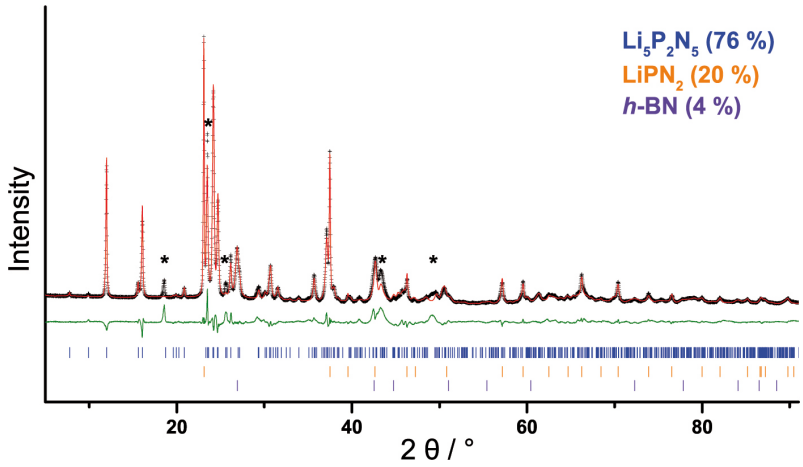

Figure S10.3 $Li_5P_2N_5$: Observed (black crosses) and calculated (red line) powder diffraction pattern as well as difference profile (green) of the Rietveld refinement. Reflection positions are marked by vertical blue bars. Peak positions of side phases are marked by vertical orange ($LiPN_2$) and violet (*h*-BN) bars.

The side phase *h*-BN can be traced back to the crucible material, which is difficult to remove from the sample. The difference of the peace profile of some peak positions is due to a further side phase, which could not be analyzed.

10.7.4 ^{31}P, ^{6}Li and ^{7}Li Solid-State MAS NMR Spectroscopy

The ^{31}P MAS NMR spectrum of $Li_5P_2N_5$ is shown in black and shows one strong resonances at 5.22 ppm and further signals at 19.42, 8.98, −7.55 and −14.36 ppm. $Li_5P_2N_5$ has three crystallographically independent P sites, which all have approximately the same chemical surrounding and bond length to N atoms. The ^{31}P MAS NMR-spectrum of $LiPN_2$ is shown in green. The resonance at 5.68 ppm corresponds to one crystallographically independent P site. The resonance at 3.13 ppm assigned to little amount of side products in the starting material $LiPN_2$.

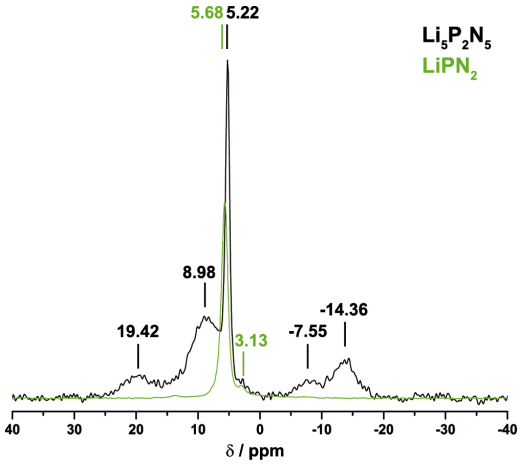

Figure S10.4 ^{31}P MAS NMR spectrum of $Li_5P_2N_5$ in black and the side phase $LiPN_2$ in green.

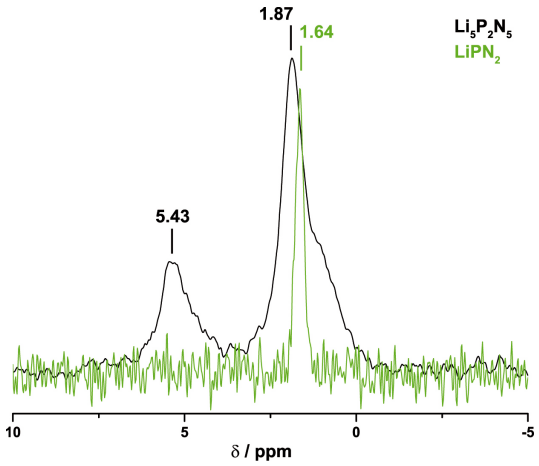

Figure S10.5 ^{6}Li MAS NMR spectrum of $Li_5P_2N_5$.

The ^{6}Li MAS NMR spectrum shows strong resonances between 5.43 and 1.87 ppm. Due to the small chemical shift differences of the signals, the differentiation of the 9 crystallographically independent sites cannot be observed in the spectrum.

The ^{7}Li MAS NMR spectrum shows two strong resonances at 4.9 and 1.7 ppm. Due to the small chemical shift differences of the signals, no differentiation of the crystallographically independent sites can be observed in the spectrum.

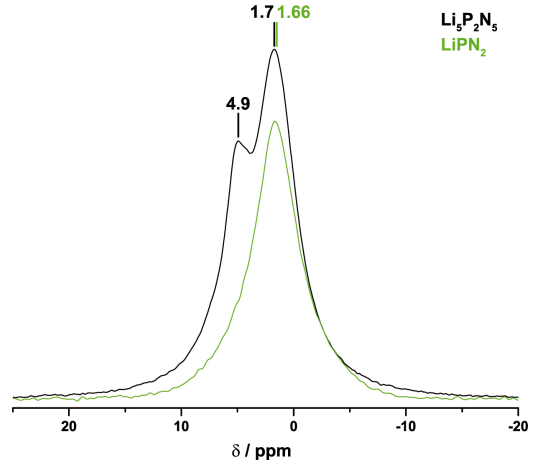

Figure S10.6 ^{7}Li MAS NMR spectrum of $Li_5P_2N_5$.

10.7.5 Details of Scanning Electron Microscopy

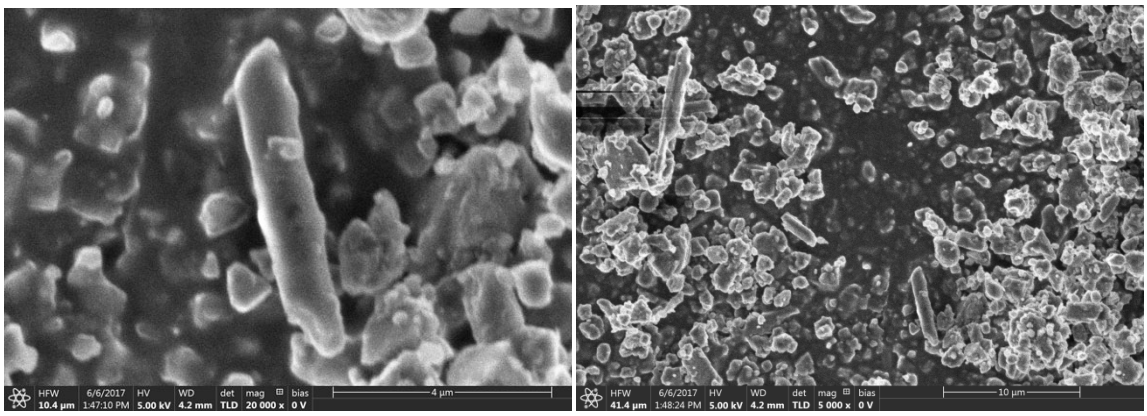

Figure S10.7 Scanning electron micrographs of $Li_5P_2N_5$.

Table S10.6 EDX analysis of $Li_5P_2N_5$

	N	O	P
EDX point 1[atom %]	63.83	6.50	29.67
EDX point 2[atom %]	67.54	4.10	28.36
EDX point 3[atom %]	67.98	4.55	27.47
Average	**66.45**	**5.05**	**28.50**
Calculated atom %	**41.7**	**0**	**16.7**

Due to hydrolysis of the sample during mounting the sample at air, oxygen can be found in the sample

10.8 FTIR Spectrum

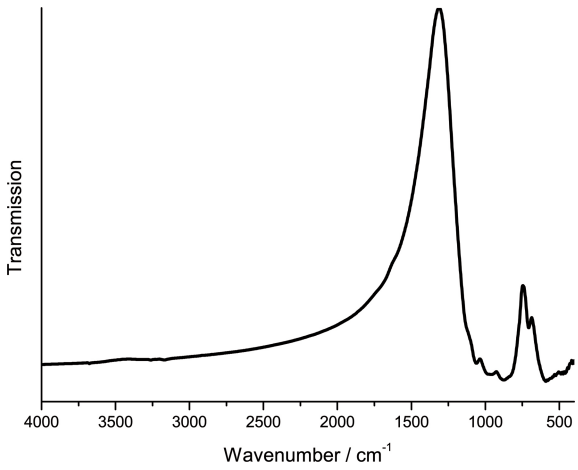

Figure S10.8 FTIR spectrum of $Li_5P_2N_5$.

Infrared spectroscopy measurements were performed on a Bruker FTIR-IFS 66v/S spectrometer. Before measurement in the range of 400–4000 cm^{-1} the sample was mixed with KBr in a glove box and cold-pressed into a pellet (Ø = 12 mm).The spectrum shows no significant valence vibrations in the region of 3000 cm^{-1}, where N–H vibrations are expected. A weak signal in that region can be explained by surface hydrolysis of the sample. Thus, the incorporation of stoichiometric amounts of hydrogen seems unlikely. Much more significant are the characteristic PN framework vibrations between 400 and 1500 cm^{-1}. The extreme background between 4000 and 1500 cm^{-1} is due to the brown side phases in the sample, which leads to a not transparent pellet.

10.8.1 Structural Analysis of Possible Lithium Migration Pathways

Possible voids and migration pathways in $Li_5P_2N_5$ were analyzed with TOPOS.[1–4]

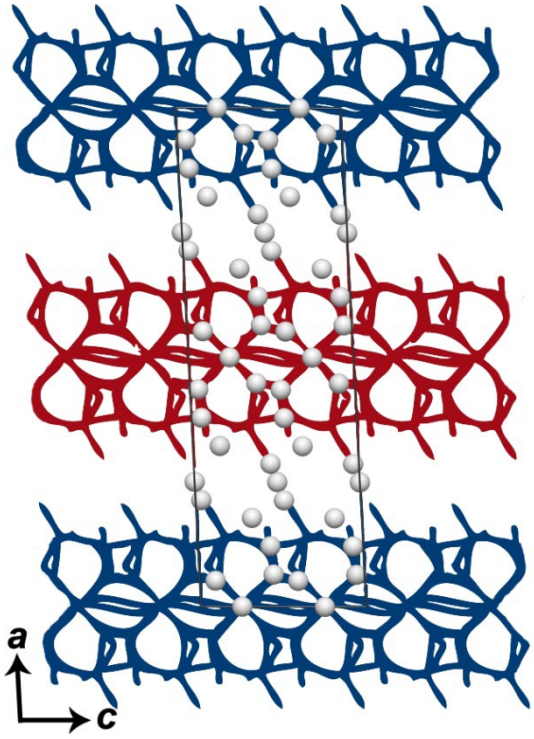

Figure S10.9 Calculated possible Li^+ pathways (blue and red) according to the voids in the structure and unit cell of $Li_5P_2N_5$. (Li: gray)

10.8.2 Density Functional Theory Calculations

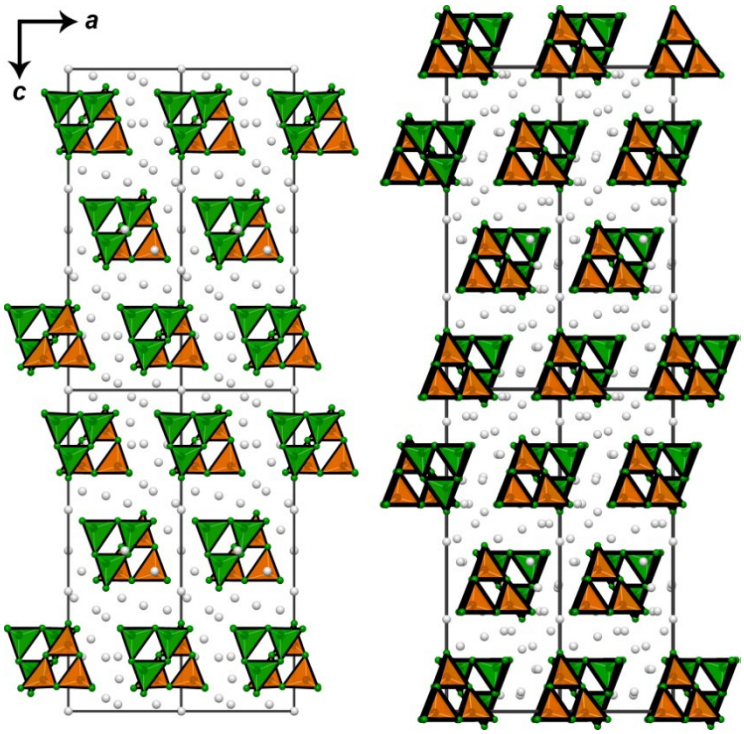

Figure S10.10 Left: unit cell of β-$Li_{10}P_4N_{10}$ with partially occupied Li position (Li9 is occupied by 2/3). Right: ordering model of β-$Li_{10}P_4N_{10}$ with fully occupied Li atoms (2/3 of Li9 positions were fully occupied), used for calculations. (P: black, N: green, Li: gray)

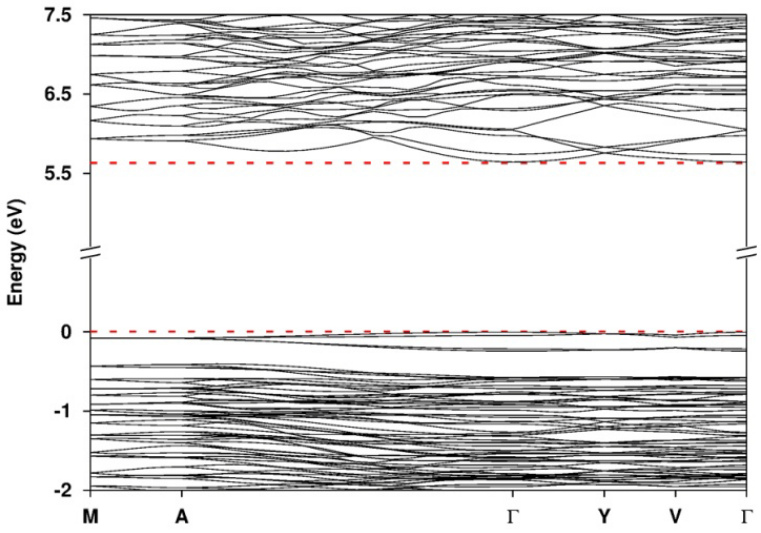

Figure S10.11 Electronic band structure along high-symmetry directions in the first Brillouin zone for $Li_5P_2N_5$.

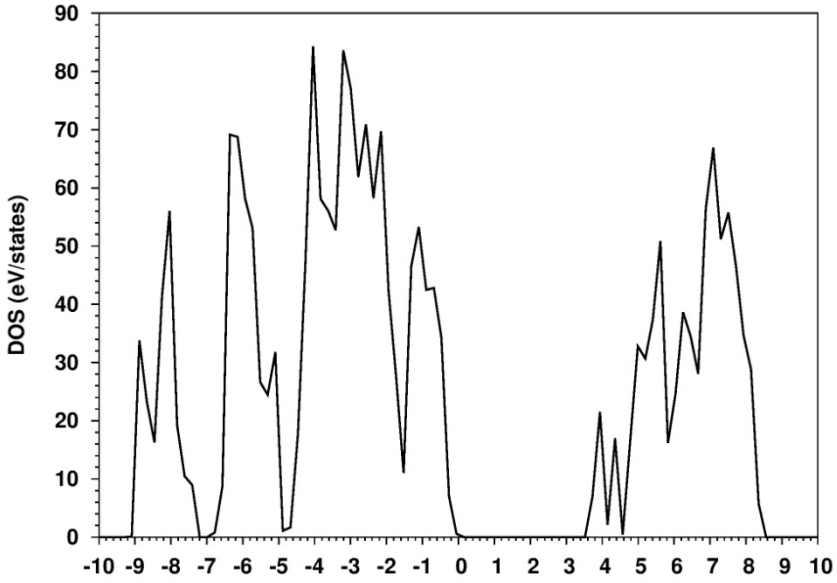

Figure S10.12 Density of states (DOS) for β-$Li_{10}P_4N_{10}$ (ordering model like in Figure S10.10). The band-gap is estimated to 3.5 eV.

10.8.3 References

[1] V. A. Blatov, Multipurpose crystallochemical analysis with the program package TOPOS, *IUCr CompComm Newsl.* **2006**, *7*, 4–38.

[2] V. A. Blatov, Voronoi–dirichlet polyhedra in crystal chemistry: theory and applications, *Crystallogr. Rev.* **2004**, *10*, 249–318.

[3] N. A. Anurova, V. A. Blatov, G. D. Ilyushin, O. A. Blatova, A. K. Ivanov-Schitz, L. N. Dem'yanets, Migration maps of Li^+ cations in oxygen-containing compounds, *Solid State Ionics* **2008**, *179*, 2248–2254.

[4] V. A. Blatov, A. P. Shevchenko, V. N. Serezhkin, TOPOS3.2: a new version of the program package for multipurpose crystal-chemical analysis, *J. Appl. Crystallogr.* **2000**, *33*, 1193.

11 *Ab initio* Exploration and Prediction of AE-containing Nitrido(litho/magneso)tetrelates (AE = Ca, Sr; Tt = Si, Ge) with $[Si_2N_6]^{10-}$ or $[Ge_2N_6]^{10-}$ Units

published in: *Dalton Trans.* **2019**, *48*, 8671–8677.

authors: Robin Niklaus, Ján Minár, Philipp Strobel, Peter J. Schmidt, Wolfgang Schnick

DOI: 10.1039/C9DT01158G

Acknowledgment: Reproduced (adapted) from *Dalton Transactions* with permission from The Royal Society of Chemistry. Copyright 2019 Royal Society of Chemistry.

Abstract Recently, a number of different structurally related nitrides characterized by pairs of edge-sharing Si–N tetrahedra forming $[Si_2N_6]^{10-}$ units have emerged *via* different synthesis methods. Concurrently, upon doping with rare earth elements (*e.g.* Eu^{2+} and Ce^{3+}), numerous applications in the field of luminescent materials were revealed, ranging from the visible spectrum to the near IR. This compound class in turn emphasizes the extraordinary large tuning range with respect to relative composition by formal cation exchange. In this contribution, we study the dynamical stabilities of the existing Si-based nitridotetrelates and hypothetical Ge analogues promising for future synthesis efforts of luminescent materials by means of extensive phonon calculations. Further calculations of electronic and mechanical properties corroborate the fundamental suitability of the predicted compounds for the applications of potential luminescent materials with regard to band gap (E_g) and Debye temperature (Θ_D). Calculated enthalpies of the reaction provide further beneficial insights for future experimental attempts. Our study hence highlights a potential range of novel stable nitridogermanates with isotypic structures and suitable electronic properties for optoelectronic applications.

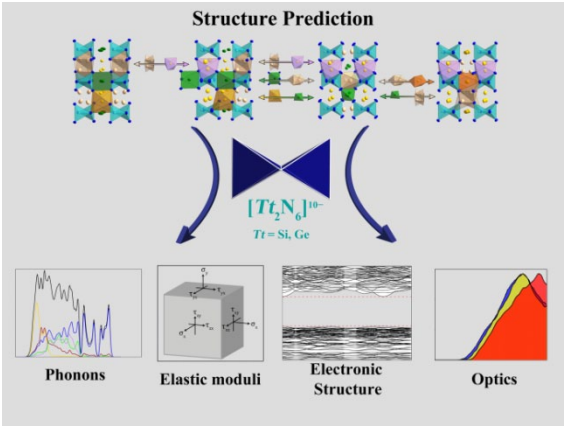

11.1 Introduction

In retrospect, over the last few decades, the focus on solid-state nitride materials has shifted from fundamental research to numerous studies dealing with potential applications revolving around high-temperature ceramics, thermoelectrics or optoelectronics.[1–7] With regard to a globally increasing environmental awareness, particular attention has nowadays been attracted towards the development of efficient phosphor materials for light-emitting diodes (LEDs), contributing to the decrease in global energy consumption.[8–11]

Herein, *e.g.* nitridosilicates and -aluminates are extensively studied subclasses owing to their highly diverse network structures in which LED light down-converting activator ions such as Eu^{2+} or Ce^{3+} may be incorporated. Prominent examples comprise nitride materials such as $CaAlSiN_3:Eu^{2+}$, $Sr_2Si_5N_8:Eu^{2+}$, $M[Mg_2Al_2N_4]:Eu^{2+}$ (M = Ca, Sr, Ba), $La_{3-x}Ca_{1.5x}Si_6N_{11}:Eu^{2+}$, $Sr[LiAl_3N_4]:(Eu^{2+}/Ce^{3+})$, $Ba_2LiSi_7AlN_{12}:Eu^{2+}$, and $Sr_4[LiAl_{11}N_{14}]:Eu^{2+}$.[12–20] One benefit of nitride materials is their ability to form diverse and highly rigid anionic framework structures made up of condensed tetrahedra. With respect to efficiency, many nitridosilicates with higher degrees of condensation have in turn proven to be suitable host structures for luminescent materials (*i.e.* LED phosphors).[5,21,22] This rigidity makes them in turn generally less prone to thermal quenching mechanisms like strong electron–phonon coupling from the incorporated activator ion. In addition, combined anionic substructures built from interconnected nitride tetrahedra with different tetrahedra centers such as Si and M (M = Li, *AE*), as present in recently discovered materials such as $(Ca/Sr)_2Li_2[Mg_2Si_2N_6]:Eu^{2+}/Ce^{3+}$ or $Ca_3Mg[Li_2Si_2N_6]:Eu^{2+}$, result in higher structural diversity. Moreover, the latter materials show promising narrow-band luminescence characteristics in the yellow, red and near-infrared spectral regions proving the venture into more complex systems rewarding.[23,24] Structurally, the latter can be characterized by edge-sharing tetrahedra building units condensed to $[Si_2N_6]^{10-}$, commonly termed bow-tie units in analogy to $[Ge_2N_6]^{10-}$ found in $Sr_3[Li_4Ge_2N_6]$.[25] Interestingly, together with $Ca_2Li_2[Mg_2Si_2N_6]$, all of the bow-tie units containing nitrides mentioned above crystallize in the space group $C2/m$ (no. 12) and structurally relate closely to each other. Formally, derived from $Ca_3[Li_4Si_2N_6]$, this series of compounds exhibit high variability toward partial Li/Mg substitution. Furthermore, the verified synthesis of $Sr_5Ge_2N_6$ and $Sr_3[Li_4Ge_2N_6]$, both isotypic to $Ca_3[Li_4Si_2N_6]$ and $Ca_5Si_2N_6$, suggests the existence of numerous analogue multinary Sr-nitridogermanates possibly accessible by similar partial substitution of Li and Mg.[25,26]

From a purely computational point of view, there are various possible starting points in order to find and potentially predict novel materials with promising properties. Such procedures regularly include the use of high-throughput screening methods generally relying on dedicated genetic algorithms and machine learning.[27–31] Although the latter often prove to be successful and come highly valued, the concomitant computational effort and resources of such calculations can still be enormous, especially for materials with an increasing number of atoms and a higher compositional order. An alternative and computationally less demanding approach can be realized by a targeted evaluation, based on chemical comprehension and observation. In our case, this connotes the abovementioned structural relations between the discussed nitridosilicates and germanates.

In our work, we predict four novel nitridogermanates $Ca_3Mg[Li_2Ge_2N_6]$, $Sr_3Mg[Li_2Ge_2N_6]$, $Sr_2Mg[Li_4Ge_2N_6]$ and $Sr_2Li_2[Mg_2Ge_2N_6]$, isotypic to their corresponding nitridosilicate analogues, by means of first principles calculations from density functional theory (DFT). By calculating the phonon density of states, we examine and validate their dynamic stability postulated in the space group $C2/m$ (no. 12). We further provide theoretical CIF files with anisotropic displacement parameters (ADPs) at room temperature as generated from PHONOPY and the Molecular Toolbox program.[32–36] Enthalpies of formation and reaction are calculated from the

elements and representative metathesis reactions based on the known (litho/magneso)nitridosilicates, subsequently providing thermodynamically favorable reaction equations that can potentially be useful to experimentalists.

All predicted nitridogermanates are isotypic to the recently synthesized compounds $Ca_2Mg[Li_4Si_2N_6]$, $Ca_3Mg[Li_2Si_2N_6]$ and $Ca_2Li_2[Mg_2Si_2N_6]$, which were also calculated in detail for comparison.[23,37] Moreover, electronic, optical and mechanical properties of the structures appear promising for optoelectronic use and potential activator doping, proving relevant for chemists in search of potential wide gap semiconductors.

11.2 Computational Details

Accurate lattice parameters for all compounds were obtained by structural relaxations of the materials with the Vienna *ab initio* simulation package (VASP).[38–40] The exchange correlation was treated in terms of the generalized gradient approximation (GGA) of Perdew, Burke, and Ernzerhof (PBE)[41,42] revised for solids (PBEsol)[43] and the projector-augmented-wave (PAW) method.[44,45] The plane-wave cut-off was set to 535 eV and the Brillouin zone was sampled on an individual *Γ*-centered *k*-mesh with divisions adapted to the setup of differing unit cells produced from the method of Monkhorst and Pack ($Ca_3[Li_4Si_2N_6]$ and $M^{II}_2Mg[Li_4Tt_2N_6]$: 9 × 6 × 9; $M^{II}_3Mg[Li_2Tt_2N_6]$: 9 × 6 × 5; $M^{II}_2Li_2[Mg_2Tt_2N_6]$: 9 × 5 × 9 with M^{II} = Ca, Sr; *Tt* = Si, Ge).[46] Total energies of the unit cells were converged to 10^{-7} eV per atom with residual atomic forces below 1×10^{-3} eV Å^{-1}. Subsequent phonon calculations were conducted based on the supercell approach in which supercells of 2 × 2 × 2 and 3 × 2 × 3 were used containing between 240 and 504 atoms. Calculations of force sets and lattice vibrations along with temperature-dependent anisotropic displacement parameters (ADPs) were calculated with the help of PHONOPY.[32,33] Conversion of the thermal displacement matrices to CIF format was achieved by utilizing the Molecular Toolbox program.[34–36] Band gaps were evaluated by additional PBEsol calculations of the standard cells in conjunction with the modified Becke–Johnson exchange potential (mBJ).[47,48] Accurate elastic tensor calculations were ensured by further increase of the plane-wave cut-off to 630 eV and calculating six finite lattice distortions of the crystal utilizing displacements of ±0.015 Å, enabling the derivation of elastic constants and moduli *via* the stress–strain relationship.[49]

11.3 Results and Discussion

11.3.1 Structural Relationship

A detailed overview of the structural relations between known lithiummagneso- and magnesiumlithonitridosilicates with bow-tie units has been published previously.[37] Figure 11.1 summarizes their main structural relations and coordination polyhedra based on their theoretically relaxed structures with ADPs derived from phonon calculations.[23,37] The latter are in good agreement with data obtained from single-crystal analyses. The bow-tie unit $[Si_2N_6]^{10-}$ provides the common denominator of all shown structures, where $Ca_3[Li_4Si_2N_6]$ can be considered to be the aristotype to the remaining structures.[37]

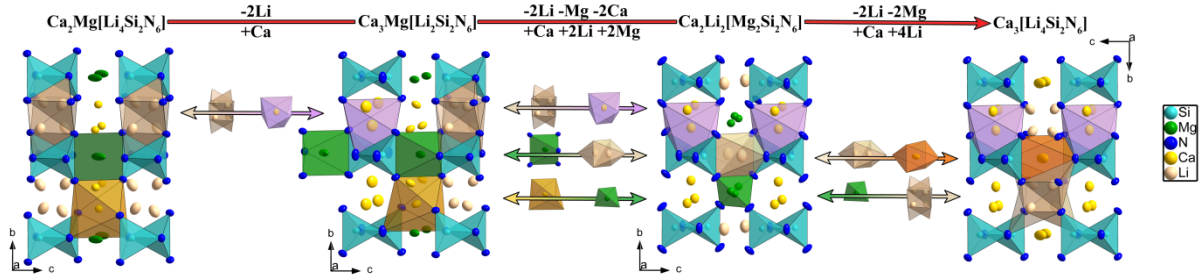

Figure 11.1 Structural relationship of different $[AE^{II}Li]^{10+}[Si_2N_6]^{10-}$ (AE^{II} = Ca, Mg) structures containing bow-tie units, all in the space group *C*2/*m* (no. 12) showcasing the interchangeability of different polyhedral units. Structures were relaxed with VASP and plotted with thermal ellipsoids (99% probability) as calculated by PHONOPY from phonon calculations with the supercell approach and extrapolated to 300 K.[32,33] The ADP data were converted to CIF format using the Molecular Toolbox program.[35,36]

All structures exhibit the same space group (*C*2/*m*, no. 12) and an overall structural similarity. The interspace between the $[Si_2N_6]^{10-}$ units apparently allows for a wide elemental flexibility and interchangeability. Of the present cations, Ca, Mg and 2 Li each can formally be substituted by one another, while maintaining charge neutrality. Such formal atomic interchange induces only minor structural distortions, mostly noticeable in the monoclinic angle of the respective unit cells shown in Table 11.1. This makes this class of materials promising for systematic studies of material properties correlations. Due to the structural flexibility between the $[Si_2N_6]^{10-}$ unit and the reported existence of the heavier $[Ge_2N_6]^{10-}$ homologues $Sr_3[Li_4Ge_2N_6]$ and $Sr_5[Ge_2N_6]$, the missing links in the germanate compound series appear promising for experimentalists. Although all discussed nitridosilicate compounds can be prepared selectively, a better understanding of how to achieve new structures is of interest for the experimentalist especially with regard to thermodynamic stability.

Table 11.1 Lattice parameters (Å) for the Si and Ge bow-tie nitrides as obtained by the Perdew-Burke-Ernzerhof GGA revised for solids (PBEsol). Experimental data is given where available. *c*/2 listed for $AE_3Mg[Li_2Tt_2N_6]$ (*AE* = Ca, Sr) for better comparability due to a doubled unit cell regarding formula units along the c-axis

	a	*b*	*c*	*c* /2	*β*[°]
$Ca_2Mg[Li_4Si_2N_6]$	5.871	9.754	5.593		94.66
Exp.[37]	5.906	9.817	5.611		94.90
$Ca_3Mg[Li_2Si_2N_6]$	5.911	9.754	11.698	5.849	99.43
Exp.[23]	5.965	9.806	11.721	5.861	99.67
$Ca_2Li_2[Mg_2Si_2N_6]$	5.543	9.803	5.988		97.06
Exp.[37]	5.547	9.844	5.997		97.13
$Ca_2Mg[Li_4Ge_2N_6]$	5.943	9.94	5.679		92.86
$Ca_3Mg[Li_2Ge_2N_6]$	5.966	10.005	11.876	5.938	97.89
$Ca_2Li_2[Mg_2Ge_2N_6]$	5.613	10.162	6.123		95.30
$Sr_2Mg[Li_4Ge_2N_6]$	6.086	10.241	5.891		94.08
$Sr_3Mg[Li_2Ge_2N_6]$	6.197	10.259	12.490	6.245	100.07
$Sr_2Li_2[Mg_2Ge_2N_6]$	5.799	10.187	6.251		96.12

Hence, we provide a detailed DFT study on the properties of the existing phases in question and their so far unknown heavier homologues.

11.3.2 Lattice Parameters

The overall disagreement for the calculated and experimental lattice parameters of the nitridosilicate compounds as listed in Table 1 is <1%, in turn corroborating an initial trustworthy prediction for structural parameters of the remaining compounds. Following the cationic exchange depicted in Figure 11.1, the lattice parameter *c* increases as Li is stepwise substituted by Ca, where the *c*-axis is doubled (respectively *c* /2 is used for comparison) in $Ca_3Mg[Li_2Si_2N_6]$, due to formally only exchanging half of the Li polyhedra. Although *b* remains mostly unaffected in each compound series, *a* widens going from $Ca_2Mg[Li_4Si_2N_6]$ to $Ca_3Mg[Li_2Si_2N_6]$ and significantly drops for $Ca_2Li_2[Mg_2Si_2N_6]$, the latter being due to the strong contraction upon formal substitution of CaN_6 for smaller MgN_4 polyhedra. β in turn is the largest in $Ca_3Mg[Li_2Si_2N_6]$ likely due to the alternating environment of the $[Si_2N_6]^{10-}$ units along *c*, owing to the substitution of only half of CaN_6 by two LiN_4 polyhedra. As expected for the substitution of heavier analogues with larger ionic radii, the calculated isotypic Ca and Sr nitridogermanates show the same trends with regard to lattice expansion within each compound series, where the overall expansion is the largest for the Sr compound series. Additional crystallographic information from the structural relaxations is given in Tables S11.1–S11.8 together with ADP values calculated from phonon calculations.

11.3.3 Enthalpies of Formation and Reaction

To estimate the thermodynamic stability of the existing and proposed Ge compounds, we calculated the enthalpies of formation (ΔH^f) next to enthalpies of reaction (ΔH^R) for representative metathesis reactions from which the Si compounds have been synthesized. The results are listed in Table 11.2. All calculated structures are stable against decomposition into the elements as seen from their negative ΔH^f values. Both $M_3Mg[Li_2Tt_2N_6]$ and $M_2Li_2[Mg_2Tt_2N_6]$ are about equally stable, while $M_2Mg[Li_4Tt_2N_6]$ is energetically elevated by about 0.14–0.2 eV for Sr and Ca, respectively. Negative reaction enthalpies ΔH^R from representative compounds used in solid-state metathesis, such as alkaline earth fluorides, hydrides and nitrides, corroborate the attainability of all Si phases according to their similar synthesis routes from the literature.[23,37] In contrast to $Ca_2Mg[Li_4Si_2N_6]$ and $Ca_2Li_2[Mg_2Si_2N_6]$, $Ca_3Mg[Li_2Si_2N_6]$ requires a change in reaction compounds due to its positive ΔH^R value for the same set. Analogues synthesis routes were adapted for the Ge substituted variants resulting in similar negative values of ΔH^R, thus appearing promising for the postulated germanates.

Table 11.2 Calculated enthalpies of formation and enthalpies of reaction for $M^{II}_2Mg[Li_4Tt_2N_6]$; $M^{II}_3Mg[Li_2Tt_2N_6]$ and $M^{II}_2Li_2[Mg_2Tt_2N_6]$ (M = Ca, Sr; Tt = Si, Ge)

Formula	ΔH^f / eV per atom	ΔH^R / eV per f.u.
$Ca_2Mg[Li_4Si_2N_6]$	-2.54	-2.17
$Ca_3Mg[Li_2Si_2N_6]$	-2.76	+0.64❶ / -6.26❷
$Ca_2Li_2[Mg_2Si_2N_6]$	-2.75	-8.20
$Ca_2Mg[Li_4Ge_2N_6]$	-2.19	-1.74
$Ca_3Mg[Li_2Ge_2N_6]$	-2.38	+0.95❶ / -5.95❷
$Ca_2Li_2[Mg_2Ge_2N_6]$	-2.41	-8.19
$Sr_2Mg[Li_4Ge_2N_6]$	-2.16	-1.29
$Sr_3Mg[Li_2Ge_2N_6]$	-2.30	+2.11❶ / -5.04❷
$Sr_2Li_2[Mg_2Ge_2N_6]$	-2.31	-6.86

$Ca_2Mg[Li_4Tt_2N_6]$

$$\mathbf{CaF_2 + {}^1/_3\,Mg_3N_2 + 4LiN_3 + 4Li + {}^2/_3\,Tt_3N_4 \rightarrow Ca_2Mg[Li_4Tt_2N_6] + 4LiF + 4N_2}$$

$Ca_3Mg[Li_2Tt_2N_6]$

❶ $$\mathbf{3CaF_2 + {}^1/_3\,Mg_3N_2 + 6LiN_3 + 4Li + {}^2/_3\,Tt_3N_4 \rightarrow Ca_3Mg[Li_4Tt_2N_6] + 6LiF + 7N_2}$$

❷ $$\mathbf{3CaH_2 + MgF_2 + 4LiN_3 + {}^2/_3\,Tt_3N_4 \rightarrow Ca_3Mg[Li_4Si_2N_6] + 2LiF + {}^{13}/_3\,N_2 + 3H_2}$$

$Ca_2Li_2[Mg_2Tt_2N_6]$

$$\mathbf{2CaF_2 + {}^2/_3\,Mg_3N_2 + 4LiN_3 + 2Li + {}^2/_3\,Tt_3N_4 \rightarrow Ca_2Li_2[Mg_2Tt_2N_6] + 4LiF + {}^{13}/_3\,N_2}$$

11.3.4 Phonon Calculations

To evaluate the dynamic stability of the postulated structures in the space group $C2/m$, we performed calculations of the absolute and partial phonon densities of states for both, the existing nitridosilicates and proposed nitridogermanates, as presented in Figure 11.2 (a–i). Figure 11.2 (a–c) corroborates the dynamical stability of the recently obtained nitridolitho- and nitridomagnesosilicates as no imaginary (negative) phonon modes are present.[32] The mere formal substitution of Si by Ge, resulting in isotypic nitridolitho- and nitridomagneso-germanates, however, leads to instabilities, as indicated by imaginary phonon frequencies, in $Ca_2Li_2[Mg_2Ge_2N_6]$ (e) and $Ca_2Mg[Li_4Ge_2N_6]$ (f). We estimate the instabilities to be likely due to the atomic size difference in Si and Ge, leading to unstable distortions by imaginary Ge, N, and Mg phonon modes, which indicate at least metastability, more likely non-existence, of both structures as calculated. In contrast, a more uniform increase by simultaneous substitution of both Si by Ge and Ca by Sr (Figure 11.2 (g–i)) leads to dynamically stable nitridogermanates isotypic to the existent nitridosilicates. Hence, synthesis efforts of those structures may prove viable, especially considering the previous synthesis of both $Sr_5Ge_2N_6$ and $Sr_3[Li_4Ge_2N_6]$.[25,26] The latter has further sparked interest with regard to its optoelectronic and mechanical properties.[50] The presented phonon density of states may further be helpful in the assignment of Raman or IR bands upon the synthesis of the predicted materials.

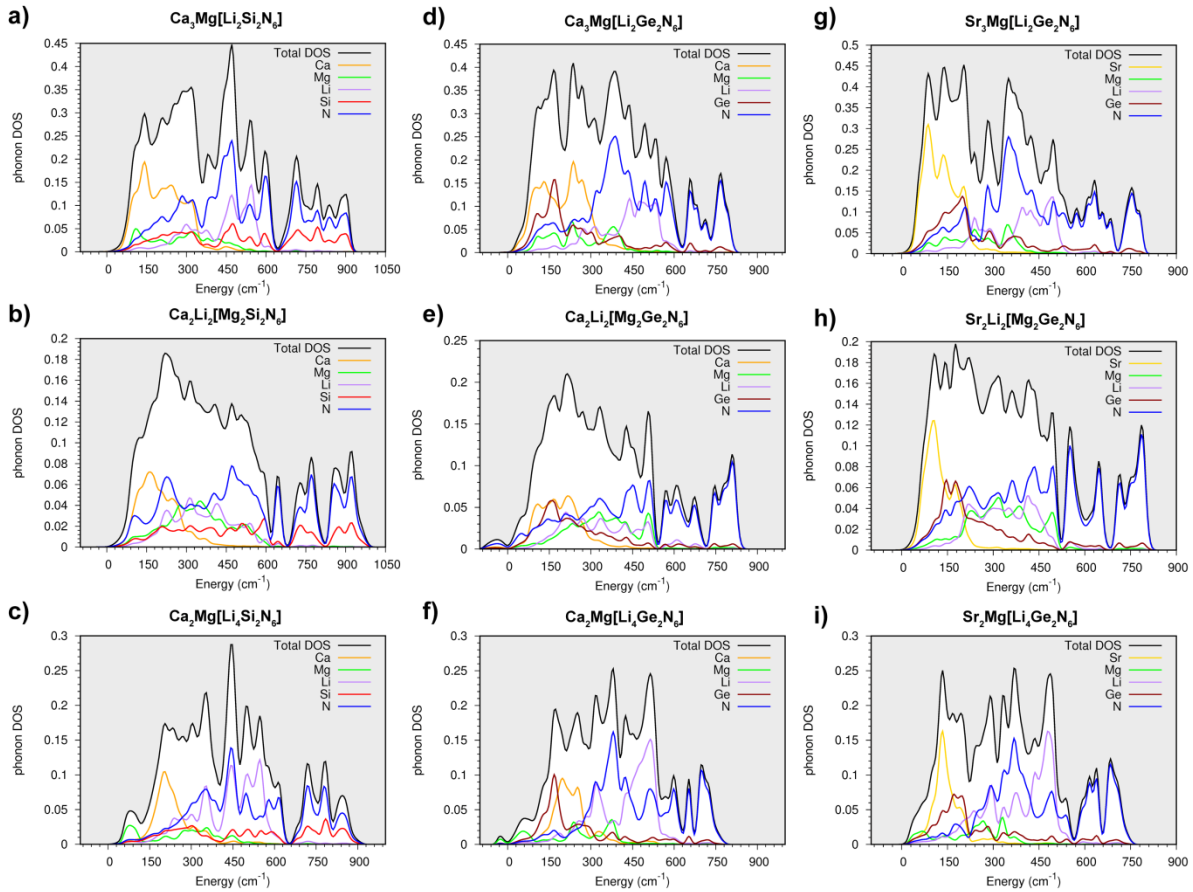

Figure 11.2 Total and partial phonon density of states for existing and predicted (litho/magneso)nitridotetrelates (a–i), as calculated from supercells within the VASP program and evaluated by PHONOPY. Imaginary frequencies present in $Ca_2Li_2[Mg_2Ge_2N_6]$ (e) and $Ca_2Mg[Li_4Ge_2N_6]$ (f) indicate dynamical instabilities.

11.3.5 Electronic and Optical Properties

In order to estimate the potential suitability of the nitridosilicate and -germanate compounds with regard to applications as luminescent host structures, their electronic and optical band gaps were evaluated and are listed in Table 11.3. The fundamental electronic E_g values were evaluated from direct transitions of the calculated band structures (see Figure S11.1) together with optical values of E_g from a joint density plot of the DOS as shown in Figure 11.3, as calculated by the mBJ exchange potential. The latter is widely established for yielding accurate estimations of E_g in general.[48] It has further led to satisfactory results in comparison with experimental band gap measurements by X-ray spectroscopy for $Ca_2Li_2[Mg_2Si_2N_6]$, whereas no detailed calculations of E_g were previously conducted for $Ca_2Mg[Li_4Ge_2N_6]$ and $Ca_3Mg[Li_2Si_2N_6]$.[51]

The partial electronic DOS (see Figure S11.2) shows that the majority of electronic transitions is expected to occur between dominant N states at the valence band edge and unoccupied Ca, Sr and N states in the conduction band. The absorption spectra calculated using the PBEsol functional in terms of consistency (see Figure S11.3) show the same trend for optical onsets of the investigated nitridotetrelates with an underestimation of the band gap, as expected from standard DFT.

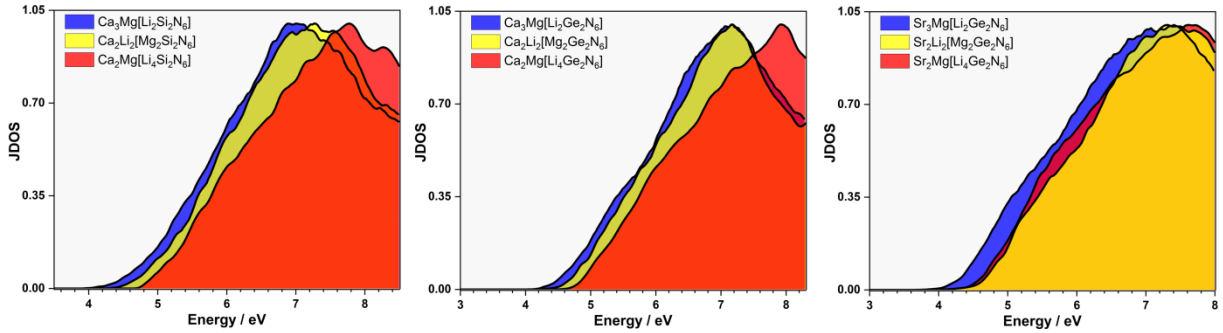

Figure 11.3 Calculated joint density of states (JDOS) with the mBJ exchange potential as an approximation of the optical band gap for the postulated compounds.

Table 11.3 Electronic and optical band gaps (E_g) in eV as calculated from the PBEsol+mBJ band structure (E_g^{mBJ}), joint DOS from PBEsol+mBJ DOS ($E_g^{JDOS\text{-}mBJ}$) and absorption from PBEsol potential ($E_g^{Opt\text{-}PBEsol}$) for the Si and Ge bow-tie nitrides

Compound	Band gap (eV)		
	E_g^{mBJ}	$E_g^{JDOS\text{-}mBJ}$	$E_g^{Opt\text{-}PBEsol}$
$Ca_2Mg[Li_4Si_2N_6]$	4.5	4.7	3.5
$Ca_3Mg[Li_2Si_2N_6]$	3.8	4.2	3.1
$Ca_2Li_2[Mg_2Si_2N_6]$	4.05	4.4	3.3
$Ca_2Mg[Li_4Ge_2N_6]$	4.1	4.6	3.2
$Ca_3Mg[Li_2Ge_2N_6]$	3.8	4.1	2.8
$Ca_2Li_2[Mg_2Ge_2N_6]$	3.6	4.3	3.0
$Sr_2Mg[Li_4Ge_2N_6]$	3.8	4.2	2.9
$Sr_3Mg[Li_2Ge_2N_6]$	3.5	4.0	2.4
$Sr_2Li_2[Mg_2Ge_2N_6]$	3.6	4.2	2.8

With fundamental E_g^{mBJ} values of 3.5–3.8 eV, the calculated electronic band gaps for all predicted nitridogermanates may be of sufficient bandwidth for activator-induced luminescence *e.g.* from Eu^{2+} or Ce^{3+} to be potentially similar to existing $Ca_3Mg[Li_2Si_2N_6]:Eu^{2+}$ and $Ca_2Li_2[Mg_2Si_2N_6]:Eu^{2+}$.

11.3.6 Mechanical Properties

The elastic moduli and Debye temperatures (Θ_D) of all investigated structures are listed in Table 4. All presented values were deduced from the individually calculated elastic constants C_{ij} according to common relations.[52–57] In recent years, Θ_D has been considered to be an important proxy for phosphor materials, due to it being in proportion to the rigidity of the crystal structure, which in turn is often correlated with thermal quenching mechanisms and quantum yield.[11,58–61] Recently, this has even led to its implementation into machine learning algorithms to identify new potential phosphor materials.[31] E_g and Θ_D values in Tables 3 and 4 of $M_2Mg[Li_4Tt_2N_6]$ (M = Ca, Sr, *Tt* = Si, Ge) are the highest within each series.

Table 11.4 Calculated elastic constants Cnm, bulk (B), shear (G) and Young's (Y) moduli in GPa, Debye temperature (Θ_D) in K and Poisson's ratio (v) for the Si and Ge bow-tie nitrides

Compound	Elastic Moduli				
	B_{VRH}	G_{VRH}	Y_{VRH}	v	Θ_D
$Ca_2Mg[Li_4Si_2N_6]$	106.9	86.4	204.2	0.18	823.1
$Ca_3Mg[Li_2Si_2N_6]$	104.8	68.8	169.3	0.23	694.2
$Ca_2Li_2[Mg_2Si_2N_6]$	106.3	64.9	161.9	0.24	690.9
$Ca_2Mg[Li_4Ge_2N_6]$	100.3	78.8	187.3	0.19	688.56
$Ca_3Mg[Li_2Ge_2N_6]$	96.6	59.7	148.6	0.24	573.7
$Ca_2Li_2[Mg_2Ge_2N_6]$	100.3	60.1	152.1	0.25	591.1
$Sr_2Mg[Li_4Ge_2N_6]$	91.6	67.4	162.5	0.20	576.3
$Sr_3Mg[Li_2Ge_2N_6]$	82.7	52.2	129.4	0.24	466.7
$Sr_2Li_2[Mg_2Ge_2N_6]$	97.1	59.3	147.8	0.25	525.0

However, surprisingly, no luminescence has been reported for doped $Ca_2Mg[Li_4Si_2N_6]$ so far, possibly indicating that luminescence might be prevented in this structural arrangement. For the remaining nitridogermanates, Θ_D ranges between 460 and 590 K, in line with the incorporation of heavier cations lowering the overall phononic contributions. The values can however still be considered to be suitable for phosphor materials considering a number of different phosphor oxosilicates with low degrees of condensation reaching the reported quantum yields of 30–85% despite having comparable Θ_D values.[11]

11.4 Conclusions

We present a systematic study of the first principles properties and stabilities of AE based nitrido(litho/magneso)tetrelates (AE = Ca, Sr; Tt = Si, Ge) with compositions $AE_3Mg[Li_2Tt_2N_6]$, $AE_2Mg[Li_4Tt_2N_6]$ and $AE_2Li_2[Mg_2Tt_2N_6]$.

The principal existence of the four novel nitridogermanates $Ca_3Mg[Li_2Ge_2N_6]$, $Sr_3Mg[Li_2Ge_2N_6]$, $Sr_2Mg[Li_4Ge_2N_6]$ and $Sr_2Li_2[Mg_2Ge_2N_6]$ was confirmed by systematic calculations of enthalpies of formation and reaction from a set of suggested starting materials in combination with extensive phonon calculations regarding their dynamical stability in the predicted space group $C2/m$ (no. 12). The existing nitridosilicates $Ca_3Mg[Li_2Si_2N_6]$, $Ca_2Mg[Li_4Si_2N_6]$ and $Ca_2Li_2[Mg_2Si_2N_6]$, isotypic to the predicted nitridogermanates, were calculated for comparability and verified to be stable and structurally in close agreement (<1%) with experimentally determined lattice parameters. Phonon calculations further allowed for the generation of CIF files with ADPs extrapolated to ambient temperatures for the predicted crystal structures using the Molecular Toolbox program. All existing and predicted structures were further analysed with regard to their electronic and mechanical properties so as to study their potential suitability as semiconductors and phosphor host structures. Although the existing nitridosilicates exhibit the largest band gaps and Debye temperatures, the predicted nitridogermanates may be still within the scope of possible applications with electronic E_g values ranging from 3.5 to 3.8 eV and Θ_D values between 466 and 576 K.

We show that a formal Li and Mg substitution of the already existing $Sr_5Ge_2N_6$ and $Sr_3[Li_4Ge_2N_6]$ might prove promising for the experimental discovery of homeotypic or isotypic new nitridogermanates with possible applications as wide gap semiconductors or phosphor materials.

11.5 Acknowledgements

The authors gratefully acknowledge the compute and data resources provided by the Leibniz Supercomputing Centre (www.lrz.de). This work was further supported by the European Regional Development Fund (ERDF), project CEDAMNF, reg. no. CZ.02.1.01/0.0/0.0/15_003/0000358 and the Czech Science Foundation (GACR), Proj. 17-1480S. Financial support by the Fonds der Chemischen Industrie (FCI) is gratefully acknowledged.

11.6 References

[1] K. H. Jack, Sialons and related nitrogen ceramics, *J. Mater. Sci.* **1976**, *11*, 1135–1158.

[2] A. Ziegler, J. C. Idrobo, M. K. Cinibulk, C. Kisielowski, N. D. Browning, R. O. Ritchie, Interface Structure and Atomic Bonding Characteristics in Silicon Nitride Ceramics, *Science* **2004**, *306*, 1768–1770.

[3] D. R. CLARKE, On the Equilibrium Thickness of Intergranular Glass Phases in Ceramic Materials, *J. Am. Ceram. Soc.* **1987**, *70*, 15–22.

[4] N. Shibata, S. J. Pennycook, T. R. Gosnell, G. S. Painter, W. A. Shelton, P. F. Becher, Observation of rare-earth segregation in silicon nitride ceramics at subnanometre dimensions, *Nature* **2004**, *428*, 730–733.

[5] M. Zeuner, S. Pagano, W. Schnick, Nitridosilicates and Oxonitridosilicates: From Ceramic Materials to Structural and Functional Diversity, *Angew. Chem. Int. Ed.* **2011**, *50*, 7754–7775; *Angew. Chem.* **2011**, *123*, 7898–7920.

[6] N. Lu, I. Ferguson, III-nitrides for energy production: photovoltaic and thermoelectric applications *Semicond. Sci. Technol.* **2013**, *28*, 074023.

[7] T. D. Moustakas, R. Paiella, Optoelectronic device physics and technology of nitride semiconductors from the UV to the terahertz, *Rep. Prog. Phys.* **2017**, *80*, 106501.

[8] S. Schmiechen, H. Schneider, P. Wagatha, C. Hecht, P. J. Schmidt, W. Schnick, oward New Phosphors for Application in Illumination-Grade White pc-LEDs: The Nitridomagnesosilicates $Ca[Mg_3SiN_4]:Ce^{3+}$, $Sr[Mg_3SiN_4]:Eu^{2+}$, and $Eu[Mg_3SiN_4]$, *Chem. Mater.* **2014**, *26*, 2712–2719.

[9] P. Pust, P. J. Schmidt, W. Schnick, A revolution in lighting, *Nat. Mater.* **2015**, *14*, 454–458.

[10] L. Wang, R.-J. Xie, T. Suehiro, T. Takeda, N. Hirosaki, Down-Conversion Nitride Materials for Solid State Lighting: Recent Advances and Perspectives, *Chem. Rev.* **2018**, *118*, 1951–2009.

[11] X. Qin, X. Liu, W. Huang, M. Bettinelli, X. Liu, Lanthanide-Activated Phosphors Based on 4f–5d Optical Transitions: Theoretical and Experimental Aspects, *Chem. Rev.* **2017**, *117*, 4488–4527.

[12] K. Uheda, N. Hirosaki, Y. Yamamoto, A. Naito, T. Nakajima, H. Yamamoto, Luminescence Properties of a Red Phosphor, $CaAlSiN_3:Eu^{2+}$, for White Light-Emitting Diodes, *Electrochem. Solid-State Lett.* **2006**, *9*, H22–H25.

[13] J. W. H. van Krevel, On new rare-earth doped *M*-Si-Al-O-N materials : luminescence properties and oxidation resistance, *Doctoral Thesis*, Eindhoven University of Technology, **2000**.

[14] H. A. Höppe, H. Lutz, P. Morys, W. Schnick, A. Seilmeier, uminescence in Eu^{2+}-doped $Ba_2Si_5N_8$: fluorescence, thermoluminescence, and upconversion, *J. Phys. Chem. Solids* **2000**, *61*, 2001–2006.

[15] P. Pust, F. Hintze, C. Hecht, V. Weiler, A. Locher, D. Zitnanska, S. Harm, D. Wiechert, P. J. Schmidt, W. Schnick, Group (III) Nitrides $M[Mg_2Al_2N_4]$ (M = Ca, Sr, Ba, Eu) and $Ba[Mg_2Ga_2N_4]$—Structural Relation and Nontypical Luminescence Properties of Eu^{2+} Doped Samples, *Chem. Mater.* **2014**, *26*, 6113–6119.

[16] C. Maak, D. Durach, C. Martiny, P. J. Schmidt, W. Schnick, Narrow-Band Yellow–Orange Emitting $La_{3-x}Ca_{1.5x}Si_6N_{11}:Eu^{2+}$ ($x \approx 0.77$): A Promising Phosphor for Next-Generation Amber pcLEDs, *Chem. Mater.* **2018**, *30*, 3552–3558.

[17] P. Pust, V. Weiler, C. Hecht, A. Tücks, A. S. Wochnik, A.-K. Henß, D. Wiechert, C. Scheu, P. J. Schmidt, W. Schnick, Narrow-band red-emitting $Sr[LiAl_3N_4]:Eu^{2+}$ as a next-generation LED-phosphor material, *Nat. Mater.* **2014**, *13*, 891–896.

[18] J. L. Leaño, A. Lazarowska, S. Mahlik, M. Grinberg, H.-S. Sheu, R.-S. Liu, Disentangling Red Emission and Compensatory Defects in $Sr[LiAl_3N_4]:Ce^{3+}$ Phosphor, *Chem. Mater.* **2018**, *30*, 4493–4497.

[19] T. Takeda, N. Hirosaki, S. Funahshi, R.-J. Xie, Narrow-Band Green-Emitting Phosphor $Ba_2LiSi_7AlN_{12}:Eu^{2+}$ with High Thermal Stability Discovered by a Single Particle Diagnosis Approach *Chem. Mater.* **2015**, *27*, 5892–5898.

[20] D. Wilhelm, D. Baumann, M. Seibald, K. Wurst, G. Heymann, H. Huppertz, Narrow-Band Red Emission in the Nitridolithoaluminate $Sr_4[LiAl_{11}N_{14}]:Eu^{2+}$, *Chem. Mater.* **2017**, *29*, 1204–1209.

[21] O. M. ten Kate, Z. Zhang, J. R. van Ommen, H. T. Hintzen, Dependence of the photoluminescence properties of Eu^{2+} doped M–Si–N (M = alkali, alkaline earth or rare earth metal) nitridosilicates on their structure and composition, *J. Mater. Chem. C* **2018**, *6*, 5671–5683.

[22] R.-J. Xie, N. Hirosaki, Silicon-based oxynitride and nitride phosphors for white LEDs—A review, *Sci. Tech. Adv. Mater.* **2007**, *8*, 588–600.

[23] C. Poesl, W. Schnick, Crystal Structure and Nontypical Deep-Red Luminescence of $Ca_3Mg[Li_2Si_2N_6]:Eu^{2+}$, *Chem. Mater.* **2017**, *29*, 3778–3784.

[24] P. Strobel, V. Weiler, C. Hecht, P. J. Schmidt, W. Schnick, Luminescence of the Narrow-Band Red Emitting Nitridomagnesosilicate $Li_2(Ca_{1-x}Sr_x)_2[Mg_2Si_2N_6]:Eu^{2+}$ (x = 0–0.06), *Chem. Mater.* **2017**, *29*, 1377–1383.

[25] D. G. Park, Z. A. Gál, F. J. DiSalvo, Synthesis and structure of $Li_4Sr_3Ge_2N_6$: a new quaternary nitride containing $Ge_2N_6^{10-}$ anions, *J. Solid State Chem.* **2003**, *172*, 166–170.

[26] S. C. Junggeburth, O. Oeckler, W. Schnick, $Sr_5Ge_2N_6$ – A Nitridogermanate with Edge-sharing Double Tetrahedra, *Z. Anorg. Allg. Chem.* **2008**, *634*, 1309–1311.

[27] W. G. Han, W. B. Park, S. P. Singh, M. Pyo, K.-S. Sohn, Determination of possible configurations for $Li_{0.5}CoO_2$ delithiated Li-ion battery cathodes via DFT calculations coupled with a multi-objective non-dominated sorting genetic algorithm (NSGA-III), *Phys. Chem. Chem. Phys.* **2018**, *20*, 26405–26413.

[28] S. U. Hong, S. P. Singh, M. Pyo, W. B. Park, K.-S. Sohn, Density functional theory calculations for the band gap and formation energy of $Pr_{4-x}Ca_xSi_{12}O_{3+x}N_{18-x}$; a highly disordered compound with low symmetry and a large cell size, *Phys. Chem. Chem. Phys.* **2017**, *19*, 16702–16712.

[29] H. Dong, A. R. Oganov, V. V. Brazhkin, Q. Wang, J. Zhang, M. M. Davari Esfahani, X.-F. Zhou, F. Wu, Q. Zhu, Boron oxides under pressure: Prediction of the hardest oxides, *Phys. Rev. B: Condens. Matter Mater. Phys.* **2018**, *98*, 174109.

[30] B. Dong, Z. Wang, N. T. Hung, A. R. Oganov, T. Yang, R. Saito, Z. Zhang, New two-dimensional phase of tin chalcogenides: Candidates for high-performance thermoelectric materials, *Phys. Rev. Mater.* **2019**, *3*, 013405.

[31] Y. Zhuo, A. Mansouri Tehrani, A. O. Oliynyk, A. C. Duke, J. Brgoch, Identifying an efficient, thermally robust inorganic phosphor host via machine learning, *Nat. Commun.* **2018**, *9*, 4377.

[32] A. Togo, I. Tanaka, First principles phonon calculations in materials science, *Scripta Mater.* **2015**, *108*, 1–5.

[33] V. L. Deringer, R. P. Stoffel, A. Togo, B. Eck, M. Meven, R. Dronskowski, Ab initio ORTEP drawings: a case study of N-based molecular crystals with different chemical nature, *CrystEngComm* **2014**, *16*, 10907–10915.

[34] R. W. Grosse-Kunstleve, P. D. Adams, On the handling of atomic anisotropic displacement parameters, *J. Appl. Crystallogr.* **2002**, *35*, 477–480.

[35] J. George, A. Wang, V. L. Deringer, R. Wang, R. Dronskowski, U. Englert, Anisotropic displacement parameters from dispersion-corrected DFT methods and their experimental validation by temperature-dependent X-ray diffraction, *CrystEngComm* **2015**, *17*, 7414–7422.

[36] J. George, R. Dronskowski, *Molecular Toolbox* **2017**.

[37] S. Schmiechen, F. Nietschke, W. Schnick, Structural Relationship between the Mg-Containing Nitridosilicates, *Eur. J. Inorg. Chem.* **2015**, *2015*, 1592–1597.

[38] G. Kresse, J. Furthmüller, Efficiency of ab-initio total energy calculations for metals and semiconductors using a plane-wave basis set, Efficiency of ab-initio total energy calculations for metals and semiconductors using a plane-wave basis set, *Comput. Mater. Sci.* **1996**, *6*, 15–50.

[39] G. Kresse, J. Hafner, *Ab initio* molecular dynamics for liquid metals, *Ab initio* molecular dynamics for liquid metals, *Phys. Rev. B: Condens. Matter Mater. Phys.* **1993**, *47*, 558–561.

[40] G. Kresse, J. Hafner, *Ab initio* molecular-dynamics simulation of the liquid-metal-amorphous-semiconductor transition in germanium, *Phys. Rev. B: Condens. Matter Mater. Phys.* **1994**, *49*, 14251–14269.

[41] J. P. Perdew, K. Burke, M. Ernzerhof, Generalized Gradient Approximation Made Simple, *Phys. Rev. Lett.* **1996**, *77*, 3865–3868.

[42] J. P. Perdew, K. Burke, M. Ernzerhof, Generalized Gradient Approximation Made Simple [*Phys. Rev. Lett.* **1996**, *77*, 3865], *Phys. Rev. Lett.* **1997**, *78*, 1396.

[43] J. P. Perdew, A. Ruzsinszky, G. I. Csonka, O. A. Vydrov, G. E. Scuseria, L. A. Constantin, X. Zhou, K. Burke, Restoring the Density-Gradient Expansion for Exchange in Solids and Surfaces, *Phys. Rev. Lett.* **2008**, *100*, 136406.

[44] P. E. Blöchl, Projector augmented-wave method, *Phys. Rev. B: Condens. Matter Mater. Phys.* **1994**, *50*, 17953–17979.

[45] G. Kresse, D. Joubert, From ultrasoft pseudopotentials to the projector augmented-wave method, *Phys. Rev. B: Condens. Matter Mater. Phys.* **1999**, *59*, 1758–1775.

[46] H. J. Monkhorst, J. D. Pack, Special points for Brillouin-zone integrations, *Phys. Rev. B: Solid State* **1976**, *13*, 5188–5192.

[47] F. Tran, P. Blaha, Accurate Band Gaps of Semiconductors and Insulators with a Semilocal Exchange-Correlation Potential, *Phys. Rev. Lett.* **2009**, *102*, 226401.

[48] J. A. Camargo-Martínez, R. Baquero, Performance of the modified Becke-Johnson potential for semiconductors, *Phys. Rev. B: Condens. Matter Mater. Phys.* **2012**, *86*, 195106.

[49] Y. Le Page, P. Saxe, Symmetry-general least-squares extraction of elastic data for strained materials from *ab initio* calculations of stress, *Phys. Rev. B: Condens. Matter Mater. Phys.* **2002**, *65*, 104104.

[50] O. Boudrifa, A. Bouhemadou, N. Guechi, S. Bin-Omran, Y. Al-Douri, R. Khenata, First-principles prediction of the structural, elastic, thermodynamic, electronic and optical properties of $Li_4Sr_3Ge_2N_6$ quaternary nitride, *J. Alloys Compd.* **2015**, *618*, 84–94.

[51] T. M. Tolhurst, P. Strobel, P. J. Schmidt, W. Schnick, A. Moewes, Designing Luminescent Materials and Band Gaps: A Soft X-ray Spectroscopy and Density Functional Theory Study of $Li_2Ca_2[Mg_2Si_2N_6]:Eu^{2+}$ and $Ba[Li_2(Al_2Si_2)N_6]:Eu^{2+}$, *J. Phys. Chem. C* **2017**, *121*, 14296–14301.

[52] N. W. Ashcroft, N. D. Mermin, *Solid state physics*, Saunders college, **1976**.

[53] R. Hill, The Elastic Behaviour of a Crystalline Aggregate, *Proc. Phys. Soc. A* **1952**, *65*, 349–354.

[54] C. Jiang, S. G. Srinivasan, A. Caro, S. A. Maloy, Structural, elastic, and electronic properties of Fe_3C from first principles, *J. Appl. Phys.* **2008**, *103*, 043502.

[55] E. Francisco, J. M. Recio, M. A. Blanco, A. M. Pendás, A. Costales, Quantum-Mechanical Study of Thermodynamic and Bonding Properties of MgF_2, *J. Phys. Chem. A* **1998**, *102*, 1595–1601.

[56] E. Francisco, M. A. Blanco, G. Sanjurjo, Atomistic simulation of SrF_2 polymorphs, *Phys. Rev. B: Condens. Matter Mater. Phys.* **2001**, *63*, 094107.

[57] J.-P. Poirier, *Introduction to the physics of the earth's interior*, Cambridge University Press, **1921**.

[58] J. D. Furman, B. C. Melot, S. J. Teat, A. A. Mikhailovsky, A. K. Cheetham, Towards enhanced ligand-centred photoluminescence in inorganic–organic frameworks for solid state lighting, *Phys. Chem. Chem. Phys.* **2011**, *13*, 7622–7629.

[59] J. Brgoch, S. P. DenBaars, R. Seshadri, Proxies from *Ab Initio* Calculations for Screening Efficient Ce^{3+} Phosphor Hosts, *J. Phys. Chem. C* **2013**, *117*, 17955–17959.

[60] K. A. Denault, J. Brgoch, S. D. Kloß, M. W. Gaultois, J. Siewenie, K. Page, R. Seshadri, Average and Local Structure, Debye Temperature, and Structural Rigidity in Some Oxide Compounds Related to Phosphor Hosts, *ACS Appl. Mater. Interfaces* **2015**, *7*, 7264–7272.

[61] Z. Wang, I.-H. Chu, F. Zhou, S. P. Ong, Electronic Structure Descriptor for the Discovery of Narrow-Band Red-Emitting Phosphors, *Chem. Mater.* **2016**, *28*, 4024–4031.

11.7 Supporting Information

11.7.1 Electronic Structure Calculations

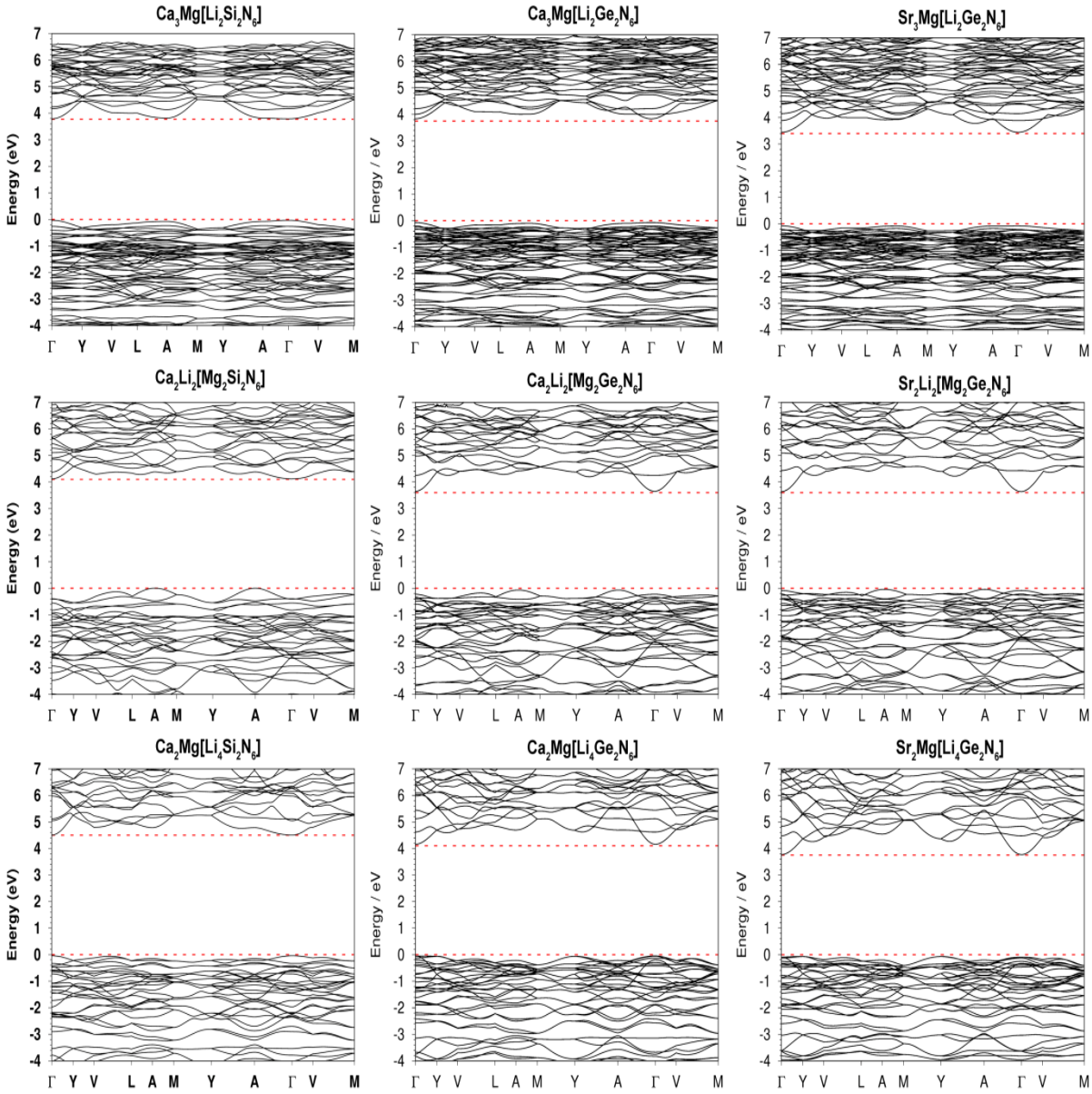

Figure S11.1 Band structure calculations along high symmetry directions for the studied nitridosilicates and nitridogermanates as calculated within the VASP program with PBEsol in conjunction with the mBJ exchange potential (PBEsol+mBJ).

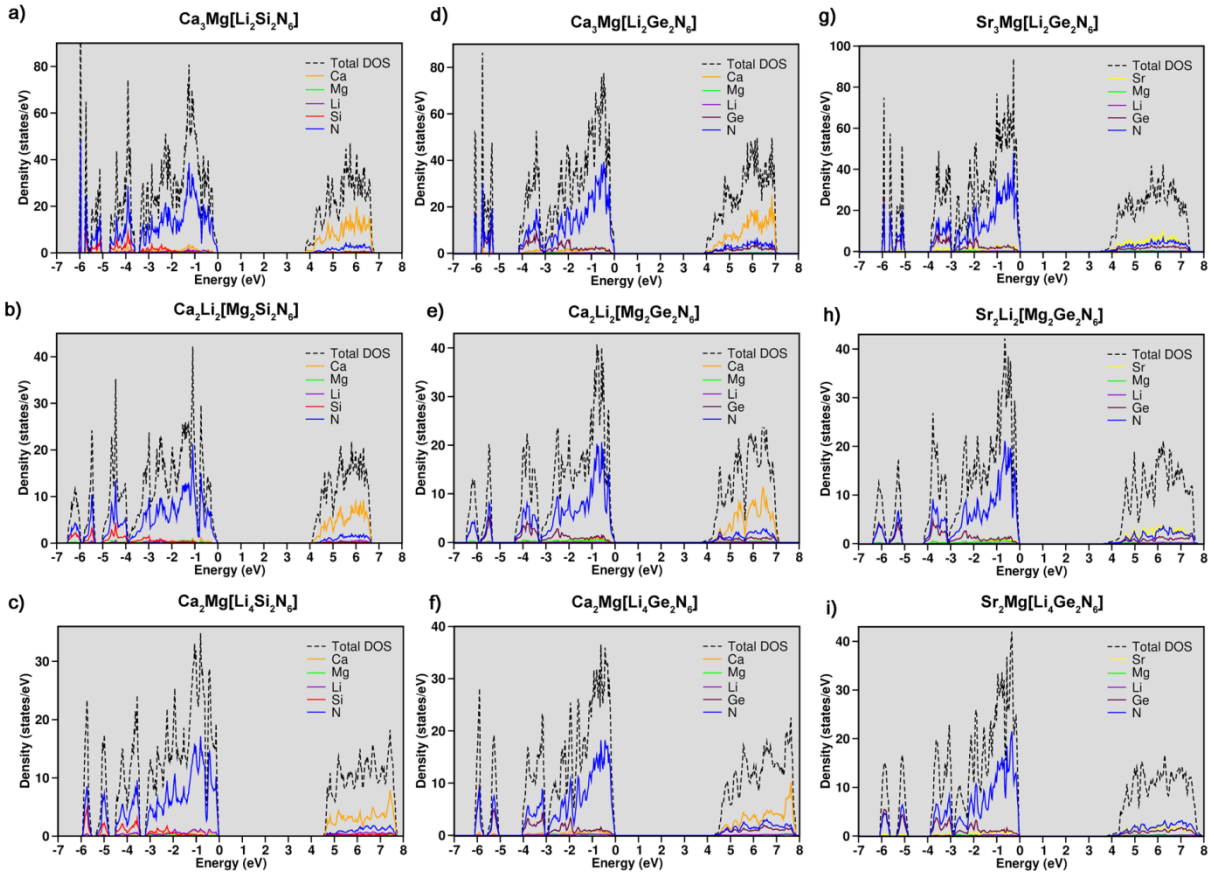

Figure S11.2 Total and atomic resolved electronic density of states for existing and predicted (litho/magneso)nitridotetrelates (a–i), as calculated within the VASP program with PBEsol in conjunction with the mBJ exchange potential (PBEsol+mBJ).

11.7.2 Absorption Spectra

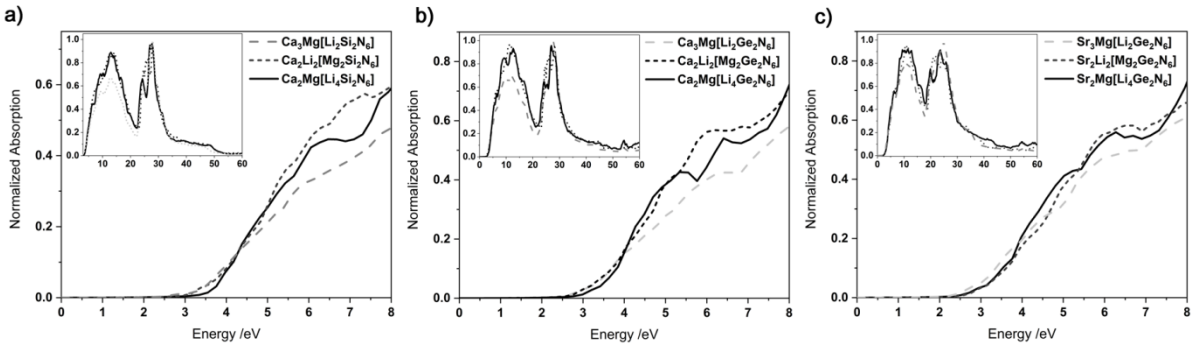

Figure S11.3 Calculated onset of optical absorption for the studied (litho/magneso)nitridotetrelates as calculated by Vasp with PBEsol.

11.7.3 Crystallographic Data Obtained by Structure Relaxations and Phonon Calculations

Table S11.1 Atomic coordinates, isotropic displacement parameters [Å^2] and site occupancies of $Ca_3Mg[Li_2Ge_2N_6]$, as calculated by DFT calculations

Atom		*x*	*y*	*z*	U_{eq}	s.o.f
Ca1	8*j*	0.0549	0.3221	0.2469	0.00803	1
Ca2	4*h*	0.0000	0.1784	0.5000	0.01853	1
Ge1	4*i*	0.3518	0	0.4160	0.0052	1
Ge2	4*i*	0.6987	0	0.0644	0.00453	1
Mg	4i	0.0768	0	0.2183	0.00903	1
Li	8j	0.1747	0.1785	0.0616	0.01213	1
N1	8j	0.2305	0.1508	0.3474	0.00876	1
N2	8*j*	0.8579	0.8498	0.1201	0.00643	1
N3	4*i*	0.3199	0	0.5755	0.01013	1
N4	4*i*	0.3840	0	0.0992	0.00653	1

Table S11.2 Anisotropic displacement parameters of $Ca_3Mg[Li_2Ge_2N_6]$, as calculated by DFT calculations, extrapolated to 300 K by PHONOPY

Atom	U_{11} / Å^2	U_{22} / Å^2	U_{33} / Å^2	U_{12} / Å^2	U_{13} / Å^2	U_{23} / Å^2
Ca1	0.00760	0.00670	0.00980	0.00170	0.00380	0.00230
Ca2	0.02290	0.01470	0.01800	0.00000	0.01500	0.00000
Ge1	0.0057	0.0048	0.0051	0	0.0006	0
Ge2	0.0046	0.0041	0.0049	0	0.0006	0
Mg	0.0099	0.0065	0.0107	0	-0.0033	0
Li	0.0131	0.0114	0.0119	-0.0012	0.0036	-0.0016
N1	0.0089	0.0084	0.009	0.0027	0.0029	0.0031
N2	0.0063	0.0052	0.0078	0.0005	0.0009	0.0006
N3	0.0071	0.0161	0.0072	0	0.0025	0
N4	0.0063	0.0073	0.006	0	0.0011	0

Table S11.3 Atomic coordinates, isotropic displacement parameters [Å^2] and site occupancies of $Sr_3Mg[Li_2Ge_2N_6]$, as calculated by DFT calculations

Atom		*x*	*y*	*z*	U_{eq}	s.o.f
Sr1	8*j*	0.0587	0.3264	0.2436	0.0077	1
Sr2	4*h*	0	0.1807	0.5	0.012	1
Ge1	4*i*	0.3520	0	0.4146	0.00476	1
Ge2	4*i*	0.701	0	0.0611	0.0048	1
Mg	4i	0.743	0	0.2168	0.00973	1
Li	8j	0.1753	0.1761	0.0576	0.01466	1
N1	8j	0.2286	0.1443	0.344	0.00873	1
N2	8*j*	0.8622	0.1466	0.1149	0.00693	1
N3	4*i*	0.3295	0	0.5673	0.01063	1
N4	4*i*	0.3934	0	0.093	0.00726	1

Table S11.4 Anisotropic displacement parameters of $Sr_3Mg[Li_2Ge_2N_6]$, as calculated by DFT calculations, extrapolated to 300 K by PHONOPY

Atom	U_{11} / Å^2	U_{22} / Å^2	U_{33} / Å^2	U_{12} / Å^2	U_{13} / Å^2	U_{23} / Å^2
Sr1	0.0077	0.0066	0.0088	0.0019	0.0032	0.0025
Sr2	0.0106	0.0146	0.0108	0	0.0054	0
Ge1	0.0051	0.0046	0.0046	0	0.0004	0
Ge2	0.0054	0.0045	0.0045	0	-0.0001	0
Mg	0.0106	0.007	0.0116	0	-0.0041	0
Li	0.0171	0.0152	0.0117	-0.0004	0.0035	-0.0018
N1	0.0095	0.0078	0.0089	-0.0027	0.0023	-0.0029
N2	0.0072	0.006	0.0076	-0.0009	0.0005	-0.0009
N3	0.0064	0.019	0.0065	0	0.0017	0
N4	0.0081	0.0079	0.0058	0	-0.0004	0

Table S11.5 Atomic coordinates, isotropic displacement parameters [Å^2] and site occupancies of $Sr_2Li_2[Mg_2Ge_2N_6]$, as calculated by DFT calculations

Atom		*x*	*y*	*z*	U_{eq}	s.o.f
Sr	4g	-0.5	-0.3157	0	0.00863	1
Ge	4i	0.1277	-0.5	0.1887	0.004333	1
Mg	4h	-0.5	-0.241	0.5	0.0064	1
Li	4i	-0.3035	-0.5	0.4130	0.01623	1
N1	8j	-0.2579	-0.1494	0.3244	0.00883	1
N2	4i	-0.1994	-0.5	0.1098	0.00840	1

Table S11.6 Anisotropic displacement parameters of $Sr_2Li_2[Mg_2Ge_2N_6]$, as calculated by DFT calculations, extrapolated to 300 K by PHONOPY

Atom	U_{11} / Å²	U_{22} / Å²	U_{33} / Å²	U_{12} / Å²	U_{13} / Å²	U_{23} / Å²
Sr	0.0072	0.0105	0.0082	0	0.0023	0
Ge	0.0048	0.0044	0.0038	0	0.0003	0
Mg	0.0064	0.0063	0.0065	0	0.0015	0
Li	0.0206	0.0177	0.0104	0	0.0025	0
N1	0.0089	0.0083	0.0093	0.0025	0.0028	0.0042
N2	0.0055	0.0146	0.0051	0	0.0009	0

Table S11.7 Atomic coordinates, isotropic displacement parameters [Å²] and site occupancies of $Sr_2Mg[Li_4Ge_2N_6]$, as calculated by DFT calculations

Atom		*x*	*y*	*z*	U_{eq}	s.o.f
Sr	4*g*	0.5	0.1759	0	0.00956	1
Ge	4*i*	0.3113	0	0.3696	0.00930	1
Mg	2*a*	0	0	0	0.03143	1
Li	8*j*	0.1608	0.1703	0.6226	0.02046	1
N1	4*i*	0.6271	0	0.3075	0.01183	1
N2	8*j*	0.1613	0.1462	0.2537	0.01140	1

Table S11.8. Anisotropic displacement parameters of $Sr_2Mg[Li_4Ge_2N_6]$, as calculated by DFT calculations, extrapolated to 300 K by PHONOPY

Atom	U_{11} / Å²	U_{22} / Å²	U_{33} / Å²	U_{12} / Å²	U_{13} / Å²	U_{23} / Å²
Sr	0.0079	0.0065	0.0143	0	0.0049	0
Ge	0.0091	0.0054	0.0134	0	0.004	0
Mg	0.0303	0.0078	0.0562	0	-0.0255	0
Li	0.0155	0.023	0.0229	0.0020	0.0051	-0.0066
N1	0.0125	0.0082	0.0148	0	0.0027	0
N2	0.0093	0.0072	0.0177	0.0012	0.0046	0.0012

12 Conclusion and Outlook

A novel lithium oxonitridosilicate oxide phosphor material $Li_4Sr_4[Si_4O_4N_6]O:Eu^{2+}$ was successfully obtained from solid-state metathesis by screening different multicomponent mixtures. DFT calculations using the Korringa–Kohn–Rostoker (KKR) method together with the coherent potential approximation (CPA), enabled for a case study showing the efficient treatment of atomic disorder for the wide band gap semiconductors $CaAlSiN_3$ and $CaGaSiN_3$. Subsequently, the KKR+CPA approach was utilized to treat the materials class of II-IV-N_2 nitrides and its solid solutions, which are promising for optoelectronic applications. Further calculations on enthalpy progression within the high-pressure phase transitions for different O/N ordering models of PON enabled the corroboration of transition pressures for cristobalite to coesite-type PON and post-coesite to orthorhombic-type PON, along with the O/N disorder observed from X-ray diffraction. The phase transitions and electronic properties of novel ternary lithium nitridophosphates were investigated in the same manner. The thesis concludes with the *ab initio* structure prediction of a series of the wide band gap alkaline earth based nitrido(lithomagneso/magnesolitho)germanates, and their optical and mechanical properties.

12.1 Accessing a Novel Luminescent Lithium Oxonitridosilicate Oxide

Until this work only a few oxonitridosilicates have been known to shown luminescence, with the only two existing Li-containing oxonitridosilicate phosphor materials $Li_{24}Sr_{12}[Si_{24}N_{47}O]F:Eu^{2+}$ and $Li_{38.7}RE_{3.3}Ca_{5.7}[Li_2Si_{30}N_{59}]O_2F$ (*RE* = La, Ce, Y).[1,2]

Within this thesis the novel phosphor material $Li_4Sr_4[Si_4O_4N_6]O:Eu^{2+}$ exhibiting orange broadband-emission (λ_{em} ≈ 625 nm; fwhm ≈ 4164 cm^{-1} | 160 nm) was found by explorative synthesis. Its structure can formally be derived from the non-luminescent layered lithium nitridosilicate nitride $Li_2Sr_4[Si_2N_5]N$[3] by oxygen substitution and incorporation. Suchlike incorporation of oxygen might further be of benefit to the expand the overall band gap, which is decreased in $Li_2Sr_4[Si_2N_5]N$ compared to $Li_4Sr_4[Si_4O_4N_6]O$, and might prevent luminescence in the former. Interestingly, the recently discovered high-performance oxonitridoaluminate phosphor material $Sr[Li_2Al_2O_2N_2]:Eu^{2+}$,[4] can be seen in a similar light when compared to the equally efficient lithium nitridoaluminate $Sr[LiAl_3N_4]:Eu^{2+}$,[5] as both exhibit very similar crystal structures with a lower band gap for $Sr[LiAl_3N_4]:Eu^{2+}$. From an analytical point of view intertwining a variety of methods, namely transmission electron microscopy, Fourier-transform infrared spectroscopy, single-crystal and powder X-ray diffraction, modelation of stacking faults, MAPLE and DFT calculations exemplifies how materials properties and structural complexity can be efficiently tackled and illuminated. Overall the experimental part of this thesis demonstrates the potential in explorative synthesis for the discovery of novel lithium oxonitridosilicates. The presented work thus, opens the scope to the targeted search of formally oxygen substituted (lithium) nitridosilicates in order to obtain potential novel wide band gap materials suitable for investigations as phosphor materials.

12.2 Treatment of Mixed Occupancy in Nitrides by KKR+CPA

Predating this thesis, only a few studies employing DFT with the Korringa–Kohn–Rostoker Green's function (KKR-GF) method and the coherent potential approximation (CPA) were known to deal with disorder or doping of nitride materials, especially such with wide electronic band gaps, including a single study employing the method to study the solid solutions of (In,Ga)N.[6]

Within this thesis, in a first step, the widely studied and characterized phosphor host material $CaAlSiN_3$,[7–11] together with recently discovered isotypic $CaGaSiN_3$[12] from ammonothermal synthesis were selected as reference systems. The equivalency between KKR and the well-established pseudopotential method was subsequently, shown for hypothetical ordered structure models of this materials class. In a second step, for both materials KKR-GF calculations with the CPA (KKR+CPA) showed a diminished electronic band gap by about 0.1 eV for the fully disordered materials with respect to structural ordering. The effect is not very pronounced for both materials compared to other experimental findings for disordered $ZnSnN_2$,[13] however, a similar trend can be observed for the investigated wide band gap semiconductors. The findings are important for considerations of phosphor materials design, as thermal quenching of the luminescence often occurs due to the 5*d* energy levels of incorporated rare earth dopants being too close to the energy level of the conduction band. Depending on the origin of the thermal quenching a widening of only 0.1 eV, resulting from structural ordering could already prove highly beneficial to the overall thermal quenching behavior of phosphor materials. This study further inspires future KKR+CPA investigations dealing with the calculation of 4*f*–5*d* energy levels of rare earth cations doped into (nitride) phosphor host materials.

Following the obtained results for wurtzite-type related $CaAlSiN_3$ and $CaGaSiN_3$, we extended our studies to the description of the electronic, magnetic and optical properties of the materials II-IV-N_2 (II = Mg, Mn, IV = Si, Ge) and Li-IV_2-N_3 (IV = Si, Ge) which had also been synthesized from the ammonothermal approach. KKR calculations for these compounds yielded optical band gap estimates in good agreement with the measured gaps from UV/Vis spectroscopy. Subsequently, also ammonothermally obtained solid solutions ($II^{A}_{0.5}II^{B}_{0.5}$) for II-IV-N_2 ($II^{A/B}$ = Mg, Mn, Zn, IV = Si, Ge), were calculated with KKR+CPA.

From the results the fundamental feasibility to selectively tune the band gap of II-IV-N_2 solid solutions was demonstrated, with the electronic band gap of the ($II^{A}_{0.5}II^{B}_{0.5}$) compositions lying in-between those of the respective boundary phases. The obtained results thus, prove the II-IV-N_2 materials class promising for future investigations of with respect to their eligibility as potential alternatives to (Al,Ga,In)N solid solutions and establish KKR+CPA as a suitable method to investigate the trends in band gap behavior for semiconducting nitride solid solutions. This is especially important since the KKR+CPA methodology enables the accurate treatment of the electronic structure, for various degrees of disorder or mixed occupancy without the need to resort to extensive supercell calculations.

12.3 *Ab Initio* High-Pressure Phase Transitions of P/O/N and Li/P/N materials

Throughout the last 30 years solid-state P/N chemistry has steadily evolved with high pressure synthesis routes contributing immensely to the structural and compositional diversity of phosphorus (oxo)nitrides and nitridophosphates.[14]

The results presented in this thesis represent important contributions to the experimentally observed high-pressure phase transitions of phosphorus oxonitride PON and the two lithium nitridophosphates $Li_{12}P_3N_9$ and β-$Li_{10}P_4N_{10}$ using density functional theory (DFT) calculations. For the observed phase transition of (O/N) disordered cristobalite-type PON to (O/N) disordered coesite-type PON the construction and relaxation of various ordered PON modifications enabled both, the corroboration of plausible (O/N) disorder in coesite-type PON for synthesis conditions beyond 15 GPa and an estimation of the transition pressure of cristobalite to coesite-type PON. In a subsequent study, analogues DFT calculations were conducted on a stishovite-related post-coesite form of PON (pc-PON) with a 5+1 coordination of P, where next to (O/N) ordering a further split position of P was accounted for within the ordering models. The pc-PON polymorph was thus, successfully confirmed as a further high-pressure phase to coesite-type PON. The Niggly formula $^{3}_{\infty}[P^{[5]}O^{[2]}N^{[3]}]$ was further deduced to be the most favorable and thus, likely local coordination of phosphorus within pc-PON from DFT relaxations from a variety of stable and ordered O/N and P models. In alignment with an additional experimentally observed transition of tetragonal pc-PON to an orthorhombic phase of PON above 20 GPa ($P4_2/mnm$ (no. 136) → $Pnnm$ (no. 58)), the transition pressure could be approximated to ca. 17 GPa from the respective DFT models.

For the interesting class of lithium nitridophosphate materials DFT calculations were utilized in a similar manner to the PON investigations. Enthalpy-pressure calculations were able to corroborate Li_4PN_3 and $Li_5P_2N_5$ as high-pressure polymorphs of $Li_{12}P_3N_9$ and β-$Li_{10}P_4N_{10}$, respectively. In contrast to the PON structures, the lithium nitridophosphates were not prone to mixed-site occupancy but instead to underoccupied Li sites, due to the mobility of Li within both Li_4PN_3 and β-$Li_{10}P_4N_{10}$. In order to arrive at reasonable estimates for the transition pressures the lithium positions were ordered within charge neutral structures models, for which the structures were optimized by relaxation. The obtained transition pressures provide further insights to the synthesis pressures necessary for structural phase transitions in lithium nitridophosphates. Further analysis of the electronic structures before and after high-pressure phase transitions also corroborated the expected ionicity between the $[P\text{-}N]^{X-}$ framework and the incorporated Li^+ where an increase in the fundamental band gap was further found for both high-pressure polymorphs.

The utilization of DFT based structural optimizations thus reveal that the utilization of (multiple) ordered structure models in combination with enthalpy-pressure derivations from calculated high-pressure transitions, proved suitable to contribute to the illumination and expansion of the high-pressure phase diagram of PON and the phase transitions in lithium nitridophosphates. Overall, the analyses of the electronic structures and phase transitions of

P/N compounds, present important contributions to their experimental characterization and provide insights relevant for materials design considerations that might inspire further investigations of potential PON polymorphs and lithium nitridophosphates from either experiment or first principle methods.

12.4 *Ab Initio* Prediction of a Series of Nitridogermanates

The exploration of novel potential (wide band gap) semiconductors from first principles represents an important subject within materials sciences with respect to (opto)electronic applications, such as phosphor materials or photocatalysts.[15–18]

Within this thesis a series of six potential, unknown quinary nitridogermanates was investigated toward their electronic and mechanical properties along with their thermodynamic stability. The chosen structure models were inspired from the previous syntheses of different, quinary nitridosilicates with promising luminescence properties. From six constructed nitridogermanate models, each isotypic to a respective nitridosilicate structure, four were verified to be dynamically stable within the space group (*C*2/*m*, no. 12). All compounds are further stable against decomposition into their elements and potentially accessible by synthesis from binary compounds. All predicted nitrido(lithomagneso/magnesolitho)germanates, $Ca_3Mg[Li_2Ge_2N_6]$, $Sr_3Mg[Li_2Ge_2N_6]$, $Sr_2Mg[Li_4Ge_2N_6]$ and $Sr_2Li_2[Mg_2Ge_2N_6]$ are wide band gap semiconductors (E_g = 3.5–3.8 eV). Together with their relatively rigid (Θ_D = 466–576 K) and isotypic structures to the nitridosilicate series they may be viable for optoelectronic application. The herein presented study not only presents four hitherto unknown predicted nitridogermanates with interesting mechanical and electronic properties, but further exemplifies that *ab initio* structure investigations can synergize with previous synthetic works from which inspirations may be drawn to efficiently target and predict novel compounds.

12.5 Concluding Remarks

Throughout the long history in research on solid-state nitrides, a multitude of structurally diverse materials with promising (opto)electronic properties and applications have been found. This work starts from an experimental approach from which a novel phosphor material emerged within the relatively unexplored material class of lithium oxonitridosilicate oxides. Combining experimental and theoretical approaches, their mutual benefits were subsequently, outlined throughout systematic density functional theory calculations regarding investigations of disordered structures and high-pressure phase transitions. This joint approach culminates within the stand-alone *ab initio* prediction of a novel compound series that takes inspiration from previous experimental efforts. As such, it may well be stated, that while first principle calculations may be a powerful tool on its own, the mutual exchange between experiment and theory may elevate both areas to unforeseen heights.

12.6 References

[1] K. Horky, W. Schnick, $Li_{24}Sr_{12}[Si_{24}N_{47}O]F:Eu^{2+}$ - Structure and Luminescence of an Orange Phosphor, *Chem. Mater.* **2017**, 29, 4590–4596.

[2] C. Maak, P. Strobel, V. Weiler, P. J. Schmidt, W. Schnick, Unprecedented Deep-Red Ce^{3+} Luminescence of the Nitridolithosilicates $Li_{38.7}RE_{3.3}Ca_{5.7}[Li_2Si_{30}N_{59}]O_2F$ (*RE* = La,Ce,Y), *Chem. Mater.* **2018**, *30*, 5500−5506.

[3] S. Lupart, S. Pagano, O. Oeckler, W. Schnick, $Li_2Sr_4[Si_2N_5]N$ - A Layered Lithium Nitridosilicate Nitride, *Eur. J. Inorg. Chem.* **2011**, *2011*, 2118–2123.

[4] G. J. Hoerder, M. Seibald, D. Baumann, T. Schröder, S. Peschke, P. C. Schmid, T. Tyborski, P. Pust, I. Stoll, M. Bergler, C. Patzig, S. Reißaus, M. Krause, L. Berthold, T. Höche, D. Johrendt and H. Huppertz, $Sr[Li_2Al_2O_2N_2]:Eu^{2+}$—A high performance red phosphor to brighten the future, *Nat. Commun.* **2019**, *10*, 1824.

[5] P. Pust, V. Weiler, C. Hecht, A. Tücks, A. S. Wochnik, A.-K. Henß, D. Wiechert, C. Scheu, P. J. Schmidt, W. Schnick, Narrow-band red-emitting $Sr[LiAl_3N_4]:Eu^{2+}$ as a next-generation LED-phosphor material, *Nat. Mater.* **2014**, *13*, 891–896.

[6] E. Salmani, A. Marjaoui, O. Mounkachi, M. Ben Ali, H. El Moussaoui, H. Ez-Zahraouy, M. Hamedoun, M. Benaissa, A. Benyoussef, Band gap engineering of (InGaN) for photovoltaic application, *2014 International Renewable and Sustainable Energy Conference (IRSEC)* **2014.**

[7] K. Uheda, N. Hirosaki, H. Yamamoto, Host lattice materials in the system Ca_3N_2–AlN–Si_3N_4 for white light emitting diode, *Phys. Status Solidi A* **2006**, *203*, 2712–2717.

[8] K. Uheda, N. Hirosaki, Y. Yamamoto, A. Naito, T. Nakajima, H. Yamamoto, Luminescence Properties of a Red Phosphor, $CaAlSiN_3:Eu^{2+}$, for White Light-Emitting Diodes, *Electrochem. Solid-State Lett.* **2006**, *9*, H22–H25.

[9] Y. Q. Li, N. Hirosaki, R.-J. Xie, T. Takeda, M. Mitomo, Yellow-Orange-Emitting $CaAlSiN_3:Ce^{3+}$ Phosphor: Structure, Photoluminescence, and Application in White LEDs, *Chem. Mater.* **2008**, *20*, 6704–6714.

[10] H. Watanabe, N. Kijima, Crystal structure and luminescence properties of $Sr_xCa_{1-x}AlSiN_3:Eu^{2+}$ mixed nitride phosphors, *J. Alloys Compd.* **2009**, *475*, 434–439.

[11] Z. Zhang, O. M. ten Kate, A. C. A. Delsing, M. J. H. Stevens, J. Zhao, P. H. L. Notten, P. Dorenbos, H. T. Hintzen, Photoluminescence properties of Yb^{2+} in $CaAlSiN_3$ as a novel red-emitting phosphor for white LEDs, *J. Mater. Chem.* **2012**, *22*, 23871–23876.

[12] J. Häusler, L. Neudert, M. Mallmann, R. Niklaus, A.-C. L. Kimmel, N. S. A. Alt, E. Schlücker, O. Oeckler, W. Schnick, Ammonothermal Synthesis of Novel Nitrides: Case Study on $CaGaSiN_3$, *Chem. Eur. J.* **2017**, *23*, 2583–2590.

[13] T. D. Veal, N. Feldberg, N. F. Quackenbush, W. M. Linhart, D. O. Scanlon, L. F. J. Piper, S. M. Durbin, Band Gap Dependence on Cation Disorder in $ZnSnN_2$ Solar Absorber, *Adv. Energy Mater.* **2015**, *5*, 1501462.

[14] S. D. Kloß, W. Schnick, Nitridophosphates: A Success Story of Nitride Synthesis, *Angew. Chem. Int. Ed.* **2019**, *58*, 7933–7944; *Angew. Chem.* **2019**, *131*, 8015–8027

[15] Y. Huang, C. Yu, W. Chen, Y. Liu, C. Li, C. Niu, F. Wang,Y. Jia, Band gap and band alignment prediction of nitride-based semiconductors using machine learning *J. Mater. Chem. C* **2019**, *7*, 3238–3245.

[16] J. Greeley, T. F. Jaramillo, J. Bonde, I. Chorkendorff, J. K. Nørskov, Computational high-throughput screening of electrocatalytic materials for hydrogen evolution, *Nat. Mater.* **2006**, *5*, 909–913.

[17] Y. Zhuo, A. Mansouri Tehrani, A. O. Oliynyk, A. C. Duke, J. Brgoch, Identifying an efficient, thermally robust inorganic phosphor host via machine learning, *Nat. Commun.* **2018**, *9*, 4377.

[18] Y. Hinuma, T. Hatakeyama, Y. Kumagai, L. A. Burton, H. Sato, Y. Muraba, S. Iimura, H. Hiramatsu, I. Tanaka, H. Hosono, F. Oba, Discovery of earth-abundant nitride semiconductors by computational screening and high-pressure synthesis, *Nat. Commun.* **2016**, *7*, 11962.Summary

13 Summary

1. Orange-Emitting $Li_4Sr_4[Si_4O_4N_6]O:Eu^{2+}$—a Layered Lithium Oxonitridosilicate Oxide

Robin Niklaus, Lukas Neudert, Juliane Stahl, Peter J. Schmidt and Wolfgang Schnick

Inorg. Chem. **2018**, *57*, 14304–14313.

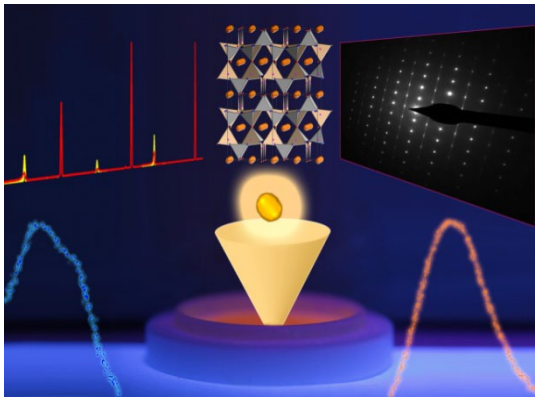

Single crystals of orange-emitting layered lithium oxonitridosilicate oxide $Li_4Sr_4[Si_4O_4N_6]O:Eu^{2+}$ were obtained as a minority phase from explorative solid-state multicomponent metathesis, carried out in Ta ampules at 950 °C. Single-crystal X-diffraction allowed for the solution and refinement of the crystal structure in space group $P4_2/nmc$ (no. 137) [Z = 2, a = 7.4833(6), c = 9.8365(9) Å, and $R1$(obs) = 0.0477]. The crystal structure consists of a layered 2D network of SiN_3O tetrahedra. The structure formally derives from non-luminescent $Li_2Sr_4[Si_2N_5]N$ by means of O substitution and incorporation. $Li_4Sr_4[Si_4O_4N_6]O:Eu^{2+}$ is prone to stacking disorder, which was corroborated by transmission electron microscopy on the initial single crystals and microcrystalline powder samples. Bulk sample reproduction was carried out at temperatures of 750 °C in Nb ampules. Based on reflections observed from powder X-ray diffraction and Rietveld refinements, together with DIFFaX simulations the extent of the stacking faults could be estimated. Energy-dispersive X-ray spectroscopy together with lattice energy, charge distribution, and density functional theory (DFT) calculations confirmed the overall elemental composition and atom assignment. DFT calculations carried out for a model free from stacking faults, yield a band gap of 4.4 eV, while experimental optical measurements on powder samples suggest an indirect gap of 3.6 eV. $Li_4Sr_4[Si_4O_4N_6]O:Eu^{2+}$ exhibits luminescence in the orange spectral range (λ_{em} ≈ 625 nm; full width at half-maximum ≈ 4164 cm^{-1}), with an internal quantum efficiency of 24% at room temperature. The study shows how synthesis can interlock with TEM investigations and DFT calculations to facilitate the understanding of materials properties relationships. As such, this study extends solid-state research toward the sparsely investigated materials class of lithium oxonitridosilicate oxides and highlights their principal suitability as phosphor materials.

2. First-principles and experimental characterization of the electronic properties of $CaGaSiN_3$ and $CaAlSiN_3$: the impact of chemical disorder

Robin Niklaus, Ján Minár, Jonas Häusler and Wolfgang Schnick

Phys. Chem. Chem. Phys. **2017**, *19*, 9292–9299.

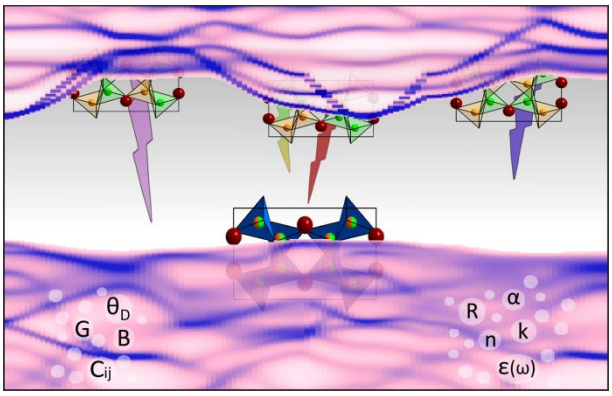

The effects of the chemical disorder with regard to the electronic structure for the mixed-occupancy phosphor host material $CaAlSiN_3$ and recently discovered isotypic $CaGaSiN_3$, have been investigated on a first principles level from density functional theory. Both materials were used as a case study to show the success of the KKR Green's function method together with the coherent potential approximation (CPA) to accurately describe the statistical disorder within nitride materials. By calculating the band structures and optical properties for three respective ordering models (each for $CaAlSiN_3$ and $CaGaSiN_3$) within the pseudopotential-based method VASP, and comparing them to the respective calculated Bloch spectral functions from the SPRKKR package the general equivalency of both programs, respectively methods was shown. Subsequent calculations on the fully disordered structures revealed a shrinking of the electronic band gap by about 0.1 eV for the introduction of complete disorder in both materials. The study shows that atomic disorder in nitrides with wide band gaps are accurately calculated by KKR without having to resort to extensive supercell calculations. The obtained results provide insights to a better understanding of chemical disorder effects, and possible materials design aspects with regard to influence the electronic band gap. Most importantly, this case study opens the scope to calculations on related solid-solution (nitride) materials. Especially for rare earth activated phosphor materials, usually doped with but a few atom percent of rare earth activator ions, KKR+CPA could prove to be a useful and cost-efficient approach to investigate the electronic structure.

3. Ammonothermal Synthesis and Optical Properties of Ternary Nitride Semiconductors Mg-IV-N_2, Mn-IV-N_2 and Li-IV_2-N_3 (IV = Si, Ge)

Jonas Häusler, Robin Niklaus, Ján Minár and Wolfgang Schnick

Chem. Eur. J. **2018**, *24*, 1686–1693.

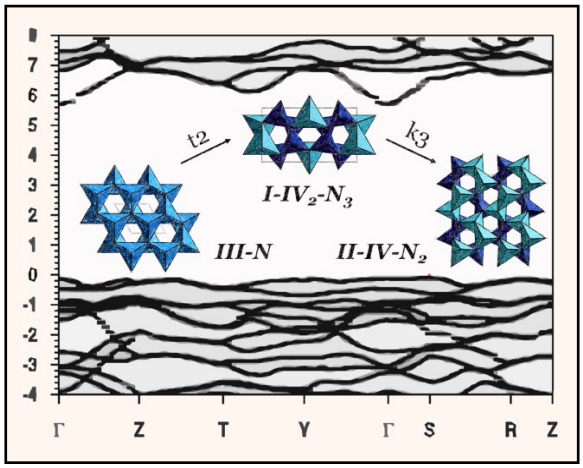

In this contribution, a new ammonothermal approach, using custom-built high-pressure autoclaves enabled the synthesis of Grimm-Sommerfeld analogous ternary nitride semiconductors. The nitride semiconductors $MgSiN_2$, $MgGeN_2$, $MnSiN_2$, $MnGeN_2$, $LiSi_2N_3$ and $LiGe_2N_3$ were successfully synthesized from the approach. The similarity to industrially used group 13 nitrides such as (Al,Ga,In,)N and their solid solutions, makes the synthesized materials class interesting with regard to their electronic and optical properties.

Together with the experimental characterization of the presented compounds, DFT calculations were employed using the SPR-KKR program. The calculations provide insights to the dispersion of the electronic band structure, their electronic transition types along with an estimate to the optical band gaps from the joint density of states with respect to corroborating the experimentally conducted UV/Vis measurements. The results demonstrate a wide range of attainable band gaps for the investigated nitrides and inspire considerations towards potential band gap engineering of Grimm-Sommerfeld analogue nitride semiconductors.

4. Solid Solutions of Grimm-Sommerfeld Analogous Nitride Semiconductors II-IV-N_2 with II = Mg, Mn, Zn; IV = Si, Ge – Ammonothermal Synthesis and DFT Calculations

Mathias Mallmann, Robin Niklaus, Tobias Rackl, Maximilian Benz, Thanh G. Chau, Dirk Johrendt, Ján Minár and Wolfgang Schnick

Chem. Eur. J. **2019**, *10.1002/chem.201903897.*

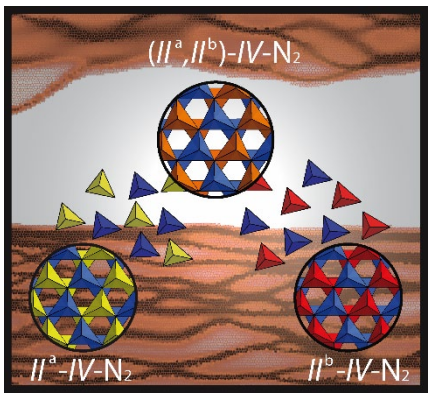

The solid solutions $Mg_{1-x}Mn_xSiN_2$, $Mg_{1-x}Zn_xSiN_2$, $Mn_{1-x}Zn_xSiN_2$, $Mg_{1-x}Mn_xGeN_2$, $Mg_{1-x}Zn_xGeN_2$ and $Mn_{1-x}Zn_xGeN_2$ ($x \approx 0.5$) were successfully obtained from ammonothermal synthesis in supercritical ammonia (T_{crit} = 405.5 K, p_{crit} = 11.3 MPa). All solid solutions crystallize in a wurtzite-type superstructure (*Pna*2_1). The optical band gaps of the compounds were determined from UV/Vis spectroscopy ranging from 2.6–3.5 eV for the different nitridogermanate solid solutions and 3.6–4.4 eV for the respective nitridosilicate solid solutions. Furthermore, magnetic measurements were conducted for the Mn-containing compounds, indicating anti-ferromagnetic behavior.

DFT calculations were employed to calculate the overall trends in electronic and optical and magnetic properties between the solid solutions and with respect to their respective boundary phases. The mixed occupancy was accounted for by the Korringa-Kohn-Rostoker Green's function method used with the coherent potential approximation. Types of electronic transitions (direct or indirect) were analyzed for the disordered solid solutions and their boundary phases from respective Bloch spectral functions. In contrast to the boundary phases no clear preference between direct and indirect electronic transitions was found for the fully disordered mixed occupancy solid solutions. The optical band gaps were further, estimated from plotting the joint density of states, showing good agreement with the experimental UV-VIS measurements. Calculations with the modified Becke Johnson potential on ordered structure models were further, used to account for the underestimation of the electronic band gap (E_g). This work shows the principal tunability of E_g in the II-IV-N_2 system, paving the way for possible future band gap engineering purposes. The Ammonothermal synthesis of the II-IV-N_2 materials and their solid solutions proves promising for potential growth of crystals and further experimental in-depth characterizations of materials properties.

5. A High-Pressure Polymorph of Phosphorus Oxonitride with the Coesite Structure

Dominik Baumann, Robin Niklaus and Wolfgang Schnick

Angew. Chem. Int. Ed. **2015**, *54*, 4388–4391; *Angew. Chem.* **2015**, *127*, 4463–4466.

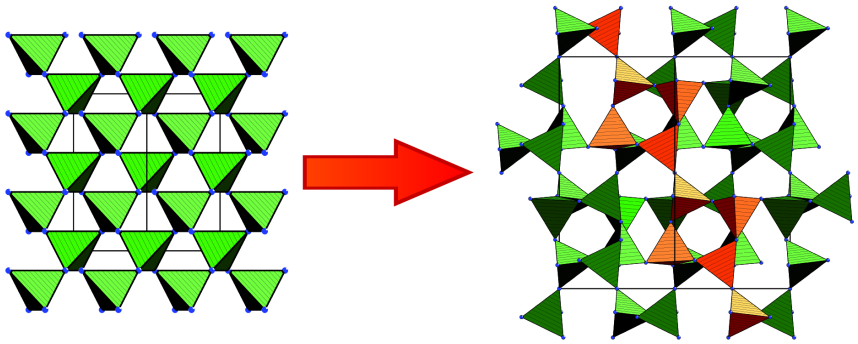

A new high-pressure polymorph to cristobalite-type PON (*ctb*-PON) was prepared in a Walker-type multianvil device. Synthesis was achieved by heating of *ctb*-PON to 1300 °C at a pressure of 15.5 GPa. The resulting polymorph crystallizes in space croup *C*2/*c* (*a* = 6.95903(8), *b* = 12.0610(2), *c* = 6.96821(8) Å, *β* = 120.0348(7)°, V = 506.33(2) Å^3, Z = 16), isotypic to coesite-type SiO_2. Phase pure coesite-type PON (*coe*-PON) could be obtained beyond 15 GPa and was characterized experimentally by (temperature dependant) powder X-ray diffraction, FTIR and MAS NMR spectroscopy.

In order to confirm the statistical occupation of O and N (O:N = 50:50) in coesite-type PON from X-ray powder diffraction, along with affirming the high pressure phase transition, DFT calculations were conducted. Using a multitude of different ordering models for both cristobalite-type PON (for which mixed occupancy is known from neutron diffraction), and coesite-type PON, the phase transition was approximated to occur between 7.5 and 10.5 GPa. The enthalpy for the different models was subsequently shown to be about equally favorable around 15 GPa. This corroborates the attributed statistical occupation observed from X-ray diffraction. Overall, the results represent a leap forward with regard to the exploration of the phase diagram of PON at high pressures.

6. Stishovite's Relative: A Post-Coesite Form of Phosphorus Oxonitride

Sebastian Vogel, Dominik Baumann, Robin Niklaus, Elena Bykova, Maxim Bykov, Natalia Dubrovinskaia, Leonid Dubrovinsky and Wolfgang Schnick

Angew. Chem. Int. Ed. **2018**, *57*, 6691–6695; *Angew. Chem.* **2018**, *130*, 6801–6805.

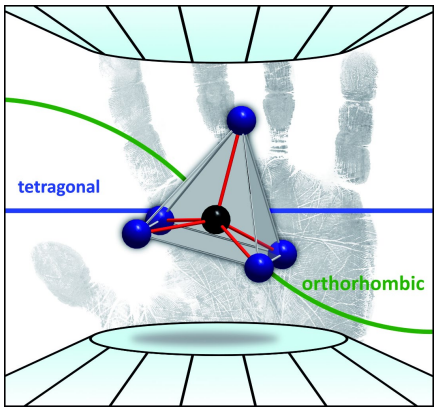

Starting from cristobalite-type PON, a high-pressure polymorph with P in (5+1) coordination and a stishovite-related structure was synthesized at 20 GPa and subsequently, heated to 1500 K by using the multianvil technique. Post coesite (pc-PON) was characterized by powder X-ray diffraction, solid-state NMR spectroscopy, TEM measurements and in situ synchrotron X-ray diffraction in diamond anvil cells ($P4_2/mnm$ (no. 136), a = 4.6184(2), c = 2.45536(9) Å, Z = 2, R_{Bragg} = 0.021). Single crystal X-ray diffraction at 1.8 GPa verified the structure model. Further, from compression in diamond anvil cells beyond 20 GPa, an additional second order phase transition ($P4_2/mnm$ (no. 136) → $Pnnm$ (no. 58)) to an orthorhombic PON phase was observed.

DFT calculations were utilized to calculate a number of supercells of possible pc-PON arrangements with regard to the O/N mixed occupancy arrangement and the split position of P, the latter of which was indicated from single-crystal data and from TEM measurements. Structural relaxations were only stable for alternating O/N arrangements, where the P atom could be seen to move into a coordination, favoring the axial N over O coordination, as expressed by the Niggly formula $^{3}_{\infty}[P^{[5]}O^{[2]}N^{[3]}]$. Using this structural model pc-PON could be confirmed as a high-pressure polymorph to coesite-type PON (coe-PON) from energy volume (EV) calculations. The phase transition to orthorhombic-type PON (o-PON) was obtained by slight lattice parameter distortions and subsequent EV relaxations at constant volume, leading to a transition pressure of about 17 GPa. The results further confirm the experimentally observed high-phase transition of pc-PON to o-PON above pressures of 20 GPa. The overall study of the high pressure behavior of PON proves promising to the discovery of six-fold coordinated stishovite-type PON .

7. $Li_{12}P_3N_9$ with Non-Condensed $[P_3N_9]^{12-}$ Rings and its High-Pressure Polymorph Li_4PN_3 with Infinite Chains of PN_4-Tetrahedra

Eva-Maria Bertschler, Robin Niklaus and Wolfgang Schnick

Chem. Eur. J. **2017**, *23*, 9592-9599.

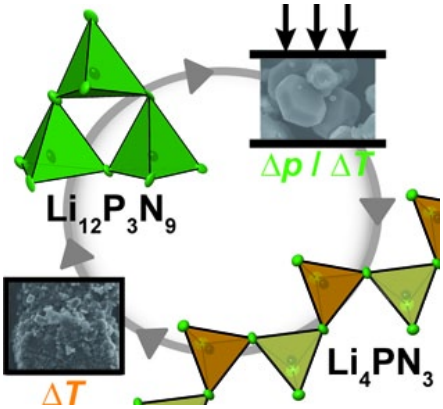

The Lithium nitridophosphate $Li_{12}P_3N_9$ (*Cc* (no. 9), *a* = 12.094(5), *b* = 7.649(3), *c* = 9.711(4) Å, *β* = 90.53(2)°, V = 898.3(6) Å^3, Z = 4) was synthesized from a Li_3N flux and P_3N_5 at 790 °C. The P-N structure consists of *dreier* rings of PN_4 tetrahedra $[P_3N_9]^{12-}$ in analogy to cyclo trisilicate $[Si_3O_9]^{6-}$. At 6 GPa and 820 °C phase transition was induced for $Li_{12}P_3N_9$ into its high-pressure polymorph, the first *catena*-nitridophosphate Li_4PN_3 (*Pccn* (no. 56), *a* = 9.6597(4), *b* = 11.8392(6), *c* = 4.8674(2) Å, V = 556.65(4) Å^3, Z= 8). Li_4PN_3 was separately synthesized from from $LiPN_2$and Li_7PN_4 at 9 GPa and 1200 °C using a Li_3N self-flux. Li_4PN_3 is made up of infinite PN_3 *zweier* chains of corner sharing PN_4 tetrahedra $^3_\infty[PN_2N_{2/2}]^{4-}$. The crystal structures of both polymorphs were solved and refined from single-crystal X-ray diffraction data. Further, the structures were confirmed by Rietveld refinement, FTIR spectroscopy and ^{6}Li, ^{7}Li, and ^{31}P solid-state MAS NMR.

In order to analyze transition pressure between both polymorphs, their electronic properties and bonding behavior, additional DFT calculations were performed. Due to the delocalized (underoccupied) Li positions a charge neutral ordered structure was modeled and relaxed for Li_4PN_3. The respective bulk moduli were obtained from fitting the respective energy volume curves. Subsequent construction of a enthalpy-pressure diagram revealed a transition pressure of about 6.5 GPa for the transition of $Li_{12}P_3N_9$ to Li_4PN_3, corroborating the latter as the high pressure polymorph being in line with the synthesis conditions of about 6 GPa. Both materials are insulators with band gaps of 5 eV ($Li_{12}P_3N_9$) and 6.1 eV (Li_4PN_3).

Overall the structural diversity of lithium nitridophosphates is expanded, giving insight to a novel approach to high-pressure/high-temperature polymerization of this materials class, along with insights to their electronic and materials properties.

8. Reversible Polymerization of Adamantane-type $[P_4N_{10}]^{10-}$ Anions to Honeycomb-type $[P_2N_5]^{5-}$ Layers under High-Pressure

Eva-Maria Bertschler, Robin Niklaus and Wolfgang Schnick

Chem. Eur. J. **2018**, *24*, 736–742.

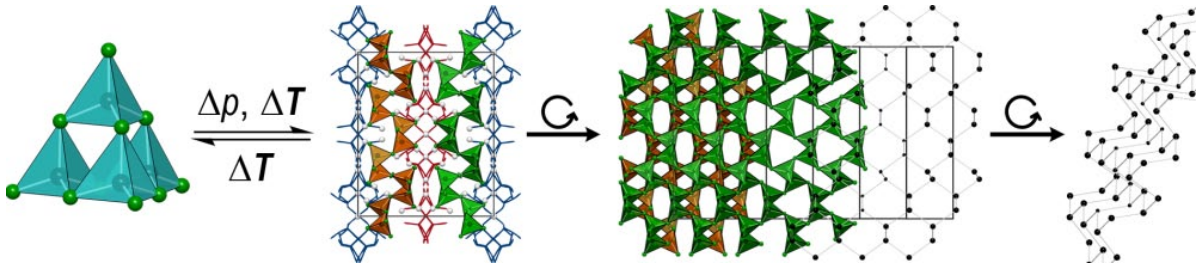

A third polymorph of $Li_{10}P_4N_{10}$ with the formula $Li_5P_2N_5$ was synthesized by high-temperature high-pressure reaction of $LiPN_2$ and Li_7PN_4 and separately directly from β-$Li_{10}P_4N_{10}$ at 9 GPa and 1000 °C, in a Walker-type multianvil assembly. Using the Li_3N self-flux method, suitable single-crystals of $Li_5P_2N_5$ were obtained. $Li_5P_2N_5$ is the first layered lithium nitridophosphate and crystallizes in *C*2/*c* (no. 15), with *a* = 14.770(3), *b* = 17.850(4), *c* = 4.860(1) Å, *β* = 93.11(3)°, V = 1279.4(5) Å3, Z = 12). Rietveld refinements, FTIR spectroscopy and ^{6}Li, ^{7}Li and ^{31}P solid-state MAS NMR were conducted to confirm the crystal structure, while EDX measurements were conducted to confirm the elemental composition. Vertex sharing PN_4 tetrahedra condensed to a corrugated layer of *sechser*-rings form the P/N substructure. The arrangement of the P atoms is analogous to the arrangement in black phosphorus. High-temperature powder diffraction indicates $Li_5P_2N_5$ as a high-pressure polymorph to β-$Li_{10}P_4N_{10}$.

The latter was further confirmed by density functional theory (DFT) calculations employing a model of β-$Li_{10}P_4N_{10}$ with fully occupied Li positions. The transition pressure could thus be estimated to 6.5 GPa. Additional electronic structure calculations revealed an increase in the band gap from 3.5 eV (β-$Li_{10}P_4N_{10}$) to 6.4 eV ($Li_5P_2N_5$) upon phase transition.

This contribution shows high-temperature/high-pressure polymerization as a suitable technique to access novel lithium nitridophosphates with high structural diversity. DFT proves to be a helpful asset in the corroboration of high-pressure transitions and in investigating the trends in the electronic structure behavior.

9. *Ab initio* exploration and prediction of AE-containing nitrido(litho/magneso)tetrelates (AE = Ca, Sr; Tt = Si, Ge) with $[Si_2N_6]^{10-}$ or $[Ge_2N_6]^{10-}$ units

Robin Niklaus, Ján Minár, Philipp Strobel, Peter J. Schmidt and Wolfgang Schnick

DaltonTrans. **2019**, *48*, 8671–8677.

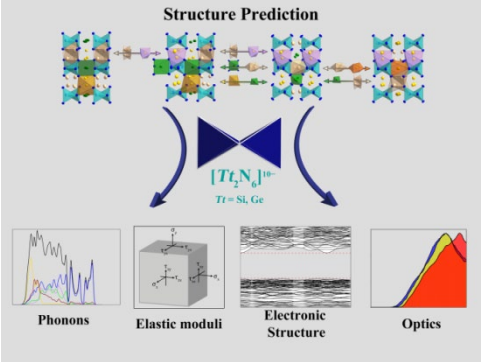

Recently a large number of structurally related lithomagneso- and magnesolithosilicates have emerged as suitable phosphor materials, showing promising luminescence properties upon doping. Together with $Ca_5Si_2N_6$ and $Ca_3Li_4Si_2N_6$ the three structures considered for this work $Ca_3Mg[Li_2Si_2N_6]$, $Ca_2Mg[Li_4Si_2N_6]$ and $Ca_2Li_2[Mg_2Si_2N_6]$ are structurally closely related to each other. Under consideration that the nitridogermanates $Sr_5Ge_2N_6$ and $Sr_3Li_4Ge_2N_6$ have already been synthesized, we employ a chemical intuitive computational approach, utilizing density functional theory (DFT) to systematically investigate the electronic and mechanical properties of the respective nitridosilicates compared to their isotypic, hypothetical compound series $AE_3Mg[Li_2Ge_2N_6]$, $AE_2Mg[Li_4Ge_2N_6]$ and $AE_2Li_2[Mg_2Ge_2N_6]$ (*AE* = Ca, Sr).

In order to analyze the dynamical stabilities of the nitridosilicate and nitridogermanate compound series in space group *C*2/*m* extensive phonon calculations were conducted, revealing stability for all nitridosilicates in accordance to their existence from experimental synthesis. Throughout the phonon calculations it could further be shown that the four nitridogermanates $Ca_3Mg[Li_2Ge_2N_6]$, $Sr_3Mg[Li_2Ge_2N_6]$, $Sr_2Mg[Li_4Ge_2N_6]$ and $Sr_2Li_2[Mg_2Ge_2N_6]$ are dynamically stable and may be promising to access from synthesis. Disregarding the presence of potential competing reactions, we further investigated the thermodynamic stability of the nitridogermanantes, with respect to their synthesis from binary compounds, in analogy to the existent nitridosilicate series. All compounds should potentially be accessible from synthesis. The electronic band gaps and Debye temperatures were further calculated for all compounds showcasing their general suitability for optoelectronic or phosphor materials applications. In conclusion four novel nitridogermanate materials are predicted by DFT. It is thus, shown that formal incorporation of Li and Mg into existing $Sr_5Ge_2N_6$ and $Sr_3[Li_4Ge_2N_6]$ might prove promising towards the experimental discovery of novel nitridogermanates with possible applications as wide gap semiconductors or phosphor materials.

14 List of Publications Within this Thesis

In the following a list of the publications included in this dissertation is presented including a list of authors and their corresponding contributions.

1. Orange-Emitting $Li_4Sr_4[Si_4O_4N_6]O:Eu^{2+}$—a Layered Lithium Oxonitridosilicate Oxide

Robin Niklaus, Lukas Neudert, Juliane Stahl, Peter J. Schmidt and Wolfgang Schnick

published in: *Inorg. Chem.* **2018**, *57*, 14304–14313.

Within this manuscript synthesis, single-crystal solution and refinement as well as UV/Vis spectroscopy was conducted by Robin Niklaus. Lukas Neudert carried out the respective TEM investigations along with corresponding interpretations thereof. Juliane Stahl contributed to this study throughout the construction of stacking variants, DIFFaX simulations and their interpretation. Peter J. Schmidt helped in the interpretation of the luminescence spectra, which were carried out in the LPC Aachen by Volker Weiler and Detlef Wiechert. The overall evaluation of the data was carried out by Robin Niklaus, along with subsidiary DFT calculations on the electronic structure. Literature research, creating graphical material and writing of the manuscript was performed by Robin Niklaus. Wolfgang Schnick supervised and directed the work. All authors revised the manuscript.

2. First-principles and experimental characterization of the electronic properties of $CaGaSiN_3$ and $CaAlSiN_3$: the impact of chemical disorder

Robin Niklaus, Ján Minár, Jonas Häusler and Wolfgang Schnick

published in: *Phys. Chem. Chem. Phys.* **2017**, *19*, 9292–9299.

Construction of the ordered and disordered structure models was carried out by Robin Niklaus along with the entirety of the DFT calculations. Ján Minár contributed to the interpretation of the obtained results from the KKR+CPA formalism and oversaw the respective calculations. Jonas Häusler synthesized the samples of $CaGaSiN_3$ and Robin Niklaus conducted the UV/Vis measurements and data evaluation. Literature research, creation of graphical materials and writing the manuscript was done by Robin Niklaus. Wolfgang Schnick directed and supervised the project. All authors revised the manuscript.

3. Ammonothermal Synthesis and Optical Properties of Ternary Nitride Semiconductors Mg-IV-N_2, Mn-IV-N_2 and Li-IV_2-N_3 (IV = Si, Ge)

Jonas Häusler, Robin Niklaus, Ján Minár and Wolfgang Schnick

published in: *Chem. Eur. J.* **2018**, *24*, 1686–1693.

Synthesis of the samples, powder X-ray diffraction analyses along with spectroscopic UV/Vis measurements in order to determine the optical band gap were carried out by Jonas Häusler. Robin Niklaus conducted DFT calculations on the electronic band structure of the materials. Analyses of the electronic transition types, fundamental band gaps and spin-polarization obtained by DFT were provided by Robin Niklaus under supervision of Ján Minár. Graphical material was created by Jonas Häusler and Robin Niklaus. The main part of the manuscript was written by Jonas Häusler, and the section on the DFT calculations with their interpretation was written by Robin Niklaus. Wolfgang Schnick supervised and directed the work. All authors revised the manuscript.

4. Solid Solutions of Grimm-Sommerfeld Analogous Nitride Semiconductors II-IV-N_2 with II = Mg, Mn, Zn; IV = Si, Ge – Ammonothermal Synthesis and DFT Calculations

Mathias Mallmann, Robin Niklaus, Tobias Rackl, Maximilian Benz, Thanh G. Chau, Dirk Johrendt, Ján Minár and Wolfgang Schnick

published in: *Chem. Eur. J.* **2019**, *10.1002/chem.201903897.*

Mathias Mallmann carried out and supervised the literature research and experimental synthesis. Maximilian Benz and Thanh G. Chau helped in conducting the ammonothermal syntheses under supervision of Mathias Mallmann. Based on the experimentally obtained structures from Mathias Mallmann, Robin Niklaus conducted the construction of the respective ordered and disordered models along with the entirety of the DFT calculations. Ján Minár helped with the interpretation of the results from the DFT calculations. Mathias Mallmann carried out the central conceptualization of the project, the interpretation of experimental data and wrote large sections of the manuscript. Robin Niklaus wrote the corresponding sections on the computational calculations. Tobias Rackl carried out additional magnetic measurements of the solid solution series under supervision of Dirk Johrendt. Final conclusions were drawn and written by Mathias Mallmann and Robin Niklaus. Graphical material was created by Mathias Mallmann and Robin Niklaus. Wolfgang Schnick directed and supervised the project. All authors revised the manuscript.

5. A High-Pressure Polymorph of Phosphorus Oxonitride with the Coesite Structure

Dominik Baumann, Robin Niklaus and Wolfgang Schnick

published in: *Angew. Chem. Int. Ed.* **2015**, *54*, 4388–4391.

published in: *Angew. Chem.* **2015**, *127*, 4463–4466.

The main part of the manuscript was written by Dominik Baumann along with the creation of graphical material and literature research. Dominik Baumann further conducted the synthesis, structure elucidation, topological analysis and the evaluation of spectroscopic data for PON. Robin Niklaus created the O/N ordered structure models for cristobalite- and coesite-type PON, performed subsequent DFT calculations and created the energy-volume and enthalphy-pressure diagram. A minor part of the main manuscript, and larger parts of the supplementary information regarding the DFT calculations were written by Robin Niklaus. Wolfgang Schnick directed and supervised the work. All authors revised the manuscript.

6. Stishovite's Relative: A Post-Coesite Form of Phosphorus Oxonitride

Sebastian Vogel, Dominik Baumann, Robin Niklaus, Elena Bykova, Maxim Bykov, Natalia Dubrovinskaia, Leonid Dubrovinsky and Wolfgang Schnick

published in: *Angew. Chem. Int. Ed.* **2018**, *57*, 6691–6695.

published in: *Angew. Chem.* **2018**, *130*, 6801–6805.

Initial synthesis, structure solution and refinement of post-coesite PON were carried out by Dominik Baumann and Sebastian Vogel. Natalia Dubrovinskaia and Leonid Dubrovinsky supplied the diamond anvil cells used for synchrotron measurements and contributed to the interpretation of observed phase transitions. Elena Bykova and Maxim Bykov oversaw the beam-time and provided the single-crystal measurements, structure solution and single-crystal refinement. Sebastian Vogel carried out the structure refinement from powder X-ray diffraction. Robin Niklaus carried out the construction and DFT calculations of O/N-ordered PON models, construction of energy-volume plots and the enthalpy-pressure diagram. Interpretation of the DFT results was done by Robin Niklaus. Sebastian Vogel, performed the literature research, created the majority of graphical material, conceptualized and wrote the main part of the manuscript. Robin Niklaus contributed in writing a section of the manuscript regarding the DFT calculations. The whole project was supervised and directed by Wolfgang Schnick. All authors revised the manuscript.

7. $Li_{12}P_3N_9$ with Non-Condensed $[P_3N_9]^{12-}$ Rings and its High-Pressure Polymorph Li_4PN_3 with Infinite Chains of PN_4-Tetrahedra

Eva-Maria Bertschler, Robin Niklaus and Wolfgang Schnick

published in: *Chem. Eur. J.* **2017**, *23*, 9592-9599.

Syntheses of the samples, their structure elucidation and topological analysis was performed by Eva-Maria Bertschler. Christian Minke carried out EDX/REM spectroscopy, Marion Sokoll the FTIR spectroscopy and Peter Mayer the single-crystal X-ray diffraction. The data thereof was evaluated by Eva-Maria Bertschler. Robin Niklaus carried out the construction of fully occupied charge neutral structure models, performed DFT calculations on the electronic structure and high-pressure phase transition along with evaluations thereof. Literature research, most graphical material construction and writing the main parts of the manuscript was carried out by Eva-Maria Bertschler. Robin Niklaus wrote a section on the DFT calculations. Wolfgang Schnick directed and supervised the work. All authors revised the manuscript.

8. Reversible Polymerization of Adamantane-type $[P_4N_{10}]^{10-}$ Anions to Honeycomb-type $[P_2N_5]^{5-}$ Layers under High-Pressure

Eva-Maria Bertschler, Robin Niklaus and Wolfgang Schnick

published in: *Chem. Eur. J.* **2018**, *24*, 736–742.

For this work, Eva-Maria Bertschler performed the syntheses of the samples, their structure elucidation, Rietveld refinement, topological analysis, and spectroscopic evaluation. The majority of spectroscopic data (solid-state MAS NMR, EDX/REM) were measured by Christian Minke, single-crystal X-ray diffraction was performed by Peter Mayer and FTIR spectroscopy by Marion Sokoll. DFT optimizations of fully occupied structure models and calculations of their electronic properties and phase transitions to one another were carried out by Robin Niklaus. Eva-Maria Bertschler performed the literature research, construction of a majority of the graphical material and the writing of the main manuscript. Robin Niklaus wrote a section on the DFT calculations and their evaluation. Wolfgang Schnick supervised and directed the project. All authors revised the manuscript.

9. *Ab initio* exploration and prediction of AE-containing nitrido(litho/magneso)tetrelates (AE = Ca, Sr; Tt = Si, Ge) with $[Si_2N_6]^{10-}$ or $[Ge_2N_6]^{10-}$ units

Robin Niklaus, Ján Minár, Philipp Strobel, Peter J. Schmidt and Wolfgang Schnick

published in: *Dalton Trans.* **2019**, *48*, 8671–8677.

Robin Niklaus performed the literature research, construction of graphical material, conceptualization and writing of the entirety of the manuscript. Philipp Strobel was involved in the early conceptualization of the work and provided insights regarding structural relations and interpretations. Ján Minár provided a portion of the computational resources and consultation in writing the manuscript. All of the presented DFT calculations on the electronic, mechanical and optical properties were performed by Robin Niklaus. Peter J. Schmidt contributed to data interpretation and evaluation of the materials properties. Wolfgang Schnick directed and supervised the manuscript. All authors revised the manuscript.

15 Publications Beyond this Thesis

1. **New Polymorphs of $RE_2FeSe_2O_2$ (*RE* = La, Ce)**
   F. Nitsche, R. Niklaus, D. Johrendt
   Z. Anorg. Allg. Chem. **2014**, *640*, 14, 2897–2902.

2. **High-pressure Synthesis of Melilite-Type Rare-Earth Nitridophosphates $RE_2P_3N_7$ and a $Ba_2Cu[Si_2O_7]$-type Polymorph**
   S. D. Kloß, N. Weidmann, R. Niklaus, W. Schnick
   Inorg. Chem. **2016**, *55*, 9400–9409.

3. **Ammonothermal Synthesis of Novel Nitrides: Case Study on $CaGaSiN_3$**
   J. Häusler, L. Neudert, M. Mallmann, R. Niklaus, A.-C. L. Kimmel, N. S .A. Alt, E. Schlücker, O. Oeckler, W. Schnick
   Chem. Eur. J. **2017**, *23*, 2583–2590.

4. **The Crystal Structure of Nitridomagnesogermanate $Ba[Mg_3GeN_4]:Eu^{2+}$ and Theoretical Calculations of Its Electronic Properties**
   C. Poesl, R. Niklaus, W. Schnick
   Eur. J. Inorg. Chem. **2017**, *18*, 2422–2427.

5. **Efficient Yellow–orange Phosphor $Lu_4Ba_2[Si_9ON_{16}]O:Eu^{2+}$ and Orange–red Emitting $Y_4Ba_2[Si_9ON_{16}]O:Eu^{2+}$: Two Oxonitridosilicate Oxides with Outstanding Structural Variety**
   C. Maak, R. Niklaus, F. Friedrich, A. Mähringer, P. J. Schmidt, W. Schnick
   Chem. Mater. **2017**, *29*, 8377–8384.

6. **Oxoberyllates $SrBeO_2$ and $Sr_{12}Be_{17}O_{29}$ as Novel Host Materials for Eu^{2+} Luminescence**
   P. Strobel, R. Niklaus, P. J. Schmidt, W. Schnick
   Chem. Eur. J. **2018**, *24*, 12678–12685.

7. **Ammonothermal Synthesis, Optical Properties, and DFT Calculations of Mg_2PN_3 and Zn_2PN_3**
   M. Mallmann, C. Maak, R. Niklaus, W. Schnick
   Chem. Eur. J. **2018**, *24*, 13963–13970.

8. **$Y_{23}Sr_{17}[Si_{38}O_{18}N_{67}]O_9$ – An Oxonitridosilicate Oxide with a Unique Layered Structure**
   C. Maak, R. Niklaus, O. Oeckler, W. Schnick
   Z. Anorg. Allg. Chem. **2019**, *645*, 182–187.

9. ***M*Be$_{20}$N$_{14}$:Eu^{2+} (*M* = Sr, Ba) –Highly Condensed Nitridoberyllates with Exceptional High Energetic Eu^{2+} Luminescence**
E. Elzer, R. Niklaus, P. J. Strobel, V. Weiler, P. J. Schmidt, W. Schnick
Chem. Mater. **2019**, *31*, 3174–3182.

10. **Syntheses and physical properties of the MAX phase boride Nb$_2$SB and the solid solutions Nb$_2$SB$_x$C$_{1-x}$ (x = 0–1)**
T. Rackl, L. Eisenburger, R. Niklaus, D. Johrendt,
Phys. Rev. Materials **2019**, *3*, 054001.

16 Conference Contributions

1. **Ab-initio Untersuchungen an nitridischen LED-phosphoren**
   Oral presentation, 41. Hirschegg-Seminar Festkörperchemie, 2015, Hirschegg (Austria)

2. **Photoemissionspektroskopie Methode und Anwendung**
   Oral presentation, 2. Obergurgl-Seminar für Festkörperchemie, 2016, Obergurgl (Austria)

3. **Quantenchemische Untersuchungen zur Auswirkung der Mischbesetzung in $CaGaSiN_3$ und $CaAlSiN_3$**
   Oral presentation, 44. Hirschegg-Seminar Festkörperchemie, 2018, Hirschegg (Austria)